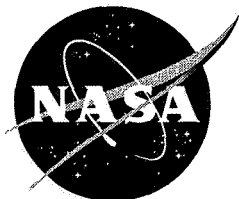


NASA/CP-2006-214290

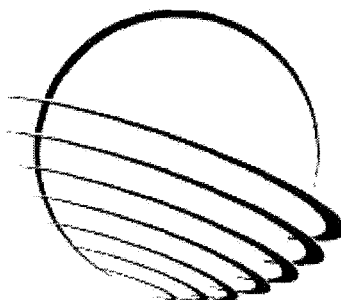


## 38<sup>th</sup> Aerospace Mechanisms Symposium

*Compiled by*

*Edward A. Boesiger*

*Lockheed Martin Space Systems Company, Sunnyvale, California*



Proceedings of a symposium hosted by  
the NASA Langley Research Center and  
Lockheed Martin Space Systems Company and  
organized by the Mechanisms Education Association  
held at the Williamsburg Marriott Hotel  
Williamsburg, Virginia  
May 17-19, 2006

---

May 2006

## The NASA STI Program Office . . . in Profile

Since its founding, NASA has been dedicated to the advancement of aeronautics and space science. The NASA Scientific and Technical Information (STI) Program Office plays a key part in helping NASA maintain this important role.

The NASA STI Program Office is operated by Langley Research Center, the lead center for NASA's scientific and technical information. The NASA STI Program Office provides access to the NASA STI Database, the largest collection of aeronautical and space science STI in the world. The Program Office is also NASA's institutional mechanism for disseminating the results of its research and development activities. These results are published by NASA in the NASA STI Report Series, which includes the following report types:

- **TECHNICAL PUBLICATION.** Reports of completed research or a major significant phase of research that present the results of NASA programs and include extensive data or theoretical analysis. Includes compilations of significant scientific and technical data and information deemed to be of continuing reference value. NASA counterpart of peer-reviewed formal professional papers, but having less stringent limitations on manuscript length and extent of graphic presentations.
- **TECHNICAL MEMORANDUM.** Scientific and technical findings that are preliminary or of specialized interest, e.g., quick release reports, working papers, and bibliographies that contain minimal annotation. Does not contain extensive analysis.
- **CONTRACTOR REPORT.** Scientific and technical findings by NASA-sponsored contractors and grantees.
- **CONFERENCE PUBLICATION.** Collected papers from scientific and technical conferences, symposia, seminars, or other meetings sponsored or co-sponsored by NASA.
- **SPECIAL PUBLICATION.** Scientific, technical, or historical information from NASA programs, projects, and missions, often concerned with subjects having substantial public interest.
- **TECHNICAL TRANSLATION.** English-language translations of foreign scientific and technical material pertinent to NASA's mission.

Specialized services that complement the STI Program Office's diverse offerings include creating custom thesauri, building customized databases, organizing and publishing research results ... even providing videos.

For more information about the NASA STI Program Office, see the following:

- Access the NASA STI Program Home Page at <http://www.sti.nasa.gov>
- E-mail your question via the Internet to [help@sti.nasa.gov](mailto:help@sti.nasa.gov)
- Fax your question to the NASA STI Help Desk at (301) 621-0134
- Phone the NASA STI Help Desk at (301) 621-0390
- Write to:  
NASA STI Help Desk  
NASA Center for AeroSpace Information  
7121 Standard Drive  
Hanover, MD 21076-1320



NASA/CP-2006-214290



# 38<sup>th</sup> Aerospace Mechanisms Symposium

*Compiled by  
Edward A. Boesiger  
Lockheed Martin Space Systems Company, Sunnyvale, California*

Proceedings of a symposium hosted by  
the NASA Langley Research Center and  
Lockheed Martin Space Systems Company and  
organized by the Mechanisms Education Association  
held at the Williamsburg Marriott Hotel  
Williamsburg, Virginia  
May 17-19, 2006

National Aeronautics and  
Space Administration

Langley Research Center  
Hampton, Virginia 23681-2199

---

May 2006

The use of trademarks or names of manufacturers in the report is for accurate reporting and does not constitute an official endorsement, either expressed or implied, of such products or manufacturers by the National Aeronautics and Space Administration.

Available from:

NASA Center for AeroSpace Information (CASI)  
7121 Standard Drive  
Hanover, MD 21076-1320  
(301) 621-0390

National Technical Information Service (NTIS)  
5285 Port Royal Road  
Springfield, VA 22161-2171  
(703) 605-6000

## **PREFACE**

The Aerospace Mechanisms Symposium (AMS) provides a unique forum for those active in the design, production and use of aerospace mechanisms. A major focus is the reporting of problems and solutions associated with the development and flight certification of new mechanisms. Organized by the Mechanisms Education Association, the National Aeronautics and Space Administration and Lockheed Martin Space Systems Company (LMSSC) share the responsibility for hosting the AMS. Now in its 38<sup>th</sup> symposium, the AMS continues to be well attended, attracting participants from both the U.S. and abroad.

The 38<sup>th</sup> AMS, hosted by the Langley Research Center (LaRC) in Williamsburg, Virginia, was held May 17, 18 and 19, 2006. During these three days, 34 papers were presented. Topics included gimbals, tribology, actuators, aircraft mechanisms, deployment mechanisms, release mechanisms, and test equipment. Hardware displays during the supplier exhibit gave attendees an opportunity to meet with developers of current and future mechanism components.

The high quality of this symposium is a result of the work of many people, and their efforts are gratefully acknowledged. This extends to the voluntary members of the symposium organizing committee representing the eight NASA field centers, LMSSC, and the European Space Agency. Appreciation is also extended to the session chairs, the authors, and particularly the personnel at LaRC responsible for the symposium arrangements and the publication of these proceedings. A sincere thank you also goes to the symposium executive committee who is responsible for the year-to-year management of the AMS, including paper processing and preparation of the program.

The use of trade names of manufacturers in this publication does not constitute an official endorsement of such products or manufacturers, either expressed or implied, by the National Aeronautics and Space Administration.



## CONTENTS

Symposium Schedule.....	viii
Symposium Organizing and Advisory Committees .....	xii
Precision Linear Actuators for the Spherical Primary Optical Telescope Demonstration Mirror.....	1
Jason Budinoff & David Pfenning	
The CRISM Motor/Encoder Assembly and Diaphragm Bearing Assembly Design .....	11
Jeffrey Lees & Ed Schaefer	
Gear Teeth Particles and Bearing Failures .....	25
William Greenwood & Jeffrey Dabling	
Failure of Harmonic Gears During Verification of a Two-Axis Gimbal for the Mars Reconnaissance Orbiter Spacecraft .....	37
Michael Johnson, Russ Gehling & Ray Head	
Stacer Driven Deployment: The Stereo Impact Boom .....	51
Robert Ullrich, Jeremy McCauley, Paul Turin, Ken McKee & Bill Donokowski	
Heritage Adoption Lessons Learned: Cover Deployment and Latch Mechanism.....	65
James Wincentzen	
Problems and Product Improvements in a Qualified, Flight Heritage Product.....	75
Chuck Lazansky & Scott Christiansen	
SoftRide Vibration and Shock Isolation Systems that Protect Spacecraft from Launch Dynamic Environments.....	89
Conor Johnson, Paul Wilke & Scott Pendleton	
Summary of the New AIAA Moving Mechanical Assemblies Standard.....	103
Brian Gore	
Lessons Learned From the Development, Operation, and Review of Mechanical Systems on the Space Shuttle, International Space Station, and Payloads .....	113
Alison Dinsel, Wayne Jermstad & Brandan Robertson	
Reliability and Fault Tolerance in ISS Thermofoil Spaceflight Heaters .....	127
Victor Bolton	
Development, Pre-qualification and Application of an Active Bearing Preload System .....	133
Simon Lewis & Martin Humphries	
Development of a Dual Mode D-Strut® Vibration Isolator for a Laser Communication Terminal.....	141
Dale Ruebsamen, James Boyd, Joe Vecera & Roger Nagel	
Design and Testing of a Low Shock Discrete Point Spacecraft Separation System.....	149
Pete Woll & Daryn Oxe	

Faying Surface Lubrication Effects on Nut Factors .....	157
Deneen Taylor & Raymond Morrison	
Torque Loss and Stress Relaxation in Constant Torque Springs .....	163
Robert Postma	
Mechanical Design of a Multi-Axis Martian Seismometer .....	169
Franck Pécal, Nicolas Paulin, Doug Mimoun & Gabriel Pont	
Commercial off-the-shelf Components in Reaction Wheels .....	187
Andrew Haslehurst	
Design of the ATMS Scan Drive Mechanism .....	197
Curtis Allmon & Dave Putnam	
Lessons Learned From the Windsat BAPTA Design and On-Orbit Anomalies .....	209
Steve Koss & Scott Woolaway	
JWST NIRSpec Cryogenic Light Shield Mechanism.....	223
Kathleen Hale & Rajeev Sharma	
Development Tests of a Cryogenic Filter Wheel Assembly for the NIRCам Instrument.....	229
Sean McCully, Charles Clark, Michael Schermerhorn, Filip Trojanek, Mark O'Hara, Jeff Williams & John Thatcher	
Cryogenic Nano-Actuator for JWST .....	239
Robert Warden	
Space Shuttle Body Flap Actuator Bearing Testing for NASA Return to Flight.....	253
Tim Jett, Roamer Predmore, Michael Dube & William Jones, Jr	
Bearing Development for a Rocket Engine Gimbal.....	269
Christian Neugebauer, Manfred Falkner, Ludwig Supper & Gerhard Traxler	
Effect of Test Environment on Lifetime of Two Vacuum Lubricants Determined by Spiral Orbit Tribometry .....	283
Stephen Pepper	
Influence of Oil Lubrication on Spacecraft Bearing Thermal Conductance .....	291
Yoshimi Takeuchi, Matthew Eby, Benjamin Blake, Steven Demsky & James Dickey	
Mars Exploration Rover Potentiometer Problems, Failures and Corrective Actions .....	303
Mark Balzer	
Mechanism Development, Testing, and Lessons Learned for the Advanced Resistive Exercise Device .....	317
Christopher Lamoreaux & Mark Landeck	
Radarsat Range Adjustment Mechanism Design .....	331
Xilin Zhang & Sylvain Riendeau	

Come-Along Tool Development for Telerobotic In-Space Servicing of the Hubble Space Telescope .....	345
Jonathan Penn	
Planetary Airplane Extraction System Development and Subscale Testing .....	359
John Teter Jr	
“Digital” SMA-Based Trailing Edge Tab Actuators for Aerospace Applications .....	373
Robert McKillip Jr	
Development of a Forced Oscillation System for Measuring Dynamic Derivatives of Fluidic Vehicles .....	387
Bo Trieu, T. Tyler , B. Stewart, J. Charnock, D. Fisher, E. H. Heim, J. Brandon & S. Grafton	

## SYMPOSIUM SCHEDULE

### WEDNESDAY, 17 MAY 2006

8:00 Wednesday Presenters' Breakfast – Terrace Room

8:00 **CHECK-IN AND REFRESHMENTS** – Auditorium

9:00 **INTRODUCTORY REMARKS** - Auditorium

James Wells, Host Chairman

NASA Langley Research Center, Hampton, VA

Stuart Loewenthal, General Chairman

Lockheed Martin Space Systems, Sunnyvale, CA

#### CENTER WELCOME

Stephen G. Jurczyk, Deputy Director

NASA Langley Research Center, Hampton, VA

9:30 **SESSION I – ACTUATORS**

Stephen Sandford, Session Chair

NASA Langley Research Center, Hampton, VA

- Precision Linear Actuators for the Spherical Primary Optical Telescope Demonstration Mirror  
Jason Budinoff & David Pfenning, NASA Goddard Space Flight Center, Greenbelt, MD
- The CRISM Motor/Encoder Assembly and Diaphragm Bearing Assembly Design  
Jeffrey Lees & Ed Schaefer, Johns Hopkins University Applied Physics Laboratory, Laurel, MD
- Gear Teeth Particles and Bearing Failures  
William Greenwood and Jeffrey Dabling, Sandia National Laboratories, Albuquerque, NM
- Failure of Harmonic Gears During Verification of a Two-Axis Gimbal for the Mars Reconnaissance Orbiter Spacecraft  
Michael Johnson, Jet Propulsion Laboratory, Pasadena, CA; Russ Gehling & Ray Head, Lockheed Martin Space Systems, Denver, CO

11:45 **LUNCH BREAK** – Box lunch is provided

1:00 **SESSION II – MECHANISMS**

Ted Hartka, Session Chair

Johns Hopkins University Applied Physics Laboratory, Laurel, MD

- Stacer Driven Deployment: The Stereo Impact Boom  
Robert Ullrich, Jeremy McCauley, Paul Turin, Ken McKee & Bill Donokowski, Space Sciences Lab, University of California, Berkeley, CA
- Heritage Adoption Lessons Learned: Cover Deployment and Latch Mechanism  
James Vincentsen, Jet Propulsion Laboratory, Pasadena, CA
- Problems and Product Improvements in a Qualified, Flight Heritage Product  
Chuck Lazansky & Scott Christiansen, Starsys Research Corp., Boulder, CO

2:30 **BREAK**



2:45 **SESSION III – “BIG PICTURE”**  
John McManamen, Session Chair  
NASA Johnson Space Center, Houston, TX

- SoftRide Vibration and Shock Isolation Systems that Protect Spacecraft from Launch Dynamic Environments  
Conor Johnson, Paul Wilke & Scott Pendleton, CSA Engineering, Inc., Mountain View, CA
- Summary of the New AIAA Moving Mechanical Assemblies Standard  
Brian Gore, The Aerospace Corporation, El Segundo, CA
- Lessons Learned From the Development, Operation, and Review of Mechanical Systems on the Space Shuttle, International Space Station, and Payloads  
Alison Dinsel, Wayne Jermstad & Brandan Robertson, NASA Johnson Space Center, Houston, TX

4:15 **SESSION IV – POSTER PREVIEW**  
Michael Johnson, Session Chair  
Jet Propulsion Laboratory, Pasadena, CA

- Reliability and Fault Tolerance in ISS Thermofoil Spaceflight Heaters  
Victor Bolton, The Boeing Company, Houston, TX
- Development, Pre-qualification and Application of an Active Bearing Preload System  
Simon Lewis, European Space Tribology Laboratory, Warrington, Cheshire, U.K.; Martin Humphries, Sula Systems Ltd., Wotton-under-Edge, Gloucestershire, U.K.
- Development of a Dual Mode D-Strut® Vibration Isolator for a Laser Communication Terminal  
Dale Ruebsamen, James Boyd, Joe Vecera & Roger Nagel, Honeywell Defense and Space, Glendale, AZ
- Design and Testing of a Low Shock Discrete Point Spacecraft Separation System  
Pete Woll, NEA Electronics, Chatsworth, CA; Daryn Oxe, Lockheed Martin Space Systems Company, Sunnyvale, CA
- Faying Surface Lubrication Effects on Nut Factors  
Deneen Taylor, NASA Johnson Space Center, Houston, TX; Raymond Morrison, The Boeing Company, Huntington Beach, CA
- Torque Loss and Stress Relaxation in Constant Torque Springs  
Robert Postma, The Aerospace Corporation, El Segundo, CA

6:30-9:30 **RECEPTION & DISPLAYS** - ADAMS BALLROOM/PROMENADE OF THE MARRIOTT  
Invited component and software suppliers display current products and provide tutorials.

#### **THURSDAY, 18 MAY 2006**

7:15 Thursday Presenters' Breakfast - Terrace Room

7:45 Light Refreshments - Auditorium

8:15 **SESSION V – GIMBALS** – Auditorium  
William Jones Jr., Session Chair  
Sest, Inc., Middleburg Heights, OH

- Mechanical Design of a Multi-Axis Martian Seismometer  
Franck Pécal & Nicolas Paulin, EADS SODERN, Limeil Brévannes, France; Doug Mimoun, IPGP, Saint Maur, France; Gabriel Pont, CNES, Toulouse, France
- Commercial off-the-shelf Components in Reaction Wheels  
Andrew Haslehurst, Surrey Satellite Technology Ltd, Guildford, Surrey, U.K.
- Design of the ATMS Scan Drive Mechanism  
Curtis Allmon & Dave Putnam, Lockheed Martin Space Systems Company, Sunnyvale, CA

- Lessons Learned From the Windsat BAPTA Design and On-Orbit Anomalies  
Steve Koss, Naval Research Laboratory, Washington, D.C.; Scott Woolaway, Ball Aerospace & Technologies Corp., Boulder, CO

10:15 **BREAK**

10:30 **SESSION VI – JWST**

Casey DeKramer, Session Chair  
Swales Aerospace, Beltsville, MD

- JWST NIRSpec Cryogenic Light Shield Mechanism  
Kathleen Hale & Rajeev Sharma, NASA Goddard Space Flight Center, Greenbelt, MD
- Development Tests of a Cryogenic Filter Wheel Assembly for the NIRCams Instrument  
Sean McCully, Charles Clark, Michael Schermerhorn, Filip Trojanek, Mark O'Hara, Jeff Williams & John Thatcher, Lockheed Martin Space Systems Company, Palo Alto, CA
- Cryogenic Nano-Actuator for JWST  
Robert Warden, Ball Aerospace & Technologies Corp., Boulder, CO

12:00 **LUNCH BREAK** – Box lunch is provided

1:00 **SESSION VII – BEARINGS & POTS**

Dino Christopoulos, Session Chair  
Raytheon Space & Airborne Systems, El Segundo, CA

- Space Shuttle Body Flap Actuator Bearing Testing for NASA Return to Flight  
Tim Jett, NASA Marshall Space Flight Center, Huntsville, AL; Roamer Predmore, Swales Aerospace, Beltsville, MD; Michael Dube, NASA Goddard Space Flight Center, Greenbelt, MD; William Jones, Jr, Sest, Inc., Middleburg Heights, OH
- Bearing Development for a Rocket Engine Gimbal  
Christian Neugebauer, Manfred Falkner, Ludwig Supper & Gerhard Traxler, Austrian Aerospace GmbH, Vienna, Austria
- Effect of Test Environment on Lifetime of Two Vacuum Lubricants Determined by Spiral Orbit Tribometry  
Stephen Pepper, NASA Glenn Research Center, Cleveland, OH
- Influence of Oil Lubrication on Spacecraft Bearing Thermal Conductance  
Yoshimi Takeuchi, Matthew Eby, Benjamin Blake, Steven Demsky & James Dickey, The Aerospace Corporation, El Segundo, CA
- Mars Exploration Rover Potentiometer Problems, Failures and Corrective Actions  
Mark Balzer, Jet Propulsion Laboratory, Pasadena, CA

3:30 **BREAK**

3:45 **SPECIAL PRESENTATION** – NASA Engineering & Safety Center, Mechanical Systems Super Problem Resolution Team

John McManamen

NASA Johnson Space Center, Houston, TX

The NESC is an organization established in the wake of Space Shuttle Columbia accident to provide an independent look at high risk, complex technical issues. Presentation will include problems the SPRT has been engaged in and focuses in more detail on an ongoing investigation regarding the Space Shuttle Solid Rocket Booster Holddown Post stud hang up problem and the completed assessment of the Orbiter Rudder Speedbrake gear micro-pitting problem.

5:30-10:30 **SYMPOSIUM BANQUET AT JAMESTOWN SETTLEMENT**

5:30 Bus leaves Marriott to Jamestown

10:00 Bus leaves Jamestown for hotel

**FRIDAY, 19 MAY 2006**

7:15 Friday Presenters' Breakfast – Terrace Room

7:45 Light Refreshments - Auditorium

8:15 **SESSION VIII – TOOLS & AIRCRAFT** - Auditorium

Gérard Migliorero, Session Chair

ESA/ESTeC, Noordwijk, The Netherlands

- Mechanism Development, Testing, and Lessons Learned for the Advanced Resistive Exercise Device

Christopher Lamoreaux & Mark Landeck, NASA Johnson Space Center, Houston, TX

- Radarsat Range Adjustment Mechanism Design

Xilin Zhang & Sylvain Riendeau, MDA Space, Inc., Ste-Anne-De-Bellevue, Canada

- Come-Along Tool Development for Telerobotic In-Space Servicing of the Hubble Space Telescope

Jonathan Penn, Swales Aerospace, Beltsville, MD

- Planetary Airplane Extraction System Development and Subscale Testing

John Teter Jr., NASA Langley Research Center, Hampton, VA

- "Digital" SMA-Based Trailing Edge Tab Actuators for Aerospace Applications

Robert McKillip Jr., Continuum Dynamics, Inc., Ewing, NJ

- Development of a Forced Oscillation System for Measuring Dynamic Derivatives of Fluidic Vehicles

Bo Trieu, T. Tyler, B. Stewart, J. Charnock, D. Fisher, E. H. Heim & J. Brandon, NASA Langley Research Center, Hampton, VA; S. Grafton, Vigyan, Inc., Hampton, VA

11:15 **PRESENTATION: An Overview of LaRC**

11:45 **TECHNICAL SESSIONS CONCLUSION**

- PRESENTATION OF THE HERZL AWARD

- CLOSING REMARKS

Edward Boesiger, Operations Chairman

Lockheed Martin Space Systems Company, Sunnyvale, CA

1:30 **BUSES DEPART HOTEL FOR LaRC TOUR**

2:00-4:00 **NASA LANGLEY RESEARCH CENTER FACILITY TOUR**

## **SYMPOSIUM ORGANIZING COMMITTEE**

**James E. Wells, Host Chair, NASA LaRC**  
**Robin Tutterow, Host Co-Chair, NASA LaRC**

**Stuart H. Loewenthal, General Chairman, Lockheed Martin**  
**Edward A. Boesiger, Operations Chairman, Lockheed Martin**

**Carlton L. Foster, NASA MSFC**  
**Claef F. Hakun, NASA GSFC**  
**Christopher P. Hansen, NASA JSC**  
**Wayne Jermstad, NASA JSC**  
**Patrice Kerhousse, ESA/ESTeC**  
**Alan C. Littlefield, NASA KSC**  
**Edward C. Litty, JPL**  
**Fred G. Martwick, NASA ARC**  
**Donald H. McQueen, Jr., NASA MSFC**  
**Wilfredo Morales, NASA GRC**  
**Robert P. Mueller, NASA KSC**  
**Fred B. Oswald, NASA GRC**  
**Minh Phan, NASA GSFC**  
**Donald R. Sevilla, JPL**  
**Mark F. Turner, NASA ARC**

## **SYMPOSIUM ADVISORY COMMITTEE**

**Obie H. Bradley, Jr., NASA LaRC (ret)**  
**Robert L. Fusaro, NASA GRC (ret)**  
**Ronald E. Mancini, NASA ARC (ret)**  
**Stewart C. Meyers, NASA GSFC (ret)**  
**William C. Schneider, NASA JSC (ret)**

# Precision Linear Actuators for the Spherical Primary Optical Telescope Demonstration Mirror

Jason Budinoff\* and David Pfenning\*

## Abstract

The Spherical Primary Optical Telescope (SPOT) is an ongoing research effort at Goddard Space Flight Center developing wavefront sensing and control architectures for future space telescopes. The Ø3.5-m SPOT telescope primary mirror is comprised of six 0.86-m hexagonal mirror segments arranged in a single ring, with the central segment missing<sup>2</sup>. The mirror segments are designed for laboratory use and are not lightweighted to reduce cost. Each primary mirror segment is actuated and has tip, tilt, and piston rigid-body motions. Additionally, the radius of curvature of each mirror segment may be varied mechanically. To provide these degrees of freedom, the SPOT mirror segment assembly requires linear actuators capable of <10-nm resolution over a total stroke of 5 mm. These actuators must withstand high static loads as they must support the mirror segment, which has a mass of ~100 kg. A stepper motor driving a differential satellite roller screw was designed to meet these demanding requirements. Initial testing showed that the actuator is capable of sub-micron repeatability over the entire 6-mm range, and was limited by 100-200 nm measurement noise levels present in the facility. Further testing must be accomplished in an isolated facility with a measurement noise floor of <5 nm. Such a facility should be ready for use at GSFC in the early summer of 2006, and will be used to better characterize this actuator.

## Introduction

Future large (>6 m) space telescopes such as the James Webb Space Telescope, SAFIR, and beyond require segmented primary mirrors to package into launch vehicle payload fairings of diameters less than their apertures. Requisite architectures to align or “phase” the individual segments into a single optical surface after launch and deployment are required. Current techniques used on large ground-based telescopes such as Keck include precision segment edge sensors<sup>4</sup> and various types of wavefront sensors<sup>5</sup>. However, phasing a large number of segments requires a significant amount of computing resources which can reduce observing efficiency. Maintaining a “phased” array of mirror segments in a challenging environment such as low-earth or L2 orbits remains to be seen. The SPOT research testbed will explore a new method of phasing segmented mirrors. The SPOT telescope architecture has possible application to a robotically assembled telescope for ISS, as shown in Figure 1.



**Figure 1. A possible application of the SPOT telescope architecture: a telescope mounted on the “top” (zenith) end of the Z1 truss**

### Wavefront Sensing and Control

A relatively recent technique utilizing image-based wavefront sensing has been pursued by the GSFC optics branch, Code 551. By placing a point source and camera at the center of curvature of a spherical

---

\* NASA Goddard Space Flight Center, Greenbelt, MD



mirror, a direct measurement of its surface wavefront error is possible. Taking various defocused images at the center of curvature and using an iterative transform solver, the phase error of the reflected wavefront can be determined<sup>3</sup>. From the phase error tip, tilt, defocus, and other Zernike terms (currently truncated to the first 15 terms) can be recovered. This information is used to position the mirror segments. To further develop this approach to phasing mirror segments, the SPOT internal research & development project was started in 2004.

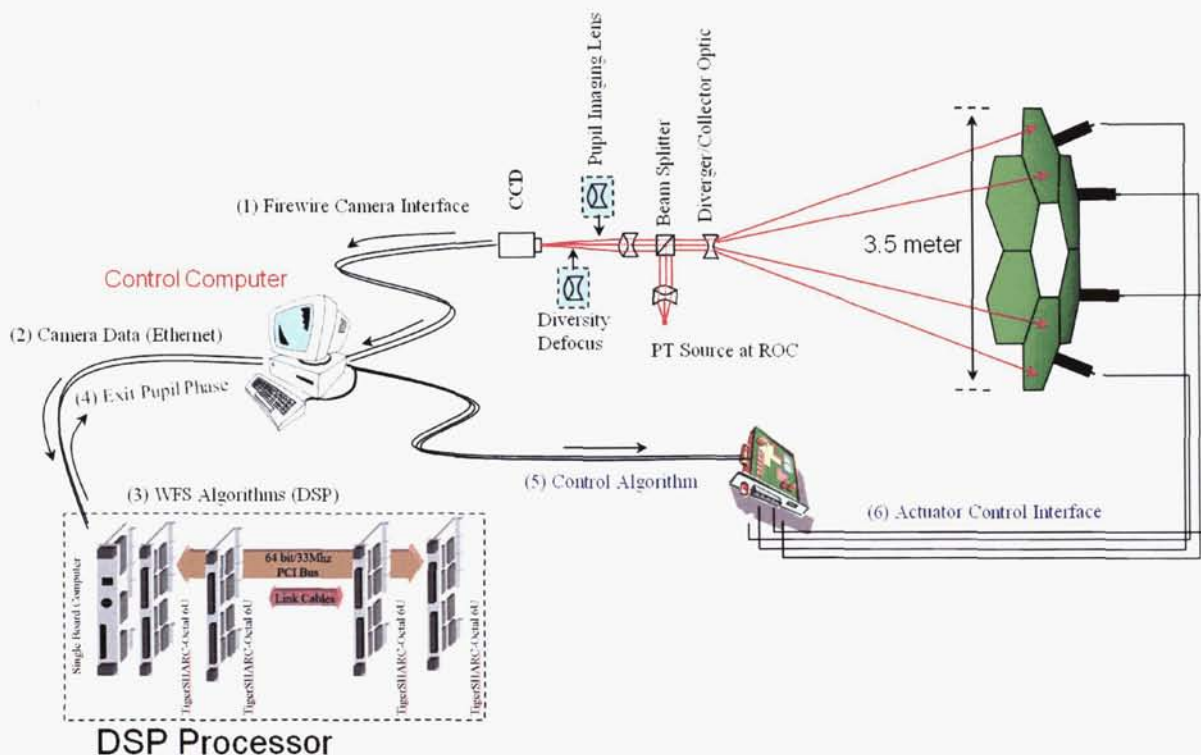


**Figure 2. SPOT Testbed Schematic**

Nanometer-level positioning of ~100-kg mirror segments was required, as well as a high-load nanometer displacement actuator to mechanically bend the mirror segments to adjust their radius of curvature. As the program had limited funding, low-cost actuators were designed to meet these requirements.

### SPOT Background

The Spherical Primary Optical Telescope (SPOT) is a GSFC internal research & development program initiated in 2003. The goal of the SPOT effort is to develop a robust architecture which will reduce the cost of large-aperture, segmented primary mirror space telescopes. The SPOT telescope architecture is based upon two key technology developments: 1) a high-rate, center of curvature, iterative transform phase-diversity phasing algorithm, and 2) a low-cost mirror segment. The SPOT demonstration telescope is a Ø3.5-m segmented spherical primary. The primary consists of 6 identical hexagonal segments measuring 876 mm point-to-point, in a 1-ring configuration, without a central segment. However, only 2 segments are being fabricated for this effort. Two segments are the minimum amount required to successfully demonstrate the phasing architecture. Each segment has rigid-body position control in tip, tilt, and piston. Each segment also has mechanical radius-of-curvature control. Some of the relevant requirements for the SPOT mirror segments are given in Table 1.

**Table 1. Pyrex™ Mirror Segment Requirements**

Mirror Requirement	Value	Units	Note
Size	Ø876 (34.5)	mm (inch)	Point-to-point hex
Radius of curvature (ROC)	5000 ± 0.20	mm	Measured before plating
Figure	1/30	waves@633 nm	ambient
Surface Roughness	40	Angstrom	
ROC adjustment range	±400	microns	
ROC adjustment resolution	1	micron	
Max Surf error for 400 micron ROC adj.	15	nm RMS	
Thermal Operational Environment	20-26	Degrees C	ambient
<b>Rigid Body Motion Requirement</b>			
Focus range	± 5 goal ± 1 min	mm	Needed to provide defocus range
Focus resolution	<10 goal 20 min	nm	Resolution required for phasing
Focus update rate	1	Hz	
Tip/Tilt Range	± 2.0	degree	
Tip/Tilt Resolution	0.05	arcsecond	As allowed by focus resolution
Tip/Tilt update rate	1	Hz	
Position Hold	0	Amp	Power-off hold
Actuator Thermal Stability		Microns/deg	As small as practicable
Static Load	35	kg	Mirror mass ~100 kg, assume 3 actuators

To provide rigid-body positioning in tip, tilt, and defocus of the segments, which will weigh ~50 kg each, a tripod mechanism with custom actuators was designed at GSFC.

### Design of the Segment Assembly Tripod

The mirror segment must have 3 rigid-body degrees of freedom: tip and tilt rotations and piston, a vertical translation. A segment assembly is shown in Figure 3.

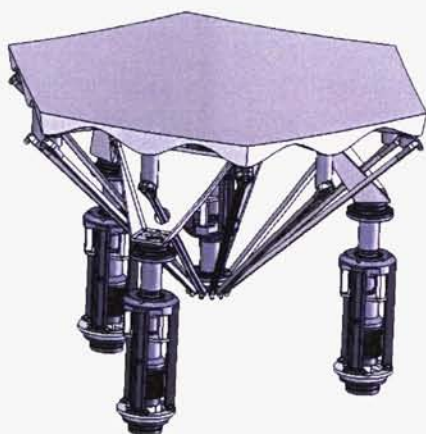


**Figure 3. The SPOT Mirror Segment Assembly Tripod**

### Kinematics of the Segment Assembly & Grübler's Mobility Criterion

The mirror requires only tip tilt and piston adjustment, 3 degrees of freedom. A hexapod would provide 6 degrees of freedom; but we don't need 6. Therefore, a tripod was selected to provide the rigid body motions required. The end joints of each strut must constrain a number of degrees of freedom. For example, a ball-in-socket joint constrains 3 translations but is free to rotate, allowing 3 rotations. From kinematics, Grübler's mobility criterion states that  $F$ , the number of degrees of freedom in a system, can be defined by:

$$F = \lambda(n-j-1) + \sum_{i=1}^j f_i$$

Where

- $\lambda = 6$ , the degrees of freedom in the space the mechanism will be operating in
- $n$  = the number of links in the system
- $j$  = the number of joints in the system
- $f_i$  = the degrees of freedom allowed (unconstrained) at the  $i^{\text{th}}$  joint

For the SPOT tripod, each leg consists of 2 links and 3 joints. Ground is considered a rigid link, and the mirror is the "end effector" or output link. For this system, the following values are used:

- $\lambda = 6$ , we shall consider the system exists in 6 degrees of freedom
- $n = 8$ , ground and the mirror are each one link, and each leg has 2 links
- $j = 9$ , each leg has 3 joints (base, linear, and upper) x 3 legs
- $f_1 = 2$ , base joint of leg 1, XY flexure allowing 2 rotations
- $f_2 = 2$ , base joint of leg 2, XY flexure allowing 2 rotations
- $f_3 = 2$ , base joint of leg 3, XY flexure allowing 2 rotations
- $f_4 = 1$ , linear joint of leg 1, allowing 1 translation
- $f_5 = 1$ , linear joint of leg 2, allowing 1 translation
- $f_6 = 1$ , linear joint of leg 3, allowing 1 translation
- $f_7 = 2$ , upper joint of leg 1, XY flexure allowing 2 rotations
- $f_8 = 2$ , upper joint of leg 2, XY flexure allowing 2 rotations
- $f_9 = 2$ , upper joint of leg 3, XY flexure allowing 2 rotations

Using the above values, the system degrees of freedom are calculated as:

$$F = 6(8-9-1) + \sum_{i=1}^9 f_i = 3$$

The number of system degrees of freedom is 3, corresponding to tip, tilt and piston. The use of XY flexures, allowing  $f_i$  (for  $i = 1..3, 7..9$ ) = 2, is justified. Ball joints could be used, but the additional passive degree of freedom at each leg (roll) would have to be subtracted out of the Grübler criterion equation to keep  $F = 3$ . The XY flexures will allow hysteresis-free angular motion at the cost of increased force proportional to displacement.

### **Actuator Design**

The actuator is shown in Figure 4.





**Figure 4. The SPOT linear actuator, shown with a six-inch ruler for scale.**

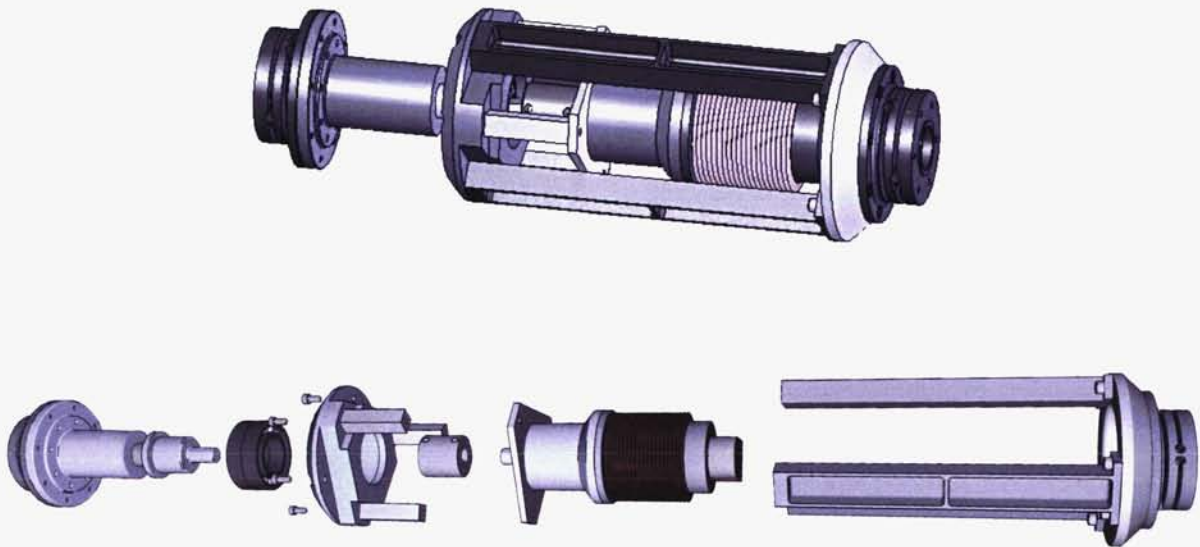


**Figure 5. An exploded view of the SPOT linear actuator**

Stepper Motor/Harmonic Drive Gearhead

ZSS 52.500.2.5.K1-HEDL-HD14/100

The HD14 100:1 harmonic Drive gearhead

Phytron 500 step per revolution or 0.72 degree step size

3-phase stepper motor, 2.5 Amp winding

Agilent HEDL 5540 500 line (A quad B = 2000 counts) incremental encoder on motor output



**Figure 6. The Phytron ZSS 52 / HD14 actuator**

#### Differential Satellite Roller Screw

Several options exist for rotary-to-linear motion: lead screw, ball screw, or roller screw. Generally the most precise of these is the satellite roller screw. A differential roller screw was selected. After several months of vendor interaction, a differential roller screw was selected and sized. The smallest, readily available precision roller screw has a pitch of 0.5 mm. A lead of this size can produce 10 nm steps using the 0.72° stepper motor and 100:1 harmonic drive.

Using a differential roller screw, the effective lead can be reduced by 2 orders of magnitude, but at the cost of a stroke limitation to ~6 mm. The theoretical attainable step size drops to 0.4 nm (see below). A Rollvis™ differential satellite roller screw utilizes equal thread pitch on the nut and the shaft, but varies the nut/shaft thread pitch diameters and the number of starts on the nut and shaft. The effective lead of such a differential satellite roller screw can be calculated by:

$$L_{eff} = \frac{P(D_n N_s + D_s N_n)}{D_n + D_s}$$

Where

$D_n$  = Nut thread pitch diameter, mm

$D_s$  = Shaft thread pitch diameter, mm

$P$  = thread pitch in threads/mm

$N_n$  = number of thread starts on nut

$N_s$  = number of thread starts on shaft, negative for opposite handedness to nut starts

For the SPOT actuator, the values were varied within reasonable limits until a minimum value for effective lead was found. Using the following values:

$D_n$  = 29 mm

$D_s$  = 19 mm

$P$  = 0.5 threads/mm

$N_n$  = 4

$N_s$  = -6

$$L_{eff} = \frac{0.5[(29)(-6) + (19)(4)]}{29 + 19} = 0.02 \text{ mm}$$

The minimum effective lead,  $L_{eff}$ , was found to be 0.02 mm per revolution, or ~21 microns per revolution. A bind condition determines the total stroke, which for this differential roller screw is ~6 mm. Rollvis Swiss S.A., a Swiss manufacturer of precision roller screws, fabricated the roller screw as Model RV160/19,02.R1.604350, custom designed for maximum resolution.

The 5 rollers roll around the shaft and are held in a rotating retainer ring at each end of the nut. A sun gear at each end of the nut and mating roller gears at the ends of each roller keep them in proper clocking as they rotate around the shaft. The shaft, nut and rollers are 410 stainless steel. The lubricant for the roller screw is Isoflex Topas NCA 52, manufactured by Klüber Lubrication. It is a synthetic oil with a calcium thickener. The differential satellite roller screw is shown in Figure 7 and 8.



**Figure 7. Custom Differential Satellite Roller Screw**

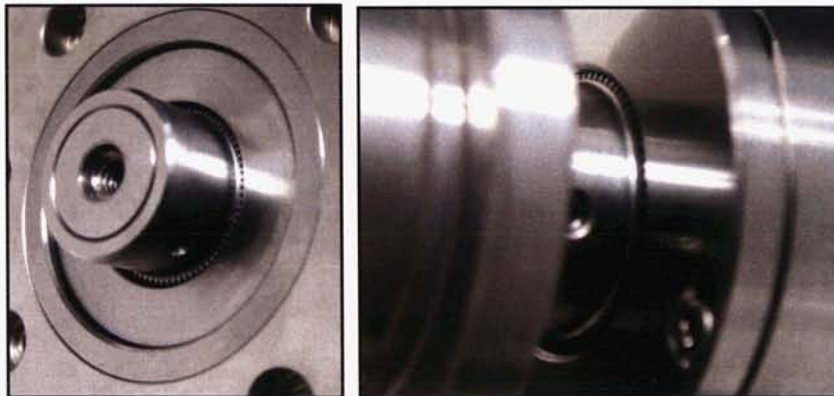


**Figure 8. Nut end details showing the timing gear teeth**

#### Helical Coupling

A standard flexible shaft coupling from Helical Products Company, Inc. was used to couple the motor output shaft to the satellite roller screw shaft. Such couplers allow torque to be transmitted despite small axial misalignments between the shafts. A model HRM-125-12mm-12mm coupling was used. This coupler uses 2 pairs of cup-point set screws to secure the motor and screw shafts. The coupling is 17-4PH H900 stainless steel. The coupling is shown in Figure 9.





**Figure 9. Helical Coupling**

#### Bearings

Barden 106HCDUL back to back duplex pair, ABEC-9, SAE52100 steel

30-mm bore diameter, 15-degree contact angle, 14 7.14-mm (9/32") diameter 440C balls, 36-kg (80-lb) heavy preload

Static load capacity 1005 kg (2216 lb)

Machined phenolic cage retainer

Winsorlube L245X oil lubricant



**Figure 10. Barden 106HC Duplex bearing pair**

#### Leg End Flexures

XY flexures

Crossed flexure

Torsional rate

Fatigue/cycle life

$$K = \frac{9\pi r^{0.5}}{2Eb t^{2.5}}$$

Where

K = torsional spring rate  
r = radius of notch cut  
E = Modulus  
b = thickness of flexure section  
t = width of notch

For the SPOT tripod, each leg consists of 2 links and 3 joints. Ground is considered a rigid link, and the mirror is the “end effector” or output link.

### Conclusion

Further testing to fully characterize nanometric step size, repeatability, and linearity must be accomplished in a quiet facility. The actuator performance will also be measured with an actuator built into a mirror segment. Actuator positioning performance will be indirectly measured by mirror radius of curvature change per commanded step.

### References

1. Budinoff, Jason G. “SPOT Mirror Segment Assembly Requirements - Revision C”, March 2004
2. Howard, Joseph “Optical Design Study for NASA’s Spherical Primary Optical Telescope” SPIE 5524-1
3. Budinoff, Jason G, Michels, Gregory J. “Design & Optimization of the Spherical Primary Optical Telescope (SPOT) Primary Mirror Segment” SPIE 5877-42
4. Dean, B, Smith, S, Budinoff, J. “Image-Based Wavefront Sensing for the Control of Space Optics” USAF AMOS Maui Technical Conference, September, 2000
5. Chanan, G., Troy, M., Ohara, C. “Phasing the Primary Mirror Segments of the Keck Telescopes: A Comparison of Different Techniques” Proc. SPIE, 4003, 188-201, 2000
6. Martinez, L.M., Yaitskova, N., Dierickx, P., Dohlen, K. “Mach Zender Wavefront Sensor for Phasing Segmented Telescopes”
7. Tsai, Lung-Wen, ‘Robot Analysis: The Mechanics of Serial and Parallel Manipulators’ ©1999 John Wiley & Sons, Inc.
8. Paros, J.M., Weisbord, I. “How to Design Flexure Hinges” Machine Design vol 37, pp151-156, 1965
9. Lobontiu, Nicolae “Compliant Mechanisms: Design of Flexure Hinges” ©2002 CRC Press LLC



# The CRISM Motor/Encoder Assembly and Diaphragm Bearing Assembly Design

Jeffrey Lees<sup>\*</sup> and Ed Schaefer<sup>\*</sup>

## Abstract

This paper will describe the thin section angular contact bearings and WS<sub>2</sub> dry film lubrication used on the compact Reconnaissance Imaging Spectrometer for Mars (CRISM) motor/encoder and diaphragm bearing assemblies.

## Introduction

CRISM will use targeted observations to search for evidence of aqueous activity and to characterize the geology and composition of surface features<sup>1</sup> on Mars (Figure 1). Global measurements acquired repeatedly throughout the Martian year will provide information on atmospheric water vapor, CO, and aerosols complementary to that from other MRO instruments.

The Optical Sensor Unit (OSU) consists of an optical system, a cryogenic system, and focal plane electronics gimbaled about a single axis to allow scanning over  $\pm 60^\circ$  from nadir. Its mechanical design builds on proven technology from previously successful APL instrument designs. The base housings are fabricated from titanium that provides high stiffness and thermal isolation within the same component. The gimbal bearings are a precision assembly designed to operate in a  $-60^\circ\text{C}$  environment. The gimbal is driven directly by a brushless DC motor paired with a BEI 20-bit incremental position encoder. The encoder disk is co-mounted directly to the bearing shaft beside the motor rotor and the read heads are mounted to the bearing housing alongside the motor stator. The electrical signals and purge are passed through a twist capsule in the center of the motor/encoder bearing assembly. A second bearing pair is mounted in a parallel diaphragm bearing housing that provides high stiffness in the lateral directions to the gimbal axis and flexibility along the gimbal axis to compensate for differential expansion of the instrument and spacecraft. The spectrometer housing is passively cooled to  $-90^\circ\text{C}$  using a flexible link to the anti-sunward radiator. The anti-sunward radiator passes through the center of the diaphragm bearings in a thermally isolated mount, and thus rotates with the OSU; its FOV is independent of gimbal position.

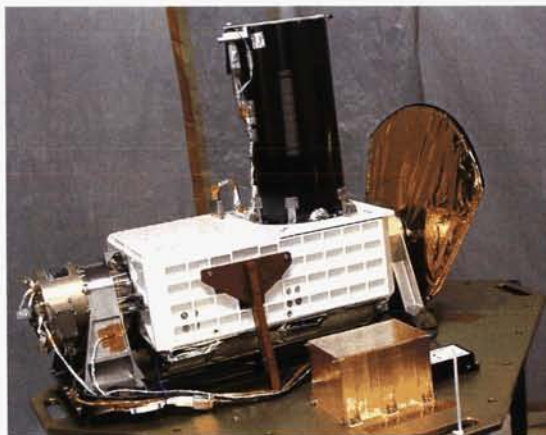


Figure 1. CRISM Instrument

---

<sup>\*</sup> Johns Hopkins University Applied Physics Laboratory, Laurel, MD



## CRISM Thermal Design

The CRISM thermal design provides both active cooling of the IR focal plane to cryogenic temperatures to reduce dark current and passive cooling of the spectrometer housing to  $-80^{\circ}\text{C}$  for low background. Simultaneously it keeps the electronics section near  $-40^{\circ}\text{C}$  (Fig. 2). Cryogenic cooling is provided by three Ricor K508 integral Stirling cryocoolers. The multi-cooler configuration requires "thermal switching" between coolers. A cryogenic diode heat pipe assembly consisting of heat pipes and a thermally isolating mounting assembly connects the active cooler with the focal plane while isolating it from the two dormant coolers<sup>2</sup>. Each of the three diode heat pipes is connected to the focal plane on one end and to a cooler on the other. The focal plane electronics are mounted in the bottom of the gimbal housing and are maintained at  $-40^{\circ}\text{C}$ . The housing along with tantalum plates provide EMI shielding and minimize cable length to the focal planes. Table 1 lists the CRISM expected flight operating temperatures.

**Table 1. CRISM Flight Operating Temperatures**

Component		Min.	Max.
Telescope	$^{\circ}\text{C}$	-75	-25
Spectrometer Housing	$^{\circ}\text{C}$	-110	-78
Optical Bench	$^{\circ}\text{C}$	-75	-25
VNIR FPA	$^{\circ}\text{C}$	-60	-20
IR FPA	K	110	120
Cryo-Coolers	$^{\circ}\text{C}$	-25	20
Diode Heat Pipes	K	95	115
Electronic Boards	$^{\circ}\text{C}$	-25	20
Motor/Encoder	$^{\circ}\text{C}$	-40	10
Shutter Motor	$^{\circ}\text{C}$	-71	0
Integrating Sphere	$^{\circ}\text{C}$	-71	0
Anti-Sunward Radiator	$^{\circ}\text{C}$	-130	-90

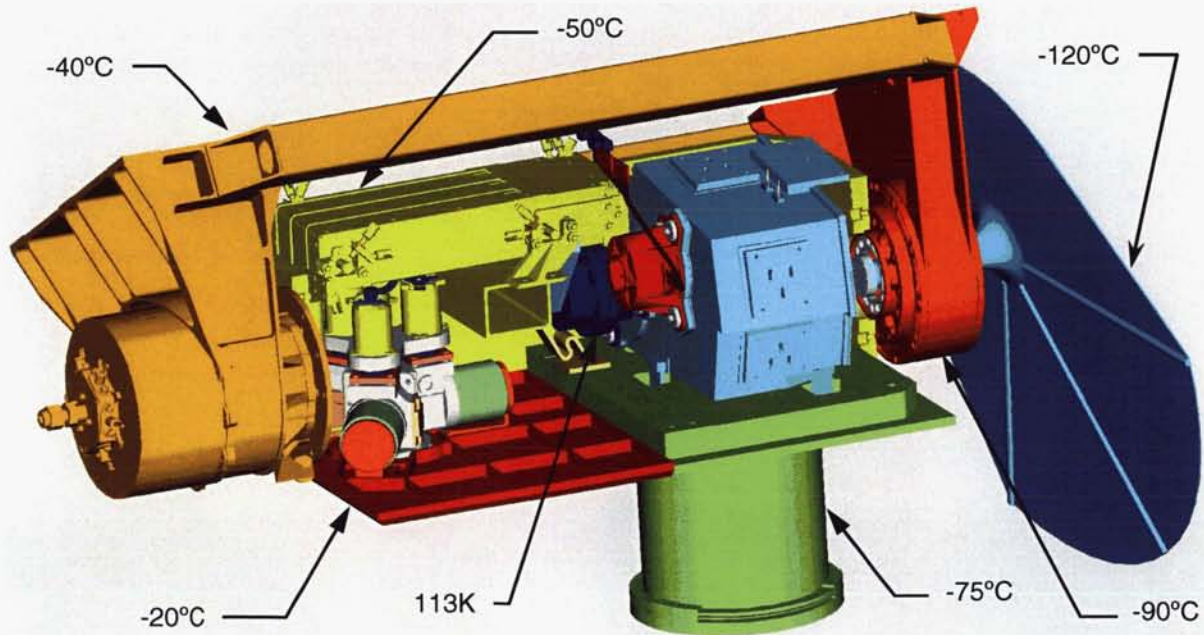


**Figure 2. CRISM Thermal Zones**



## CRISM Bearing System

The CRISM instrument rotates the OSU  $\pm 60^\circ$  from nadir. The OSU weighs 20.9 kg (45.9 lbf) and is supported by the motor/encoder (Figure 3) and the diaphragm (Figure 4) bearing assemblies. The motor-encoder side used a thin-section angular-contact duplex pair mounted back to back and was designed to take the non-axis moments, the entire thrust load, and its share of the radial loads associated with launch event (Figure 5). These bearing were designed for a 266.9-N (60-lbf) axial preload. The diaphragm side used a thin-section angular-contact duplex set mounted face to face and was designed to take only the radial loads associated with the launch event. The diaphragm bearings were designed for a 66.7-N (15-lbf) axial preload.

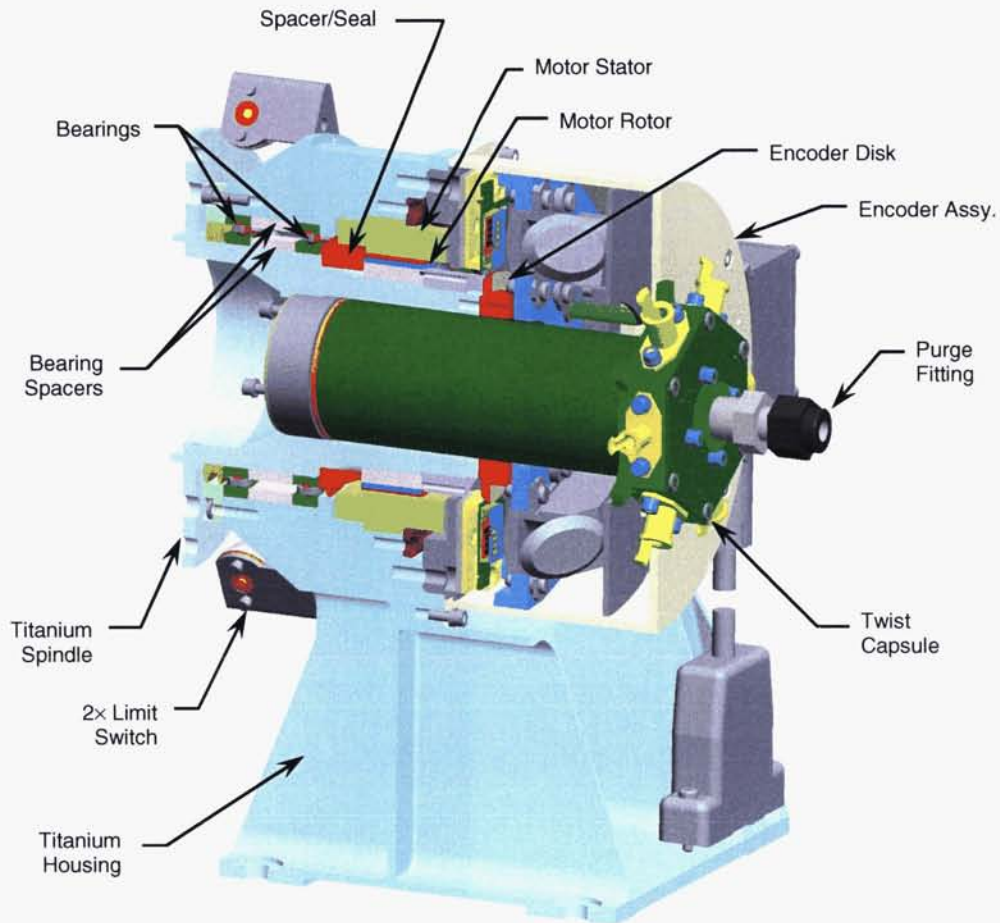


**Figure 3. CRISM Motor/Encoder Assembly**

## Preloading

Angular contact bearings should be preloaded as lightly as necessary to achieve the desired results. A duplex pair is a pair of bearings that have a pre-determined amount of preload built into them. This was accomplished by grinding the inner or outer ring a sufficient amount to eliminate all internal clearance within the bearing commonly referred to as the preload offset. There are, however, several disadvantages to preloading bearings:

- Increased running torque
- Sensitivity to differential thermal expansion
- Sensitivity to misalignment

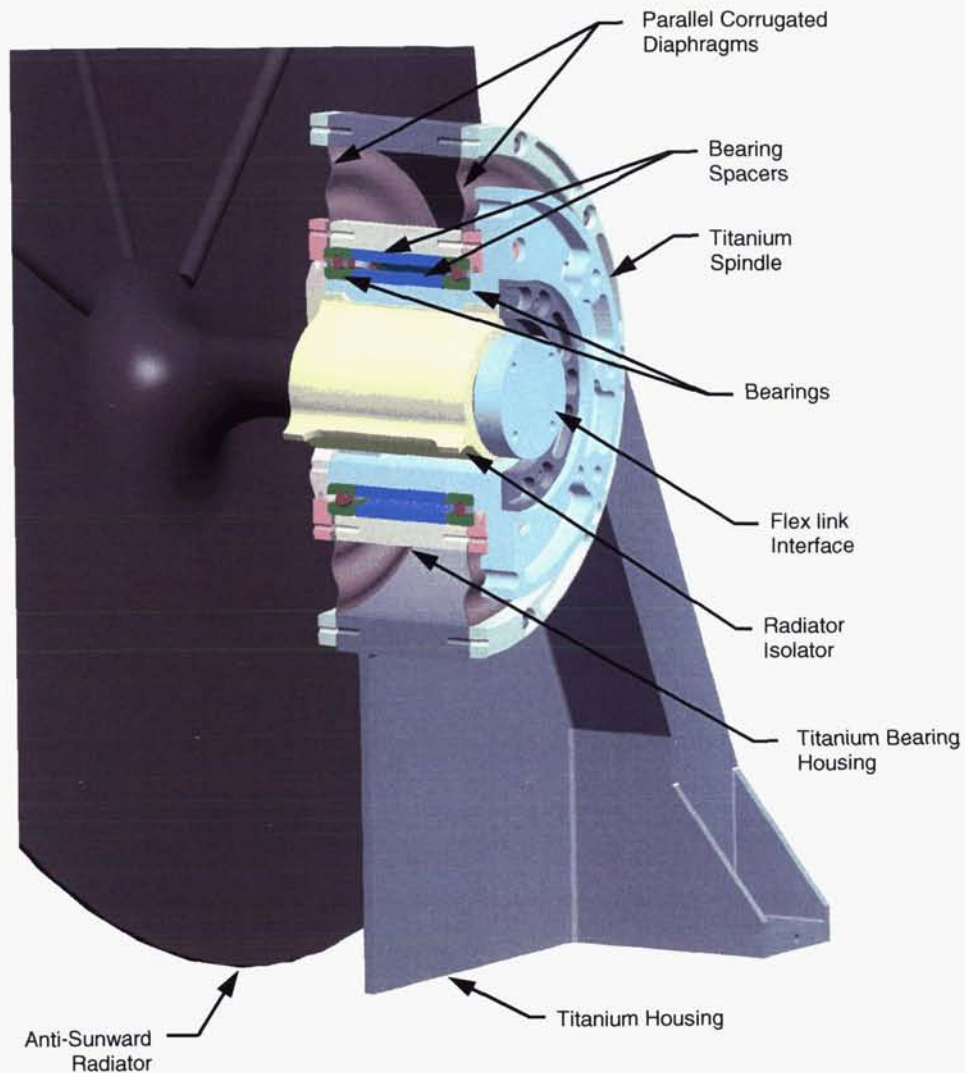


**Figure 4. CRISM Diaphragm Bearing Assembly**

The CRISM duplex bearing pairs were separated by titanium spacers so that the preload offset would remain constant over temperature. However, the difference between the 440C inner and outer rings and the titanium shaft and housing resulted in a reduction of clearance as temperature decreased (Figure 6). A reduction of clearance results in a decrease of the contact angle. However, the bearings are only going to experience substantial axial loads during the launch. The bearings were tested to  $-196^{\circ}\text{C}$  and continued to rotate freely. The few disadvantages of preloading are more than offset by the following advantages:

- Reduces axial and radial runout of the rotating shaft. Required for the encoder disk to read head alignment
- Reduces the shaft deflection under load and improves its assembled stiffness
- Removes free play in the bearing set, keeping the bearing set loaded in-order to avoid skidding of the balls
- Minimizes the peak stresses that occur during the maximum loading events by ensuring the load on the bearings is shared by more balls in each bearing
- Decreases bearing noise

In addition to the axial preload, the CRISM bearings employed a light interference fit,  $12.7\text{ }\mu\text{m}$  (0.0005 in) in the bearing/shaft fit and  $15.2\text{ }\mu\text{m}$  (0.0006 in) in the bearing/housing fit.



Figure 5. CRISM motor/encoder spindle

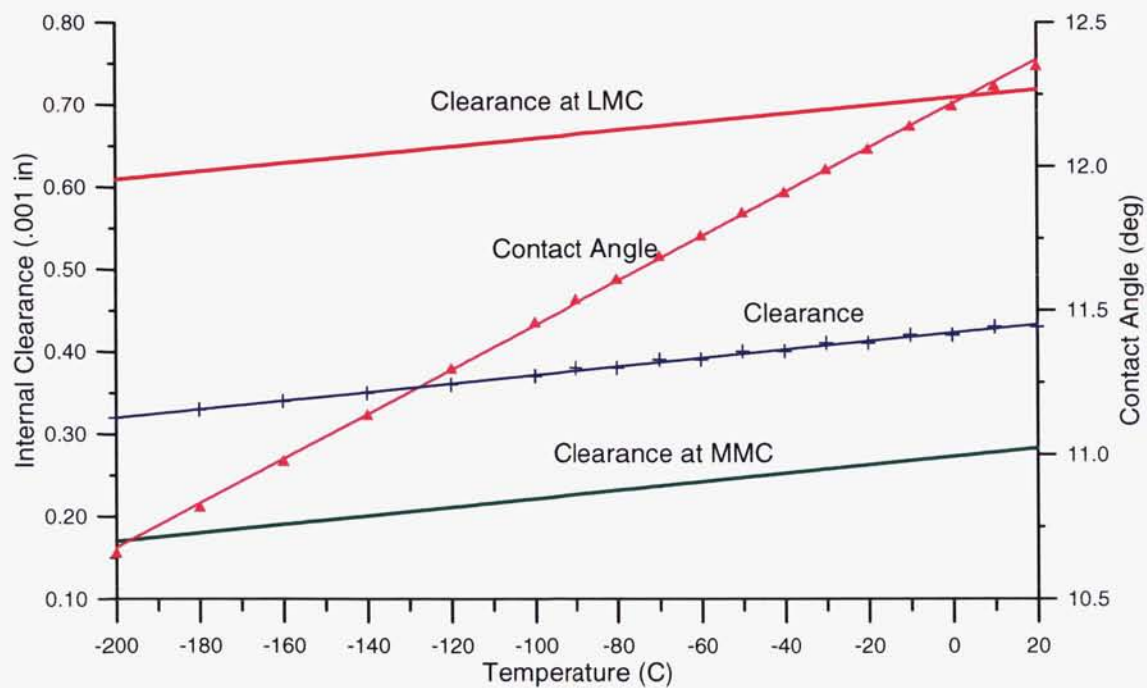


Figure 6. CRISM motor/encoder bearing clearance



## CRISM Bearing Lubrication

The thermal analysis of the CRISM motor/encoder and diaphragm bearing assemblies indicated that they would operate at -40°C and -90°C respectively. The analysis indicated that the diaphragm bearing assembly would be too cold for oil or grease lubrication. Our tests showed that -40°C was beyond the acceptable temperature range for Pennzane synthesized hydrocarbon based oils and greases and -90°C was beyond the accepted range for perfluorinated polyether based Brayco oils and greases. It was desired to use identical lubrication in both bearing assemblies for the following reasons:

- To have nearly identical bearings and identical lubrication in both bearing assemblies
- To simplify bearing/lubrication testing
- Once the bearings and lubrication were selected, a single qualification test could be applied to both assemblies

The three choices of dry film lubrication that were considered were:

1. Ion plated lead
2. Sputtered MoS<sub>2</sub> (molybdenum disulfide)
3. WS<sub>2</sub> (tungsten disulfide)

Ion-plated lead bearings were successfully used in the Compact Remote Imaging SPectrometer (CRISP) tracking mirror assembly on the Comet Nucleus TOUR (CONTOUR) spacecraft. The CRISP tracking mirror assembly bearings were a Barden precision angular contact duplex pair with a bronze cage. They were purchased through BEI as part of their motor/encoder assembly. This was done since they were the same bearings used in the BEI motor/encoder and they had used an identical set previously in the SABER<sup>3</sup> instrument on the TIMED spacecraft. However, we were unable to procure ion-plated lead thin-section bearings at the time. If it were possible to procure them in the future, we would definitely recommend trying them.

There is a great deal of literature touting the benefits of sputtered MoS<sub>2</sub>. Dry film lubrication tests for MoS<sub>2</sub> and WS<sub>2</sub> were conducted for the CRISP cover and release mechanism<sup>3</sup>. Sputtered MoS<sub>2</sub> is supposed to work great in vacuum, however, moisture absorption can cause severe performance degradation. Most of the CRISP cover and release mechanism qualification testing was conducted in ambient conditions including a test on NASA's Low Gravity Experiment aircraft (the "Vomit Comet"). Tests comparing sputtered MoS<sub>2</sub> and WS<sub>2</sub>, showed WS<sub>2</sub> to be clearly superior to sputtered MoS<sub>2</sub> for this application. Sputtered MoS<sub>2</sub> seemed to exhibit tremendous stiction in tests conducted in ambient conditions where as stiction was virtually undetectable with WS<sub>2</sub>. In fact, we believe that the cover and release mechanism would not have worked at all using sputtered MoS<sub>2</sub> in ambient conditions. Sputtered MoS<sub>2</sub> was also used in the bearings for the MDIS instrument on the MESSENGER spacecraft launched in 200X. In addition to the well known issues of sputtered MoS<sub>2</sub>, this instrument suffered two additional issues:

1. Smoothness
2. The sputtered MoS<sub>2</sub> coating is a hard and brittle coating

The MDIS instrument was able to meet its performance requirements with the sputtered MoS<sub>2</sub> coated bearings. However, the initial flight assembly had to be replaced and a new assembly built up because the sputtered coating had become cracked and resulted in large unacceptable torque spikes. Based on our experiences, we would NOT recommend sputtered MoS<sub>2</sub> coatings.

WS<sub>2</sub>, Dicronite, was chosen for the CRISM motor/encoder and diaphragm thin section bearings. However, we were unable to locate any specific examples or find any heritage on WS<sub>2</sub>-lubricated bearings used in space applications in the available literature. However, based on our previous success with WS<sub>2</sub> on the CRISP instrument, we were optimistic that WS<sub>2</sub> could also work in bearings. We also knew that the bearing companies offered it as an option and that the WS<sub>2</sub> coaters coated bearings. We decided to conduct our own WS<sub>2</sub> coated thin-section Teflon-toroid bearing test.

### CRISM Bearing Tests

Identical sets of sputtered  $\text{MoS}_2$ -coated and  $\text{WS}_2$ -coated thin-section Teflon-toroid angular contact duplex-pair bearings were purchased simultaneously (Figure 7). Prior to running the tests, an initial set of pictures using a scanning electron microscope were taken of both types of bearings (Figure 8 through Figure 10). Figures 8 through 10 show that  $\text{MoS}_2$  appears to have a much rougher surface than  $\text{WS}_2$ . We believe this is why the MDIS bearings never “felt” smooth.

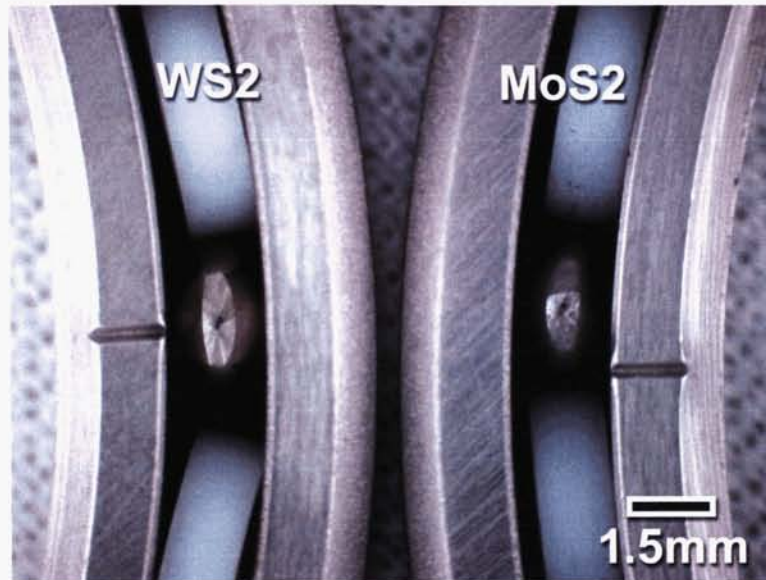


Figure 7.  $\text{WS}_2$  and  $\text{MoS}_2$  life test bearings

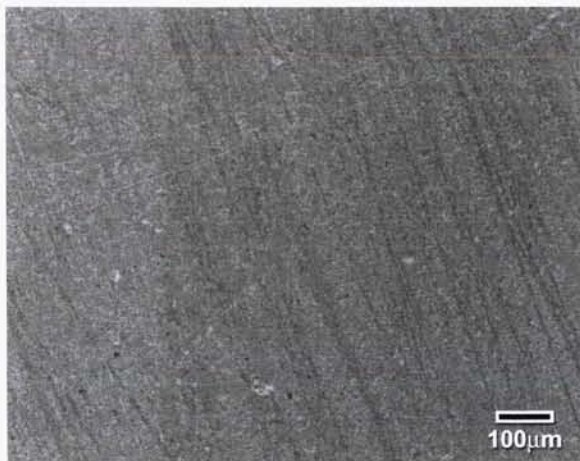


Figure 8a.  $\text{WS}_2$  Coating

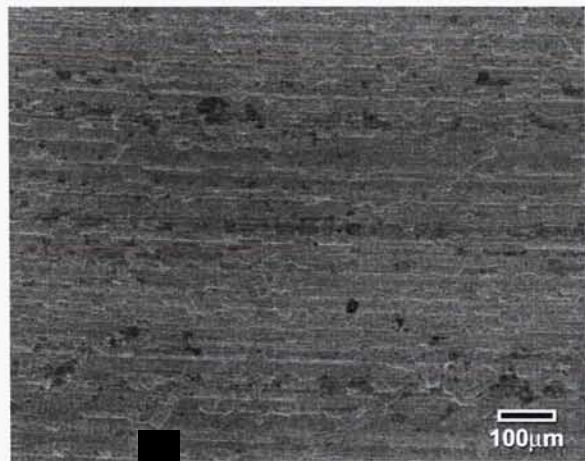
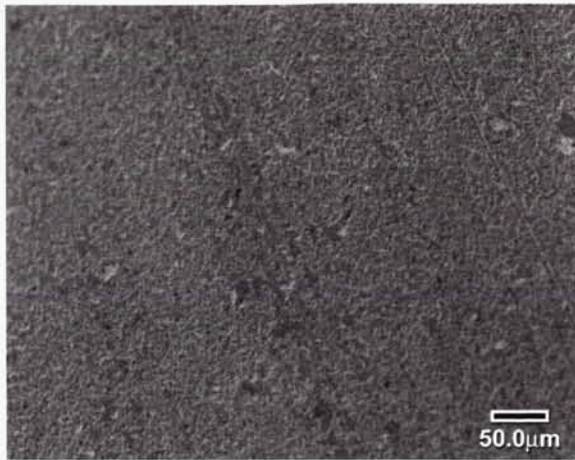
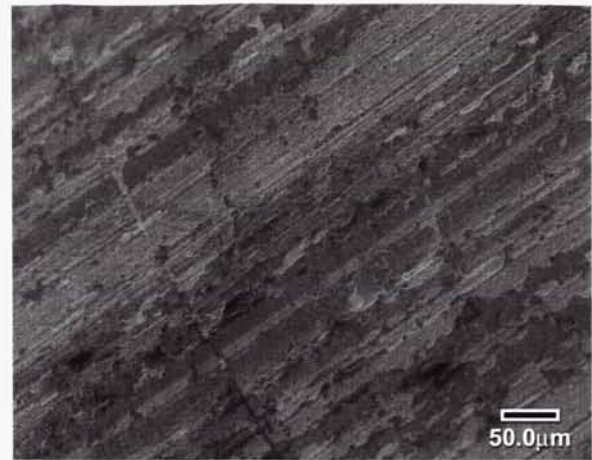


Figure 8b.  $\text{MoS}_2$  Coating



**Figure 9a. WS<sub>2</sub> Coating**



**Figure 9b. MoS<sub>2</sub> Coating**

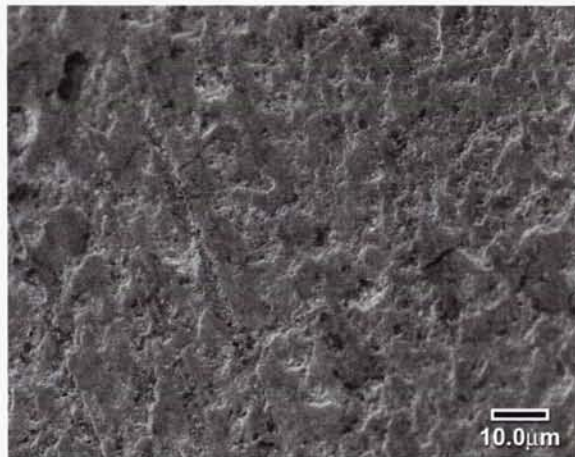


**Figure 10a. WS<sub>2</sub> Coating**

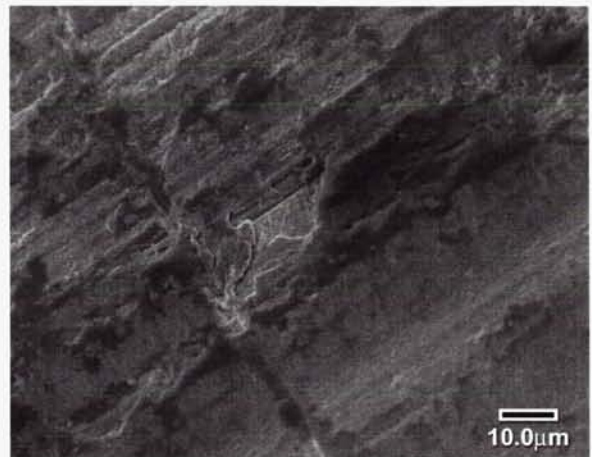


**Figure 10b. MoS<sub>2</sub> Coating**

Following the test of the WS<sub>2</sub>-coated bearings in which 57952 cycles were completed, we were concerned that the bearings seemed much rougher than they were prior to the test. After a visual inspection of the bearings, a significant amount of debris in the bearings was found. Post-test pictures were taken with a standard microscope, Figure 11 through Figure 13. There were several types of contamination found:

- White particles
- Brown particles on the toroids
- Brown film on the raceways

We were concerned that the contamination found in the bearings following the test would present a real problem, both in terms of lifespan and smoothness. However, upon review of the data, the rougher feel was not adversely affecting the motor control system. The bearings were disassembled and further inspected. We could find no evidence of wear in the raceways or the WS<sub>2</sub> coating. The life test was also significantly longer than the expected lifetime of the instrument at Mars.

#### Bearing Test Conclusion

The WS<sub>2</sub> coating is more than adequate for a slow moving oscillating gimbal requiring dry film lubrication. We were satisfied enough with the WS<sub>2</sub> performance that we did not test the sputtered MoS<sub>2</sub> bearings, we had found the solution we were looking for. The Teflon toroids would likely continue to break down and contaminate the bearings with additional particles that the instrument may no longer be able to rotate as precisely as is required. We believe the Teflon toroids will ultimately be the life limiting factor of these



bearings. Although this may be an advantage for continuously rotating higher speed mechanisms acting as an additional lubricant.

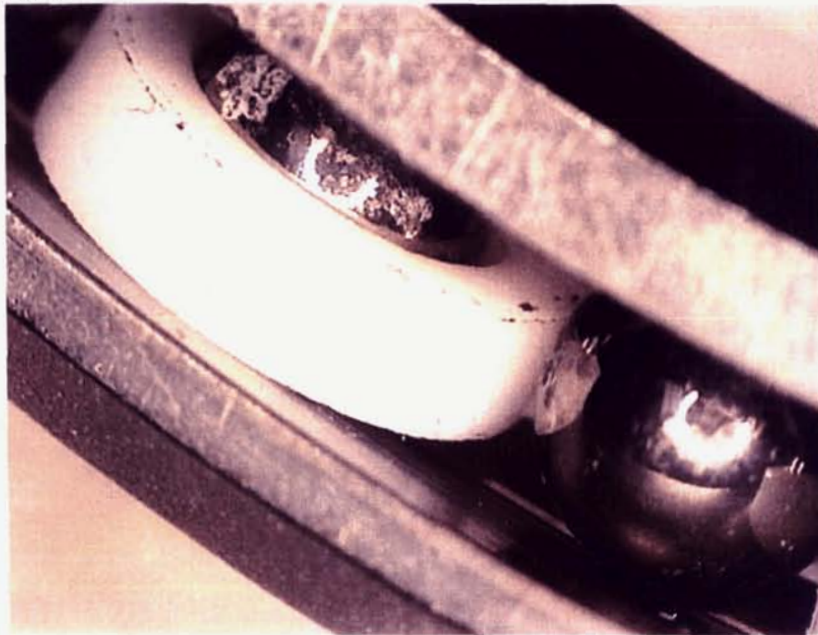


**Figure 11. Post life test bearing**



**Figure 12. Post life test bearing raceway**



**Figure 13. Post life test bearing raceway**

### **CRISM Bearing Anomalies**

#### Bearing Ball Spacing

The APL Space Department has used different sizes of thin-section Teflon-toroid-spaced bearings on several programs and tests. One feature that we have always noticed with these types of bearings is the potential for a "large" gap to occur between a ball and toroid (Figure 14).

We attribute both the high running torque and the poor feel to the non-uniform ball-toroid spacing. We believe that non-uniform ball-toroid spacing can result in some various amounts of pressure between all the toroids and balls. This can result in unpredictable friction between the ball and toroid causing an increase in the running torque. It may also result in a stick-slip situation between the ball and toroid resulting in torque spikes or non-smooth rotation. Additionally, it could lead to rapid wear of the toroid. The toroid wear particles could wind up in the raceways as contamination, also causing anomalous



torque spikes. Grease and oil lubricated bearings may exhibit the same problems as the CRISM dry film lubricated bearings to a far less noticeable degree due to the grease or oil between the ball and toroid. The evidence for this conclusion with the CRISM bearings is two fold:

1. The significant amount of Teflon contamination found in the bearings following the run-in procedure described in Appendix 1
2. The drastic change in torque level and smoothness following the high-pressure air blow through cleaning procedure described in Appendix 1

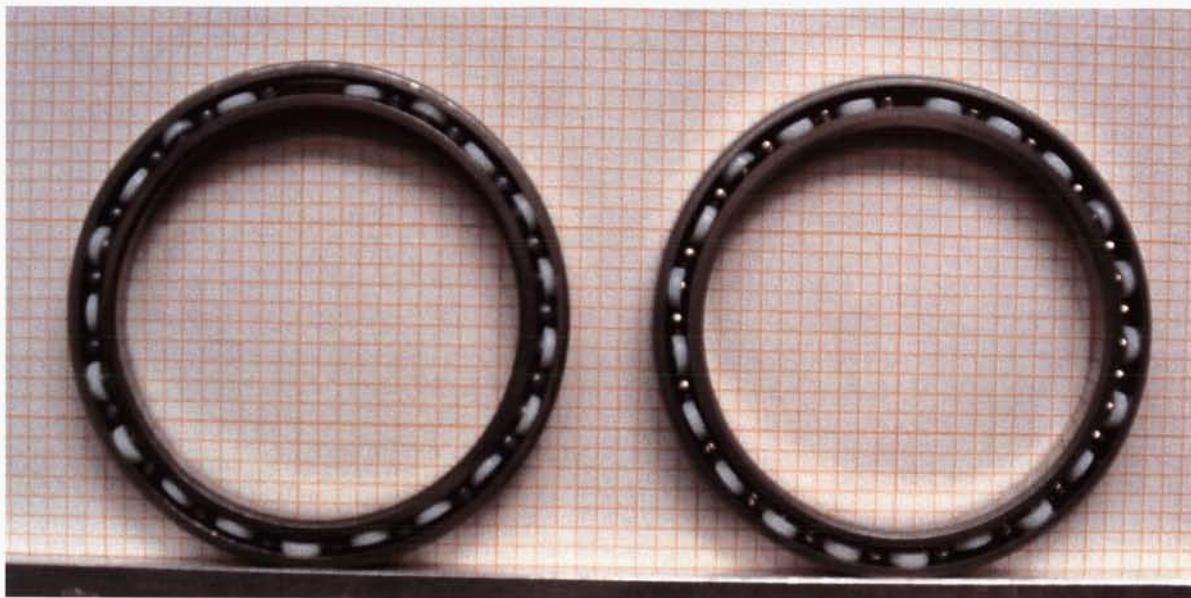


**Figure 14. Thin section bearings, same size, different manufacturer**

#### Reproducible Torque Spikes

Another type of torque spike was also noticed with the CRISM bearings that could be easily reproduced based on the operation of the spindle. During the run-in procedure in Appendix 1, unidirectional rotation resulted in extremely smooth running torque. However, CRISM was intended to oscillate  $\pm 60^\circ$ . A reproducible torque spike occurred following a change in direction of rotation. Rotating the spindle backwards and forwards, sometimes referred to as "safe cracking", torque spikes, equal to or greater than the nominal running torque, would result within several degrees of rotation following the reversal. A ball can never remain rolling between surfaces that form an angle to each other<sup>5</sup>. All angular-contact ball bearings create an angle between the two raceways. Therefore, as the bearings rotate, the balls produce a gyroscopic motion in addition to rolling. Pressure or drag friction between the toroid and the adjacent balls also seems to deflect the toroids based on the direction of rotation. Thus, the gyroscopic motion of the balls and pressure between toroids and adjacent balls appears to cause the toroids to align themselves based on the direction of rotation. This behavior appears to be attributable to the vast majority of toroids aligning themselves (Figure 15). When the spindle reverses, as do the balls, the toroids flip and align themselves in the opposite direction (Figure 16). As the toroids flip and align themselves in the opposite direction, a torque spike resulted. This effect was significantly reduced following the cleaning procedure. Once the balls and toroids became more evenly spaced, the drag friction between the toroid and adjacent balls was reduced, thus reducing the ability of the toroids to align themselves. This was also noticed following the Christmas holiday. As the bearings sat over the holiday, pressure between the balls and toroids either slightly re-spaced the balls or caused the Teflon to cold flow resulting in bearings the felt much better after having sat for an extended period. However, following another run-in, the bearings quickly resorted to their pre-holiday behavior.





**Figure 15. Toroids in "down" position**



**Figure 16. Toroids in "up" position**

Unfortunately, we never photodocumented this effect, thus, it was extremely difficult to find pictures of the flight hardware demonstrating this effect clearly. Figure 15 clearly shows all the toroids uniformly aligned in the "down" position. Figure 16 shows most of the toroids in aligned in the "up" position, including most of the ones at the top of the bearing. This effect can not be reproduced with a single un-mounted bearing.

### **CRISM Bearing Assembly Procedure**

The CRISM bearings were removed from the manufacturer's packaging and visually inspected to verify that they conformed to the documentation and were marked properly (Figure 17). Once we were sure that the bearings were correctly marked and free of contamination, they were assembled as follows:

1. The bearings and spacers were stacked and aligned per drawing and documentation (Figure 18)
2. The bearings and spacers were placed in an assembly fixture (Figure 19) specifically designed to keep them aligned during assembly
3. The bearing retainer was placed on the assembly (Figure 20)
4. The bearing shaft (Figure 21) was cooled in liquid nitrogen
5. The cooled bearing spindle was quickly assembled in the bearing assembly fixture. Weights were placed on the assembly to ensure that it remained seated against the top bearing.
6. The bearing assembly was quickly placed in a  $N_2$  purged vessel and allowed to equilibrate for 24 hours (Figure 22)
7. The spindle bearing assembly was then visually inspected and checked for "feel". It was noted that there was a significant amount of pressure on the spacers between the two bearings on both the Engineering Test Unit (ETU) and the flight unit. The ETU and the flight assembly were the first bearing assemblies with spacers that we had assembled using the liquid nitrogen technique. Previously, the bearings were duplex pairs without spacers. We were concerned that with the shaft being significantly cooler than the bearings and spacers, that as it warmed and expanded, there would be very little pressure between the bearings and spacers or worse, a gap. However, that never materialized
8. The entire spindle bearing assembly was then cooled in liquid nitrogen
9. The cooled spindle bearing assembly was quickly assembled in the titanium motor/encoder/bearing housing
10. The assembly was then purged and allowed to equilibrate for 24 hours
11. The assembly was visually inspected and checked for "feel"
12. We were not happy with the "feel" of the flight assembly and took the steps outlined in Appendix 1

There were two main issues with the flight bearing assembly, 1) high running torque; 2) torque spikes that made the assembly not feel smooth as it rotated. We were confident that contamination was not the problem from pre- and post-assembly inspections causing either of these problems.



**Figure 17. CRISM flight bearings**



**Figure 18. Bearings stacked and aligned**



**Figure 19. CRISM bearing alignment fixture**



**Figure 20. Bearing assembly**



**Figure 21. CRISM bearing shaft**



**Figure 22. Purging bearing assembly**



## Appendix 1

Table 2 lists the operations and measurements made to the flight motor/encoder bearing assembly. Most measurements were an average running torque. Some measurements were a peak torque when there was a significant torque spike to the running torque. On several tests where many measurements were made, an average value is reported and denoted by and Avg. in the Torque column.

**Table 2. Bearing Assembly Operations**

Date	Operation	Torque mN-m (oz-in)
12/04/2003	Initial torque measurements	111.6 (15.8)
12/16/2003		111.6 (15.8) nominal 190.7 (27.0) peak
	Run-in @60 RPM, 19 minutes (1140 Revolutions)	143.0 (20.25) Avg.
	Run-in @60 RPM, 25 minutes (1500 Revolutions)	381.3 (54.0)
	Cool off	254.2 (36.0)
12/23/2003	Loosen retaining nut	158.9 – 190.7 (22.5 – 27.0)
	Tighten retaining nut, 14.2 N-m (10.5 ft-lb)	158.9 – 190.7 (22.5 – 27.0)
	Tighten retaining nut, 20.3 N-m (15 ft-lb)	254.2 – 286.0 (36.0 – 40.5)
	Loosen retaining nut, 17.0 N-m (12.5 ft-lb)	190.7 (27.0)
	Tighten retaining nut, 19.0 N-m (14.0 ft-lb)	190.7 (27.0)
	Run-in @60 RPM, 22 minutes (1320 Revolutions)	508.5 (72.0)
	Loosen retaining nut	
	Tighten retaining nut, 17.0 N-m (12.5 ft-lb)	286.0 (40.5)
	Loosen retaining nut	
	Run-in @60 RPM, 20 minutes (1200 Revolutions)	158.9 (22.5)
	Tighten retaining nut, 17.0 N-m (12.5 ft-lb)	190.7 (27.0)
12/24/2003- 1/4/2004	Stored in N2 purged container in cleanroom	
1/5/2004	Loosen retaining nut and re-measure torques	
	Set-1	238.7 (33.8) Avg.
	Set-2	317.8 (45.0) Avg
	Changed torque measuring method for all future measurements.	
	Peak torque measurements	208.3 (29.5) Avg.
	Tighten retaining nut, 10.2 N-m (7.5 ft-lb)	240.8 (34.1) Avg.
	Run-in @60 RPM, 20 minutes (1200 Revolutions)	
	Peak torque measurements	182.2 (25.8) Avg
	Best “feel” so far	
	Tighten retaining nut, 13.6 N-m (10.0 ft-lb)	317.1 (44.9) Avg
	Run-in @60 RPM, 20 minutes (1200 Revolutions)	
	Peak torque measurements	148.3 (21.0) Avg.
	The best these bearings have ever “felt”	
1/6/2004	Removed retaining nut, rotor, and spacer	

	Noticed bearings had many small particles on the balls and races	
	Flushed with Isopropyl alcohol	
	Blow dry with high pressure filtered air	
1/7/2004	Re-install spacer and stator. Tighten retaining nut, 13.6 N-m (10 ft-lb)	
	Peak torque measurements	76.3 (10.8) Avg.
	Silky smooth, perfect feel	

### Acknowledgements

This work was performed at Johns Hopkins University Applied Physics Laboratory under a contract with the National Aeronautics and Space Administration. The authors would like to thank all those who helped design, fabricate, integrate and test the CRISM instrument. Reference herein to any specific commercial product, process, or service by trade name, trademark, manufacturer, or otherwise does not constitute or imply its endorsement by the United States Government or the Johns Hopkins University Applied Physics Laboratory, Laurel, MD.

### References

1. S. Murchie et. al., "CRISM (Compact Reconnaissance Imaging Spectrometer for Mars) on MRO (Mars Reconnaissance Orbiter)", Instruments, Science, and Methods for Geospace and Planetary Remote Sensing, SPIE Vol. 5660, pp. 66-77.
2. Bugby, D., J. Garzon, B. Marland, C. Stouffer, D. Mehoke, M. Fasold, "Cryogenic Diode Heat Pipe System for Cryocooler Redundancy," SPIE Optics and Photonics Conference, Cryogenic Optical Systems and Instruments XI, San Diego, CA, 31 July -4 August, 2005.
3. J. Lees, E. Schaefer, "Design and Testing of the CRISP Tracking Mirror Cover and Release Mechanism", Proceeding of the 36<sup>th</sup> Aerospace Mechanisms Symposium, Glenn Research Center, April, 2002, NASA/CP-2002-211506, pp.63-76.
4. Esplin, Roy. A satellite-based multichannel infrared radiometer to sound the atmosphere (SABER). In Optical Remote Sensing of the Atmosphere held in Salt Lake City, Utah, 5-9 February 1995. pp.130-132.
5. Harris, Rolling Bearing Analysis, 3<sup>rd</sup> Edition, John Wiley & Sons, Inc., pp.451-452.

# Gear Teeth Particles and Bearing Failures

William H. Greenwood\* and Jeffrey G. Dabbling\*

## Abstract

Torque is transmitted from rotary solenoids to rotate drive arms that advance a ratchet wheel as part of a safety mechanism in missile warheads. The small volume constraint led to single gear teeth to transmit the torque from the rotary solenoid. High contact forces and compliant gear teeth caused many fine particles to be generated at the rubbing surfaces of the gear teeth. The particles were pulled into the ball bearings of the adjacent solenoids causing early failure while having no ill effect on the ball bearings of the drive arms. A temporary solution of custom plastic shields allowed the prototype units to proceed to environmental and flight tests. A subsequent build replaced the gear teeth with ball bearing followers.

## Introduction

Missile warheads and bombs usually have safety mechanisms [1] to prevent unintended explosions in the event of accidents. These safety mechanisms are small and made of stainless steels for high temperature integrity in the event of accidents involving jet fuel or propellant fires. The safety mechanisms often have ratchet-type wheels, and are usually driven by rotary solenoids (Figure 1).



Figure 1. Mounting plate, ratchet wheel, and rotary solenoid

---

\* Sandia National Laboratories, Albuquerque, New Mexico

A new generation of safety mechanisms is nearing production. The safety mechanism of Figure 1 is among the new generation and transmits torque from the rotary solenoid to the drive arms by way of gears. Due to the limited stroke of the solenoid and the volume constraint, the gears are actually single gear teeth cut as part of the solenoid rotor and drive arm (Figure 2).



**Figure 2. Rotary solenoid and single gear teeth**

Earlier generations of these safety mechanisms often used full gears to transmit torque from the ratchet type wheels to other shafts for thousands of ratchet wheel cycles. One life test of the first generation of safety mechanisms involved 10,000 ratchet wheel cycles; the main gear had teeth that were no longer involutes but appeared triangular. Much wear debris was adjacent to the gear but did not migrate to ball bearings or cause operational failure.

The first units of the new intent safety mechanism were operated in January 2003 and failed to operate after only a dozen to a few hundred ratchet wheel cycles, as shown in Table 1. A failure to operate at such low number of cycles was unexpected. The original units had molybdenum disulfide ( $\text{MoS}_2$ ) applied to the gear teeth, but had no lubrication on the ball bearings of the solenoid or the drive arms. Molybdenum disulfide is used since the mechanisms must sit for decades unused and then be called upon to function. The safety mechanisms are usually hermetic units and have a nitrogen and helium atmosphere, although the ratchet cycle tests in this report were all performed in the laboratory atmosphere as part of early qualification. The ball bearings are generally lubricated but a new process for the bearings was not yet ready, so the early ratchet wheel cycle tests were performed with dry (non-lubricated) ball bearings.



**Table 1. Ratchet wheel rotations to failure, MoS<sub>2</sub> on gears, no MoS<sub>2</sub> on bearings**

Unit #	Date	Wheel cycles	Observations
CP007	13 Jan 2003	160	Powder at gear teeth
CP009	21 Jan 2003	12	Powder at gear teeth
CP004	28 Jan 2003	50	Powder at gear teeth
CP010	28 Jan 2003	40	Powder at gear teeth
CP005	30 Jan 2003	34	Powder at gear teeth

### **Initial Investigation**

The energized stroke of the solenoid is on the order of five milliseconds and the spring (de-energized) return of the drive arms is also on the order of five milliseconds. The initial investigation by high-speed video of the mechanism in operation showed erratic operation times for the inboard rotor during energized strokes when the unit was close to failure. Failed units were disassembled and visually examined. Drive arm bearings and drive springs showed no problems, and no rubs were detected between the arms and adjacent surfaces. The wear zone on the gear teeth showed a powdered layer rather than a burnished appearance as shown in Figure 3. The powdered layer was 0.1 to 0.2-mm thick at the edges and 0.05 mm or thinner in the center. The powdered layer was composed of many micron size particles and was readily scraped or wiped away from the gears. In addition, many small dark particles were observed on the mounting plate under the gear teeth and at stop pins. The quantity of particles was much greater than observed in previous safety mechanisms.

An additional troubleshooting test was a higher than expected minimum operate voltage. The minimum operate voltage occurs when the solenoid torque is nearly equal to the drive arms spring torque. The solenoids were designed to operate the mechanism as low as 16 volts and up to the maximum supply voltage of 22 volts. The ratchet wheel cycle tests are operated at 22 volts to give more solenoid torque and greater forces and loads on the bearings and pins. From the measured solenoid torque and the measured drive spring forces, the ratchet wheel units were expected to operate at 14 volts but when initially assembled were measured to operate at about 15 volts. This higher minimum operate voltage indicated a small loss, in the solenoid bearings, gear teeth or drive arm bearings, and the gear teeth contact between the solenoid and the drive arms was suspected as the probable cause. The powdered layer that was observed at the gear teeth contact in the first wheel cycle tests gave more evidence than the gears had substantial sliding contact and not the rolling contact desired in well-formed gear trains. The solenoid torque at 22 volts is approximately double the solenoid torque at 15 volts. The failure to operate after dozens or a hundred ratchet wheel cycles at 22 volts means an apparent frictional loss increased from near zero at the start to approximately 50% of the solenoid torque. If the large frictional loss was solely at the gear teeth, then slower and erratic spring return times of the drive arms and solenoid rotors were also expected but not seen in the high-speed videos.

The powdered layer at the gear contacts was obviously troubling, but it did not appear that the gear teeth interaction caused such high loss of torque. From the failed units, a solenoid rotor was manually stroked and no high friction was measured. Several failed units were cleaned of the powdered layer at the gear teeth contact, and the minimum operate voltage improved somewhat to 18 to 20 volts, but was still significantly higher than the initial 15-volt measurement. The powdered layer at the gear teeth did not appear to be the high friction loss that caused the units to stop at 22 volts.





**Figure 3. Gear tooth wear zone has a powdered layer.**

The solenoids from failed units were rotated manually and some roughness in rotation was noted. However, a quasi-static torque test of the solenoid at 16 and 22 volts showed nearly the same torque as measured before the installation into the ratchet wheel assembly, but the measured friction at zero volts was somewhat higher. The solenoid bearings in failed units were visually examined at 10x magnification, and the balls in the bearings in the inboard rotor had a roughened or a worn surface (Figure 4). The solenoid ball bearings were replaced, and the solenoids were re-assembled into their failed ratchet wheel units. The rebuilt units were then measured for minimum operate voltage and found to be 15 volts, the same as new units. The parts that degraded as the ratchet wheel units were operated were the solenoid bearings. The rebuilt units (with new solenoid bearings) were then cycle tested again and failed at similar cycles as those of Table 1.

The solenoid bearings could be degrading due to high dynamic loads or from particles from the gear teeth entering the bearings during operations. The axial load from the magnetic forces when the coil is energized was calculated to be 71 N (16 lbf) compared to the dynamic load rating of 116 N (26 lbf). The small oscillatory solenoid stroke of 0.2 rad (12 degrees) is a more severe service than continuous rotations since only a small portion of the balls see the load repeatedly. Therefore, the high axial magnetic force could be degrading the unlubricated bearings in such a few cycles. However, the innermost bearings of the rotors support all of the axial forces; whereas the failed units showed bearing wear to be most severe in the inboard rotor and approximately equal from the innermost and outermost bearings of the inboard rotor. The rapid bearing degradation did not appear to be caused by the relatively high dynamic axial load.



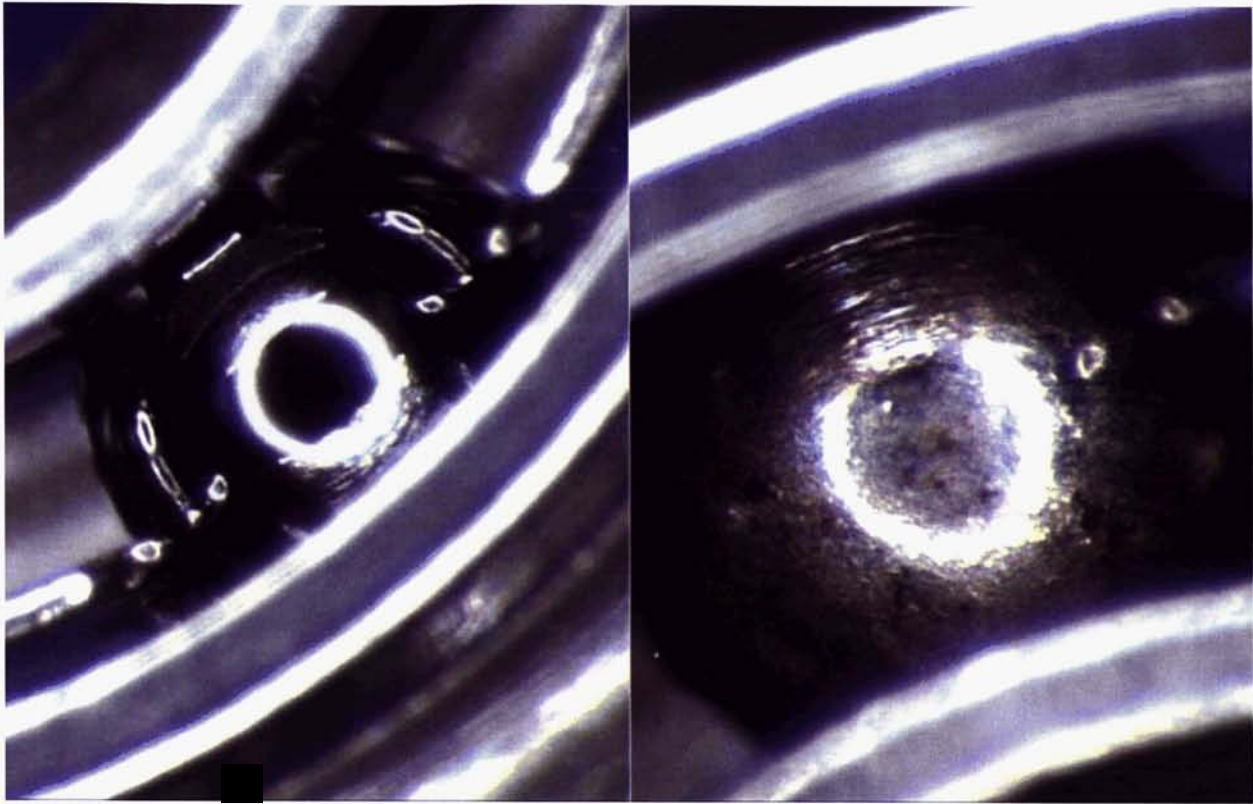


**Figure 4. Solenoid ball bearings before (left) and after (right) life cycle test.**

When ball bearings fail from high loads, the initial signs are many small pits as bearing material spalls, then the ejecta from the pits are rolled into the bearing surfaces that cause more localized high loads and accelerated degradation and eventually a non-rotating (seized) bearing. As the bearings were visually scrutinized, many patches or scabs were observed and some indentations but not pits. The scabs appeared to be a particle or perhaps several particles that are rolled into the balls as the bearing is operated. The scabs were foreign particles and not bearing ejecta. The parts that degraded and caused the early wheel cycle failure were the solenoid bearings; the cause of the bearing degradation was the particles from the gear teeth. The problem resolution was to sharply reduce the particles generated at the gear teeth.

#### **Attempts to Reduce the Gear Teeth Particles**

The gear teeth were lubricated with a proprietary molybdenum disulfide process. A tribological investigation showed some alumina particles imbedded in the surface where the solid lubricant was applied. The lubricant applicator did indeed prepare the surfaces with alumina beads. A possible cause was identified; some of the alumina beads from the surface preparation were imbedded into the gear surface and caused grinding at the mating gear surfaces and generated the great amount of metal particles.

Gear teeth surfaces were cleaned of the  $\text{MoS}_2$  and alumina beads and were then life cycle tested, but the same failure to operate after a few hundred ratchet wheel cycles was observed (Table 2). The post-mortem inspection again showed many metal particles at the gear teeth wear zones and scattered on the nearby mounting plate and stop pins. The inboard solenoid rotor had much rougher manual rotation than the outboard rotor. The wear zone on the inboard rotor gear tooth was broader at the base as shown in Figure 3, rather than a more parallel wear zone observed in the outboard rotor gear tooth.

**Table 2. Ratchet wheel rotations to failure, no MoS<sub>2</sub> on gears, no MoS<sub>2</sub> on bearings**

<i>Unit #</i>	<i>Date</i>	<i>Wheel cycles</i>	<i>Observations</i>
CP005	01 Feb 2003	82	Rough manual rotation
CP008	12 Feb 2003	180	Rough manual rotation
CP009	14 Feb 2003	260	Rough manual rotation

The original outboard gear on the solenoid was Ph 13-8 Mo, condition H1150, as were the drive arms. A wear-resistant stainless steel, Nitronic 60 by Armco, was used as a trial for the outboard rotor gear. Even though the high-speed videos showed slow and erratic return of the inboard rotor, the outboard gear was a part that could be quickly made with a new material and if successful in producing fewer wear particles, then the drive arms could be made with the wear resistant material.

Several units with the wear resistant outboard gear were tested with the same disappointing result: the units failed to operate after a few ratchet wheel cycles, and there was a thick powdered layer at the wear zone on the gear teeth (Table 3 and Figure 5). The wear zone on the new outboard gear appeared to be even heavier than the wear zone on the trials from Tables 1 and 2. The rotors spun roughly after the life test. The bearings were observed to have a roughened surface on the inboard rotor, but only slightly roughened on the outboard or stator bearings. The long stringers observed in Figure 5 on the edge of the gear are composed of many fine particles that are magnetized. These magnetized stringers appear at the edges of other parts as well as the gear teeth. A schematic of the solenoid is shown in Figure 6. The solenoid bearings from left to right will be numbered 1 through 4 in many of the descriptions to follow. The outboard rotor bearings are 1 and 2 while the inboard rotor bearings are 3 and 4.

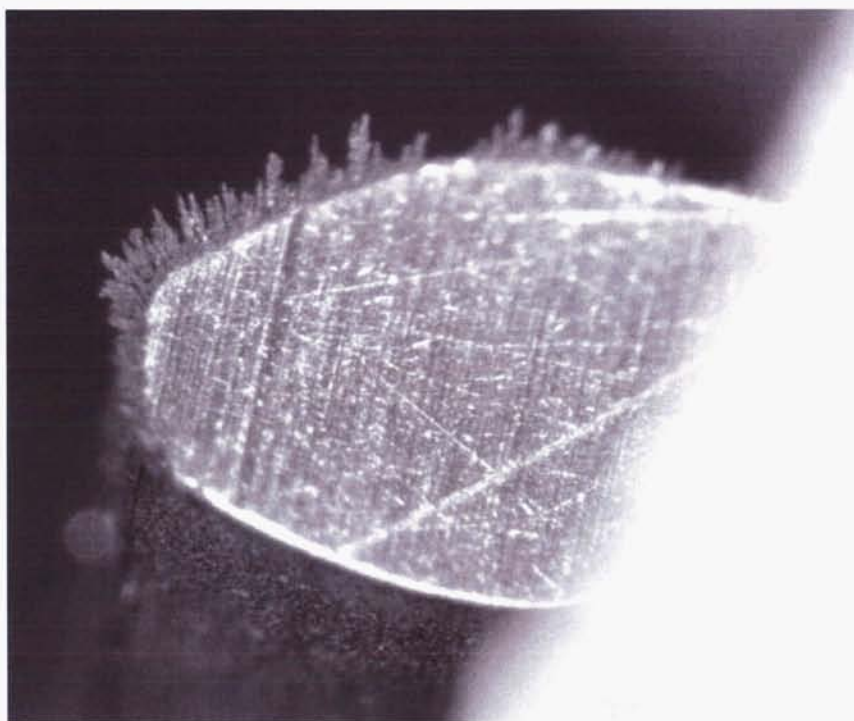


**Figure 5. Wear particles generated due to a Nitronic 60 gear tooth interface**



**Table 3. Ratchet wheel rotations to failure, Nitronic 60 gear, no MoS<sub>2</sub> on gear or bearings**

	<i>Date</i>	<i>Wheel cycles</i>	<i>Observations</i>
CP011	20 Feb 2003	72	Bearings 3 and 4 bad, bearings 1 and 2 fair
CP037	20 Feb 2003	280	Bearings 3 and 4 bad, bearings 1 and 2 fair
CP034	21 Feb 2003	220	Bearing 3 very bad

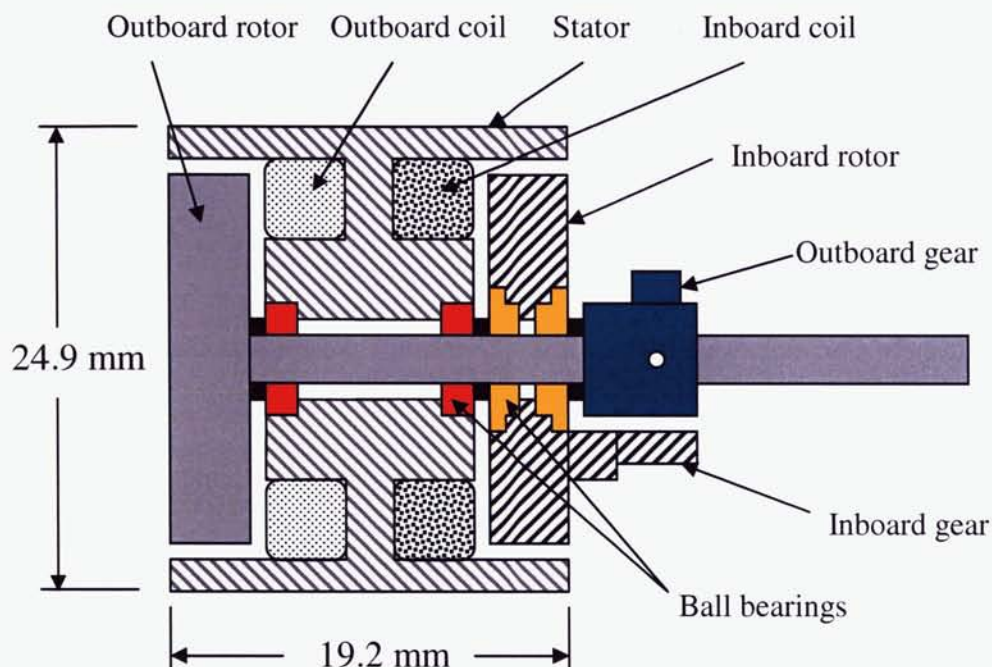


**Figure 6. Double rotary solenoid; outboard and inboard rotors move independently.**

A new trial was performed with MoS<sub>2</sub> to the applied gear teeth, but with the surfaces prepared by acid etching rather than alumina bead blasting as in the original condition of Table 1. The desire was a drastic reduction of wear particles at the gear teeth. Again, low ratchet wheel cycles to failure were measured and a heavy powdered layer at the gear teeth was again observed (Table 4). The third replication that failed at wheel cycle 518 was encouraging, but the two replications that failed at low cycles indicate that the condition of Table 4 is similar to the first three conditions. The unit that failed at 518 cycles was examined carefully in the post-mortem, but resulted in no clues regarding its much longer operating life.

**Table 4. Ratchet wheel rotations to failure, MoS<sub>2</sub> on gears without grit blasting**

<i>Unit #</i>	<i>Date</i>	<i>Wheel cycles</i>	<i>Observations</i>
CP045	27 Feb 2003	110	--
CP054	27 Feb 2003	90	Inboard rotor rotates very roughly
CP021	03 Mar 2003	518	Inboard rotor bearing seized

The baseline condition of Table 1 and the trials or fixes of Tables 2, 3 and 4 all had similar results. The units failed to operate at low number of wheel cycles, there were many wear particles at the gear teeth, the high speed videos showed erratic and stalled energized strokes of the inboard rotor, and the inboard rotor bearings were very worn while the outboard rotor bearings wear showed little or moderate wear.

### **A Temporary Solution – Bearing Shields**

As our early efforts to decrease particle generation at the gear teeth were unsuccessful (Tables 2-4), we looked for a quick solution; so that environmental and flight tests could continue. A shielded bearing was suggested as a way to prevent the gear teeth particles from entering the solenoid bearings. However, there is not room for standard shielded bearings. The inboard rotor is 3.8-mm thick; the original bearings are 1.6 mm thick, which leaves a 0.6-mm gap between the ball bearings. A shielded bearing of the same inside and outside diameters has a thickness of 2.4 mm that for a pair of bearings is wider than the rotor. The temporary solution was to make thin washers, 50 microns (.002") thick, out of acetate plastic that had the same inside and outside diameters as the bearings and were placed next to the bearings of the inboard rotor. Plastic was used since they could be made quickly. One shield was placed on the inboard rotor bearing next to the outboard gear (bearing 4) as shown in Figure 7, and the other shield was placed between the inboard rotor bearing (bearing 3) and the stator bearing (bearing 2).

These shields were placed in test units with no  $\text{MoS}_2$  on the gears or bearings and had encouraging results as shown in Table 5. Finally, most units run at least 500 wheel cycles. The initial solenoid torque tests showed no increase in friction due to addition of the plastic shields. After the life tests, the shields showed a darkened annulus where the bearings were sliding, but the plastic was not grooved. A workable solution appeared possible. The shields appeared to be protecting bearings 3 and 4 since tested units now had some bad bearings at position 1 with some good bearings at position 4.

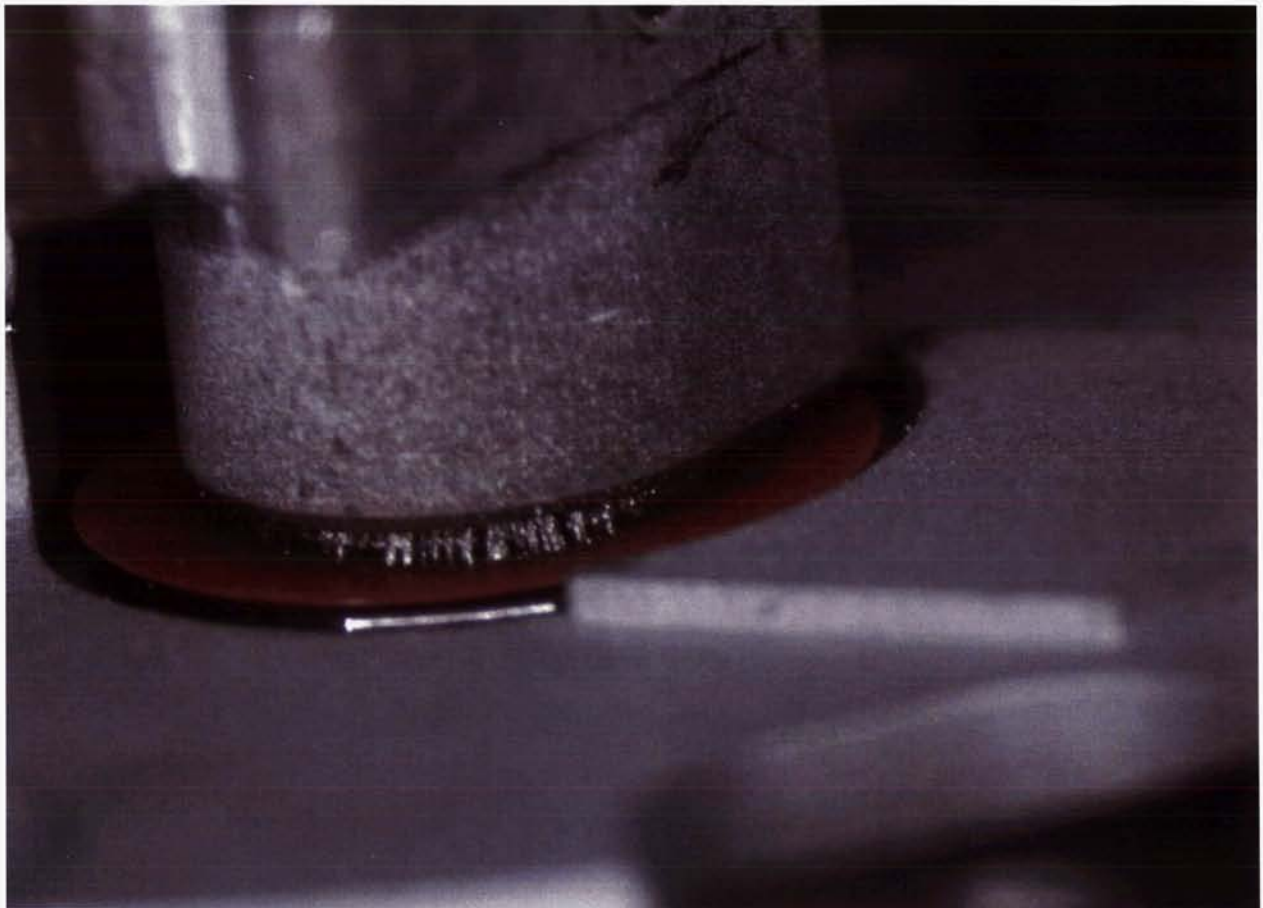


**Figure 7. Plastic shields were used to keep particles out of the solenoid bearings**



**Table 5. Wheel rotations to failure, plastic shields over bearings, no MoS<sub>2</sub> on gears or bearings**

<b>Unit #</b>	<b>Date</b>	<b>Wheel cycles</b>	<b>Observations</b>
CP046	03 Mar 2003	524	Failed, bearing 1,3, 4 – bad, bearing 2 - good
CP014	03 Mar 2003	520+	No failure, bearing 1 – bad, 2 – fair, 3, 4 - good
CP020	04 Mar 2003	820+	No failure, bearing 1,3 – bad, , bearing 2,4 - good
CP016	13 Mar 2003	404	Failed, bearing 1, 4 – bad, bearing 2 , 3 - fair

Ball bearings with MoS<sub>2</sub> lubricant were received and put into solenoids with the plastic shields next to the inboard ball bearings and were cycle tested with very favorable results (Table 6). A fix or a solution to our early wheel cycle failure was found. The solenoid used in the first test of CP028 showed an unrelated assembly issue, resulting in a frictional rub between the inboard rotor and the stator. After being rebuilt with an additional 13-micron shim added under the inboard rotor but with the original bearings, the second cycle test of CP028 performed very well.

**Table 6. Wheel rotations to failure, plastic shields over bearings with MoS<sub>2</sub>, no MoS<sub>2</sub> on gears**

<b>Unit #</b>	<b>Date</b>	<b>Wheel cycles</b>	<b>Observations</b>
CP046	21 Mar 2003	1014+	No failure, bearing 1, 2, 3, 4 - good
CP048	25 Mar 2003	1000+	No failure, bearing 1, 2 – fair, bearing 3, 4 - good
CP028	25 Mar 2003	52	Failed, bearings – good, inboard rotor rub
CP028	26 Mar 2003	1000+	No failure, bearing 1, 3, 4 – good, bearing 2 - fair

As previously discussed, the dynamic axial load was 71 N versus the manufacturer's rated load of 116 N. Since our load condition is a small reversing stroke rather than continuous rotation, the duty is more severe than the rated condition. The dry film lubrication used in the bearings of the units of Table 6 appears beneficial when compared to the dry bearings of Table 5 and confirms the bearing manufacturer's recommendation that lubrication becomes more important as the bearings are more severely loaded.

The drive arm bearings are very close to the gear teeth but did not show any wear when compared to the solenoid bearings. Many of the gear particles stayed on the gear teeth as shown in Figures 3 and 5, but some of the particles will migrate to other parts as shown in Figures 7 and 8. The electric coils in the solenoids produce a magnetic flux field when the coils are energized. The flux field is in the shape of a toroid that makes a complete loop about the coil from the inside coil diameter to the outside coil diameter. Most of the flux passes through the rotor and stator due to the high permeability of electrical iron, but some flux passes through the air between the races of the bearings. Loose magnetic particles will align on these flux lines and then move along the flux lines to high magnetomotive force. Some of the particles are pulled into the bearings where they become scabs as the balls roll against the races.

The large axial loads on the solenoid rotors are present only when the coils are energized. The wear particles are pulled into the bearings and rolled flat when the coils are energized; the rotors are returned to their home positions by helical extension springs. Hence, the slower and erratic motion of the rotor was observed during the energized stroke only and not during the return stroke. Likewise, a manual rotation and a zero-volt solenoid torque test would not show the large friction that is present when the coil is energized. The inboard rotor motion was erratic and caused the operational failure since the inboard rotor bearings are very close to the gear teeth and the resulting wear particles. When the plastic shields are in place as shown in Tables 5 and 6, the inboard bearings (3 and 4) are not consistently worse than the outboard bearings (1 and 2).



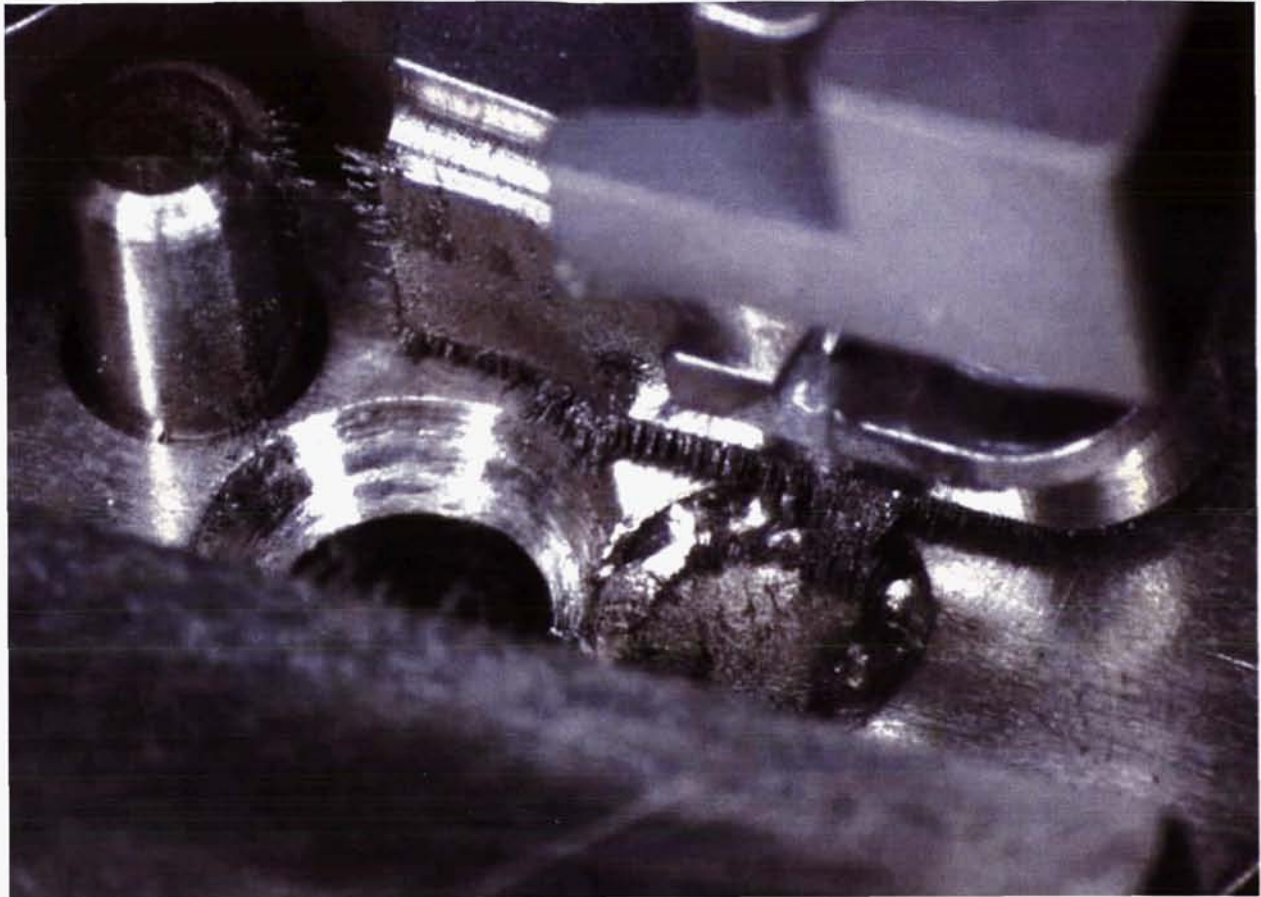


**Figure 8. Particles scattered on the mounting plate**

### **Why so many gear teeth particles?**

The tribological investigation continued to evaluate material pairs or lubrication that would decrease the gear particles. Some standard pin on disk tests at a high contact stress showed long life of the  $\text{MoS}_2$  lubricant and little particle generation. This caused us to calculate the Hertzian contact stress [2] at the gear teeth. The contact stress was 753 MPa (109 ksi). This exceeds the yield strength of the Hiperco 50A, 365 MPa (53 ksi), used for the inboard rotor, the wear resistant stainless steel, Nitronic 60, 414 MPa (60 ksi), used for the outboard gear in one of the trials, and the drive arms PH 13-8 Mo, condition H1150, 620 MPa (90 ksi). The contact stress was undoubtedly higher on the single cantilevered gear tooth of the inboard rotor since it deflects during loading and the wear zone on the tooth was more triangular than rectangular. Figure 3 shows just such a wear zone on the drive arm gear tooth that mates with the inboard rotor gear tooth. The single gear tooth was analyzed for bending stresses at the base during the initial design but the Hertzian contact stresses were not calculated for the contact load at the gear teeth. The high contact stresses mean plastic deformation at the load zones, non-rolling contact and resultant particle generation.

### **Long term solution – eliminate the gear teeth**

The plastic shield was a fix that permitted further testing of the first build. However, the many particles were undesirable and created a potential for other problems. A long-term solution was desired where few particles were generated. Increasing the gear pitch or the length of the gear teeth to decrease the contact stress by a factor of two or three was not possible due to the volume constraints. In addition, the single gear tooth on the inner rotor and the drive arms made these expensive parts and difficult for part



acceptance. Changing the solenoid design from a single shaft to two solenoids side by side was considered, but rejected as too drastic a change.

The change selected was to use ball bearings as followers between the solenoid and drive arms. The space was limited but the small 1.0-mm by 3.2-mm ball bearing could be made to fit. See Figure 9 and compare to Figure 2. The contact load was high but within the manufacturer's limits of 4,000 MPa (580 ksi). This change was implemented on the subsequent group build, and has been successful with long ratchet wheel cycles before mechanism failure. There are a few dark particles after a ratchet wheel cycle test, but they are located at stop pins and not at the bearing followers that actuate the drive arms.

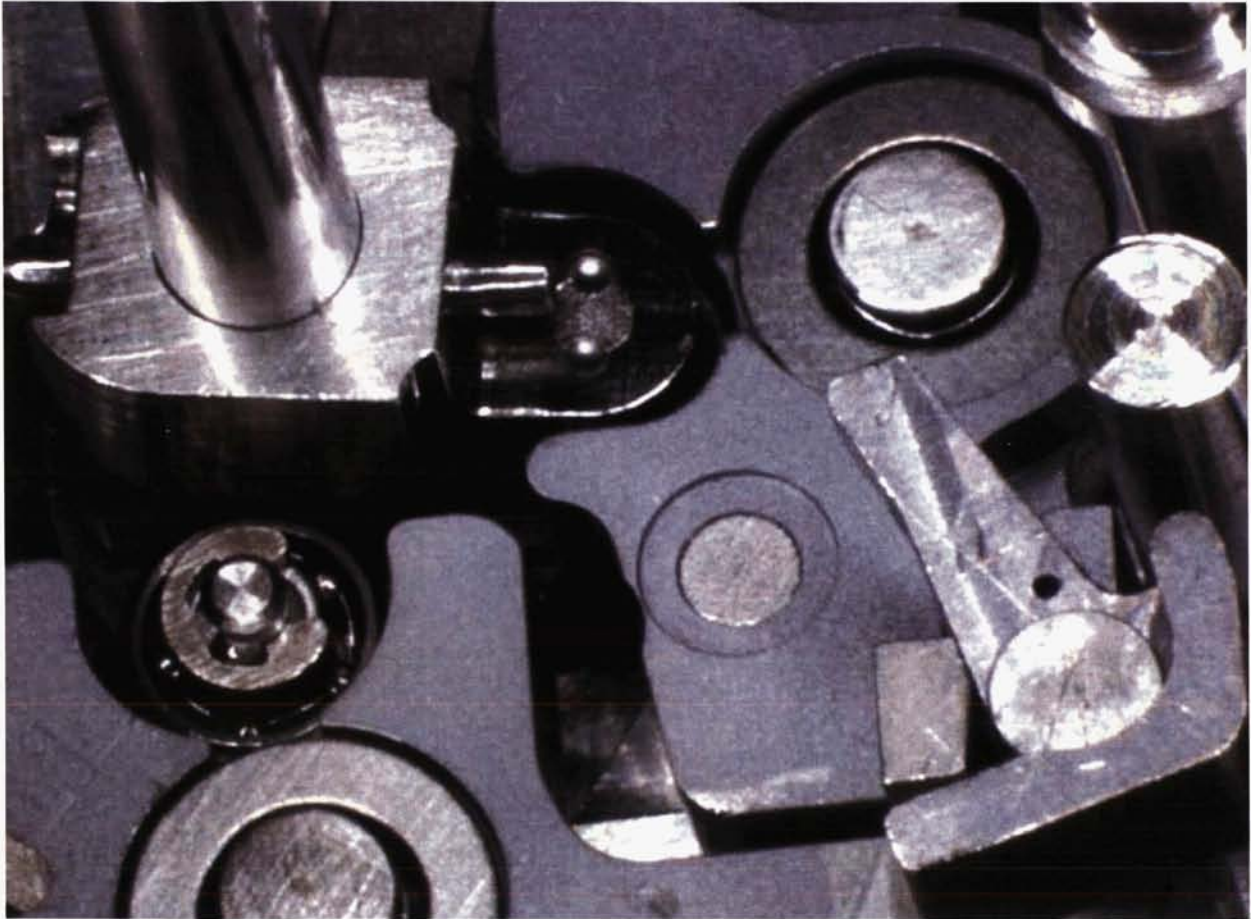


**Figure 9. Ball bearings now transfer the torque from the solenoid to the drive arms**

### **Conclusion**

Due to volume constraints and the desire for a simple assembly, single gear teeth were made as integral part of arms and rotors in a small safety mechanism. The gear teeth were discovered in the prototype to generate many very small particles that were pulled into the bearings of the adjacent solenoid and caused very early failures in life tests. The cause of the particle generation was contact stresses exceeding the yield strength of the gear teeth. The lesson learned was to prioritize our efforts in analysis and failure mode prediction on new or unfamiliar design concepts that are incorporated into a mechanism. An ancillary lesson is to consider and evaluate additional concepts when moderate or high risks are identified in the base design.

## References

1. D.W. Plummer and W.H. Greenwood (1993). *A Primer on Unique Signal Stronglinks*, SAND93-0951, Sandia National Laboratories, Albuquerque, NM.
2. J.E. Shigley and C.R. Mischke (1989). *Mechanical Engineering Design*, 5<sup>th</sup> edition, McGraw-Hill, New York City, NY.

# **Failure of Harmonic Gears During Verification of a Two-Axis Gimbal for the Mars Reconnaissance Orbiter Spacecraft**

Michael R. Johnson\*, Russ Gehling\*\*and Ray Head\*\*

## **Abstract**

The Mars Reconnaissance Orbiter (MRO) spacecraft has three two-axis gimbal assemblies that support and move the High Gain Antenna and two solar array wings. The gimbal assemblies are required to move almost continuously throughout the mission's seven-year lifetime, requiring a large number of output revolutions for each actuator in the gimbal assemblies. The actuator for each of the six axes consists of a two-phase brushless dc motor with a direct drive to the wave generator of a size-32 cup-type harmonic gear. During life testing of an actuator assembly, the harmonic gear teeth failed completely, leaving the size-32 harmonic gear with a maximum output torque capability less than 10% of its design capability.

The investigation that followed the failure revealed limitations of the heritage material choices that were made for the harmonic gear components that had passed similar life requirements on several previous programs. Additionally, the methods used to increase the stiffness of a standard harmonic gear component set, while accepted practice for harmonic gears, is limited in its range. The stiffness of harmonic gear assemblies can be increased up to a maximum stiffness point that, if exceeded, compromises the reliability of the gear components for long life applications.

## **Introduction**

### The Mars Reconnaissance Orbiter Mission

During its two-year primary science mission, the Mars Reconnaissance Orbiter will conduct eight different science investigations at Mars. The investigations are functionally divided into three purposes: global mapping, regional surveying, and high-resolution targeting of specific spots on the surface. This detailed mapping of the surface of Mars will provide future landed missions with the high resolution data required to land safely in a desired area. The instruments on board the MRO spacecraft consist of five types: cameras, a spectrometer, a radiometer, a radar, and engineering. Refer to Figure 1 for an overall view of the MRO spacecraft's science deck.

### Cameras

#### HiRISE (High Resolution Imaging Science Experiment)

This visible camera can reveal small-scale objects in the debris blankets of mysterious gullies and details of geologic structure of canyons, craters, and layered deposits.

#### CTX (Context Camera)

This camera will provide wide area views to help provide a context for high-resolution analysis of key spots on Mars provided by HiRISE and CRISM.

#### MARCI (Mars Color Imager)

This weather camera will monitor clouds and dust storms.

### Spectrometer

#### CRISM (Compact Reconnaissance Imaging Spectrometer for Mars)

This instrument splits visible and near-infrared light of its images into hundreds of "colors" that identify minerals, especially those likely formed in the presence of water, in surface areas on Mars not much bigger than a football field.

---

\* Jet Propulsion Laboratory, California Institute of Technology, Pasadena, CA

\*\* Lockheed Martin Space Systems, Denver, CO



#### Radiometer

##### MCS (Mars Climate Sounder)

This atmospheric profiler will detect vertical variations of temperature, dust, and water vapor concentrations in the Martian atmosphere.

#### Radar

##### SHARAD (Shallow Radar)

This sounding radar will probe beneath the Martian surface to see if water ice is present at depths greater than one meter.

#### Engineering

The engineering instruments facilitate spacecraft navigation and communications.

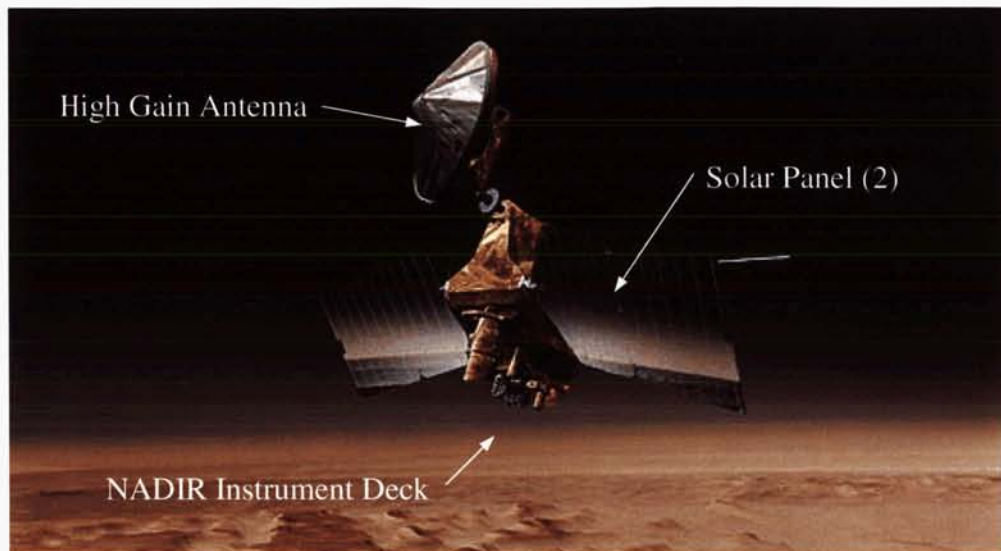


**Figure 1. Artist's Rendering of MRO Spacecraft in Mars Orbit**

Once the science phase is completed (two years after the mapping orbit is established), the MRO mission enters a second phase, communications relay. In this phase, the communication equipment on-board MRO will be used as a communications relay between the Earth and landed crafts on Mars that may not have sufficient radio power to communicate directly with Earth on their own. This capability allows landed crafts to use smaller antennas with reduced mass, improving the lander's science complement potential.

Due to the mapping nature of the mission, the instrument deck of the spacecraft must always be facing the surface of Mars. Additional pointing requirements include maintaining sun pointing of the solar panels and keeping the High Gain Antenna Earth pointed for communication purposes. The solution to this extreme panel and antenna pointing choreography was to put a two-axis gimbal at each of the appendages: two solar array wings and one High Gain Antenna.

The path from Earth to Mars orbit and mapping of the surface consists of launch, cruise, orbit insertion, aerobraking, and mapping phases. The spacecraft configuration of the solar array and the High Gain Antenna are different for each of these phases. During launch, the solar array wings are folded in half and the High Gain Antenna is positioned directly over the spacecraft bus to fit into the launch vehicle fairing (Figure 2). Once MRO is launched and in the cruise phase of the mission, the solar array and High Gain Antenna are pointing in roughly the same direction to capture sunlight and communicate with Earth (Figure 3). For Mars orbit Insertion and aerobraking, the appendages are moved slightly from the cruise configuration to produce an aerodynamically stable configuration. The High Gain Antenna and the solar array wings are the predominant source of atmospheric drag on the spacecraft and must be positioned to keep the spacecraft stable throughout the aerobraking maneuvers, which last for about 6 months (see Figure 4). For the mapping phase of the mission, the solar array wings and High Gain Antenna are almost



continuously articulated so the wings remain sun pointed and the High Gain Antenna maintains a lock on Earth. This continuous motion must be performed while the spacecraft maintains precise pointing for high resolution imaging and high-speed data transmission to Earth (see Figure 1 for a mapping configuration). Because of the stringent pointing stability requirements, the gimbals were required to be exceedingly smooth and quiet.

The different phases for the MRO appendages lead to a large range of requirements for the two-axis gimbal assemblies. The gimbals must be capable of carrying launch loads through their output bearings for the launch phase. The cruise phase is very benign with minimal load on the gimbals. The orbit insertion and aerobraking phases put a significant load on the output bearings and gears, since the loads have a significant component in the backdriving direction for the gimbal actuators. Once the spacecraft is in the mapping phase, the high resolution capability of the instruments on board require that the gimbal assemblies do not produce any significant disturbance to the spacecraft platform while they are continuously scanning to maintain the required pointing of the attached appendage. The gimbals must withstand all of these load combinations and still maintain extreme pointing accuracy and smooth operation once at Mars. In addition to the smooth motion, the lowest structural frequency in the mapping configuration is determined by the natural frequency of the deployed appendages. A major contributor to the frequency of the deployed appendage is the gimbal actuator output stiffness for each axis.



**Figure 2. MRO Launch Configuration**



**Figure 3. MRO Cruise Configuration**



**Figure 4. MRO Orbit Insertion & Aerobraking Configuration**

#### Gimbal Actuator Configuration

Each two-axis gimbal consists of two identical gimbal actuators, structurally connected with application specific components. The core of the actuator is a 130-mm diameter two-phase brushless dc motor with a large number of poles in order to maintain smooth rotor velocity. The brushless motor is commutated using a resolver with the same number of poles as the motor to simplify the commutation logic. The motor directly drives the wave generator of the output harmonic gear component set through a bellows coupling. The bellows coupling was used to minimize speed ripple that would cause disturbances while operating. The harmonic gear is a size-32 HDC, standard-cup-type unit. The flexspline is mounted to the actuator housing and provides the torque reaction mount. The circular spline is mounted in a pair of preloaded angular-contact ball bearings. A multi-speed output resolver is installed between the angular-contact bearings for a compact assembly that measures the output position to the accuracy required for the MRO mission pointing. This arrangement of drive components provides a zero-backlash actuator with minimal mechanically generated disturbance sources and applies all of the externally generated loads directly to the harmonic gear teeth. A photo of a completed flight gimbal actuator assembly is shown in Figure 5.





**Figure 5. Flight Gimbal Actuator Assembly**

The need for the harmonic gear to take the external loads led to the selection of the size of the harmonic gear in concert with the required output stiffness. The available volume and mass allocation for the actuators was minimal on the MRO spacecraft, requiring use of the smallest gears possible to achieve the required load and stiffness capability. The loads from the Mars orbit insertion and aerobraking phases needed to be taken into account along with all other applied loads during the mission. The mass of the solar array wings and the antenna assembly loading the output gear teeth in the acceleration environment of orbit insertion was one source of applied load. The force from aerodynamic loading on the large area array and antenna during aerobraking was another source of loading. These conditions together defined the magnitude of the loads that would be applied to the harmonic gear output teeth in flight. It was determined that the applied loads could be carried with appropriate margins by a size-32, cup-type harmonic gear component set.

The output torsional stiffness of the actuator axes affects the spacecraft dynamics. The spacecraft sensitivity to jitter disturbances and the attitude control system authority dictated a minimum natural frequency for the deployed solar array wings and High Gain Antenna. Since the gimbal actuator was a significant contributor to the overall appendage stiffness and the harmonic gear teeth were the load reacting devices, an output stiffness was required of the chosen harmonic gear that exceeded its standard specification significantly. The magnitude of this stiffness increase for the selected size of harmonic gear was within the range of experience for this type of application on other programs. Since there was no significant difference in the stiffness requirement when compared to other heritage programs, this was not considered a significant risk to the program.

The selection of the harmonic gear materials from the available set involved comparing the MRO requirements with those of previous flight programs in order to maintain as much heritage as possible. A fundamental tenet for this and many programs was to use only corrosion resistant materials in all space mechanisms as is commonly done in the medical, semiconductor, and food processing industries. The materials of the various pieces of the MRO harmonic gear component set are listed in Table 1. This combination of materials had been used successfully in several programs with stiffness and total lifetime revolutions requirements that were similar to MRO. Table 2 lists the other heritage applications of the same material combination with similar functional requirements. To maximize the life cycle capability of all



of the actuator components, Penzane 2001-3PbNp Oil was utilized in the motor bearings and Rheolube 2004 grease was chosen for the lubricant throughout the harmonic gear. Other flight applications with the same material combinations for the harmonic gear components had also used Braycote® because of a much lower operating temperature requirement than MRO. Since the required operating temperature range did not necessitate the use of bray oil or grease, the Penzane lubricant family was chosen since it tends to demonstrate more life capability over the Bray series when the operating temperatures are moderate.

**Table 1. Commercially Available Materials for  
MRO Gimbal Actuator Harmonic Drive Components**

Component	Material	Processing
Circular Spline	15-5 PH	H1075
Flexspline	15-5 PH	H1075, Melonite case harden
Wave Generator	15-5 PH	H1075
Bearing	440C	

Note: The Melonite process is a Nitrocarburizing case hardening per SAE-AMS-2753B

#### Hardware Verification

The motor and gearbox assembly was the same for all of the six axis applications on MRO, allowing one life verification to be performed on the worst case loaded design that would encompass all of the other five axis applications on MRO. The life verification program for these actuators consisted of operating a harmonic drive assembly alone in ambient environment with standard lubrication, followed by operation of an assembled flight-like actuator assembly in a vacuum with thermal cycling and a representative wiring harness for loading of the output gear.

The lone harmonic drive gear assembly was operated in a standard gear test fixture used at the harmonic drive vendor. This was performed at ambient pressure and temperature in a bath of low viscosity commercial oil at an input speed of 1750 RPM and with an applied load on the output that matched the cable loading from harnesses. The wave generator was driven for 32 million revolutions with no sign of unusual wear or failure of the bearing or the gear teeth. This was done without incident to a rotational life of five times the flight requirement of 6.2 million input revolutions, indicating harmonic gear rotational lifetime was a low risk.

Next an Engineering Development Unit (EDU) actuator was operated in a flight-like configuration. The EDU actuator used the flight housings with output hardware that supported the High Gain Antenna cable management system. The cable management system was incorporated to cycle the cabling as well as provide flight like output loading to the harmonic gear. The High Gain Antenna application was chosen because it has the largest number of cables across any of the gimbal axes. The EDU actuator was operated over a total output angle of 340 degrees. The EDU actuator was run in a thermal/vacuum environment, with the temperature slowly cycled from -25°C to +40°C at the rate of one thermal cycle every 18 hours. The actuator was driven at a motor rate of 125 RPM for approximately 3.8 million input revolutions, and then run at 65 RPM for the remainder of the time. The EDU motor was driven with an industrial stepper motor driver, severely limiting visibility into the performance of the actuator. The stepper motor driver was used for this operation for several reasons: flight actuator drivers were not available for the start of the running, the motor is a two-phase brushless dc (not three phase), and the rotary life was believed to be low risk so the limited visibility was not considered to be significant. The EDU life setup is shown in Figure 6.

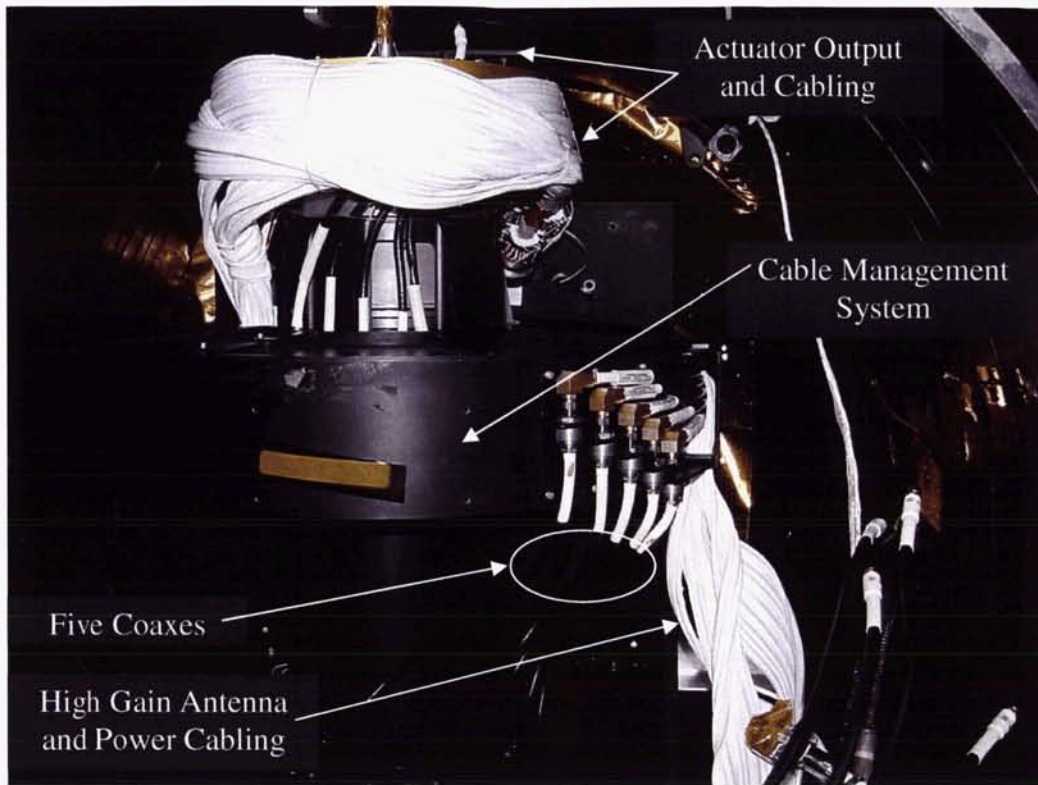


**Figure 6. Engineering Development Unit Configuration in Vacuum Chamber**

**Table 2. Materials and Surface Finishes of Heritage Hardware from Previous Programs with Similar Stiffness and Life requirements as the MRO Applications**

<b>Program (Harmonic Drive Size)</b>	<b>Circular Spline</b>	<b>Flexspline</b>	<b>Lubricant</b>
MRO (size 32)	15-5 PH H1075	15-5 PH H1150 Melonite	Penzane 2001-3Pb Rheolube 2004
Program #1 (size 20)	15-5 PH H1075	15-5 PH H1150 Melonite	Braycote 602 Bray 815Z oil
Program #2 (size 25)	15-5 PH H1150	15-5 PH H1075 Melonite	Penzane 2001-3Pb Rheolube 2004
Program #3 (size 32)	15-5 PH H1150 Melonite	15-5 PH H1075	Penzane 2001-3Pb Rheolube 2004
Program #4 (size 40)	15-5 PH H1150 Melonite	15-5 PH H1075	Penzane 2001-3Pb Rheolube 2004
Program #5 (size 32)	15-5 PH H1075	15-5 PH H1150 Melonite	Rheolube 2000 with 3% lead Napthenate

The EDU actuator operated up to 6.1 million input revolutions, when the output telemetry indicated the actuator was not following the input signals properly. Later analysis revealed there were indications of improper operation as early as 4 million input revolutions that were not diagnosed due to limitations in the test setup with the stepper motor driver. The EDU actuator was removed from the chamber, disassembled, and inspected. Figures 7, 8, and 9 show the condition of the harmonic gear teeth at this inspection. Note that the tooth profile was completely obliterated and damaged across the entire width of the flexspline teeth and most of the width of the circular spline.

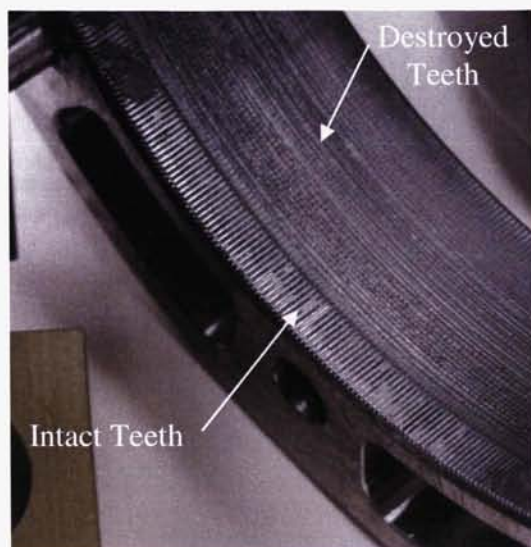


**Figure 7. EDU Circular Spline Life Damage**



**Figure 8. EDU Flexspline Life Damage**

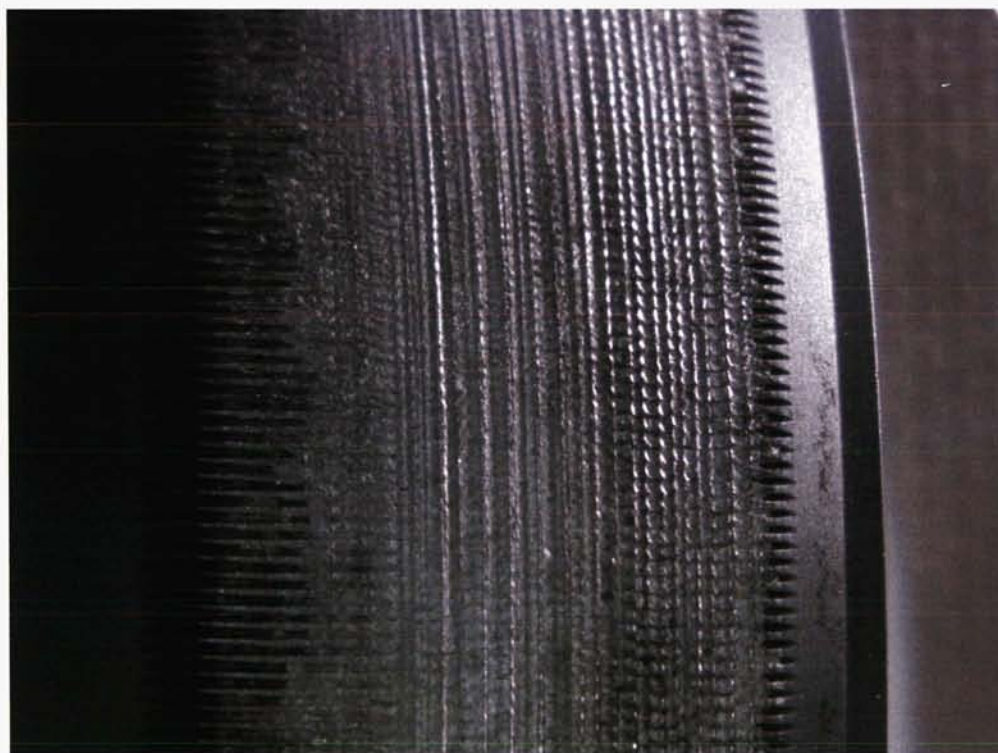


**Figure 9. Magnification of EDU Flexspline Life Test Damage**



Once the dramatic failure of the harmonic gear assembly was seen, a detailed review of the manufacturer's documents uncovered that there were some problems with the Melonite coating on the group of flexsplines that included the life unit, labeled Lot B. Two additional Melonite processing groups of flexsplines had been received at the time of the failure, labeled Lot C and Lot D. Operation of these units was started to determine if the Melonite processing on the EDU life test unit was the source of the failure. A harmonic assembly from each of the two remaining Melonite process groups was placed in a harmonic gear fixture (not in the gimbal actuator) and operated in vacuum with thermal cycling over a 12-hour period, an output load, and an input speed of 130 RPM. Additionally, one of the two units was tested using the same Penzane family of lubricants as the EDU and the other was tested using Braycote® 602. Both assemblies failed at approximately two million input revolutions. Figure 10 shows the failed splines that were tested with the Penzane family of lubricants. Figure 11 shows the failed splines that were tested with the Braycote® 602 lubricant. A significant result of these two tests was that the lubricant type made no difference at all, with both assemblies failing at nearly the same number of revolutions with the same type and level of damage.

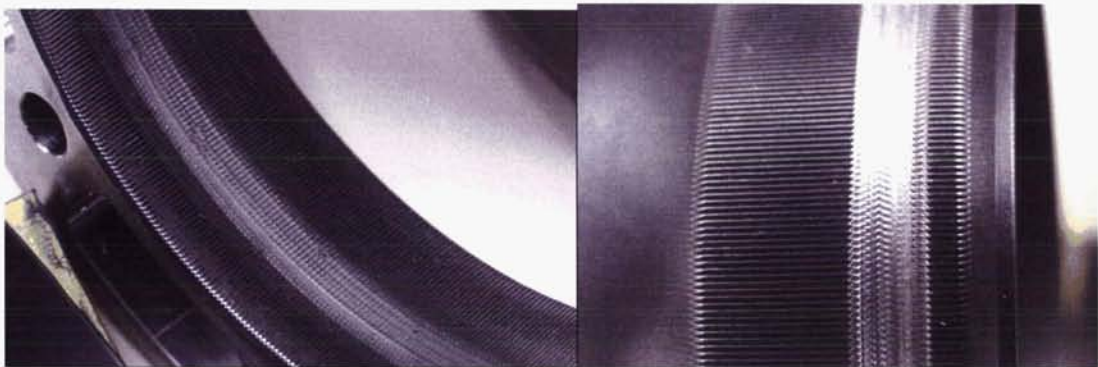


**Figure 10. Circular Spline and Flexspline from Harmonic Only Test #1  
Tested with Penzane**

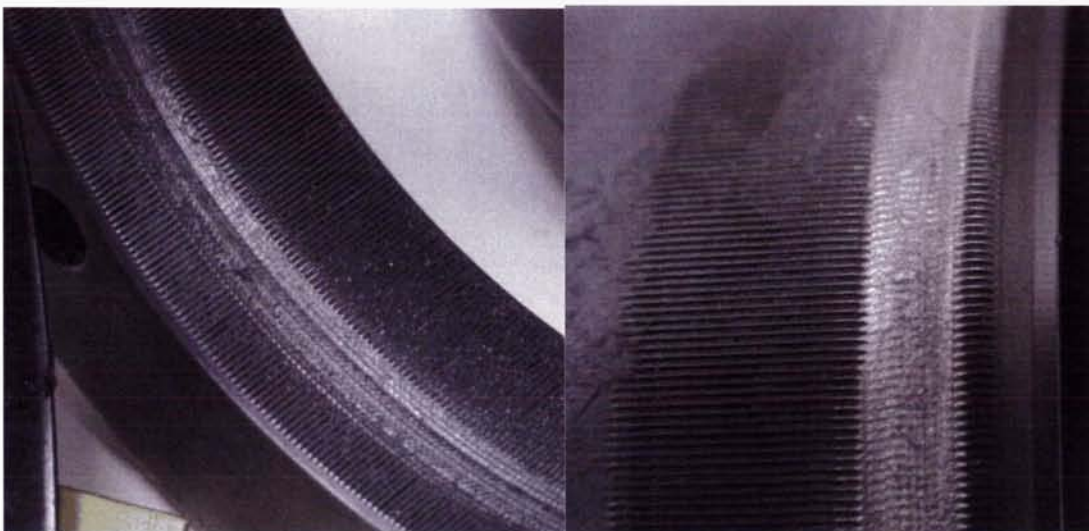


**Figure 11. Circular Spline and Flexspline from Harmonic Only Test #2  
Tested with Braycote® 602**



Since the lubricant type made absolutely no difference in the life capability of the harmonic drive gear teeth, it was clear the problem was related directly to the material combination of the components and their internal stress level. The appearance of the failure surfaces gave the impression of a possible galling condition at work, but it was not clear if galling was the initiator of the failure or a consequence of the damage once the failure had been initiated. Rough mathematical analyses were performed to estimate the contact stress at the harmonic gear teeth from the preload and under the applied load in the operation. The constant external load in the harmonic fixture runs represented the worst-case load from the cable management system and was responsible for a roughly 40% increase in tooth contact stresses over the preload. The estimated contact stresses in the EDU life test were in the realm of 750 MPa. The galling threshold listed for a 15-5 PH stainless steel contact pair is around 14 MPa. This indicated that the contact stresses compared to the galling threshold for the selected materials was a strong candidate for the cause of the failures. To minimize the schedule time to a solution, the next group of tests used Nitronic 60 (another available harmonic gear material) with a listed galling threshold value greater than 345 MPa. Nitronic 60 was identified as a candidate in addition to other standard commercial materials for the harmonic gear assemblies, like nodular iron. Also, the output stiffness of the assembly was reduced so the internal harmonic gear preload (and with it the internal tooth stresses) could be reduced as well. At this point in the project schedule, the flight solar array panels had been fabricated and their stiffness was measured, allowing reduction of the stiffness margin for these panels in the MRO spacecraft stability analysis. This made it possible to reduce the gimbal actuator stiffness requirement significantly.

To investigate these issues within the remaining program schedule, three readily available harmonic drive assemblies were procured with different material combinations and tested on the harmonic gear fixture. The material combinations consisted of a unit with a nodular iron circular spline and an E4340 flexspline. The second unit had a Nitronic 60 circular spline and an E4340 flexspline. The third assembly was composed of a Nitronic 60 circular spline with an E4340 flexspline processed with a Melonite surface. Additionally, the internal preload of the harmonic gear (to obtain the new required output stiffness) was reduced in order to lower the gear tooth internal stresses. Table 3 lists all of the life test units and the material and lubrication configuration for each.

**Table 3. Selected Harmonic Gear Material and Lubricant Configurations**

Test Unit	Circular Spline Material	Flexspline Material	Flexspline Surface Treatment	Lubricant
Harmonic drive vendor Unit #1	15-5 PH, H1075	15-5 PH, H1075	Melonite, Lot C	Rheolube 2004 grease Nye 2001-3PbNp oil
EDU Assembly #1 (in actuator)	15-5 PH, H1075	15-5 PH, H1075	Melonite, Lot B	Rheolube 2004 grease Nye 2001-3PbNp oil
LM Harmonic Assembly #1 (same unit as Harmonic drive vendor Unit #1)	15-5 PH, H1075	15-5 PH, H1075	Melonite, Lot C	Rheolube 2004 grease Nye 2001-3PbNp oil
LM Harmonic Assembly #2	15-5 PH, H1075	15-5 PH, H1075	Melonite, Lot D	Braycote® 602
LM Harmonic Assembly #3	Nodular Iron	E4340 Steel	None	Rheolube 2004 grease Nye 2001-3PbNp oil
LM Harmonic Assembly #4	Nitronic 60	E4340 Steel	None	Rheolube 2004 grease Nye 2001-3PbNp oil
LM Harmonic Assembly #5	Nitronic 60	E4340 Steel	Melonite, Lot E	Rheolube 2004 grease Nye 2001-3PbNp oil
EDU Assembly #2	Nitronic 60	E4340 Steel	None	Rheolube 2004 grease Nye 2001-3PbNp oil

Note: LM stands for Lockheed Martin

The test units for LM Harmonic Assemblies #3, #4, and #5 were tested in the harmonic drive test fixture, in the environment, with the applied load and input speed listed in Table 4. The stiffness of the units was measured at the start of the testing as shown in column 2 of Table 4. The life tests already discussed are listed in Table 4 for completeness.

**Table 4. Life Unit Stiffness, Environments, Conditions, and Revolutions at Failure**

Test Unit	Initial Stiffness with 45/140 N·m Applied Torque (N·m/rad)	Environment	Applied Load on Output	Input Speed	Approx. Revolutions to failure
Harmonic drive vendor Unit #1	Approx. 68,000	Ambient	11.3 N·m	1750 RPM	No Failure
EDU Assembly #1 (in actuator)	> 56,000	Vacuum, -25°C/+40°C 18 hour cycles	HGA Cable Harness	125 RPM & 65 RPM	4M
LM Harmonic Assembly #1 (same unit as Harmonic drive vendor Unit #1)	Approx. 68,000	Vacuum, -15°C/+40°C 12 hour cycles	11.3 N·m	130 RPM	2M
LM Harmonic Assembly #2	69,000/75,000	Vacuum, -15°C/+40°C 12 hour cycles	11.3 N·m	140 RPM	2M
LM Harmonic Assembly #3	56,000	Vacuum, -15°C/+40°C 12 hour cycles	11.3 N·m	140 RPM	4M
LM Harmonic Assembly #4	55,600/60300 56,500 (28 N·m) 43,800 (28 N·m)	First 3M revs Vacuum, -15°C/+40°C 12 & 24 hour cycles Next 3M revs Vacuum, +23°C constant Next 8M revs Vacuum, -10°C constant	11.3 N·m	140 RPM	No Failure @ 14M
LM Harmonic Assembly #5	54,600/61,000 43,800 (28 N·m)	Vacuum, -10°C/0°C constant	11.3 N·m	140 RPM	No Failure @ 9.1M
EDU Assembly #2	37,300 to 46,300 (28 N·m)	Vacuum, -10°C/+10°C constant	HGA Cable Harness	60 RPM	No Failure @ 13M

Key results of the above are as follows:

- The high input speed of the harmonic gear only operation performed at the harmonic drive vendor allows the lubricant to support high contact stresses that would otherwise result in complete failure of the gear teeth.
- The difference from the EDU Assembly #1 unit and the LM Harmonic Assembly #1 was the Melonite lot and coating details. The results of the LM Harmonic Assembly Unit #1 showed that the Melonite coating was not involved in the failure.
- The applied output load, while small when compared to the maximum torque capability of the harmonic gear, made a difference in the revolution life to failure. Note that the EDU life unit exhibited failure around 4 million revolutions, while assemblies #1 and #2, with a constant applied load, failed at 2 million revolutions. This difference could be due to the EDU assembly #1 using a cable wrap harness, with a variable load depending on output position, compared to a constant load.



- LM Harmonic Assemblies #1 and #2, with failure at a similar number of revolutions using very different lubricants, indicated the lubricant was not a significant player in the failure mechanism. This eliminated the lubricant as a variable in further failure investigation.
- The LM Harmonic Assembly #3, with nodular iron and a reduced preload, had a longer life to failure than the stainless steel, supporting the galling hypothesis. Note the regions of damage in Figure 12.
- The LM Harmonic Assemblies #4 and #5 used Nitronic 60 for the circular spline, the highest galling threshold material that could be obtained in a harmonic gear assembly. The late date of the testing permitted a reduction of the output stiffness to two-thirds of the initial values used for the gimbal actuators. The stiffness of the unit in Harmonic Assembly #4 was reduced as the operation progressed and a method of setting the harmonic gear preload was established. The result of the run was no failure at all with some minor wear of the harmonic gear teeth, as shown in Figure 13. The schedule dictated that the first successful combination be used, so the final material selection was a Nitronic 60 circular spline and a flexspline of E4340 with no additional surface processing. Note that schedule dictated changing more than one variable at a time.
- The setting of the internal preload of the harmonic gear assembly during assembly at the harmonic drive vendor was critical in achieving the required output stiffness without compromising the reliability of the harmonic gear assembly.

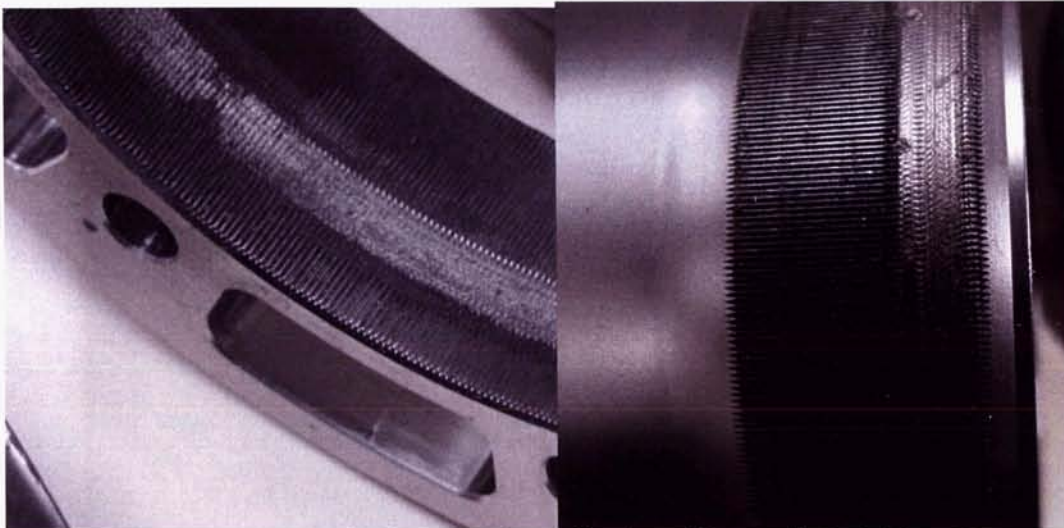


**Figure 12. Circular Spline and Flexspline from Harmonic Only Test #3**

Note the damaged regions show where the flexspline was engaged with the circular spline.

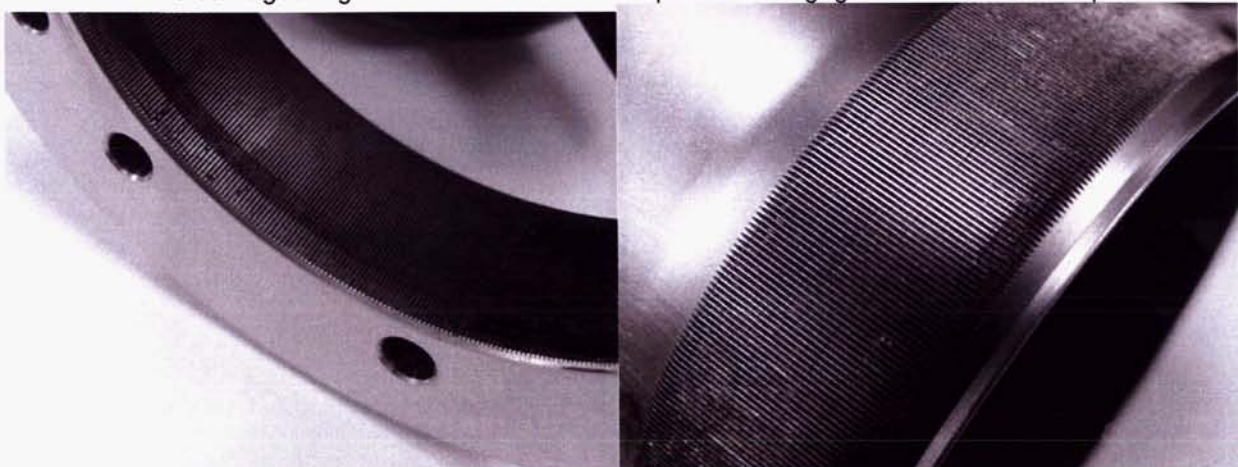


**Figure 13. Circular Spline and Flexspline from Harmonic Only Test #4**

Note the slight wear region on the circular spline showing where the flexspline was engaged with it.



#### Harmonic Gear Assembly Internal Preload Setting

The cup type harmonic gear assembly has zero backlash due to the angle of approach, along the rotation axis, of the flexspline teeth relative to the circular spline teeth (Figure 14). This arrangement leads to a two-sloped stiffness curve of the output of a harmonic gear. As torque is applied to the gear, the cup flexes to allow more of the width of the teeth to engage with the circular spline. As more tooth area is engaged, more load sharing occurs and the stiffness increases. Once the angle between the teeth of the splines is reduced to near zero, the stiffness has reached its maximum value. As the torque is increased from this point, the stiffness is related to deflection of the individual teeth and the change in roundness of the housing and circular spline. Figure 15 shows a stiffness curve for a typical harmonic gear assembly prior to increasing the internal preload for stiffness improvement.

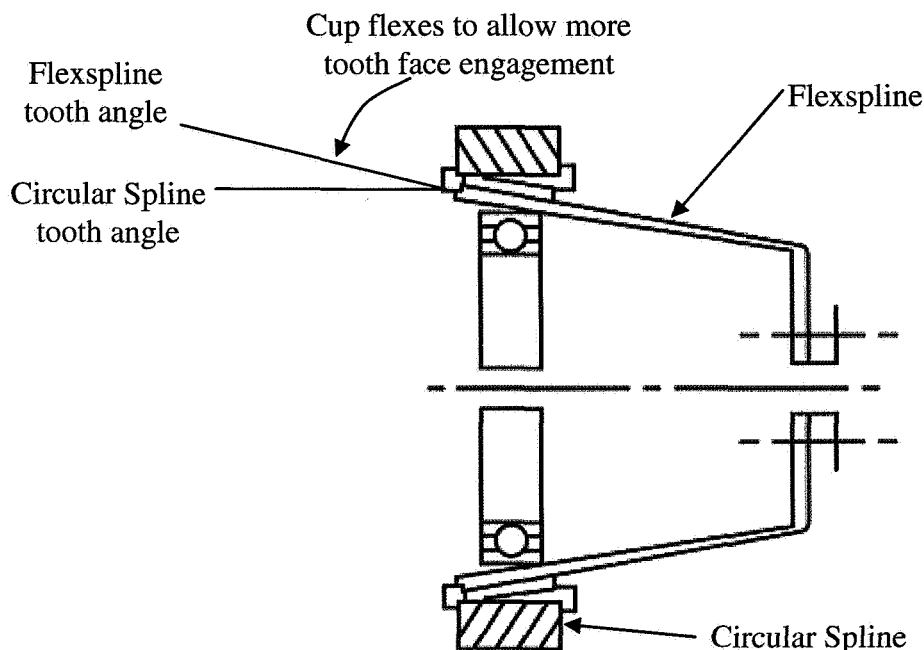


**Figure 14. Harmonic Drive Cross Section Showing Significant Source of Variable Stiffness**

Note the largest stresses on flexspline teeth occur at the point of initial contact, the open end of the cup.

*Drawing courtesy of Harmonic Drive, LLC*

Increasing the output stiffness of a harmonic drive assembly involves increasing the diameter of the wave generator in the area where it forces contact between the teeth of the two splines. This is accomplished by using a different wave generator plug with a larger major diameter of the oval. As the diameter is increased, the flexspline cup is deflected in the direction of engaging more of the face of the teeth. This has the same effect as increasing the torque on a nominal unit in the low stiffness region. As the wave generator plug size is increased, the low stiffness region gets smaller. This trend continues until the stiffness curve is essentially straight. At this point, a further increase in the diameter of the wave generator plug will increase the overall gear assembly stiffness and significantly increase the internal tooth stresses. Figures 16 through 19 show the how the shape of the stiffness curve changes with different wave generator plugs in a harmonic drive assembly. The low stiffness region is very evident in Figure 16. A larger plug, after insertion into the wave generator bearing may nearly eliminate the low stiffness region, as seen in Figure 17. Figures 18 and 19 show the next two larger size wave generator plugs, without a significant change in the shape of the stiffness curve. The desired operating point for the flight plug is smallest wave generator plug that exhibits a fairly straight curve. If there is any uncertainty between units, the smaller one would always be installed to guarantee that the gear teeth were not being jammed together with high, and unknown, internal stresses. The wave generator plug used in this example would be Figure 17's.

### Measured Initial Harmonic Drive Stiffness

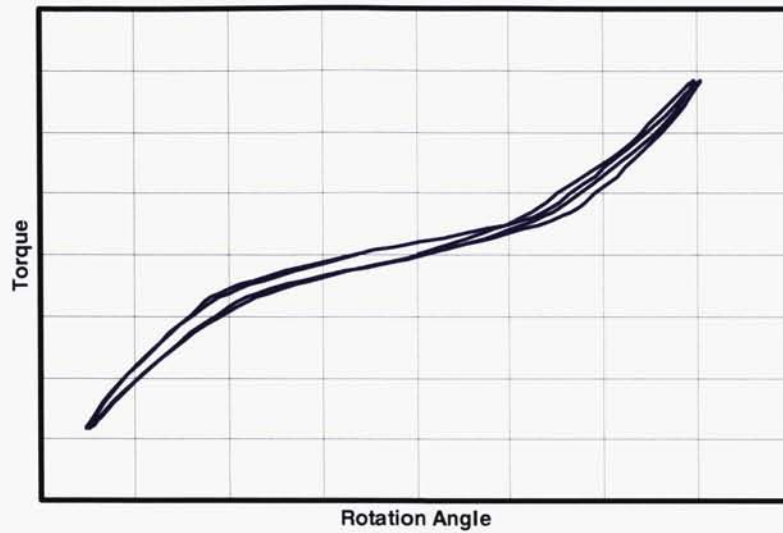


**Figure 15. Typical Harmonic Gear Assembly Stiffness**

Note two regions of stiffness: low near zero torque and larger at high torques.

The following figures are from measured data on the flight harmonic gear assemblies:  
(Note: the following figures' axes are rotated relative to Figure 15)

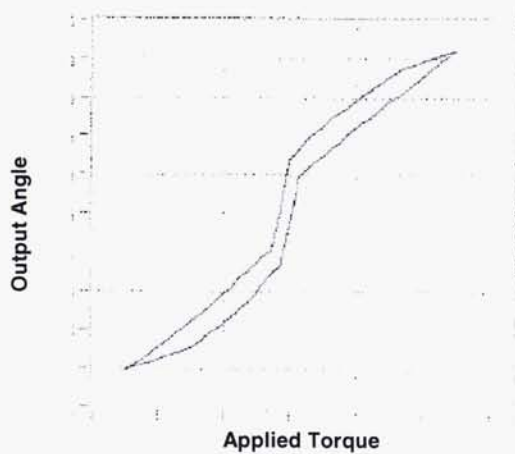


**Figure 16. Stiffness Curve Showing Low Stiffness Region**

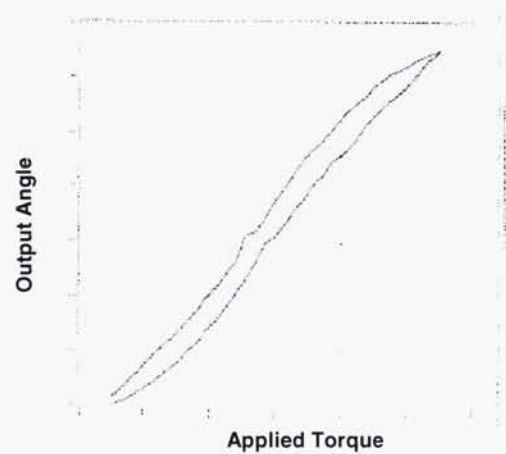


**Figure 17. Stiffness Curve with Minimal Low Stiffness Region**

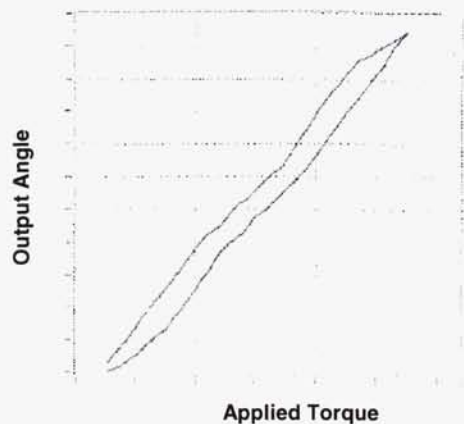


**Figure 18. Next Larger Plug Size Over Figure 17 Showing Little Change**

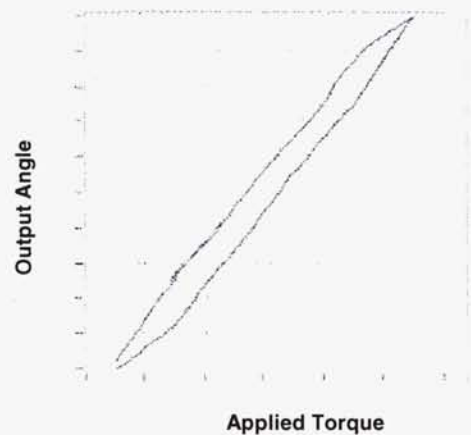


**Figure 19. Next Larger Plug Size Showing Showing a Small Change in Shape**

### **Conclusions and Lessons Learned**

The most significant result of the failure investigation was determining that the internal stresses due to the preload and the cable harness loading caused the premature failure of the EDU harmonic gear assembly. In order to maintain reliability for long life applications, increasing the wave generator plug size (a service provided by the harmonic drive vendor) is an acceptable technique up to the point where the low stiffness region is eliminated. This is the maximum stiffness enhancement achievable without compromising the reliability of the gear assembly for long life. Any further increase in the wave generator plug size will increase the stiffness at the cost of reducing the life of the unit. For minimal life applications, increasing the stiffness beyond this point may still be acceptable.

Stiffness enhanced harmonic gears are very sensitive to the externally applied load and test environment. Since the failure mode is galling, the presence of any gas (nitrogen, for example) severely compromises the test results. Life capabilities from previous heritage programs had been successful and so the initial gear material for the MRO gimbal actuators was considered acceptable and robust. However, some of the heritage operation had been performed in nitrogen, instead of vacuum. When enhanced stiffness is required in a harmonic gear application and it is not being used in a preload configuration represented by Figure 16, the situation is sensitive to possible galling of the harmonic gear teeth. Performing harmonic gear component operation at loads above the planned level to increase the tooth contact stresses should be considered. This will demonstrate if internal stress margin exists in the hardware. Also note that running a harmonic gear at a high input speed to reduce the operating time is not adequate. The high-speed condition may function with no incidents while low speed operation may catastrophically quit functioning. Finally, operating a unit at nominal contact stress levels to a larger number of revolutions than planned is a necessary, but not complete, margin demonstration program. A catastrophic failure may be lurking just a few megapascals away from the nominal value.

### **References**

Harmonic Drive, LLC web site, [www.harmonic-drive.com/support/principals.htm](http://www.harmonic-drive.com/support/principals.htm), description of harmonic gear assembly operation

### **Acknowledgements**

This work was performed at Lockheed Martin Space Systems, Denver, Colorado under a spacecraft system contract to the Jet Propulsion Laboratory, California Institute of Technology, under a contract with the National Aeronautics and Space Administration. Reference herein to any specific commercial product, process, or service by trade name, trademark, manufacturer, or otherwise does not constitute or imply its endorsement by the United States Government, the Jet Propulsion Laboratory, Pasadena, California, or Lockheed Martin Space Systems, Denver, Colorado.



# Stacer Driven Deployment: The Stereo Impact Boom

Robert Ullrich\*, Jeremy McCauley\*, Paul Turin\*, Ken McKee\* and Bill Donokowski\*

## Abstract

The Impact<sup>1</sup> Booms carry 3 scientific instruments each on the twin NASA Stereo<sup>2</sup> satellites. When stowed for launch the boom is 1.54 m in length, when deployed the boom extends to 5.80 m. The boom consists of 5 concentric graphite epoxy (Gr/E) tubes extended by the spring force of a Stacer. The Stacer is fabricated from a flat strip of Elgiloy<sup>®</sup> spring material, rolled with a constant diameter and fixed helix angle. It supplies the motive force for deployment, and requires no external power once released. The deployed boom exhibits excellent rigidity, the natural frequency first mode occurring at 1.96 Hz. Discussed is the implementation of a Stacer to deploy the 5 segment telescoping boom and some of the activities performed during its design, qualification and testing.

## Mission Introduction

The NASA Stereo mission consists of twin, three-axis stabilized satellites orbiting and viewing the Sun in the plane of the ecliptic at ~1 AU. Spacecraft A (Ahead) will be sent into an Earth preceding path with an Earth-Sun-Spacecraft angle increasing at a rate of 22° per year, while Spacecraft B (Behind) is sent into an Earth lagging orbit, also at a rate of 22° per year. The imagers on board will yield true 'stereoscopic' views of coronal mass ejections, while other instruments perform concurrent in-situ measurements of a large portion of the electro-magnetic spectrum. The telescoping boom was conceived to interface 3 instruments from the Impact suite: the Magnetometer (Mag), the Solar Wind Electron Analyzer (SWEA), and the Supra-Thermal Electron – Downward looking instrument (STE-D) to the Stereo spacecraft. The program requirements demanded a new concept, as existing hardware was deemed too expensive or unsuitable. The boom was initially developed via three 'proof of concept' models for the tube locking mechanism, and a final mock up using the Stacer to deploy four concentric, telescoping graphite/epoxy tubes from the center of the fixed 5<sup>th</sup> tube. An engineering model (EM) was then built to verify end to end design via qualification testing. The challenge for this mechanism was demonstrating that the design met the requisite GEVS SE<sup>3</sup> force (torque) margin. Two flight models (FMs) were then produced, with the EM being refurbished as a flight spare. The FMs are currently mounted to the spacecraft and mission I & T is progressing. Launch is scheduled for May 2006 from Cape Kennedy on a Delta II.



Figure 1 Magnetometer, SWEA and STE-D mounted on the end of the (stowed)

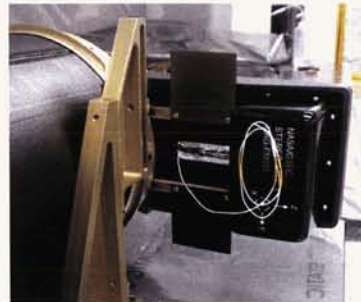


Figure 2. Magnetometer

\* Space Sciences Lab, University of California, Berkeley, CA

<sup>1</sup> In-situ Measurements of Particles And Coronal mass ejection Transients

<sup>2</sup> Solar – TErrestrial RElations Observatory

<sup>3</sup> See References Section



## The Science Flowdown Requirements

The requirements for the Impact boom were based on the scientific needs of the three instruments mounted to it: the Mag (built at Goddard Space Flight Center); the SWEA, supplied by CESR, Toulouse, FR; and the STE-D, supplied by UCB - SSL. The magnetometer for this mission is very sensitive: the magnetic (**B**) field at 1 Au heliocentric orbit is ~ 3 to 4 orders of magnitude smaller than near Earth. This slight field strength was a driver for the EMI/EMC design for the spacecraft and the devices near it. To avoid 'sensing' the spacecraft, the Mag needed to be 3 meters away from it. This requirement set the minimum boom length. To ensure a low magnetic signature from the boom assembly, no ferritic alloys were allowed for its construction.

Titanium screws were used to mount the magnetometer to its tray on the 4<sup>th</sup> tube element and the tray itself is made of carbon impregnated PEEK, a high-strength, conductive engineering plastic. To lower Mag exposure to any eddy currents present in the harness or structure of the boom, the mounting tray offset the Mag 200 mm from the nearest metal on the tube. Additionally there were not to be any other instruments closer than 1 m to the Mag. To allow accurate inter-experiment correlation of data, the angular alignment accuracy and repeatability requirement has an allowable deviation of  $<0.88^\circ$  (52.5 arcmin) between the Impact boom mounting feet and the magnetometer housing from the stowed condition to the deployed state, for the two axes that form the mounting plane of the Mag.



**Figure 3. SWEA / STE**

The second experiment mounted on the Impact boom is the Solar Wind Electron Analyzer (SWEA, supplied by CESR, Toulouse, FR). The SWEA has two variably charged hemispheric surfaces that attract electrons into an anode assembly which counts them as they impinge on to it. The SWEA would have a limited field of view when mounted directly to the spacecraft deck, hampering its ability to characterize the electron regime in the volume around it. Proximity to the spacecraft also causes deflections of the electrons due to the almost unavoidable static fields that develop near the spacecraft surface. Since this effect is difficult to model, a better solution was found. The implementation of the SWEA on the Stereo mission is extremely good: it is mounted on the extreme end of the boom, allowing a full  $2\pi$  radians x  $135^\circ$  field of view (FOV). The demands of the SWEA for

mounting to the boom are not complex: power lines, command lines supplied to it, data return lines from it.

The final instrument is the STE, a Supra-Thermal Electron detector, mounted on the side of the SWEA pedestal. It needs a clear  $80^\circ \times 80^\circ$  field of view looking along the plane of the ecliptic at a  $45^\circ$  angle (aligned with the Parker spiral), and to stay at  $\sim -40^\circ\text{C}$ .

The fixed base of the Impact boom is pointed towards the Sun for all science activities, and the only off-points scheduled are for momentum dumping. The boom deploys away from the Sun, so that there is minimal solar input to the boom suite, giving very low operational temperatures for the instruments. Thermal control was a large concern for the instrumenters.





**Figure 4. Solid Model Section View of Stowed Impact Boom**

### Impact Boom Mechanism

The Impact Boom consists of five concentric Gr/E Tubes, ranging from 50 mm to 210 mm in diameter, with a pair of aluminum rings bonded to each end. Each ring pair contains three lock pins, pointing outward at the Sun-ward end, and inward pointing at the release mechanism end, and three sockets, in their corresponding orientations. The pins are spring loaded, and have rollers mounted in their tips. When released, the Stacer spring extends the tubes until the end of travel where the pins drop into sockets, locking the assembly rigid. The mounting feet are integral to the outermost rings on the Ø210-mm tube. There is a spool for the electrical harness while stowed, a flyweight brake to govern the deployment speed, a shape memory alloy release mechanism with pretensioning adjustment, deployment assist rods and kick springs to initiate the deployment. Combs at each end hold the tubes in alignment prior to deployment, and during vibration/launch. A provision for individually adjusting the combs to remove any play in the stowed tubes due to fabrication tolerances is also provided. The design was performed in Solidworks™, utilizing its 3-dimensional solid modeling and multiple configuration capabilities.

#### Tube Details



**Figure 5. Tube End Detail**

The use of telescoping concentric tubes is not a new idea. Each telescope application brings its own set of challenges however. For the Impact Boom, the tubes needed loose tolerances on their cylindricity callout to allow for simple tube manufacture. The deployment / locking scheme required compliance regarding the inter-tube fit since there is a relatively low force available from the Stacer. The boom needed to be very rigid when deployed, so locking pins were utilized at end of travel, rather than relying on spring force to hold them in place. The tubes have three longitudinal concave grooves equispaced about their circumference, running their length, with a precise profile that doesn't jam the rollers. These grooves kept the pins on track to be aligned with the sockets at the far end of the tube. The tubes are a five-layer Gr/E composite designed to be quasi-isotropic: three 0°-90° layers interleaved with

two 45° layers of 0.12-mm woven epoxy pre-impregnated material (Fiberite Hy-E 1034C prepreg). The tubes were fabricated by Vision Composites of Signal Hill, California on internal mandrels, with a slight taper to enhance ease of extraction after cure. The cure regimen was specified to be 'dry': the ratio of epoxy to carbon filament was held to a minimum to ensure low surface resistance. This was achieved by using a higher autoclave pressure with a slower 'warm up to cure' temperature ramp and a thick layer of absorbent over the bleeder sheet. The process determination was somewhat lengthy, however, the final result met requirements.



**Figure 6 Partially Deployed Tubes**



At both ends of each tube there are inner and outer interlocking aluminum rings that 'sandwich', and are bonded to, the Gr/E. After an extensive search, Loctite Hysol 9309NA was used to form the bond. The thermal environment for the boom is rather severe: it will be in the shadow of the spacecraft for all of the science activity; thermal analysis estimates put the operating low temperature at 30K. There is very little data for epoxies at this temperature, so we performed an FEA for the bond between the aluminum and the Gr/E to establish what parameters minimized the stresses in the glue, the weakest part. Several cases for the glue design were examined: thickness of the bond, edge conditions of the bond and effects of the aluminum ring thickness (internal and external) on the joint stresses. Optimized, the glue line was

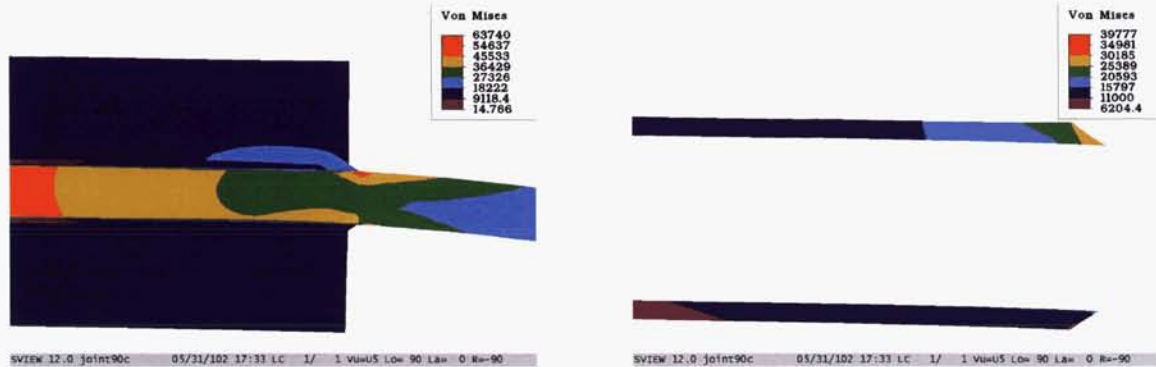


**Figure 7. FEA of Aluminum Ring – Glue Line - Gr/E – Glue Line – Aluminum Ring**

chosen to be ~0.4-mm thick, with a fillet onto a tapered aluminum ring edge. This best case predicted a stress value of 110vMPa (16 ksi)<sup>4</sup>, which exceeded the glue published maximum stress value of 38 MPa (5.5 ksi)<sup>5</sup>.

There was concern that the joint would not be sound after exposure to the thermal gradient, so an actual test was needed. A test GR/E tube / aluminum ring assembly was fabricated, with a large cantilever mass attached at the extremity providing ~2X expected loads for this test. This test 'tube' assembly was installed in a cryogenic liquid helium chamber, which was then installed into a cryogenic liquid nitrogen chamber in turn was placed inside of a refrigerated chest. We performed a multiple cycle thermal test (in a dry air environment), utilizing four candidate glues. The cold temperature was set to 25K (-248°C), and warm was 150K (-123°C). The 9309 performed nominally, with no crazing or cracking and was



**Figure 8. Epoxy Thermal Test Chamber**

accepted for use. As a side note, only one of the tested epoxies exhibited any signs of thermal distress. As a hedge against exceeding our thermal predicts, small solar absorbers were attached to the two joints in the mid boom. These little flags raise the expected temperature by ~5 degrees, buying some margin for the assembly (Figure 6).

<sup>4</sup> Besuner Consulting, Madera, CA 93638

<sup>5</sup> Loctite Hysol Applications Note, April /01, Loctite Aerospace, Bay Point, CA 94565



#### Lock pin details

Once the rings are bonded to the tubes, the locking pins / rollers are installed into precision radial bores in these inner and outer rings. When the segment locks, the pins are pushed into the sockets by custom wound torsion springs, two for each pin. The 'arms' of the springs also provide alignment for the pins, keeping the roller in the groove. The pin / roller combination allows any tube dimensional change to be insignificant during the deployment, as the spring compliance takes up any bumps or dips. When the tube section reaches end of travel, the locking pins are pushed into tapered holes, causing the tubes to become rigid with respect to each other. Guide ramps are provided at the end of travel to ensure that the pins are aligned with the sockets. Each locking pin has a slight taper (i.e.,  $<20^\circ$  included angle) that fits into the corresponding tapered socket. This gives a 'self-locking' feature to the pin, offering increased rigidity and prevents the pins from backing out under slight vibrations. With six lock pins engaged per joint, three inward acting, three outward, the boom exhibits great rigidity, and offers redundancy in the event that one pin (or more, up to three maximum, as long as they are not in same ring) does not lock.



**Figure 9. 50-mm Tube End Lock Pins (EM)**

Rollers are fitted to the tips of the locking pins to minimize deployment drag when rolling in the tube's grooves. Repeated deployments have shown no signs of wear to the tube or the rollers. To provide conductivity, the tapered portion of the pins and sockets were Alodined, while the sliding cylindrical parts were Type III black anodized to give good wear and low friction sliding properties. The Gr/E exhibits a low surface resistance too, enabling the boom to easily meet the surface resistance requirement of  $<10^8$  ohms per square, throughout its stroke. The drag was measured to be 3.1 N on average for the assemblies. The main function of the rollers is to keep the tubes aligned during deployment, so that the pin engagement is virtually guaranteed at the end of stroke.

#### Shape Memory Alloy Release (SMAR) details

The SMAR uses the interesting phase change properties of a 50% titanium – 50% nickel alloy (trade named Nitinol initially) to provide the actuation of the Impact Boom. This device, pioneered by TiNi Aerospace<sup>6</sup> in cooperation with UCB-SSL, takes advantage of the ~4% dimensional change in the drawn alloy wire when heated above its transformation temperature to let a ball detent assembly release a large spring loaded retracting pin. Since there was a large design load (50 Gs),  $>2.5$  kN retraction force was needed. A force amplifier was added to the TiNi standard P50 (~200-N [50-lb] pin puller). The force amplifier contains a stack of Belleville washers, preloaded and held by the P50 pin in another ball detent assembly, providing a final pull force exceeding 3 kN. When an electric current is passed through the Ti-Ni wire, it changes phase, elongates, releasing the primary pin, which then retracts and releases the main pin, which retracts with great force, allowing the Stacer to deploy. The main benefit of using an SMAR, aside from increased safety as no explosives are used, is that the flight unit can be tested over and over again (hundreds of cycles), and is simply resettable with a hand tool, with no temperature or time dependant constraints.



**Figure 10. Shape Memory Alloy Release Assembly**

#### Flyweight Brake

After the SMAR has been triggered, kick springs push the tubes out of the combs and the deployment assist device pushes the Stacer out of the canister with a force of ~90 N, giving the assembly a good initial velocity. The Stacer continues to provide force throughout the travel, so the deployment velocity would continue to increase until a balance between drag and push is achieved. This balance is never reached by the boom, so the deployment velocity reaches a 'run-away' condition rapidly, with the possible issues of lock pin shearing, ring-tube separation or other damage as consequences. As with every Stacer, a means to limit deployment velocity is incorporated. For the Impact Boom, a flyweight brake mechanism is attached to

<sup>6</sup> TiNi Aerospace, San Leandro, CA 94577



the Stacer via a woven Dacron (parachute shock) cord. Similar to the device found on (old) dial telephones that prevented the dial from being rotated faster than an old telephone exchange could count, the flyweight brake supplies braking force proportional to the rotational speed of its weight assembly. If the force (speed) increases, the brake shoes are centripetally accelerated against the brake drum, increasing the braking force and slowing the rotational velocity. Over a wide range of forces, the brake typically can control the speed to  $\pm 10\%$ . For the Boom, a deployment velocity of  $\sim 0.5$  m/s was chosen. This allows a certain momentum to build, but is slow enough to avoid shearing damage to the lock pins at the end of travel.

#### Harness and Spool

The power and electrical signals between the data processing unit and the instruments are carried by a cable routed down the center of the tubes, and is stowed on a spool for launch. This harness is a custom-fabricated conductor assembly consisting of seven coaxial cables and five twisted shielded pairs. Built of silver-plated copper with Gortex<sup>®</sup> dielectric, the harness is wound onto a bobbin when stowed and is pulled off when the boom deploys. This 'straight through' design provides greater signal strength, higher reliability and allows longer harness length as there are no slip rings or other connections between the data processing unit and the instruments. Care is taken to prewind the harness to avoid kinking or 'birdnesting' when stowing.

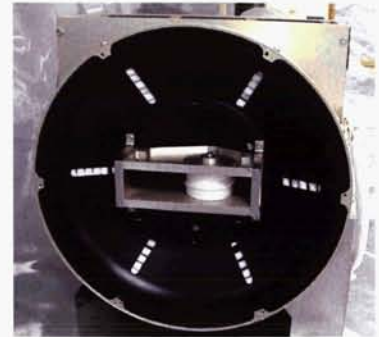


**Figure 11. Flyweight Brake & Harness Spool**

#### The Stacer

The Stacer is a rolled, constant helical pitch, fixed diameter flat spring. The strip width, thickness, roll diameter, and helical pitch are selectable for each application, allowing each Stacer to be tailored for optimum properties. Stacers range in size from  $<1$  m to  $>10$  m in length, from 4 mm to 55 mm in diameter at the tip, and can provide extensive force from almost nothing to 200 N. Trade studies can balance mass versus length, force, etc. In the last 30 years, more than 650 units have been utilized in aerospace applications, from sounding rocket sensors to gravity gradient booms with large masses on the end. What makes the Impact Boom unique is the use of the Stacer as a spring 'motor' without using it as the structure or sensor surface. Most applications have the Stacer with the sensor(s) mounted directly on it, or the Stacer as the sensor, for example as an antenna (a total of six 6-m-long beryllium copper Stacers are used on the Stereo satellites for the Swaves experiment in this manner).



**Figure 12. Picture of a Stacer**

To accommodate the Mag requirement of low magnetic signature for the boom, Elgiloy<sup>®</sup> was selected as the spring material over the more traditional beryllium copper (Be-Cu). This alloy was chosen to minimize any eddy currents that could be developed between the SWEA / STE and the spacecraft. Originally invented in the late 1940's in Elgin, IL for use in watches, it has been used for exacting Stacer applications several times. Its internal resistance is higher than copper, and cuts down the eddy currents accordingly. It has a higher modulus (E), and can provide greater force in the same physical volume as the Be-Cu. Elgiloy is a cobalt 'super-alloy', having an E  $\sim 190$  GPa and a yield strength of  $\sim 1600$  MPa<sup>7</sup>.

<sup>7</sup> Matweb, <http://www.matweb.com/search/SpecificMaterial.asp? = Elgiloy>



At deployment, the formation of the Stacer starts with the initial coil winding out of the storage canister onto a cylindrical tip piece, which is slightly larger than the free coil diameter of the Stacer. Thus the Stacer grabs the tip piece tightly, and the subsequent coils 'stack' up on the prior, producing the characteristic spiral appearance. The typical helix angle provides for significant overlap, such that a section taken at any point along the Stacer would yield at least two thicknesses of strip material. Since the 'outer' layer of strip is rolled to the same diameter as the inner layer, the outer grips the inner with a force normal to the surface. So between layers, significant inter-coil friction exists and prevents inter-coil slipping for small disturbances. This gives the Stacer one of its more useful properties: it behaves as a thin walled tube for small displacements, with similar bending strength and stiffness. If a larger displacement occurs, the coils slip, dissipating the strain energy, serving as a friction damper. The damping ratio value is typically 5 – 15% for the non-slipping regime, and can reach 30 – 40% with the slipping. Of course, the displacement limit is buckling, as any tube would experience when taken beyond its yielding strength.

As described, the motive force for the deployment is a Stacer. When compressed (stowed) it is a very compact package: it fits in a cylinder Ø50 X 130-mm long. When the Stacer is stowed, the strip is flexed into the canister, laying each coil inside its predecessor, and wound tightly to the outside of the can. When released, this stored strain energy is reclaimed, giving the motive effort needed to move the tubes along their path. The Stacer generates a higher force at the beginning of stroke, ~46 N for this application, and the force curve dropped to 1 N at the end of stroke (this was an isolated minimum value obtained from one force test). The force that the Stacer provides is shown in the polynomial fit curve in Figure 13.

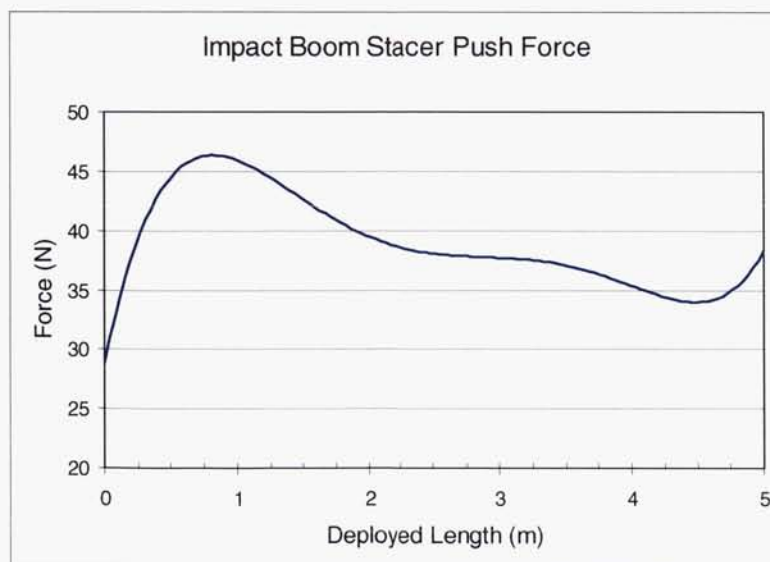


**Figure 13. Stacer Force**

For the purposes of torque (force) margin analysis, the initial push is 45 N, final thrust 18 N (the lowest value obtained). This lower value was used to bound the design force available for deployment. The Torque (force) Ratio ( $t_R$ ) requirement from *GEVS SE (Sec. 2.4.5.3)* is:

$$t_R = t_{\text{avail}} / t_{\text{required}} \geq 3.0 \quad (\text{Equation 1})$$

and the Torque (force) Margin ( $t_M$ ) requirement from *GEVS* is:

$$t_M = t_{\text{avail}} / t_{\text{required}} - 1 \geq 2.0 \quad (\text{Equation 2})$$

for systems dominated by resistive torques due to friction. This assumes worst case for the boom, taking the lowest force for the Stacer and applying it to the entire stroke. There is additional margin as there is a significant mass at the end of the boom SWEA / STE-D which contributes momentum towards full deployment stroke. Using the given values it can be shown that the force available, the minimum Stacer force of 18 N, divided by the force required, the tube drag of 3.1 N yields a torque ratio of 5.8, and a torque margin of 4.8. The Stacer satisfies the force requirements by analysis. Still, the device must show functionality to prove that manufacturing has been in accordance with design.

The graph shows the need for a deployment initiator. The stowed Stacer is in a 'meta-stable' condition. If left by itself, it would partially deploy in either direction, therefore a back plate on the canister is required. To ensure that it deploys a deployment assist device (DAD) is incorporated. The final upturn in the force curve is an artifact of how the force was measured. The Stacer in this case is 5-m long, and when it is fully deployed, the coils have tightened onto themselves. The force value was taken at the moment the Stacer began to slip back into the canister. For this case, the coil needs to be expanded significantly, and requires greater effort.

There is an additional use for the Stacer after deployment as the secondary EMI/EMC shield. While each of the conductors in the harness is shielded, the mission's low noise requirement demanded a second, 'over-shield' for all conductors. Since the harness runs down the center of the Stacer, the Stacer was tied to ground, and serves this purpose.

### Deployment Sequence

Deployment is initiated when a TiNi Aerospace shape memory alloy release device (SMAR, Model P50-810-1RS) is triggered causing the restraint pin to pull out of the tail of the Stacer tip piece. To give the stacer and tube deployment an initial 'kick', a deployment assist device (DAD) is incorporated between the SMAR mount plate and the 50-mm tube base. The DAD consists of three long coil springs compressed when stowed, and when released provide ~90 N of push at the very beginning of the stroke. After the first 100 mm of travel, the initial coils of the Stacer are fully formed around the tip piece, and the flyweight brake has been spun up to speed. At this time the DAD has completed its stroke. The Stacer is attached to the base of the 50-mm tube via a swivel, allowing the Stacer to wind down while extending, recapturing the strain energy stored when the Stacer was wound 'out' against the canister. At the end of the 50-mm tube travel, the six lock pins pop into their sockets, and transfer the Stacer push force, as well as momentum, to the 90-mm tube, pulling it along until it latches; the process continues with the 130-mm tube and the 170-mm tube, and finally the entire four tube rigid assembly locks onto the 210-mm tube, which is fixed to the spacecraft. While the actual sequence follows this description fairly closely, occasionally the tube drag would cause one or another tube to partially deploy. There is no provision or requirement for any tube to deploy in any set sequence. To control the velocity of the tubes during deployment, the flyweight brake is attached to the 50-mm tube via a lanyard, limiting the speed of deployment to ~0.5 m/s, giving a total deployment time of ~10 sec. There are position alignment blocks for stowed (launch) condition holding the tubes aligned



**Figure 14. Impact Boom after a thermal vacuum deployment**



relative to each other, and carrying the vibration loads. These also incorporate 'kick' springs to aid in their deployment, and to alleviate any possible "stiction" from the alignment blocks.

The boom is not retractable once deployed. Re-stowing is achieved by removal from the spacecraft, and hand retraction of each set of pins followed by each tube segment being (de) telescoped; after which the Stacer is compressed into its canister; and the harness and flyweight brake are rewound. Finally, the SMAR is reset reinstalled, and preload is set.

### Verification

The Impact Boom's qualification activities were based on GEVS SE, as modified by JHU-APL for mission specific needs. The test regime selected for the Stereo mission was Protoflight, meaning new (unflown or non-heritage) hardware is tested with a combination of prototype (EM) levels (i.e., temperature or vibration) with flight (FM) durations. This method is typically used to shorten development times by eliminating the engineering / qualification model fabrication and test period. However, the Impact Team did build up an engineering model, and tested all 3 assemblies to the protoflight levels. The main changes and additions pertinent to this paper: Level 300 cleanliness, UV + Visible light inspection, no silicones used for fabrication, and testing for silicone residuals. Vibration levels were taken from the Delta II user's manual<sup>8</sup> modified by APL analysis for the 'stacked' configuration. Stringent EMI/EMC levels were levied, due to the extremely sensitive radio receiver and magnetometer on board.

Testing procedures were standard NASA mission fare. The main tasks to be performed for this application were: demonstration of sufficient force (torque) margin for extension of telescoping sections throughout the Boom's stroke; thermal design validation at 25K (discussed previously); and thermal vacuum cycling and deployment verification at hot and cold operational temperatures.

As the team worked on the testing it became clear that Stacer thrust force is not easy to measure accurately or repeatably. The deployment of a Stacer is a 'stick – slip' affair: and once stopped, it sticks, then when released slips, giving a wide range of force values due to the hysteresis built into the inter coil friction. For consistency, the force value used at any point was the force needed to start the Stacer being pushed back into the canister, after overcoming the 'stiction'. This does not accurately convey the sliding force, but is as close as can be statically measured. Attempts to measure Stacer force dynamically were fruitless. Another difficulty lay in measuring the drag from rollers and harness. Each tube has a 1.1-m stroke, and pulling steadily for that distance vertically while monitoring force is a challenge. The weight of the tube assembly was subtracted from the pull out force, giving the drag value.

Finally it was seen that proving force margin analytically was not conclusive as the uncertainties in each measurement, when combined, exceeded the margin requirements. A different path was chosen: show that the boom deploys while using 1/3 of the available Stacer force. By definition, there is sufficient margin. This is how the boom was verified.



**Figure 15. Thermal Vacuum Chamber**

<sup>8</sup> Delta II Payload Planner's Guide, The Boeing Company, Huntington Beach, CA 92647



When testing deployables, the desire is to prove beyond question that the mechanism will deploy in space, however, it must be tested here on the ground first. How many times? GEVS provides a minimum, and each program defines how many additional operations. This brings up wear margin: the design must show that it is sufficiently robust to survive testing and flight without degradation. The EM served this purpose, getting many deployments more than the FMs did. After identifying these values, a test plan was developed, reviewed and implemented.

Testing large deployables in a simulated space environment is difficult, and ensuring that the test actually verifies functionality is critical. Deploying the boom horizontally was initially considered since it is easier to develop a 6-m-long test rig that rests on the floor. After a few small efforts in this orientation, it was realized that the only way to ensure that roller drag on the tubes was representative of actual orbital deployment would be to deploy the boom vertically. While several interim off load pulley systems were used, all the verification deployments were performed on the thermal vacuum gantry.

To this end, a tall vacuum chamber was designed and built to allow the tests to be performed (Figures 14 & 15). Inside the chamber 'chimney' a gantry that allowed a counterbalance pulley system to provide G negation was installed (Figure 16). The distance from the top of the boom to the pulley was maximized to provide the least possible restorative (centering) force to the sections of the boom during deployment.

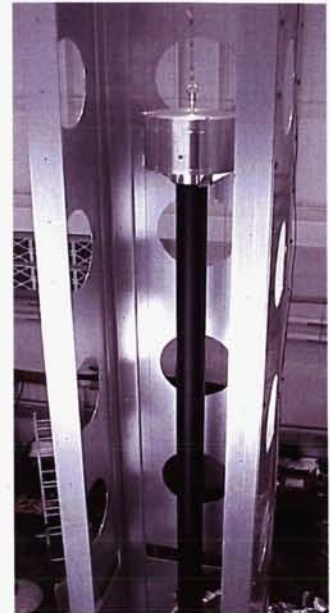


**Figure 16. Gantry Detail**

#### Counterweight Description

To demonstrate the force (torque) margin, the masses to be used for the counterbalance force had to be chosen to show that the Stacer would be energetic enough to deploy the boom. The mass of each of the tubes (in flight configuration) was added to give neutral balance, plus the Stacer neutralization mass (determined by bare Stacer vertical deployments to be 164 g). This mass (5214 g) was decreased by 2/3 of the Stacer minimum force ( $31 \text{ N} \times 0.67 = 20.7 \text{ N}$ , converted to kg:  $20.7 \text{ N} / 9.98 \text{ kgm/s}^2 = 2.07 \text{ kg}$ ) and subtracted from the counterweights. All 10 verification deployments were 'force margin' deployments and were successful. After deployment, each boom was inspected for wear, with no signs of degradation of rollers or Gr/E. The EM has been deployed ~20 times, and is still in good condition.

Initially, the counterweights far exceed the G negation requirements for deployment as only one tube is being deployed, while it is being pulled by the counter weight for 4 tubes. This is not invalid for our testing needs, as the flyweight brake dissipates the extra force, keeping the velocity in correct range. The area of interest is the very end of travel, where the Stacer force is lowest, and the full mass is being acted on. It was this point that the gantry design was built on.

#### Magnetometer Alignment Verification

After deployment, the alignment of the Mag needed to be measured to determine compliance with the specification. A very accurate digital level (resolution:  $0.01 \text{ degree} \pm 0.02$ ) was used for this activity. The measurements were taken relative to the origin and coordinate system established in the Interface Control Document (ICD)<sup>9</sup> for the boom. The relative angles for the mounting feet for the X – Z and X – Y planes were recorded at the mounting foot. The angles for the same planes (translated out to the Mag tray) were then measured. The difference was taken, yielding the deviation of the Mag tray from the mounting plane. Figure 17 shows the measured differences of the deviations for the FMs for each plane.

<sup>9</sup> See Appendix A for ICD Details



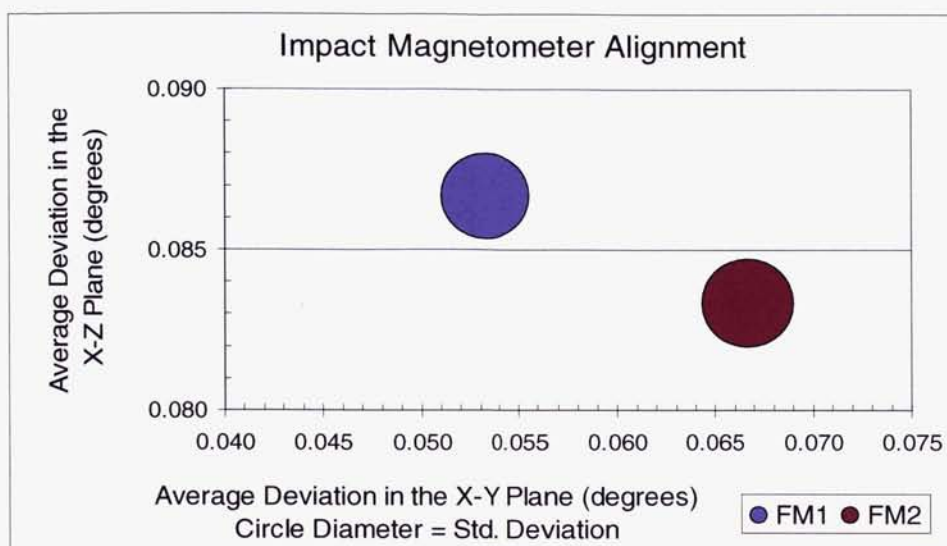


**Figure 17. Magnetometer Alignment Error**

For the final determination of pointing error, the root of the sum of the squares was calculated to give the magnitude of the deviation (the direction is not of interest as long as the specification is met). Flight Model 1 measured deviation "used up"  $0.10^\circ$  of its allowable  $0.88^\circ$  margin, while FM2 used  $0.11^\circ$ . The Impact Boom deploys accurately, repeatably, and exceeds requirements by a large margin.

### Lessons Learned

#### Design for test.

The final validation of any design is complete when the device performs as expected in its orbital environment. GEVS SE gives guidelines, developed over many programs, as to what tests must be run, and how much extra (or over-) testing is needed. For the boom to be tested, a vacuum chamber was required to be built in a vertical orientation. The initial plan had been to use a horizontal track, using an existing facility. This plan did not give sufficient demonstration of the booms ability to deploy in a straight line as the track would have given alignment to the sections through out their travel. Additionally, the drag induced by the lock pin rollers when the tubes deploy horizontally far exceeded the Stacer deploy force. At the time the decision was made to go vertical, the Stacer should have been sized to allow a non-counterweighted deployment. There would have been a mass hit, but being able to leave off the gantry would have been a great savings, as the chamber would not have had to be as tall.

#### Safety

One person was injured during initial installation of the stacer into its canister. As the final portion was stowed, the safety retaining pin would not fit into the hole provided for it. When additional force was tried, the operator lost control of the stacer and it deployed in an uncontrolled manner to ~1 m, when it was grabbed, cutting their finger deeply through two sets of latex gloves.

Some points arose from the review of the accident:

a) Check fit all safety related parts, sub-assemblies and fixtures. The size + tolerance of the hole for the safety pin were too small after plating to allow the pin to be inserted. This would have been an easy test, prior to assembly.

b) Have back up hardware and personnel: the operator was working virtually alone, and had no back up person there to hold the stacer while the pin was being inserted. After the finger was cut, a colleague from another part of the lab had to run to help control the stacer and finger damage. Another

point for spring loaded deployables: don't rely on a single safety path. A lock down plate in front of the stacer assembly would have caught the stacer, preventing damage. These recommendations have been implemented in the procedures, and stowing fixture used now: the stowing procedure has a minimum requirement of two persons to proceed.

#### Materials Specifications

Often materials can be useful beyond supplier's data, one only needs to verify what limits to the previous testing exist. The search for a cryogenic temperature suitable glue was fruitless. In the end a test was performed to establish suitability, after much effort. The question to add after "At what temperatures does the product perform satisfactorily?" is "Has it been tested beyond that?" A fair number of days could have been saved by realizing the manufacturers don't have all the information.

#### Margin

While most programs have a margin requirement, it is good to carry some margin for additional mass demands while designing. This is almost rhetorical. The proposal mass for the instruments at the end of the boom was 1.2 kg. After deliberation, it was determined that the data would be significantly better if pre-processing were done closer to the detector, so additional circuit boards were added out at the end, raising the deployed end mass to 2.2 kg. This drove the size of the release mechanism from being 'off the shelf' to a new, custom version, requiring additional testing, with the usual learning curve associated with new mechanisms. The entire structure needed 'beefing up' to accommodate the added loads.

### **Summary**

The Impact Boom has completed qualification and acceptance verification for use in flight for the NASA Stereo mission. This application has shown the use of a Stacer spring can be implemented for major deployables as a motive force, not only as a sensor or sensor support. This represents a major cost savings from traditional motor driven deployables, with their associated high cost electronics. Currently, the launch is planned for 26 May 2006, with deployment of the boom occurring within a 3 - 30 day window after launch.

### **Acknowledgements**

Thanks go to Dr. Janet Luhmann, Principle Investigator for the Impact Suite, and the entire Impact Boom Team at the University of California Berkeley, the Space Sciences Lab. Also to NASA Goddard Space Flight Center for working with us to get this new hardware off the ground, and to all the reviewers whose inputs and criticisms helped make the boom robust enough to survive qualification. Thanks also go to the Stereo crew at APL for their continued support for the program.



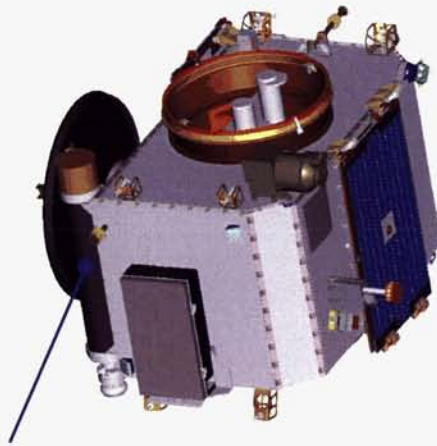


**Figure 18. Stereo "B" Spacecraft: Impact Boom location**

### References

Space System Reliability and Safety Office, Code 302; "General Environmental Verification Specification for STS and ELV, Rev A"; (June 1996), National Aeronautics and Space Administration, Goddard Space Flight Center, Greenbelt, MD 20771; June, 1996; §2.4.5.3 – 2.4.6.2

### Appendix A

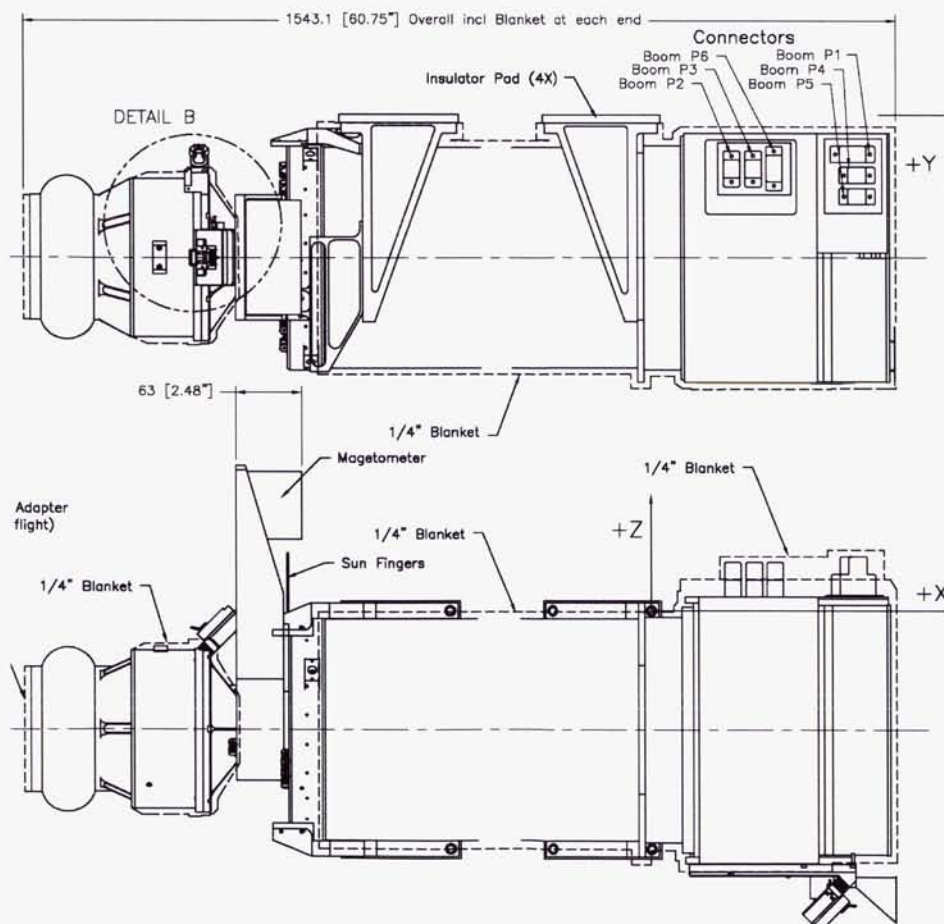


**Figure 19. Impact Boom ICD Detail: "B" Stowed**

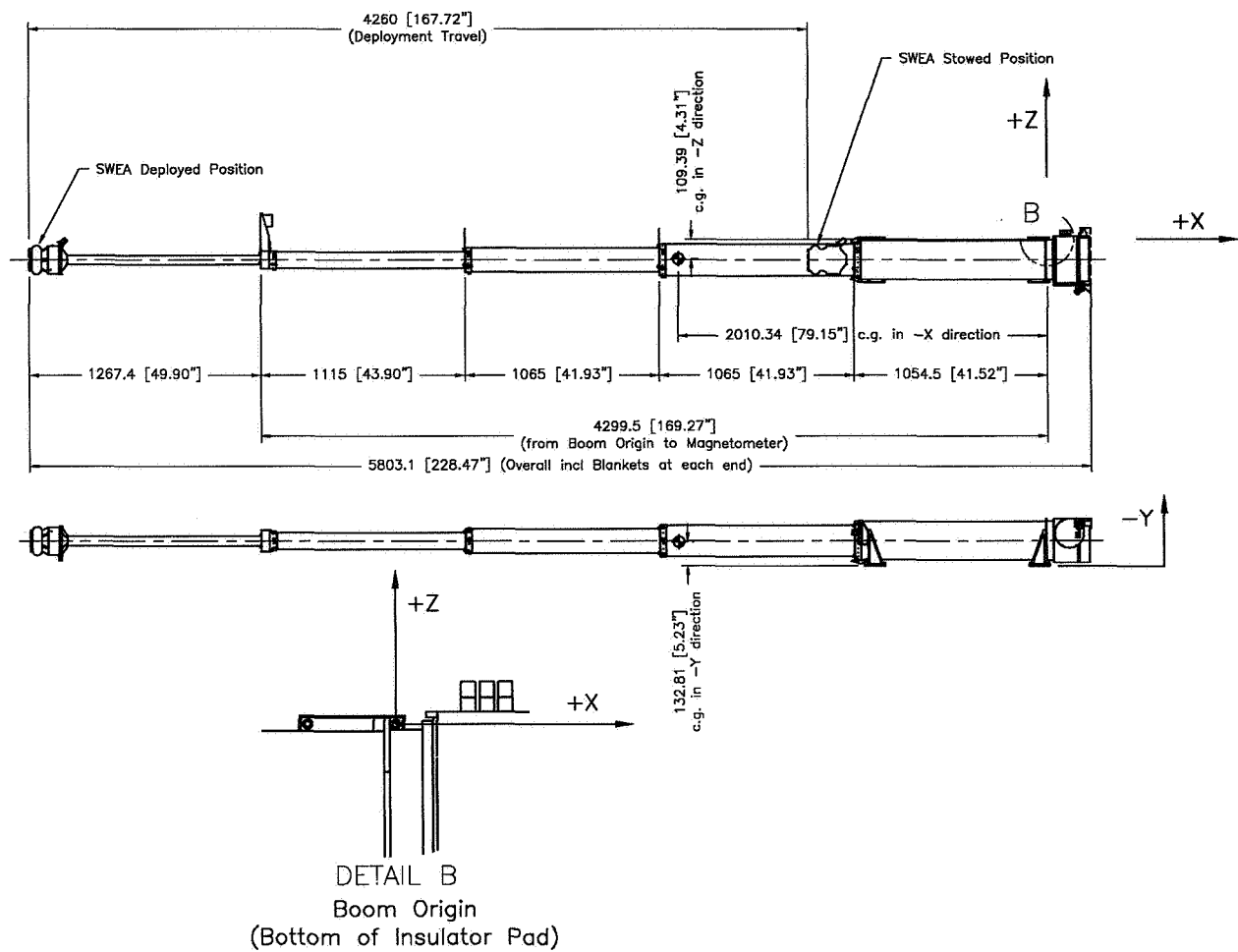


**Figure 20. Impact Boom ICD Detail: "B" Deployed**

# **Heritage Adoption Lessons Learned: Cover Deployment and Latch Mechanism**

James Wincentzen\*

## **Abstract**

Within JPL, there is a technology thrust need to develop a larger Cover Deployment and Latch Mechanism (CDLM) for future missions. The approach taken was to adopt and scale the CDLM design as used on the Galaxy Evolution Explorer (GALEX) project. The three separate mechanisms that comprise the CDLM will be discussed in this paper in addition to a focus on heritage adoption lessons learned and specific examples. These lessons learned will be valuable to any project considering the use of heritage designs.

## **Introduction**

Because of future JPL mission needs for meter class space telescopes, there was an internal technology demonstration to develop a complete mechanism set for single-time deployable cover to protect the optics. Because the task was tracked for a fast technology development, the decision was made to fully adopt the GALEX cover deployment design early in the project cycle to save cost and schedule. For reference, the baseline design aperture opening diameter was 0.83 m (32.7 in) and the outer diameter of the instrument was 1.1 m (43.3 in) in diameter, roughly twice the size of GALEX.

## **CDLM Overview**

The three mechanisms that comprise the CDLM are the Latch, Hinge, and two Energy Absorbers. When the Latch releases the cover, two push off springs and the Hinge mechanism rotate the cover approximately 4.66 rad (267 deg) and impact the crushable honeycomb filled Energy Absorbers. Deployment time is approximately 3.4 seconds. The Hinge mechanism is un-dampened. After deployment, the cover remains against the canister. An overview of the instrument and placement of the mechanisms are presented in Figure 1.

## **Latch Mechanism**

The Latch mechanism, attached to the cover, employs a Starsys paraffin thermal actuator as the prime mover. An interfacing slotted Latch Arm is affixed to the Cover Ring. The Latch Arm is spring loaded to rotate away from the aperture opening upon release. A detail view of the latch area is shown in Figure 2, the Latch Arm is shown in Figure 3, and a cross section of the Latch mechanism is shown in Figure 4. The Locking Piston passes through and retains the Latch Arm. The Push Piston has a small-diameter tip and passes through the Latch Arm slot. To deploy the cover, the actuator heater is energized, which translates both the Push Piston and Locking Piston, forcing the Locking Piston clear of the Latch Arm. Once the Locking Piston is clear of the Latch Arm, the Push Piston slips through the Latch Arm as it rotates. The mechanism locks open by means of torsion spring loaded arms that snap into a groove on the Locking Piston. Microswitches sense the motion of the arms and provide telemetry of the mechanism state.

Power to the actuator is discontinued once one of three criteria are met: Hall effect sensors mounted on the Energy Absorbers register a deployed cover (discussed later), PRTs mounted on the actuator reach a maximum temperature, or a time limit circuit is exceeded. Both the temperature and time are based on a look up table derived from thermal vacuum Latch test data. After power is terminated and the actuator

---

\* Jet Propulsion Laboratory, Pasadena, CA



cools, a Push Piston return spring resets the actuator for further ground testing. Resetting of the cover and Latch Arm is manually performed.

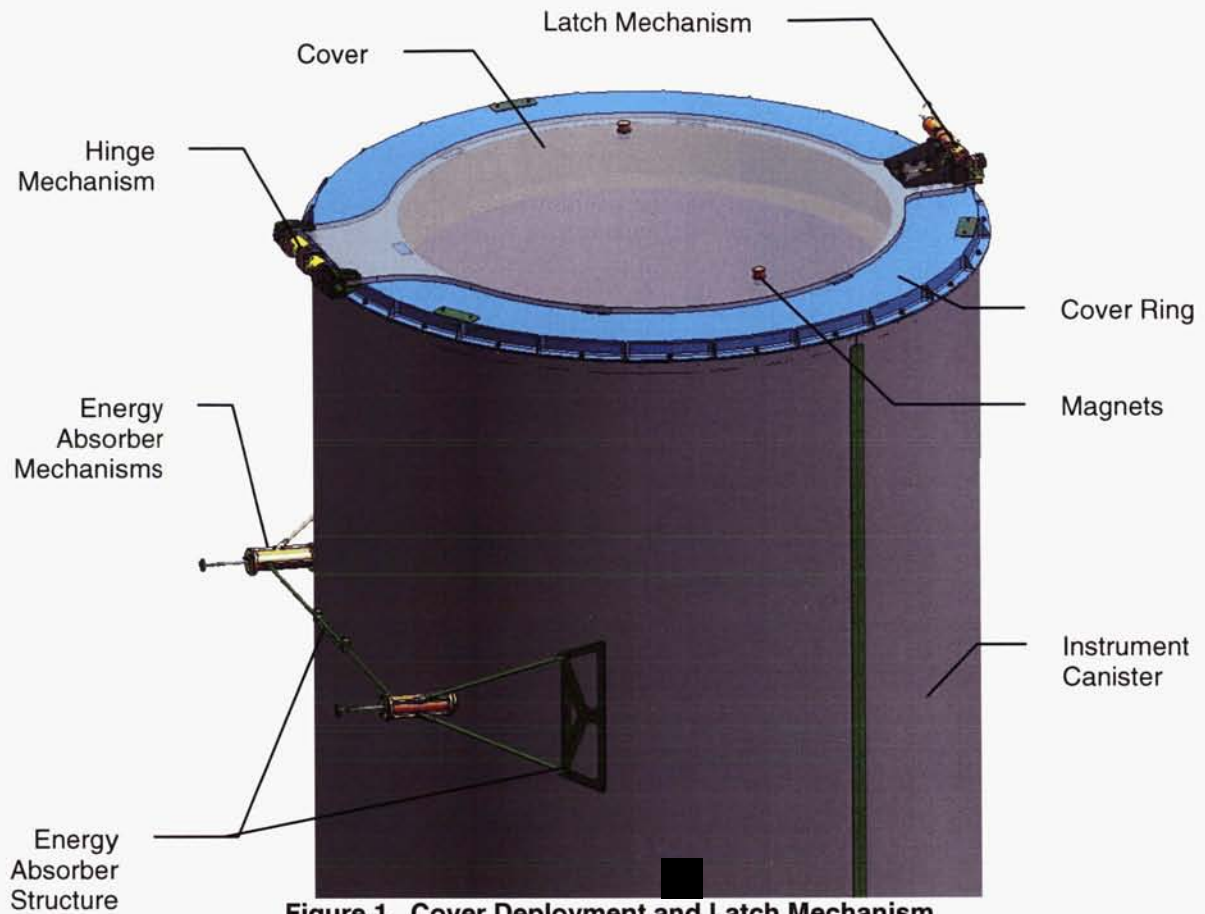


**Figure 1. Cover Deployment and Latch Mechanism**

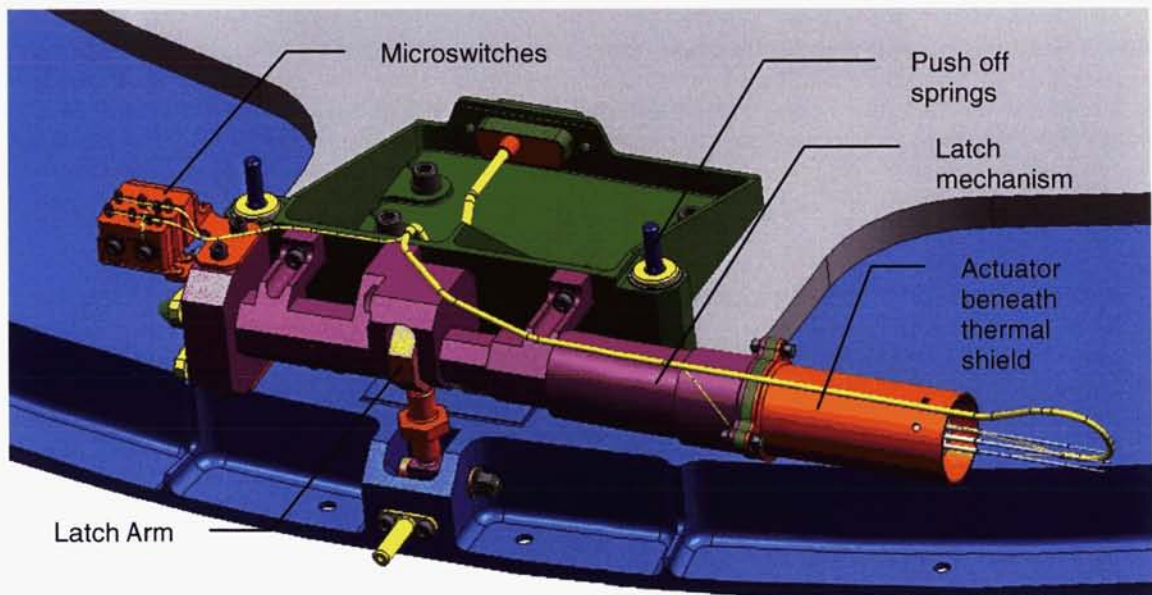


**Figure 2. Latch mechanism and Cover/Cover Ring**

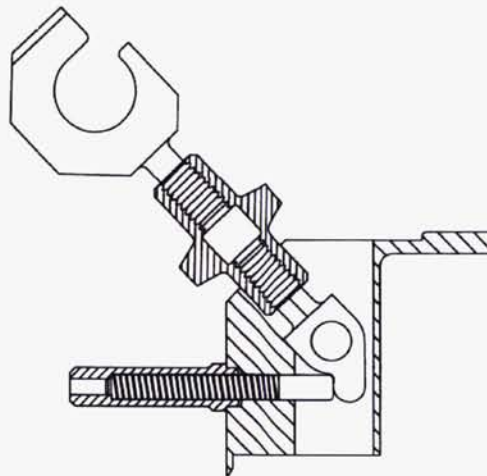


**Figure 3. Latch Arm assembly, rotated**

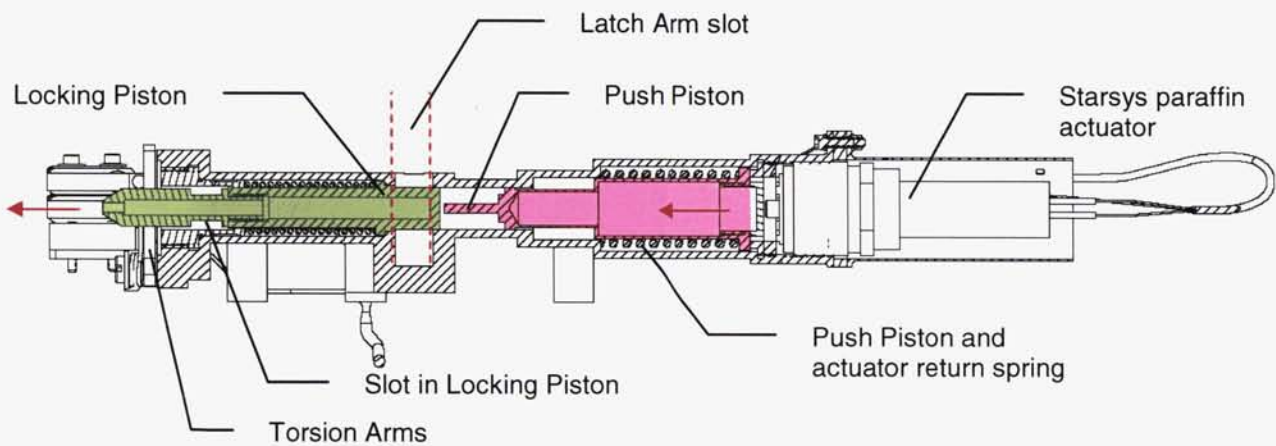


**Figure 4. Latch mechanism cross section**

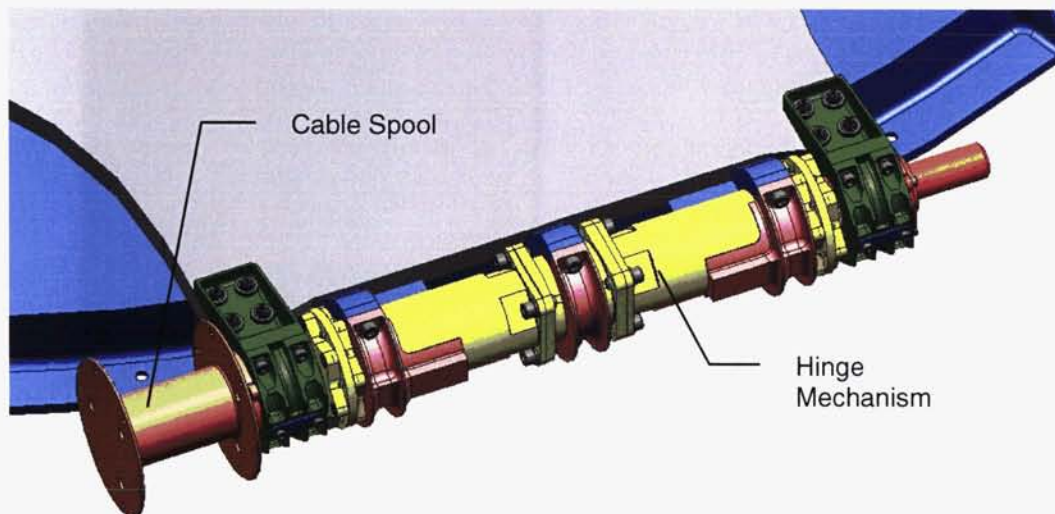


**Figure 5. Hinge Mechanism**



## Hinge Mechanism

The Hinge mechanism works by means of two sets of nested compression springs acting against a lead screw / carrier nut combination. A clever and complex design, the Hinge is fully single fault tolerant. For some failure modes, such as the loss of a spring, the Hinge is two-fault tolerant. A graphic of the Hinge mechanism is presented in Figure 5 and a cross section is shown in Figure 6.

In the cover-closed position, the compressed springs react against the Hinge mid section and the spring support end, which are restrained from rotation by shoulder screws and rollers running in slots in the housing. Attached to the spring support end is the lead screw, which is also restrained from rotation. The lead screw passes through a carrier nut, which is constrained from translation, but allowed to rotate. As the lead screw translates, the carrier nut rotates. The cover is attached to the clevis, which in turn is fitted on roller bearings on the carrier nut. Pins fixed in the carrier nut and clevis engage during rotation, driving the cover open. Each side of the hinge mechanism works independently of the other. If one side jams, the Clevis rotates freely on the bearings. If a Clevis bearing freezes, the carrier nut and Clevis can rotate on the inner bearing.

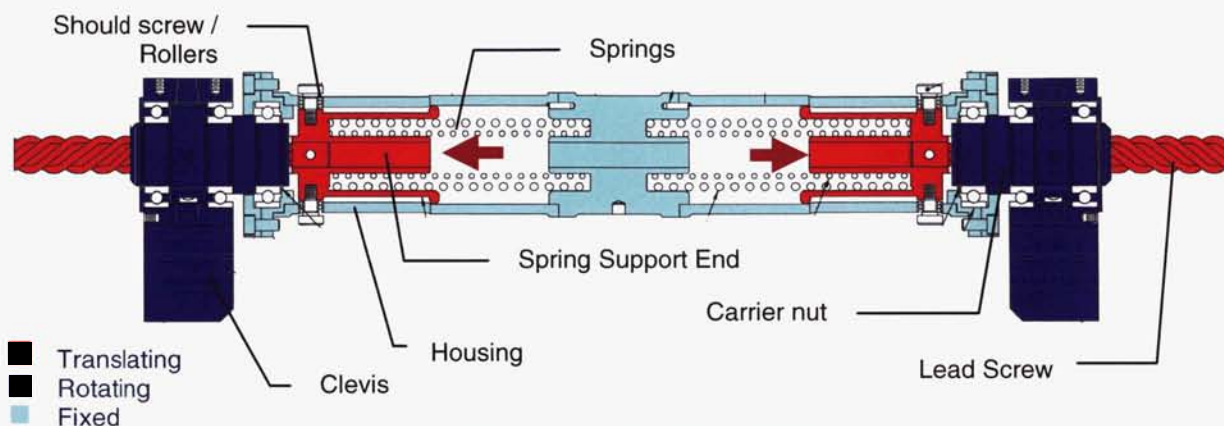


**Figure 6. Hinge mechanism cross section**

## Energy Absorber Mechanism

The GALEX Energy Absorber used a compression spring in combination with a ratcheting plunger. Once the plunger was pushed in, the ratchet held the plunger and compressed spring fixed. Hall effect sensors imbedded in the striker and magnets mounted on the cover provided telemetry of a deployed cover. The cover magnets also served to latch the cover open. One disadvantage of the GALEX design was that after each cover deployment test, the Energy Absorber had to be disassembled to be reset. It was requested by the project to simplify the GALEX Energy Absorber design with replaceable, crushable honeycomb.

We desired to keep the new energy absorber function as similar as possible to the GALEX mechanism due to the support structure design. The housing and Hall effect sensor striker were left relatively unchanged, but the compression spring and ratcheting device were replaced with crushable honeycomb core. The honeycomb core is bonded to a simple disposable aluminum plate which is attached to the plunger. The push rod and Hall effect sensor striker are then attached to the plunger, creating the plunger subassembly. As the magnets mounted on the Cover impact the striker during a deployment, the core is crushed against the Energy Absorber End Cap. See Figure 7 for an exploded view of the crushable honeycomb Energy Absorber mechanism and Figure 8 for a graphic of the Plunger subassembly.

The Energy Absorber honeycomb core is replaced after each cover deployment. The Push Rod is segmented in two pieces with a left-hand thread so that the Hall effect sensor striker and front segment



Push Rod can be removed from the plunger subassembly without stressing or twisting the sensor leads. The mechanism is reset by first removing the striker and Front Cap and then the Plunger subassembly is removed from the housing and the core replaced.

During prototype cover deployment tests, several types of honeycomb were experimented with, for the goal of reducing cover bounce-back and obtaining the cleanest cover capture. Aluminum core, 3/8-5052-1.0, foil thickness 0.018 mm (0.0007 in) and crush strength of 172 KPa (25 psi), trimmed to three cells was found to work well, however the 50.8-mm (2-in) long samples available came close to bottoming out. New core, 88.9-mm (3.5-in) long, was selected to allow for enough travel with margin (see following paragraph for more detail). Deployment with this core proved to be the best and the cover bounce back was limited to approximately 0.04 rad (2.5 deg) (the cover does not rebound off the striker; instead the Plunger is pulled back to its limit stop). Because of the core's long length compared to its cross-sectional area, the core appears to initially buckle uniformly, then folds between the mid-section to base. Crush tests were conducted with the core and the force required to continue crushing gradually dropped from the initial buckling. This result corresponded well for this application as the impact force falls off considerably after some energy is absorbed. See Figure 9 and Figure 10 for before and after cover deployment images of 50.8-mm (2-in) and 88.9-mm (3.5-in) core respectively.

The kinetic energy of the deployed cover and energy to be absorbed is equal to that of the Hinge mechanism compression spring's potential energy at the cover closed position. The average crush load multiplied by the crushed length gives the energy absorbed, and thus, with some extra length for margin, defined the length of required core.<sup>1</sup> Figure 11 is Hexcel's honeycomb crush strength curve, which illustrates the peak load, average crush load, and the energy absorbed. Core used in the Energy Absorbers were pre-crushed slightly to remove the peak force spike. Crush test data from the three-cell, 88.9-mm (3.5-in) long core is presented in Figure 12.

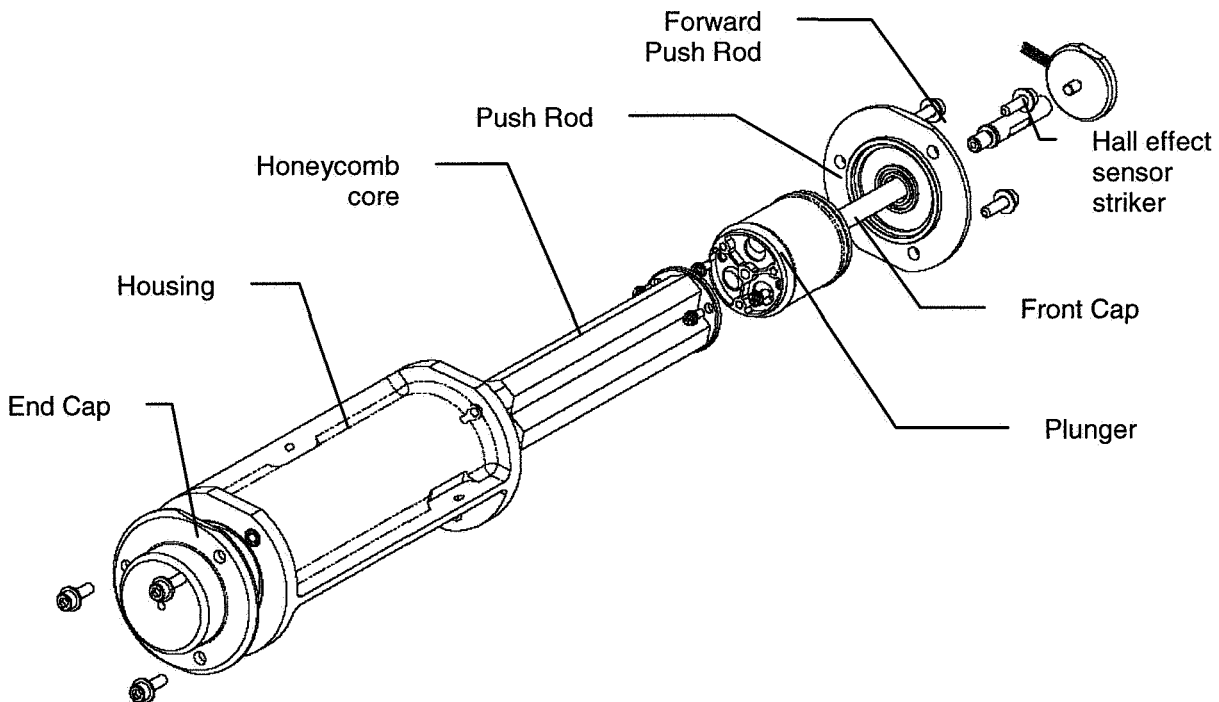


**Figure 7. Energy Absorber exploded view**



**Figure 8. Energy Absorber Plunger subassembly; note core pre-crushed.**



**Figure 9. Three-cell core, 50.8-mm (2-in) long**



**Figure 10. Three-cell core, 88.9-mm (3.5-in) long**

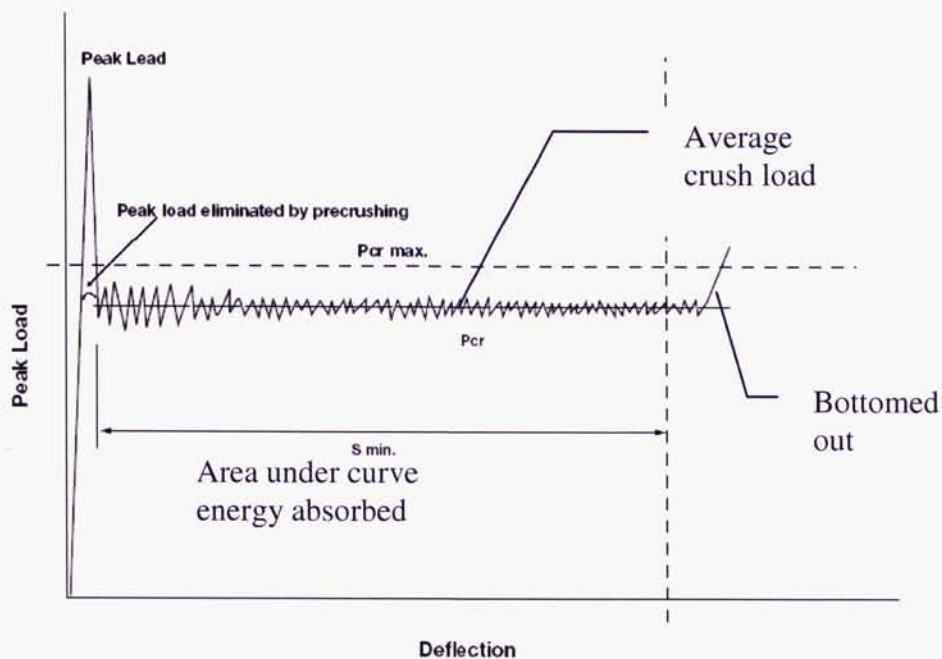


Figure 11. Hexcel Honeycomb crush strength curve<sup>1</sup>

3/8-5052-.0007, 3 Cell, 3.5in Samples  
Displacement vs Force

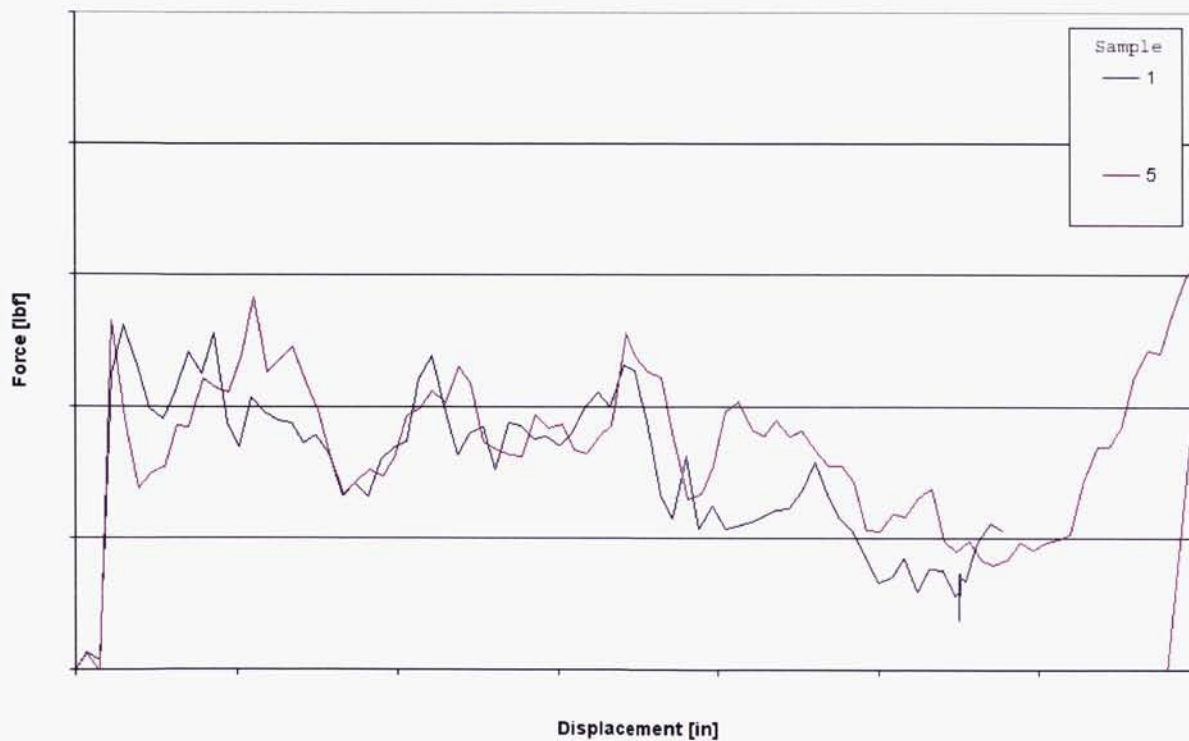


Figure 12. Force / Displacement graph for 3-cell, 88.9-mm (3.5-in) core



## Heritage Adoption Lessons Learned

Sufficient review of a heritage design is necessary before adoption as heritage designs may impose unnecessary limitations, constraints, or failure modes on interacting mechanisms or systems. Additionally, a flight readiness review of a heritage design is necessary, as it can not be assumed that all necessary information regarding the design, such as as-built drawings, assembly instructions, test procedures and test data, are available. Of particular interest are the GALEX heritage adoption lessons learned during the CDLM technology development.

GALEX cover deployment mechanism was obviously built to a redlined set of drawings; however, these drawings were not available during this task. As GALEX was an aggressively “faster, better, cheaper” mission, it is thought that resources were not available to complete the drawing package. Much of any schedule savings in using the heritage design was exhausted going through more than 70 drawings to look for, and correct, interference, material, and lubrication issues. Some issues were found only after fabrication and assembly, necessitating the rework or re-fabrication of built parts. Accurate build and assembly histories are required to adopt heritage designs.

Very limited test data, such as cover deployment time and cover impact force, was available from GALEX. The lack of test data necessitated the building of a schedule intensive deployment test fixture and mockup cover and duplicating cover deployment tests. Fortunately, a spare Latch mechanism and an engineering model Hinge mechanism were available for testing. An image of the deployment fixture is shown in Figure 13.



**Figure 13. Deployment Test Fixture**

Early adoption of the Hinge mechanism restricted the design of the crushable honeycomb Energy Absorbers. Not until the deployment test fixture and prototype energy absorbers were built and tests run did it become apparent that the cover impact force was much lower than expected. If the honeycomb crush strength was too high, the cover would bounce off the Energy Absorbers as the impact force dropped off during impact. Conversely, the honeycomb had to be strong enough to resist the Plunger subassembly inertial loads during vibration. It was found during testing that the impact force necessary to sustain honeycomb crushing, and to effectively keep the cover from rebounding, required the Hinge torque output to be *increased* (by the use of larger springs). By increasing the un-dampened Hinge torque output, the amount of kinetic energy to absorb was also increased. This was further complicated by adopting the same GALEX composite cover thickness, even though the cover grew substantially in size. An alternative design, with a stiffer cover, could have placed the crushable honeycomb on brackets close to the hinge axis where the impact forces would be higher, allowing for a more stable and compact

honeycomb design and reducing the torque output and energy absorption. The overall design would have been much simpler, reducing drawing, fabrication, and installation costs and schedule with the removal of the Energy Absorber structure and simplification of the Hinge mechanism. Additionally, the crushable honeycomb would have been replaceable without disassembly of the Energy Absorber mechanism.

GALEX placed the Latch mechanism on top of the cover due to mounting surface constraints and contamination control. However, the proposed configuration could have allowed the Latch mechanism to be mounted to the Cover Ring instead of on the cover. This would have removed the necessity of routing Latch cabling over the Hinge, eliminating cable parasitic torque drag. Additionally, the simplified cabling could have received cable stiffening micrometeorite shielding. With the Latch mechanism mass removed from the cover, the crushable honeycomb could have been placed close to the hinge axis instead of along the canister.

Cover deployment depended on Latch Arm rotation. The GALEX latch arm was positioned close to the instrument aperture opening and was rotated away from the aperture to reduce stray light issues. The rotation of the latch arm rotate introduced some potential single point failures. After the GALEX latch arm was adopted, it was discovered than an earlier mission that originally designed the Latch mechanism instead utilized a fixed latch arm with a slot in the path of cover deployment. Because the proposed design did not face the same stray light issues as GALEX, a potential failure mode was unnecessarily adopted and additional work was necessary to reduce risk.

The Latch mechanism is zero-fault tolerant in some cases as it depends on a single actuator (with redundant heaters) and a single set of pistons to translate prior to cover deployment. An alternate latch mechanism design using two Starsys pin pullers in a toggle type configuration could have been more desirable and would have been fully single fault tolerant. Additionally, the mechanism would have been less complex and would possibly have fewer parts and less expensive to fabricate.

Both the Latch and Hinge mechanisms were complex, with many tightly toleranced parts. These mechanisms were expensive and schedule intensive to fabricate. Simpler alternate designs described above would have potentially saved more schedule than building the heritage designs.

The Hinge mechanism is only capable of cover deployment with the Hinge axis aligned with gravity (vertically). It would have been preferable to incorporate a hinge mechanism that was capable of deploying the cover in any orientation as the instrument will not be positioned vertically during I&T and ATLO, making an end-to-end test impossible. Instead, cover deployment tests will be conducted before CDLM delivery to I&T. Once in I&T and ATLO, first motion tests will verify Latch mechanism functionality and the cover will be sweep to ensure there are no obstructions.

The Energy Absorber honeycomb was finalized before flight-like cable was installed over the Hinge axis during prototype cover deployment tests. It was expected that the cable could be wrapped in a way to provide a positive torque to aid the cover rotation, but was initially found not to be possible. Further prototype deployment tests with the cable showed that the honeycomb needed to be changed.

The crushable honeycomb Energy Absorber prototype effort cost significant schedule. In keeping the Energy Absorber housing similar to GALEX (and thus limiting the redesign of the support structure), the Energy Absorber still must be disassembled to be reset after a cover deployment test. This disassembly is only moderately less time consuming than a GALEX Energy Absorber reset.

While the residual end-of-travel Hinge torque output and magnetic latch provide enough force to keep the cover captured during spacecraft maneuvers, a positive latch mechanism would have been more preferable.

## **Conclusion**

Heritage designs offer projects an attractive means of reducing cost and schedule. However, without a thorough review and investigation of the state of readiness, a heritage design may impose unnecessary limitations and restrictions, in addition to cost and schedule impacts. It is recommended that trade studies be completed of designs similar in function to that of the proposed heritage design prior to adoption. Only then, potential shortcomings of the heritage design may become apparent.

Before adopting a heritage design:

- Perform trade studies of designs similar in function to that of the heritage hardware. Look for best solution.
- Thoroughly review heritage drawing package for completeness
- Verify the heritage design will meet project requirements
- Review heritage test data and test plans and verify they meet current projects requirements. If they do not, study impact and feasibility of revised testing.
- Review heritage design for failure modes. It can not be assumed that all modes were found, or that new modes will not be introduced.
- Perform all prototype testing with as flight-like hardware configurations as possible

## **Acknowledgements**

The research described in this paper was performed by the Jet Propulsion Laboratory, California Institute of Technology, under contract with the National Aeronautics and Space Administration.

The author gratefully acknowledges the contributions of JPL team members: Mark Balzer, Kevin Burke, Keith English, Ted Iskenderian, Mike Johnson, Ellyn McCoy, Doug Packard, Don Sevilla, and Brad Swenson.

## **References**

1. "HexWeb Honeycomb Energy Absorption Systems, Design Data", Hexcel Corporation, March 2005.



# Problems and Product Improvements in a Qualified, Flight Heritage Product

Chuck Lazansky\* and Scott Christiansen\*

## Abstract

This paper will discuss improvements to an existing, qualified, flight heritage launch restraint and release mechanism. The changes made to the design are the result of customer feedback, test failures, and optimization of performance margins. Specific test failures and their resolutions will be discussed. Impacts to field units, process controls, product heritage, and qualification status will be summarized. Conclusions and lessons learned will include aspects of what "qualified product" means and insights around what is required to improve a product based on lessons learned through production and customer use.

## Introduction

A Launch restraint/release device must meet a demanding set of requirements to be reliable and robust. Most importantly, the device must never release prior to command (during ground handling, transportation, launch, etc.) and must always release when properly commanded. A combination of redundancy and robust design features are typically used in pursuit of meeting these demanding requirements. The QWKNUT has been designed with these goals in mind, and has been shown through qualification and flight use to meet these requirements.



Figure 1. Gen 1 QWKNUT Mechanism

## Product Description

The QWKNUT is a device which utilizes a segmented nut to maintain and release an axial preload. The device accepts a standard, hardened,  $\frac{1}{4}$ -28 bolt to carry the nominal 13345-N (3000-lbf) load. Preload is released when the four nut segments are opened by activating the mechanism. Release of the device is initiated by a redundant pair of shape-memory alloy (SMA) wires within the QWKNUT, which are linked directly to the latch. The QWKNUT requires an electrical pulse (3-5 Amps, ~10-75 msec) similar to that used for pyrotechnic release devices. The pulse causes resistive heating of the SMA wire above its transition temperature, resulting in a strain of the wire and release of the latch.

Functionally, the mechanism can be separated into two parts: the **preload-bearing part**, and the **latch-release part**. The preload-bearing part consists of four nut segments (Figure 3). Axial load from the bolt exerts a radial load on these nut segments, which are retained radially by a set of rollers and a bearing outer race. This outer race has slots which correspond to each roller, such that rotation of the race allows the rollers to drop into these slots, allowing the nut segments to open and release the bolt. The outer race is preloaded with redundant coil springs acting to rotate the race and release the device.

---

\* Starsys Research Corporation, Boulder, CO

The outer race is prevented from turning by two latch pawls (called “toggles”) that engage the OD of the race. The ***latch-release part*** of the mechanism consists of a lever-arm which reacts the radial load from the toggles, and retains them in the outer race (Figure 2). Nominally, the lever arm is held against a stop feature, in the latched position, by a retention spring. The lever arm is acted on directly by the SMA wire, which upon activation rotates the lever arm and frees the toggles, causing release of the mechanism.

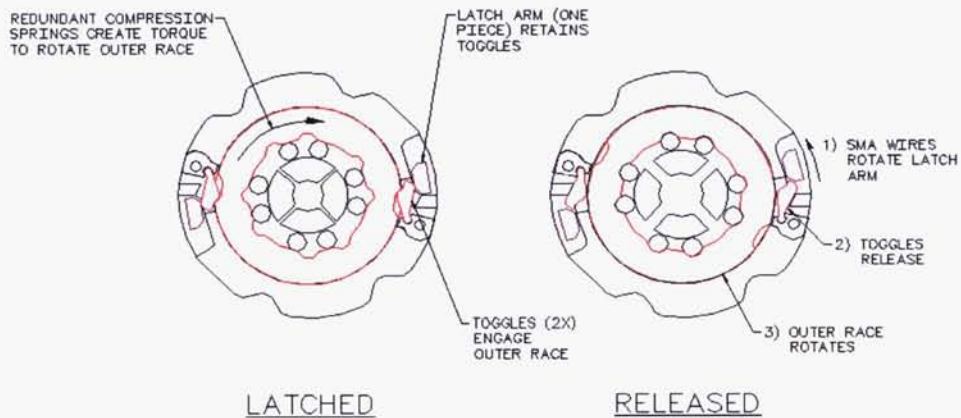


**Figure 2. Latch-Release Section Detail**

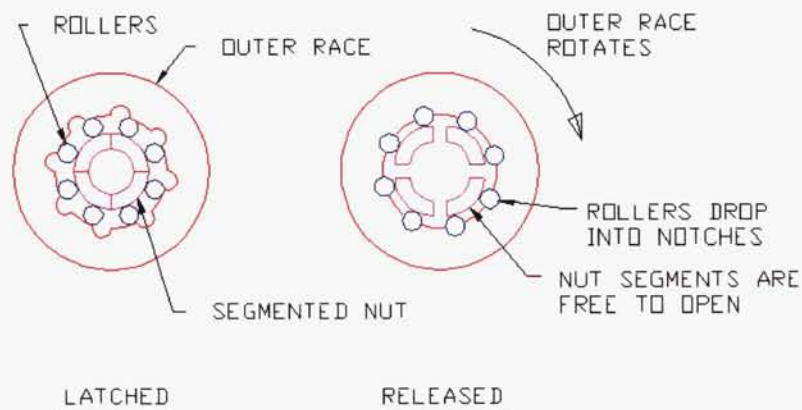


**Figure 3. Preload-Bearing Section Detail**

A key feature of the QWKNUT is that it is fully resettable. The reset procedure entails using a small tool to rotate the outer race back towards its latched position. The reset process is the exact reverse of the release sequence. Once the outer race is rotated, the rollers move radially inward closing the nut segments. The toggles then re-engage the outer race, and the lever arm, which is spring loaded, moves over both toggles to latch the mechanism. The straightforward reset process and multiple use capability is an attractive feature in a release device, allowing a “test as you fly” approach to ground verification. For additional ease of ground use, the original version of the QWKNUT contains cutoff switches, which discontinue power to the SMA circuits once release occurs. The switches are not rated for Flight use, and additional lead wires are included which bypass the cutoff switches for Flight.

## **History of Product**

The product was developed and fully qualified in 1999 with two test units. The initial production run of 4 units was delivered, and successfully flown, with the FalconSat1 program. Following the initial run, roughly six production runs were completed for various programs, totaling roughly 50 units. During this time, we became aware of improvement opportunities as we worked to support customers with specific flight applications. These were primarily usability issues related to damage during handling and operation, and included:

- Cutoff switch arm breakage
- Reset difficulty
- SMA wires burned by excess pulse energy
- Mechanism damage due to bolt over-engagement
- Strain relief of lead-wires

Some of these issues were addressed with engineering changes during these first 6 production runs. In 2004, engineering proposed more extensive design changes and an internal research and development effort was initiated. Production of the original design (Gen 1) was to continue until the new design(s) (Gen 2 and 3) and the delta-qualification program was completed. There were two versions of the new design to be qualified to suit different programmatic needs. The Gen 2 design did not include an in-line current shut-off feature. The Gen 3 design included a redundant, in-line current shut-off rated for Flight use as well as ground operation. While the above designs were being developed, the final planned production lot of the Gen 1 design was in process (circa May 2004). During this time, we encountered a failure in vibration testing of several Gen 1 Engineering units at levels well below qualification.

## **Test Failures**

Four significant test failures have occurred during the product life to date. These failures occurred sequentially and were linked together as the process of investigation and resolution were carried out for each. As each of the failures was investigated, our understanding of the mechanism increased. In some cases, the failures required an exhaustive process of properly addressing any and all affected hardware in the field. As painful as it was, the investigation process created invaluable opportunities to roll improvements into the Gen 2 and 3 designs, resulting in an extremely robust final product.

Starsys' FRB (Failure Review Board) process involves a systematic approach to failure resolution, utilizing tools such as failure trees, fishbone diagrams, and detailed tracking of closure actions. Regular reporting of progress and senior technical oversight continue until root cause and corrective action plans are determined, and the investigation is closed. From June of 2004 until November of 2005, the QWKNUT was under nearly continuous FRB activity for each of the failures described. These failures are an example of how a qualified design can fail, and evolve, over the product life-cycle.

## **Engineering Unit Vibration Failures**

In June of 2004, an Engineering Unit QWKNUT (Gen 1) undergoing development vibration testing released the nominal 13345-N (3000-lbf) preload under the relatively low level of 12 Grms compared to the 35 Grms qualification level. In reviewing the test setup, there were a number of potential causes including cross-axis noise on the vibration table, and a non-standard, massive bolt interface. However, two more EDU units at Starsys Research were vibration tested and also showed an intermittent release of preload at levels below the 35 Grms qualification. We initiated an FRB action to investigate the anomaly. With roughly 38 Gen 1 flight units delivered to customers and staged for flight use, there was concern regarding the scope of the anomaly and status of units in the field.

The engineering team generated a complete failure tree. As potential causes were eliminated, the failure tree pointed to the latch release portion of the mechanism. High-speed video of the failure event showed the lever arm moving slightly during vibration with respect to the toggles, and then moving suddenly, and fully, in the direction of release. A cause for this behavior could not be found initially. Physical and dimensional inspection of the parts did not reveal any clear discrepancies. The engineering analysis



showed relatively low inertial forces on the lever, which could not overcome the lever retention spring and drive the lever in the direction of release.

Tests were developed to assess latch performance. The lever retention spring force was measured, and also the net force required to release the lever arm from the toggles (force-to-release, or FTR). The results of the testing were that some units showed low lever spring force (up to 50% below nominal), and this was strongly correlated to vibration failure at 35 Grms. All units which failed in vibration showed spring force below nominal values. The low spring force was traced to yielding of the spring caused by installation damage, as well as overstress during manual releases. Though low spring retention force was strongly correlated to vibration failure, it did not explain the physical cause of the lever motion under vibration.

The true root cause was elusive. Driven in part by the need to resume production, the vibration performance was initially addressed by increasing latch retention spring force. This was accomplished with the addition of a second retention spring. The dual-spring design provided strong margin for load-holding under vibration, and was not vulnerable to handling damage. Validation testing of the proposed change supported the assertion that release margins and vibration margins were better balanced with the second spring, and that cycle life was not impacted. A formal Delta-Qualification test program of the new configuration was planned in parallel with production. The latch performance tests were also added to the production process as additional screens. However, when production resumed, the in-process testing showed inconsistent results for FTR screening. There was variability within a single mechanism that could not be explained. Production was stopped, and the investigation resumed with the focus on the dry-film lubrication layer at the latch interface. The lubrication was to be removed from the lever of a production unit to determine the source of the inconsistent FTR measurements.

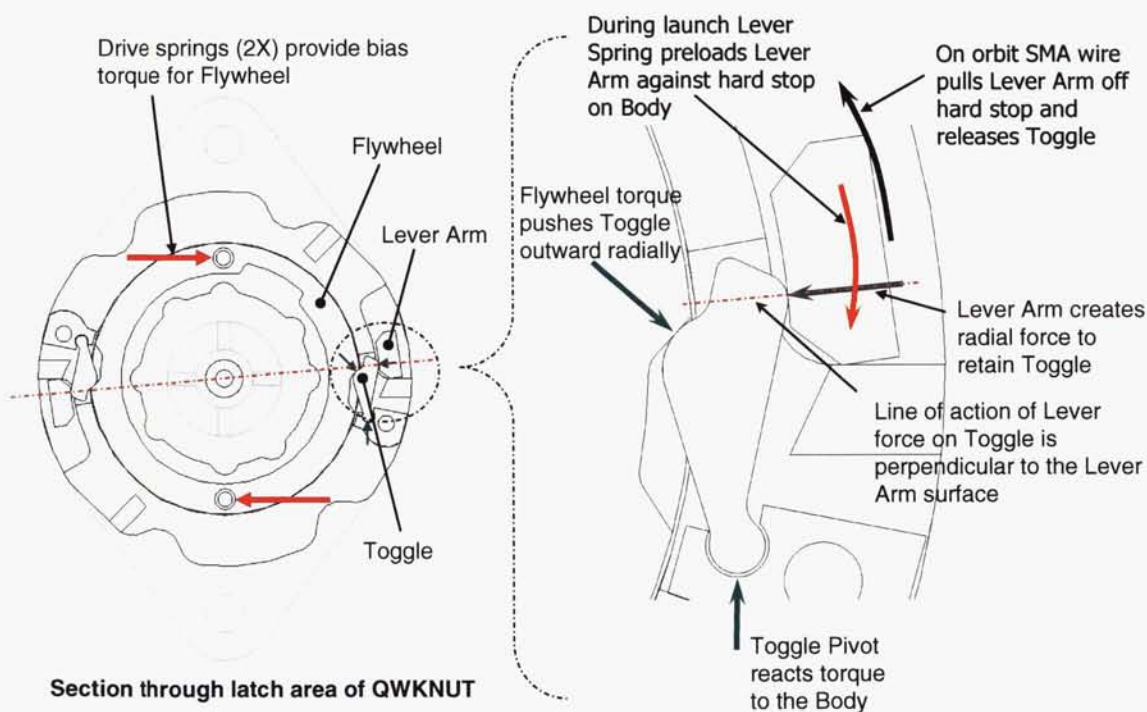


**Figure 4. Latch-Toggle Section Detail**

#### Failure Mechanism

The physical cause of the failure was discovered when lubrication was removed from the critical latch surface on the lever. The shape of the surface did not meet the intent of the design. The curved surfaces contained "flat" areas approximately 0.76 mm (0.030 in) in width, at each end (Figure 5). These flats were not easily seen with the dry-film lubrication present. The presence of the flats immediately explained the



intermittent vibration behavior and the variability in release force measurements. If the toggle is on the "flat" area of the lever, a tangential driving force results and leads to release of the device. If a toggle is located on the curved surface of the lever, no driving force is present and no release occurs (Figure 4). The width of the flats corresponds closely to the nominal location of toggle contact when the device is latched. In this case, small variations in toggle position on the critical surface caused the variability in latch performance. The physical cause was confirmed when the discrepant lever arm in the failed unit was replaced with a conforming part from another lot, and the unit passed 3 repetitions of vibration exposure (35 Grms, 3 minutes).

#### Root Cause

The root cause of the failure was found to be inadequate form control of the critical latch surface. Though the latch surface was depicted on the drawing with a continuous curvature, the dimensional controls were not adequate to ensure this. A total of 5 production lots of lever arms were received. The first 4 production lots of parts met the design intent. The 5<sup>th</sup> lot was procured from a new supplier who used a different machining process, which did not produce the intended surface at the critical latch point. The inspection process did not detect the different geometry since the drawing did not specifically control the feature shape. The inadequate drawing controls, combined with variation in manufacturing process (change of vendor, machine, or even machinist) created the opportunity for the discrepancy. Fortunately, the discrepant lot of levers was confined to the current production run, and no field units were affected.

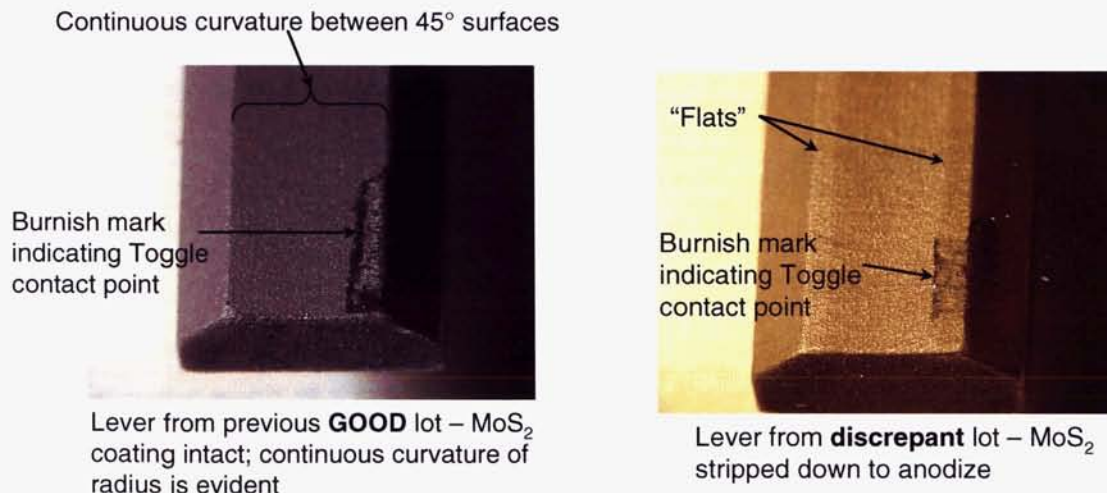


**Figure 5. Lever Surface Discrepancy**

#### Corrective Actions

The corrective actions for the vibration anomaly included adding proper engineering controls to the critical lever surface to ensure design intent is met. The curved surface is now tightly controlled on the drawing using runout and true position callouts. 100% inspection of this surface is required per an inspection process defined on the drawing, followed by engineering review before parts are certified and released. Process controls were also added at the assembly level to verify proper latch performance. These include measurement of retention spring force and force required to release the latch and defined pass/fail criteria (Figure 6). The latch release point is also screened against pass/fail criteria. The dual-spring design change was implemented (and delta-qualification tested) to improve margins for vibration performance, and prevent handling damage. Finally, acceptance level vibration testing under nominal preload is performed on all units.

Once the lever surface was restored to the intended geometry, the device has proven to be extremely robust with respect to vibration exposure. Delta qualification tests were performed at greater than 42 Grms with the lever arms intentionally shimmed 0.508 mm (0.020 in.) in the direction of release (to approximately 70% of the release point) and all units passed the test.





**Figure 6. QWKNUT Latch In-Process Test Fixture**

#### Discussion and Lessons Learned

The vibration anomaly is an example of how insufficient controls on critical features will, in time, cause a failure. The first four production lots were not discrepant, and there was no indication of a shortcoming in the design -- the problem was simply dormant. Design intent must be clearly communicated in engineering drawings. This requires a thorough understanding of which features are critical to performance. If adequate engineering controls are not in place, the discrepancy will eventually emerge with enough repetition (or opportunity). Parts from different lots may both meet the same drawing requirements but perform differently in a mechanism. Proper identification and inspection of critical features is essential, and in-process screening at the assembly level provides redundancy in detection of variation.

Failures are sometimes created as a result of two or more prevailing conditions. Care must be taken to ensure root cause and all contributing causes are identified before the investigation process is concluded. Low spring force was initially thought to be the cause because with a certain minimum spring force, even the discrepant lever geometry could not cause a vibration failure. Increasing spring force did resolve vibration release, but did not create consistent latch performance. Proper performance under vibration loads is now ensured by a combination of geometric drawing controls, a rigorous inspection plan, assembly level screening tests, and finally ATP. These added controls, and a deeper understanding of the design, were some benefits of the investigation process.

#### **Failure to Release during ATP**

Following the resolution of the vibration anomaly, production of the QWKNUT resumed with the vibration corrective actions fully implemented. The "Gen 1A" QWKNUT configuration now contained dual-springs for lever retention, and flight units were assembled in parallel with Delta-qualification activity. During acceptance testing, a flight QWKNUT failed to release preload during an ambient functional test. The unit operated nominally using the primary SMA circuit, but did not release when the secondary SMA wire circuit was activated. The testing was stopped and the FRB team was again convened.

Physical observation of the failed unit helped guide us quickly to the physical cause. The lever on the activated side of the mechanism had disengaged properly from its toggle, but on the opposite side, the lever was still engaged with its toggle (Figure 7). This prevented the outer race from rotating and releasing the mechanism. The lever arm appeared to be tilted at an unusual angle, and one end was in contact with the underside of the cover, which is directly above the lever. The mechanism was in a partially released condition. In this condition, the mechanism could be released with further travel of the lever arm. Minimal added force was required, on either side of the lever, to pull the lever free from the engaged toggle. When the partially released mechanism was activated with the opposite (redundant) SMA wire circuit, it released full preload. This distinguishes the condition from a "jam" in which increased force is encountered with mechanism movement. What we observed was a stable lever position at a point in the travel which should have resulted in complete mechanism release.



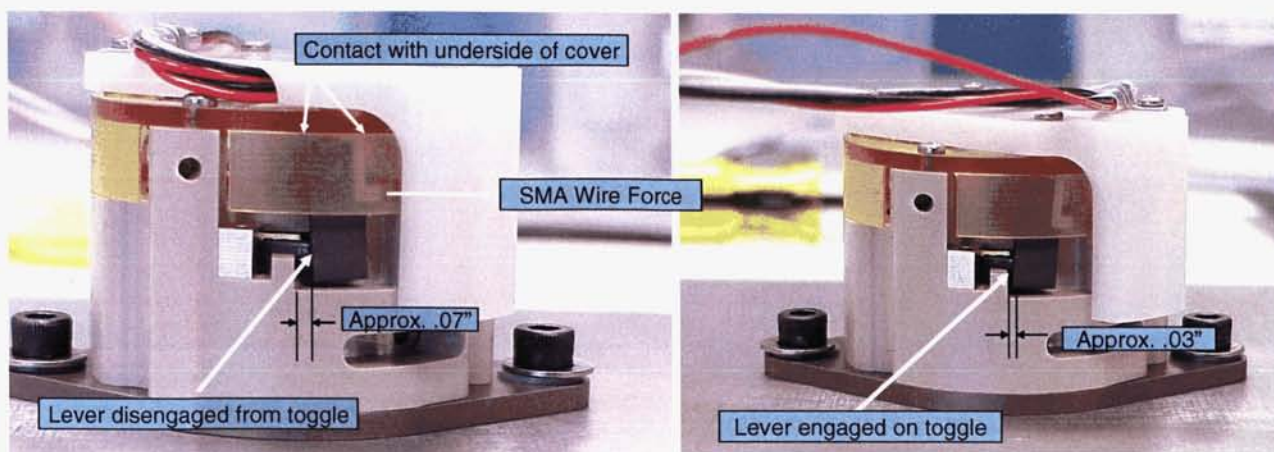


**Figure 7. QWKNUT in Partially Released State**

#### Failure Mechanism

The tilted lever arm in the failed unit had been stroked about 1.78 mm (0.070 in) from its stop. Previous testing had shown that only 1.02 mm (0.040 in) of lever travel will release the mechanism. It was determined that the addition of the second spring changed the force balance on the lever arm during actuation. The result was the observed tilting motion of the lever during release, which extended the nominal latch release point from 1.02 mm (0.040 in) to over 1.78 mm (0.070 in). Figure 8 shows how forces acting on the lever, including the added spring force, contribute to the anomalous tilting motion. The extended release point is only part of the failure mechanism.

The SMA wire stroke expected from analysis and early development tests was 2.29 mm (0.090 in). It was unclear why the unit had not released even with the extended release point. This led us to measure actual SMA wire strokes for the entire lot using high-speed video. Measurement of the 7 units in the failed lot showed a mean stroke of 1.85 mm (0.073 in) and a variation of  $\pm 0.305$  mm (0.012 in), well below the expected 2.29 mm (0.090 in). The unit which failed had the lowest recorded stroke in the lot (1.55 mm, or 0.061 in). If the failed unit had the expected SMA stroke it would have released, but the stroke was not available. The extended release point in combination with reduced SMA wire stroke produced the failure. Both are required for a partial release to occur. This failure is essentially one of low performance margins. The stroke margin on the failed unit was less than zero.

In addition, the partial release behavior was only displayed when the mechanism was under preload. However, the process screenings were all performed with no applied preload, and the anomaly was not detected until test. All units in the failed lot displayed the partial release behavior during screening once preload was applied. In addition, the forces required to release the latch increased significantly with the presence of preload. A majority of units in the lot showed unacceptably low actuation force margin.

The described anomaly was present only on units with the dual return springs. Single spring units were not affected. Fortunately, though we did not have the margins we expected in the dual-spring design, acceptable margins were confirmed in the single spring units. This limited the scope of affected units in the field.

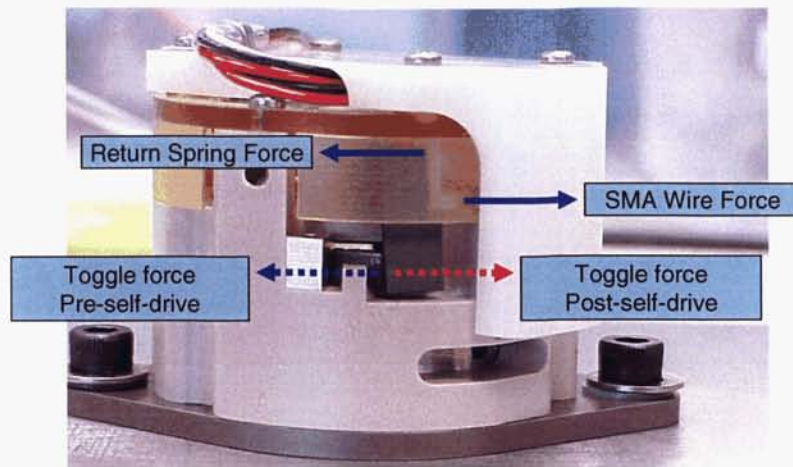


**Figure 8. Forces Acting on Lever Arm**

#### Root Cause

The change to the dual spring design created an anomalous lever motion during release. The tilting motion that was introduced to the lever required significantly more stroke from the SMA wire than the single spring design. The motion of the lever arm was not properly constrained in the design, but until the second spring was added, there was no impact to performance. The tolerances in the latch assembly allowed for the anomalous tilting motion, and this was a root cause of the failure.

The other root cause was variability in the manufacturing process. SMA wire stroke was found to be lower, and more variable, than expected by previous test results and analysis. Wire stroke measurement was not part of the manufacturing process for the QWKNUT. There was inherent process variability that had not been characterized. The wire setting process had also drifted with ongoing production lots and different operators since its development. Without in-process measurement of stroke, the drift was not detected.

Finally, a contributing cause was that the in-process latch screening tests were not performed under load. An assumption was made that load bearing part of the mechanism performed independently of the latch portion, which was not correct. Preloading the mechanism for the screening tests takes more time, and adds cycles, but it is necessary. In designing screening tests, care must be taken to ensure the tests accurately represent true operating conditions.

#### Corrective Actions

Corrective actions for the Release Anomaly were:

1. A stabilizing washer was added to control lever arm release motion and eliminate "tilt" and the partially released state.
2. The SMA wire setting process was improved to increase the mean stroke and reduce variation (was reduced by 30%). Actual SMA wire stroke was to be measured on each unit.
3. New process controls were added to measure latch release point and SMA wire stroke, and determine actual performance margins present in each flight unit. Existing process controls were now to be performed with the mechanism under nominal preload, which better reflects true operating conditions.



4. A process for adjusting stroke margin was developed, consisting of a shimming operation at the stop feature for the lever. This allowed us to tune the latch release point to match SMA wire stroke capability, so that acceptable stroke margin is achieved.
5. Lever retention spring force was tuned to a range, and controlled with a maximum. This ensured adequate release force margins. Force margin is verified on each of unit as part of the production process.
6. All field units with the dual lever return spring were recalled under a Technical Bulletin for measurement of stroke and force margins. With some schedule impacts, all units which had been built with dual springs were rebuilt and re-tested with the new stabilizing washer, process controls, and delivered with full margins for Flight use.

#### Discussion and Lessons Learned

The primary challenge of a release device is to maintain high performance margins for both pre-load retention and operation. It is interesting that anomalies have been encountered in both these areas, sequentially. The vibration anomaly focused attention on the preload retention aspect, and the analysis showed that margins would be balanced with the dual spring. With the focus on improving vibration performance, we added spring force and disturbed the release performance. Sometimes in an effort to resolve one failure mode, we accidentally introduce another one. This is especially true when failure investigations are performed under tremendous schedule pressure. In our case, the dual spring solution was tested with greater than 400 life cycles prior to implementing the change, but the test unit had positive stroke margin. Though the test unit passed, a variation in manufacturing process created a failure of the revised design in a subsequent lot. The release anomaly is an example of unintended consequences of a simple change, and insufficient controls on critical processes. The change to the spring was necessary, and carefully implemented. But even with careful steps taken to validate the change, there was an impact to mechanism performance.

When evaluating a qualified product, the variability of the production environment must be considered. It is impractical and expensive to attempt qualification testing with all design tolerances at worst case. However, worst case production results should be enveloped by the qualification program. In general, this means that a production process control plan should be developed prior to qualification activities. A qualified product must be manufactured with stable, controlled processes or future production lots will not be similar to the original product.

Another lesson from this anomaly is that analysis of performance margins should always be verified by actual measurement. Force and stroke margins on the QWKNUT were measured during development, but not as part of the ongoing production process. The release anomaly led us to verify actual performance margins, and ultimately these margin measurements were made a permanent part of the production process. Stability of the performance margins over the product's cycle life has also been verified. The overall result is more robust hardware.

The investigation process was difficult and expensive, and impacted deliveries to several programs. It is painful to have to recall flight hardware which has been delivered. However, the process has been instrumental to the advancement of the design. We would not have discovered low SMA stroke and variable performance margins had we not made the change to the dual spring. All 3 design generations have been enhanced by the investigation of this anomaly.

Once the corrective actions were implemented, we proceeded to qualification of the "Gen 1B" design with optimized design and manufacturing process.

#### **Life-Test Pin Failure**

Delta-Qualification of the Gen 1B design proceeded, using two test units which were rebuilt from the failed lot in the release anomaly. The units passed all tests and proceeded into an extended life test, at the end of which another failure was encountered. In each unit, one of the two spring posts ("flywheel



pins”) on the main drive element broke. The life test is a 200 cycle test, to support a 100 cycle life rating for the device. The failure occurred at a thread relief on the pins in both units. The fracture surface displayed characteristic signs of a low-cycle fatigue failure. This type of failure had not been seen before in previous life tests.

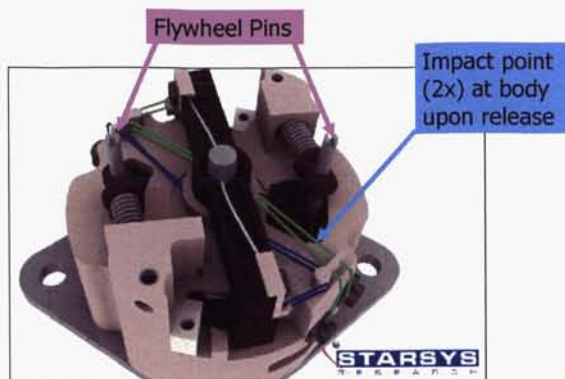


**Figure 9. Flywheel Pins in QWKNUT**

#### Failure Mechanism

The flywheel pins in the QWKNUT transmit force from the main drive springs to the outer race (or “flywheel”). They also serve to limit travel of the outer race following release, and are subject to an impact load with each cycle (Figure 9). The initial investigation steps were to measure the corner radii and estimate the total number of impact cycles seen by the pins. Sample pins taken from the failed lot showed that the corner radius at the point of failure was undersized, and measured between 0.000 and 0.051 mm (.000 and .002 in). The pin drawing controlled the corner radius only by block tolerance to a minimum of 0.076 mm (0.003 in), and the parts were therefore discrepant per the drawing.

When the number of cycles on the failed units was counted, we found they had over 450 documented releases, and an indeterminate number of un-documented manual releases. This inordinately large number of cycles was due to all the activities from the previous two investigations. This included in-process checks, multiple rebuilds and confidence tests, and finally, the qualification cycles. When number of impact cycles and the undersized radius were considered in a fatigue analysis, the failure should have been expected. The physical cause of the failure was a classic combination of stress concentration and cyclic loading.

A total of 5 lots of flywheel pins were procured since product inception, and only the most recent lot had a corner radius below the block tolerance of .076 mm (.003 in). Analysis showed that with a radius of  $> .089$  mm (.0035 in), the mechanisms would have a predicted cycle life of at least  $10^4$ , which confined the hardware affected by the failure to the current lot.

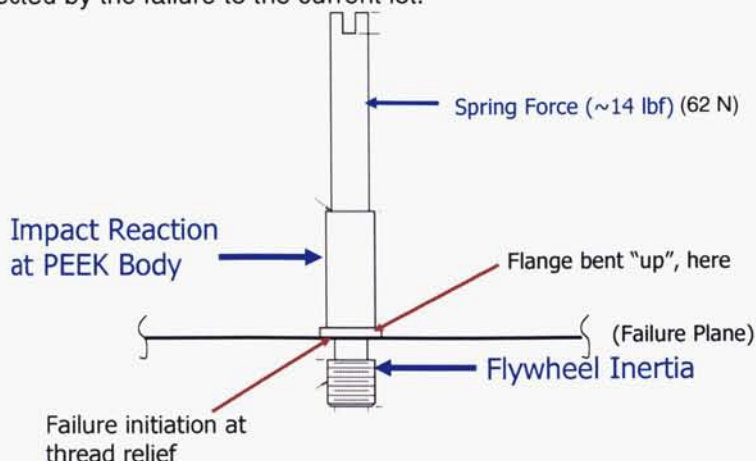


**Figure 10. Force Balance on Flywheel Pin**

### Root Cause

The physical cause of the failure was the discrepant corner radius. The failed lot of pins was machined with a sharp corner which violated the block tolerance. However, the discrepancy was not caught at inspection since it was only a thread relief subject to block tolerances. Even though the parts were discrepant per the drawing, it is clear that the critical radius was not adequately tolerated. Given the exposure to cyclic impact loading, a specific radius callout was needed along with inspection requirements for the feature.

A contributing factor to the failure was the high number of cumulative cycles on the test units, without which the failure would not have occurred.

### Corrective Actions

Corrective actions implemented as a result of the failure include addition of a healthy radius (.305-.432 mm or .012-.017 in) at the thread relief on the pin, and a countersink in the mating part. These were flagged as critical inspection features on the drawings. The mechanisms in the failed production lot were rebuilt with the improved geometry. Life tests were performed and confirmed essentially infinite fatigue life with the revised radius callout. In addition, a cycle log is now maintained during production to monitor all mechanical releases of the device, to preserve as-delivered mechanism life.

### Discussion and Lessons Learned

During a failure investigation, unintended overstress of components can occur even with a careful approach. Prior to this failure, we were not concerned about any life-limiting component in the mechanism. The need to develop the process controls and characterize the hardware was real and the cycles were not believed to be stressful to the units. The mechanisms in this lot were first produced as single spring units (Gen 1), then rebuilt as dual-spring units (Gen 1A), and rebuilt yet again with the stabilizing washer (Gen 1B). If the mechanisms had not been operated and tested so extensively in the previous investigations, they would have easily passed the Delta-qualification test. Again, focused on failure resolution and developing adequate process controls, we overstressed the hardware and introduced another failure mode.

A more obvious lesson: always ensure a proper corner radius is specifically called out at corners of thread reliefs – especially on shoulder bolts subject to cyclic loading.

The pin failure is an example of a vulnerability in the design which only required repetition (multiple lots) to create the conditions for a failure. Even the most careful design reviews will not eliminate all areas of vulnerability. In commercial manufacturing, process variation and scrap occur even on the best production lines because of recurring opportunity for variations. The same is true in production of aerospace hardware. Small lots of space hardware which pass a single qualification program are not necessarily without areas of sensitivity in the design. With repetition in procurement and manufacture of future lots, the failure modes will be revealed.

A new failure mode was not a welcome development in our path to complete the last of the Gen 1 production lots. There was concern for the impact to field units before the full lot history of the pins was completed. Fortunately, no delivered units were affected.

## **Gen 2 Design and Roller Position**

About the time the pin failure was resolved, the Gen 2 qualification test program was starting. The Gen 2 design incorporated significant revisions for usability and manufacturability, and was subject to intensive review. During qualification level pyroshock testing on the Gen 2 design, 2 test units were exposed to out-of-spec shock levels, and released preload. Though the over-test condition was a clear physical cause, a thorough investigation process revealed an underlying, physical root cause to the preload release. In the process of changing a feature for the Gen 2 design, the nominal position of the 8 rollers was inadvertently shifted relative to their detent slots in the outer race.



**Figure 11. Section View of Rollers (2 of 8 shown)**

#### Root Cause

A Slot in the body was enlarged to allow room for a larger diameter flywheel pin. The pin was enlarged to allow for threads in the pin, to add a fastener to secure the main drive spring connection. This change was made to address usability feedback from customers regarding difficulty with reset. What was not considered at the time of the change was that the body slot was a stop feature for the roller cage, which locates the rollers relative to flywheel in the latched condition (Figure 11). The result was that the rollers were moved closer to detents in latched condition compared to the Gen 1 design. The new position was nominally on the radius transition into the detent. This did not adversely affect nominal operation, but under pyroshock exposure, especially in an over-test environment, a loss of preload occurred.

#### Corrective Actions

The problem was corrected by relocating the stop feature on the cage, returning the rollers to a nominal position. The roller location was revised to be slightly further from the detents than the original position to allow for tolerance stack-up and achieve a more balanced roller position. Units which were retested in pyroshock with the corrected design did not lose preload. The change was implemented and the qualification program was re-started with the corrected cage corrected design. All Gen 2 units were rebuilt with the corrected roller location, and the Gen 3 design was similarly revised.

#### Discussion and Lessons Learned

This failure is an example of an unintended consequence of a simple change that was made from Gen 1 to the Gen 2 designs. The reason for the change was to prevent the difficulty resetting the mechanism that can occur when the main drive spring rides up on the pin. The pin was enlarged to allow a fastener to retain the spring, and the body feature was revised to accommodate the pin. Revising the body feature shifted the roller position and affected mechanism performance. This change, along with other changes made between Gen 1 and Gen 2 designs, was heavily reviewed on multiple occasions. Even with thorough review, subtle interactions can be missed and changes can have unintended consequences.

#### **Product Status**

Gen 1 production has been phased out. The Gen 2 and Gen 3 qualification programs are underway and contain all cumulative engineering improvements and lessons learned. Tolerances, fits and geometry of all parts have been extensively reviewed and optimized for these next generation designs. The programs are due for completion in mid-2006.

At present, there are at least 30 Gen 1 QWKNUTs integrated for pending flight missions. While this delivered Gen 1 hardware has met all test requirements and remains extremely flight-worthy, the robustness of the product has been greatly enhanced as a result of problems we've addressed.



## Overall Conclusions and Lessons Learned

A “qualified” product is typically held as proven, stable, and unchanging in a world of carefully assessed program risk. Yet, change is necessary over a product’s lifespan as limitations in a design are discovered. These limitations range from feedback on usability from customers to full-blown failures. How can this contradiction – that change is both inevitable and discouraged – be resolved? A “qualified” product should not be considered frozen or static in its configuration, since change will be required as production continues. The process of engineering changes to qualified hardware must be carefully managed. As potential design issues are discovered, a difficult process of assessment of field units, and possible recall, may be required. While design changes to established products are essential to improve reliability, usability, and robustness, the risks of unintended consequences must be understood and discipline in the assessment and incorporation of changes must be maintained.

Qualified, Flight heritage products are sensitive to a large number of variables. Proper engineering controls (print requirements, inspections, screening, etc.) can reduce or detect variability, but not eliminate them. Every design has areas of sensitivity waiting to be revealed by real-world variations. Any problem which can potentially occur eventually will, given enough time and repetition. This is part of the reason for holding ample design margins. However, sometimes these areas of sensitivity are not analyzed and escape the design team’s awareness. The pin which failed in life-test had reported mechanical margin of >10. In a low-cycle fatigue environment, this part failed. Expect problems and variations in performance, and expect a constant effort to identify and eliminate sources of variation. This mindset supports overall product reliability more than a rigid notion that a design is qualified and therefore not subject to variation.

The importance of thorough analysis and review of a design goes without saying. Design intent must be clearly communicated in engineering drawings. We must understand all features of the design which contribute to performance, not just the critical features, in order to understand the impact of changes. This is not as easy as it appears. Discipline in assessment of changes is crucial, since well intentioned, seemingly innocuous design changes can have unintended consequences.

Definition of a qualified product must go beyond passing a single test program:

- Qualification programs are bounded by the realities of cost and schedule, and may be driven by an individual risk assessment for a given program.
- Number of qualification units is typically limited.
- Testing is normally confined to one production lot.
- Testing at extremes of piece part tolerances is not feasible.

The point is to understand the limitations of a “qualified” product. In addition to qualification testing the product, the process for manufacturing and testing that product must also be qualified. Ask:

- What are the critical design features, and how are they to be controlled and inspected?
- What screening steps and process controls are needed ensure expected performance?
- What are the greatest sources of variability in production and how can they be mitigated?
- Can performance margins be verified in-process, or at least periodically?

A well developed process control plan is critical to keeping variability in check. Thorough in-process and acceptance test programs combined with inspection plans can be effective at detecting process escapes and discrepancies. Consider periodic re-qualification activities, such as a first article “qualification” with new production lots of critical parts, especially if a new supplier or process was used.

Flight Heritage is only one factor in assessing reliability of Flight components. Other arguably more important criteria are robustness of design, stability of processes, rigor of the test program (acceptance and qualification) and demonstration of margins. Do not rely on analysis (or manufacturer claims) alone to verify margins. Perform tests, and incorporate tests into the recurring process. Reality frequently has more variability than the analysis, and its supporting assumptions, can capture. Though our analysis

showed ample stroke margins in the QWKNUT, the variability of the production environment resulted in margins well below the analysis.

When failures do occur, a disciplined approach to investigation is vital to ensure true root cause is identified and corrected, and that the approach does not compromise hardware. During a failure investigation, multiple tests, combined with non-standard testing to resolve a specific issue, can lead to over-stress of other parts in the system. In addressing the vibration failure, we did not expect to trigger another failure due to overstress. We can frequently become so consumed with solving one problem that we create another problem with the hardware. Continued testing and resolution can sequentially fail one part, then the next, and so on. This can be a painful process, but ultimately one that makes the hardware better.

Failures present an opportunity to make significant improvements in a product. Close scrutiny of a design during failure investigations allows discovery and resolution of issues outside the scope of the failure, resulting in a more robust product. The learning that takes place during a failure investigation can far surpass the most effective design review process. In the course of our investigations we found ourselves saying *"we never would have discovered this problem if..."* Specifically, if the discrepant lot of levers had not caused a vibration failure, the dual spring design change would not have been made. Performance margin variation would not have been detected, and the mature process controls now in place may not exist. Though our industry can be intolerant of products with a history of anomalies, the investigation process is an effective and perhaps necessary path to a truly robust and reliable product.

# SoftRide Vibration and Shock Isolation Systems that Protect Spacecraft from Launch Dynamic Environments

Conor D. Johnson\*, Paul S. Wilke\* and Scott C. Pendleton\*

## Abstract

Reduction of the vibration and shock loads seen by spacecraft during launch greatly reduce the risk that the spacecraft and its instruments will be damaged during their ascent into orbit, and also allow more sensitive equipment to be included in missions. Protecting the satellite from these loads by whole-spacecraft vibration and shock isolation systems has now been demonstrated. The basic concept of whole-spacecraft isolation is to isolate the entire spacecraft from the dynamics of the launch vehicle. This paper discusses two different systems: the SoftRide system and the ShockRing system. This paper discusses each of these types of systems and presents flight data that demonstrates their effectiveness.

## Introduction

Satellites are perhaps among the most amazing products in use today, used for many purposes from communications to reconnaissance to weather prediction, and much more. Like all other products, satellites undergo design, fabrication, test, and shipment. However, the shipment of a satellite to its final destination in orbit is far more complicated than for all other products. Since the launch of the world's first satellite in 1957, the capability and reliability of launch vehicles have improved dramatically. What has not improved in 48 years of launching satellites is the launch vehicle-induced vibration and shock environment that a satellite must endure on its trip to orbit. Excessive dynamic and shock loads can be a satellite killer causing permanent damage to electronics, optics, and other sensitive equipment. To compensate for the harsh dynamic environment, payloads must be designed and tested to very high dynamic levels, greatly increasing the cost of many payload components. An excellent alternative is to reduce the launch dynamic loads through the use of whole-spacecraft passive vibration isolation.

Whole-spacecraft vibration isolation has been developed to attenuate dynamic loads for some launch vehicles<sup>1,2</sup>, has been successfully flown several times, and is in development for other vehicles and loading conditions. Whole-spacecraft vibration isolation systems can be discussed as systems that significantly reduce the dynamic loads in both the low frequency range (coupled loads analysis range) and in the high frequency range (shock loading range) or systems that only reduce the high frequency shock loads (Figure 1).

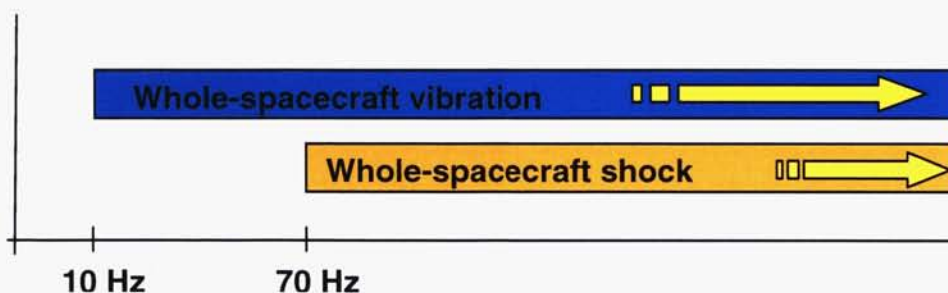


**Figure 1. Frequency ranges for attenuation for shock and vibration isolation systems**

Whole-spacecraft vibration isolation systems have typically been designed to date to attenuate launch dynamic loads from about 12 Hz and upward. This is very useful for mitigation of vibration loads on launch

\* CSA Engineering, Inc., Mountain View, CA



vehicles and also functions to isolate higher frequency shock loads. Whole-spacecraft shock isolation systems, on the other hand, are being designed to attenuate launch shock loads from about 70 Hz and upward. Most damaging shock loads have their most significant magnitude in the 1000 Hz and upward frequency range, however dynamic loads between 100 Hz and 1000 Hz are still considered to be shock loads and this frequency range has been known to be a real source of problems for some launch vehicles.

So the logical question is: Why not always use a vibration isolation system, as opposed to a shock isolation system, and get the isolation benefit from the lowest possible frequency? The answer lies in the relationship between the isolation system, the launch vehicle guidance, navigation, and control (GNC) system, and coupled loads analysis. The whole-spacecraft vibration isolation system is lower in frequency and stiffness than a shock isolation system and is carefully sized, for each mission, using coupled loads analysis. The first bending modes of the satellite are typically reduced by the introduction of a vibration isolation system and therefore must be designed in concert with the GNC system such that control instabilities are not introduced. Again, this is possible, and has been done successfully on several flights. The whole-spacecraft shock isolation system, on the other hand, is relatively high in frequency and stiffness and has little or no effect on the GNC system or on coupled loads analysis. For missions that do not anticipate any problems with lower frequency vibration loads, a shock isolation system will be easier to include with only minimal effort.

Under a number of contracts from the Air Force Research Laboratory, Space Vehicles Directorate, CSA Engineering has been working on the concept of whole-spacecraft vibration isolation and shock systems (hereinafter referred as the SoftRide system) since 1993. A number of design and performance analyses were performed on a variety of liquid-fueled and solid-fueled launch vehicles, all of which showed great promise. However, it was not until the launch of the GFO spacecraft on Orbital Science's Taurus launch vehicle in February 1998 did an isolation system designed to vibration-isolate the complete spacecraft actually fly. Since that time, two different types of systems have flown, and design work has been performed on several additional launch vehicle/spacecraft combinations. The following sections discuss each type of system, show hardware pictures, and present flight results.

### **SoftRide Vibration Isolation Systems**

Typical vibration isolation systems work by connecting the isolated structure (payload) to the base structure (launch vehicle) by means of a resilient mount or mounts. The resilient mounts have low relative stiffness as compared to the base and payload, and some degree of structural damping. The stiffness of the resilient mounts is tuned so that the frequency of vibration of the supported payload on the resilient mounts is a specified value (isolation frequency). Damping in the resilient mounts reduces the amplitude of response of the payload at the isolation frequency when the system is under external excitation. The resilient mounts must allow relative motion between the vibrating base structure and the payload at the isolation frequency, which is referred to as the isolator stroke.

Because the spacecraft is a major structural component of the launch vehicle/spacecraft dynamic system, variations in the isolation frequencies greatly effect the dynamics of the launch vehicle/spacecraft system. Any unpredicted changes in the dynamics could have an adverse effect on the control system of the launch vehicle and cause instability and thereby loss of the mission. Therefore, the stiffness properties of the isolation system must be predictable for the duration of the flight. This requires a linear isolation system under all load cases, including preloads from  $-2g$ 's to  $+6g$ 's accelerations of the launch vehicle. This eliminates using an elastomeric material (i.e., rubber mounts) as the stiffness component of the isolation system. Owners of spacecraft, which costs tens to hundreds of millions of dollars, demand a metallic connection between the spacecraft and the launch vehicle. This connection, which is the SoftRide system, must also provide a fail-safe connection, must be able to handle, without overstressing, the deflections due to the sum of the dynamic and quasi-static acceleration loads of the spacecraft, and must be of minimal height (reduces payload volume) and weight (reduces payload weight).

On expendable launch vehicles, spacecraft are attached to the launch vehicle at their base either at discrete points or by a band clamp. If the attachment stiffness is made soft in the axial or thrust axis, then we refer to that type of isolation system as an axial system. Axial systems can provide isolation in the axial and two rocking directions and therefore can isolate against both axial and bending modes of the launch vehicle. If the attachment stiffness is made soft in the in-plane directions at the attachment points, then

that type of isolation system will be referred to as a lateral or shear isolator. Whole-spacecraft vibration isolation systems may also be a combination of these.

The SoftRide whole-spacecraft vibration isolation systems have flown on two different launch vehicles to date: Orbital Science Corporation's Taurus launch vehicle and the Air Force Minotaur launch vehicle (Figure 2). This paper discusses axial and combined axial + lateral SoftRide systems designed for and flown on these launch vehicles. Even though these systems were designed to reduce transient vibration loads below 80 Hz, they performed extremely well at reducing high-frequency loads. Whole-spacecraft vibration isolation systems are now offered as a launch option in the Taurus Launch System Payload User's Guide<sup>1</sup> and in the Minotaur Payload User's Guide<sup>2</sup>. Minotaur is a four-stage, ground-launched solid propellant, inertially guided spacelift vehicle from Orbital Sciences Corporation. It uses the first two stages from the Minuteman II intercontinental ballistic missile (ICBM) combined with the upper two stages, structure, and fairing from the orbital Pegasus XL air-launched space vehicle<sup>3</sup>.



**Figure 2. The Taurus and Minotaur launch vehicles**

### **Passive Whole-Spacecraft Vibration Isolation Systems**

Two types of passive whole-spacecraft vibration isolation systems have been flown. These are (1) a patented uniaxial damped flexure system called SoftRide UniFlex, and (2) a patented multi-axis damped flexure system called SoftRide MultiFlex. These systems are intended to attenuate low-frequency launch vibration loads from about 20 Hz and higher.

The SoftRide vibration isolation systems seek to reduce dynamic loads on a payload by blocking the transmission of dynamic loads present in a base structure to which the payload is attached. The design of classical vibration isolation systems typically assumes that the base is rigid and the isolated payload has dynamics only well above the isolation frequency. Contrary to this, the design of a SoftRide system must be done with full knowledge that the structures on either side of the isolation system, namely the launch vehicle and the spacecraft, are both very rich in dynamics. This necessitates that the SoftRide system must be approached from the perspective of system-level dynamics.

Some of the typical design constraints are weight, volume, and strength. Two other major constraints on the design of the isolation systems are:

- Do not introduce excessive spacecraft to fairing relative displacement.
- Do not introduce modes that are too low in frequency or high in amplitude such that they interfere with the LV attitude control system.

The design of the isolation system therefore requires coupled-loads analysis (CLA), along with detailed design analysis. The basic procedure involves the following steps:

- Preliminary CLA with worst load cases to optimize system-level isolator performance and get component-level requirements
- Isolator concept design to meet component-level performance requirements
- Isolator loads analysis to determine design loads for isolator strength design



- Isolator detailed design to arrive at a design that meets all strength and performance requirements
- Complete CLA using final detailed isolator models in the system model to verify system-level performance

The CLA must be performed with actual launch vehicle and spacecraft models. The typical procedure at CSA is to obtain LV models and loads for worst case conditions from the LV manufacturer and perform CLA with the latest model of the spacecraft supplied by its manufacturer. Once the detailed isolator design analysis is completed, then a model of the isolation system is delivered to the LV manufacturer for a complete and final CLA.

The following sections describe the isolation systems and present flight telemetry data.

#### SoftRide UniFlex

The patented SoftRide UniFlex whole-spacecraft vibration isolation system is intended to reduce dynamic launch loads that are predominantly axial (thrust-direction) in nature. The design procedure requires CLA to accurately predict the responses of the spacecraft with an isolation system. As an example, CLA showed that the isolation system significantly reduced spacecraft responses due to the resonant burn load. For example, the spacecraft net C.G. response in the axial direction was reduced by a factor of seven by using the isolation system (Figure 3).

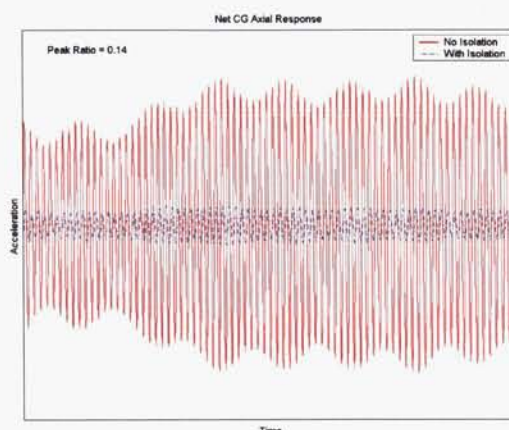


**Figure 3. Spacecraft axial C.G. response, resonant burn load**



**Figure 4. SoftRide UniFlex and its installation**

The stiffness and damping of the isolators are sized to mission-specific requirements for reduction of these dynamic loads. This system consists of a set of damped flexure elements that connect the spacecraft to the launch vehicle. Figure 4 shows a UniFlex isolator. This consists of a titanium flexure and a constrained layer damping treatment. The metallic load path of this isolator allows a strong, predictable, stable connection between the spacecraft and the launch vehicle. The damping treatment provides sufficient damping to control resonant amplification of loads. The typical application of this isolation system is to replace each bolt at a field joint with a UniFlex isolator element, as shown in Figure 4. The typical location for the isolation system is just aft of the spacecraft separation system.

#### SoftRide MultiFlex



The patented SoftRide MultiFlex whole-spacecraft vibration isolation system is intended to reduce dynamic launch loads that are both axial (thrust-direction) and lateral in nature. Again, CLA is required to design the MultiFlex for the particular LV / spacecraft. Sample results for the design analysis showing responses non-isolated and isolated is given in Figure 5.

The stiffness and damping of the isolators are sized to mission-specific requirements for reduction of these dynamic loads. Similar to UniFlex, this system consists of a set of damped flexure elements that connect the spacecraft to the launch vehicle. Figure 6 shows a MultiFlex isolator.

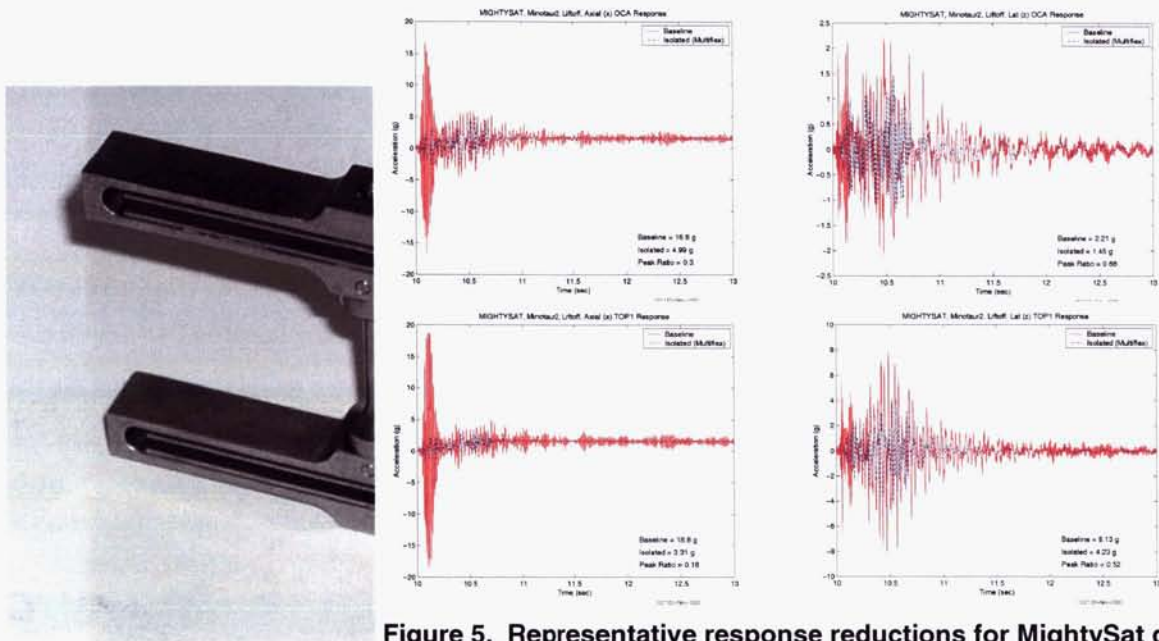


Figure 5. Representative response reductions for MightySat due to the SoftRide system

Figure 6. SoftRide

MultiFlex and its installation

This consists of a pair of UniFlex isolators separated from one another by a central post. The axial isolation is achieved by virtue of the UniFlex isolators in series with one another. The lateral isolation is achieved by the shearing of the assembly with bending occurring in the flexures. The typical application of this isolation system is to replace each bolt at a field joint with a MultiFlex isolator element, as shown in Figure 6.

### Flight Heritage of Whole-Spacecraft Vibration Isolation

There is significant flight heritage for whole-spacecraft vibration isolation. These systems have, to date, flown on six separate missions. Flight telemetry data indicating the flight performance of the isolation systems is available from all missions except the MightySat mission and will be presented in the following sections. Table 1 summarizes the missions on which SoftRide has flown.

Table 1. Summary of SoftRide Flight Heritage

Launch Vehicle	Spacecraft	Isolation System
Taurus	GFO	UniFlex
Taurus	STEX	UniFlex
Minotaur	JAWSAT	MultiFlex
Taurus	MTI	UniFlex
Minotaur	MightySat	MultiFlex
Taurus	QuickTOMS OrbView4	Uniflex
Taurus	QuickTOMS OrbView4	Uniflex
Minotaur	XSS-11	Uniflex



### Taurus 2 / GFO

The GFO spacecraft interface was instrumented with six accelerometers that measured axial and lateral vibration during the flight. A single accelerometer was mounted in the flight direction just forward of or on the soft side of the isolation system. The remaining spacecraft interface accelerometers were mounted aft or on the hard side of the isolation system. The accelerometers were sampled at 4000 samples per second with 8-bit resolution. Variable capacitance accelerometers were used which measured both the steady state and transient acceleration. An overplot of the time history of the response, during the first stage burn, from accelerometers mounted on the launch vehicle side and on the satellite side of the isolation system is shown in Figure 7. The reduction due to the spacecraft isolation system is readily apparent by comparing the two time histories. The isolation system significantly reduces the vibration level to the payload by 50% for all load events.

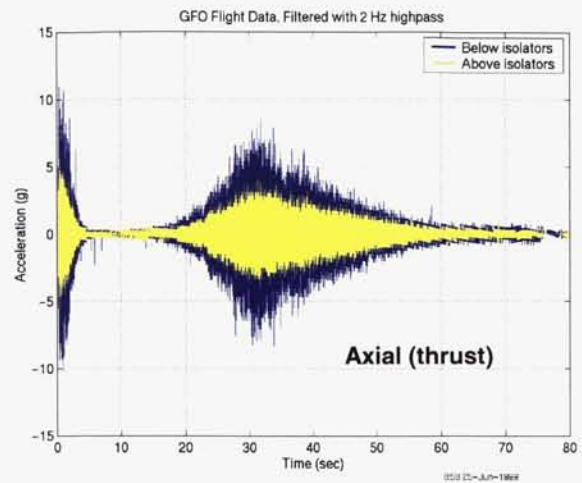


**Figure 7. GFO flight data – below and**

### Taurus 3 / STEX

The Taurus/STEX SoftRide isolation system was very similar to that of GFO but “tuned” for this mission. The STEX spacecraft was heavier than the GFO and therefore the isolation system was larger. With one successful flight of this system, the program offices allowed a slightly more aggressive design (lower in frequency) to be flown. Finite element models of the LV and spacecraft were obtained and full coupled-loads analyses were performed to design the isolation system. While the first mission (Taurus/GFO) required both component-level and system-level testing of the isolation system, only component-level tests were performed on the Taurus/STEX system.

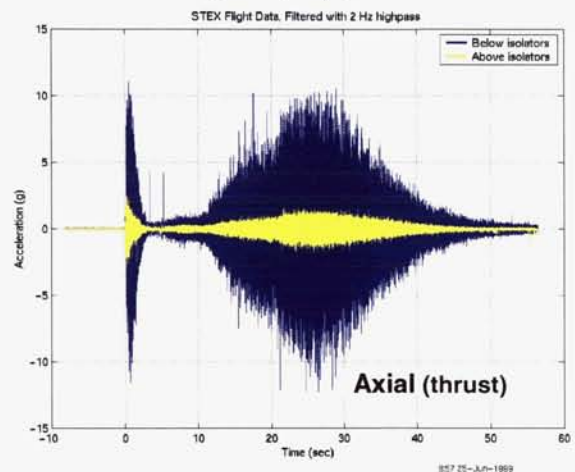


**Figure 8. STEX flight data - below and above isolators**

For the Taurus/STEX mission, data from two accelerometers, again one below and one above the isolators, was obtained. An overplot of this data is shown in Figure 8 (this data has been high-pass filtered to eliminate the quasi-static accelerations). This data shows a factor of five reduction in the broadband acceleration levels above the isolators.

It is of great interest to examine the performance of the SoftRide isolation system in the frequency domain. This allows inspection of the broadband attenuation characteristics of the SoftRide system. The dynamic system made up of the launch vehicle and spacecraft is non-stationary due to continual propellant depletion and stage separations. Also, the highly transient nature of most launch load events precludes digital signal processing of the flight data averaged over the entire launch window. Therefore, the frequency content of the transient flight data is best observed by creating waterfall PSD plots. These plots show the PSDs of 2-second windows of transient data, overlapped by 1 second, and stacked up next to each other.

Figure 9 shows the waterfall plots for the axial acceleration below and above the isolators from the STEX flight. Note that the sample rate of 4000 Hz only allows data to be examined up to 2000 Hz. Examination of these plots shows that the SoftRide system provided significant reductions in the acceleration levels across the broadband spectrum. The high frequency accelerations below the isolators may be due to structural-borne acoustic energy. The SoftRide system has greatly reduced the structural-borne acoustic vibration on the spacecraft.

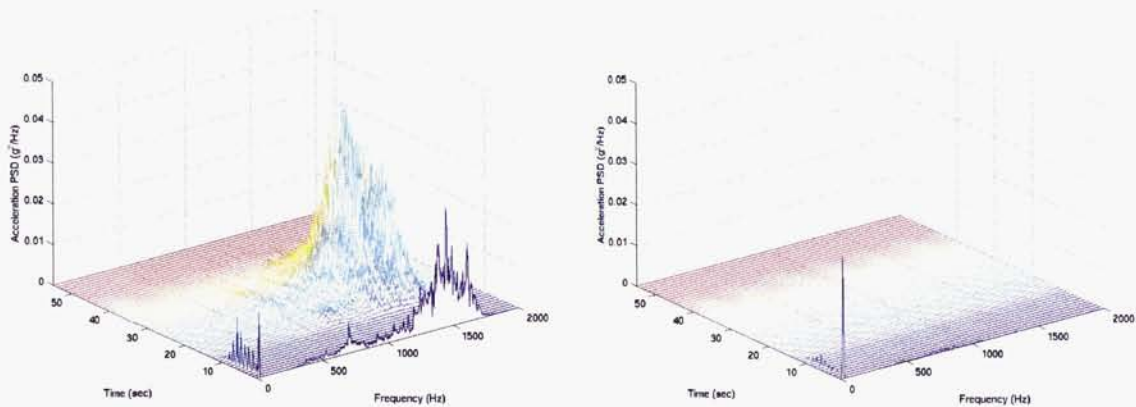


**Figure 9. Waterfall PSD of STEX data - below and above the isolators**

#### Taurus 5 / MTI

For the Taurus/MTI mission, flight telemetry data was obtained below and above the isolators in both the axial and the radial directions. The instrumentation and data processing were done similarly to the GFO and STEX missions. Transient data and waterfall PSD plots for the axial direction are similar to the previous flight data. Transient data plot for the radial direction is shown in Figure 10. Note that the UniFlex isolation system not only provides attenuation in the axial direction, but also provides significant reduction in dynamic responses in the radial direction.

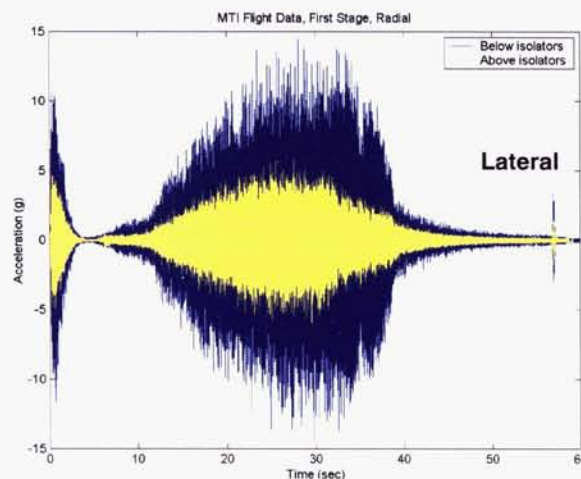


**Figure 10. MTI flight data - below and above isolators**

#### Taurus 6 / QuickTOMS & OrbView4

The Taurus 6 /QuickTOMS & OrbView 4 mission (see Figure 11) was the first dual mission where both satellites were protected by separate SoftRide systems. Flight telemetry data was obtained below and above the isolators in the axial direction for both satellites. Transient data plots for the axial direction are shown in Figure 11 for both QuickTOMS and OrbView4. This data shows that the isolators provided excellent response reductions, similar to other Taurus flights.

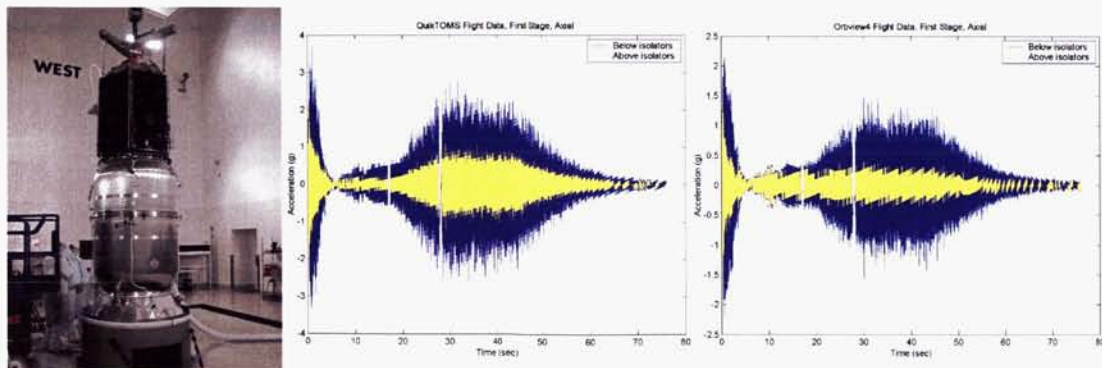




**Figure 11. QuickTOMS and OrbView4 satellites in the launch configuration and flight data**

#### Minotaur 1 / JAWSAT

The Air Force funded a significant data acquisition system on Minotaur for the purpose of assessing the performance of the SoftRide vibration isolation system. A total of 18 accelerometers were flown for measuring accelerations on both the launch vehicle side and the spacecraft side of the isolation system. These accelerometers were arranged into 6 triaxial sets: three triaxial sets on the hard side and three triaxial sets on the soft side. Flight data was examined and the trends observed agreed very well with the predictions of coupled loads analyses. An example of some SoftRide acceleration flight data from the JAWSAT mission is shown in Figure 12.

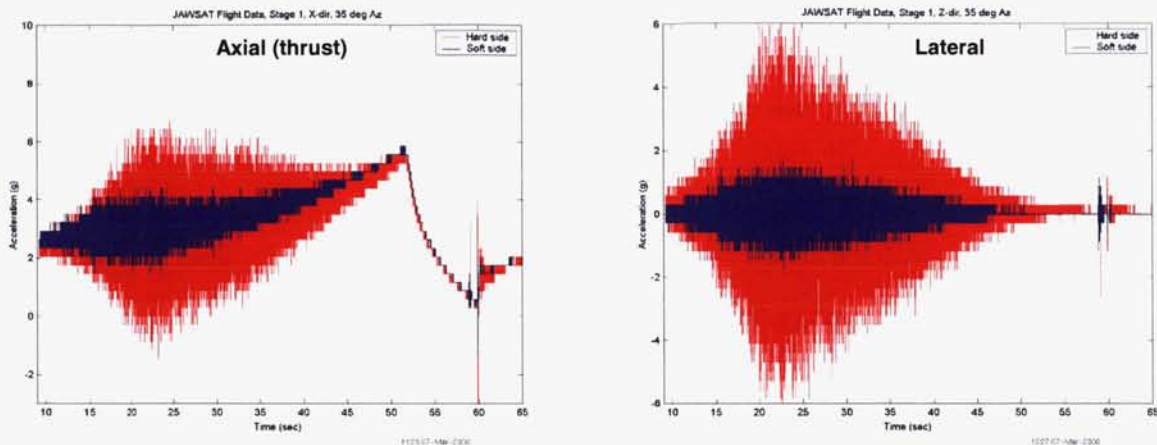


**Figure 12. Typical SoftRide flight data from the Minotaur/JAWSAT mission**

The quasi-static acceleration measurements have not been filtered out of this data. Note that excellent vibration isolation was achieved in both the axial (thrust) and the lateral directions.

Data showing the fairing separation shock event from the Minotaur/JAWSAT flight is shown in Figure 13. The flight accelerometers were not shock accelerometers and therefore some clipping of the high-level "hard side" shocks has occurred. However, the isolated "soft side" shows greatly reduced shock inputs to the base of the spacecraft.

#### Minotaur 2 / MightySat

The Minotaur/MightySat mission was the second flight of the Minotaur launch vehicle. The auxiliary data acquisition system for collecting SoftRide performance data was not flown on this mission so telemetry data is not available. The launch was a complete success and the MightySat spacecraft, after its soft ride to orbit, began operation as planned.

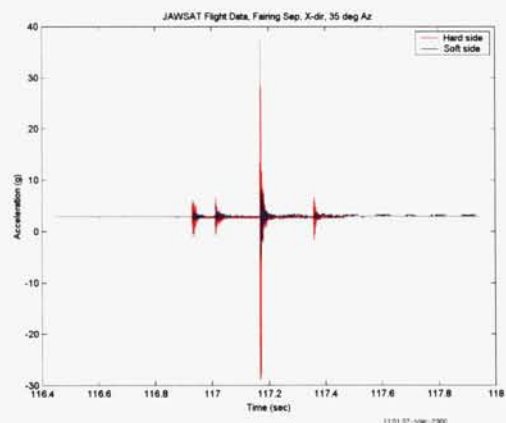


**Figure 13. Fairing separation shock flight data showing SoftRide attenuation**

### **SoftRide Shock Isolation Systems (ShockRing)**

Whole-spacecraft shock isolation systems have been designed, analyzed, tested, and flown and others are currently in development. These isolators are optimally located in the stack just aft of the satellite in order to attenuate all shock loads from the launch vehicle. Candidate locations include (1) at the top of the payload attach fitting (PAF), just below the satellite separation system (Figure 14), (2) at the bottom of the PAF, or (3) integrated somewhere within the PAF. One patented design for a whole-spacecraft shock isolation system is shown in Figure 14. This is a continuous ring made of a series of highly damped flexures. The designed-in compliance, the high damping, the contorted shock path, and the assembly joints all combine to make this an effective light-weight isolation system. This isolator design, along with several other designs that are in development, have been tested and results will be presented in the following discussion. Flight results from the first flight are also presented.

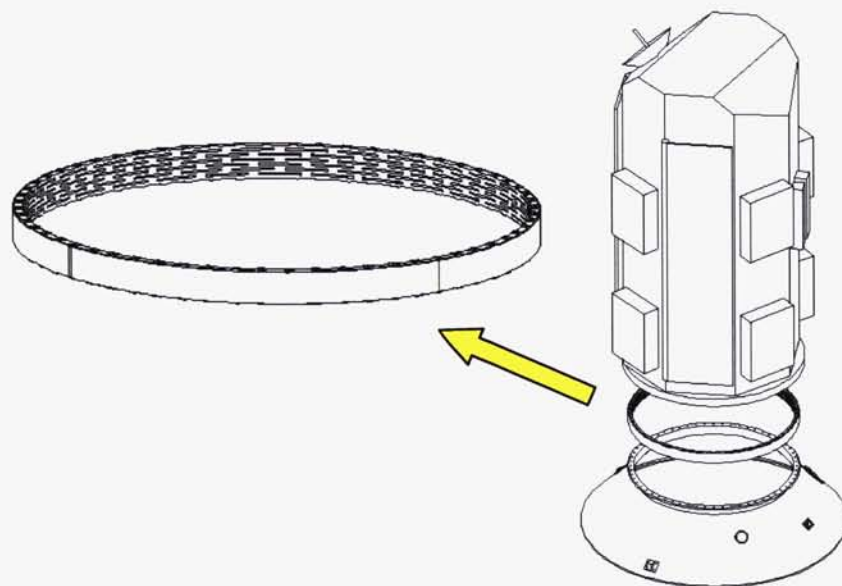


**Figure 14. Whole-spacecraft shock isolator at top of PAF**

Whole-spacecraft shock isolation systems are currently under development for the purpose of attenuating shock inputs from the launch vehicle to the spacecraft. The major source of these shock inputs is typically fairing separation shock, dual payload attach fitting (DPAF) separation shock, stage ignitions, and stage shutdowns. While UniFlex and MultiFlex vibration isolation systems are tailored to mission-specific requirements for low frequency isolation, the shock isolation system is planned to be more of an "off-the-shelf" component. It is envisioned that, for each class of launch vehicle, the shock isolator will be a "couple sizes fits all" type of system for the purpose of attenuating launch dynamic loads from frequencies of about 70 Hz and higher, depending on the design. Several patented shock isolators are shown in Figure 15. The largest is over 180 cm in diameter.



**Figure 15. Patented whole-spacecraft shock isolation systems (ShockRing)**



During the initial development phase of the whole-spacecraft

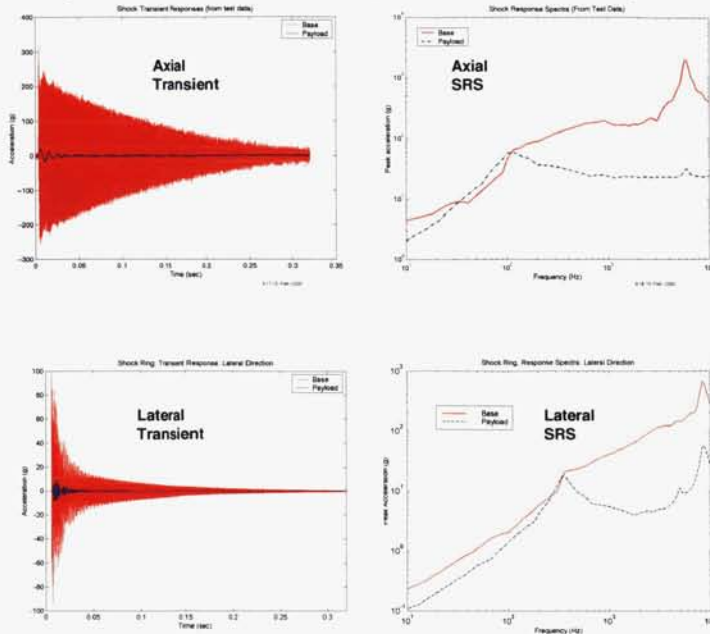


**Figure 16. Transient responses and shock response spectra from impact test**

shock isolation system, prototypes were fabricated and shock tested using a pneumatic impact gun. The shock isolator was attached to two rigid steel blocks and suspended from a test frame. The impact occurred on the steel block referred to as the “base” and the accelerations were measured on both the base and the “payload” steel blocks. Acceleration time histories and their corresponding shock response spectra for a typical test are shown in Figure 16. Above the isolation frequency of this shock isolator (100 Hz in the axial direction and 250 Hz in the lateral direction) over a magnitude of attenuation is achievable.

This testing is very useful for development of shock isolators. However, this type of testing is missing two essential ingredients to prove the shock isolator’s ability to attenuate shock loads. The launch community will place more credibility on the shock isolator testing if it includes (1) flight-like

pyrotechnic excitation and (2) flight-like flexible adjoining structures as opposed to rigid blocks.

Shock tests were subsequently conducted using primacord for pyrotechnic excitation, launch vehicle components, and a spacecraft emulator. The amount of primacord was experimentally adjusted until flight-like shock acceleration levels were measured at the spacecraft interface. Accelerations were measured in all directions at several locations. Figure 17 shows acceleration time histories and shock response spectra from the test of a whole-spacecraft shock isolator. Data is shown for accelerometer locations both forward and aft of the isolator. The excellent attenuation performance of the shock isolator can be seen in both the time and frequency domains.



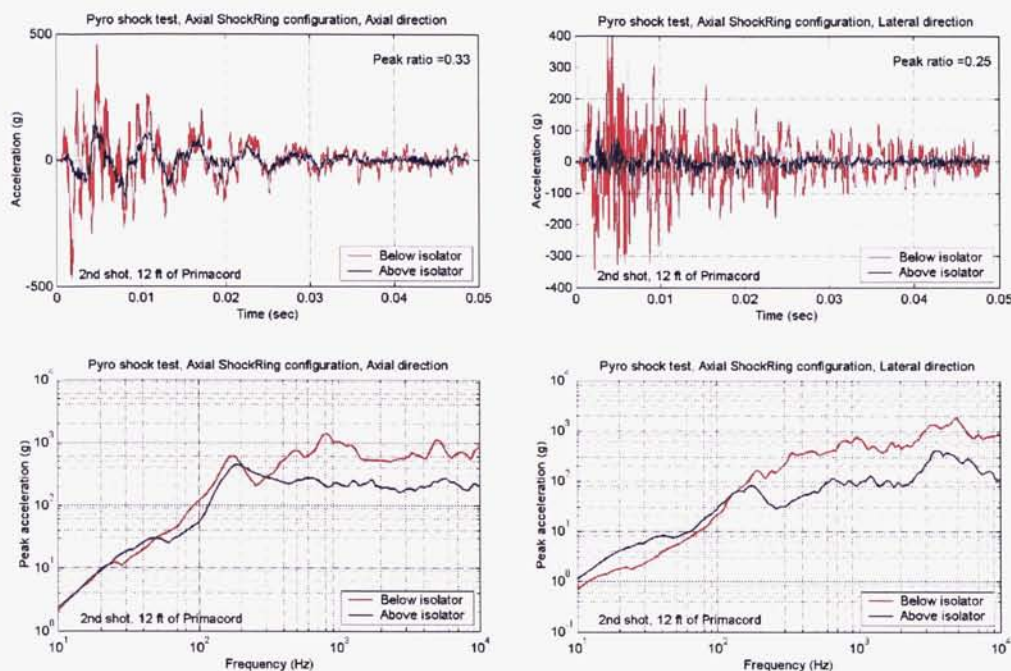


**Figure 17. Pyrotechnic shock test results of a shock ring**

#### VALPE Flight Experiment

The Air Force Research Laboratory and the Air Force Space Test Program sponsored a program called VALPE, Vibro-Acoustic Launch Protection Experiment. VALPE demonstrated several vibration/acoustics reduction techniques on board two flights of a NASA sounding rocket, the Terrier Improved-Orion. Passive and hybrid (passive-active) whole-spacecraft vibration isolation was one component of this program. For the first flight, only a passive SoftRide ShockRing isolation system was flown. For the second flight, an active vibration isolation system was also implemented using the ShockRing as the passive stage. This launch vehicle produces very high quasi-static acceleration loads (up to 20 g's) and very high dynamic loads (up to 40 g's). Therefore, designing the isolation system for strength while maintaining the required flexibility was a challenge.

The first flight was launched from NASA Wallops Flight Facility at Wallops Island, VA in November 2002. Figure 18 shows the flight one payload hardware prior to integration into the launch vehicle. Due to the small payload envelope for this experiment, the ShockRing was a compact design. The ShockRing, mounted just below the payload electronics, has a diameter of 32 cm and a height of 4.5 cm. The ShockRing was designed to protect the mission specific electronics for monitoring the experiment launch environment. Figure 19 shows the launch vehicle and the lift-off.

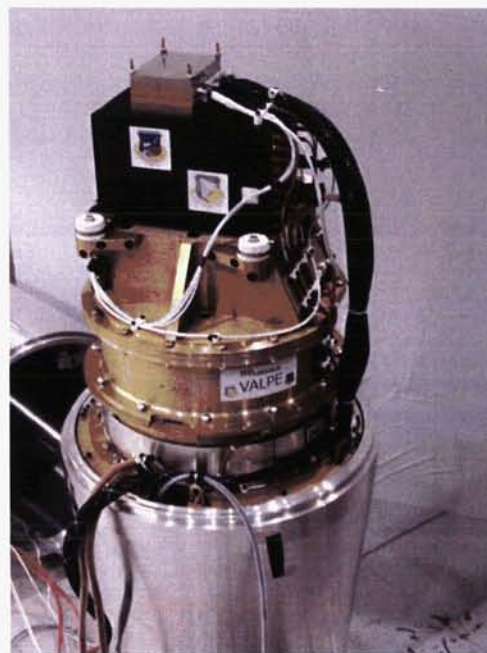


**Figure 18. VALPE flight one payload hardware**



**Figure 19. VALPE Terrier Improved-Orion on launch rail and November 02 launch**

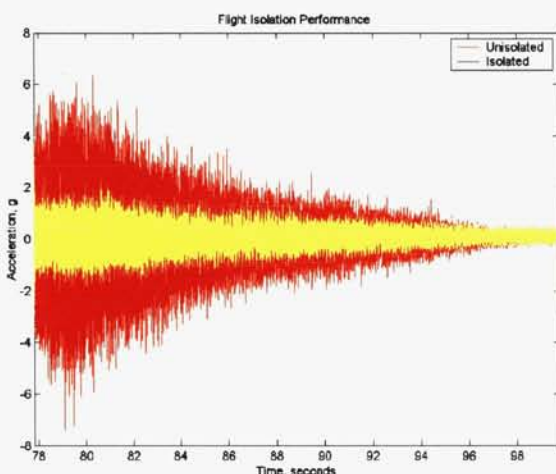


**Figure 20. VALPE flight data from last 20 seconds of flight, below and above the isolation system**

Flight data was recovered by telemetry from the entire flight. Flight data for the lateral direction for the second stage burn is shown in Figure 20, where the data in red is below the isolation system and data in yellow is on the payload side. This data shows that the ShockRing reduced the acceleration levels even in the lateral direction, which is not as compliant and highly damped as the axial direction.

### FalconSat-3

In 2006, under a program sponsored by the Air Force Research Laboratory, a whole-spacecraft ShockRing developed for the Air Force Academy's FalconSAT-3 satellite will provide high frequency attenuation during launch on an Atlas V launch vehicle. FalconSAT-3 is a 50 kg experimental satellite that will be one of the first secondary payloads to fly on ESPA. FalconSAT-3 is a unique satellite that has a boom that protrudes into the center of ESPA and through the center of the ShockRing. The ShockRing provides an open center for the FalconSAT-3 boom, attenuate in both the satellite axial and lateral directions and provides a rigid connection to ESPA.

The ShockRing isolation system adds just over five centimeters to the stack height of the system and just over 3 kg to the assembly. Figure 21 below shows the FalconSAT-3 qualification model during testing with the ShockRing mounted directly underneath. Figure 22 is test data from system level vibration tests performed with and without the ShockRing isolation system. Acceleration data was recorded at the top of the satellite during an axial direction high level random test. Overall grms levels were reduced from 21 grms to 8 grms. Currently CSA is on schedule to deliver flight hardware to the Air Force Academy in early 2006.



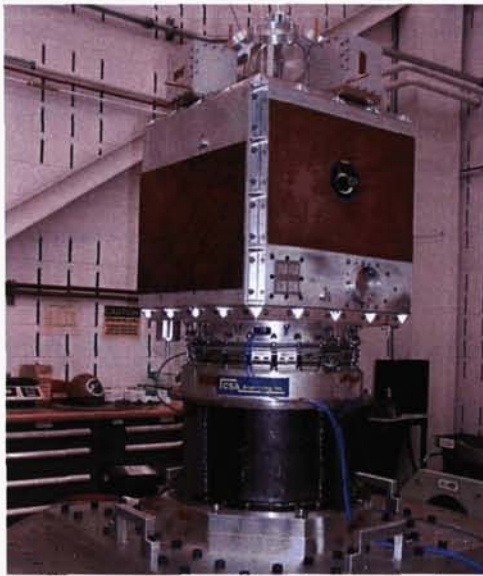


**Figure 21. Qualification tests of a ShockRing stack on the shaker**

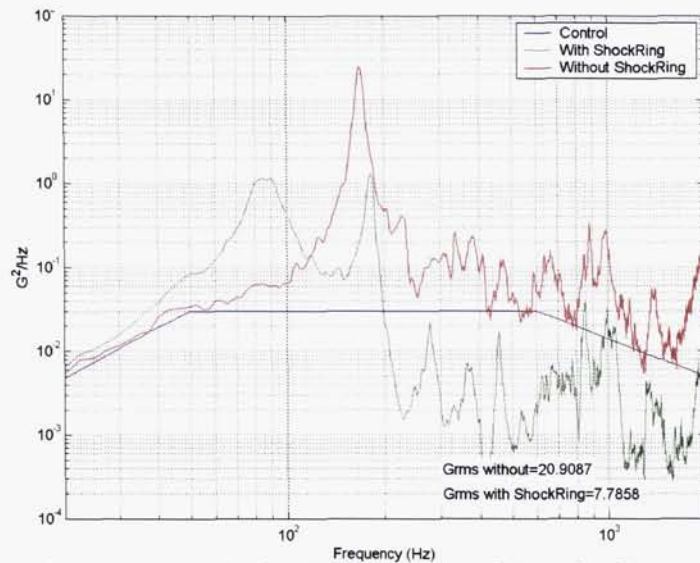


**Figure 22. Axial direction test data with and without the ShockRing**

### Conclusion

There is a need to reduce launch loads on spacecraft so that spacecraft and their instruments can be designed with more concentration on orbital performance rather than launch survival. A softer ride to orbit will allow more sensitive equipment to be included in missions, reduce risk of equipment or component failure, and possibly allow the mass of the spacecraft bus to be reduced. These benefits apply to military as well as commercial spacecraft.

For all of the missions flown to date, the patented SoftRide UniFlex, MultiFlex, and ShockRing whole-spacecraft vibration and shock isolation systems have proved to be a very effective means of reducing spacecraft responses due to the broadband structure-borne launch environment.

From both the transient data and the waterfall PSDs, it is clear that the SoftRide whole-spacecraft vibration isolation systems performed very well to reduce structure-borne vibration levels transmitted to the spacecraft. The isolation system was designed specifically to reduce the effects of solid motor resonant burn in the 45 Hz to 60 Hz frequency range, which it did very well. It should also be noted that the SoftRide vibration isolation system provided extreme reductions of shock and structure-borne acoustics at higher-frequencies.

The isolation system hardware design was elegant in its simplicity, which ultimately played a great part in its acceptance by both the spacecraft and launch vehicle manufacturers. The SoftRide isolation systems are simply inserted at an existing field joint. No flight hardware changes were required. The only change was to the guidance and control algorithms to account for bending frequency changes introduced by the isolation system. In the end, the choice to fly the isolation system proved to be a tremendous risk-reduction for the spacecraft by drastically increasing the spacecraft margins. Because of the success of these flights, this isolation system design is being used on several upcoming flights.



## **References**

1. Orbital Sciences Corporation, "Taurus Launch System Payload User's Guide", Release 3.0, September, 1999
2. Orbital Sciences Corporation, "Minotaur Payload User's Guide", Draft version, April 26, 2001
3. Schoneman, S., Buckley, S., et. al, "Orbital Suborbital Program (OSP) "Minotaur" Space Launch Vehicle: Low Cost Space Lift For Small Satellites Using Surplus Minuteman Motors", AIAA Paper AIAA-2000-5068, AIAA Space 2000 Conference, September 19-21, 2000, Long Beach, CA.

# Summary of the New AIAA Moving Mechanical Assemblies Standard

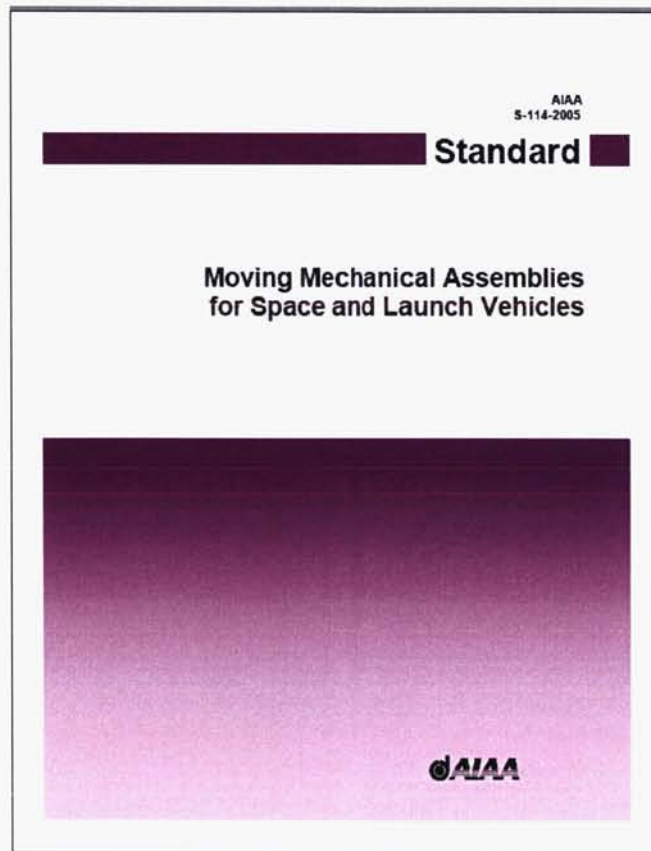
Brian W. Gore\*

## Abstract

A new American Institute of Aeronautics and Astronautics (AIAA) standard entitled "Moving Mechanical Assemblies for Space and Launch Vehicles," AIAA-S-114-2005, has been created. It is based on Military Specification MIL-A-83577B, which was cancelled by the Department of Defense in the mid-1990's. The new standard supersedes a Technical Operating Report (TOR) (prepared by Brian W. Gore of The Aerospace Corporation with support from the Air Force Space and Missile Center and the National Reconnaissance Office, which was a "cleaned-up," same-format version of MIL-A-83577B) and has already been used as a compliance document in several recent acquisitions and Requests For Proposals. This paper outlines some of the more significant changes and additions made in the new AIAA MMA Standard since the previous TOR and MMA specification were released.

## Introduction

The U.S. Air Force (USAF) Space and Missile Center (SMC) and the National Reconnaissance Office (NRO) have recently established policies supporting and requiring government, industry, and professional society specifications and standards for new acquisitions.



---

\* The Aerospace Corporation, El Segundo, CA

The new AIAA standard, AIAA-S-114-2005, is one of the first products of the recent Specifications and Standards Revitalization Program undertaken by the USAF's SMC. They asked the AIAA to engage appropriate subject matter experts to develop five consensus standards to be used as compliance documents for SMC (and potentially NRO) acquisition activities. These five standards were:

1. AIAA-S-110-2005, "Space Systems – Structures, Structural Components, and Structural Assemblies
2. AIAA-S-111-2005, "Qualification and Quality Requirements for Space-Qualified Solar Cells"
3. AIAA-S-112-2005, "Qualification and Quality Requirements for Space-Qualified Solar Panels"
4. AIAA-S-113-2005, "Space Systems – Criteria for Explosive Systems and Devices Used on Launch and Space Vehicles"
5. AIAA-S-114-2005, "Moving Mechanical Assemblies for Space and Launch Vehicles"

Three other standards are currently beginning the same development process, as of the time of publication of this paper; these involve

1. Space System Electrical Power System Design,
2. Space System Electromagnetic Compatibility Requirements, and
3. Space System Mass Properties Control

A memorandum from USAF Lt. Gen. Brian Arnold to SMC dated 14 January 2003 and titled "Policy Letter on Specification and Standards Usage at SMC" outlines the framework for using specifications and standards as a key part of their acquisition, contracting, and program management. Some key excerpts from that memo include:

"The unintentional result (of reducing the use of specifications and standards as compliance documents through "Acquisition Reform") was that technical baselines and processes were compromised."

"There is no intent to return to the pre-acquisition reform approach of using an excessive number of specs and standards. A list of high priority critical specs and standards is being...established for appropriate use."

"The baseline list of specs and standards will be used in a less prescriptive manner than in the past."

With these ideas in mind, the Moving Mechanical Assembly Standard was created with the utmost thought toward incorporating those requirements that are common to most MMAs for space and launch vehicles. The requirements stated are a composite of those that have been found to be cost-effective for high reliability space and launch vehicle applications.

The standard is the result of contributions received from many individuals, most notably those on the AIAA MMA Committee on Standards (CoS). Although the committee started out about twice as large, at the time of approval the actively participating members of the AIAA MMA CoS were:

Stephen Brock, Liaison  
Ken Emerick, Co-Chair  
Brian Gore, Co-Chair  
Michael Pollard, Co-Chair  
Dave Putnam  
Dave Richman  
Paul Reynolds  
Bert Timmerman

AIAA  
Space Systems/Loral  
The Aerospace Corporation  
Lockheed Martin Corporation (Denver)  
Lockheed Martin Corporation (Sunnyvale)  
The Boeing Company  
Northrop Grumman Corporation  
Hi-Shear Technology Corporation



The above consensus body approved the document and the AIAA Standards Executive Council accepted the standard for publication in June 2005. It can be downloaded for purchase (\$39.95, or \$31.95 for AIAA members) from the AIAA website at

<http://www.aiaa.org/content.cfm?pageid=363&id=1366&Type=StoreProduct&LayerID=51>

### **Description**

The new AIAA MMA standard specifies general requirements for the design, manufacture, quality control, testing, and storage of MMAs to be used on space and launch vehicles. It is applicable to the mechanical or electromechanical devices that control the movement of a mechanical part of a space or launch vehicle relative to another part. The requirements apply to the overall MMA as well as to the mechanical components and instrumentation that are an integral part of these mechanical assemblies.

Not all requirements in the standard are of equal importance or weight. They have been divided into three categories of importance, ranging from requirements that are imposed on all applications to examples of acceptable designs, items, and practices. The relative weighting of requirements is an important consideration when tailoring the standard to specific applications and in making trade studies of alternatives. Three weighting factors are incorporated in the standard:

1. "Shall"
2. "Shall, where practical"
3. "Preferred/Should/May"

Note that the old MMA specification designated four separate weighting factors, with this standard essentially combining the lowest two in the hierarchy. The use of the weighting factors in the standard is intended to assist in the tailoring of requirements to specific applications and to assist contractors in the design process. Detailed definitions and scope of these weighting levels are described in the standard.

Unlike the uniform, one-format-fits-all of many military specifications, this particular document reflects the general consensus of the industry in what is required for today's MMAs from a design, build, inspection, and test perspective. The document was designed to be more "user-friendly" than the old MMA specification as it was consciously re-organized to flow simultaneously from general to specific, as well as along the design and development life of MMAs. To provide an illustration of this new organization, the chapters and major subheadings are listed in Table 1.

**Table 1. Organization of MMA Standard**

1	Scope
2	Tailoring
3	Applicable Documents
4	Vocabulary
5	General Design Requirements
5.1	Performance Requirements
5.2	Environmental Design Requirements
5.3	Physical Requirements
5.4	Electrical and Electronic Requirements
5.5	Structural Requirements
5.6	Reliability
6	Component Design Requirements
6.1	Fasteners
6.2	Retention and Release Devices
6.3	Pivots and Hinges
6.4	Cable Systems
6.5	Springs
6.6	Dampers
6.7	Stops
6.8	End-of-Travel Latches
6.9	Bearings
6.10	Electric Motors
6.11	Power and Signal Transfer Components
6.12	Switches
6.13	Gears
6.14	Pressurized Components
7	Parts, Materials, and Processes Requirements
7.1	General Parts, Materials, and Processes
7.2	Materials
7.3	Lubricants
7.4	Hard Coatings
7.5	Contamination
8	Testing and Inspection Requirements
8.1	Parts, Materials, and Process Controls
8.2	Test Fixtures
8.3	Test Instrumentation
8.4	Test Plans and Procedures
8.5	Development Tests
8.6	Qualification and Proto-qualification Tests
8.7	Component and Subsystem Level Acceptance Tests
8.8	Vehicle Level Acceptance Tests
8.9	Pre-launch Validation Testing and Inspection
8.10	Modifications, Rework, and Retesting
9	Bibliography
Annex A (Informative)	Static Torque or Force Margins at Different Coordinate Points

## Highlighted Changes

### Overall flow – easier to use/find information

As stated above, it was an early and deliberate action by the CoS to reformat the AIAA MMA Standard to be easier to use and find information than the previous military specification document. Before any work was done on the technical content, the co-chairs spent a notable – and ultimately worthwhile – amount of time determining the current organization, deleting obvious subject items and inserting placeholders that were later filled in regarding new areas of interest and importance.

The co-chairs then rearranged the remaining text into the corresponding sections of the new format, and the committee went to work to generate and compile a list of discussion comments. It was this list that formed the focus of the CoS efforts. Teleconferences on a bi-weekly, then weekly, then almost daily basis toward the end were the main forum of CoS communication, augmented by a members-only, AIAA-hosted website which stored and organized pertinent and necessary documentation.

### Approximately 400 comments generated, submitted, and dispositioned.

After the CoS reviewed the base document and compiled the aforementioned list, they used the teleconferences and two, multiple-day, face-to-face “summit” meetings to work through the list. Several of the committee members passed the working document [initially issued as The Aerospace Corporation Technical Operating Report TOR-2004(8583)-1] to their colleagues or certain specialists to solicit additional insightful comments. The CoS spent the majority of these meetings discussing the merits of the particular comments submitted, grouped as either general, editorial, or technical; a breakdown of the comments in the list is shown in Figure 1.

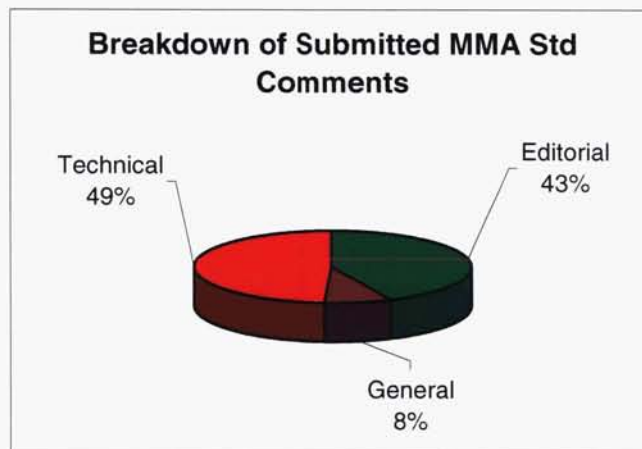


**Figure 1. Breakdown of Submitted MMA Standard Comments**

Moreover, after the final draft of the standard was prepared, AIAA initiated a 30-day public review period, which yielded still more comments, for a grand total of approximately 400 submissions by members of Aerospace, many contractors, NASA, etc. Figure 2 illustrates the approximate number of comments by submitting individuals. Some of the people listed were points of contact from their entire organization.



## Comments by Contributor

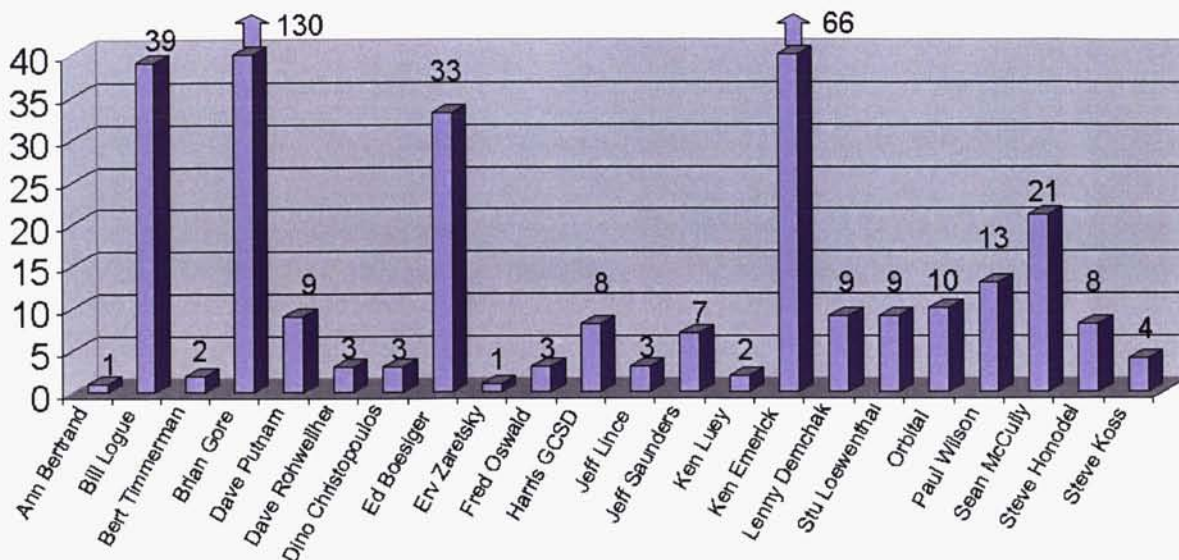


**Figure 2. Number of Comments by Contributor**

### Conciseness/deletion of peripheral areas

There were many areas of the old MMA specification that were deemed by consensus to be out of scope for a modern moving mechanical assembly standard. Since we were no longer bound by the standard template, there was freedom to make this document more relevant overall. As such, several sections were deleted altogether in recognition that there were virtually always other documents or specifications, either governmental or internal to contractors that existed to govern those areas. Some of these subject areas included identification and marking, certain details on processes and controls, structural requirements, specific environmental conditions, etc. However, many such sections were minimized and maintained as a consideration guide for younger engineers, or simply as a reference pointer to the appropriate document, such as the new AIAA Structures Standard, MIL-STD-1540E (the environmental testing standard), etc. This scope is one of the main utility features for which the CoS was striving. One metric of this conciseness may be indicated by the relative word counts of the documents, as illustrated in Table 2.

**Table 2. Word Count of Evolving MMA Documents**

Document	Approx. Word Count
MIL-A-83577B	23,000
TOR-2004(8583)-1	24,000
AIAA-S-114-2005	19,000

### Areas rechecked for modern validity

There were several peripheral areas relating to MMAs that were also verified for modern validity, such as contamination, lubrication, electrostatic discharge, etc. For these particular areas, Aerospace and contractor experts were consulted to obtain an insight as to what governing documents existed for their respective disciplines. These were, in turn, referenced in the MMA standard where appropriate, leaving the details to those other documents, unlike the original MMA specification that contained many of the details.

#### Applicable documents

One evident change that appears early in the document is the far fewer number of Applicable Documents called out in the AIAA standard. The only documents in this section of the standard are the ones specifically mentioned in the body of the text. In a parallel effort, each one of the documents named in the original MMA specification was validated regarding its status (active, cancelled, superseded, etc.). Many of them, if not mentioned in the text, were moved to the new Bibliography section at the end, provided the CoS consensus agreed that they still contained useful information. One important note to point out is that, simply because the government decided to cancel a document during acquisition reform, it does not mean the contents of that specific document are automatically null and void. After all, the MMA specification falls into the “cancelled” category and the industry still recognized it as valid, just not eligible as a contractual compliance document.

#### Acceleration term removed from static torque margin

After significant debate, the CoS decided to remove the acceleration term from the equation to calculate static torque margin. Since the true meaning of this particular margin is to show how much force exists above and beyond all static resistances, the acceleration term was deemed irrelevant. A moving mechanical assembly must have sufficient motive force to begin motion, as evaluated with a free-body diagram. Forces required for a given acceleration are deemed performance requirements, and are thus captured in the dynamic force margin requirement.

#### New section on stepper motor margin in force/torque margin section

One of the areas without clear definition in previous forms of this document was the lack of attention given to force/torque margins with the use of stepper motors. A section was added which describes two ways to calculate stepper motor margin:

1. using motor available torque (pull-in torque) and comparison to friction loads, and
2. using a step stability analysis

Guidelines and conditions are also given regarding which of the two methods should be used in various applications.

#### Expansion of related electrical and electronic requirements

Although seemingly contradictive of the section above describing the deletion of peripheral areas, it was recognized that there are a significant number of electrical/electronic subjects that are particularly germane for design and testing of MMAs. A short paragraph exists for each of the following subjects:

- Cables and Wiring
- Connectors
- Cable Supports and Strain Relief
- Cable Loops
- Current Draw
- Grounding
- Electromagnetic Interference/Electromagnetic Compatibility (EMI/EMC)
- Electrostatic Discharge
- Flight Instrumentation

For some subjects, little more is given than a statement of consideration to ensure an area is not overlooked, but for others, pertinent reference documents are cited, and lessons learned are described. Again, the CoS was focused on MMA-related requirements, but felt at least this level of detail was justified.

#### Additional recognition of newer, common devices

Since the last release of the MMA specification in 1988, many new technologies have been developed and/or are more widely used, and thus warranted recognition. Non-explosive devices, including wax actuators, shape memory actuators, and split spool release devices are examples of these “next-generation” items. There is actually a reduction of information in this standard regarding pyrotechnic

devices, instead deferring to the new AIAA Standard for Ordnance, AIAA-S-113-2005. Clampbands and retention cables are also included in a new section. Although these hardware items were used prior to 1988, no considerations or requirements were provided in the former MMA specification.

#### Bearing stresses for new steel materials

The development and increased use of hybrid bearing material combinations such as  $\text{Si}_3\text{N}_4$  (silicon nitride) balls and M62 (bearing steel) races required a certain level of attention. Allowable stress levels in prior documents only corresponded to 440C, but the new standard recognizes and provides requirements for 52100, M50, and M62 steels as well. Varying levels of allowable stresses for all of these materials are provided for quiet-running as well as non-precision, short duration applications.

#### Life testing for long life mechanisms

In one of the more significant changes, and one that easily generated the most discussion and debate by the CoS, life test requirements were revisited, motivated by the increasing duration of today's missions as compared to those typical of two and three decades ago. A distinction is now made between "low-cycle MMAs" (such as release devices, spring driven "one-shot" deployables, etc.) and "high-cycle MMAs" (such as solar array drives, momentum wheels, tracking gimbals, etc.), with different corresponding life requirements now given for each.

#### Run-in testing modifications

Another moderately noteworthy change in the testing requirements involves run-in testing. Run-in testing can be expressed in terms of cycles or a percentage of expected life. A slight reduction in the potential number of minimum run-in cycles has been incorporated. This was a result of some common sense being applied, particularly in the area of release devices, or other "one-shot" MMAs. It is generally accepted that the design life for these types of mechanisms is about 50 cycles, given the number of expected tests on the ground, plus on-orbit use(s), plus margin. The current minimum number of required cycles in the AIAA standard brings it closer to correspondence with the minimum percentage of life for these types of MMAs.

#### "Informative" annex on static torque/force margins at different coordinate points

This was the subject of a paper at the 37<sup>th</sup> Aerospace Mechanism Symposium by R. W. Postma of The Aerospace Corporation, and it was chosen to be included as an informative appendix, not necessarily subject to contractual compliance. This section describes the basic methodology overview for MMAs that have drive forces (or torques) and resisting forces (or torques) applied to mechanical elements that do not all move at the same velocity. A common example would be the ratio of the rotation of a jackscrew relative to its translation (e.g., rad/in).

### **Summary**

U.S. Air Force (and effectively NRO) policy is swinging back to previous practices of requiring the use of specifications and standards. Subsequently, several subject matter documents have been reviewed, edited, and updated. Incorporation of those documents has started in the proposal phase of new acquisitions. One of the first new standards to be developed under these new guidelines is the AIAA Standard, "Moving Mechanical Assemblies for Space and Launch Vehicles," AIAA-S-114-2005. It is based on the former MMA military specification, but reorganized and technically scrutinized by a committee of industry experts to reflect the current state of the art in designing, fabricating, and testing space mechanisms. This standard will begin to be required as a compliance document for future Air Force space acquisitions, and can be purchased through the AIAA website.



## References

- AIAA-S-114-2005, Moving Mechanical Assemblies Standard for Space and Launch Vehicles, American Institute of Aeronautics and Astronautics standard, July 2005.
- MIL-A-83577B, Military Specification – Assemblies, Moving Mechanical, For Space And Launch Vehicles, General Specification For, 1988.
- Gore, Brian W., Moving Mechanical Assemblies Standard for Space and Launch Vehicles (Draft 1), The Aerospace Corporation Technical Operating Report, TOR-2004(8583)-1, July 2004.

## Acknowledgements

The author recognizes several individuals who not only made this paper possible, but were supportive of the entire effort behind its subject matter. Mr. Dave Davis of SMC/AX, through Valerie Lang, John Ingram-Cotton, and Joe Meltzer from the Aerospace Office of the Chief Engineer, provided the funding necessary to complete all of the work in getting the TOR and AIAA Standard prepared and released. Ken Emerick of Space Systems/Loral and Mike Pollard of Lockheed-Martin (Denver) were loyal and admirable co-chairs on the AIAA MMA Committee on Standards. Their leadership work is to be commended. Stephen Brock of AIAA served as CoS Liaison, and without him, the CoS would still be trying to figure out how to use the CoS website, and probably still be editing changes. Certainly not to be forgotten, Mike Hilton, Tom Trafton, Leon Gurevich, and Al Leveille (retired) of The Aerospace Corporation helped get the ball rolling in the right direction by providing some historical perspective on the MMA specification and its contents.



# **Lessons Learned From the Development, Operation, and Review of Mechanical Systems on the Space Shuttle, International Space Station, and Payloads**

Alison Dinsel\*, Wayne Jermstad\*, and Brandan Robertson\*

## **Abstract**

The Mechanical Design and Analysis Branch at the Johnson Space Center (JSC) is responsible for the technical oversight of over 30 mechanical systems flying on the Space Shuttle Orbiter and the International Space Station (ISS). The branch also has the responsibility for reviewing all mechanical systems on all Space Shuttle and International Space Station payloads, as part of the payload safety review process, through the Mechanical Systems Working Group (MSWG). These responsibilities give the branch unique insight into a large number of mechanical systems, and problems encountered during their design, testing, and operation. This paper contains narrative descriptions of lessons learned from some of the major problems worked on by the branch during the last two years. The problems are grouped into common categories and lessons learned are stated.

## **Introduction**

The Mechanical Design and Analysis Branch at JSC is responsible for the technical oversight of over 30 mechanical systems flying on the Space Shuttle Orbiter and the ISS. The branch houses the MSWG, which has the responsibility to review all mechanical systems on all Space Shuttle Program (SSP) and ISS payloads to verify compliance with the fault tolerance requirements as part of the payload safety review process. These responsibilities give the branch unique insight into a large number of mechanical systems, and problems encountered during their design, development, testing, and operation.

This paper describes some of the recent problems worked by the branch, and lessons that can be learned from them to improve future mechanical systems. The paper contains narrative descriptions of some of these problems. The problems are grouped into common categories and lessons learned are stated. The categories used are derived from the Mechanical Systems Safety memorandum [1]. The letter has 11 key design implementation and verification provisions to be followed to help ensure that credible failure modes have been reliably and effectively controlled as a result of a thorough design, build, and test process for mechanical systems. For this report, some categories will be combined, some omitted, and others expanded upon, to arrive at the list of categories: binding, jamming, and seizing; fastener locking and preload; strength; positive indication of status; and testing. Following each example, lessons learned are stated.

## **Binding/Jamming/Seizing**

This provision addresses the prevention of mechanism binding, jamming, and seizing. Appropriate design features include dual rotating surfaces or other mechanical redundancies, robust strength margins such that self-generated internal particles are precluded, shrouding and debris shielding, proper selection of materials and lubrication design to prevent friction welding or galling, and others. Adequate dimensional tolerances on all moving parts are needed to ensure that functional performance will be maintained under all natural and induced environmental conditions. Tolerances associated with mechanical adjustment (or rigging) must also be taken into account. Mechanical system designs must ensure compatibility of lubricants used with interfacing materials, other lubricants used in the design, and the natural and induced environments. Designs must also ensure that appropriate quantities of lubricant are specified.

---

\* NASA Johnson Space Center, Houston, TX



### Nose Landing Gear Uplock Mechanism

The Space Shuttle Orbiter's nose landing gear, nose landing gear door, and nose landing gear uplock mechanism, shown in Figure 1, are interconnected, and must be rigged and operated together.

Following replacement of the door environmental seal, rigging was performed to achieve proper seal compression. During nose landing gear cycling, the gear uplock indication did not illuminate because the mechanism did not reach the full uplock condition. Binding in the rotational fitting between the uplock fitting and the bellcrank prevented the uplock mechanism from going to the full over-center position for gear uplock. Measurements of the width of the bellcrank and the internal width of the fitting showed an interference fit between the two assemblies. Rework on the bushings per specification requirements removed the interference condition, allowing the bellcrank to move freely.

***Lesson Learned: Proper tolerancing and inspection are critical to preventing interferences in mechanical systems.***

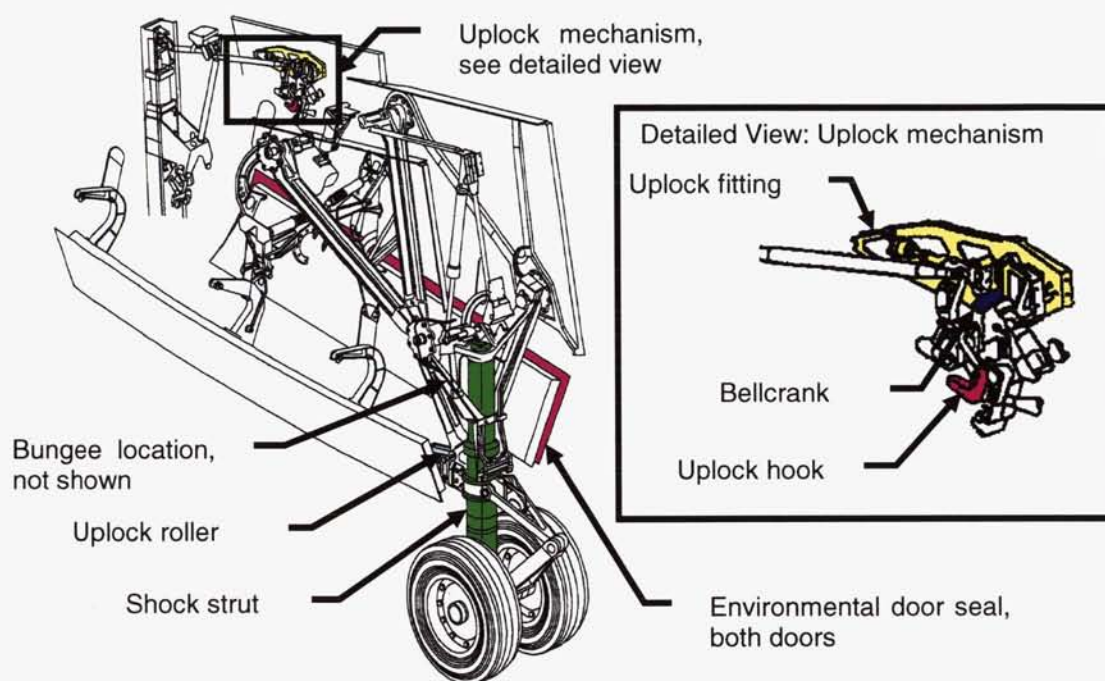


**Figure 1. Nose Landing Gear Mechanisms**

During subsequent nose landing gear retract operations, there was an early indication that the gear uplock mechanism was in the gear-up position. As the shock strut was entering the wheel well and bringing the doors closed, the gear stalled prior to being fully up and locked. After an immediate halt to operations the gear fell freely to the down position. It was observed that the uplock hook was in the gear-up position, thus preventing the uplock roller from engaging. Upon investigation, it was discovered that when hydraulic pressure was applied to retract the gear, the uplock actuator immediately drove the uplock hook closed to the gear-up position. Normally, the mechanism is in a gear-down over-center condition and cannot move prior to gear uplock roller engagement. When the gear uplock roller enters the hook, the roller pushes the mechanism out of its over-center position and allows the uplock hook to engage with the strut and bring the gear to the up-and-locked over-center position. A new source of binding in the mechanism had prevented the hook from being in the full down position. During the rework of the mechanism for the binding described above, inadvertent damage was imparted on the bungee spring. Tooling used to assist in the rework efforts described above is believed to have caused bent/raised metal on the bungee end cap. The resulting binding in the bungee prevented the mechanism from freely going to the full down over-center position. A replacement bungee was installed, and rotational pins and linkages in both the

gear uplock and in the door uplock mechanisms were inspected with no signs of damage observed. The mechanism now properly “snaps” into both the gear-up and gear-down over-center positions.

***Lesson Learned: Repair and rework of mechanical assemblies can cause collateral damage.***

#### Video Camera Support Assembly

The Video Camera Support Assembly (VCSA) is used to mount video cameras in any of 14 potential positions on the truss segments, nodes, laboratory module, or habitation module on the exterior of the ISS. As shown in Figure 2, the VCSA is mechanically attached to ISS primary structure with a threaded bolt that is installed by an astronaut during an extra-vehicular activity (EVA).

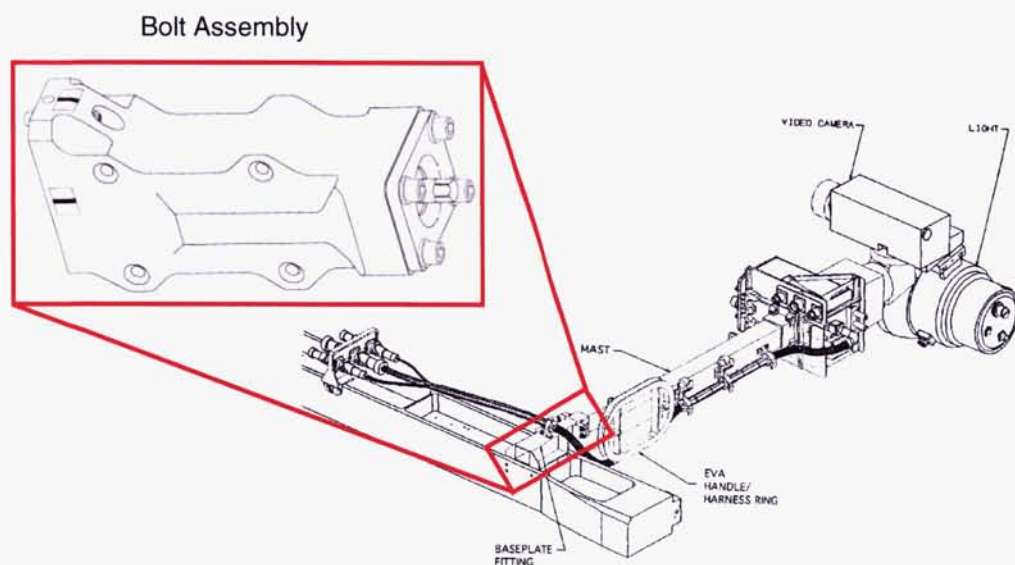


**Figure 2. Video Camera Support Assembly**

During testing, the VCSA bolt experienced extremely high running torques. The recorded running torque values were higher than the Pistol Grip Tool, which was to be used to drive the bolt during an EVA, was able to generate. Investigation revealed that no lubricant thickness was specified on the bolt drawing, and that the dry film lubricant thickness on the bolt was 10 times thicker than the requirement by the application specification, causing an interference with the female threads. In addition, the surface of the bolt was not bead-blasted prior to lubricant application, as required by the application specification. To resolve the issue, the dry film lubricant was removed and the bolts were returned to print by first bead-blasting the surface, and then reapplying the lubricant.

***Lesson Learned: Dry film lubricant thickness is important and the appropriate surface preparation must not be overlooked.***

#### **Fasteners**

Fasteners remain one of the most problematic areas on mechanical systems. The problems can generally be grouped into two subcategories, the first related to secondary locking features (or lack thereof), and the second related to fastener installation torque and the resulting fastener preload.



### Secondary Locking Features

For decades, dating back to the development of aircraft engines, the response of fastened joints to vibration environments has been a critical issue. Failures of critical fastened joints led to the development of “secondary” locking features that served as a method to guarantee that fasteners would not rotate and back out under vibration environments. Preload was recognized as a “good” method to prevent bolt rotation, but it was neither highly reliable nor predictable. So, “positive” locking methods were developed for highly critical joints, such as lockwire, cotter pins, locking tab washers, and safety cable. These locking methods are very reliable, but are also very labor intensive and thus expensive. To decrease labor, prevailing torque locking features were developed that rely on friction to help decrease propensity for bolts to rotate. Prevailing torque locking features include lock nuts, deformed thread keenserts, helicoils, and various types of locking patches and pellets.

Liquid Locking Compounds (LLCs) including epoxy have also been used as secondary locking features, but these have proven to be unreliable. LLCs are very sensitive to application process and environmental factors and cannot be verified after installation without breaking the bond. At JSC, the Engineering Directorate has been critically evaluating use of LLCs and has implemented policies restricting its use.

Many of the problems with secondary locking features can be traced to a lack of well-defined requirements. Using explicit language such as this can help:

“Each bolt, screw, nut, pin, or other fastener used in a safety critical application shall incorporate two separate verifiable locking features. Preload may be used as one of the features combined with a conventional aerospace secondary locking feature that is positive locking and vibration rated [2].”

***Lesson Learned: Clear secondary locking feature requirements need to be specified in program and project requirements documents.***

Over the past two years a significant number of problems have been encountered on many different pieces of hardware relating to either the lack of a secondary locking feature or the improper use of such features.

### External Stowage Platform 2

The External Stowage Platform 2 (ESP-2) was a payload mounted in the payload bay of the Space Shuttle Orbiter on STS-114. ESP-2 had several space station Orbital Replacement Units (ORUs) attached to it. After docking, the ESP-2 was removed from the payload bay and mounted to the external airlock on the ISS.

Following a test failure caused by migration of an uncured LLC, NASA Materials and Processes (M&P) and Structures and Mechanisms personnel advised both the ISS and Shuttle programs to closely restrict the use of LLCs and to develop application procedures for its use. As a result of the policy, an investigation of all uses of LLCs on ISS began. It was determined that an LLC had been used in some locations to assemble the ESP-2. The NASA ISS M&P System Manager advised the ISS Program that the installation procedures for ESP-2 did not call out the use of primer on the titanium inserts as recommended and that the design should be corrected by using a standard, verifiable locking feature.

It was decided to attempt qualification of the hardware with the LLC as configured, while following a parallel path to fix the hardware if the test was not successful. A conservative vibration test used to generically qualify secondary locking features was adapted to the ESP-2 LLC configurations. The test was performed at lower-than-flight preloads to help isolate performance of the secondary locking feature from preload. Five samples each of five different configurations were tested. All samples were assembled using the same process as on the ESP-2 flight hardware. All 25 samples showed various degrees of rotation following testing and were therefore determined to be failures. Upon disassembly of several of the samples, it was observed under microscopic inspection that the LLC had cured, but had failed to adhere to the titanium properly. The bolts with LLC were removed and replaced with bolts that had a verifiable locking feature, a Mylar locking patch, to resolve the issue.



***Lesson Learned: Liquid locking compounds are very application process-sensitive and not verifiable, and therefore are not recommended for use as a secondary locking feature.***

An interesting observation during the testing was that there appeared to be a relationship between fastener preload and LLC adhesion, which may warrant further study. For details, refer to JSC-62850 [3].

#### Resupply Stowage Rack

The Resupply Stowage Rack (RSR) is used to carry pressurized cargo to the space station in the Multi-Purpose Logistics Module (MPLM). The RSR consists of various sizes of locker compartments. These compartments, which accommodate individual stowage trays or bags, are bolted into the rack structure. The compartments have structural doors with latches, shown in Figure 3.



**Figure 3. RSR Latch Mechanism**

Only one month prior to the scheduled launch of STS-114, an issue was discovered with the locker door mechanism on the racks installed into the MPLM. The locker doors were held closed by a 90-degree latch that was held in the closed position by a single thumb screw. The thumb screws thread into locking inserts, but all had zero running torque due to numerous installation cycles. In addition, the engineering drawings required the thumb screws to be torqued "hand-tight". Testing was quickly performed to determine that a maximum of approximately 0.34 N-m could be achieved, far less than a fastener of this size would be nominally torqued. The fasteners essentially had no secondary locking features, and very low preloads. One of the lockers contained a 36.3 kg component with a high-pressure tank, which created a safety concern if the fasteners backed out and allowed the component to fall out of the open locker door.

Any fix to the lockers required opening the Payload Canister and the MPLM hatch, which had already been closed out for flight. Because of this, a decision was made to temporarily fix all of the lockers (about 40) with Permacel Tape. The tape worked because it did not have to prevent the loss of preload, only locker latch rotation. While not very elegant, this was an acceptable fix for STS-114. Prior to any future flights, a secondary locking feature is being added to this system. The proposed concept consists of a slider, which fits over the existing handle and prevents the thumb nut from backing out, and can be slid away to permit operation.

***Lesson Learned: Measure running torque during each fastener installation cycle and keep a record for verification. Replace locking features that do not exhibit running torques within design specifications.***

***Lesson Learned: Fasteners and locking inserts are not the proper locking feature solution for latch designs requiring many cycles.***

#### Bearing Motor Roll Ring Module Spanner Nut

The Bearing Motor Roll Ring Module (BMRRM) is part of the space station Beta Gimbal Assembly (BGA), which provides mounting and gimbaling for the space station solar arrays. The BGA and BMRRM are shown in Figure 4.

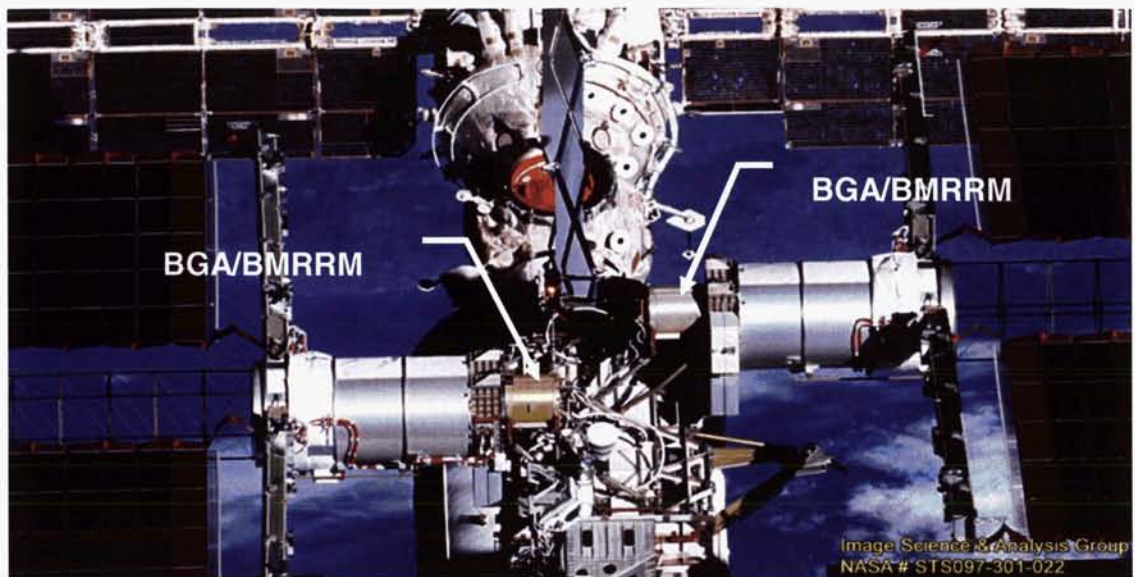


**Figure 4. BGA and BMRRM**

The BGA BMRRM assembly was experiencing anomalous behavior after acceptance vibration testing: it would rotate smoothly in one direction, but would rotate slightly then seize when rotated the opposite direction. A layer of debris was also noted on the exterior of the assembly, as shown in Figure 5. Disassembly and inspection revealed that a large spanner nut, which was used to capture and preload the internal components of the roll ring and housed inside the BMRRM, had loosened and rotated out. As the nut rotated out, it closed up the clearance in a labyrinth gap as shown in Figure 5, resulting in metal to metal contact between the rotating and fixed parts of the housing components and generating the debris.

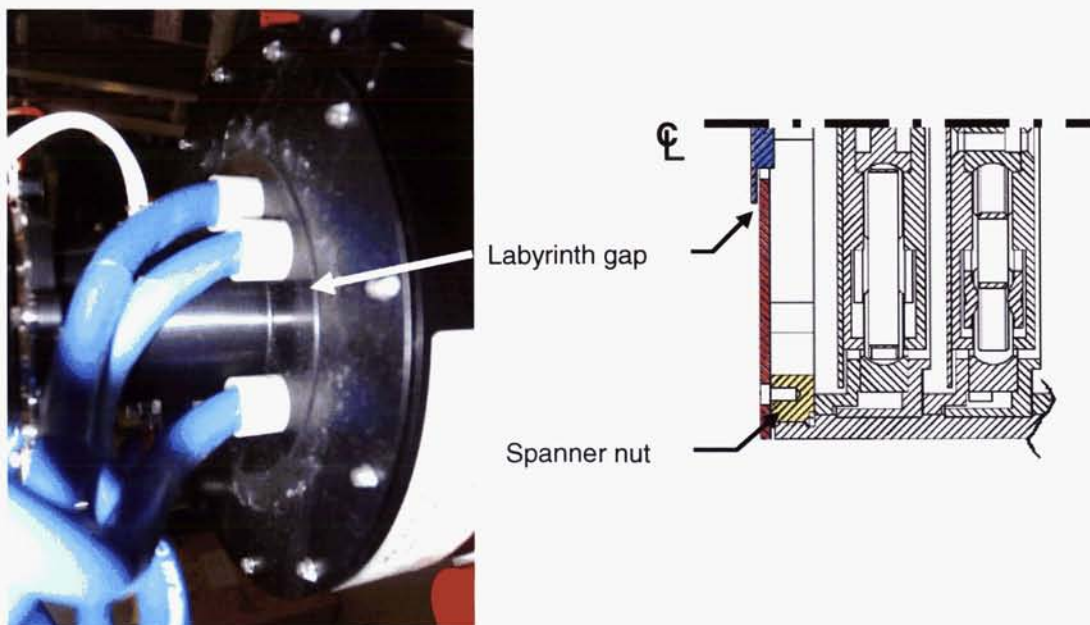


**Figure 5. BMRRM Debris and Labyrinth Gap and Spanner Nut**



Pre-delivery photographs and post-installation photographs taken with a borescope were evaluated to determine if multiple units had experienced a similar loosening problem. No other units were found with this problem.

A review of the drawings and build processes revealed that the nut design used a light preload and a small amount of LLC on its threads as its primary and secondary locking features. Due to a general concern for the locking design and the inability to define the exact cause of the failure, a mechanical lock was devised to fix the problem. The lock will be installed on all seven serviceable units. The three on-orbit units cannot be serviced.

While the vendor had what appeared to be a properly documented and controlled application process, the LLC had failed, allowing the nut to loosen. When the situation was discussed with the LLC manufacturer, they noted that the application fell outside of the recommended usage for their product because of the large size of the spanner nut and low preload and therefore would not guarantee its function.

***Lesson Learned: Liquid locking compounds cannot be depended upon when used in applications outside of manufacturer's guidelines.***

Pre-test, post-test, and post-installation photos were used as a non-destructive method to identify any other instances of nut movement. Since the units are not visible after being fully assembled into their next higher assembly, a borescope was used to obtain the photographs needed to clear the units.

***Lesson Learned: Maintain photo documentation of mechanical systems during assembly and subsequent testing and usage with similar viewing angles to allow for comparisons.***

***Lesson Learned: Provide access for inspection of mechanical systems.***

#### Torque/Preload

A significant number of issues have been worked during the past two years relating to fastener installation torque and the resulting fastener preload. Many of these issues were the result of the improper installation torque being applied to the fasteners. Others were the result of an improper torquing sequence applied to a fastener pattern. A recurring theme has been a lack of understanding of the torque-tension relationship.

#### Inspection Boom Assembly and Shuttle Remote Manipulating System

The Inspection Boom Assembly (IBA) supports components of the Orbiter Boom Sensor System, including sensors and video cameras used by the crew for situational awareness and inspection of the Orbiter. The IBA and Shuttle Remote Manipulator System (SRMS) are mounted in the payload bay of the Orbiter. During flight the IBA is removed from the payload bay and operated as an extension of the SRMS, as shown in Figure 6.



**Figure 6. IBA on SRMS**

An installation drawing review of the IBA handrails revealed that unusually high torque values had been specified for some of the IBA fasteners, for which the vendor was not able to supply any supporting test data. An analysis assessment showed that several fastener groups within the IBA could potentially be



torqued above the yield strength of the fasteners. Similarly, a stress assessment for the SRMS bolts revealed that several SRMS fasteners could potentially be torqued above their yield strength as well.

A series of tests was conducted at JSC to evaluate the suitability of this condition. Torque-tension tests were performed on four different fastener groups, two from the IBA and two from the SRMS, to directly measure the relationship between torque and preload. The tests were able to show that the IBA and SRMS were acceptable to fly in their current condition. For more details refer to JSC 63083 [4].

***Lesson Learned: Ensure torque tables are substantiated by relevant test data, accounting for the materials, lubricants, and installation process. Lubricants or sealants can significantly alter torque-tension relationships.***

#### Flight Releasable Attachment Mechanism

The Flight Releasable Attachment Mechanism (FRAM) provides a generic structural and electrical interface between spare ISS hardware components, called ORUs and either the Shuttle or ISS. The FRAM consists of an active half, which is mounted on the ORUs, and a passive half, which is connected to Shuttle payload bay carriers and on-orbit stowage locations. This provides interchangeability between storage locations.

After acceptance vibration testing of the FRAM, a post-test functional test and inspection revealed that a locking collar was loose and minor damage to an ACME thread was noted. The locking collar is shown in Figure 7.

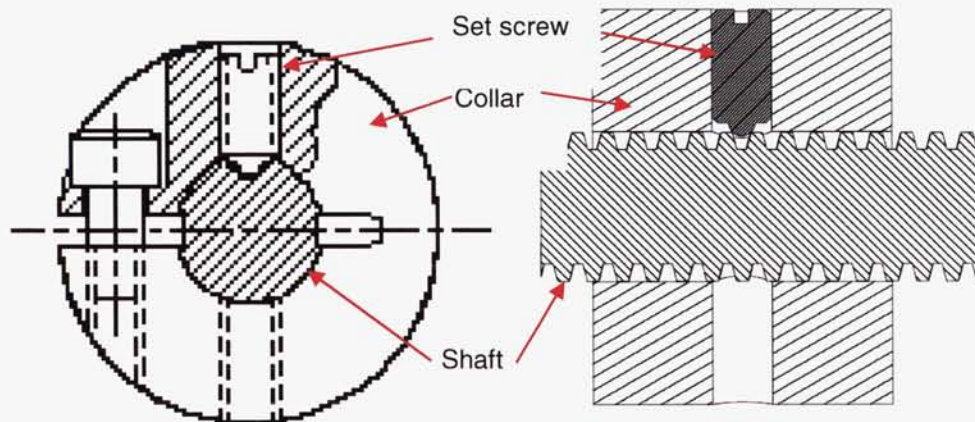


**Figure 7. FRAM Locking Collar**

It was discovered that improper torquing of the locking collar clamping fasteners resulted in a loose collar and that the ACME thread on the shaft was damaged during the testing. The fasteners had been torqued to their full level individually and were not alternated or checked a second time around to ensure that the tightening of one fastener had not reduced preload in another. Unfortunately in this case, the clamping force of the collar was very sensitive to the order and manner of torquing the fasteners. To correct the problem, the fasteners were incrementally torqued to their full torque, while alternating between the two fasteners.

***Lesson Learned: Use proper torque sequence in multi-fastener patterns.***

## Strength

Mechanical system components and linkages need to be designed with sufficient strength to tolerate an actuation force/torque stall condition at any point of travel and maintain a positive margin of safety with an ultimate factor of safety applied. Mechanical systems that incorporate end of travel mechanical stops need positive strength margins for worst case dynamic loading conditions, considering variables in inertia properties, actuation force/torque, drive train resistance, and other environmental conditions. Exposed mechanical system components, protective shrouds and covers, and mounting structure need to accommodate inadvertent impact loads from manipulator systems, payload operations, and crew activity.

### Main Landing Gear Door Retract Mechanism

The Space Shuttle Orbiter main landing gear (MLG) door retract mechanism is shown in Figure 8. The door retract mechanism is a four bar over-center linkage, with the orbiter structure forming the fixed link. A spring-loaded bungee is also part of the mechanism and helps to hold the mechanism over-center when the door is open.

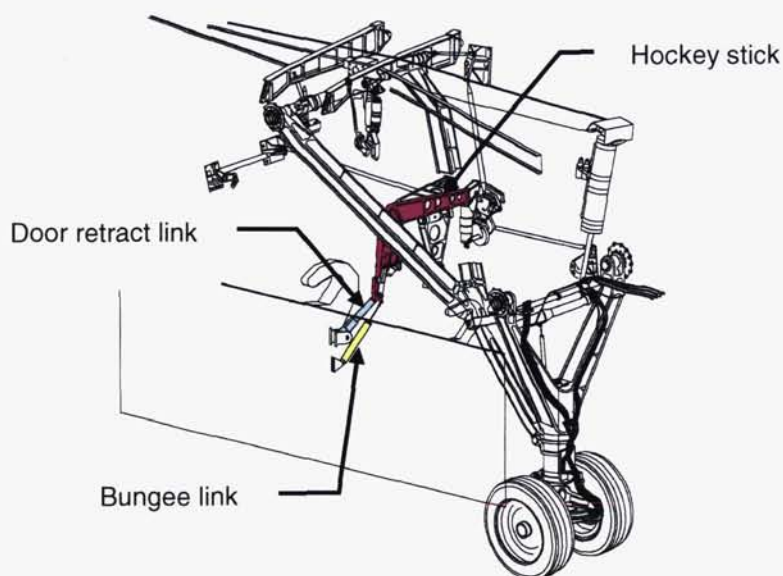


**Figure 8. MLG Door Retract Mechanism**

The door retract link on the starboard main door retract mechanism of Atlantis (OV-104) was found to be bent and cracked during a routine inspection. Figure 9 shows the damaged link in comparison with its counterpart on the port side.



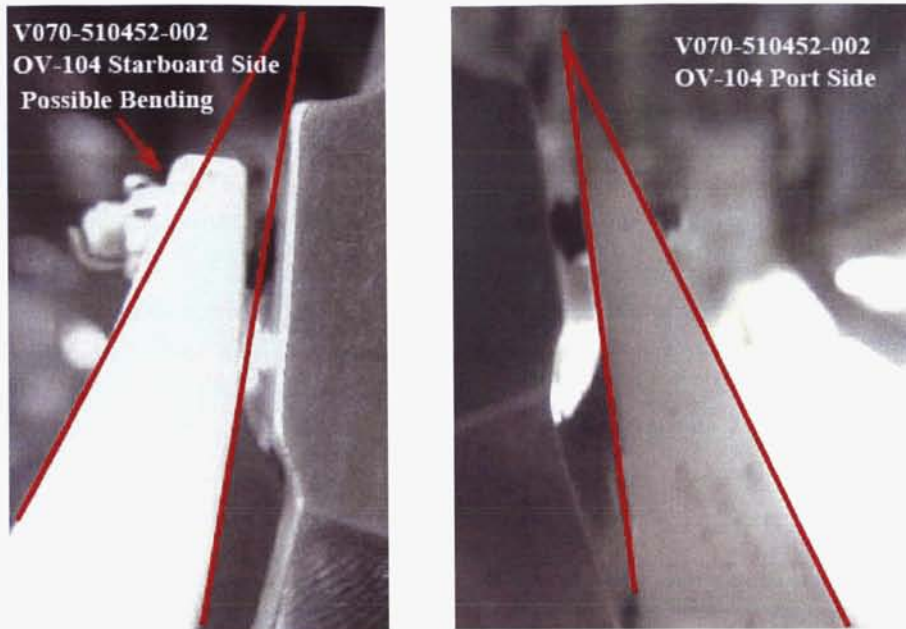


**Figure 9. Comparison of Starboard and Port 452 Links**

Extensive failure analysis including metallography of the failed part, historical data retrieval, dimensional verification, loads analysis, and borescope inspection of Discovery, were conducted to understand the scope of the problem. It was concluded that the damaged part had adequate design properties, and that this part was damaged during replacement of the O-ring seals in the piston axle assembly of this main landing gear strut. This ground operation involved using a hoist to support the lower part of the main gear from overhead by attaching ground support equipment to the hockey stick. The over-center link was overloaded during this procedure, causing the damage. The vehicle flew two flights in this condition.

Discovery was inspected to ensure that it did not have a similar problem, and the damaged over-center link on Atlantis was replaced with a good link borrowed from Endeavour. Ground servicing procedures will be changed to prevent this problem in the future.

***Lesson Learned: Ensure that strength analyses are performed for planned ground operations of mechanisms, and prior to any unplanned ground operations.***

#### **Positive Indication of Status**

All movable mechanical systems should provide positive indication that the mechanism has achieved its desired position (i.e., ready-to-latch, latched, open, closed, etc.) and end of travel stops should be provided for all movable mechanical systems.

#### Limit Switches

Limit switches are often used to provide positive indication of status for mechanisms. Limit switches are small electronic devices not capable of sustaining high mechanical loads, and are typically protected by an actuating lever mechanism. Limit switches require ground rigging to set the actuation lever in the proper location. Due to their size, there is usually a small adjustment window in which the switch will indicate the proper status.

One example of an SSP mechanism that incorporates limit switches is the payload bay door drive mechanism. This system has switches that sense the position of its rotary actuators, and also indicate the location of the door. The rotary actuator limit switches are internal to the actuators, and are therefore protected from extreme thermal gradients between the hardware that is being sensed. The limit switches



that indicate the position of the door are incorporated into the bulkhead switch module, which is installed on the payload bay bulkheads, and are exposed to space.

There have been numerous failures during missions with the bulkhead limit switch module and other limit switch applications. The switches do not accurately change status as the mechanism is operated, and take a few seconds to hours to flip to the proper indication. These failures do not always repeat themselves on the ground. The phenomenon is not currently understood, and despite tearing down the limit switch assembly, rebuilding, reinstalling, and ground rigging, the failures tend to repeat on orbit, and are attributed to thermal effects.

Extra effort should be made to locate limit switches so they are not subjected to extreme thermal environments. In the event that the switches must be installed in these environments, redundancy should be built into the limit switch system and extensive testing should be done to understand the interaction between the various components of the system under the applied thermal gradients.

***Lesson Learned: Ensure that thermal effects have been considered in the design and analysis of limit switches, and have been reproduced during environmental testing.***

#### External Tank Door Mechanisms

Following the External Tank (ET) jettison, the ET doors are used to close out the aft areas where the Space Shuttle Orbiter was attached to the ET. The doors, shown in Figure 10, are open for launch and ascent and then must be closed while on-orbit and remained closed for entry.

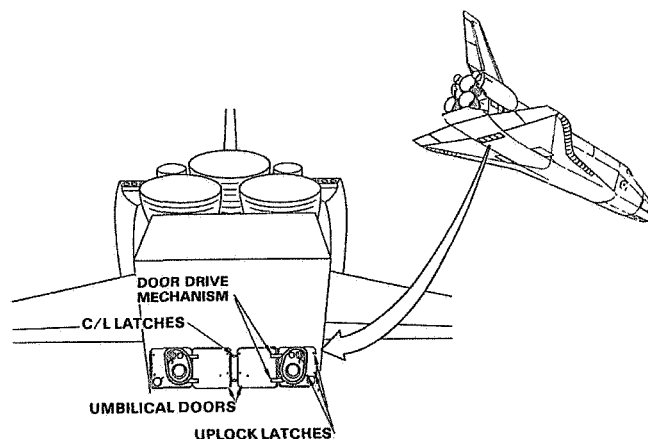


**Figure 10. ET Doors**

A centerline latch mechanism holds the doors open. Once the latches have been released, the ET door drive mechanism is used to drive the doors into a nearly closed, ready-to-latch position. The uplock mechanism then operates to pull the doors into a closed position.

For the ET door drive and uplock mechanisms, mechanical limit switches are incorporated into the actuators. This provides an indication that the actuator has rotated the proper amount, but does not directly indicate the status of the doors. If, for example, debris became wedged between the door and the frame, the actuator might be able to turn the correct number of degrees but the door opening might actually not be fully sealed. Given the external tank foam-shedding problem, this was a concern during the STS-114 return to flight mission. A better way to determine the true door status is being developed.

***Lesson Learned: Provide true indication of status for all safety critical mechanisms.***

## Testing

Proper testing of mechanical systems is extremely important, and cannot be over-emphasized. A comprehensive test program, including run-in tests, functional and environmental acceptance tests, qualification tests, and design life verification tests, is recommended to ensure that mechanical systems operate properly on-orbit. In addition, development testing, done early with prototype hardware, is extremely valuable and has proven to be cost effective by catching problems early when there is time to fix them.

One aspect of testing that is often overlooked, which will be discussed below, is the interaction of hardware inspections and functional verifications.

### Payload Bay Door Mechanisms

Each Space Shuttle Orbiter Payload Bay Door (PLBD) is comprised of multiple sections that are permitted to float along dry film lubricated shear pins. There are multiple requirements to inspect these expansion joint shear pins after a predetermined number of flights. At the same time, there are multiple door functional verifications for the operation of the PLBD mechanical systems (drive mechanism, bulkhead latch mechanism, and centerline latch mechanism). The shear pins are critical to the proper operation of the doors. In the event that the pins are replaced following a door functional, the door functional test must be repeated with the newly installed pins in place. Over the life of a vehicle, unanticipated actuations like these can add many cycles to mechanisms that were not necessarily accounted for during the original design phase.

In an integrated vehicle of various systems, there will be some overlap between hardware inspections and functional verifications. Numerous examples of this interrelation of maintenance requirements and functional verifications exist within the space shuttle program, including the interaction between tile replacement work and the cycling of the landing gear doors, star tracker doors, air data probe doors, vent doors, external tank door, etc.

***Lesson Learned: Design life of mechanisms should consider maintenance cycles of interfacing systems.***

***Lesson Learned: Processing work should be planned such that the fewest number of functional tests are performed, and cycles on mechanical systems should be tracked.***

## Summary

Several lessons learned have been presented in this report. A complete summary of the lessons are presented in Table 1. These lessons may prove to be of benefit for anyone who designs, develops, evaluates, or operates mechanical systems, regardless of the program.

**Table 1: Summary of Lessons Learned**

Category	Lesson
Binding, Jamming, and Seizing	Proper tolerancing and inspection are critical to preventing interferences in mechanical systems.
	Repair and rework of mechanical assemblies can cause collateral damage.
	Dry film lubricant thickness is important and the appropriate surface preparation must not be overlooked.
Fasteners: Secondary Locking Features	Clear secondary locking feature requirements need to be specified in program and project requirements documents.
	Liquid locking compounds are very application process-sensitive and not verifiable, and therefore are not recommended for use as a secondary locking feature.

Category	Lesson
	Measure running torque during each fastener installation cycle and keep a record for verification. Replace locking features that do not exhibit running torques within design specifications.
	Fasteners and locking inserts are not the proper locking feature solution for latch designs requiring many cycles.
	Liquid locking compounds cannot be depended upon when used in applications outside of manufacturer's guidelines.
	Maintain photo documentation of mechanical systems during assembly and subsequent testing and usage with similar viewing angles to allow for comparisons.
	Provide access for inspection of mechanical systems.
Fasteners: Torque/Preload	Ensure torque tables are substantiated by relevant test data, accounting for the materials, lubricants, and installation process. Lubricants or sealants can significantly alter torque-tension relationships.
	Use proper torque sequence in multi-fastener patterns.
Strength	Ensure that strength analyses are performed for planned ground operations of mechanisms, and prior to any unplanned ground operations.
Positive Indication of Status	Provide true indication of status for all safety critical mechanisms.
	Ensure that thermal effects have been considered in the design and analysis of limit switches, and have been reproduced during environmental testing.
Testing	Design life of mechanisms should consider maintenance cycles of interfacing systems.

### Acknowledgements

The authors wish to acknowledge the team members that contributed to the resolution of the problems that have been described in this paper: Mechanical Systems Working Group, ISS Structures and Mechanisms System Problem Resolution Team, and SSP Mechanical System PRTs.

### References

1. Mechanical Systems Safety, MA2-00-057, NASA JSC, Sept. 28, 2000.
2. Materials Control Plan for JSC Flight Hardware, JSC-27301D, NASA JSC, Feb. 2000.
3. Use of Liquid Locking Compound on ESP-2, JSC-62850, NASA JSC, Jan. 2005.
4. Inspection Boom Assembly and Shuttle Remote Manipulator System Fastener Test Report, JSC-63083, NASA JSC, Aug. 2005.





# Reliability and Fault Tolerance in ISS Thermofoil Spaceflight Heaters

Victor J. Bolton\*

## Abstract

Extra-vehicular avionics systems and mechanisms used on the International Space Station (ISS) typically require redundant survival heaters due to cold thermal extremes. Two such survival heater systems have completely failed to date. These designs were not truly fault tolerant because a failure within the heater patch would bring down both the prime and redundant systems. This report is intended to make designers and operators of mechanisms requiring survival or operational heaters for spaceflight applications aware of common issues that contributed to in-flight failures.

## Introduction

A dual element thermofoil heater is in essence set of two resistive elements laminated together. Failures in either element can easily propagate to the other by damaging other element or the laminate structure. Figure 1 illustrates a layered, dual element design.

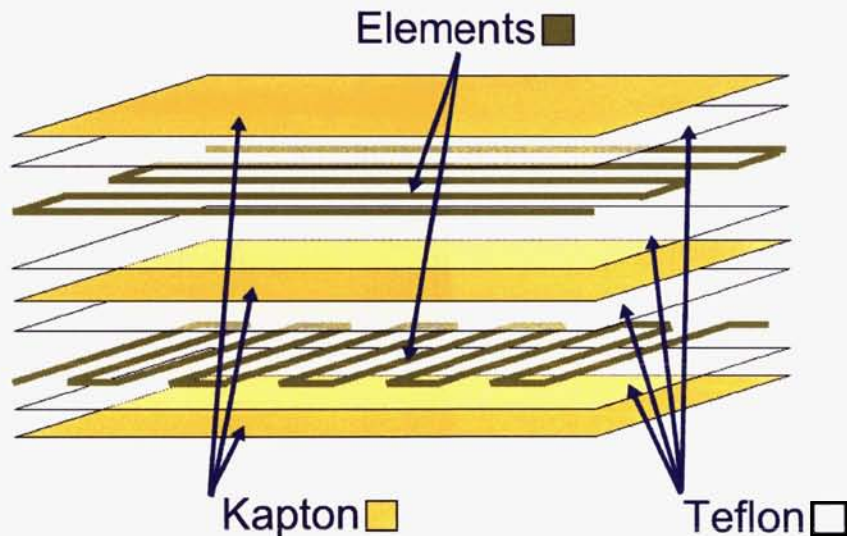


**Figure 1. Layered Design Flexible Heater Exploded View**

Heaters are often treated exclusively as electronic components; however, standard electronics qualification and acceptance testing is insufficient to certify a heater design. Flight history lessons learned lead directly to design and testing recommendations for mechanism heaters. Survivability in particular was not thoroughly examined in the design and testing process.

Failures are presented with a short description to provide data points that suggest areas to pursue alternative designs. Recommendations are meant as solutions to these known problems and other sensitivities of heater patch design and installation. History and descriptions presented here were developed through in depth analysis of failure telemetry, and by direct interview of hardware designers, manufacturers, and operators.

\* Boeing ISS Structures and Mechanisms, Houston, TX

By reviewing the lessons learned from these failures we can create more robust designs that significantly reduce risk and are tolerant of severe conditions: high watt density, over-voltage, complex installation and unknown stress. These lessons are consolidated in the design and testing recommendations section.

### Failure History

Requirements for survival or operating heaters were determined after much of the hardware design process, leaving this critical system as an afterthought. Flexible heaters have a long flight heritage within the US space program. In the ISS program to date we have seen at least three failures of flexible heater systems on-orbit: Auxiliary Power Converter Unit discharge resistor (not used for heating purposes), Nitrogen Tank Assembly (NTA) survival heaters, and the Segment-to-Segment Attach System (SSAS) Capture Latch Assembly survival heaters. We have also seen one failure in on ground testing, the Flex Hose Rotary Coupler Flight Support Equipment survival heaters. The Nitrogen Tank Assembly and Segment-to-Segment Attach System Capture Latch Assembly cases are presented in this paper.

#### Nitrogen Tank Assembly (NTA)

The NTA uses two separate heater patches with layered elements. Each layer within the patches was wired in series to form two circuits that spanned both patches (Figure 2). As a result, failing both layers in a single patch would completely fail both strings of heaters.

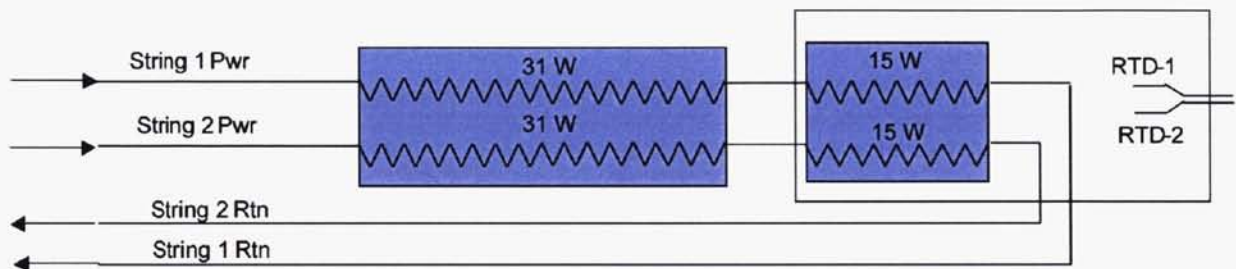


**Figure 2. NTA Heater Strings**

On January 17, 2003 (GMT 2003\_017:16:00) both heater strings failed. The NTA heater assembly cannot be inspected until it is replaced with a spare and returned for analysis. After the failure of the NTA heaters, all similar ISS heaters were identified for further analysis.

#### Suspect Condition Action Notice (SCAN) 044

After the failure of the NTA heaters, a Suspect Condition Action Notice (SCAN) was issued across the entire ISS program to check for similar issues. Many heaters were identified by the search criteria:

1. Multiple elements in a single patch.
2. Greater than  $0.46 \text{ W/cm}^2$  ( $3.0 \text{ W/in}^2$ ) watt density.

Once identified, the true redundancy of the elements, software control, and possible impacts were evaluated. The majority of station heaters have watt densities under  $0.46 \text{ W/cm}^2$  ( $3.0 \text{ W/in}^2$ ); unfortunately, several systems contained multiple elements in a single patch.

The critical impact of the suspect condition to ISS operations was mitigating the hazard presented by activating both elements in a layered patch simultaneously. Simultaneous activation effectively doubles the watt density of a heater, greatly increasing the risk of failure. Suspect software controlled heater activation set-points were offset to reduce the possibility of this type of failure. Set-point adjustment was not possible for thermostatically controlled heaters on orbit, and operational procedures were modified to minimize this risk during power up.



#### P1-P3 Segment-to-Segment Attach System (SSAS) Capture Latch

On May 25, 2004 (GMT 2004\_146:20:01), both heaters on the Port side, segment 1-3 SSAS capture latch failed. This heater was a single patch with dual element, layered design. Figure 3 gives a general view of the capture latch mechanism. The heater patch wraps around the gearbox at the base and would not be readily visible in this view. Telemetry was available at the time of failure and automated warning alarms were activated when cold limits were approached.

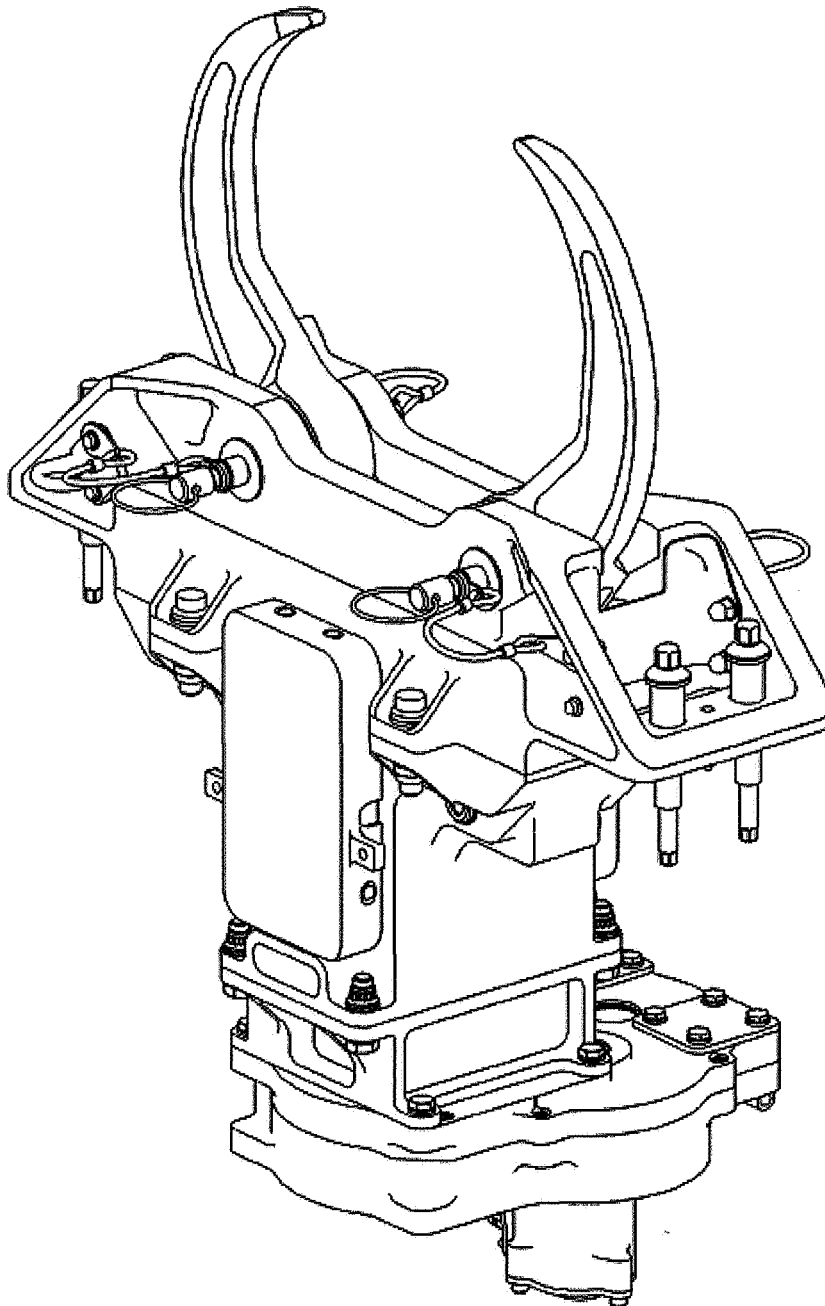


**Figure 3. ISS P1 Truss SSAS Capture Latch**

Failure of both elements was simultaneous. The last short peak in both traces in Figure 4 represents the failure point. The temperature of the system began to decay, and system temperatures did not begin

recovery until the Integrated Motor Controller Assemblies (IMCAs) were activated to provide self heating. The IMCAs are rectangular motor assemblies that bolt to the gearbox at the base of Figure 3. They will actuate the capture latch to berth the P3/P4 truss. Until the P3/P4 truss arrives on flight 12A, the IMCAs will run continuously to mitigate this failure.

At the time of failure only one of the two layers was powered; however, software changes to avoid simultaneous activation of both strings may have helped to prevent this failure. The most likely cause of the failure is heater patch burn-through. This heater assembly is permanently installed to structure and cannot be returned for failure investigation.

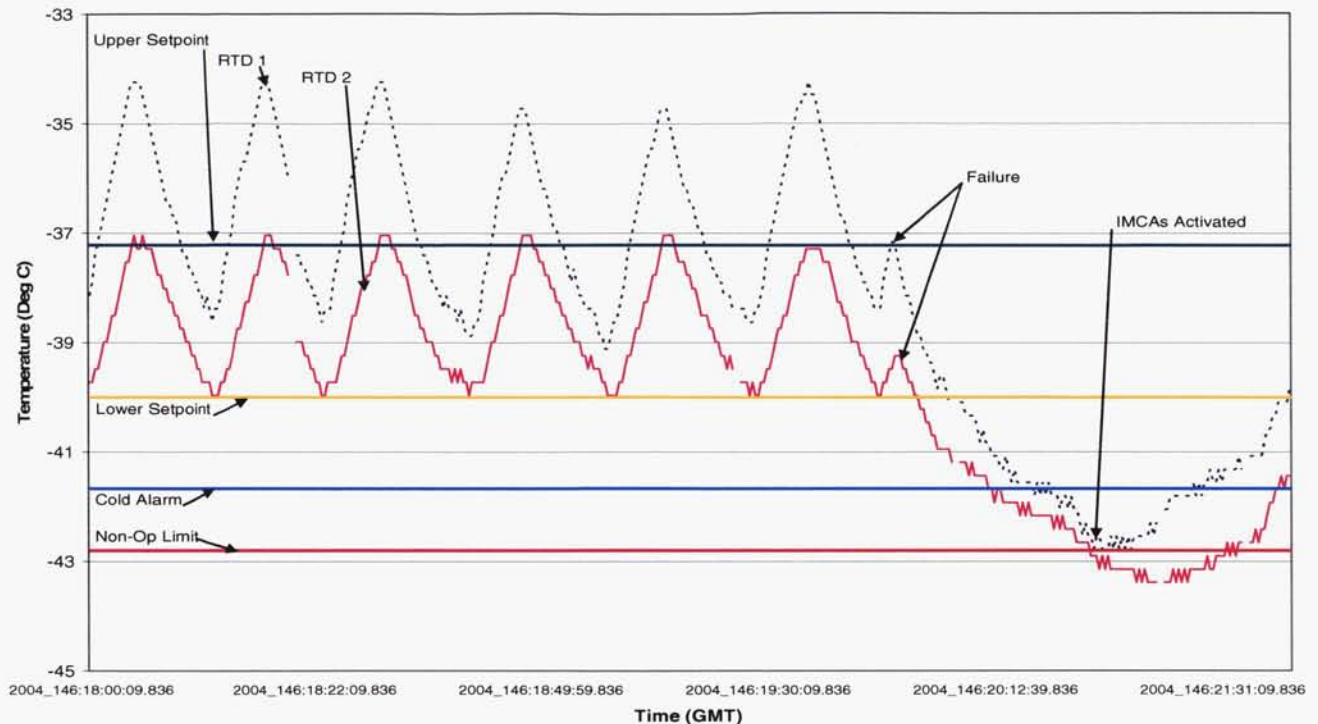


**Figure 4. Failure Temperature Traces**

#### Progressive Failure in a Thermofoil Heater

Progressive failure or burn-through is the result of overheating within an element. Many things cause overheating: over-voltage, necking in the element trace, bubbles under the element, incomplete or improper installation, or delamination within the patch. Once the overheating begins, the stages of failure typically follow these steps:

- Temperatures increase within the element, increasing resistance.
- Melting temperature for the Teflon is reached and the patch delaminates. In this process the Kapton film may char.
- Once delamination occurs, there is no direct conductive path for heat transfer and radiation becomes the dominant mode of heat transfer.
- Unable to release the heat, the heater element foil continues to increase in temperature until it melts or fractures and loses electrical continuity. At this point the heater has failed irrecoverably.

- In dual element heater patches the local delamination will likely cause failure to propagate between both elements, in both side-by-side and layered conditions.

A heater is typically considered failed when it delaminates. The remaining steps lead to failure of the element and an open circuit. There is no data available to determine a critical flaw size. As a result, any visible delamination would be considered unacceptable.

## **Design and Testing Recommendations**

### Design Recommendations

Due to their physical proximity, elements in a dual element heater patch are highly likely to fail simultaneously, even if they are not layered directly on top of one another. They do provide system redundancy for other failures that occur in the power system leading up to the heater patch, but any failure within the patch itself will fail all elements. Multiple element heater patches do NOT provide fully redundant thermal conditioning. Dual element heaters are inappropriate for situations that require true redundancy and fault tolerance unless survivability is addressed.

Individually, high watt density, layered design, and installation difficulty would not necessarily be a significant driver towards failure for a flexible heater; however, the combination of multiple higher risk design elements into an individual heater patch creates sensitivity to conditions that increase the risk of failure. Because layered design has been common across all discovered failures to date it should be approached with a high level of caution. Each individual issue further erodes the margin for error.

Heater systems should be integrated as early in the design process as is possible. Earlier inclusion in the design process would allow for specifications of system components that would permit a large, flat area for heater installation.

Heater patch effective area should be maximized and watt density should be minimized within the bounds of required heat generation: An ideal heater system will be as large, simple, flat and low-watt density as possible. As watt density increases, the importance of effective heat transfer from the element to the heat sink increases. Installation conditions must be carefully examined and fully understood to mitigate overheating.

### Testing Recommendations

Acceptance and qualification testing of thermofoil heaters is specified similarly to standard electronic components; however, this approach is not sufficient to determine all three crucial criteria: Suitability of the design for the intended use, Capability of the design to maintain the desired temperature under minimum power conditions, or Survivability of the design under extended use and maximum power conditions. Survivability verification under worst-case use conditions must be part of acceptance testing.

Survivability in particular has not been part of heater acceptance and qualification testing programs. ISS voltages historically have been running near the upper end of the acceptable range of 113-126 volts. Heaters were typically tested with the minimum voltage (or ambient equivalent) to verify they would produce sufficient heating in a worst-case environment, but never tested to verify they could survive the highest available voltages indefinitely. A 25% increase in heater power can lead to failures not found in qualification testing at 113 V.

Testing under vacuum conditions in particular will create a more realistic environment for verifying survivability of a heater system design. Ideally, all hardware would be fully tested in a thermal vacuum environment, but cost and schedule constraints can prohibit this level of testing. When planning the testing regime, additional planning and analysis should be spent to ensure that the heater has seen an equivalent duty cycle. Because vacuum conditions drastically change the thermal environment, testing of a heater design under vacuum attached to an appropriate heat sink would be a reasonable compromise.



## **Conclusions**

Flexible thermofoil heaters have failed several times in the ISS program. We must look at and seriously consider the processes going into design, testing, and installation of heater patches on spacecraft. Suitability and capability of the designs to fulfill their functions have generally been understood and analyzed in depth; however, survivability has not always been treated with sufficient rigor. Qualification and acceptance testing must include steps to verify heater survival.

Overestimation of the ability of the system to survive high voltages, extended use, or inadequate installation undermines all design effort spent on the system. If the heater itself does not survive, failure of the thermal system jeopardizes mission objectives. If no resolution can be found, the system could be a total loss. Mitigating the impacts of these failures consumed substantial time and resources within the ISS program. The most critical lesson learned is to do everything possible to maintain the survivability of the mechanism via heater patch design by incorporating knowledge from previous failures during initial design.

## **References**

1. Bolton, Victor J "SCAN 044 Response for Structures and Mechanisms," Boeing memo A92-J383-STN-M-VJB-04-032, February 2004.
2. Bares, Geoffrey "PRACA 3661: P1 Nitrogen Tank Assy (NTA) Heater Failure," Boeing presentation, February, 2003.

# Development, Pre-qualification and Application of an Active Bearing Preload System

Simon Lewis\* and Martin Humphries\*\*

## Abstract

This paper describes the development to pre-qualification status of a novel and widely applicable technology development known as a Bearing Active Preload System (BAPS). The BAPS can be thought of as a “smart bearing housing” which replaces a conventional bearing or mechanism housing and whose function is to permit ball bearing preload variation on command. An overview of typical BAPS requirements, its design, the range of actuation options and some performance data are provided. A number of historical and recent bearing applications are reviewed and the benefits realizable by a capability to vary preload are highlighted. These can include order of magnitude improvements in lubricant lifetime, reductions in bearing torque, mechanism mass, cost and complexity.

## Introduction

Ball bearings are preloaded to provide adequate rotor location and bearing stiffness, as well as to protect the bearings themselves from damage due to “hammering” during launch. However, increased preload also has some undesirable effects discussed below.

Grease- or oil-lubricated bearings have essentially two main torque components, namely a speed and temperature dependent “Viscous” component and a load dependent “Coulombic” torque component. At low- to moderate-speeds, the Coulombic component can be dominant, such that mean bearing torque is approximately proportional to preload<sup>4/3</sup>. This relationship is also true at all speeds for solid- and self-lubricated bearings. Furthermore, peak Hertzian ball-raceway contact stress is proportional to preload<sup>1/3</sup> [1].

In ESTL much work has been done in the past concerned with characterization of bearing torque and lifetime, particularly for self-lubricating (e.g., Duroid or PGM-HT) and solid-lubricated (e.g., thin films of MoS<sub>2</sub> or lead) bearings. A review of some of the highlights of this experimental work [2-5] demonstrates that preload (or peak Hertzian contact stress) has a very significant effect, both on film lifetime for solid lubricated bearings, and on separator (cage) wear for self-lubricating bearings as shown in Figure 1. For liquid lubricated bearings too (especially PFPE-based oils and greases), though the lifetime may be often be longer, ultimately lubricant degradation due to shear or chemical reaction at ball/raceway asperities and separator stability/wear issues are aggravated by high bearing preload.

In summary, the use of a high preload throughout life not only increases the Coulombic torque and therefore motor mass/power requirements for the bearing, but also decreases the potential operational lifetime significantly. Furthermore, since in most applications the high bearing stiffness required for launch is no-longer essential once in-flight, the capability to operate in-flight at relatively low preload is highly desirable, particularly in long-lifetime applications and those with challenging thermal requirements (e.g., those having a particularly wide operational temperature range, large or adverse thermal gradients).

Historically bearing “off-load devices” or “launch-locks” have been used to protect bearings during launch by providing an alternative load path in those relatively few applications where the launch loads necessarily exceed the capacity of the bearings, or more often where the low-torque or long-life requirement dictated a moderate to low preload should be selected (e.g., Giotto de-spin bearings [6]). However, bearing off-load devices are relatively mass inefficient and need to be tailored to the application.

---

\* ESTL (European Space Tribology Laboratory) - ESR Technology Ltd., Warrington, Cheshire, U.K.

\*\* Sula Systems Ltd., Wotton-under-Edge, Gloucestershire, U.K.

The BAPS concept provides a bearing cartridge structure that is of appropriate stiffness and load capacity to enable the maximum loads (combination of preload and externally applied launch loads) for the particular bearing size to be applied and a factor of approximately 10 high/low preload ratio. This ratio permits at least a halving of Hertzian contact stress, with commensurate bearing torque and life benefits.

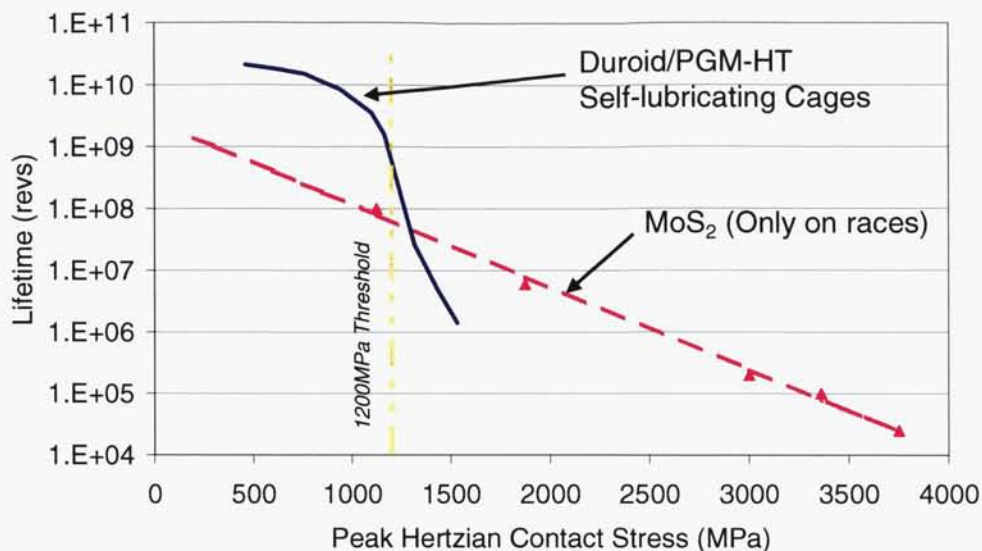


**Figure 1. Lifetime v Contact Stress for Bearings Lubricated by Duroid/PGM-HT or MoS<sub>2</sub>**

### BAPS Requirements

The BAPS device requirements were determined via a comprehensive Market Survey of current or near term applications in which more than 34 space companies were contacted. Responses to the questionnaire indicated that over 20 applications could benefit from BAPS technology, for example deployment hinges, steering devices, APM's, various instruments, actuators, reaction/momentum wheels, CMG's, solar array drives and scan mechanisms for microwave sounding and radiometry. Design drivers from the Survey were ranked in order of priority as Reliability, Envelope, Mass and Cost.

The Survey suggested most potential users would require a bi-stable BAPS device capable of switching from a single high-preload (State 1) to a single low-preload (State 2), however a significant minority of respondents also foresaw applications where the ability to continually vary preload could be valuable. A wide range of bearing sizes was identified, from 25-190 mm bore, but the most popular size range was 50-100 mm bore. The number of operations required of a bi-stable BAPS (assumed to exclude qualification margins) was enveloped as <20 on ground and 1 in-flight. For a variable type device, up to 2 million operations were envisaged.

Envelope constraints were also deduced from the Survey, together with thermal requirements. Excluding the relatively infrequent cryogenic or high-temperature applications, the majority of applications were enveloped by an operational temperature range of -40°C to +80°C.

### BAPS Concept Derivation and Description

By combining the results of the Market Survey and the experience of the team, a generic requirements specification was generated together with a number of concepts potentially capable of meeting these requirements. The concepts were subjected to an initial filtering using "killer criteria" (i.e., criteria which all viable concepts MUST meet) after which surviving concepts were then subjected to a formal trade-off against criteria again reflecting the aspirations/concerns expressed in the Market Survey returns ranked using a rigorous paired comparison method.



As part of the trade-off process an assessment was made of the flexibility of each candidate design for adoption with 4 candidate design cases ranging from small (25-mm bore ISO 10 section, e.g., SNFA EX25 with State 1 preload of 200 N), to medium (50-100 mm bore, thin section) and large (>150 mm bore thin section, e.g., Kaydon KA075ARO, with State 1 preload of 3000 N) bearing envelopes. From these design cases, a single so-called “enveloping design case” was established as a most-challenging case for the Breadboard Model (BBM). The enveloping case was based on the thin-section SNFA SEA55 (7CE3) bearing, having a preload ratio of 3000 N (State 1) / 200 N (State 2) generating a peak bearing Hertzian contact stress ratio of approximately 2000 MPa / 850 MPa.

In the trade-off winning concept, which is based on the monolithic titanium structure shown in Figure 2 below, the bearings (not shown) are located by upper (floating) and lower (interfacing) thrust rings. These rings are linked via a series of “suspension beams” which provide the required structural stiffness characteristics for launch. By monitoring the strains induced in these features due to changing relative axial displacements of the two rings the bearing preload can be determined.

Rotation of a central “synchro-ring” by a few degrees adjusts the spacing of the upper and lower rings by some microns and so modifies bearing preload. The upper and lower rings remain parallel despite the rotation of the synchro-ring because they are linked through a series of flex-struts to the upper and lower rings preventing misalignment. These features also provide an over-center toggle action such that the preload is stable un-powered in two synchro-ring positions. For the high preload state the central synchro-ring is retained just away from top-dead-center (TDC) in a stable configuration (in contact with an end-stop). To set the bearings to low preload, a “Self-Release” force is applied to displace the synchro-ring such that the flex-struts are pushed over TDC and to a stable low-preload position used for flight. This position is maintained by application of a “Holding Force”. For the BBM, the high (3000 N) preload state is at a synchro-ring position of +100  $\mu\text{m}$ , and low (200 N) preload at -600  $\mu\text{m}$  as shown in Figure 3. A maximum “Reset Force”, around 100 N on the BBM must be applied.

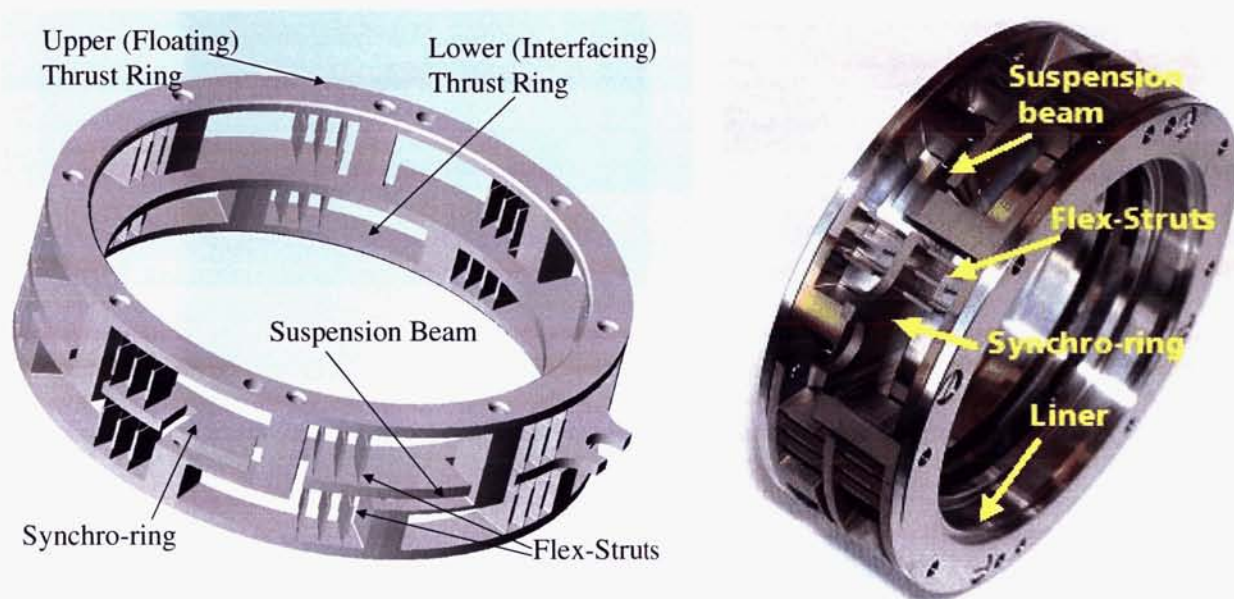


**Figure 2. Monolithic Titanium Alloy Structure Concept and Hardware**  
(includes liners to interface with bearings)

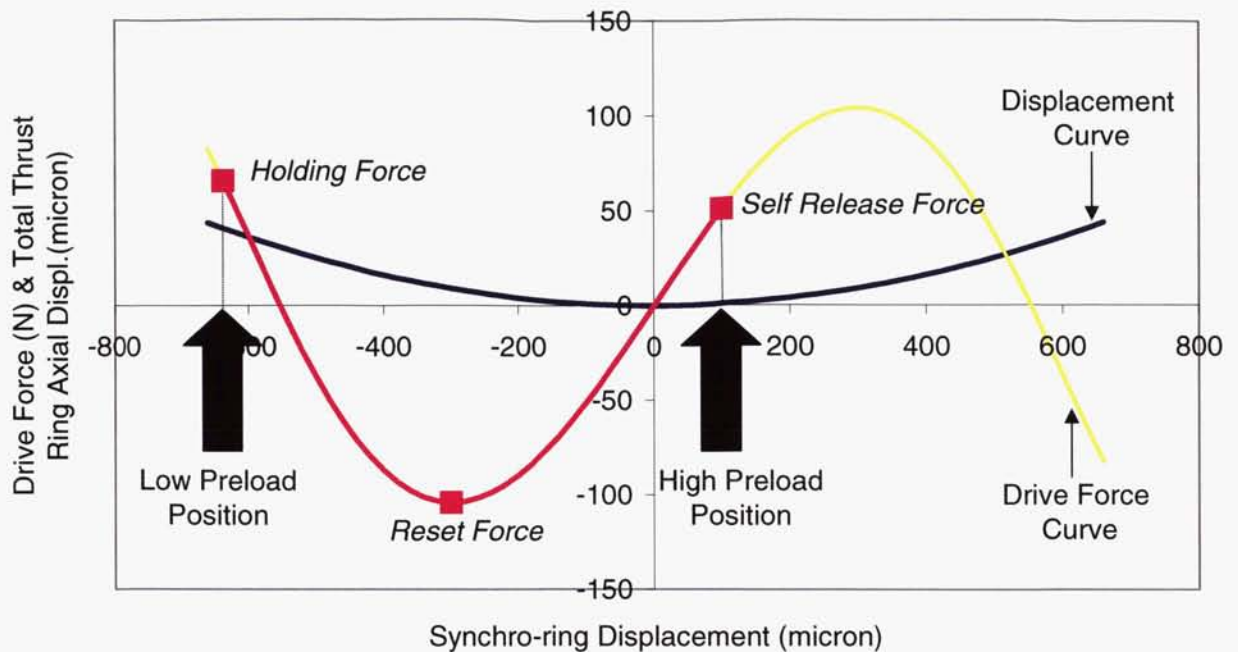


**Figure 3. Predicted Drive Force and Thrust Ring Displacement Curves for SEA55 BAPS**

### Practical Experience with Hardware

Highlights of the performance of the breadboard model (BBM) BAPS, which contains bearings lubricated by a PFPE-based grease thickened by PTFE particles are provided below.

Dimensional inspection showed the BBM to have been manufactured to tolerances in-line with requirements, especially when considering bearing seating tolerances. No significant misalignment of the bearings on assembly or during BAPS operation was measurable. On assembly the BBM structure introduced  $<100 \mu\text{rad}$  of angular misalignment and when operated at most a further  $20 \mu\text{rad}$ . These values are well within even the permissible groove-face misalignment for the bearings themselves (e.g., for ABEC 9 grade bearings of this size,  $200 \mu\text{rad}$  PER BEARING is allowed). This figure is also much less than the known face-face target misalignment for good performance of solid-lubricated bearings, which is around  $300 \mu\text{rad}$ .

As expected, because the BAPS is a purely elastic system, the strain gauges used to monitor displacement of the suspension beams were found to be very linear (sensitivity typically  $20 \mu\epsilon/\mu\text{m}$  of BAPS total axial displacement) and repeatable (within  $1\text{--}2 \mu\epsilon$  when BAPS is repeatedly switched from high- to low-preload), demonstrating accurate, repeatable preload switching even after vibration.

The target preload ratio of  $3000 \text{ N}$  (State 1) /  $200 \text{ N}$  (State 2) which would have provided bearing mean torques at room temperature of  $1400 \text{ gcm}$  and  $110 \text{ gcm}$  respectively was not quite reached due to the effects of elastic strain in the bearing seats. The achieved preload values were  $2500 \text{ N}$  and  $300 \text{ N}$  for which the measured torques were around  $1100 \text{ gcm}$  and  $200 \text{ gcm}$  (Figure 4).

However a positive effect of this bearing seat elasticity was that because strain energy is stored in the BAPS, bearings AND the bearing seats, on switching from high to low preload much less force is needed to hold the device in against the low-preload end-stop position than is predicted based on a model which excludes bearing seat effects, as can be seen in Figure 4.



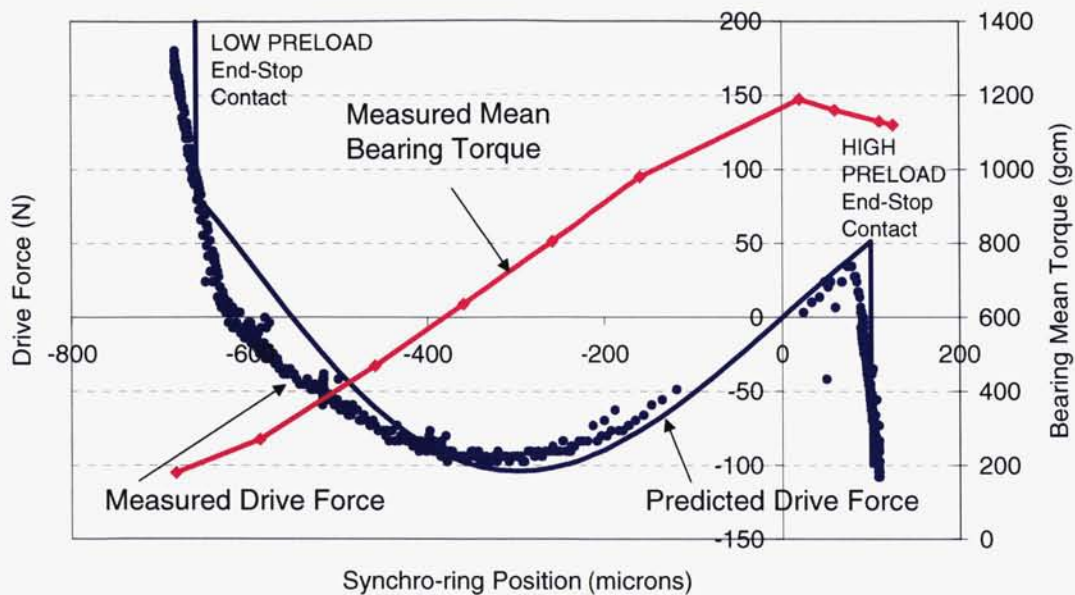


**Figure 4. Measured torque and Drive Force Performance of BBM BAPS Unit**

#### **Actuation Options**

The BAPS can be actuated by several means depending on the application. Most commonly a direct linear actuation will be used for which, all that is required is to provide up to around 60-70 N force and around 700  $\mu\text{m}$  of total linear displacement. For the majority of applications where a typical operational temperature range of  $-40$  to  $+80^\circ\text{C}$  is demanded, then actuation will be via a Shape Memory Bender or High Output Paraffin Actuator. Both devices have the advantage of reset-ability and ease of redundant implementation. However, the BAPS can also be entirely passively actuated, for example by exploiting differential thermal expansion for applications that have high or low temperature requirements, or indeed implemented in a fully-variable form. In the latter case, use of a rotary piezomotor is an attractive option.

#### **How Designs Could Change Post-BAPS**

A number of historical and more recent applications are reviewed (and summarized in Table 1). For each we identify some of the main potential design changes and resulting engineering benefits of use of a BAPS device in similar future applications.

##### Optical Pointing and Tracking (e.g., GOMOS SFA on ENVISAT)

The GOMOS Steering Front Assembly (SFA), currently flying on ENVISAT, is an optical acquisition and tracking mechanism for stars. The mechanism includes a coarse pointing azimuth stage that provides a wide pointing range by allowing a mirror and turntable to rotate. The bearing configuration would ideally support the mirror and turntable during launch. However, given the need for low torque noise emission and reliable operation the bearings required a soft, low preload, and a relatively small outside diameter. However, high strength and stiffness were required during launch, and these conflicting demands could only be met by use of a massive and complex motorized launch protection system (bearing offload device or BOLD).

Using BAPS, a more elegant design using large, thin-section bearings could have been adopted, capable of meeting the launch design case, yet also providing low and soft bearing preload on-orbit. Preliminary analysis suggests that a pair of back-to-back thin-section bearings having a bore of 200 mm could have met the launch load and stiffness requirements. This approach would have yielded very significant savings in mass, cost and complexity.



**Table 1. Summary Historic/Recent Application Details**

Application	Back-Back: BB Face-Face: FF	Size (Type or Bore Dia.)	Supported Load and Offset	Launch Frequency or Stiffness/Preload Used	Special Constraints
GOMOS SFA	BB & Diaphragm	SEA60 /SEA55	16 kg / 100 mm	>100 Hz / 250 N	BOLD used
Giotto De-Spin	BB & Diaphragm	SEA55	5 kg / 150 mm	>100 Hz / >100 N	BOLD used
Optical Terminal	FF/BB	KA075	2 kg / 120 mm	>160 Hz / Minimize (e.g., 30-300 N)	Large bore, severe mass/power constraints
APM with RF Feedthrough (Bepi- Colombo)	BB or Super- Duplex	~50-85 mm	10-14 kg cantilevered – but with 3 <sup>rd</sup> hold-down points (Launch loads ~ 1.5-3 kN plus 102 Nm)	> 5.4x10 <sup>5</sup> Nm/rad / 1200 N (min) for launch stiffness	Bore to accommodate RF joint High launch loads and moments
SADM (BAPTA)	BB & Diaphragm	25 mm	Unknown	>100 Hz / 45 N in flight	BOLD used, released on-orbit stiffness must support solar array
Reaction/Momentum Wheel/CMG	BB or FF & Spring/Diaphragm	20 mm (typ.)	Up to 1-2 kg	>100-150 Hz	Life target 5x10 <sup>10</sup> revs
Swash Plate APM	4 Pt Contact BB Hard Preload	177 mm	Unknown	>100 Hz / 1500 N	Stiffness on-orbit adequate for payload
Push-Broom Scanner (EGPM)	BB	>100 mm	>60 kg	>70 Hz	6x10 <sup>9</sup> Nm/rad. On orbit

**Despin Mechanism (e.g., GIOTTO De-spin)**

In common with many deep space missions, GIOTTO the last European deep space mission using a spin stabilized spacecraft, required a de-spun antenna to maintain a high-data-rate communications link to Earth. The key issues for this type of mechanism are to support the antenna during launch yet provide long life, low friction and reliable operation in adverse thermal conditions (e.g., with wide fluctuations in temperatures and temperature gradients).

To maximize bearing/lubricant life while maintaining insensitivity to adverse thermal gradients a low preload was required and applied by means of compliant diaphragm. But launch loads and frequency constraints for the application could only be met by employing a separate bearing off-load device (BOLD).

Had BAPS technology been available this application could have avoided the need for the BOLD even if a bearing pair with virtually the same diameter were selected.

**Optical Communications**

Laser Communications Terminals for inter-satellite communications links are a major application for pointing mechanisms. One device currently under development is a Course Pointing Assembly. This device is required to gimbal a high precision mirror through large angles. The bearing must be almost free of stick-slip effects and must provide a through-bore sufficiently large to allow the passage of an optical beam (typically 15-mm dia.) through the azimuth gimbal. To achieve both of these requirements in a mass- and cost-effective manner ideally requires high bearing preloads during launch and very low preloads once on-orbit.

A preliminary assessment suggests that launch requirements could be fully met at low risk if launch preload could be set at 2000 N, provided preload is released to less than 200 N once on orbit. The use of BAPS could provide an even larger range than this and would provide a lower risk solution than the use of a fundamentally lower fixed preload and snubbers to limit rotor motion during launch vibration. The latter conventional approach allows hammer like contact at the bearing and drive gear contacts which increase risk of degraded life-time and in-orbit performance.

#### Two Axis Antenna Pointing Mechanisms (APM's) with RF Feedthrough

There are a number of current/near future applications for two-axis APMs that require integrated R/F rotary joints within their azimuth actuators. The applications cover both commercial LEO constellations through to dedicated science missions such as the Bepi-Colombo mission to Mercury. These applications need to accommodate internally mounted rotary RF joints that call for high precision and repeatable co-alignment of R.F. choke faces. The bearings themselves are required to be stiff during launch to support the antenna but must provide low friction torques once on-orbit even when subjected to inverted temperature gradients caused both by R.F. losses at the shaft and in some cases by the operational environment.

The major risks associated with these mechanisms are their sensitivity to thermal gradients and installation tolerances given the lack of elastic preloading. In the unique Bepi-Colombo case, an operational temperature range of +50°C to +250°C is envisaged with 70% of the expected life at the hot case and with adverse temperature gradients which could be up to 30°C across the bearings.

It is foreseen that the use of a BAPS for these applications would significantly enhance performance and reduce risk. It may be an advantage for applications to control bearing stiffness at actuator level in order to maximize the overall structural efficiency of the combined APM and Antenna Launch Configuration, with the Antenna in its stowed configuration. To implement BAPS in for example the Bepi-Colombo application, a pair of angular contact bearings would replace the baselined hard-preloaded super-duplex bearings (without significant impact on radial envelope) and titanium housing. For launch, the BAPS could be set to provide a high-preload in excess of the currently specified 1200 N (enhancing launch stiffness, eliminating bearing gapping during launch and further minimizing risks of fretting damage to gears). On-orbit the preload could be reduced, and more importantly the preload-stiffness achievable with BAPS is low, compared to a conventional hard-preloaded system thus rendering the bearings much less sensitive to the significant and adverse thermal environment.

#### Medium Power SADM (BAPTA)

The BAPTA was developed for early satellite programs, e.g., OTS, ECS, Marecs. It became the baseline SADM for a later series of defense satellites transferring up to 900 W of array power and associated signal lines.

The SADM design uses a pyrotechnically released internal bearing off-load system providing bearing protection and adequate launch stiffness to the solar array. In orbit, the bearings are compliantly preloaded.

Use of a BAPS for this type of SADM would replace a complicated system of compliant preloading, hard bearing-offload and pyrotechnic release mechanisms. Final preload could be set on station for required torque performance and maximum power efficiency. Such a device would be suitable for small to medium mass arrays on small satellites.

#### Reaction/Momentum Wheel/Control Moment Gyros

Reaction/momentum wheels and Control Moment Gyros run continuously and allow transfer of momentum/torque as required by the orbital control system. Ideally the operating case requires a minimum of bearing preload to minimize power loss, torque disturbances and motor mass/volume. The rotating elements supported on bearings have significant mass and require correspondingly high stiffness, both to prevent damage during launch and in the case of the CMG to provide structural efficiency during slew maneuvers. Cage instability and wheel whirling instability are also factors to be considered.

Use of BAPS for wheels would prevent gapping on launch yet allow minimum preload and hence torque loss value for in-orbit operation thus improving power consumption and wheel performance per unit mass. Such a capability is particularly important for solid-lubricated wheels sometimes used in Smallsat and Microsat applications for which life benefits may be significant. With a variable type BAPS, preload could be varied to alleviate cage or resonant frequency problems in reaction/momentum wheels or to permit tuning of CMG stiffness characteristics and energy dissipations.

#### Push-broom Earth Scanner (e.g., EGPM)

The now postponed EGPM mission requires an earth-scanner using the push broom scan approach. The main instrument rotor and reflector (mass >70 kg) rotate at a constant speed up to 32 revs per minute over a nominal 15 year mission, resulting in >250 million revolutions. The instrument rotor must be supported rigidly during launch and rotated about a precise axis in-flight.

The main issue is related to the high instrument rotor mass and the relatively large C of G offset of the instrument rotor in relation to the scan mechanism. This leads to combination of high lateral and axial forces and very high moment loading during launch. Therefore the current instrument configuration incorporates a dedicated hold-down system that supports the rotor at its outer extremities at four locations for launch. These are released once on-orbit and then the instrument rotor is supported purely by the scan mechanism. While the primary launch protection is able to rigidly secure the bulk instrument structure, due to the size and supported mass of the instrument equipments mounted within the instrument there are also local panel modes between the scan mechanism interfaces with the instrument lower panel and the spacecraft side wall. It is not possible to accommodate these modes by allowing relative internal movements within the mechanism due to a number of critical internal operating gaps (e.g. at the motors, sensors and power/signal transfer devices) Therefore the scan mechanism must react the local forces and moments associated with constraining these local modes, which leads to significant local forces and moments across the mechanism. The bearings of the scan mechanism are required to have a bore of greater than 100 mm due to internal design constraints and so in principle the mechanism is capable of reacting significant loads. The use of BAPS technology allows the bearings to react these launch loads without introducing any significant internal movements and provides a relatively stiff fifth hold down point at a location where it is most mass effective. This is done without compromising the mechanism's on orbit performance, in particular the long life and the critical on orbit nodding frequency.

Note that although a bi-stable BAPS is currently base-lined, there would be some benefits in this application in the use of a fully variable BAPS that would enable on-orbit tuning of instrument rotor preload in order to achieve an ideal rotor stiffness.

### **Conclusions**

This paper demonstrates that the novel BAPS device can be used in a wide variety of the more demanding spacecraft mechanism applications to improve both system level and mechanism performance and lifetime. The examples used demonstrate that for maximum benefit, the BAPS concept needs to be incorporated within the design from an early stage in the system development.

The BAPS is currently at the pre-Qualification stage of development, but it is expected that it will be Qualified during 2006.

### **References**

1. Roberts E.W. (Ed.) *ESTL Space Tribology Handbook*
2. *Performance Guide – Self-lubricating Bearings* Prepared by NCT, June 1976
3. Anderson M.J. "Duroid Replacement Material Requirements Specification" *ESTL/TM/20* (July 1998)
4. Lewis S.D. "GERB Phase 3b Post-Test Review" (Unpublished Experimental Work) ESTL (2000)
5. Stevens K.T. & Todd M.J. "Parametric Study of Solid Lubricant Composites as Ball Bearing Cages" *Tribology International* Oct. 1982 (pp293-302)
6. Felici F. "The Giotto Mechanisms and Their Functions" *Proc. 1<sup>st</sup> ESMATS, Neuchatel 1983*, ESA-SP-196



# Development of a Dual Mode D-Strut® Vibration Isolator for a Laser Communication Terminal

Dale T. Ruebsamen\*, James Boyd\*, Joe Vecera\* and Roger Nagel\*

## Abstract

This paper provides a review of the development by Honeywell of a dual mode D-strut® vibration isolator for long range communication instrument. This paper reviews the basic design requirements for the dual mode isolator, the D-strut® isolator design drivers, the prototype D-strut® isolator design, and the results of prototype D-strut® isolator testing.

## Introduction

Honeywell is developing a dual mode D-strut® vibration isolator to isolate the sensitive instrument from the spacecraft bus during launch vibration and during in-flight operation (spacecraft bus vibration disturbances). This paper will describe the design challenges that led to a new isolator design meeting the stringent requirements of this sensitive instrument, and the issues that were identified as a result of testing a set of prototypes of the new design.

Two isolator design options were considered for this application. The first option was to launch lock mount the instrument to the spacecraft and design the instrument to survive the launch loads, and then release the instrument once in flight allowing the isolator to isolate the instrument from the spacecraft bus disturbances. The second (dual mode) option uses the same isolators to isolate the instrument from the launch environment and the spacecraft bus disturbances. In both cases, the isolators are configured in an optimized hexapod configuration (also known as a "Stewart Platform") to provide the desired isolation. The dual mode isolator configuration was chosen to minimize the loads into the instrument due to launch and still provide the required in flight isolation due to the spacecraft bus disturbances.

There are several requirements that define the new isolator design. The requirements for the D-strut® isolator are that the weight of the isolated system is 48.1 kg (106 lb) maximum; the quasi-static acceleration is 16.25 g's maximum during launch. The vibration requirement means that the peak axial load into each D-strut® isolator is approximately a factor of over 2.0 times the previous dual mode design. The higher loads also required that the stroke in each isolator increase by almost a factor of 1.6. These increased loads and strokes needed to be accommodated without changing the length of the isolator.

The D-strut® isolators are three parameter isolation systems. The parameters defined for the three parameter isolators are static stiffness ( $K_a$ ), dynamic stiffness ( $K_a + K_b$ ), and damping factor ( $C_a$ ). These are the parameters Honeywell uses to size the main machined spring, the tuning spring, and the damper annulus gap filled with the proper damping fluid.

Honeywell has submitted a patent application for a new isolator design that meets the load and stroke requirements needed to support the instrument. In the new isolator design, the sealing bellows in the damper assembly are externally pressurized instead of internally pressurized. The new configuration allows for a significant increase in the load capacity and stroke of the isolator without increasing the overall length of the isolator. To demonstrate that the new isolator design would meet the requirements, Honeywell built two complete isolator assemblies to measure the isolator parameters and fabricated the fixtures needed to test the isolators in a bipod configuration up to the maximum quasi-static accelerations.

---

\* Honeywell, Defense and Space, Glendale, AZ

To characterize a bipod of the new Isolator configuration, we performed a series of sine vibration tests with a 18.1-kg (40-lb) mass attached at 0.25 g, 2.5 g's, 7.5 g', 12 g's, and 16.25 g's from 5 Hz to 1 kHz; we performed a random vibration test from 10 Hz to 2000 Hz at a level of 9.1 Grms the results of which will not be discussed here because of the similarity to the sine test results; we also performed a 900 G-SRS Shock Beam test with a 18.1-kg (40-lb) payload mass and a 31.8-kg (70-lb) payload mass. These tests characterized the isolator and showed how the "Q" (amplification factor) at the isolator resonant frequency compared at the different input "g" levels. The testing also found that the lateral mode of the isolator was very well damped and that there was an undamped machined spring surge mode at 615 Hz. All the testing was performed in the Honeywell Vibration Lab.

This paper will describe the development of the new isolator D-strut® for the Laser Communication Terminal and the testing performed on the development bipod.

### Design Requirements and Analysis

The design requirements for the D-strut® are not finalized at this stage of the program. However, there are some preliminary design requirements that are design drivers for the sizing of the D-strut® isolator for the instrument. The original desire was to use an existing D-strut® isolator<sup>1</sup> design that Honeywell had qualified for launch and on-orbit isolation for another application. See Reference 1 for detailed description of the existing qualified D-strut® isolator design. The original qualified system had been developed for a smaller payload, lower environmental loads, and the system isolation requirements were less stringent. A comparison of the requirements for the previous system and the new system is shown in Table 1. The impact of these design requirements differences and how they affect the design will be discussed in the following paragraphs.

**Table 1. Design Requirements Comparison**

Requirement Item	Previous "Dual Mode" System Design Requirements	New D-strut® System Design Requirements	Change in Requirements
Payload Weight	32.25 kg (71.1 lb)	46.7 kg (103 lb) (Design Value)	+ 1.45 X
Peak Damper Force	29.2 N (130 lb)	87.7 N (390 lb)	+ 3.0 X
Peak Static Spring Force	85.4 N (380 lb)	193.3 N (860 lb) (Due to 16.25 g static load)	+ 2.3 X
Peak Dynamic Force	97.3 N (433 lb)	192.3 N (882 lb) (Due to 16.25 g Sine Sweep)	+ 2.0 X
Limit Load (Qualification Level)	11.7 g's	16.5 g's	+ 1.41 X
Weight of the D-strut® Hexapod system	2.36 N (10.5 lb) (Spec) 8.5 lb (Actual)	3.37 N (15.0 lb) (Spec goal) 16.1 lb (Actual)	+ 1.9 X (Actual)
Dynamic Stroke (w/o Margin)	± .51 cm (± 0.20 in)	± .813 cm (± 0.32 in)	+ 1.6 X

#### Impact of Requirements on the new D-Strut® Isolator Design

The peak damping force requirement was one of the limiting factors in the previous D-strut® isolator design. The existing design would have to be redesigned to meet the new design requirements. The new design is a through shaft system with externally pressurized sealing bellows. By externally pressurizing the sealing bellows, there is no squirm pressure limitation. The externally pressurized bellows design is stable, i.e., increasing the pressure does not cause the bellows to try to move to one side since the fluid is always pushing in. The limitation of the externally pressurized bellows is the strength of the bellows materials resisting the pressure and external loads. Because of this difference in the design, the new design capabilities exceed 87.02 kPa (600 psi) which is a factor of 2 over the previous qualified isolator design.

Another limiting factor in the existing qualified D-strut® isolator design is that the dynamic stroke of ±5.1 mm (0.20 inch) will not meet the new requirement of ± 8.13 mm (± 0.32 in). The new D-strut® isolator design contains externally pressurized bellows and does not have the limiting pressure issue; therefore, the bellows stroke capabilities can be increased by adding more convolutes and increasing the bellows

length. The stroke capability of the new D-strut® isolator damper assembly is in excess of  $\pm 8.13$  mm ( $\pm 0.32$  in), as required. The original D-Strut® Isolator is shown in Figure 1 and the new patent pending D-Strut® Isolator is shown in Figure 2. It needs to be noted that the mounted lengths for both of the isolators are the same, 21.03 cm (8.28 inches).



**Figure 1. Original D-Strut® Isolator for previous program**

The original D-Strut® Isolator shown above was used in a previous program to provide launch and on orbit isolation for an instrument which has already flown. The environmental loads for a new payload instrument exceed the capabilities of the existing D-Strut® isolator.



**Figure 2. New D-Strut® Isolator for Customer**

The new D-Strut® Isolator shown will be used to provide launch and on orbit isolation for the Laser Communication Terminal Experiment which is under development. The launch loads for the Laser Communication Terminal required the design changes. There is a patent pending on this new design.

#### Design Analysis

The loads from the derived requirements in Table 1 were used to determine the stresses in the components that make up the new D-strut® isolator. The analysis of the sealing bellows and compensation bellows was performed by the bellows supplier using proprietary methods. The flexure,  $K_B$  spring, and main spring analyses were performed using finite element analysis modeling methods with I-DEAS® application software. There was a requirement that the factors of safety be 1.1 to the material yield limit and 1.25 to the material ultimate limit. We calculated the loads, predicted the stresses, and calculated the factors of safeties for all the critical structural parts in the new D-Strut® Isolator. The limiting part in the new D-Strut® Isolator, from this set of analysis that needs further evaluation is the  $K_B$  spring with a minimum factor of safety to the yield strength is 1.14 and the minimum factor of safety to the ultimate strength is 1.22. Once detailed requirements are defined, the loads in the parts will be further analyzed.

#### **Isolator Bipod Test**

The new D-strut® isolator bipod testing was performed in August, 2005 with the isolators mounted to an 18.1-kg (40-lb) mass. This configuration proved that the isolators were capable of meeting the extreme load case defined for the launch quasi-static environment of 16.25 g's. The testing was performed up to 2000 Hz. The configuration is shown in Figure 3. The suspended mass was 18.1 kg (40 lb) so that the bipod first mode would align with the predicted system hexapod bounce mode of approximately 40 Hz. We reconfigured the shock test setup to test with a Shock Beam methods using both the original 31.8-kg (70-lb) mass and the new 18.1-kg (40-lb) mass. We attached the bipod (with the masses suspended) to a shock beam and provided the shock levels by impacting the beam with a weight on a pendulum. The shock beam test setup is shown in Figure 4.



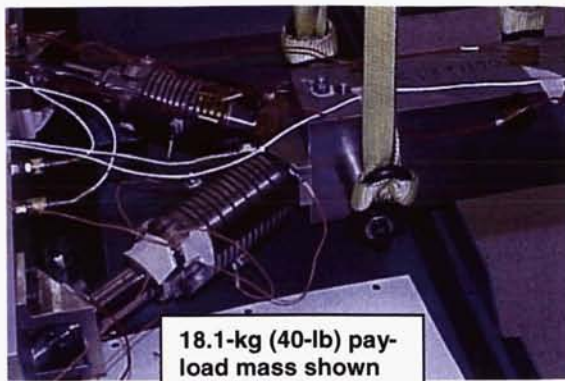


**Figure 3. Bipod Vibration Configuration**  
Electro-Dynamic shaker Input is at Bipod Base on the left with the payload mass placed in-line to the input. This configuration minimized the suspended mass modes in the measured response.



**Figure 4. Shock Beam Test Fixture Set-up.**  
This set-up was used to provide a shock to the base of the Bipod using the impact mass suspended on the chain. The impact mass is allowed to swing and impact the shock beam to produce the shock required at the bipod base on the far end of the shock beam.

#### Shock Beam Test

When performing the shock beam test, we used an 18.1-kg (40-lb) mass and a 31.8-kg (70-lb) mass. The test setup is shown in Figure 4. Figure 4 shows the actual setup of the shock beam. There was an array of accelerometers placed on the new D-strut® isolator bipod and fixtures to measure the shock input and the response of the isolators and payload mass. Only the in-axis input and in-axis response of the payload mass will be discussed in this paper. The set up was the same for both of the masses. The test results for each of the payload masses were much the same; therefore, only the results from the 18.1-kg (40-lb) payload mass test will be presented.

The locations of the accelerometers were selected to provide information on the isolator spring body axial surge modes, isolator spring body lateral modes, and the mass response. The locations of the accelerometers are shown in Figures 5. In order to ensure that the shock input to and response of the payload mass were captured, we used shock accelerometers at the channel 1 location, and the channel 8 location.

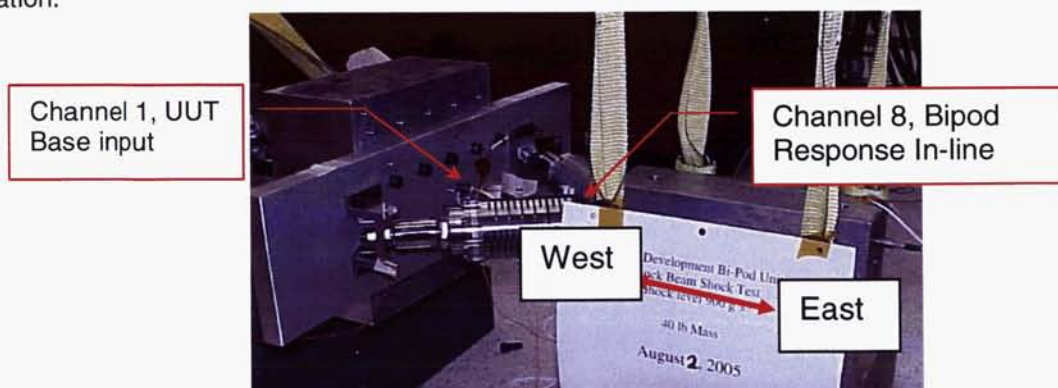


**Figure 5. Shock Beam Test Accelerometer Locations**

From this view, five of the accelerometers can be clearly seen. The accelerometers of interest which indicate how each of the isolator body modes affect the payload mass are channel 1 and channel 8.

The SRS's of the shock pulses are shown in Figure 6 and the time histories of the pulses are shown in Figure 7.

The response of the payload mass was measured with accelerometers at the locations shown in Figure 5. The peak response of the mass was measured at the channel 8 (in axis) accelerometer location. The peak response from the shock pulse was peak input value of 805 g's and a peak response of the payload mass was 21.2 g's. This was a reduction of 31 dB. The amount of isolation due to base shock input can be seen by viewing the base input time history on the same plot as the mass response as plotted in Figure 7.

The SRS of the 18.1-kg (40-lb) mass to both of the shock pulses is shown in Figure 6. The SRS of the response reflects the fact that, in the higher frequencies, the first input shock pulse is higher and this is reflected in the response of the mass. One noticeable artifact of the mass response in Figure 6 is that there is a peak between 560 Hz and 630 Hz even though the break frequency of both pulses is around 800 Hz. The 630 Hz peak is very close to known surge frequency of the isolator main springs. The sine vibration data only goes to 2 kHz; therefore, the correspondence to the peaks in the SRS data can only be tracked to 2 kHz.

#### Conclusions about the Shock Beam Test Results

The following conclusions can be made about the test results.

- The shock beam test was able to achieve the input levels required by the potential isolation system.
- The isolators in the bipod configuration were able to decrease mass responses relative to the maximum input by 30 dB or more. **These Isolators eat shock!**
- The isolator surge modes do contribute to the response of the payload mass due to the base shock input; but, the contribution is not as great as previous testing indicated.

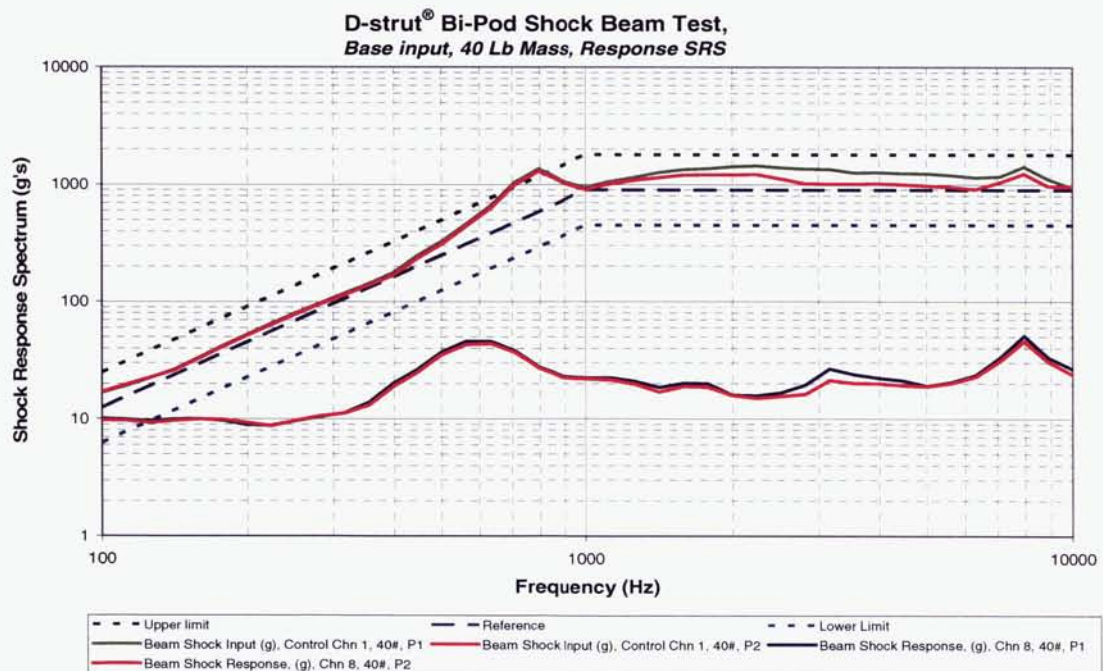


**Figure 6. Bipod 18.1-kg (40-lb) Mass response SRS, both Pulses**

The isolated calculated SRS of the payload mass is significantly lower than the input SRS. The spring surge mode at around 620 Hz can be observed in the above plot.



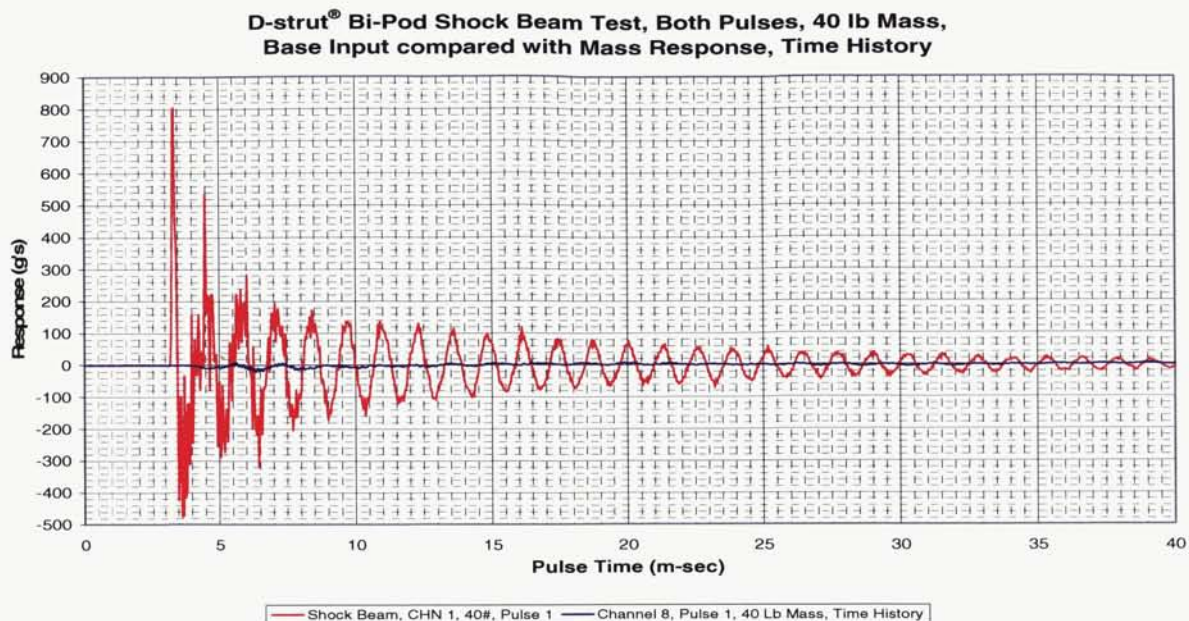


**Figure 7. Comparison of Shock Input and Mass Response, 18.1-kg (40-lb) Mass, Shock Beam Test**  
The time history for the recorded shock pulses is shown along with the mass response. This plot shows the amount of reduction in the response of the bipod mass due to the isolation of the shock input. The effective reduction of the mass response due to the base input is over 30 dB.

### Sine Vibration Test

#### Sine Vibration Test Setup

The test setup for the sine and random vibration test is shown in Figure 15. The picture in Figure 16 shows the actual setup of the sine and random vibration testing. The bipod and mass were instrumented with 15 accelerometers. The accelerometers were placed to measure the response of the isolators and payload mass with-in the limitations of the available instrumentation. The locations of the accelerometers were selected to provide information of the in-line spring surge modes, the isolator spring body lateral modes, and what the mass response was at those modes. The locations of the test accelerometers are shown in Figure 8. The testing was performed with only the 18.1-kg (40-lb) mass. This was done to characterize the equivalent system bounce mode and to characterize the isolator spring body lateral mode, spring body in-line surge mode and harmonics, which are not affected by the bipod suspended mass.

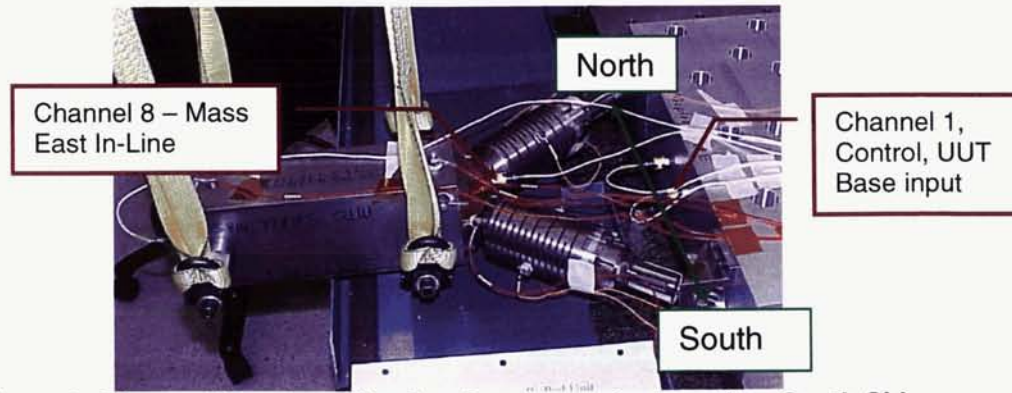


**Figure 8. Sine and Random Vibration Accelerometer Location, South Side**

The north (top) and south (bottom) isolator with the location of the visible accelerometers are shown. The slip plate and the adapter plate are to the right with the suspended 18.1-kg (40-lb) mass to the left.



### Sine Test

There were a total of six different test input levels of 0.25 g's initial, 2.5 g's, 7.5 g's, 12 g's, 16.25 g's and finally 0.25 g's. The input at the base was limited for the 7.5 g's, 12 g's, and 16.25 g's to achieve a peak response at the payload mass of 16.25 g's. The mass responses for the 0.25 g's and 2.5 g's test levels are not limited. Reviewing the mass response provides an indication of the affect of the isolator structural modes on the payload mass. It is best to determine the performance of the isolators by reviewing the transfer function of the isolator which is a ratio of the response relative to the input. Using the Transfer function the different input levels can be compared to each other.

### Sine Test Transmissibility Data (Transfer function)

Prior to performing the vibration test, we identified which response channels we wanted to compare to the reference channels so that the transmissibility of the isolator could be evaluated without consideration to the input level. For the purposes of this paper, we will discuss the calculated transmissibility of mass response accelerometer, channel 8, to the bipod base.

The transfer function for all the base input different levels is plotted in Figure 9. In this plot, the bipod break frequency is shown, the lateral mode of both of the isolators can be clearly identified, the spring body surge mode with its very high response can be clearly identified, and there are modes above 1000 Hz that are evident.

In order to evaluate the mass response and the bipod structural modes, we will break the plot in Figure 9 up into three different ranges, 10 Hz to 100 Hz, 100 Hz to 1000 Hz, and 1000 Hz to 2000 Hz. First, we will examine the break frequency of the bipod shown in the plot from 10 Hz to 100 Hz. The bipod break frequency shows shifts with the change in the base input level. Care was taken to ensure that the temperature of the isolator was at room temperature before the start of each test. The break frequency and calculated transmissibility changed slightly as the input level increased. This is consistent with the theory for the isolator. An explanation of the three parameter isolator theories that predict shift in frequency and change the isolator break frequency and damping is included in Reference <sup>2</sup>. The isolator design is such that as the damping (Ca) decreases because of the heating of the isolator, the isolator is more closely tuned to the input level which slightly decreases the break frequency and the isolator calculated transmissibility. We measured the temperature rise of the damper housing during the 16.25 g test and the increase in temperature was 18.8 °C (34 °F). The effect of the temperature change is clear in Figure 9.

In the frequency range from 100 Hz to 1000 Hz we see that there is a lateral mode of both of the isolators in the bipod at 215 Hz and the isolator spring body modes at 615 Hz. This data is consistent with the data collected in previous testing. The 615-Hz mode can be used to evaluate the transmissibility of the main spring surge mode. The worst-case transfer function peak of the 615-Hz mode is approximately 0.9. If there was no mode at this location, the mass response should be approximately 0.02 therefore, the calculated transmissibility of the mass response due to the spring surge mode is approximately 45. This is likely an optimistic estimate since this measurement is not in-line with the isolator.

In the frequency range from 1000 Hz to 2000 Hz, there are some structural modes of interest in the payload mass response transfer function. The first mode of interest is at 1190 Hz. The transfer function approaches a calculated transmissibility of 0.12 or a factor of 8 below bipod base input. There are additional modes above 1190 Hz but there levels are even lower. Evaluation of the higher modes is still in progress.

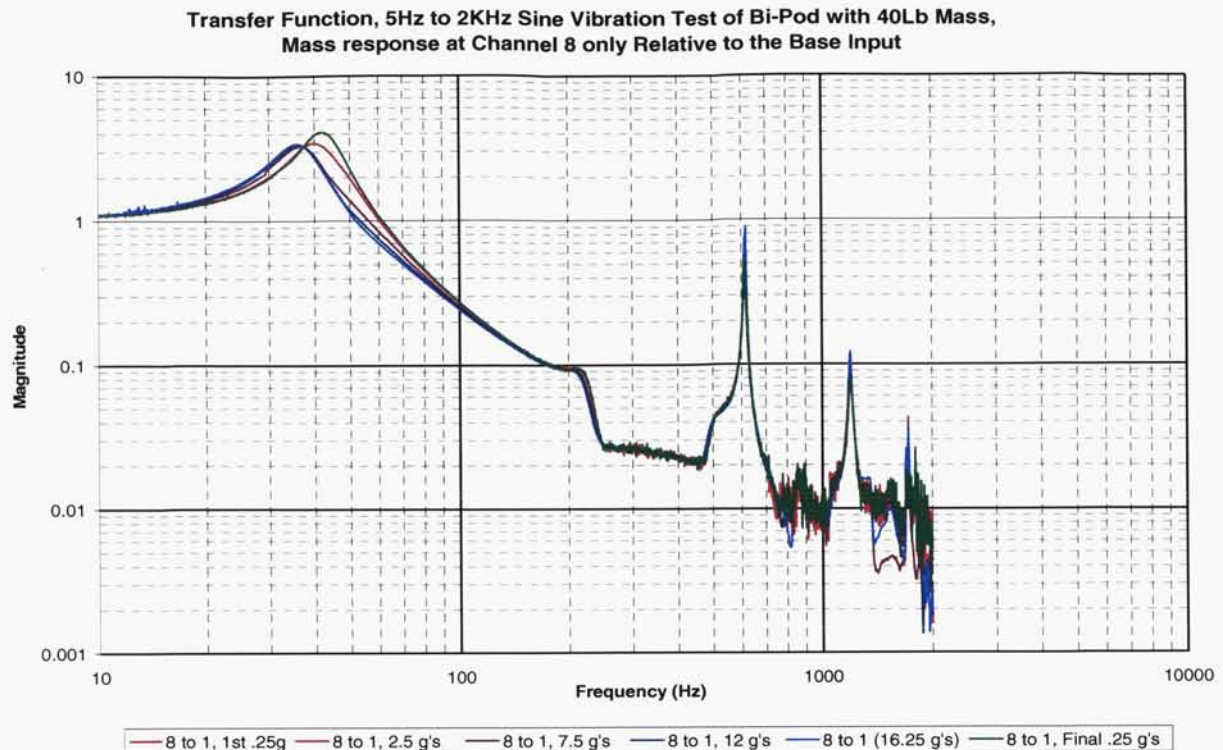


**Figure 9. Transfer Function of the Mass Response only at the Bipod Interface.**

Since the in-line response of the mass is much the same in both accelerometers, the plot in this figure is just the mass response at the bipod interface to the 18.1-kg (40-lb) mass. These Isolators work so well that for low inputs (0.25 g's), the high frequency response is less than the accelerometer noise floor

### Final Conclusions

A new D-Strut<sup>®</sup> isolator has been developed for a Laser Communication Terminal experiment. This new D-Strut<sup>®</sup> isolator advances the state of the art for dual mode isolators in the space environment. This new D-Strut<sup>®</sup> isolator increases launch load capacity by at least a factor of two with the limiting factor now being the structure and not the damper bellows as in previous designs. This new D-Strut<sup>®</sup> isolator was exposed to a sine vibration environment of 16.25 g's and still functions properly afterwards without changing it's isolation capabilities. This new D-Strut<sup>®</sup> isolator reduces the shock environment by a minimum of 31 times (-30 dB).

A customer concern with the new D-Strut<sup>®</sup> isolator is the main spring surge mode at 615 Hz. This mode may affect the line of sight pointing capability of the Laser Communication Terminal instrument. To solve this problem we have completed testing using constrained layer damping, or the using Tuned Mass Dampers on the spring to reduce the main spring surge mode. At the time of this writing, we have not completed the evaluation of the test results but firs indications is the constrained layer damping has no effects on the surge mode and tuned mass damping has significant effects. We will have some conclusions about the additional damping methods available in a future paper.

### References

- 1 "Performance of a Launch and On-Orbit Isolator", Jim Boyd, T. Tupper Hyde, Dave Osterberg, Torey Davis; Presented at the Smart Structures and Materials Conference; SPIE, March 2001
- 2 "Advanced 1.5 Hz Passive Viscous Isolations System"; Porter Davis, David Cunningham, John Harrell; presented at the 35<sup>th</sup> AIAA SDM Conference, April 1994.

# Design and Testing of a Low Shock Discrete Point Spacecraft Separation System

Pete Woll<sup>\*</sup> and Daryn E. Oxe<sup>\*\*</sup>

## Abstract

A separation system was designed for use on a standard Lockheed Martin satellite bus structure to allow the satellite to separate from standard launch vehicles. The separation system had two key design requirements: six discrete point attachments and a low shock separation (<1600 G's). The design solution was a system utilizing a heritage separation system component and a previously unused low shock release device for booster separation, a Split Spool Release Device (SSRD). This paper describes the overall design of the system as well as the unique challenges encountered during component and system level design and test. The challenges were primarily associated with achieving the low shock requirement imposed on the system and the integration of previously unused components into a new separation system.

## Introduction

The Discrete Point Spacecraft Separation System key requirements are: six discrete point attachments and a low shock separation. These requirements were dictated by the spacecraft bus structural design and the use of shock sensitive electronics. The structure is comprised of hexagonal bulkheads that are connected to a central cylinder via radial panels. The radial panels are the primary mounting location for all component electrical boxes on the spacecraft. They are also the primary load path for all launch loads and the location of the discrete point attachments. In order to meet the low shock requirement, a new low shock device had to be implemented because a standard pyro-actuated separation nut could not meet the low shock requirements. After evaluating several candidate device designs, a Split Spool Release Device (SSRD) was chosen as the restraint device in the separation system. This device has never been used in a spacecraft separation system to date and there were many challenges associated with using this relatively new device.

## Design Description

The LM900A spacecraft bus does not mount directly to a standard Payload Attach Fitting, instead using a secondary structure called a Booster Adapter Assembly (BAA). By using a secondary structure, the separation plane as well as all associated separation components can be tested with the spacecraft to minimize the amount of testing that occurs at the launch base. This allows a separation demonstration to be performed prior to shipment to the launch base. The BAA is a large cylindrical ring that bolts on to an industry standard 66" Payload Attach Fitting. Attached to the cylindrical ring of the BAA are 6 A-frame brackets. These brackets are where the six SSRD's are mounted along with six Spring Mechanisms. The SSRD's provide the restraint of the spacecraft during launch and provide a low shock release upon command. The Spring Mechanism provides the separation tip-off force for the spacecraft during separation. Shear loads between the launch vehicle and space vehicle during launch are carried by a cup/cone interface. The A-frame brackets contain the conical half and the cup half is located in the aft bulkhead of the spacecraft. Mounted inside the radial panels of the spacecraft, is a custom designed low shock Retraction System used in conjunction with the SSRD's. The Retraction System ensures the preload bolt clears the separation plane after release and provides positive retention for the life of the spacecraft. The Discrete Point Separation System and the components have been completely qualified for use in a space environment and several system-level separation demonstrations have been performed. Figure 1 shows the basic components of the Discrete Point Separation System.

---

<sup>\*</sup> NEA Electronics, Inc., Chatsworth, CA

<sup>\*\*</sup> Lockheed Martin Space Systems Company, Sunnyvale, CA



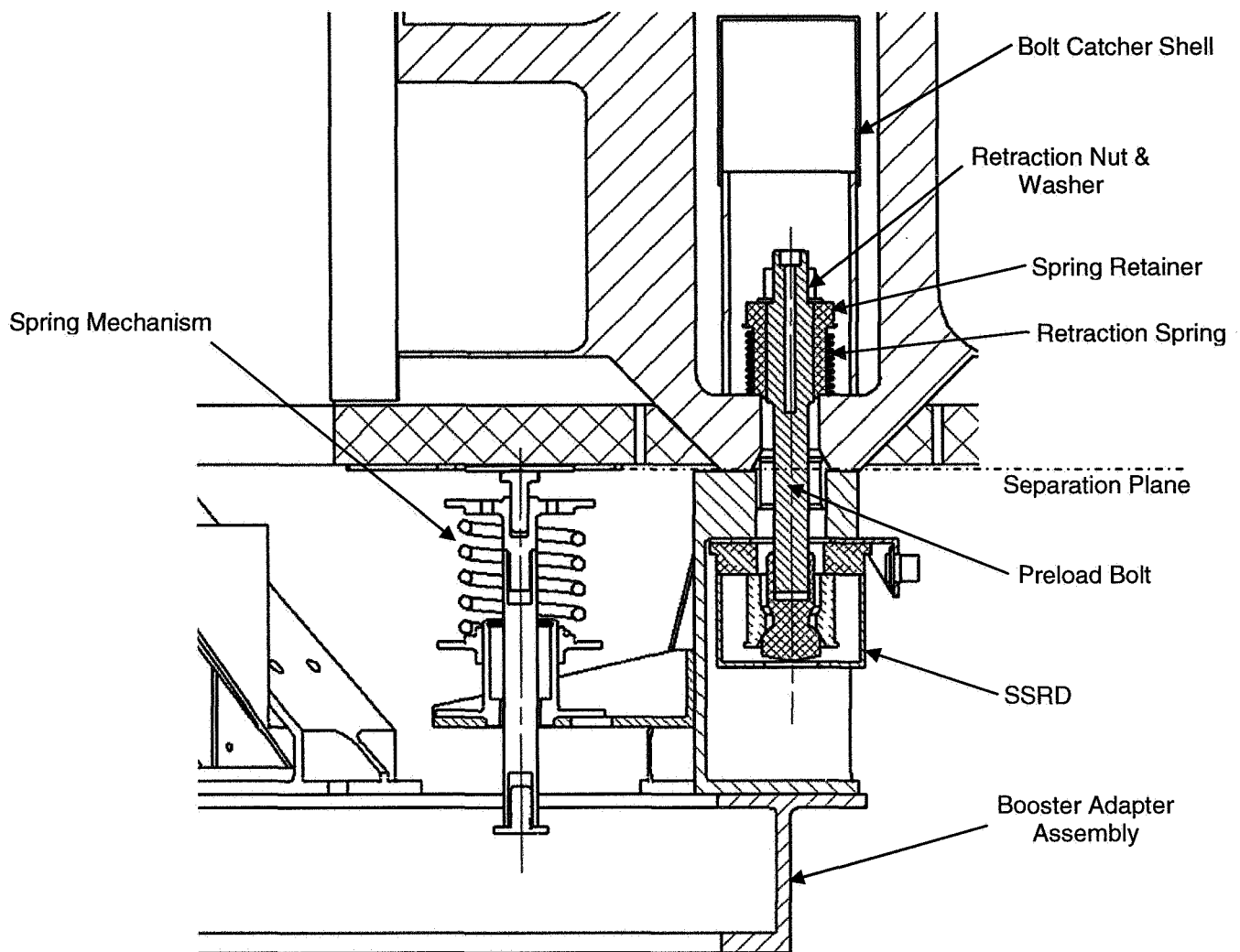


**Figure 1. Discrete Point Separation System Components**

The heritage component of the separation system is the Spring Mechanism. The Spring Mechanism has extensive flight history and was also used in the previous iteration of this separation system design. The Spring Mechanism's primary purpose is to provide the separation tip-off force from the booster vehicle. It delivers this separation force by utilizing a spring-loaded plunger configuration of which there are nine configurations capable of 225 - 525 N of force. The Spring Mechanism also has adjustment capability that allows each unit to exert an exact force and allow for mounting adjustments. These design features allow the Spring Mechanism to be used in a variety of applications and meet a wide range of requirements with only a slight impact to the weight of the unit.

Several years ago, NASA and ESA expressed a need for an alternative to traditional explosive actuators. NEA Electronics Inc. satisfied this objective by developing a reliable, fast-acting, sure release, low shock output, redundant, non-explosive separation mechanism called a Split Spool Release Device. The SSRD is an electromechanical separation nut-release mechanism that eliminates the residue and shock produced by explosive devices and are factory refurbishable for extended use. The device has significant flight heritage primarily as a hold down and release mechanism of deployable structures (solar arrays, antennas, etc). This is the first spacecraft/booster discrete point separation system design utilizing the SSRD as the restraint device. The SSRD is a mechanically and electrically redundant and in this application is capable of 55.6 kN of preload. The typical generated shock output of a single device at maximum preload is less than 500 G's. Table 1 shows a brief list of capabilities of the device used in the discrete point spacecraft separation system.

**Table 1. Specification for the 55.6-kN Split Spool Release Device**

Requirement	Capability
Ultimate Load	69,500 N
Max. Rated Release Load	55,600 N
Source Shock	<500 G's @ 55,600 N preload
Actuation Circuit	4 A @ 6 VDC per circuit
Actuation Time	25 msec max.
Qual. Temperature Range	-60°C to +105°C
Weight	816 g max.

The device consists of a load-bearing spool that is split in half. These spool halves capture a spherical rod end and represent the primary load path of the unit. The spool halves are wrapped with a restraining wire that keep the spool halves from moving laterally when load is applied to the spherical rod end. The restraining wire is fixed to one of the spool halves on one end and restrained with two fuse wires on a toggle on the other. The restraining wire puts a small preload on the fuse wires

when the unit is "set". Upon receipt of the actuation signal, the fuse wire heats up which decreases its tensile strength. The toggle breaks through one or both of the fuse wires depending on the type of actuation signal and the restraining wire starts to uncoil from around the spool halves. The unrestrained spool halves are then gradually driven apart by the preload until the rod end is no longer captured and "drops" through the device. The actuation of this device is very unique in that it gradually relieves the preload, which is the biggest contributor to shock output, and releases the constrained end of the joint. Refurbishment of the unit is achieved by replacing the restraining wire and fuse wire assemblies after actuation and can be done numerous times to allow for ground test. In the Discrete Point Separation System, the SSRD assemblies are jettisoned with the Booster Adapter Assembly after actuation. Figures 2 and 3 show external and internal views of the 55.6-kN SSRD.



**Figure 2. External View of 55.6-kN SSRD**

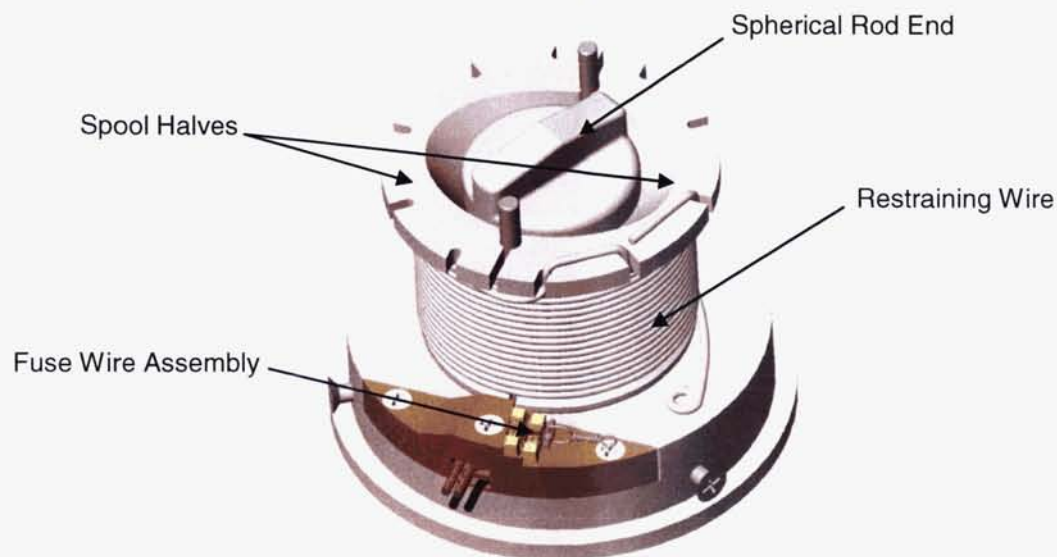


**Figure 3. Internal Components of a Typical SSRD**



In similar separation devices, an external system is utilized to ensure retraction of the preload bolt or rod. However, in this application existing hardware was not compatible with the SSRD nor would it meet the low shock requirements, therefore a new Retraction System was designed. The primary purpose of the Retraction System is to carry the preload in the separation joint and retract the spherical rod end out of the SSRD. The system is made up of a Preload Bolt, Retraction Spring, Spring Retainer, Shock Absorber, and Bolt Catcher Can. The Retraction System is assembled in place after the BAA is mated to the spacecraft. The Preload Bolt is threaded into the spherical rod end in the SSRD through the separation fittings. The Spring Retainer and Retraction Spring are then fed over the Preload Bolt and the spring is compressed. Once compressed, a washer and nut are threaded onto the Preload Bolt and the preload is applied. Preload verification is done via a strain gage within the Preload Bolt to assure proper preload. After applying the preload, the Bolt Catcher Can is installed to contain the assembly inside the spacecraft. When the SSRD is actuated, the spring retracts the Preload Bolt and Spherical Rod End out of the SSRD and across the separation plane, eliminating the possibility of hang up during separation. The Retraction Spring also ensures positive retention of the Preload Bolt and Spherical Rod End throughout the lifetime of the spacecraft. Figure 1 shows the components of the Retraction System.

### Design Challenges

The majority of the design challenges were associated with using an SSRD as the primary restraint device. As stated earlier, this device has never been used in a spacecraft separation system and had a significant impact on the design of the Retraction System. There were two key design drivers on the Retraction System related to the design of the SSRD: torque retention capability and mechanical redundancy.

By design, the SSRD has no torque retention capability within the unit except for a key on the spherical rod end. This posed a significant challenge on how the unit is preloaded. The spherical rod end within the unit needs to be held fixed in its orientation such that the friction critical surfaces between the rod end and spool halves are not damaged while preloading the unit. There were two potential solutions to this challenge. The first solution was to react the torque through the key in the rod end. The key is accessible through the SSRD housing but reacting a torque load equivalent to the 55.6-kN preload proved to be risky.

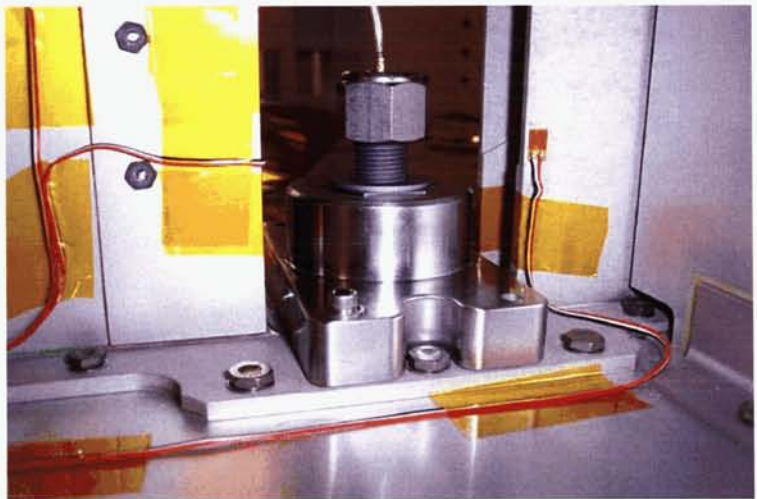


**Figure 4. SSRD Torque Retention Tool**

The second and chosen solution was a unique hardware design used in conjunction with a torque tool to react the torque through the bus structure and not the SSRD. The preload bolt has an external hex feature on the rod that interfaces with an internal hex feature on the spring retainer. The fit between these two component parts allows relative axial motion but both will rotate as an assembly. The spring retainer also has an external hex feature that allows a tool to be installed and bolted to the aft bulkhead of the spacecraft. This tool constrains the rotation of the spring retainer and preload bolt, but allows the bolt to stretch applying a preload. When torque is applied to the preload nut bearing against the spring retainer, the torque is reacted through the tool and onto the aft bulkhead of the spacecraft and not the SSRD.

A key feature of the SSRD is it is a mechanically redundant device. It achieves this redundancy because only one of the split spool halves needs to move laterally in order for the rod end to be released. However, this is only true as long as the rod end is not constrained from exiting the unit. In order to maintain mechanical redundancy at the system level, the retraction system needed to be designed such



that its functional motion did not inhibit the rod end from exiting the SSRD. Using the baseline designs of the Retraction System, SSRD, Booster Adapter Assembly, and Spacecraft Bus Structure an in depth analysis was done to determine if redundancy would be achieved at the system level. This analysis took into account tolerances on all components as well as utilizing conservative constraints within the system. The results of this analysis showed the baseline design would not work unless slight modifications were made to the SSRD, Retraction System, and Booster Adapter Assembly. All modifications were incorporated into their respective designs and redundancy testing with the Retraction System was successfully performed during SSRD component-level qualification testing.

### Test Challenges

In addition to design challenges there were several test challenges as well. These included minimizing the shock output from the retraction system as well as characterizing the shock output from the SSRD. During spacecraft separation, there are two distinct shock sources from the actuation of an SSRD. These are the shock output from the SSRD unit and the shock output from the Retraction System. The shock in an SSRD is caused by several components within the unit. These are the restraining wire unwinding, a spool valve hitting the inside of the housing, the rod end hitting the base washer as it exits, or a combination of these. The shock from the Retraction System is caused by the preload bolt hitting the top of the bolt catcher can. These two shock sources dictated a course of action: minimize the shock output from the Retraction System and characterize the shock output from the SSRD.

As described earlier, the Retraction System consists of a retraction spring that pulls the preload bolt and spherical rod end out of the SSRD. The spring force is sized to ensure retraction of the Preload Bolt and Spherical Rod End; however, this force also causes a sizeable impact of the Preload Bolt into the Bolt Catcher Can Cover. In order to minimize the impact and associated shock output, a shock absorbing material was incorporated into the Bolt Catcher Can design. A development test effort was undertaken to determine the type of material to be used as well as optimize the design. Initially, two candidate shock absorbing materials were considered: Poron and Aluminum Honeycomb. Preliminary test results showed the Poron to be a poor shock absorbing material; however, favorable results were shown for the aluminum honeycomb. The test setup consisted of a Bolt Catcher Can, Spring Retainer, Retraction Spring and a rod and nut of roughly the same mass as the flight designed hardware. The aluminum honeycomb test specimen was cut to the same inner diameter as the Bolt Catcher Can and placed inside the cover at the end of the can. The test specimen was a 2.5-cm nominal piece of aluminum honeycomb pre-crushed to a thickness of 2.22 cm. Tri-axial accelerometers were mounted at the base in two locations 90° apart and on top of the Bolt Catcher Can. Figure 5 shows the test setup.

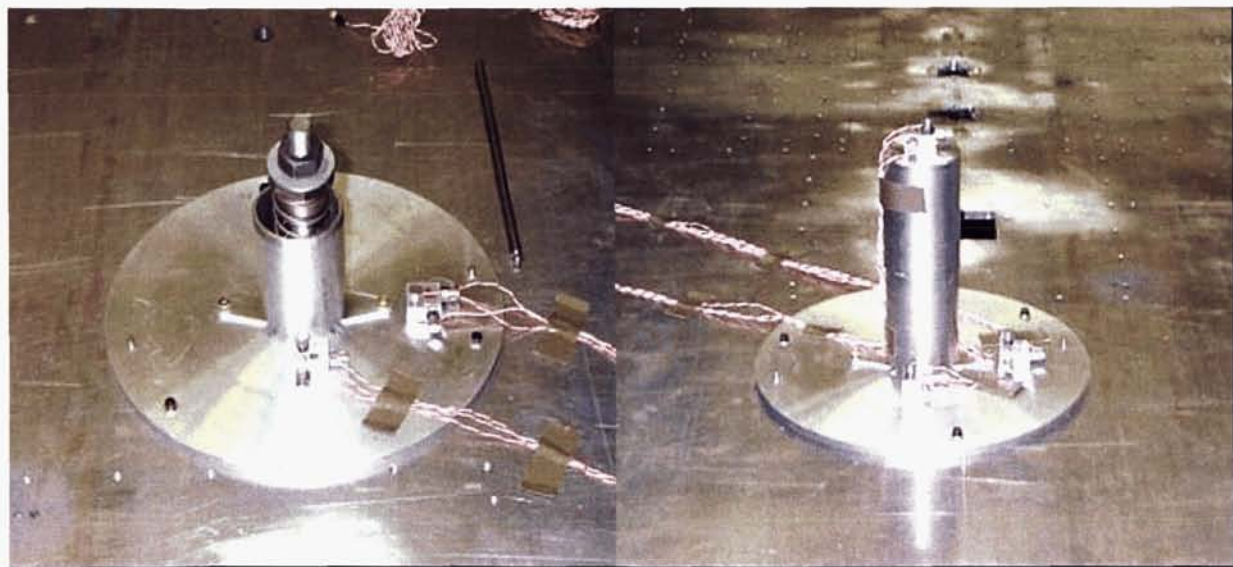


**Figure 5. Internal and External View of the Aluminum Honeycomb Shock Test**



Four configurations of the aluminum honeycomb were tested in order to find the configuration to minimize the shock output. Each honeycomb configuration went through two test runs and the data was evaluated. Table 2 lists the aluminum honeycomb configuration, and Table 3 lists the maximum shock levels at the three accelerometer locations, and crush depth in the honeycomb due to the rod of each configuration.

**Table 2. Aluminum Honeycomb Configuration**

Honeycomb Parameter	Honeycomb Configuration			
	-007	-013	-015	-017
Density (kg/m <sup>3</sup> )	16.0	32.0	110.5	104.0
Cell Size (mm)	9.53	4.76	4.76	9.53
Crush Strength (kPa)	172.4	482.6	3930	3516.3
Foil thickness (mm)	0.018	0.018	0.064	0.064

**Table 3. Aluminum Honeycomb Shock Data**

Data Information		Honeycomb Configuration				
		-007	-013	-015	-017	None
Run 1 (G's)	1X	167.631	27.025	1240.894	1233.103	622.312
	1Y	138.727	17.238	1465.170	1117.588	382.616
	1Z	233.268	29.820	2143.589	1270.930	516.098
	2X	170.565	18.846	1367.840	1238.719	516.545
	2Y	101.467	11.751	787.916	564.251	239.809
	2Z	257.538	23.989	1863.343	1664.746	431.611
	3X	410.757	289.466	1985.165	1739.393	1635.516
	3Y	1090.883	530.638	1321.610	1538.292	1915.143
	3Z	875.323	510.677	1476.057	2168.708	8648.191
Crush Depth (mm)		2.34	13.4	Full	3.23	N/A
Run 2 (G's)	1X	231.644	64.948	1214.254	1046.520	
	1Y	96.620	57.218	1192.590	976.103	
	1Z	174.474	84.268	1354.503	1047.692	
	2X	165.453	75.830	1415.292	1218.642	
	2Y	144.440	39.914	610.162	524.657	
	2Z	229.765	112.594	1880.607	1670.163	
	3X	167.832	474.099	2114.571	1060.538	
	3Y	126.101	390.583	2122.250	1352.893	
	3Z	357.979	726.983	2180.538	1950.895	
Crush Depth (mm)		Full	13.77	2.92	3.00	

The data collected during the development testing showed that the -013 configuration honeycomb had the best shock absorbing characteristics. This was based on data collected on Accelerometers 1 & 2 which were mounted at the base of the Bolt Catcher Can. As the data in Table 2 shows, the shock levels using the -013 configuration honeycomb are much lower than any of the other configurations for all test runs. Data collected at Accelerometer 3 was used for reference purposes but is also lower for the -013 configuration in all but one test run. It's interesting to point out that when compared to no honeycomb the levels significantly lower but the levels seen for the -015 and -017 configuration were higher. This was

possibly due to the honeycomb increasing the shock impact surface area. These two configurations had a significantly higher stiffness which lends some validity to the observation.

Another testing challenge occurred during the component qualification testing of the SSRD. Since this was the first time an SSRD was used in a discrete point booster separation system, the shock output of the unit needed to be characterized fully and extensive generated shock testing was performed. The test setup consisted of a 75-cm square aluminum plate that had a flight-like interface. The interface included a flight like cup-cone interface as well as the A-frame bracket. The SSRD was mounted to the A-frame bracket and the preload was applied through the center of the aluminum plate. The test was performed with the flight designed Retraction System and the crushable honeycomb shock absorber. Tri-axial accelerometers were used to collect data at locations 7.5 cm, 15 cm, and 30 cm from the center of the plate. Figure 6 shows the test setup for generated shock testing.

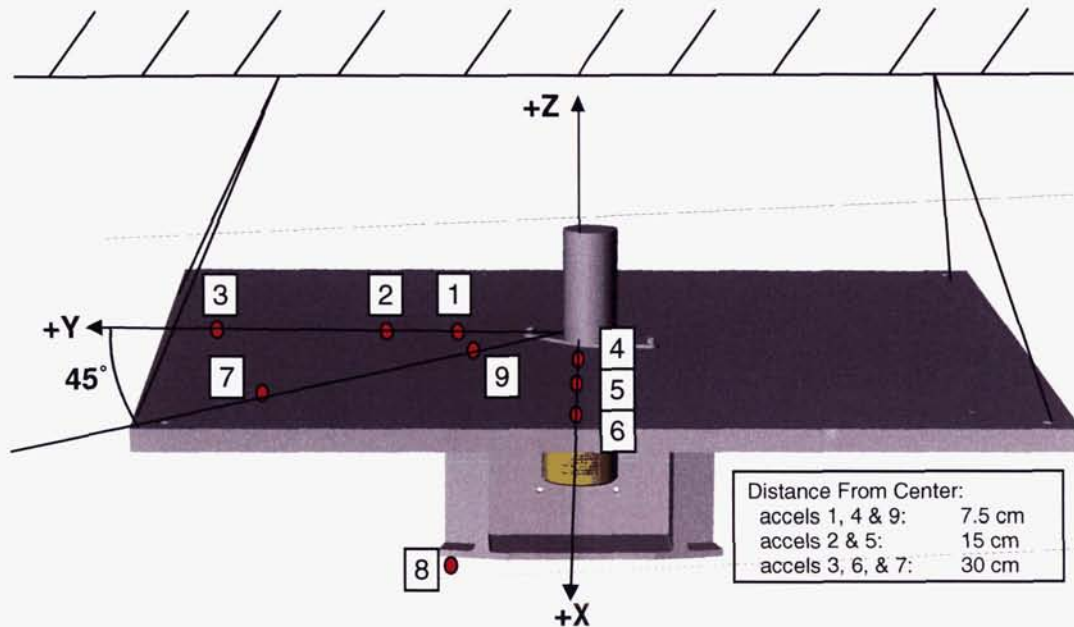


**Figure 6. Generated Shock Test Setup**

The design of the test setup was meant to mimic the exact flight configuration in the preload path; however, for conservatism, the large aluminum plate was incorporated to collect shock levels at varying locations and did not represent the flight honeycomb panel configuration. This created a major challenge during the component-level shock testing because configuration as well as accelerometer location had some bearing on the data.

In addition to the component-level generated shock tests, there was a system-level separation and shock test. The purpose of this test was to demonstrate the separation system and to measure the shock output of the system. The BAA was attached to the spacecraft with all the component parts of the separation system. The spacecraft bus was instrumented with 255 tri-axial accelerometers to measure the shock at various locations on the spacecraft bus. The entire assembly was suspended from an overhead crane for the separation test. The SSRD's were actuated in pairs that were diametrically opposed from each other. Upon actuation of the last pair, the BAA separated successfully from the spacecraft and fell into padding below the suspended spacecraft. Data collected during the three actuation events showed shock readings well within specified limits for the spacecraft.



## **Conclusions**

The Discrete Point Separation System was able to bring together a heritage component with a new low shock restraint device and successfully complete space flight qualification. There were many design and test challenges that needed to be overcome throughout the Qualification Program that show the difficulties of implementing a new component. However, understanding the components interaction and their impacts the design and test challenges are able to be overcome.

# Faying Surface Lubrication Effects on Nut Factors

Deneen M. Taylor<sup>\*</sup> and Raymond F. Morrison<sup>\*\*</sup>

## Abstract

Bolted joint analysis typically is performed using nut factors derived from textbooks and procedures from program requirement documents. Joint specific testing was performed for a critical International Space Station (ISS) joint. Test results indicate that for some configurations the nut factor may be significantly different than accepted textbook values. This paper presents results of joint specific testing to aid in determining if joint specific testing should be performed to insure required preloads are obtained.

## Introduction

During review of International Space Station analysis documentation and build paper it was discovered that one of the International Partners had overtorqued the installation bolts on the Common Berthing Mechanism (CBM) Ring on each of their elements. The build paper also raised questions concerning lubrication and whether or not it had been applied to the faying surfaces of the bolt head/washer in addition to the threads. The CBM is a mechanism built and qualified by Boeing and furnished to the other partners for use with the pressurized elements. Too high of a preload could overload the bolts when combined with on-orbit thermal and mechanical loads and potentially cause failure. Too low of a preload could cause the joint to gap and leak atmosphere overboard on orbit. Due to this out of configuration condition, it was decided that joint specific testing would be run to quantify the effects of the torque and lubrication.

## Background

The testing was implemented to determine the nut factor, K, of three different bolt materials, A286, MP35N and Inconel in combination with A286 helicoil inserts and nuts, with and without lubrication on faying surfaces. To remove any uncertainties of previous contamination to the bolts, all bolts were cleaned before testing. All bolts are about 6.3-mm (exactly ¼ inch) diameter. Countersunk CRES washers were placed under bolt heads and A286 passivated flat washers under the nuts. Helicoils and nuts came from the manufacturer with standard locking features and lubrication. Lubrication applied during testing to bolts was Braycote 815Z oil. The bolted material is anodized aluminum. The different permutations of the tests are shown in Table 1.

Although the objective of this testing was to verify that the higher torque did not yield the bolts and to obtain actual nut factors for these specific configurations, due to the numerous tests and various configurations some interesting trends became apparent. It is important to note that the lubrication was added between cycles not just for the first cycle, reflective of the flight hardware. In addition, the max/min nut factors cited are inclusive from all previous cycles, not just the max and min from the noted cycle.

---

<sup>\*</sup> NASA Johnson Space Center, Houston, TX

<sup>\*\*</sup> Boeing, Huntington Beach, CA

**Table 1. Permutations of tested bolt configurations**

Test	Bolt	Insert/nut	Lubrication	Tighten via	Samples	Cycles	Min K	Max K
Case 1-1	A286	Helicoil	Threads only	Bolt head	9	10	.18	.56
Case 1-2	A286	Helicoil	Threads and faying surfaces of bolt	Bolt head	10	10	.14	.18
Case 2-1	MP35N	Nut	Threads only	Nut	10	10	.08	.18
Case 2-2	MP35N	Nut	Threads only	Bolt head	10	10	.23	.49
Case 2-3	MP35N	Nut	Threads and faying surfaces of bolt	Bolt head	5	10	.10	.21
Case 3-1	Inconel 718	Nut	Threads and faying surfaces of nut	Bolt head	4	5	.13	.45
Case 3-2	Inconel 718	Nut	Threads and faying surfaces of nut	Nut	4	5	.12	.17
Case 4-1	Inconel 718	Helicoil	Threads and faying surfaces of bolt	Bolt head	5	5	.11	.14
Case 4-2	Inconel 718	Helicoil	Threads only	Bolt head	5	5	.21	.51

**Test Cases 1-1 and 1-2**

Test cases 1-1 and 1-2 compared the effects of lubrication on threads only with lubrication on threads and faying surface under bolt head for the A286 bolts. Both cases were tightened at the bolt head. Data indicates that for bolt/insert configurations, lubrication on the faying surfaces under the head of a bolt significantly reduces the maximum nut factor and the scatter (Figure 1). After 10 cycles, the faying-surface lubricated bolts had a  $K_{\max} = 0.18$  and  $K_{\min} = 0.14$ , whereas the threads-only lubricated bolts had a  $K_{\max} = 0.56$  and  $K_{\min} = 0.18$ . Without lubrication on faying surfaces, increasing bolt cycles also significantly increases nut factor. This is presumed to be because lack of lubrication on the faying surface induces wear under the washer, then additional cycles exacerbates the wear increasing the nut factor (Figure 2).

**Test Cases 2-1, 2-2 and 2-3**

Test cases 2-1 and 2-2 compare the affect of tightening the MP35N bolts via nut versus tightening via bolt head. Both cases had lubrication on the threads only. Bolt tightened tests were significantly higher. After 10 cycles, nut-tightened nut factors were  $K_{\max} = 0.18$  and  $K_{\min} = 0.08$ . Bolt-tightened nut factors were  $K_{\max} = 0.49$  and  $K_{\min} = 0.23$ . This is an increase of almost 75% (Figure 3).

Test cases 2-2 and 2-3 compared the affects of lubrication on threads only with lubrication on threads and faying surface under bolt head for the MP35N bolts. Both cases were tightened via bolt head. Data indicates that for bolts with lubrication applied only to the threads the nut factor will be much higher than for bolts with lubrication applied to the faying surfaces under the bolt head in addition to threads. After 10 cycles, the threads-only lubricated bolts had a  $K_{\max} = 0.49$  and  $K_{\min} = 0.23$  whereas the faying-surface lubricated bolts had a  $K_{\max} = 0.21$  and  $K_{\min} = 0.10$ . This is an increase of over 100% (Figure 4).

**Test Cases 3-1 and 3-2**

Test cases 3-1 and 3-2 are a comparison of tightening Inconel bolts via bolt head with tightening via nut. Both cases had lubrication added to threads and to the faying surfaces at the nut. The bolts tighten via bolt head had similar nut factors as those tightened via nut for the first cycle, but after just 2 cycles bolt-tightened cases had significantly higher maximum nut factors. Bolt-tightened cases produced nut factors of  $K_{\max} = 0.45$  and  $K_{\min} = 0.13$ . Nut-tightened cases produced  $K_{\max} = 0.17$  and  $K_{\min} = 0.12$  (Figure 5).

**Test Cases 4-1 and 4-2**

Test cases 4-1 and 4-2 compare the affects of lubrication on threads only with lubrication on threads and faying surface under bolt head for the Inconel bolts. Both cases were tightened via bolt head. The bolts that had lubrication both on threads and on faying surface under bolt head had lower nut factors than those bolts lubricated at threads only. After 5 cycles, the faying-surface lubricated bolts had a  $K_{\max} = 0.14$  and  $K_{\min} = 0.11$  whereas the threads-only lubricated bolts had a  $K_{\max} = 0.51$  and  $K_{\min} = 0.21$  (Figure 6).



A286 CRES Bolt, CRES helicoil, CRES countersunk washer

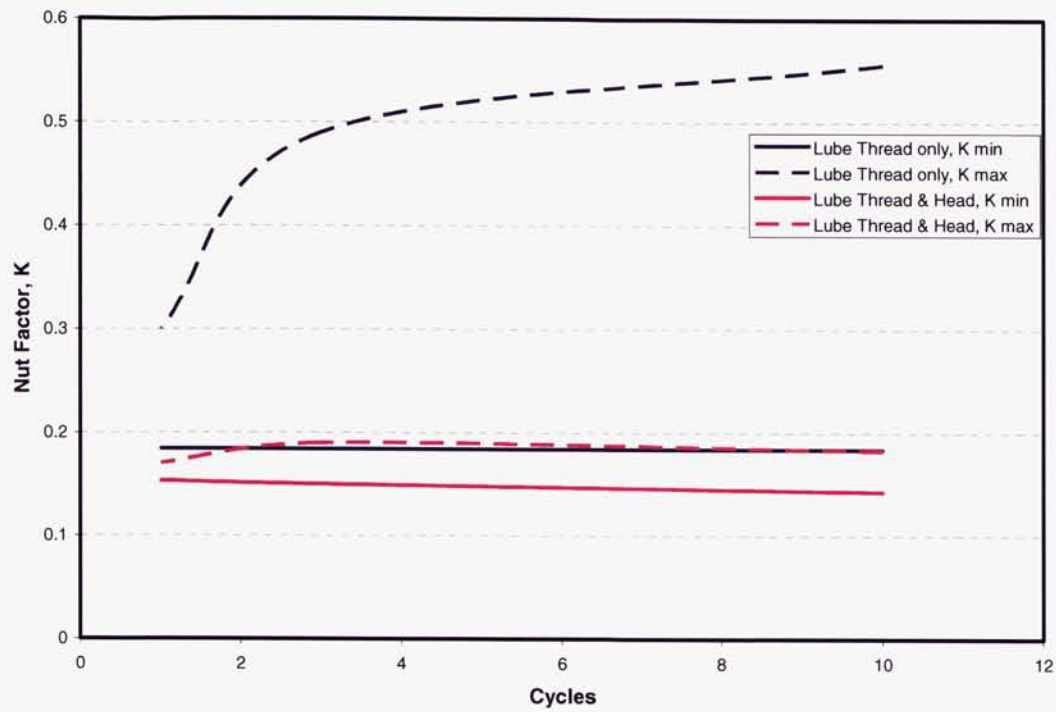


Figure 1. Comparison of test cases 1-1 and 1-2.

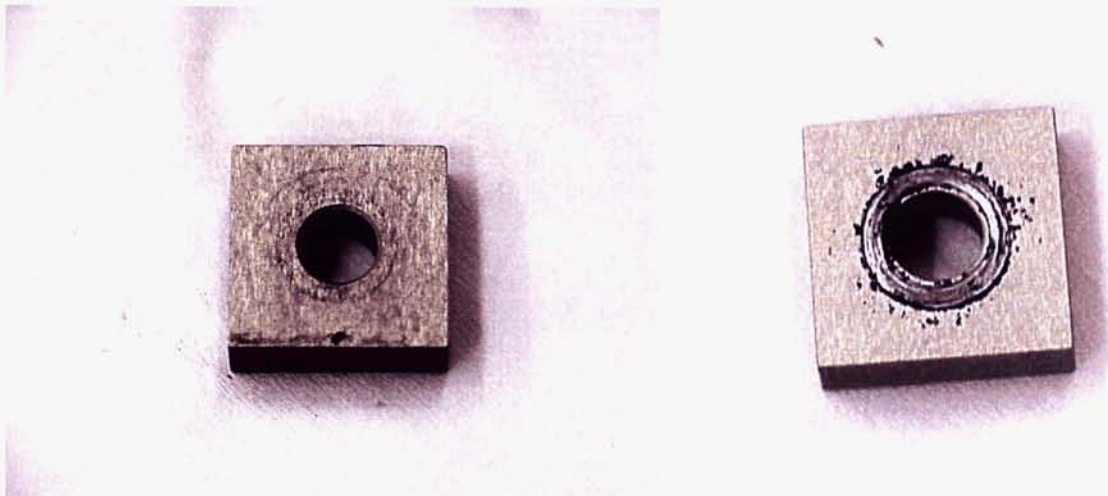
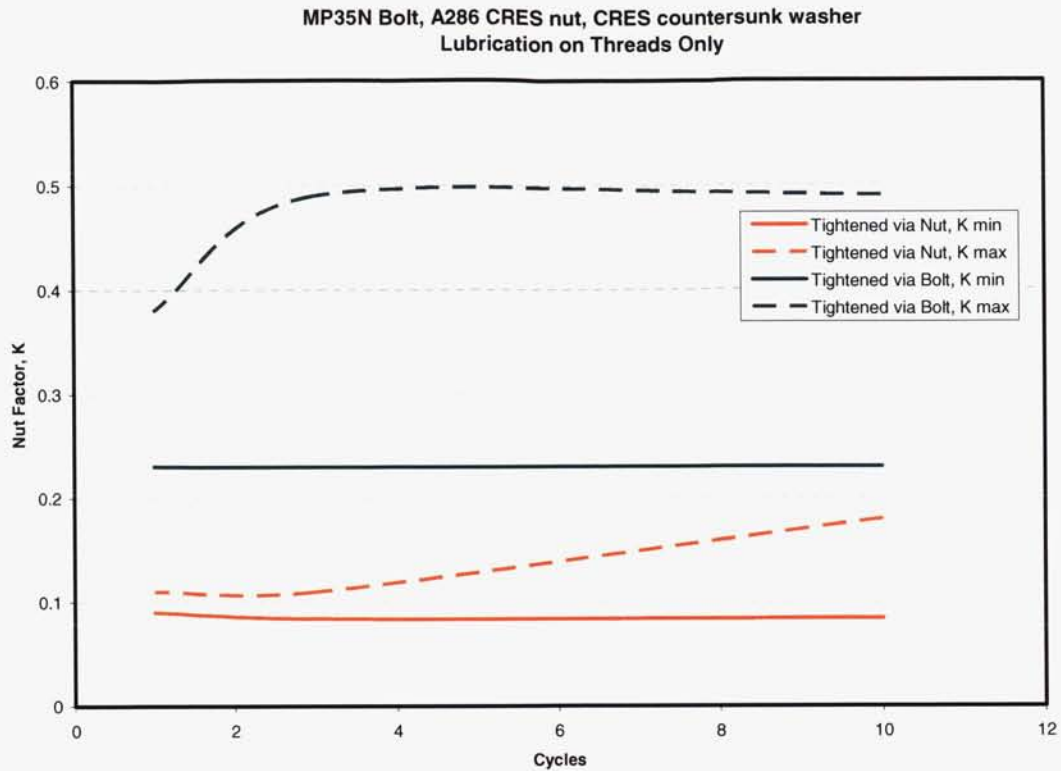
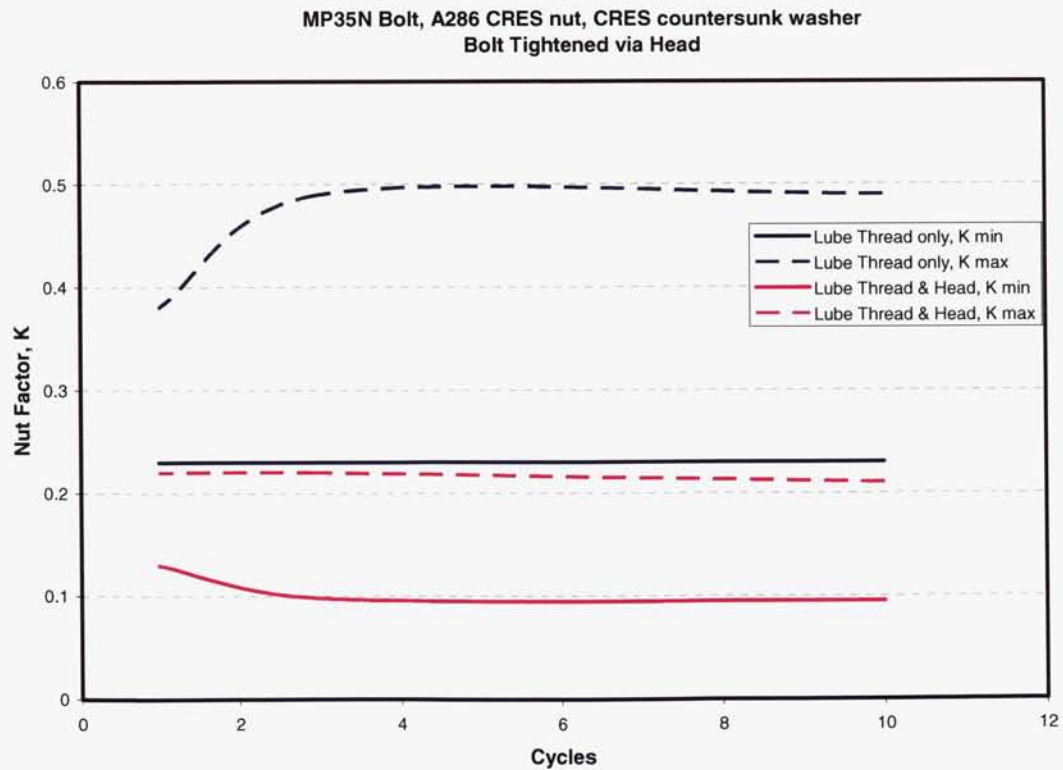


Figure 2. Photo on left from Test Case 1-1, max preload 15 kN (3400 lb)  
Photo on right from Test Case 1-2, max preload 8.0 kN (1800 lb)



**Figure 3. Comparison of test cases 2-1 and 2-2.**



**Figure 4. Comparison of test cases 2-2 and 2-3.**

Inconel 718 Bolt, A286 CRES nut, CRES countersunk washer  
 Lubrication on Threads and Faying Surfaces of Nut

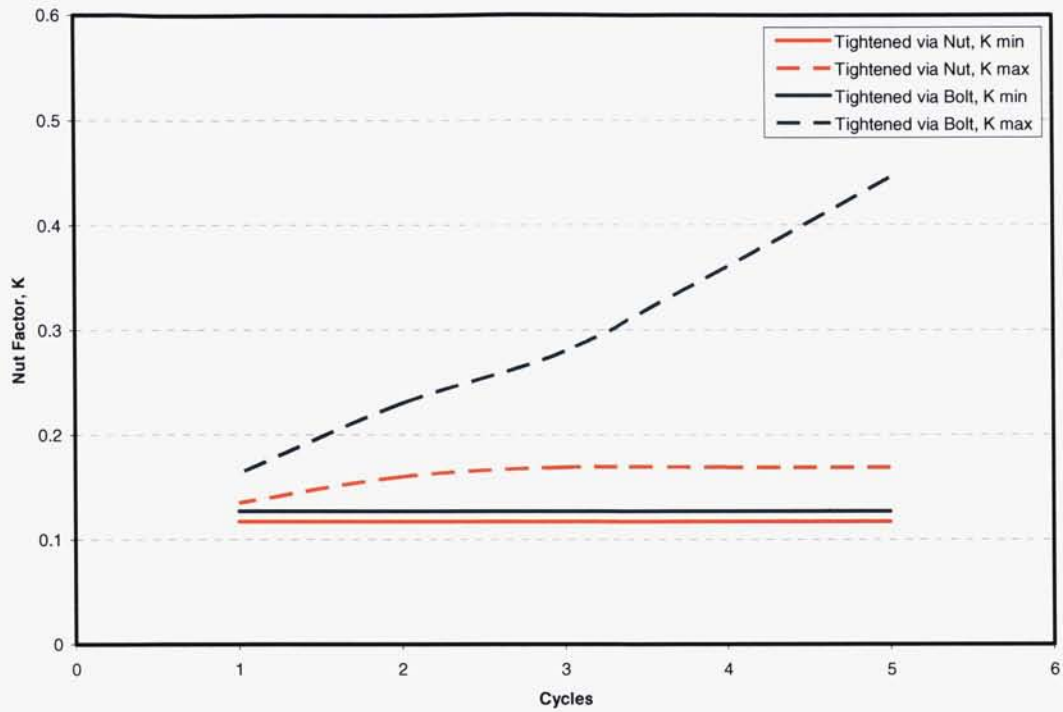


Figure 5. Comparison of test cases 3-1 and 3-2.

Inconel 718 Bolt, CRES helicoil, CRES countersunk washer

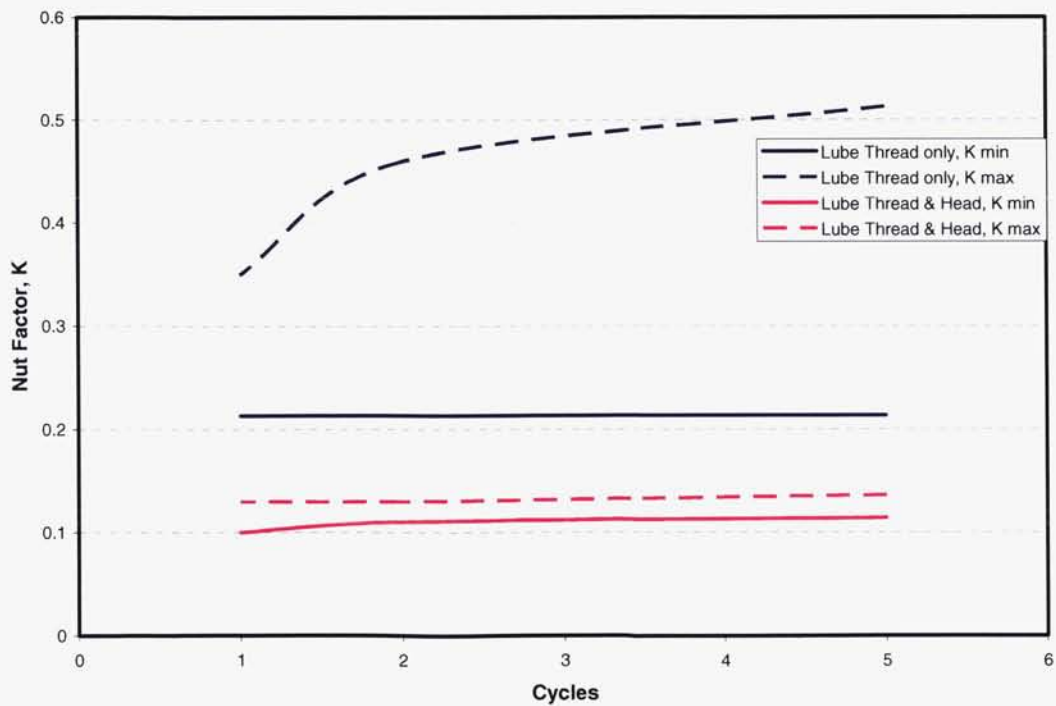


Figure 6. Comparison of test cases 4-1 and 4-2.



## Conclusion

In conclusion, bolts that were tightened via nut (test cases 2-1 and 3-2) produced similar nut factor ranges ( $K = 0.11$  to  $0.18$ ) as those typically found in literature for “lubricated” steel bolts ( $K = 0.12$  to  $0.20$ ) regardless if lubrication was added to the faying surface under the nut or not. In all published sources reviewed, if the term “lubricated” was defined it meant lubricated at the threads and “non-lubricated” would mean no lubrication was added to “as-received” condition, but bolts were not specially cleaned to remove any residuals from machining/processing. Of course, if lubrication is added to the threads it can very easily migrate to the nut faying surfaces hence explaining the similarity. However, for bolts tightened at the head, there are some significant differences. If lubrication exists on the faying surface of the bolt head (test case 1-2, 2-3 and 4-1), nut factor ranges typical for nut-tightening were produced ( $K = 0.10$  to  $0.21$ ), but if there was no lubrication on the faying surface of the bolt head (test cases 1-1, 2-2, 3-1 and 4-2), the nut factor ranges were significantly larger ( $K = 0.18 - 0.56$ ). It made little difference for the bolts tightened via head whether it was threaded into a nut or insert.

A fairly comprehensive literature search was performed to look for nut factor data on bolts tightened at the head or effects of additional faying surface lubrication. Nothing specific was found. However, one source had a very brief statement that acknowledged  $K$  values could be “up to 50% higher” for bolt head tightening [1]. It is very clear from this testing that general “text-book” nut factors values can not be assumed to be appropriate for non-lubricated faying surface bolts tightened at the bolt head.

Testing demonstrates that as early as the second cycle the nut factor increases significantly when tightened at the head without lubrication at the faying surface. This change in nut factor needs to be considered for reworking of a nonlubricated bolted joint or where a mix of installation cycles exists in a critical joint to maintain the desired preload.

Torque tension joint specific testing was not required for the majority of ISS Space Station hardware. Test results indicate that for future programs, testing should be considered for critical joints where it is not possible to apply lubrication at the faying surface.

## References

1. Engineering Sciences Data Unit “Applying, Measuring and Maintaining Pretension in Steel Bolts.” ESDU Item Number 86014, July 1986
2. National Aeronautics and Space Administrations. “Standard, Threaded Fasteners, Torque Limits for” MSFC-STD-486 Rev B, November 1992.
3. Gibson, James N. “Torque Tension Tests for the Common Berthing Mechanism (CBM), International Space Station” Boeing Report M&P-3-1638, June, 2005
4. Morrison, Raymond F. Analysis of CBM Bolts for Overtorque Condition” Boeing Report D684-12216-01, June 2005
5. Shigley, Joseph E., and Mischke, Charles R. (1996). *Standard Handbook of Machine Design*. 2<sup>nd</sup> ed. New York: McGraw-Hill.
6. Bickford, John H. (1995). *An Introduction to the Design and Behavior of Bolted Joints*. 3rd Rev ed. New York: Marcel Dekker.

# Torque Loss and Stress Relaxation in Constant Torque Springs

Robert W. Postma\*

## Abstract

Constant torque springs are manufactured from spring steel strip that in some applications is stressed beyond the yield strength to achieve maximum torque-to-weight ratio. An adverse consequence of a high state of stress is torque loss resulting from stress relaxation, which typically occurs over a prolonged period of time, accelerated by thermal cycles or continuous elevated temperatures. This poster paper discusses a case of torque loss resulting from thermal cycling of a spacecraft hinge spring manufactured from Type 301 corrosion resistant steel strip, cold worked to the extra hard condition.

The equations governing the design of the constant torque (Neg'ator®) spring are reviewed. Included is a discussion of ongoing work to better understand the design, manufacturing, and stress relieving of constant torque springs, particularly in regard to stress relaxation and delayed cracking from sustained high stress levels in aerospace environments.

## Introduction

Constant torque springs are sometimes stressed beyond the yield strength, by design, in order to obtain maximum torque-to-weight ratio. The springs are initially fabricated as a tightly wound coil of steel strip, and may have multiple laminates. The material is stress relieved, possibly before and after forming into the coil, at temperatures up to 425°C. When installed on the hinge, the spring is reverse flexed from the take-up spool onto the spool driving the output shaft (Figures 1 and 2).

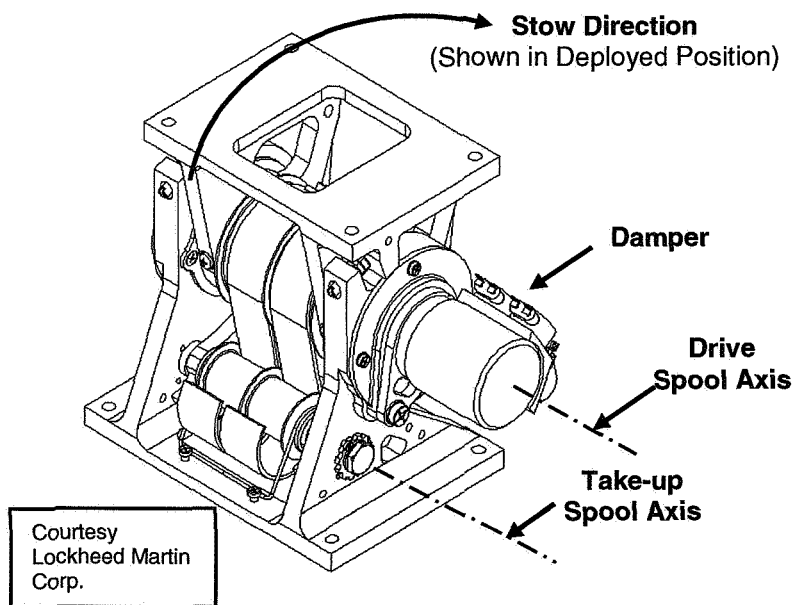


**Figure 1.**  
**Two Constant Torque Springs**  
**Installed in 90-degree Hinge**

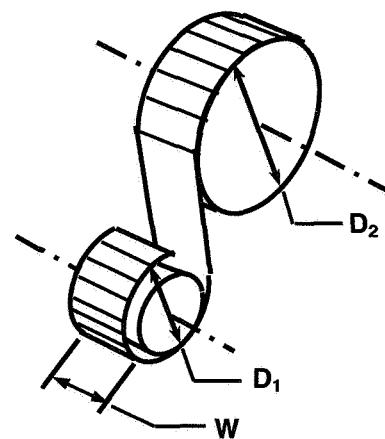


**Figure 2.**  
**Constant Torque Spring**  
**Critical Dimensions**

\* The Aerospace Corporation, El Segundo, CA

This work was initiated following loss of torque in spacecraft hinge mechanisms after a number of temperature cycles during thermal vacuum testing. The torque loss at the end of the deployment motion for one of the 180-degree hinges was 10 percent, as shown in Figure 3. (For a 90-degree hinge, as pictured in Figure 1, the torque loss was 7 percent). Note that the torque at the stowed position remains unaffected. Evidently, it is the slope of the deployment curve that is affected by the thermal cycling during this particular test. On tests of other hinges, however, the slope remained approximately the same, but the mean torque level decreased.

### Empirical Analysis of Torque Loss

After considering a number of other possible explanations, it was concluded that the 10 percent thermal cycling torque loss was due to stress relaxation. The most likely other explanation, increase in interlaminar friction, was eliminated by a special test using only one laminate. (The torque loss was about the same amount). Since stress relaxation is a function of time, temperature, and stress level, it can be further surmised that the 37°C elevated temperature portion of the thermal cycles, combined with high bending stress levels, are the primary factors contributing to the observed torque loss.

The Figure 3 data also shows  $\pm 7$  percent hysteresis and an initial negative slope of 15 percent of the maximum torque. It is also surmised (tentatively) that these adverse effects can be attributed in some measure to high bending stresses.

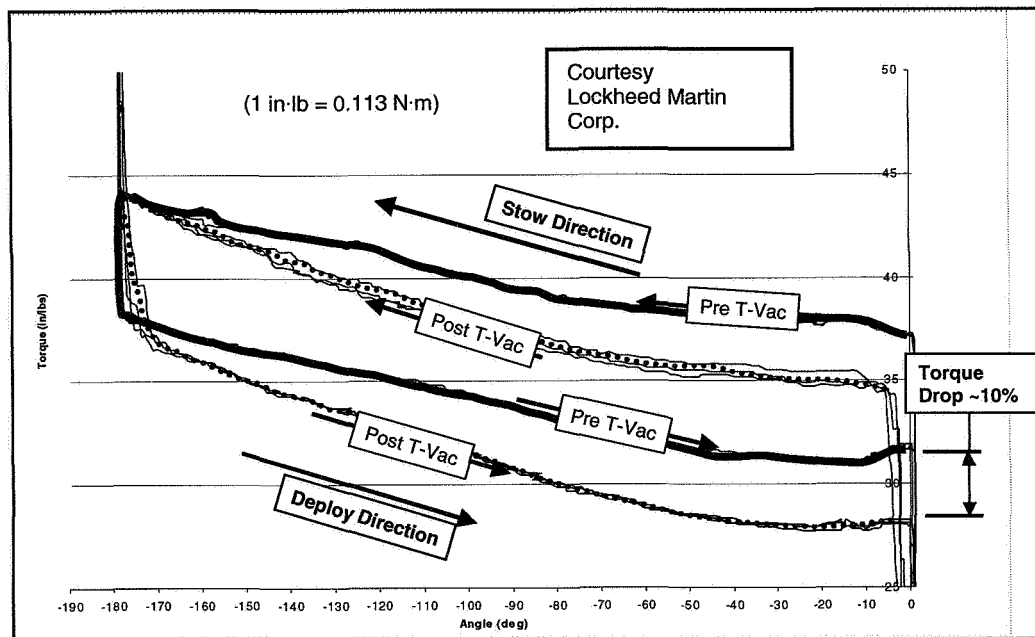


**Figure 3. Torque vs. Angle for 180-degree Hinge**

As the torque loss analysis proceeded, calculations were made that indicated that the springs were stressed beyond the yield strength (discussed in the following section). This conclusion is supported by examination of springs used for development testing, shown in Figure 4. Yielding of the spring stock from the high operating stress and strain levels after being reverse flexed is evident from observed distortion of the springs. The material is Type 301 corrosion-resistant steel, 0.0229-cm (9-mil) thick, cold worked to the extra hard condition (60 percent cold reduced). It is seen from Figure 4 that after being removed from the hinges, the springs are no longer in a tightly wound coil, but are expanded out of shape into a loose spiral. It can be concluded that being stressed beyond yield, combined with thermal cycling, contributes to stress relaxation and the associated reduction of torque.





Courtesy  
Lockheed Martin  
Corp.

**Figure 4. Springs Showing Various Degrees of Yielding**

To find out if performing multiple thermal cycles has resulted in the springs achieving a state of stress stability, a special test was performed where the torque output was measured after every three thermal cycles. It was found that the torque became essentially constant between 9 and 15 cycles at a level that still allowed sufficient torque margin. Additional thermal cycles are planned to confirm this.

### **Stress and Strain Analysis**

The practice of operating constant torque (Neg'ator®) springs at high stress, sometimes beyond yield, derives from general usage where the design stress level is based on low cycle fatigue requirements and the number of operational cycles. The invention of this type of spring is credited to Frank A. Votta Jr. In his technical paper<sup>1</sup>, he based the number of allowable cycles on a formula for (what he called) stress factor,  $f_s$ , shown here in Equation (1).

$$f_s = t \left( \frac{1}{D_1} + \frac{1}{D_2} \right) \quad (1)$$

$f_s$  = Stress Factor

$t$  = Spring Strip Thickness

$D_1$  = Fabricated Diameter (Fig.2)

$D_2$  = Drive Spool Diameter (Fig. 2)

This is identical in form to the usual formula from strength of materials for calculating bending strain in the outer fibers.

$$\epsilon_b = t \left( \frac{1}{D_1} + \frac{1}{D_2} \right) \quad (2)$$

$\epsilon_b$  = Bending Strain

The first term,  $t/D_1$ , is the bending strain from the change of curvature during the transition from the original coiled diameter  $D_1$  to the straight section between the coils. The second term,  $t/D_2$ , is the strain from further changing the curvature by reverse flexing the spring from the straight transition to the diameter of the drive spool  $D_2$ .

### **Stress vs. Strain Characteristics of Spring Steel Strip**

If one were to calculate the quasi-linear bending stress on the assumption that the modulus of elasticity in simple tension were constant and equal to the compression modulus, we would come to the impossible finding that the calculated bending stress would exceed the ultimate stress. The spring represented by Figure 3 has a calculated bending strain of 1.1 percent. Based on a modulus of elasticity of  $E = 193,000 \text{ MPa}$  (28,000,000 psi) and a Poisson's ratio of 0.3, the linear formula for bending stress

(Equation 3) would give a value of 2330 MPa (338,000 psi), which is well above the characteristic ultimate tensile strength of 1860 MPa (270,000 psi) for extra hard Type 301.

$$\sigma_b = \frac{\epsilon E}{(1 - \nu^2)} \quad (3)$$

$\sigma_b$  = Bending Stress (in Outer Fibers)

E = Modulus of Elasticity in Tension

$\nu$  = Poisson's Ratio

This formula represents the quasi-linear change in bending stress from the state of residual stress in the fabricated spring coil. (This method of calculating the bending stresses in a constant torque spring is summarily discussed in the Associated Spring Design Handbook<sup>2</sup>, which also cites Votta's paper). The spring manufacturer can intentionally pre-stress the spring in a process called strain hardening, to induce residual bending stresses of opposite sign, and thus reduce the stresses when the spring is installed on the hinge or spring motor. (It is tentatively believed that this was not done for the particular springs involved in this case of stress relaxation).

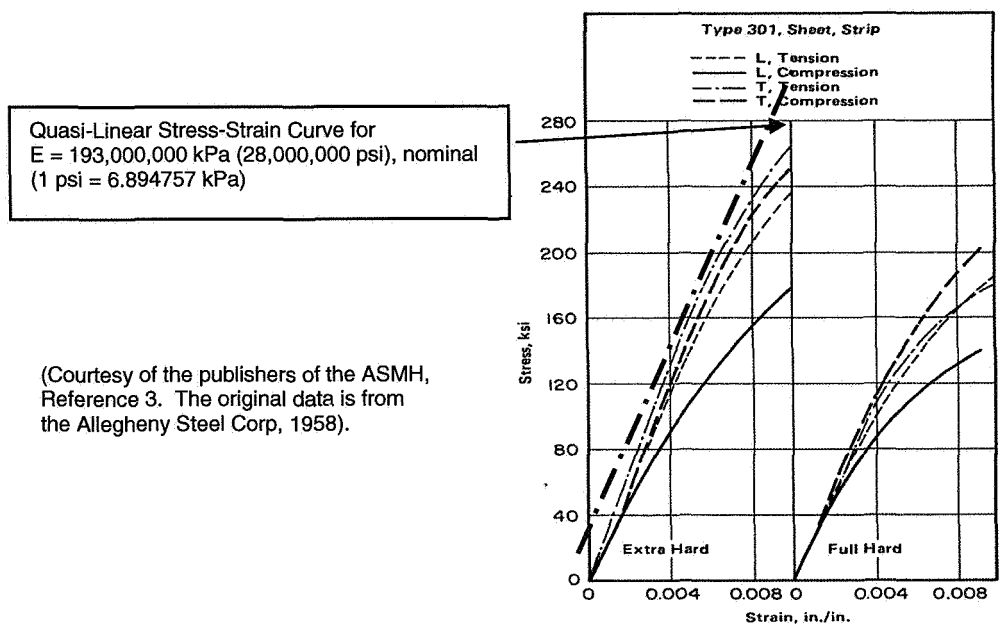


FIGURE 3.0212. STRESS-STRAIN CURVES FOR SHEET AND STRIP COLD ROLLED TO FULL-HARD AND EXTRA-HARD TEMPER (11)

**Figure 5. Stress/Strain Curves for Type 301, Extra Hard Condition**

Tensile and compression test curves for extra hard Type 301, from the Aerospace Structural Metals Handbook<sup>3</sup> (ASM), are shown in Figure 5. A hypothetical (quasi) linear curve is added to the graph. From comparison of calculated operating strains for constant torque springs with typical published tensile or compression test data (as shown in Figure 5), it can be concluded that the behavior of steel strip at high strain levels is different in bending compared to pure tension and compression. Type 301 extra hard shows higher values of elastic modulus in tension than in compression. The tensile and compression curves start to droop near peak values, such that the ultimate failure stress is less than would be predicted by the nominal assumption that the stress strain/curve is linear all the way to ultimate. Stress/strain curves published in the ASM for extra hard Type 301 typically terminate at 1.0 percent strain, (although some of the numerical data in the ASM state elongation to failure greater than 1.0 percent).

Another example that infers greater elongation to failure in bending compared to simple tension is the required bending test for a slightly less cold worked material, Type 301 full hard. (Stress/strain curves for

Type 301 full hard are also shown in Figure 5). Type 301 full hard is required by MIL-HDBK-5F<sup>4</sup> to be capable of being bent around a rod of diameter six times the thickness of the spring material, without the occurrence of surface cracking. Using Equation 2, the average bending strain calculated for 0.0254-cm (10-mil) thick strip bent around a 0.1524-cm (60-mil) diameter rod (neutral surface assumed at the 0.1778-cm (70-mil) mean diameter) is 14.3 percent, compared to the MIL-HDBK-5F requirement for minimum elongation to failure in simple tension of 8 percent. No similar bending requirement is given for the extra hard Type 301, as this level of cold work is not controlled by MIL-HDBK-5 or by ASTM specifications. Accordingly, it is prudent for the end user to provide specifications for the extra hard version, rather than rely entirely on the spring vendor's judgment and practice.

For a limited number of cycles at ambient temperature, strains beyond the yield strength (based on 0.2 percent offset) can be tolerated without failure. From a graph in Votta's paper, his recommended allowable stress factor (strain) for less than 5000 cycles is 2.0 percent, for what he calls "safe design", using 1095 carbon steel. In the Associated Spring Design Handbook<sup>2</sup>, a graph is presented showing an "allowable" (quasi-linear) stress of 2,760 MPa (400,000 psi) for fewer than 260 cycles. In actual practice, however, the design of constant torque springs is based on empirical data, rather than Votta's formulas. In a couple of other major spring manufactures' design guides, Type 301 is rated at up to 2000 cycles for strains above 1.0 percent or greater. (Typically 50 to 100 cycles are considered adequate for life testing of deployables that only operate once in orbit, plus the cycles needed during manufacture and testing).

Normally, one would not be concerned over delayed cracking in typical spacecraft storage environments. However, for springs stowed at stress levels beyond yield over prolonged periods, this aspect merits some consideration. Type 301 is on the list of materials considered to be resistant to stress corrosion cracking; however, when cold reduced to the full hard or extra hard state, a phase transformation from austenite to martensite occurs, which would logically obviate a totally exempt status. Looking into this further, the storage atmosphere is typically at controlled humidity, and at the launch site the spacecraft is usually in an air-conditioned payload housing. One reference, by Phelps and Loginow<sup>5</sup>, cites an exposure test to atmospheric corrosion at Kure Beach, N.C. of Type 301, 60 percent cold reduced, for periods of 240 to 370 days, during which the test specimens showed "excellent resistance to stress corrosion". However, these specimens were only stressed to 75 percent of the stated yield strength of 1640 MPa (238,000 psi). Data for springs stressed beyond yield, sustained over typical aerospace storage periods of five years, has not been located. On the other hand, neither has breakage of this type of spring been reported, due to delayed cracking (or for any other reason) in aerospace usage.

### Torque Determination

In Votta's technical paper, he gives a formula for calculating the torque on a constant torque spring motor. The formula currently derived (Equation 4), based on strain energy, is almost the same as Votta's except for the factor in the denominator involving Poisson's ratio.

$$T = \frac{EWD_2t^3}{12(1-\nu^2)} \left( \frac{1}{D_1} + \frac{1}{D_2} \right)^2 \quad (4)$$

T = Torque

W = Width (Figure 2)

This factor also appears in the quasi-linear stress formula, Eqn. 3, and is conventionally used to adapt the standard handbook formulas for beam bending of exceptionally wide beams. It results from an elastic state called "plain strain", which is applicable to a thin, wide beam (strip) in bending. (An interesting comment from A. M. Wahl, a noted authority in spring design of that era, was published in the "Discussion" portion of Votta's paper. Wahl stated that this factor should have been present in Votta's formula. Votta's response was that their test data showed that this factor did not apply because of energy lost in transverse [anticlastic] curvature of the straight length of spring between the two spools.)

Equation 4 implies that the torque should be constant with angular displacement. However, as seen from Figure 3, there is a fairly linear, negative slope to the deployment curve. It is surmised that stresses beyond yield contribute to the magnitude of the negative slope. Hysteresis is another component of



torque loss that adds to the total loss. From tests with single laminates it was found that interlaminar friction is not a significant cause of the hysteresis. (The single laminate has approximately the same hysteresis as multiple laminates). As of now, it is not known how much of the hysteresis is internal to the material from stress related yielding of the spring stock, and how much is due to bearing friction.

One broad objective is to better understand why the physics (applied mechanics) behind the theoretical formula for torque (Equation 4) does not account for the downward slope of the torque vs. deflection curves. This will assist in design optimization of the relationships between the variables affecting torque and torque loss. It may be that optimum design would be achieved at lower stress levels, by reduced laminate thickness and increased number of laminates. It is desirable to minimize this decreasing torque slope, because the maximum torque is usually needed at the end of deployment to actuate end-of-travel latches or wind-up cable bundles.

### **Conclusions and Recommendations**

This poster paper has discussed how general practice for the design and manufacturing of constant torque springs using empirical design data provides springs that may be stressed beyond the yield strength. Typically, highly stressed springs are subject to stress relaxation and related torque loss under prolonged load and elevated temperature conditions.

It appears that torque loss due to thermal cycling, for the springs cited herein, had achieved a state of stability, in that the torque output of the unwound spring actuated hinges was not continuing to decrease with each successive cycle. Additional cycles are expected to confirm this. It also remains to be determined whether maintaining stresses above the yield strength over periods of prolonged storage in aerospace environments can be done without excessive loss of torque from stress relaxation and without loss of immunity to delayed cracking.

The final outcome from this work will likely be that Type 301 extra hard corrosion resistant steel will continue to be an optimum material for one-time operation in space of constant torque spring actuated hinges. Particularly for the extra hard condition, which is not controlled by ASTM or military specifications, the end user and spring manufacturer should be mutually cognizant of spring material requirements, such as yield and ultimate strength and ductility, and stress relieving and pre-stressing procedures.

### **Acknowledgments**

This work has been conducted interactively with the Lockheed Martin Corporation, Sunnyvale CA. The Lockheed Martin portion of the investigation is under the cognizance of Stuart Loewenthal. The hinge drawing (Figure 1), test data (Figure 3), and sample springs (Figure 4), were provided by Lance Lininger, courtesy of Lockheed Martin. Usage of the single figure from Reference 2 has been verbally approved by telephone discussion with the publisher, Purdue University.

### **References**

1. "The Theory and Design of Long-Deflection Constant-Force Springs", F. A. Votta, Jr., ASME Paper No. 51-F-11, June 11, 1951.
  2. Design Handbook, Engineering Guide to Spring Design, Associated Spring, Barnes Group Inc., 1987 Edition.
  3. Aerospace Structural Metals Handbook, 39th Edition, Vol. 2; Code 1301, Original Code 1301 Author – W. D. Kloop, March 1988; Published and Updated by Purdue University.
  4. Metallic Materials and Elements for Aerospace Vehicle Structures, MIL-HDBK-5F, DOD, Nov. 1, 1990.
- "Stress Corrosion of Steels for Aircraft and Missiles", E. H. Phelps, and A. W. Loginow, Feb. 3, 1960, 16<sup>th</sup> Annual Conference of Corrosion Engineers, March 14-18, 1960.

# Mechanical Design of a Multi-Axis Martian Seismometer

Franck Pécal\*, Nicolas Paulin\*, Doug Mimoun\*\* and Gabriel Pont†

## Abstract

A planetary seismometer intended to fly onboard future missions to Mars has been developed by SODERN as the industrial partner of IPGP and CNES. This seismometer is a Very Broad Band seismometer (VBB). Its main purpose is to measure the Martian seismic activity. It is included in the Geophysical Package of the ESA ExoMars mission (to be launched in 2011).

This paper describes the mechanical architecture of the seismometer and identifies the main challenges that were overcome. In particular, the paper points out how SODERN managed the requirements for the extremely high sensitivity of the seismometer and coped with the very low size and mass budgets together with the very harsh mechanical and thermal environments specific to Martian missions (especially very low temperatures and severe shock when landing).

The lessons learned from the full test program results are presented.

## Introduction

Since 1992, EADS SODERN has been the industrial partner of IPGP (Institut de Physique du Globe - Paris) and CNES (Center National d'Etudes Spatiales) for the development and the industrialization of planetary seismometers. Following the launch failure of the Mars 96 mission and the subsequent loss of the seismometer "OPTIMISM", in 2002 CNES and IPGP selected SODERN as their partner in the development of a new multi-axes seismometer.

This seismometer is a Very Broad Band seismometer (~0 to 20 Hz). It is intended to measure the Martian seismic activity in a network of seismometers. It was initially developed for the joint CNES/NASA "NetLander" mission. Although this mission was stopped in 2003, development went on until the end of the B phase (preliminary design). The VBB is now part of the geophysical package instrument suite of the ESA Exomars mission, to be launched in 2011.

The aims of this B phase were to demonstrate:

- The seismometer detection performance with a Breadboard model
- The mechanical robustness and stability under thermal and mechanical environments with a Structural and Thermal Model (STM)
- The compliance of the definition of a future Flight model with regard to the main requirements for the Martian missions

The VBB is currently the only planetary seismometer available for a launch towards Mars in 2011. Its characteristics make it compatible with Mars, Moon and Mercury environments. With some modifications, it may be compatible with the "telluric" satellites of the outer planets such as Europa and Titan.

---

\* EADS SODERN, Limeil Brévannes, France

\*\* IPGP, Saint Maur, France

† CNES, Toulouse, France

## General Description

### Principle

The seismometer is based on the principle of an inverted pendulum with an angle of  $35.25^\circ$  wrt vertical axis (Figure 1). This kind of configuration gives a high sensitivity for a low mass and reduced volume. It also allows detection in the horizontal and vertical directions with the same sensor. The pendulum equilibrium is realized when the leaf spring moment balances the gravity moment.

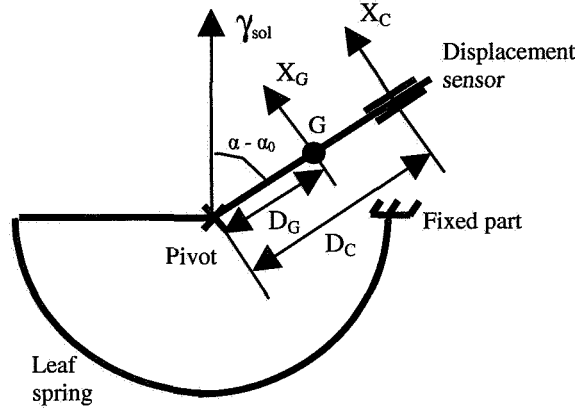


Figure 1. Seismometer model

The leaf spring transmits the movement to the mobile mass when a quake occurs. The mobile mass vibrates and oscillates around the axis of the pivot. The position of the center of gravity is governed by Eq. (1):

$$(1) \quad J \frac{d^2 \alpha}{dt^2} + \beta \frac{d\alpha}{dt} + k(\alpha - \alpha_0) = -mgD_g \sin(\alpha - \alpha_0) + mD_g \gamma_{sol}$$

with:

$\alpha$ : angular position of mobile part  
 $J$ : moment of inertia of the mobile part  
 $\beta$ : coefficient of viscous friction  
 $k$ : stiffness of the assembly pivot-spring  
 $m$ : mass of the mobile part  
 $g$ : gravity

The transfer function between the displacement of the mobile part  $X_c$  and ground acceleration  $\gamma_{sol}$  follows Eq. (2):

$$(2) \quad FT(p) = \frac{X_c(p)}{\gamma_{sol}(p)} = - \frac{G_{mec}}{1 + \frac{1}{Q \cdot \omega_0} \cdot p + \frac{1}{\omega_0^2} \cdot p^2}$$

with:

$$\omega_0^2 = \frac{k - mgD_g \cos(\alpha)}{J} \quad Q = \frac{\omega_0^2 \cdot J}{\beta}$$

$$G_{mec} = \frac{mD_g D_c}{J \cdot \omega_0^2}$$

The displacement of the mobile part is measured by two sensors: a short term sensor called DCS (Differential Capacity Sensor) and a long term sensor called OCS (Oscillating Cavity Sensor).



A feed-back system, based on a magnetic coil actuator, is used to control the mobile part position and set it at the equilibrium position. A closed-loop system is necessary to widen the measurement bandwidth of the system and to give a representative output voltage of the ground acceleration. Another digital feedback loop is used to compensate for the long term and daily thermal effects.

The principle of the seismometer is illustrated by the diagram block Figure 2:

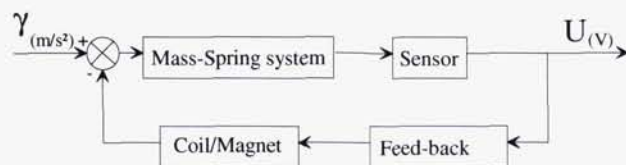


**Figure 2. Block Diagram of the VBB seismometer**

### VBB sensor

The Breadboard model of the Very Broad Band sensor developed during the R&D program is described in Figure 3.

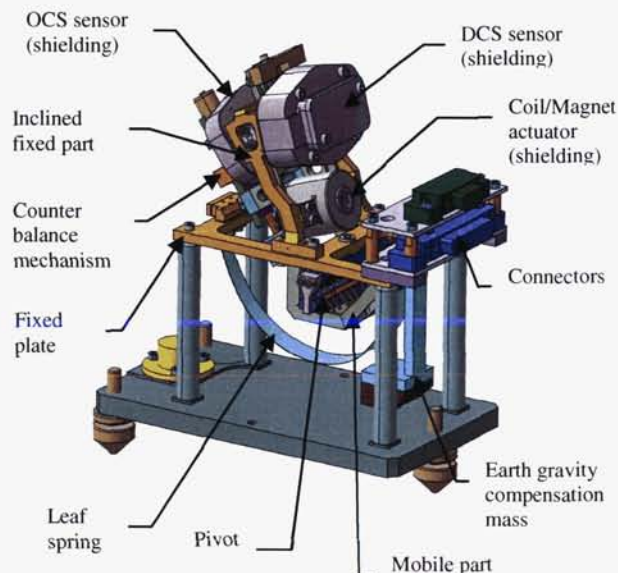


**Figure 3. Breadboard model of the VBB sensor**

In addition to the main parts of the seismometer, two other components are essential to operate the seismometer. A counter balance mechanism is used to adjust the equilibrium position of the mobile part. This adjustment is necessary according to the uncertainty of the local Martian gravity or the drift due to the thermal sensitivity. An additional mass is also used to balance the VBB sensor, designed for Mars gravity, during Earth testing.

Except the design of the housing structure, this breadboard model is very close to the flight model.

### Sphere

“Sphere” is the name given to the seismic sensor part of the multi-axes Martian seismometer. The sphere, in flight model configuration, consists of the following components:

- 2 VBB seismometers in opposite sensing directions
- Inclinator, vacuum sensor, thermal sensors
- Getters
- Flex-rigid cables and feed-through
- Inner plate with insulating blocks
- Radiative screen
- Spherical covers
- Structural ring (diameter of about 140 mm)
- Sealing pipe

Vacuum is set in the sphere in order to reduce the viscous damping and the buoyancy (Archimède thrust) on the mobile part. Figure 4 presents an overview of the flight model of the sphere, without the upper cover.

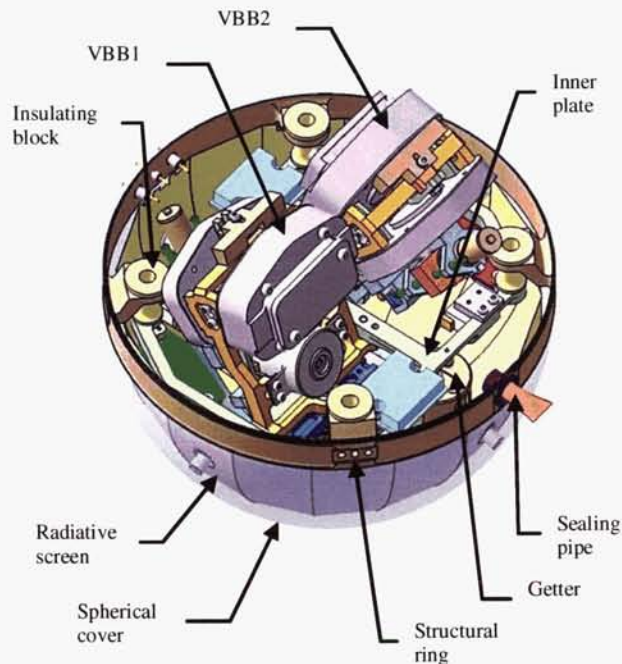


**Figure 4. Flight model of the Sphere**

The breadboard model of the sphere offers the same functions as the flight model. The breadboard sphere, intended to test on the Earth ground, is composed of the breadboard models of the VBB sensor. Consequently, the breadboard sphere volume and mechanical interfaces are a little bigger. There is no radiative screen on this model.



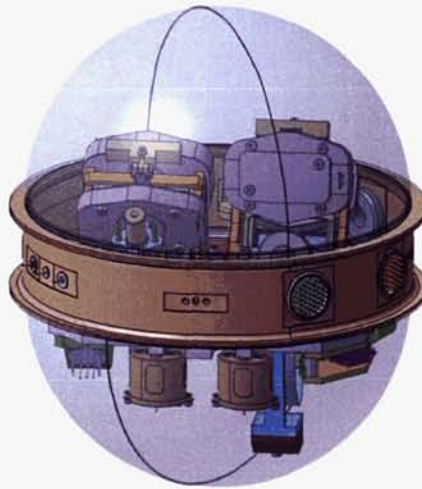


**Figure 5. Breadboard model of the Sphere**

### **Technical Challenges Overcome**

#### Struggling for a low mass

The total mass allocated to the Martian seismometer, including sphere, installation device and electronics, is 2.4 kg. The mass budget allocated to the sphere is only 540 g.

At the end of this Phase B, we managed to get very close to the mass budget with 570 g, which almost ensures matching the specification mass in a phase C. It is the result of a trade-off between seismic performance, mechanical resistance and thermal sensitivity. Huge efforts were made to miniaturize all functions and match with the mass specification while matching at the same time with the necessary robustness.

#### Low mass vs. seismic performance

Theoretically, the bigger the mobile part mass is, the better the seismological performance is for an open-loop seismometer (the sensitivity of a seismometer varies with  $m/k$ , with  $m$  the mass and  $k$  the stiffness). For example, the seismometer STS2 which is the current reference on Earth weighs 11 kg. The use of a feed-back loop on the mobile part position is a way to reduce its mass. Concerning the fixed part, some rather heavy but, unfortunately compulsory components – the getter and the shielding for instance – makes the “fight” for a low mass even more challenging.

#### Low mass vs. mechanical resilience

As an other big issue with regard to a low mass, the structural part has to be stiff enough to not interfere with the oscillations of the ground and resistant enough to withstand the landing on Mars. The mass of the structural part has been reduced by calculations on a finite element model and especially thanks to the use of stuck glued and welded assemblies (instead of bolts and screws).

#### Low mass vs. thermal sensitivity

Finally, concerning the materials, the choice was led by the thermal sensitivity and the need of vacuum. Titanium (TA6V or T40) was selected for all the parts participating in the oscillations measures (ring, plate, fixed part and mobile part) except for the insulating blocks. Titanium is of course an additional difficulty with regard to the low mass objective.

For the covers, an alternative to the titanium was explored. With a composite material in carbon covered with a metal deposit, the mass of the covers can be reduced by 40% (35 g). Unfortunately the current technologies of deposit on composite materials do not guarantee a sufficient level of



tightness for the vacuum desired inside the sphere. Consequently the covers are made of titanium (T40) by hydroshaping with a 0.3-mm thickness only. This thickness represents the very limit of this kind of technology. The mass of the DCS and OCS shielding has been optimized by the use of aluminium with a 0.4-mm thickness.

#### High thermal insulation from Mars environment

The thermal environment on Mars is very tough. The minimum temperature can be as low as  $-120^{\circ}\text{C}$  in the polar region and the daily amplitude is about  $110^{\circ}\text{C}$ . This environment imposes a very high thermal insulation to allow the operation of the electronics and to reduce the thermal sensitivity of the sensors. A thermal regulation inside the sphere is not possible because of the perturbations it would cause on the seismic signal.

The internal insulation of the sphere has been reached by a drastic reduction of the conductive and radiative heat transfer. In fact, there are mainly three thermal paths between the inside and the outside of the sphere.

The first thermal path is the conduction through the structure. Although the titanium TA6V has a rather low conductivity, it is not sufficient. The high thermal resistance expected has been raised up thanks to four insulating blocks in Torlon<sup>TM</sup> (composite material with short fibers). This assembly (Figure 6) gives a huge thermal resistance of about 2000 K/W. Such value also requires that the block be fixed by an adhesive joint on the structural ring.

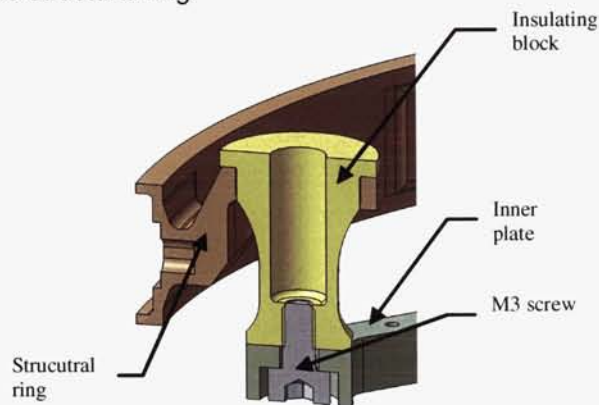


**Figure 6. Insulating block assembly**

The second thermal path is the conduction through the internal harness. Indeed, many electrical signals have to be shielded and these shields constitute a real thermal path. The thermal resistance on this path has been increased thanks to the use of flex-rigid cables. Also interesting for the integration, this solution allows an optimal section of the wires and especially the thermal insulation of the electronic shielding. The electrical connection of the shielding is made in a very local way with a thin track.

Finally, the third main thermal path is the radiative exchange with the covers. This exchange was reduced by the set-up of radiative screens and by the use of a gold coating. The 2 radiative screens (upper and lower) are made from a sheet of titanium of only  $50\text{ }\mu\text{m}$  in thickness. Then, this sheet is shaped and welded by point to recreate the spherical shape of the covers. This part cannot be obtained by machining or hydroshaping. Little insulating blocks in Torlon<sup>TM</sup> are also used for the screen assembly (Figure 7). They are stuck on both sides on the covers and the screen.

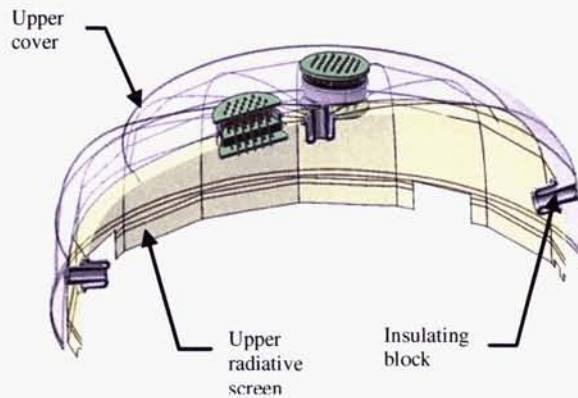


**Figure 7. Upper radiative screen assembly**

#### Withstanding the shock when landing

When the surface module that contains the seismometer, lands on Mars a very violent shock is generated. This shock, equivalent to a half-sine 200 g – 20 ms, is relatively long and thus very energetic. The seismometer resistance to this shock is a real challenge for all the subassemblies but especially for the mobile part because of the absence of a locking mechanism. The power and mass budgets do not allow using any locking devices.

Good performance was obtained by stiffening the structure and by placing mechanical final stops. Much work was carried out on the pivot because it is the most sensitive element as far as mechanical requirements. The pivot Figure 8 is based on a flexible blades assembly. The flexible blades are stuck on two rigid parts (fixed and mobile part). Consequently, the pivot supports all the loads of the mobile part and permits only a limited movement.

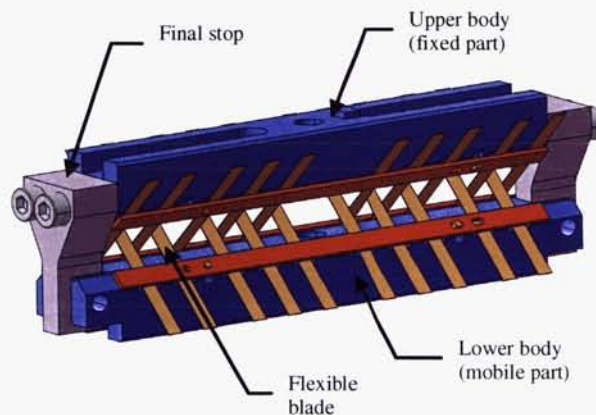


**Figure 8. Pivot 20 blades**

In order to have acceptable stresses in blades, mechanical final stop are designed to limit the deformation of the blades at  $\pm 50 \mu\text{m}$ .



### Thermal sensitivity avoidance

Because of the great amplitude of temperature and the small stroke of the mobile part (200  $\mu\text{m}$ ), the VBB sensor has to be insensitive as possible to temperature variations. Our requirement is a mobile part displacement of 2  $\mu\text{m}$  for a temperature variation of 1°C (measured at the DCS level).

To reach this very critical requirement, material homogeneity is essential in order to avoid any shift of the center of gravity of the mobile part. All structural parts of the VBB sensor are titanium TA6V. However, this is not enough and the use of a very specific material for the leaf spring, the THERMELAST, is necessary. The advantage of this material is the possibility to adjust the thermoelasticity coefficient  $\beta$  (Eq. (3)) with an appropriate heat treatment.

$$(3) \quad \beta = \frac{1}{E} \cdot \frac{\Delta E}{\Delta T}$$

with:

$E$ : Young modulus

$T$ : temperature

For the THERMELAST,  $\beta$  values can be adjusted in the  $\pm 16 \cdot 10^{-6} \text{ K}^{-1}$  range. For example, when the temperature is cold (lower than the integration temperature), the dilatation makes the distance to the center of gravity smaller and pulls the mobile part upward. If the leaf spring is less rigid when the temperature is cold ( $\beta > 0$ ), a moment balancing can be found.

### Obtaining and keeping vacuum

To reduce the viscous damping and the buoyancy (Archimède thrust) on the mobile part of the seismometer, vacuum is necessary inside the sphere. The vacuum level at the end of the nominal mission (2 years) must be less than  $10^{-2}$  mbar. This requirement imposes a sealed volume, a very low outgassing for the materials placed inside the sphere, and a passive pumping after the sphere sealing. The tightness is obtained by laser welding for the covers and by brazing for the feed-throughs and sealing pipe assemblies. The sealing pipe (copper tube) is used for the pumping and the closing of the sphere.

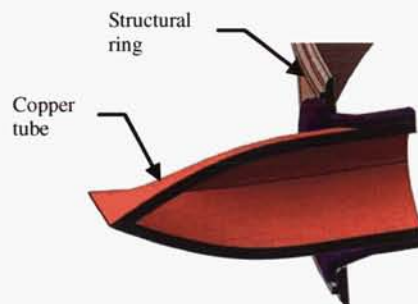


**Figure 9. Section of the sealing pipe assembly**

A low outgassing requires adapted material (plastics have to be avoided or minimized) and a preparation before sphere sealing. A preliminary outgassing under vacuum is performed for all the sphere components in order to evacuate the solvents molecules. Then an oven drying of the sphere at 120°C during the pumping is done to evacuate the water molecules. The oven drying at 120°C is extremely challenging for the material and adhesive joint choice.



In spite of all these preparations, the materials keep on outgassing inside the sphere which is not acceptable. Getters are necessary to absorb these gasses and thus ensure vacuum (the getter material works as a sponge with the gas molecules).

Unfortunately, the use of this technology leads to some very tough thermal constraints. When activated, the getter's temperature raises up to 900°C (current of 8 A). As a consequence, the getter has to be strongly thermally insulated. The getter assembly (Figure 10) was designed with insulating braces made out of ceramic, and surrounded with radiative screens. Screens are opened and placed so as to mask the getter from the outside.

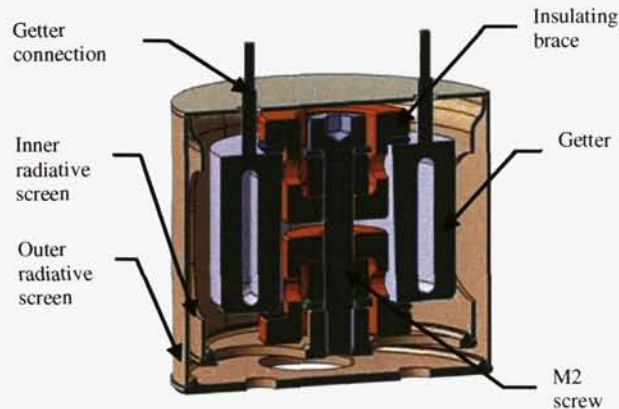


**Figure 10. Getter assembly**

#### High level of integration

Beyond the studies, the seismometer integration is also a big challenge. For example, the OCS and DCS assemblies (Figure 11) are made with M1.6 screws. The gaps between the fixed and mobile electrodes of these sensors (6 electrodes) are adjusted at 250  $\mu\text{m}$  with an accuracy of  $\pm 10 \mu\text{m}$ . These adjustments are reached thanks to measurements on an optical bench.

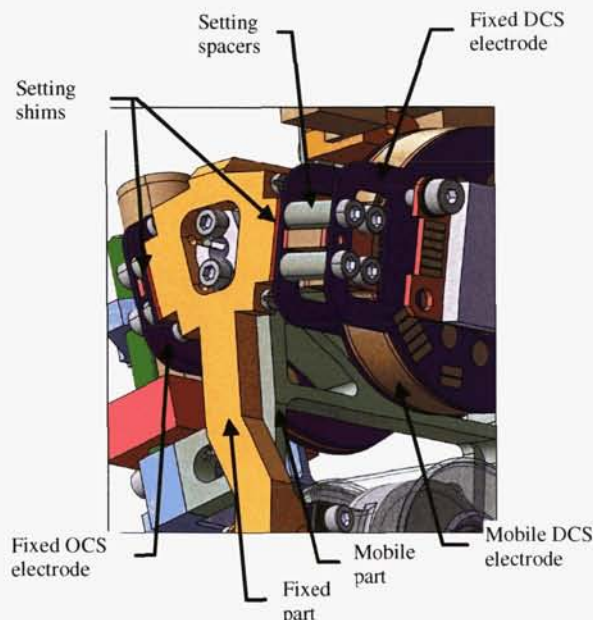


**Figure 11. DCS and OCS assembly**

The wiring is also an example of the high level of integration. First, the pivot is used to make the electric interconnection between the fixed and mobile parts. It requires a precise number of blades for the pivot and also requires that the blades be insulated from the structure. The need of 20 blades for the VBB sensor makes the pivot assembly very hyperstatic and thus leads to a relatively wide distribution of the pivot stiffness.

On the other hand, the wiring is made by using flex-rigid cables. The flex-rigid cables make their way through the structure towards each component (OCS, DCS, coil, mechanism...). These flex-rigid cables are composed of 4 layers of 12.5  $\mu\text{m}$  in thickness for the electric signals and their shielding. Figure 12 shows the wiring of the mobile part with the pivot.

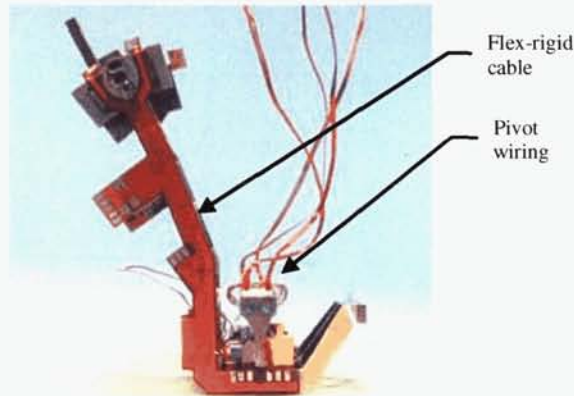


**Figure 12. VBB mobile part wiring**

Finally the wiring requires specific feed-throughs to take out the electric signals of the sphere under vacuum. There are 2 feed-throughs for the getter power supply and 2 feed-throughs of 42 pins for the VBB sensors wiring (Figure 13).



**Figure 13. VBB Sensor feed-through**

## **Modelling**

### VBB sensor modelling

The mechanical modelling of the VBB sensor is essential to reach the performance required for the pendulum resonance, the mechanical sensitivity, the thermal sensitivity and the shock withstanding. The VBB sensor was modelled on ABAQUS because of non-linear calculations (contacts on the final stop and large displacements for the leaf spring). Great care was taken to achieve the simplified model of the VBB (Figure 14) in order to give the best predictions. The model is based on shells, beams and concentrated masses. Each component was updated on tests or on detailed models.

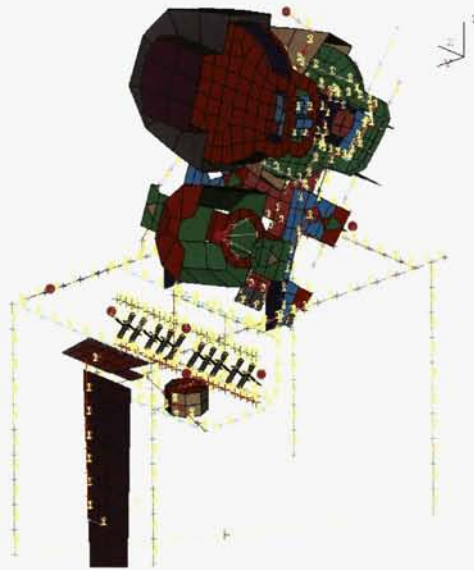


**Figure 14. Finite element model of the VBB sensor**

Concerning the performance, Table 1 presents the modelling results. After the stiffening of the pivot (upper and lower body), the shock calculations give positive margins on stresses and efforts in the assemblies. These results validated the final stop setting at 50  $\mu\text{m}$ .

**Table 1. Modelling results of the VBB sensor**

<b>Modal analysis</b>	Earth config.	Mars config.
Pendulum	0.35 Hz	0.70 Hz
Spring	81 Hz	81 Hz
Pivot	90 Hz	96 Hz
Fixed part	137 Hz	
<b>Mechanical sensitivity (m/k)</b>	Earth config.	Mars config.
Vertical sensitivity	$1.39 \cdot 10^{-2} \text{ s}^2$	$2.38 \cdot 10^{-2} \text{ s}^2$
Horizontal sensitivity	$1.99 \cdot 10^{-2} \text{ s}^2$	$3.38 \cdot 10^{-2} \text{ s}^2$
<b>Thermal sensitivity</b>		
Leaf spring	$7.3 \mu\text{m}/^\circ\text{K}$ $\beta = -16 \cdot 10^{-6} \text{ K}^{-1}$	$0.9 \mu\text{m}/^\circ\text{K}$ $\beta = +16 \cdot 10^{-6} \text{ K}^{-1}$

#### Mechanical design

The mechanical design of the sphere structure was verified and optimized based on a finite element model of the sphere (Figure 15). The model was developed on I-DEAS.



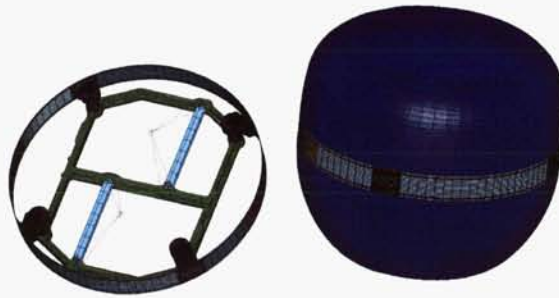


**Figure 15. Structural model of the Sphere**

The following calculations were applied:

- Modal analysis to check the stiffness of the structure
- Quasi-static load at 200g to simulate the shock (pessimistic case)
- Loading under pressure at 1 bar on the covers to simulate the vacuum set up
- Thermo-elastic to simulate the storage ( $\Delta T$  of  $-140^{\circ}\text{C}$ ) and oven drying ( $\Delta T$  of  $+100^{\circ}\text{C}$ )

Several iterations were carried out to obtain the best compromise between mass, rigidity and thermal resistance. For example, much work was done on the insulating block. To withstand the shock in the transversal direction a bigger section was necessary but this decreased dramatically the thermal resistance. A compromise was found by widening the block in the upper part and especially by optimizing the blend radius (Figure 16).

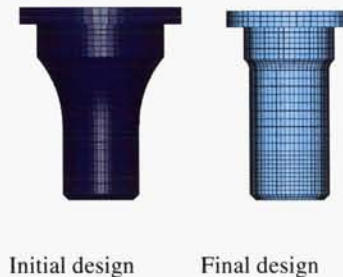


**Figure 16. Insulating block optimisation**

Specific tests were made to validate the use of the composite material (Torlon<sup>TM</sup>) for the insulating block as a structural part. Static tests on the whole insulating block assembly showed good results even after thermal cycles at  $+120^{\circ}\text{C}$  and  $-120^{\circ}\text{C}$ .

Finally, the results of the mechanical modelling gave positive margins for all structural parts.

#### Thermal design

A modelling of the thermal design of the sphere was developed on I-DEAS TMG (Figure 17).

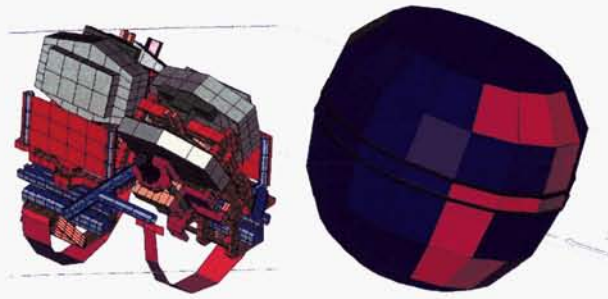


**Figure 17. Thermal model of the Sphere**

The analysis gave the thermal behavior inside the sphere for hot and cold dynamic cases. Figure 18 shows the efficiency of the insulation: in the cold case with only 70 mW inside the sphere (electronics), the minimum temperature is  $-93^{\circ}\text{C}$  for an ambient temperature at  $-122^{\circ}\text{C}$  and the thermal amplitude during a Martian day is reduced from  $110^{\circ}\text{C}$  to  $45^{\circ}\text{C}$ .

However, Figure 19 shows higher thermal amplitude inside the sphere with  $58^{\circ}\text{C}$ . This is a potential problem because of the thermal sensitivity of the VBB sensor. With such thermal amplitude, the mobile part could come on the final stop and not allow measurement for several days.

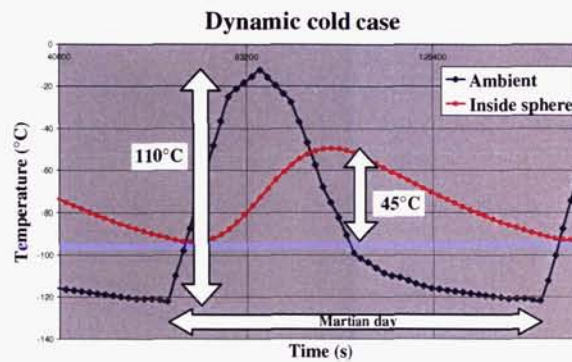


**Figure 18. Dynamic cold case**

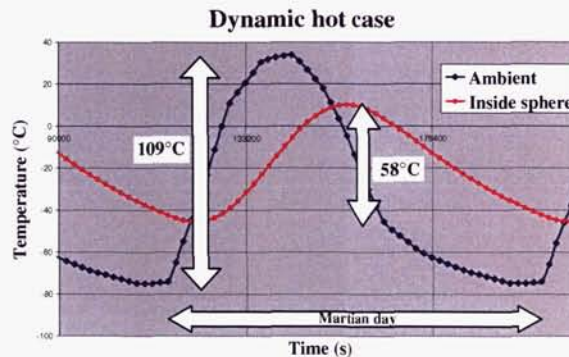


**Figure 19. Dynamic hot case**

## Testing

### Seismological performance

The first Breadboard model of the VBB sensor (Figure 20) was tested in a seismic cellar at St Maur near Paris by the IPGP team.



**Figure 20. Breadboard model of the VBB sensor**

With several earthquake detections, for example the Sandwich Islands one on September 6, 2004 (Figure 21), the IPGP characterized the VBB sensor performance.

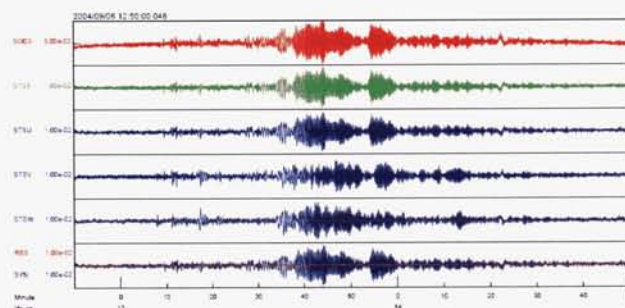


**Figure 21. Sandwich Islands earthquake detection**

The measured performance is presented in Table 2. They show results relatively close to the modeling. Furthermore, the comparison measurements between the VBB sensor and the STS2 seismometer, the current reference on earth, confirmed the high performance of this Martian seismometer.

### Thermal & Mechanical qualification

#### Shock test on a pivot mock-up

A preliminary mechanical qualification test with random vibrations and shocks was performed on a pivot mock-up (Figure 22). The aim of this test was to validate as soon as possible the pivot design and the use of the final stop on the mobile part.



**Table 2. Testing results of the VBB sensor**

Modal analysis	Modeling	Testing
Pendulum	0.35 Hz	0.50 Hz
Mechanical sensitivity	Modeling	Testing
Vertical sensitivity	$1.39 \cdot 10^{-2} \text{ s}^2$	$1.73 \cdot 10^{-2} \text{ s}^2$
Horizontal Sensitivity	$1.99 \cdot 10^{-2} \text{ s}^2$	$2.45 \cdot 10^{-2} \text{ s}^2$
Thermal sensitivity	Modeling	Testing
Leaf spring	$4.1 \text{ } \mu\text{m}/^\circ\text{K}$ $\beta = +1 \cdot 10^{-6} \text{ K}^{-1}$	$4.8 \text{ } \mu\text{m}/^\circ\text{K}$ $\beta = +1 \cdot 10^{-6} \text{ K}^{-1}$

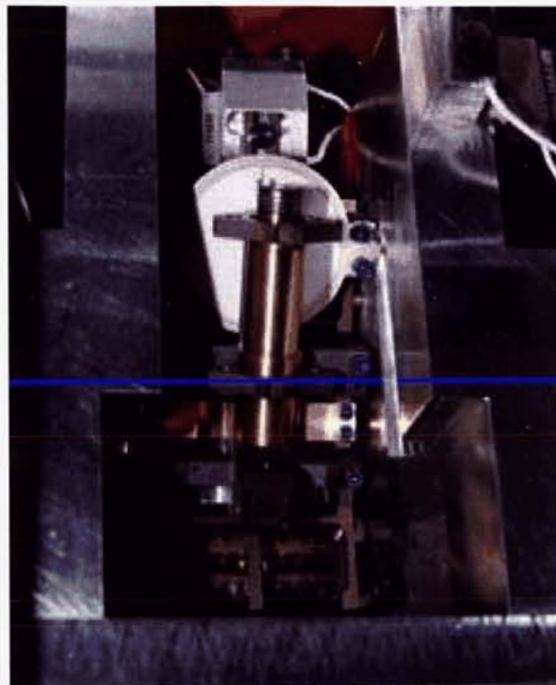


**Figure 22. "Pivot" mock-up during shock testing**

The shock test performed at CEA/CESTA was successful: the pivot performance was conserved and no degradation was noticed. We did learn from the shock test that the torque of the M3 fixation screw of the pivot had to be increased to avoid any slip.

#### Qualification on a Structural/Thermal Model of the Sphere (STM)

The STM is representative of the flight model except for the functional aspects. It includes the structural parts and all the critical assemblies like the pivot, the getters, the sealing pipe, the radiative screen and the feed-throughs. The STM cavity is not under vacuum but the covers are welded onto the structural ring.

A complete qualification test of the seismometer design was performed on the STM. The STM was opened (cut) after mechanical and thermal environment tests for visual inspection.



**Figure 23. Sphere STM during integration**

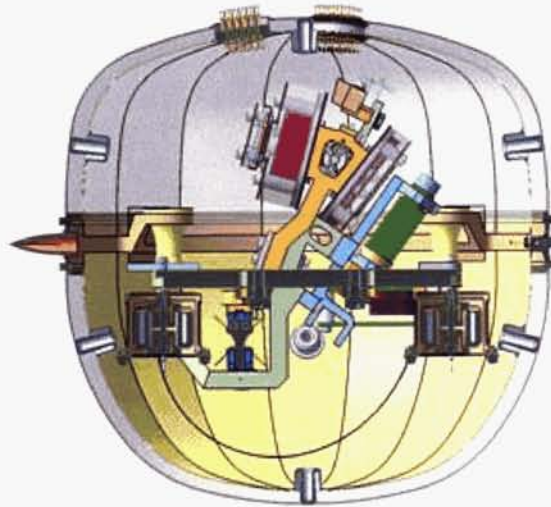


**Figure 24. Section of the STM CAD model of the sphere**



**Figure 25. STM on shaker**



During the mechanical qualification, the STM had to undergo a 9g RMS random vibration test and a 200g-20ms shock on all axes (2 shocks per axis). The STM was instrumented to measure the structural eigenmodes frequencies and the dynamic responses.

The random vibration test was performed in SODERN's lab on a 40-kN (9000-lb) shaker. The low sine tests performed before and after the random test did not show any discrepancy on the eigenmode frequencies which gave a first clue that there was no damage, before sphere opening and visual inspection. The main concern was the evolution of the eigenmode amplification factors after the test; from -35% to +50% depending on the eigenmode frequency and measurement location. There is still no reliable explanation of this phenomenon apart maybe from the use of non-metallic materials (glueings and composite material of the insulating blocks or the presence of an unlocked mobile part) and mechanisms.

The 6 shock tests were performed at CEA CESTA in France. The Low Sine tests performed after the shock test did not show any frequency drift.

After the mechanical environment tests, the sphere was opened for visual inspection (cut by machining). No damage was noticed.



**Figure 26. STM Sphere opening**



**Figure 27. STM Sphere ready for thermal balance**

In addition to the mechanical tests, thermal cyclings in the extreme specified temperature range [-120;+120°C] were successfully performed at the IGP in the Martian environment simulator and in Sodern facilities. No damage was observed.

#### Thermal balance test

A thermal test of the STM Sphere was performed in SODERN's EV5 vacuum chamber in order to update the mathematical thermal model and the thermal studies of the Sphere. Fifteen (15) thermocouples were used in order to measure the temperature at various locations and correlate with the mathematical model predictions in static and dynamic cases. Heaters were used to simulate the power dissipated by the real electronics (70 mW).

The test showed that the thermal insulation of the sphere was lower than predicted. The representativity of the mathematical model w.r.t the test conditions was analyzed and confirmed. In particular, an additional test with only two thermocouples was performed and confirmed that the wires of the 15 thermocouples were not doing an undesired thermal shunt. A sensitivity analysis was also performed with the thermal mathematical model (I-DEAS) showing that a refinement of the model assumptions (more accurate material data, more representative geometry, radiative exchanges modeling improvements) and few corrections were able to suppress most of the discrepancies



between test and mathematical result. This correlated thermal model will be of course very useful for any further analysis.

An improvement of the thermal insulation of the Sphere has still to be worked out in Phase C in order to reduce the sensitivity of the seismometer to temperature variations between night and day. It is however not really an issue and the use of MLI around the sphere should help a lot.

#### Getter activation tests

Functional tests were carried out on the getters. Firstly, preliminary tests were performed on a getter mock-up to determine the best getter activation parameters (power supply, activation duration). Secondly, a fully representative test was carried out with the STM. Both tests were performed under vacuum of course.

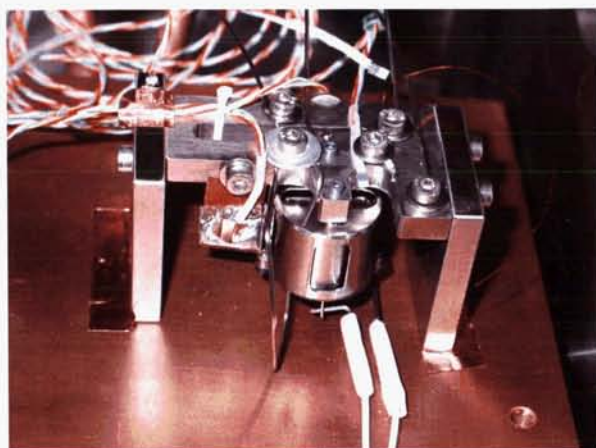


**Figure 28. Getter Breadboard**

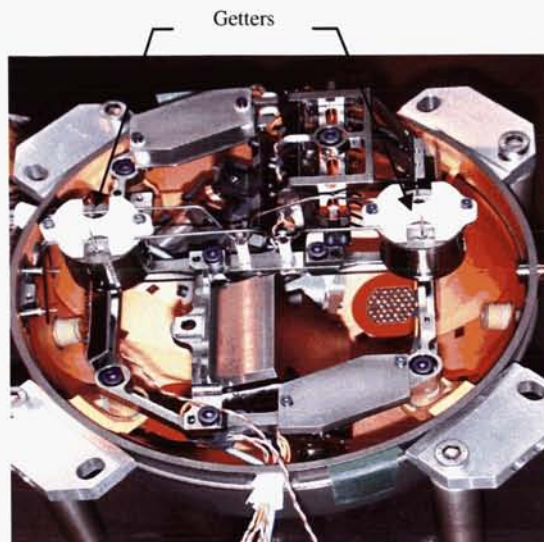


**Figure 29. Getters in Sphere STM**

The getter Breadboard was made of the getter itself and the parts of the seismometer located close to the getter in order to check they were not damaged during the getter heating. This test helped us to determine the maximum acceptable temperature of the getter in order to prevent any damage of the surrounding parts, actually 600°C. The activation duration needed to obtain the expected vacuum level will be defined precisely in Phase C with a fully representative model of the Sphere. Indeed it is very dependant of the material amount and outgassing properties.

A second getter activation test was performed on the STM. The goal temperature of 600°C was not reached on the 2 getters and the insulating blocks were locally damaged because of the temperature of getter power supply wires. The cause of this problem is clearly understood and it can easily be fixed. It is due to the electrical resistance of the feed-through. A larger feed-through solves the problem. This has been successfully confirmed by complementary tests.

#### **Conclusion**

At the end of this phase B, the most critical points of the design of the very core of the seismometer, the detection sphere, have been successfully verified. The few last points to be improved or adjusted are clearly identified. The expected high performance was confirmed on the Breadboard and the global consistency of the design with regard to the requirements was also confirmed.

SODERN is now ready to start a C/D phase for any future seismological planetary mission and will be a very serious candidate on the ESA EXOMARS 2011 mission.

# Commercial off the Shelf Components in Reaction Wheels

Andrew Haslehurst\* and Guy Richardson\*

## Abstract

This paper presents the approach adopted by Surrey Satellite Technology Ltd (SSTL) for development of reaction wheels incorporating commercial components and the accelerated life test / qualification philosophy. The paper focuses on the mechanical development and re-qualification of reaction wheel which has flown successfully on many missions having conducted years of in orbit operation. The scope of the requalification was to verify the wheels performance with ground testing for new missions where an increased life was required, with some re-design where applicable.

## Introduction

The Microsat Reaction Wheel (MRW) or Micro Wheel was developed at SSTL in the mid-nineties and is unique in its design from the simple drive electronics which are enclosed in the base of the wheel to the commercial brushless DC motor using dry lubrication, to the wheel volume at approximately 100\*100\*100 mm<sup>3</sup> all weighing in at under 1 kg, this wheel was succeeded by the Enhanced Microsat Reaction Wheel (EMRW) in the year 2000.

The aim of the new Superior Microsat Reaction Wheel (SMRW) was to build on the heritage and success of the MRW and EMRW increasing the performance and extending the life in terms of revolutions of the wheel. Figure 1 shows the MRW, EMRW and SMRW wheels. At the time of writing this paper the SMRW is integrated onto the protoflight model of 5 imaging micro satellites currently being built at SSTL and due for launch towards the end of 2006.

The Microsat wheels have led the way forward for the development of the next generation of larger more powerful wheels which use similar electronics and lubrication systems. Although this wheel is not discussed here in the paper, four smallsat reaction wheels also incorporating dry lubricated bearings have been integrated onto the GIOVE A spacecraft ready for launch at the end of December 2005.



Figure 1. SSTL Microsat reaction wheels

## Background

The small satellite market (<500 kg) is particularly demanding not only for the small budgets involved or the mass and power requirements but also for the fact that a typical program for SSTL from contract to in orbit operation is normally from 18 – 24 months which leaves a very short period of time for development and qualification.

---

\* Surrey Satellite Technology Ltd., Surrey Space Centre, Guildford, Surrey, U.K.



One approach that SSTL uses builds on its philosophy of “affordable access to space” by flying new developments as back-up or experimental units on missions. Hence, flight qualification can be achieved without the need for lengthy and costly ground qualification. The market SSTL is addressing is changing though and there are now fewer opportunities to qualify in this manner with customers demanding proven reliability and heritage.

To achieve the rapid development and qualification with wheels a different approach needs to be taken from the typical wet (oil or grease) bearing lubricated systems. This simplifies the design, not requiring reservoirs for the oil and anti-creep barriers but allows for an accelerated life test. Due to the properties of wet bearing lubricated systems preventing acceleration of life tests with either speed or bearing preload, wet lubricated systems have to perform real time life tests (at flight speed). This leads to very long, potentially costly wheel qualification programs, which can lead to launch occurring before wheel qualification is complete.

All of SSTL early spacecraft were microsats approximately 50-kg spacecraft 360-mm square by 750-mm long in launch configuration. The AOCS system of these microsats did not rely on reaction wheels to provide attitude stability. The spacecraft design used a gravity gradient boom to keep it nadir pointing. Yaw motion was controlled using magnetorquers. Augmenting the AOCS with wheels allowed much better control of yaw and the potential to off point from nadir to increase the imaging opportunities of a particular target. Early SSTL wheels were flown as experiments providing enhanced performance above the baseline mission requirements. This allowed development cost to be kept down by reducing ground testing to a minimum.

All SSTL wheels to date and the current EMRW, SMRW and SRW use self-lubrication in the form of a PGM-HT cage. Fortunately for such self-lubricating bearings, there is an increasing body of life test data, which shows there to be a quite strong correlation between wear rate (i.e. bearing lifetime) and peak Hertzian ball- raceway contact stress. Much of this data was recently generated by ESTL (European Space Tribology Laboratory) as part of an ESA-funded campaign to source, fully characterize and qualify a replacement material for the Duroid 5813 material at the time it ceased production. Taken as a whole, this data includes both in-vacuum long lifetime application data with PGM-HT and Duroid 5813 materials and an in-air test campaign of approximately 3000 bearings aimed at generating design guidelines for industrial applications of this type of bearing. Further information can be found in [1], [2]. The graph presented in Figure 2 shows the relationship between preload and life which comes from experimental data from tests and predictions from design analysis,

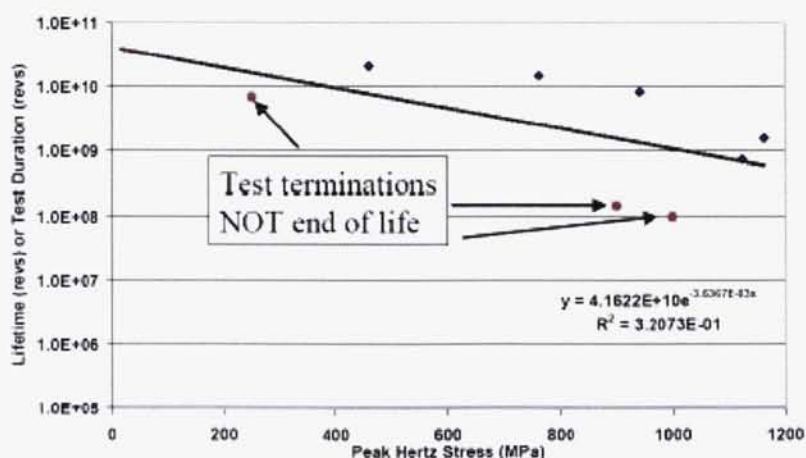


**Figure 2. Preload V's life graph**

Use of solid lubricants in reaction and momentum wheel bearings is clearly quite rare. One reason for this is the higher torque noise of some solid lubricated bearing systems, their perceived short lifetime and intolerance to misalignment, competing against the long-established heritage of liquid lubricated solutions



which offer high lifetime (though often this is achievable only with the addition of a wheel re-lubrication system). The disadvantage of the conventional approach for an accelerated wheel development program is that to qualify a liquid-lubricated wheel, no strict tribologically valid method exists which can accelerate the life test without modification to the lubricant regime in a manner which risks significant under-test. For a solid-lubricated wheel however testing can be relatively straightforwardly carried out at high speed without significant impact on the lubricant wear behavior.

SSTL's approach with such bearings can be thought of using the cage as providing a lubricant reservoir with solid lubricant being transferred from cage to balls and ultimately onto the raceways as a so-called "transfer film". Bearing lifetime is limited by ultimate wear-out of the cage pockets or by excessive or lumpy transfer, which may in some applications create unacceptable torque noise.

For SSTL's first generation of reaction / momentum wheels, which were successfully flown, the lifetime requirement was not particularly high and the self-lubricating bearings were adopted and used in a relatively commercial manner. However, for this latest generation of wheels, there was a requirement to demonstrate a much higher lifetime nominally 2.2 billion revs for a 7-year DMC type mission (including a factor of 2) with low torque noise, combined with a programmatic need to demonstrate the life within an approximate 12 month testing window.

With this change in requirements for lifetime there is an on going investigation into extending life by using novel hybrid lubricant combinations, which are not presented in this paper.

## **MRW**

### Background / Development

The first experimental MRW flew in 1995 on FASat-Alpha which unfortunately failed to separate from the launch vehicle upper stage. FASat-Bravo was built to replace FASat-Alpha and was successfully placed into orbit in 1998. The experimental reaction wheel worked well and encouraged development and use of similar reactions wheel on future missions.

Between 1997 and 1999 three reaction/moment wheels were developed: a nanosat momentum wheel, a minisat reaction wheel and a modified microsat reaction wheel. All of these wheels were based on commercial motors and with the exception of the nanosat momentum wheel, which used vacuum grease lubrication, all used dry lubricated bearings.

The most successful of these wheels was the modified microsat reaction wheel, which flew on Thai Phutt (TMSat), Tiungsat-1. TMSat and Tsingsat-1 each had a single wheel that was used for experimental operations only. Tsinghua-1 had 3 reaction wheels and was operated in three-axis reaction wheel control for months before its gravity gradient boom was deployed, during this time one wheel biased at 500 rpm conducted over  $-6.59 \times 10^8$  revolutions.

The modified microsat reaction wheel used for Thai Phutt, Tiungsat-1, Tsinghua-1 was the basis of the EMRW. The EMRW is a primary attitude control component on six SSTL spacecraft currently in orbit. The first of the spacecraft to use the EMRW was AISat-1 this was the first spacecraft of the DMC constellation, launched in 2002. This spacecraft used two wheels in combination with a gravity gradient boom. Since the lifetime requirements for the AISat-1 wheel were largely met by the on orbit operation of the Tsinghua-1 wheels and the design of the wheels were similar, extensive ground testing and requalification was not carried out.

UK-DMC, NiSat-1 and BiSat-1 were the next spacecraft to use the EMRW. These three were launched together in 2003 and also form part of the DMC constellation. The core platform design of UK-DMC and NiSat-1 was the same as AISat-1. However, BiSat-1 was first of a new generation of SSTL spacecraft designed to be more agile and have a longer mission life (seven years instead of five). It was not conclusive from the available data at that time that the EMRW design would have sufficient life to meet the mission requirements of BiSat-1. Hence, as a contingency, BiSat-1 also included a deployable boom to allow gravity gradient ADCS operation in the event of a wheel failure.

At this time ESTL performed a life test on a MRW motor miss aligning and loading the bearings to their maximum capacity in an attempt to purposefully cause an early failure. The wheel conducted 0.6-billion revolutions (proving mission life taking into account an acceleration factor) showing no signs of failure at which point the test was stopped and the bearings inspected. Some pitting was observed on some balls and these were examined under a SEM, which can be seen in Figure 3, the damaged areas showing delaminating are typical with high sub surface stress and although not desired the wheel was operating nominally.

The cages were weighed pre / post test and seen to have negligible cage weight loss. Assuming cage wear limits the life then it is predicted that lifetime in the order of tens of billions revs could be achieved. Although these tests fundamentally proved the motor was fit to meet current mission life requirements it was thought the life could be extended even further. Hence, it was determined that bearing misalignment should be taken out by some small design changes, which are presented in the development the SMRW.



**Figure 3. MRW (SR4) Bearing inspection after life test**

Since their launch the EMRW wheels in these spacecraft have performed millions of revolutions without anomaly. On orbit data can be seen from two wheels of the UK-DMC spacecraft, in this case of operation mode operating around zero. Table 1 summarizes the wheel parameters for the MRW, EMRW and SMRW.

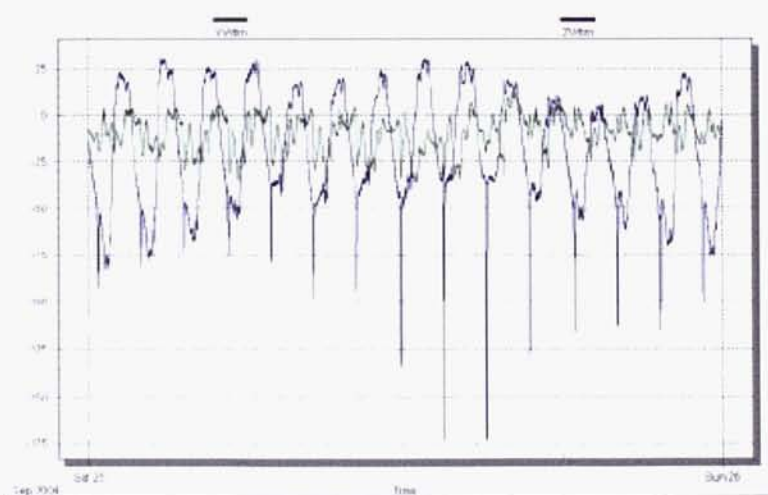


**Figure 4. Snap shot of in orbit data from a UK-DMC spacecraft showing speed (RPM) against time**

**Table 1. Micro wheel spec overview**

Parameter	MRW	EMRW/SMRW
Mass	<0.75 kg	<1.1 kg
Volume	100*100*100 mm <sup>3</sup>	105*105*105 mm <sup>3</sup>
Voltage	11-14 V (12 nominal)	24-32 V (28 nominal)
Power	0.4 W (constant speed) 3.0 W (peak torque)	1.2 W (constant speed) 5.0 W (peak torque)
Momentum	0.21 Nms	0.42 Nms
Torque	3 mNm	10mNm
Life	>1X10 <sup>9</sup> revs	>2.2X10 <sup>9</sup> revs

## SMRW

### Background / Development

There were two main design changes to the SMRW from the EMRW:

- The introduction of a cover, deemed necessary due to increased harness packing around the spacecraft which lead to concerns of harness clashing with the unprotected inertia disk.
- The re-housing of the motor magnetics to increase the size and alignment of the bearings thus striving to increase the life.

For reasons explained later in the paper with regards to ground testing the motor was partly reengineered to provide:

- a) a very low but repeatable bearing preload, thus low contact stress
- b) a supplementary angular snubber for launch vibrations
- c) a very high degree of bearing alignment

Figure 5 shows a cross section of the SMRW. The motor is supported on a cone that attaches to the housing, which supports the electronics including optical encoder below. The motor houses the bearings above the magnetics, which was a change from the EMRW to increase the alignment accuracy as the EMRW bearings were supported at either end of the shaft in two different housings.

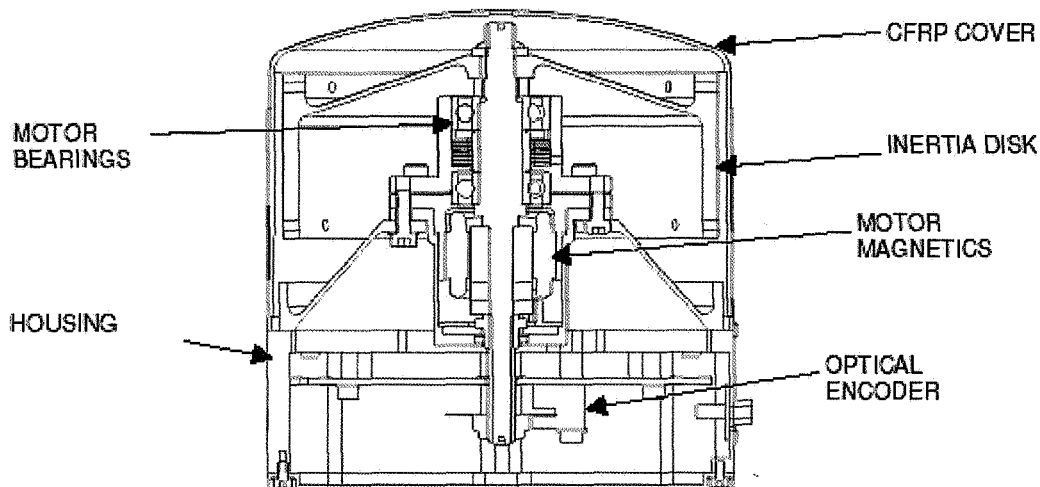


**Figure 5. Cross section of the SMRW**

The bearings are arranged in a back-to-back configuration using a deep groove type made from 440C stainless steel. The size was increased size from the EMRW SR4 type to an SR6 size, both of which are standard catalogue parts with relatively short lead times from European suppliers costing about 50 GBP each (\$100). This is very affordable when considering that some bespoke bearings and cages can be orders of magnitude more expensive.



As previously mentioned the lubrication system is dry by means of a transfer cage. The cages are a standard snap on design using PGM-HT, which is a PTFE base using chopped glass fibers for cage strength and it is impregnated with  $\text{MoS}_2$ . As small particles of the cage transfer to the balls and raceways they get squashed out leaving a thin film that provides the lubrication.

The increase in bearing size was also necessary to increase the load capability as the launch environments on some new missions are increasing. There was also a change to preload the bearings (the EMRW bearings were shimmed to 50 microns with no preload) using a (standard catalogue part) crest-crest spring to apply a low preload, the spring also simplifies assembly due to the high deflection to low force characteristics of the spring thus designing in simple assembly and keeping the cost down.

The motor magnetics were primarily kept the same but a magnetic overlap that provides some preload on the EMRW was removed thus removing the axial preload from the design so a lower preload can be achieved to maximize the life.

The electronics are nominally unchanged from the MRW consisting of a simple power stage utilizing commercial components and a main PCB which houses the optical encoder and can be seen in Figure 6. All the electrical components are readily available commercial parts, which do go through some increased screening at SSTL upon inspection on critical and delicate components such as the DC-DC converters, which have glass-isolating beads around their legs. Further detailed information on electrical commercial components can be found in [3], [4].

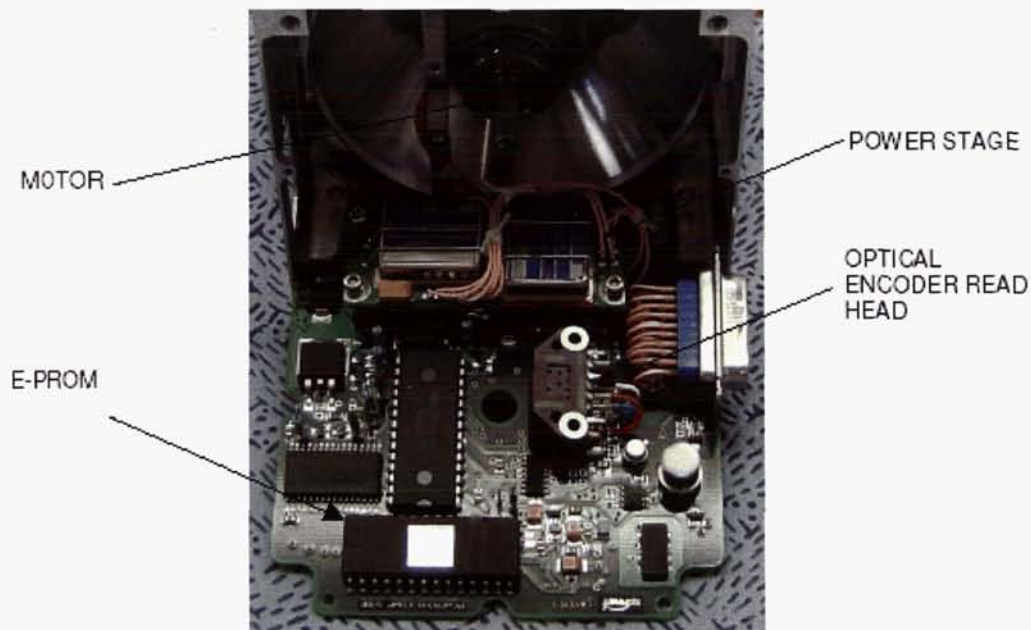


**Figure 6. Micro wheel electronics**

#### Qualification testing

The testing mentioned above and documented by ESTL clearly shows two effects. Firstly that using this class of self-lubricating material above a critical peak Hertzian contact stress of around 1200MPa results in very poor lubrication and should be avoided. Secondly, that below this stress there is a clear relationship between ball raceway peak Hertzian contact stress and lifetime which suggests that acceptably high lifetimes CAN be achieved with self-lubricating materials IF the contact stress between balls and raceways are maintained at a sufficiently low level. Furthermore, because of the well defined relationship between contact stress and wear rate (i.e. lifetime) it is possible to define a highly accelerated test program in which not only the speed is increased (say by a factor 5), but also an additional acceleration factor is obtained by increasing the bearing preload to some higher value than nominal for the application. In this way life test acceleration factors of order 20-30 can be justifiably achieved.

One additional benefit of using solid lubricants at low Hertzian contact stress is that the torque noise, which is in part related to lumpy and uneven transfer of the cage material onto the raceways, is reduced. The disadvantages of using this approach are relatively modest; firstly some extra care must be taken during ground testing (at low preload the rotor mass and 1-g effects can be significant) and reduced angular stiffness of the wheel shaft during launch vibration.

Given the improvements to the SMRW over the original unit, and by extrapolation of data from the design guide and other test programs, lifetimes of order  $1\text{-}2\text{E}10$  revs were predicted to be achievable even in the absence of the improved bearing alignment.

Two SMRW wheels have successfully passed the following qualification program:

- Vibration (to 23.5 Grms)
- Micro vibration
- Life test (to a factor of 2 on life in thermal vac performing hot / cold cycles)<sup>1</sup>
- Micro vibration

<sup>1</sup> Including two different spacecraft operational scenarios, QM#1 nominal four-wheel operation in a tetrahedral configuration biased at constant speed of 300 RPM with a higher preload (6.1 N) to allow accelerated testing, and QM#2 degraded spacecraft mode with three wheels biasing around zero and constantly crossing zero with a nominal flight preload of 2 N.

Over a typical mission life of seven years in nominal mode this equates to 2.2 billion revolutions including a factor of 2. Taking into account acceleration philosophy mentioned above the life test only needs to run for a few months.

The nominal operational mode also included operational scenarios from orbital maintenance maneuvers, which increase the wear on the cage due to the acceleration of the wheel. During these maneuvers the wheels are spun up from their nominal speed to around 4500 RPM to stabilize the spacecraft during thruster firings. They are then driven slowly back to nominal speed using the spacecraft's magnetorquer rods to dump the momentum. These maneuvers have been scaled to take into account the increased speed of the life test covering a representative number of revolutions at the correct rate of acceleration. This equated to performing approximately 1 slew cycle per minute at 3 RPM per second acceleration, Figure 7 shows the predicted profile.

The degraded spacecraft mode with the wheels constantly crossing zero was performed nominally from  $\pm 100$  RPM at approximately 2 crossings per minute for over 156 thousand zero crossing. The wheel was set up in a fully flight configuration including cover and the bearing preload was set at 2 N.

During the life test, both wheels also demonstrated hot and cold survival ( $-30^{\circ}\text{C}$  /  $+60^{\circ}\text{C}$ ) / operational  $20^{\circ}\text{C}$  /  $+50^{\circ}\text{C}$ ) cycles including start ups at the beginning and end of test at the temperature extremes.

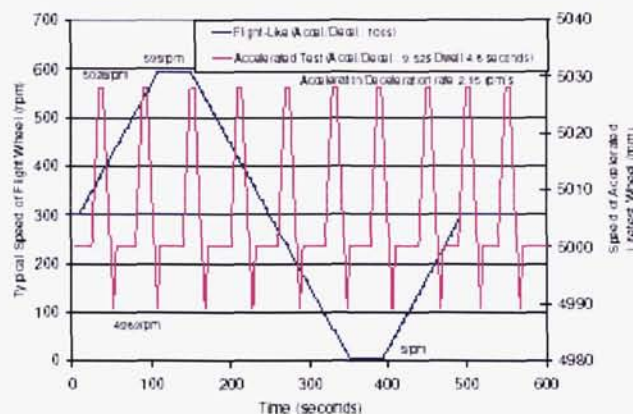




**Figure 7. Typical flight like orbital maneuvers imposed over the accelerated life test profile**

QM#1 (nominal operation)

During vibration it is not uncommon to see responses at the inertia disk in the order of 60g. This relates to a peak Hertzian contact stress around 3500 MPa, which is pushing the bearing to its limits with the onset of sub surface plastic deformation at 4000 MPa. No visible damage was evident on any bearing surfaces ball or race as was seen with the MRW.

Figure 8 shows a snap shot from the life test of the high slew maneuvers. There is some difference between the predicted acceleration rates, which is due to the way the wheel was controlled during the test. This actually gave the bearings a slightly harder time, as the higher acceleration rates increase wear. The wheel conducted over 113 thousand slew cycles at high speed with no anomalies.

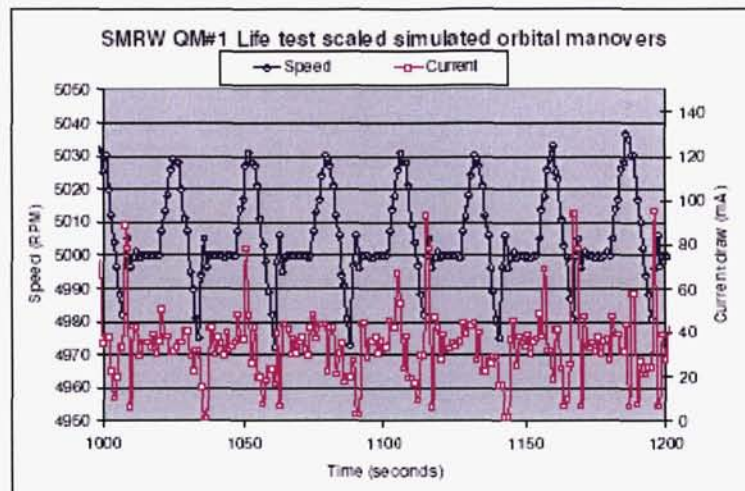


**Figure 8. SMRW QM#1 Snapshot of life test data**

Micro-vibration was conducted on the wheels pre and post life test to investigate the size of the effect cage degradation has on the micro-vibration, a plot from post life test can be seen in Figure 9. The bearing fundamental frequencies such as cage / ball frequencies can be seen tracking as predicted up to about 350 Hz and showed a small increase in amplitude. The main increase in noise was in two frequency bands, 400-500 Hz and around 1000Hz bands where there is a slight increase in amplitude. This ties in with modes of the inertia disk around 400Hz and 1000 Hz that can be seen from vibration sine sweeps.



Analysis of the jitter testing is still ongoing with spacecraft system models to gain a better understanding of the effects of wheel micro vibration through the spacecraft with particular interest to imaging missions.

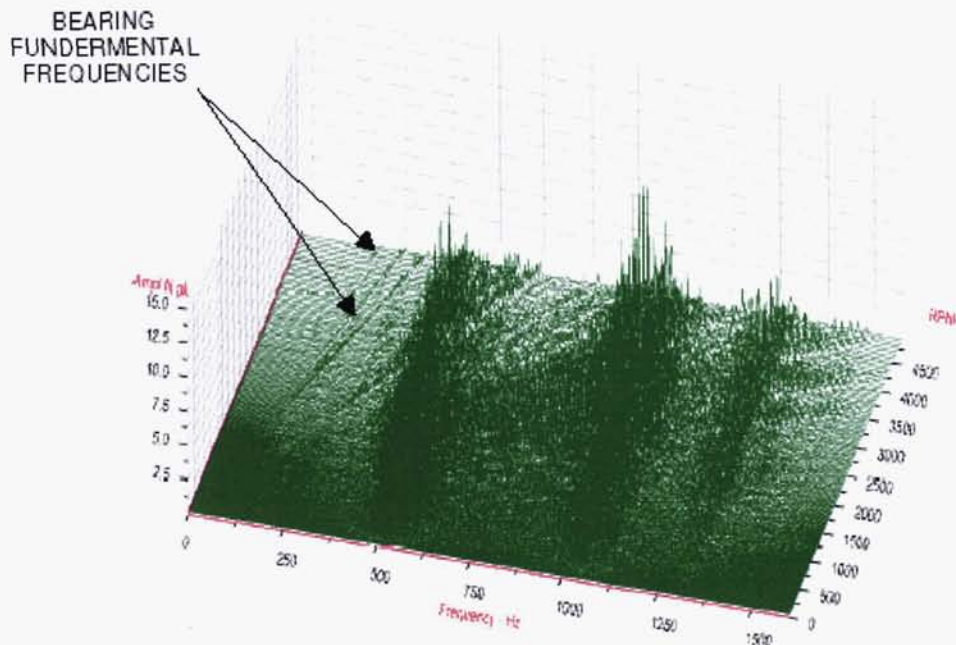


**Figure 9. Waterfall plot showing coast down micro vibration post life test**

#### QM#2 (Degraded mode)

The wheel operated nominally throughout the life test with no anomalies performing over 130 thousand zero crossing.

#### Post life test inspection

The bearings were stripped down, inspected and the cages weighed pre and post life test to ascertain the amount and characteristics of the wear. Photos from the strip down can be seen in Figure 10, with even wear around the pocket, clear and even transfer of PTFE material onto the race ways.

Both QM1 (6.1-N preload) and QM2 (2.3 N) exhibited very low cage wear on successful completion of the life tests carried out compared to that expected. Typically the cage mass loss was of order 1% or less of the QM1 initial cage mass (with on-loaded bearing cage wear rate being higher than that operated at the nominal preload). For QM2 the measured cage wear rate was still lower, in fact on the threshold of measurement for QM2. According to the lifetime model, and previous experimental data, QM1 bearing cages could have been expected to have lost up to 15% of their cage mass due to wear (0.1g) by the end of the accelerated life test. The excellent condition of the cages in both QM1 and QM2 suggests that the improved bearing alignment achieved has a large impact on the wear rate observed comparing to the EMRW life test.

Extrapolation of wear rates is slightly hazardous because typical wear processes follow a so-called "bathtub" curve with high initial and final wear rates but a long period of low wear rate equilibrium performance. Given this a linear extrapolation of mass is likely to under-estimate lifetime, but using such an approach, it may be concluded that the ultimate lifetime of the bearings in the SMRW wheel may be considerably in excess of  $1E10$  revs, that is permitting a lifetime with margin of in excess of 16 years at 300 RPM. Clearly however the ultimate lifetime achievable will need to be determined by further testing/flight experience.

The torque performance of the bearings during the life tests was also very good. After the initial run-in, the torque noise generated improved with lifetime. For example in QM1, the Standard deviation torque

noise during reversals was around 2.5 gcm initially and slightly improved, to a value of 1.8 gcm by completion of testing.

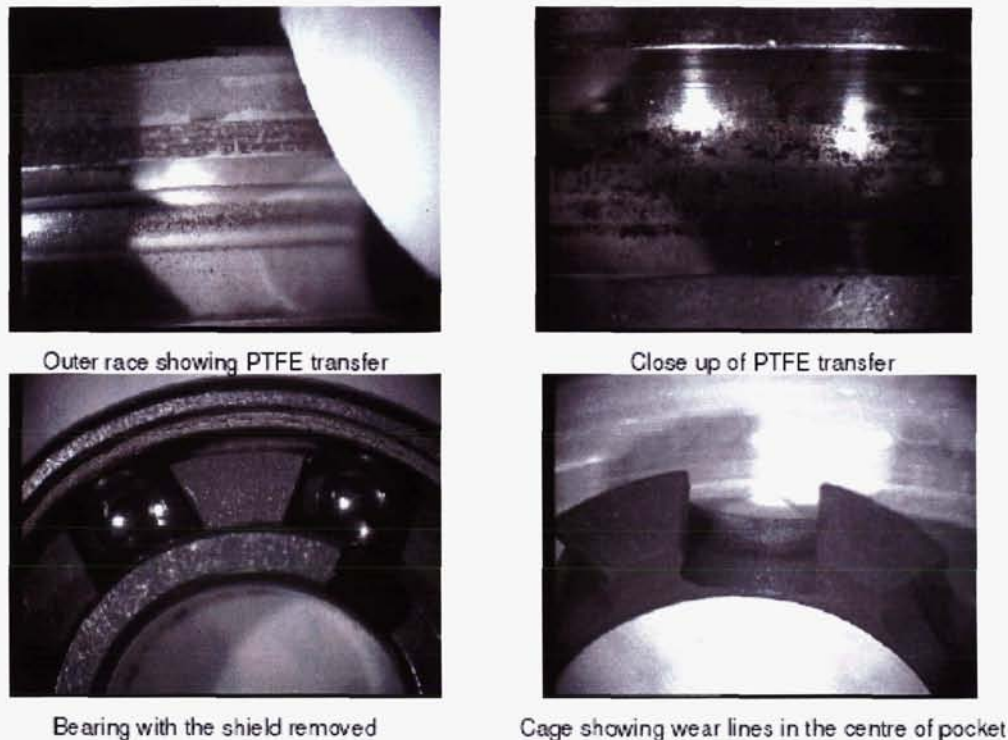


**Figure 10. Close up photo of the wear of one of the SMRW QM#1 bearing cage after life test**

### **Conclusion**

Both SMRW life tests were successfully concluded with both wheels meeting and exceeding their requirement; lifetimes substantially in excess of these values may well be achievable.

No SSTL wheel has had a mechanical failure on orbit. All wheels are either still working or were working nominally when the spacecraft was decommissioned. To date the MRW and the SMRW (through on ground qualification) have outlived spacecraft life and have still been operating nominally when the spacecraft has been de-commissioned proving self lubrication is fit for this type of wheel application.

The EMRW, SMRW and SRW covered in the paper are available commercially from SSTL under the trade names MicroWheel and SmallWheel.

### **References**

1. Ball bearing tests to evaluate duroid replacements - ESTL
2. Performance guide; self lubrication bearings, NCT Guide, 1976-ESTL
3. 30 Years of Commercial Components in Space: Selection Techniques without Formal Qualification-SSTL
4. 25 Years Experience With Commercial Components in Space – SSTL, California Paper



# Design of the ATMS Scan Drive Mechanism

Curtis Allmon\* and Dave Putnam

## Abstract

The Advanced Technology Microwave Sounder (ATMS) scan drive mechanism is a torque-compensating single-axis dual-mirror gimbal assembly. The scan drive mechanism will fly as part of ATMS on both NOAA's NPOESS (National Polar-orbiting Operational Environmental Satellite System) and NASA's NPP (NPOESS Preparatory Project). The ATMS, a weather monitoring instrument under development by Goddard Space Flight Center, measures microwave energy emitted by the atmosphere which aids weather forecasting. The material covered in this paper will focus on the mechanical design of the scan drive mechanism. The topics covered include the design features of the scan drive mechanism and the methods used to minimize the transmitted torque disturbances from the scan drive mechanism to the spacecraft.

## Introduction

The ATMS scan drive mechanism is a single-axis continuous-rotation gimbal that feeds microwave frequency data into the ATMS instrument. The microwave data generated by the scan drive mechanism is used to develop layered maps of the Earth's atmosphere by measuring the temperature and humidity at different altitudes. Figure 1 shows the orientation of the scan drive mechanism and ATMS instrument in flight and a composite plot of the temperature layers showing a developing tropical storm.

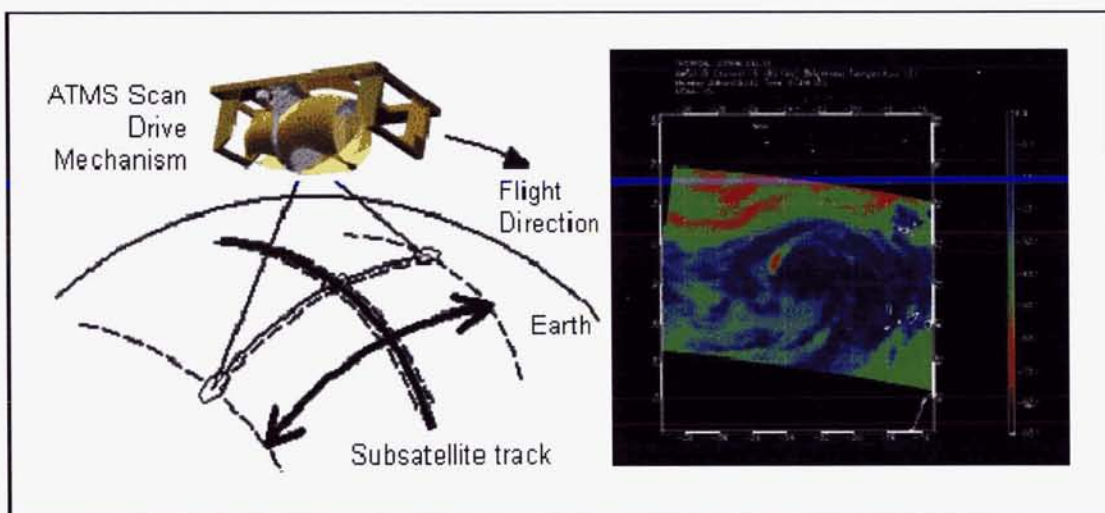


**Figure 1. ATMS scan drive mechanism flight pattern and data from earlier generation AMSU showing a tropical storm developing in November 2005. The ATMS Scan Drive Mechanism is the 3<sup>rd</sup> generation scanner to provide atmospheric temperature and humidity data from space for weather prediction.**

The ATMS scan drive mechanism is the third generation in a family of scan drives that reaches back to 1978. The ATMS scanner offers a three times improvement over the current generation AMSU scanner in number of scans per orbit. For comparison, the first generation MSU scanner rotated one scan or one revolution over 25 seconds. The AMSU second generation scanner rotates one revolution every 8

\* Lockheed Martin Space Systems Company, Sunnyvale, CA



seconds, and the ATMS scan drive mechanism rotates one revolution once every  $8/3$  seconds. To achieve the improved scan rate, the ATMS scan drive mechanism inserts three periods of acceleration and deceleration into each revolution as shown in Figure 2.

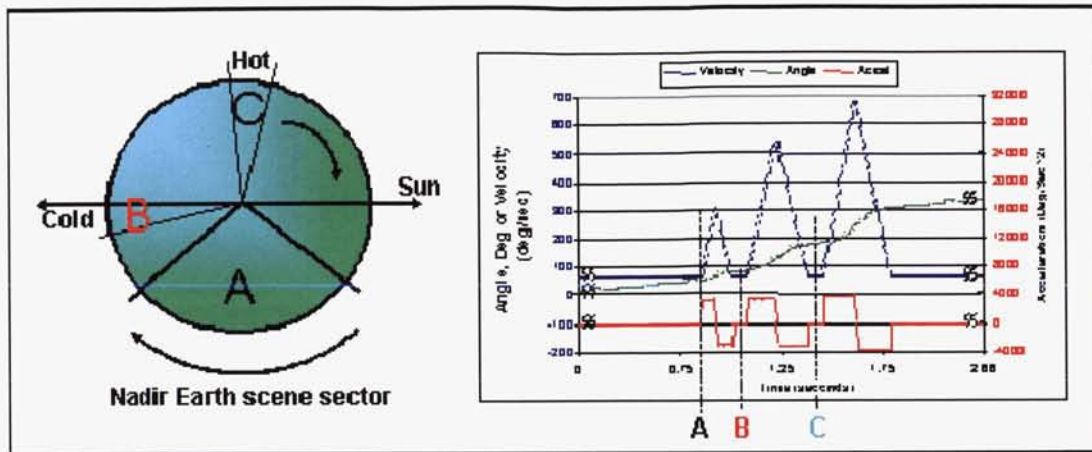


**Figure 2. Scan Drive Mechanism Scanning Pattern:** When in scanning mode, the Scan Drive Mechanism rotates at a constant velocity through the Earth scan and the Cold and Hot calibration scans. It rotates with constant acceleration or deceleration between these scans

As with every new design, there were things done very well in the scan drive mechanism and things that could have been improved upon if time permitted. In the category of things that were done well were the packaging design, the design for manufacturability, and the disturbance torque minimization features. One of the things we wished went better was the EMI/radiated susceptibility design and in a middle category (some good, some bad) was the bearing procurement and testing.

### Scan Drive Mechanism Design

#### Packaging and Overall Design.

The overall envelope and packaging of the scan drive is in the category of things that went well. As can be seen in Figure 3 the scan drive mechanism needed to fit in a very compact space on the ATMS instrument. The space between the two reflectors had to house two motors, two resolvers, two pairs of bearings, and a flywheel. The details of packaging the components in this space are illustrated in the Figure 4 cross section. One unique feature that aided in packaging the gimbal in this small space was the use of single-string (non-redundant) motors and resolvers. The single-string main and flywheel motors were driven by redundant wiring and electronics but by making the motors non-redundant we were able to achieve higher torque margin in a smaller package than possible with a redundant winding design of the same size. The motors were also an ironless core construction, which used a significantly thinner stator than a conventional brushless DC motor.

As shown in Figure 4, the scan drive mechanism is made up of main and compensating subassemblies. The main subassembly rotates the reflectors while the compensating subassembly limits the disturbance torque into the instrument by driving a flywheel in the opposite direction. The scan drive mechanism can be driven in both a compensated and uncompensated mode. In the uncompensated mode, the flywheel is not powered and torque compensation is eliminated.

Weight was another key requirement that went well. The weight and other requirements for the scan drive mechanism are given in Table 1. To achieve the required weight, the reflectors and the main and compensating subassembly housings were made of beryllium. The reflector material selection was important for weight as well as inertia. The spherical shrouds around each reflector were made of 6061-T6



aluminum. Other materials were considered for the shrouds but aluminum was selected for both for weight and manufacturability.

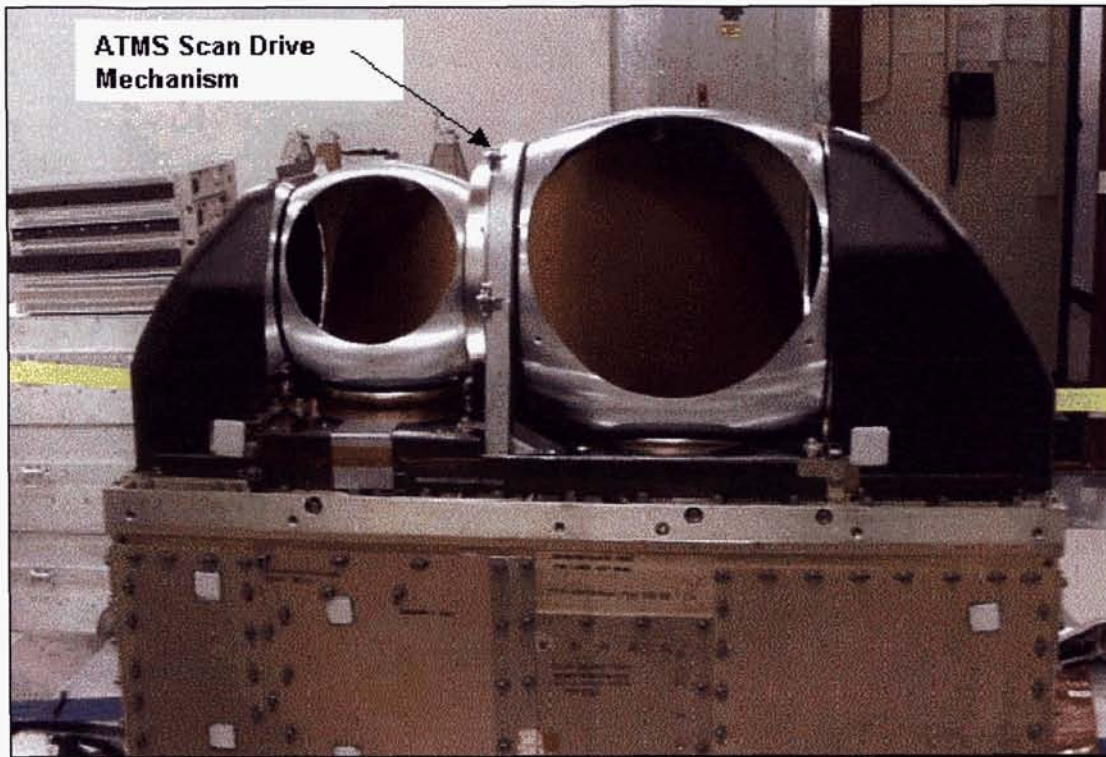


**Figure 3. The Scan Drive Mechanism mounted on the ATMS instrument illustrates the packaging challenge of this design. Two motors, two resolvers, two pairs of bearings, and a flywheel must fit in the center section between the two spherical shrouds.**

#### Design for Manufacturability.

The scan drive mechanism design not only met very tight packaging goals and weight requirement but was created as a modular assembly that allowed assembly, disassembly (when required), and test as subassemblies. This approach provided schedule and work load flexibility during assembly and test. The modular design of the scan drive mechanism can be seen in Figure 5 where the main motor subassembly and compensation flywheel subassembly are on the work bench together. The subassembly approach also allowed for the separate balancing of the main assembly with the reflectors and the compensating assembly with the flywheel.

Fabrication of the spherical shrouds and a repeatable method of assembling and disassembling the shroud halves with the scan drive mechanism was another important manufacturing challenge. The shrouds attach to rings that have floating nut plates and locating pins for repeatable reattachment of the shrouds. The shrouds are split along a horizontal seam to allow removal of the upper shroud half during reflector alignment verification (see Figure 6). The shrouds are rough machined out of one piece of aluminum and then split along the horizontal seam. The spherical shape of shrouds provided a maximum view factor for each reflector and covered the warm calibration source inside the ATMS during earth scan.

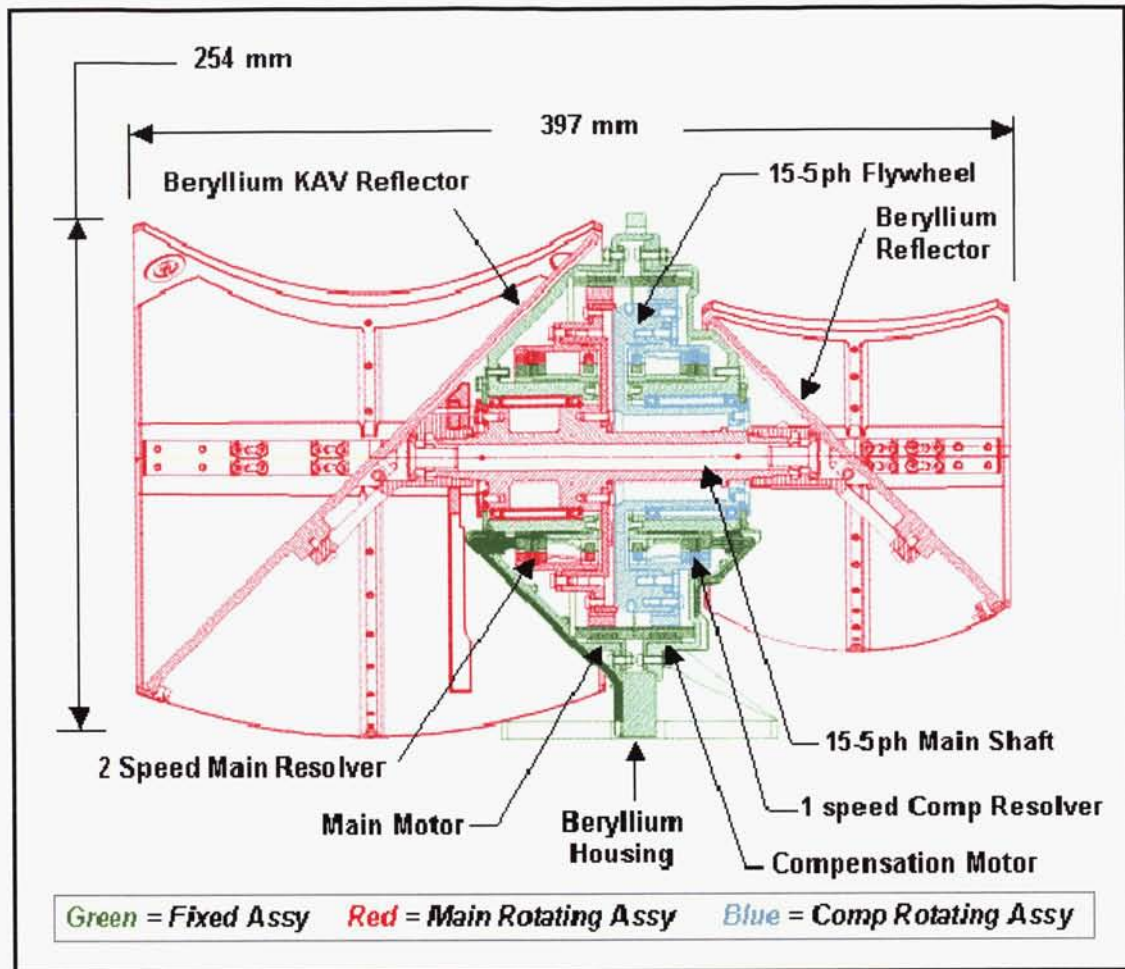


**Figure 4. Cross Section of the Scan Drive Mechanism illustrates compact packaging and materials selection used to meet weight and envelope requirements**

#### Reflector Alignment

The reflectors mounted to the main shaft with titanium spiders that allowed axial and rotational alignment. The spiders attached to the shaft using tapered square holes to ensure repeatability of position during successive assembly and disassembly operations. In order to meet the required alignment, as shown in Table 1, there were shims between the spider and the reflector. The shims were pre-machined in thickness increments of 0.01 mm (0.0005 in). This shim kit allowed for rapid alignment of each reflector to the spin axis on a coordinate measuring machine (CMM). The CMM was used to define the true angle of the reflector relative to the spin axis by defining multiple planes whose normal vectors defined a cone. The upper half of the split shroud was removed during alignment to allow full access across the entire reflector.

#### Radiated Susceptibility.

The cable harnessing and EMI design on the scan drive mechanism were things that fell into the category of things-not-done-so-well. Cabling is often one of the last features considered by mechanical designers and the scan drive mechanism was no different. The scan drive mechanism has two harnesses with connectors that extend a short distance out of the gimbal. Inside the gimbal the harness travels on the surface of the gimbal housing inside a cable tray. The harness was originally sheathed with braided shielding and the surfaces of the cable tray and gimbal housing were coated for conductivity. Despite these seemingly normal precautions, the scan drive mechanism dramatically failed the first radiated susceptibility test. Instead of providing a required 60 dB of attenuation in the 1 to 4 GHz frequency range, the scan drive mechanism harness and shielding were effectively acting like an antenna.



**Table 1. Requirements and capability for the ATMS Scan Drive Mechanism – to achieve a 3x increase in the scan rate, the single-axis SDM is accelerated and decelerated between measurement and calibration scans**

Parameter	Requirement
Scan profile period	8/3 seconds
Reflector to Scan Axis misalignment	<10mdeg
Earth View Sector Control Accuracy	+/- 35mdeg
Disturbance torque into spacecraft	<0.003 N-m between 0.01 and 1.0 Hz <0.1 N-m above 33 Hz
Torque capability	function under 3X worst case drag
Life (continuous service)	11 years
Mass	<10.9Kg
Average Power	<13W

There were numerous causes for the radiated susceptibility failure:

1. The beryllium housing halves and cable tray were attached with fasteners spaced too far apart and there were no provisions for EMI gaskets (the gaps were radiation sources).
2. There were no provisions for terminating the harness shield to the cable tray or to the entry into beryllium housing necessary to make a continuous Faraday cage.
3. The beryllium housing mesh air vent was installed with non conductive RTV – an ungrounded air vent can propagate RF energy.
4. The harness inner shield was tied to the outer shield inside the connector backshells - both shields terminated at one end can act as an RF antenna.
5. Motor and resolver harnesses were routed together providing coupling paths inside the harness.

Unfortunately these shortcomings were not uncovered until late in the testing program and schedule did not permit major design changes to fully correct the problem.

The fixes as shown in Figure 7 consisted of caulking the cable tray and housing halves with silver-filled epoxy, using silver-filled epoxy to ground the vent screen, and wrapping the harnesses with copper foil over the braided shielding. These fixes fell short of the required 60-dB attenuation, but fortunately the requirement was lowered to 40-dB attenuation and the reworked scan drive mechanism passed the radiated susceptibility test. The painful lesson from this experience is that every wire harness and EMI task is not necessarily similar to the last design and a quick discussion with a subject area expert can save weeks of time.

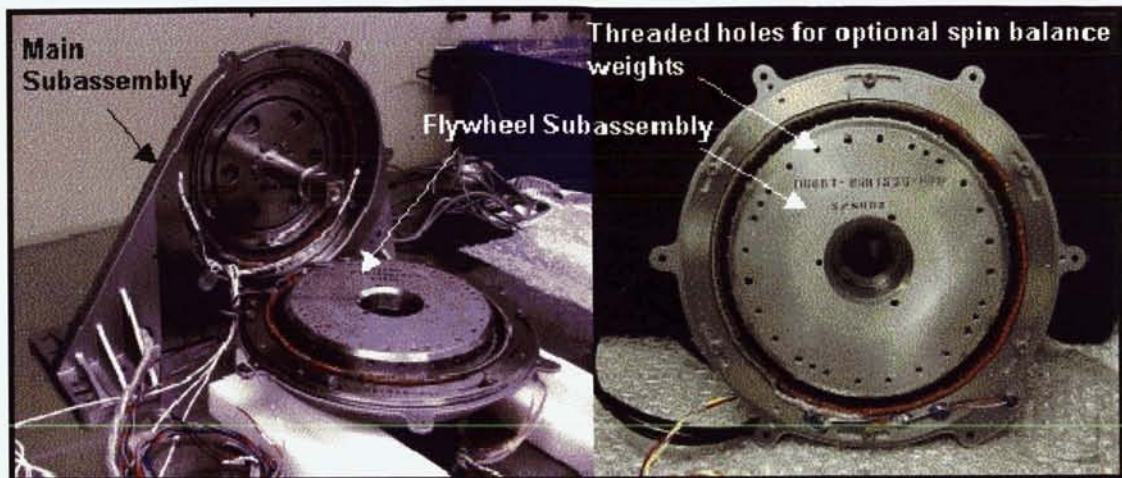


Figure 5. Torque compensation flywheel. The torque into spacecraft due to accelerating and decelerating the reflectors is compensated for by active control of the counter rotating flywheel. The flywheel inertia is lower than the inertia of the rotating reflectors so the flywheel is accelerated at the inertia ratio times the changing rotation rate of the main rotating assembly.

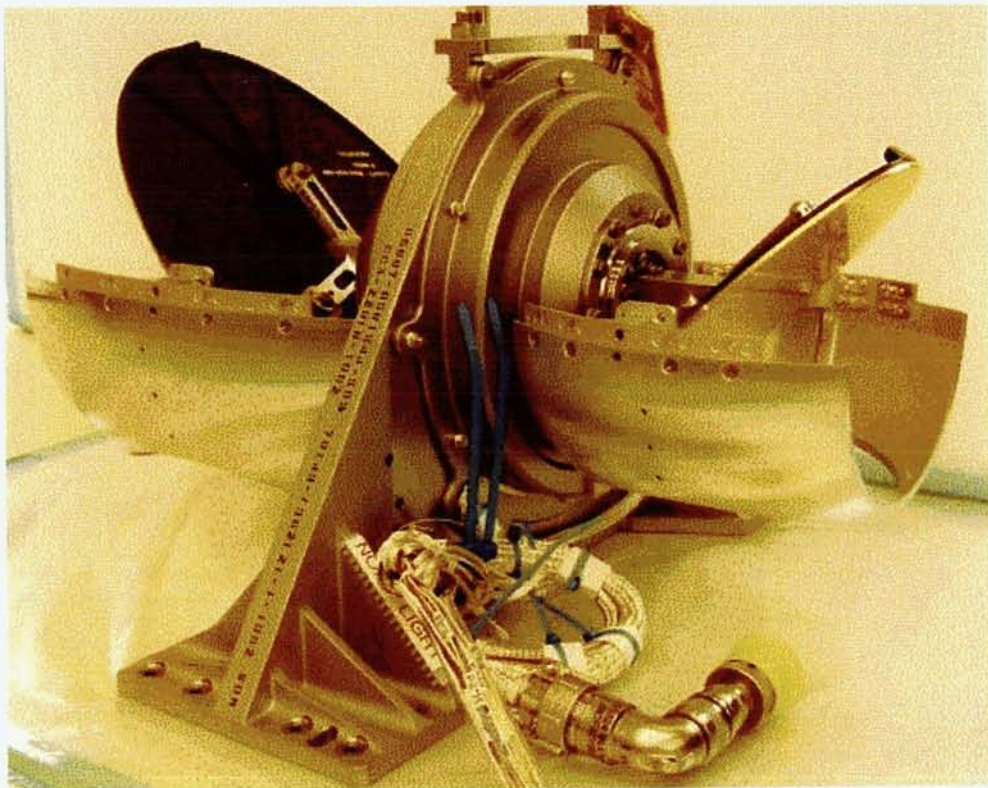


Figure 6. Upper half of Scan Drive Mechanism shroud is removed to verify alignment of reflectors and rotation center before and after each environment



### Gimbal Bearing Handling

The manufacturing handling of the gimbal bearings was good news, bad news story. On the plus side, bearing torque characterization tests were implemented as part of the manufacturing plan to detect torque irregularities. On the down side, the bearings did not have sufficient cleanliness controls. The bearings in the scan drive mechanism were designed for a life of 130 million revolutions for the reflector shaft bearings and 230 million revolutions for the flywheel bearings. Cleanliness of the bearings and lubricant was absolutely essential to achieve bearing life and smooth torque performance. Fortunately, we had a bearing torque test after the bearings were installed in the gimbal and on the third scan drive mechanism we found a noisy torque trace on a flywheel bearing duplex pair and on closer inspection we found debris in the bearing. The most likely sources of debris were:

1. Metallic debris was found and was most likely from tooling used for torque testing at the supplier. Inspection of the supplier tooling found metallic debris in threaded holes on the tooling.
2. White fibers were found and were most likely from cleanroom wipes or hair bouffants.

Although disassembly and replacement of the bearing was a painful schedule hit, the bearing contamination was caught before entering acceptance test. None of the other gimbal bearings ever showed erratic torque performance and a recommended cleanliness program was implemented by our bearing supplier to eliminate future contamination. Figure 8 shows our bearing torque set-up and samples of the debris found in the bearing.

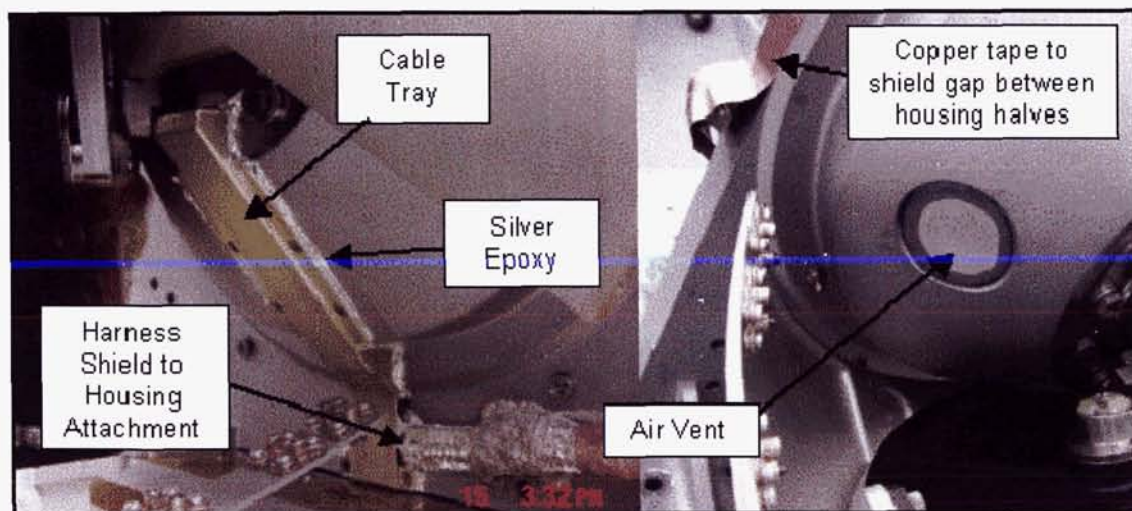


**Figure 7.** During radiated susceptibility testing in the 1 to 4 giga-Hertz frequency range, the scan drive mechanism harnessing acted as an antenna causing interference with the ATMS receivers. Various fixes were implemented to reduce the interference but adding the right EMI features earlier in the design process would have worked better.



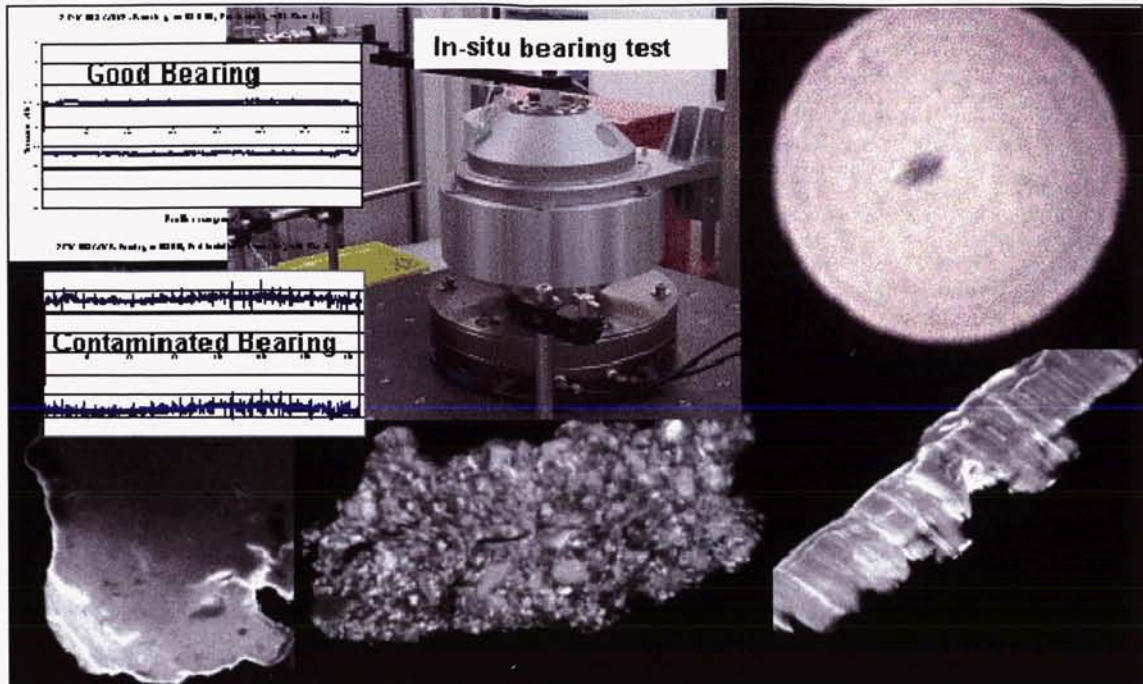


**Figure 8.** Contamination was found in the flywheel bearing of flight unit 3. The in-situ bearing torque test was invaluable at identifying bearing problems during the assembly of the gimbal. Fortunately disassembly features were built into the design of the scan drive mechanism.

#### Disturbance Torque Reduction.

Torque reduction was an aspect of the scan drive mechanism that went well. The level of torque disturbance allowed by the scan drive mechanism as shown in the Table 1 is less than 0.027 in-lb (0.003 N-m) across the 0.01 to 1.0 Hertz frequency range. To achieve this level of quiet operation, a number of disturbance reduction techniques were required. The first was to use a counter-rotating flywheel to compensate for the torque disturbance caused by accelerating and decelerating the reflectors three times each scan rotation. Other techniques used to achieve quiet operation included accurate balancing both the main antenna rotation assembly as well as the flywheel, and careful selection of parts including low run-out bearings and low cogging motors for both main and flywheel assemblies.

One of the primary reasons for designing the scan drive mechanism as two subassemblies was to allow access for balancing the main reflector rotation subassembly and flywheel compensation subassembly. In Figure 5, radial and axial threaded holes for balance weights can be seen on the flywheel subassembly. The balance weight holes were filled with set screws as required to achieve a 80,935 g-mm<sup>2</sup> (4.4 oz-in<sup>2</sup>) dynamic balance and 216 g-mm (0.3 oz-in) static balance. Figure 9 illustrates the features on each reflector shroud that allowed balancing of the main shaft and reflector subassembly. The main subassembly was difficult to balance due to the cutout in the shroud for reflector viewing. The cutout was balanced by placing a tungsten weight on the hole side of the reflector assembly. Several other smaller masses were added around the shrouds to account for other inconsistencies in geometry. The main subassembly was balanced to the same level as the flywheel subassembly.

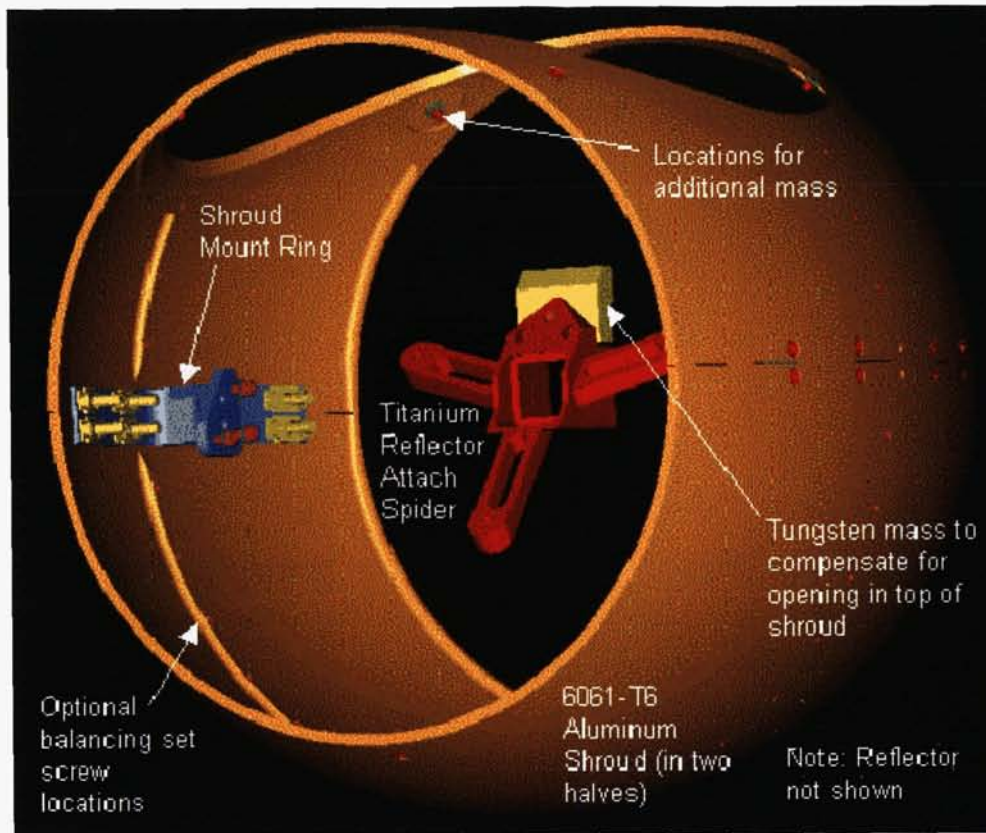


**Figure 9. To minimize uncompensated torque disturbances, balancing features inside each shroud allowed dynamic and static balancing of the rotating main assembly.**

One of the unique features of the scan drive mechanism was the counter-rotating flywheel used to minimize the torque generated by accelerating and decelerating the reflector each scan cycle. The scan drive mechanism acceleration/deceleration pattern (Figure 2) shortened the scan period and increased overall gap coverage but generated undesirable torque disturbances. The counter-rotating flywheel cancelled 92% of the torque from the reflector acceleration profile. The success of this approach is shown in Figure 10 where the scan drive mechanism was run both with and without the flywheel compensation.

#### Pointing Performance

The final link in the scan drive performance was the earth scan pointing. Pointing performance success was a combination of mechanical alignment and motor and resolver selection. As noted the brushless DC motor was a low-cogging ironless-core design which resulted in very low torque ripple. The main motor and reflector assembly position was controlled by a 64-speed and single-speed brushless resolver. The resulting pointing performance is shown in Figure 11.



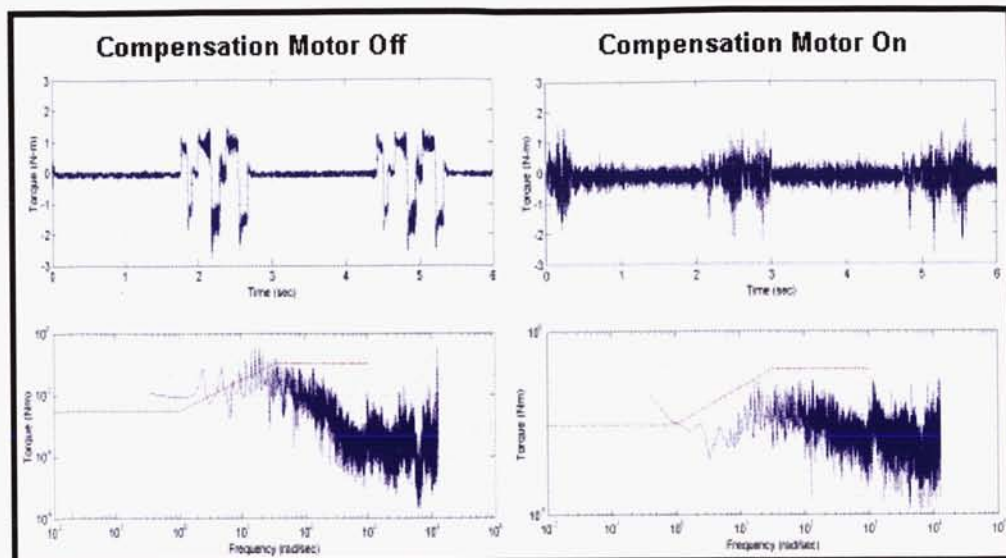


Figure 10. Reaction torque cancellation is successful with the compensation flywheel motor on. The Scan Drive Mechanism can operate in reduced mode (greater torque disturbance) using only the main motor.

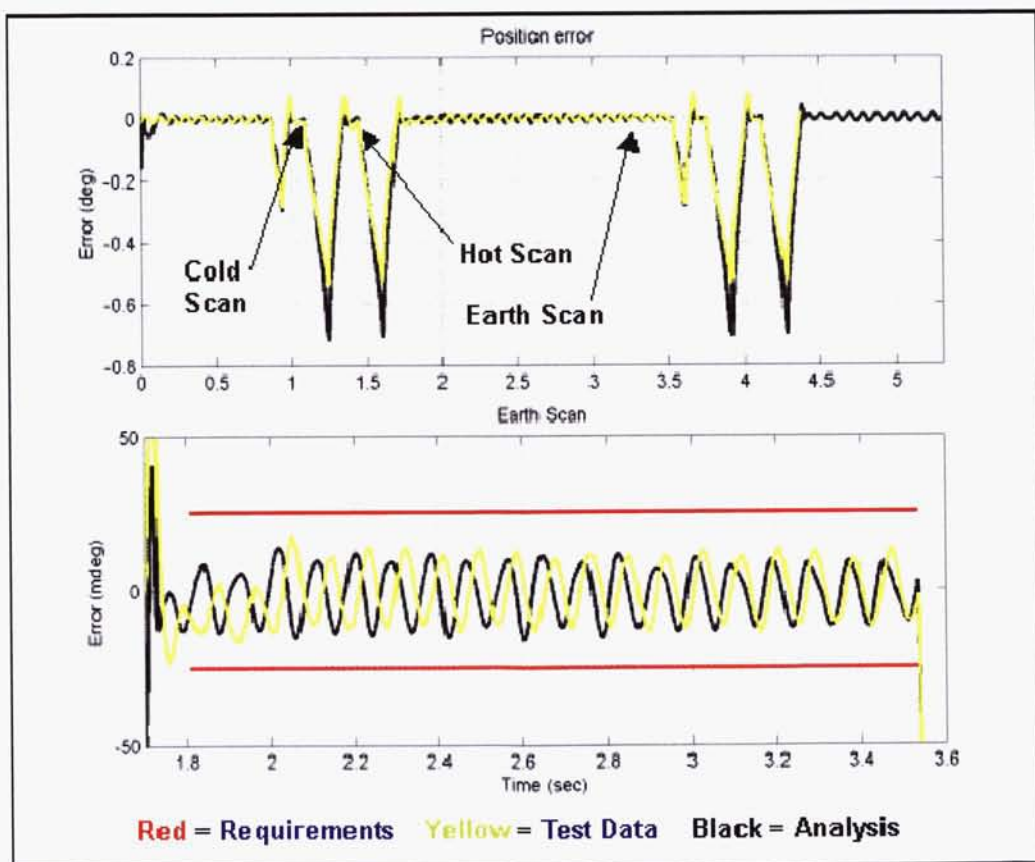


Figure 11. The Scan Drive Mechanism meets the ultimate test of pointing accuracy for earth scan as well as during hot and cold calibration. Acceleration/deceleration periods offer the ability to provide more earth scans per orbit.



### **Acknowledgements**

Every successful major project results from the combined efforts of many people. It is with great regret we don't have the space to list all of the many people who contributed time, effort, and talent to the ATMS Scan Drive program. None-the-less, most of those who participated in the Scan Drive program would agree that the following people were key to the success of the mechanism part of the program. Goddard Space Flight Center: Sergey Krimchansky, Robert Lambeck, Rick Schnurr; Northrop Grumman Electronic Systems: Dennis Lord, Terry O'Brien; Lockheed Martin: Ed Boesiger, Caesar Ching, Jeff Fisher, Patrick Herbert, Stu Loewenthal, A.J. Maher, Larry McGovern, Gordon Smith, Nic Mercer and Julie Price.

### **References**

- 1) Advanced Technology Microwave Sounder on NPOESS and NPP, Christina Muth, Paul Lee, Sergey Krimchansky, James Shiue, Allan Webb. NPOES IPO Information center, No. 06125, 06-16-2004, [http://140.90.86.6/IPOarchive/SCI/sensors/ATMSDraftBriefv4\\_AlanWebb.pdf](http://140.90.86.6/IPOarchive/SCI/sensors/ATMSDraftBriefv4_AlanWebb.pdf)
- 2) AMSU temperature plots: <http://pm-esip.msfc.nasa.gov/amsu/>



# Lessons Learned From the Windsat BAPTA Design and On-Orbit Anomalies

Steve Koss<sup>\*</sup> and Scott Woolaway<sup>\*\*</sup>

## Abstract

The Windsat spin drive assembly is a high precision constant speed drive assembly with challenging design requirements. Many difficulties were encountered during the design and build of the spin drive assembly. Additionally, after 2 years of nominal on-orbit operation the Windsat spin drive assembly spun out-of-control, resulting in a temporary cessation of the Windsat/Coriolis mission. After a lengthy investigation, telemetry analysis revealed that the resolver based tachometer data was likely being corrupted by two distinct kinds of slip ring noise. Workarounds were devised to successfully bring Windsat back on-line, and another similar spin anomaly was recovered from 5 months later. This paper will concentrate on the many lessons learned from the Windsat spin drive development and subsequent on-orbit anomaly. Additionally, the goal of the paper is to convey the "key things that were done well" as well as the "things that should be done different next time" (good vs. bad heritage).

## Introduction

Windsat is the primary payload on the Coriolis spacecraft. The Windsat payload size is roughly 2-meters square by 3-meters tall with a mass of 450 kg. Windsat is a demonstration program to evaluate the ability to exploit passive microwave polarimetry to measure the full ocean surface wind field (wind speed and wind direction) from space. This payload is very similar to the NPOESS CMIS payload currently under design. The Windsat payload instrument spins continuously at 31.6 revolutions per minute via a spin drive mechanism called the Bearing And Power Transfer Assembly (BAPTA). For accurate geolocation, the BAPTA is a precision device with a spin rate accuracy of  $\pm 0.05\%$  and a position feedback accuracy of

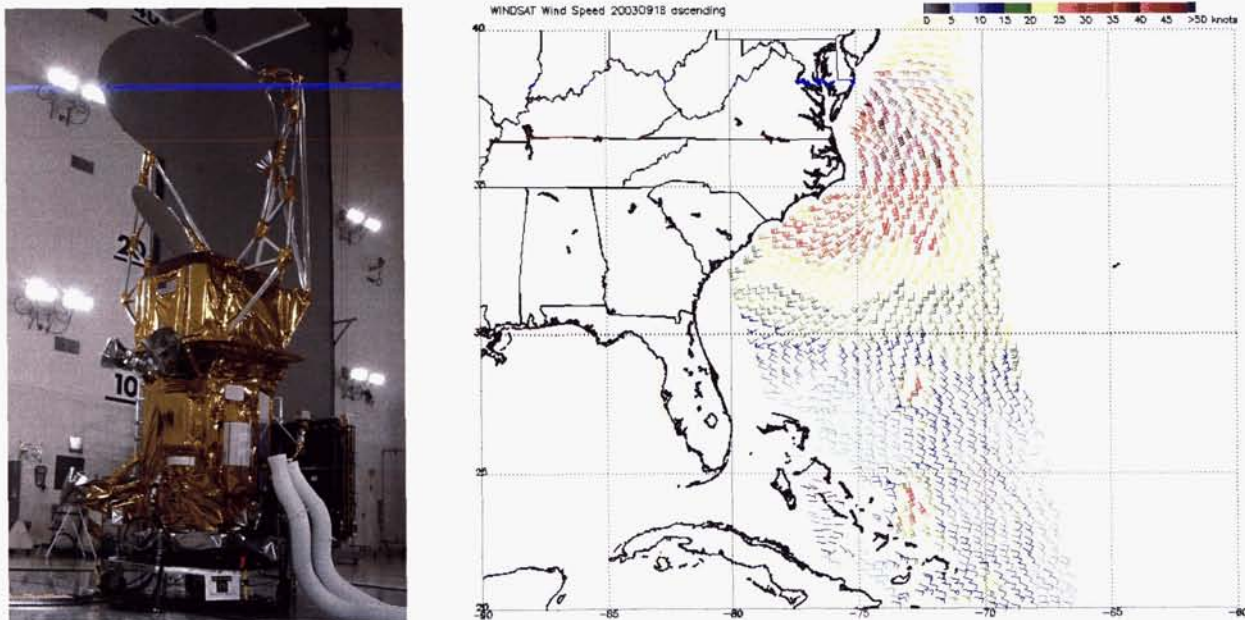


Figure 1. Windsat/Coriolis (left) and Wind Speed/Direction Data (right)

<sup>\*</sup> U.S. Naval Research Laboratory, Washington, DC

<sup>\*\*</sup> Ball Aerospace Corp, Boulder CO



$\pm 0.0055$  degree. To provide a zero momentum payload a 189 Nms momentum wheel spins in the opposite direction of the payload. During operation, the Windsat payload and BAPTA speed control is “slaved” to track the momentum wheel speed. This system performed nominally for 2 years on-orbit (33 million revolutions), until February, 2005 when the BAPTA abruptly spun out-of-control.

### BAPTA / Slip Ring Design Overview

The BAPTA design (Figure 2) incorporates a “bolt-on” slip ring assembly which provided ease of integration & test and “modular functionality” of the separate units. The BAPTA was designed with a redundantly wound three phase brushless DC torque motor and redundant dual speed (1X & 64X) resolvers. The resolvers provided 18-bit position resolution and better than 16 bit accuracy after conversion via a resolver to digital converter. This also enhanced the servo “stiffness” to maintain the tight  $\pm 0.05\%$  speed control required. Two angular-contact machine spindle bearings supported the aluminum-beryllium rotating housing, resulting in a very stiff, robust structural design.

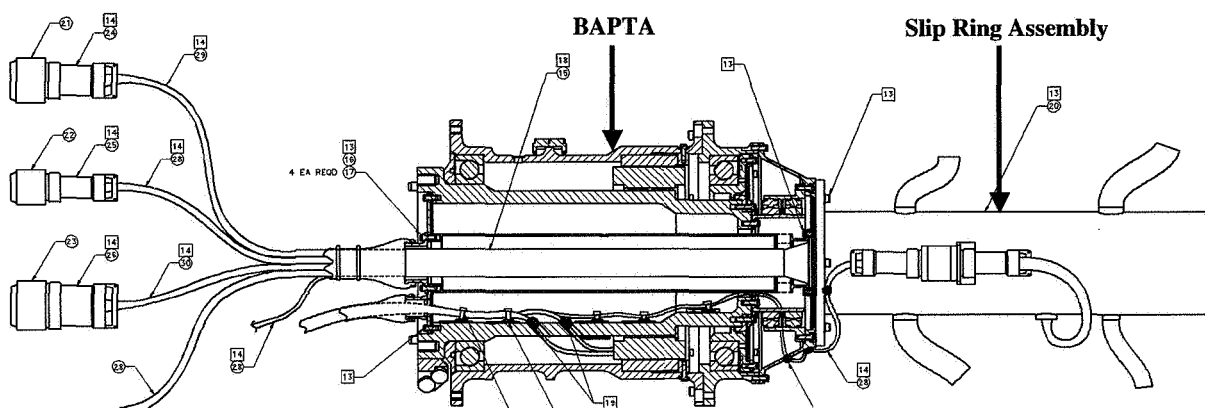


**Figure 2. BAPTA/Slip Ring Assembly**

The slip ring performance was the most challenging aspect of the BAPTA. The design life for Windsat is 3 years at 31.6 rpm, which translates to 50 million revolutions. Many spacecraft slip ring applications are for solar array drives that have rotational life requirements several orders of magnitude lower. The Boeing 376, NGST/Ball DSCS II spun/despun satellites, and a few others, have the only slip rings with life requirements in this class. The Boeing slip rings use silver rings with silver/MoS<sub>2</sub> brushes, whereas the DSCSII used a gold-on-gold slip ring design. However, unique to Windsat was the requirement to pass high-rate 1553 digital data and resolver transmitter signals across the slip ring, which are much more sensitive to high-frequency slip ring noise than these previous applications. Much life test data existed for slip rings, but little if any high frequency noise data existed for slip rings at the time of Windsat design. Fortunately, a 1968 vintage DSCS II program slip ring unit was found that had been through a 200 million revolution life test in the 1970's. This unit was tested in 1999 with a comprehensive slip ring test set, designed to monitor & record high-frequency slip ring noise. After several hours of noisy operation, the brushes pushed the significant amounts of wear debris to the side (Figure 3) and the slip ring noise went away. This test data gave us confidence that this type of slip ring would work, while another life test on a new unit closer to the flight design was run in parallel to the fabrication of the flight slip rings. The Windsat & DSCS II slip ring designs are of the oil-lubricated, gold-brush / gold-ring variety, but differ from any other gold-on-gold designs. The Windsat slip ring design consists of hard gold alloy brushes made from wire that is swaged to a rectangular cross section (Figure 4). The brushes were swaged flat instead of round in an attempt to accommodate more wear debris under the brush. Since Windsat & DSCS II spin in only one direction, a pair of trailing rings sit in a “W” shaped contact groove compared to the more common bidirectional “stubbing” & trailing round wire in a “V” groove configuration. The “trailing only” design is less prone to brush bounce compared to a “stubbing” design. Additional details on the DSCSII slip rings can be found in reference 1. Since there was great concern for slip ring noise problems, 100% parallel redundant rings were used for all signal rings resulting in 4-8 contacts per wire (4 vs. 8 contacts

depending on how the brush might “lift off” due to debris). Additionally, unlike the typical gold plated rings, the Windsat rings are solid soft gold with a hard gold flash coating on top (Figure 4).

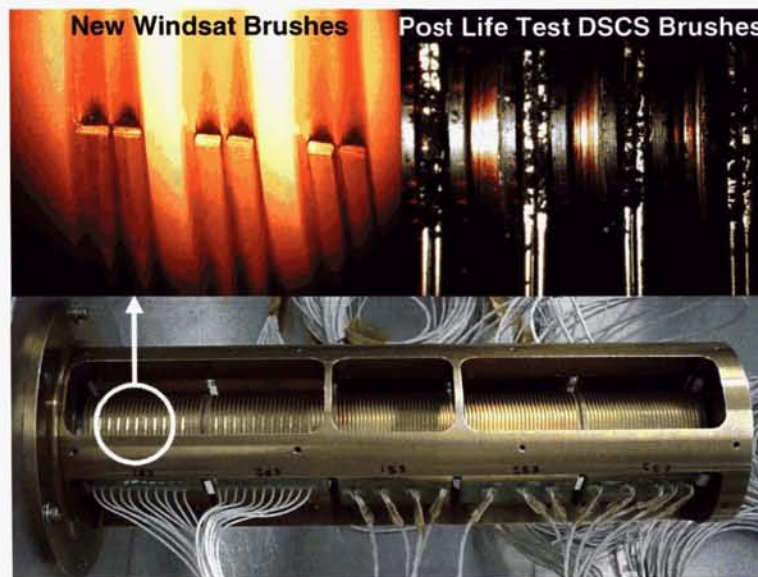


**Figure 3. Windsat / DSCS Slip Rings**

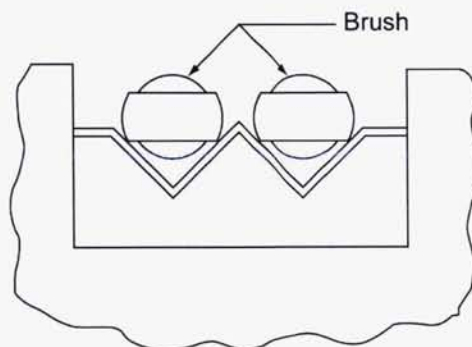


**Figure 4. Windsat / DSCS Slip Ring/Brush Contact Cross Section**

### **Design & Manufacture Lessons Learned**

There were numerous lessons learned during the design, build, and test phase of the Windsat BAPTA and slip rings. What will be discussed are the “key things that were done well” as well as the “things that should be done different next time”

#### Test Validated Torque Margins

The performance test program for the Windsat BAPTA required it to meet its rate and position accuracy requirements when operating under a 4X worst-case drag torque. This test was performed by measuring the cold drag torque (worst-case) and driving the BAPTA against an open loop torque motor (acting as a brake) to produce the 4X drag torque. The BAPTA was found to function well under this load but the increased BAPTA motor current caused the resolver based tachometer feedback signal to get noisy. The noise was due to secondary power supply feedback into the resolver-to-digital chip under high load. Adding an R/C filter and a Zener Diode circuit between the secondary power supply and the resolver-to-digital chip eliminated this noise. By performing performance testing at worst-case torque, this problem

was fixed on the ground allowing us to fully utilize our torque margin with full closed loop servo performance. It is common to demonstrate margin by analysis only or via friction torque measurements but less common to verify closed-loop servo torque margin performance. Only the closed-loop servo torque margin test performed would have caught our resolver noise problem. Additionally, the large margins built into all aspects of the design helped in the decision to fly “as-is” with numerous problems/defects that will be described hereafter.

#### Design/Test For Indefinite Stall At Hot TVAC

The NRL standard test program for the Windsat BAPTA required testing the BAPTA under stalled conditions at worst case hot thermal vacuum until the BAPTA reached thermal equilibrium. Designing the BAPTA to survive these conditions and performing this test gave us the confidence that it was extremely difficult to damage the BAPTA by mistakes or anomalies on the ground or on-orbit. As point of fact, during the Windsat on-orbit anomaly the BAPTA drive motor was hammered back and forth with full stall current at 13 Hz for 15 minutes with no damage.

#### Don't Put Precision Feedback Device (Resolver) In A Load Path

The Windsat BAPTA resolver was mounted at the end of the BAPTA, which supported the cantilever, mounted slip ring assembly. As such all cantilevered slip ring launch loads were transmitted through the resolver mounting structure. While this structure was capable of handling these loads, the resolvers are precision bonded to this structure and some slight settling of the resolver position was seen after the first BAPTA vibration and thermal vacuum testing. After this initial “set” the position did not drift noticeably and was thus more of a “headache” than a real problem. The layout of the Windsat BAPTA does not leave many optional locations for locating the resolver (i.e., out of a load path). However, for future designs consideration should be given to placement of precision feedback devices relative to load paths.

#### Blind Holes, Filtered Vents & Labyrinth Seals Prevent Contamination Problems – Both Going In And Coming Out – Especially On Slip Rings

The Windsat BAPTA and slip rings had a design requirement for blind holes whenever possible and filtered vents and/or labyrinth seals to prevent contamination problems. Many drives have suffered anomalies due to contamination in bearings or air gaps. This is especially critical on designs with slip rings. Slip rings with the life requirements of Windsat create significant amounts of wear debris. Managing this debris and keeping it out of bearings, air gaps, (and shorting rings) is a crucial part of the design. In the Windsat design the slip ring assembly had labyrinth seals that kept the slip ring debris contained within the slip ring and away from bearings, motors, and resolvers. Slip ring barriers were made with heights large enough to prevent debris buildup ring shorts. Additionally, all power + rings were grouped together and all returns were grouped together to minimize potential shorting paths. On the signal side we had alternating “odd & even” side brush blocks for consecutive signal wiring and ring assignments of shield, +, -, shield (4 rings per twisted shielded pair, Figure 5) to prevent adjacent circuit shorting and minimize noise and crosstalk. A final lesson was learned from inspecting the old DSCSII slip ring life test unit, which was full of wear debris. It was found that the oil impregnated reservoirs used to help replenish the relatively high vapor pressure oil used in the 1970's had a side benefit of acting as a “fly trap” to collect a thick layer of wear debris away from the critical brush/ring interface. Thus while the new low vapor pressure oil used on the Windsat slip rings did not need oil reservoirs, they were maintained for their “wear debris management” function.

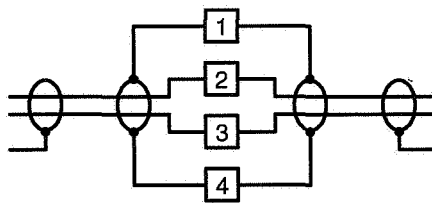


**Figure 5 – Signal Rings – Twisted Shielded Pairs**



### Motors - Not Challenging But Acts Like a "Magnet" For "Mundane" Problems

For various reasons spaceflight motors seem to have an unusual amount of minor manufacturing problems, which at best impact schedule and at worst impact reliability. As such, special attention should be paid to the motor contract and it is strongly recommended that an extra thorough pre-ship test/inspection/documentation review be conducted at the motor vendor prior to accepting motor delivery. On Windsat, motor manufacturing defects drove us to procure motors from 2 different vendors and neither vendor produced defect-free motors – in the end we flew the motor that had the least defects. A listing of problems that have been encountered with both the Windsat BAPTA motors as well as a few on other programs follows:

- 1) Windings potted in Stycast thermally conductive epoxy. Stycast cracked (Figure 6) after thermal cycling as a result of CTE mismatch between Stycast & copper windings. Resulted in X-rays of motor to look for crack induced strain on windings. Also resulted in "painting" the Stycast with Urelane in an effort to contain any pieces of Stycast that might pop off and jam the air gap or bearings. On the Windsat BAPTA, we ended up flying a motor that had the least cracks in the Stycast. While Stycast winding encapsulant may not cause a problem on small motors, on large motors like the 147-mm-diameter Windsat BAPTA motor it is probably best to avoid potting windings in Stycast.

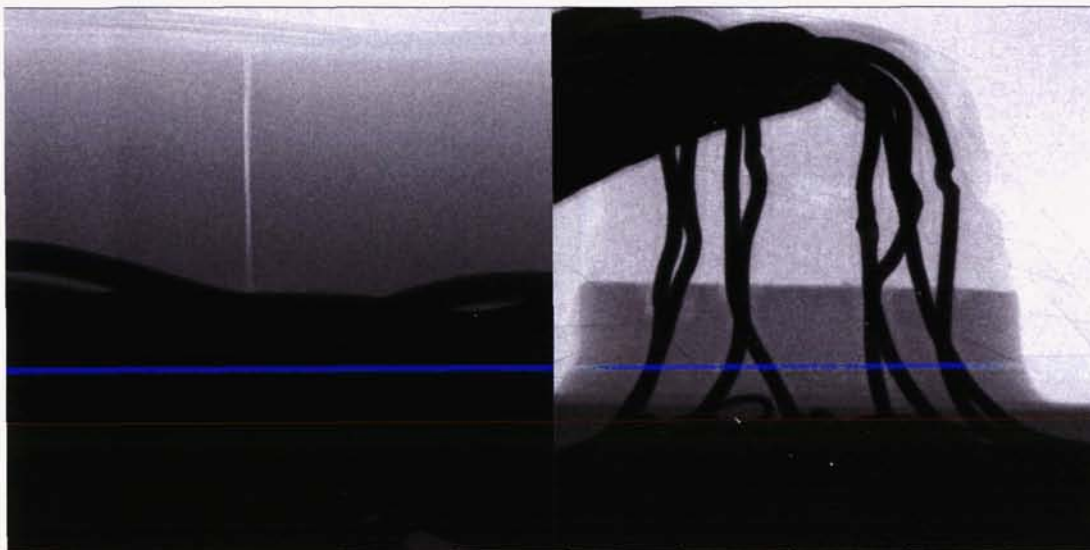


**Figure 6. Fine-Focus X-Rays, Cracked Stycast (left), Nicked Hookup Wires (right)**

- 2) Lamination stack painted with "fluidize". Problems with fluidize adhesion/flaking off. Risk/concern that fluidize flakes could get into bearings.
- 3) Magnets or non-corrosion resistant backiron nickel plated. Problems with nickel plating adhesion/flaking off. Problems with epoxy washcoat bubbling/peeling off. Risk/concern that plating/coating flakes could get into bearings. Use corrosion-resistant materials to the greatest extent possible to minimize need for plating & epoxy coating. When coating is required perform tape test & detailed inspections.
- 4) Hookup wire strain relief problems. Various instances of insufficiently designed strain relief in multiple vendors/designs wherein wire insulation damaged (Figure 6) or wires broken. Strain relief is something that rarely gets enough attention.
- 5) Problems with air gap tolerances. Tolerance stack analysis required both at room temperature and worst-case temperatures. Analysis should be verified by test/measurement.
- 6) Problems with motor cleanliness. Particulate contamination, which could get into bearings & reduce lubricant life. In extreme cases debris in tapped/helicoiled holes, which could jam, air gap or bearings. (Watch out for helicoil tangs, small tap pieces, etc)



- 7) Finally, while not necessarily a problem, a very faint motor “ticking” sound was found wherein the tick corresponded to the commutation frequency of the motor (6-step commutation) and the intensity of the sound was proportional to motor current. This was first noticed during Windsat EMI in the “soundproof” EMI chamber. The drive had been listened to with a mechanics stethoscope earlier as standard practice but the faint tick was not noticed. However, the stethoscope test was done in a clean room next to the air handling system so it is quite possible the “tick” sound was always there but not noticed until the dead quiet EMI chamber. The tick might have been just the magnetostrictive contraction of the armature and normal – it is not known for sure. The ticking sound was tracked through system level vibe, TVAC, etc and it never changed and the source was never isolated. A lesson learned is to turn off all noise sources (air handlers, etc) when listening to something and to use a microphone to provide an audio record that is subsequently analyzed by sound /frequency analysis software if possible.

#### Value Of Screening Torque Traces On Bearings – Especially Thin Section

The Windsat slip rings were built as a standalone assembly with their own bearings. This was done for ease of integration and to minimize potential conflicts with the slip ring integration and test schedule. The bearings used were angular contact thin section (50.8-mm (2”) ID, 63.5-mm (2.5”) OD, 6.35-mm (0.25”) cross section, 42 balls). Since the slip ring vendor had limited bearing design/analysis capabilities, NRL helped them with bearing design and analysis. Additionally NRL provided the bearings and assisted with installation. During bearing screening torque tests conducted at NRL prior to installation, several bearing pairs were rejected as a result of torque spikes at the bearing cage frequency (Figure 7). The bearing had very thin “rubber band like” one-piece phenolic retainers, which were difficult to dimensionally control. Many of the cages were out-of-round and would pinch the riding land of the bearing, resulting in torque spikes at the cage frequency. The torque screening tests ensured that these bearings were rejected and after several iterations acceptable bearings were obtained and flown.



**Figure 7. Screening Torque Trace (left) & Thin Section Bearings (right)**

#### Analysis & Life Test Data For Couplings Cannot Be Overlooked

The Windsat BAPTA design used two different bellows shaft couplings. Shaft couplings are often a “necessary evil” when multiple shafts must be connected and small amounts of misalignment would result in large/unacceptable bearing loads. On the Windsat BAPTA the shafts in question were aligned with high precision, however, there was no solid analytical prediction for coupling life. One of the couplings was a “catalog” design with a published fatigue life/misalignment capability. When the vendor was pressed to back up the published data, however, it was found that it was extrapolated off tests of the first few couplings made 50 years ago and that “you really should run a test”. A life test was run on one of the couplings with the flight misalignment duplicated. The life test was stopped after the required design life of 3 years / 50 million revolutions as it was deemed unlikely that a fatigue failure would occur past that point (and because the life test gearbox wore out). There are many different styles/designs of shaft couplings, the more common being Oldham and Bellows. The Oldham can wear and have backlash issues whereas the bellows can fail by fatigue (either in vibration testing or operation). An assessment of the life-limiting



impacts on the design should be done, and if necessary, a life test should be conducted. The program did not have the time or funds to conduct a life test on the second bellows coupling used and the program accepted that risk. This has been borne out by the fact that the BAPTA has so far seen over 40 million revolutions to date without a failure.

#### Many Commercial Slip Ring Vendors Can Use Help When Designing For Space, Especially When it Comes To Thermal Design & Bearings

There several slip ring vendors being used for space in the USA. All of the slip rings vendors are primarily "commercial" slip ring vendors wherein space is a sideline business. As such, it is recommended that special attention/oversight be given to the slip ring vendor to ensure the unique design and reliability aspects related to space are satisfied. For instance, none of the slip ring vendors have special expertise in bearing design, or detailed thermal analysis that is typically required for long-life high reliability space applications. As such, NRL and Ball assisted the slip ring vendor with the bearing design and purchased, lubricated, screened, and helped install the bearings. NRL also performed a detailed thermal analysis and provided the information to the slip ring vendor to assist in temperature and thermal expansion/brush alignment analyses. The detailed thermal analysis NRL performed on the Windsat slip rings was critical in ensuring adequate performance from the slip rings as well as enabling us to understand and recover from the Windsat BAPTA on-orbit anomaly. This will be discussed further in the next section "On-Orbit Anomaly Lessons Learned."

#### Slip Rings – "Devil is in the Details"

Slip rings are a fairly 'low tech' device. However, for high reliability, long-life space applications "the devil is in the details" to ensure proper performance and reliability. When passing high-frequency signals across slip rings this problem is multiplied greatly. On the Windsat slip rings many "detail problems" were encountered such as the following:

- 1) As mentioned previously the Windsat slip rings were solid "soft" gold with a thin hard gold flash top coating. The slip rings were sent to Ball Aerospace for cleaning and lubrication. After cleaning a microscopic inspection was performed wherein it was noticed that several of the slip rings were cracked (Figure 8). After the first cracks were discovered a 100% microscopic "mapping" of the slip rings were performed and other cracks were found. The rings were also eddy current inspected, which also uncovered a few faint cracks. None of the cracks affected the ring resistance/impedance, and the brush wear actually tended to smear over the cracks in a beneficial manner so it was decided that the cracks were acceptable. Finding cracks on solid "soft" gold slip rings was surprising. It was determined that the cracks were caused by plating with a current density that was "in-spec" but at the high end of the spec. Subsequently the current density tolerance was revised and the second, flight spare slip ring was plated with no cracking. While the cracking was not desirable, no problems were ever caused by the cracks.

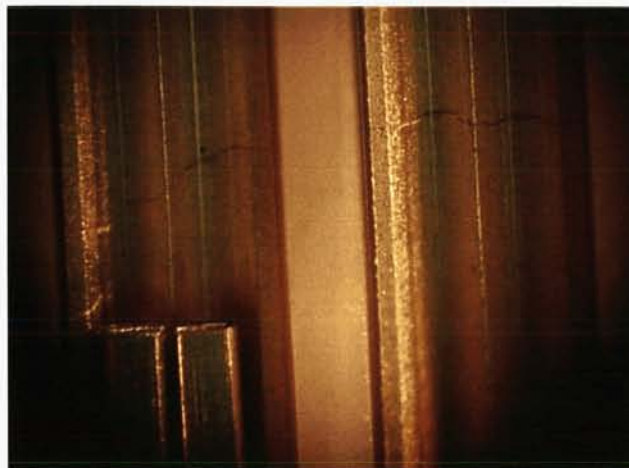


**Figure 8. Cracked Slip Rings**



- 2) The slip ring wires used Tefzel wire insulation per MIL-W-22749/44 and M27500-28SR2S23. There were numerous instances wherein the wire insulation cracked at bend radiuses (Figure 9). This required a lot of tedious repair work and inspection. Similar problems were also seen on the Tefzel motor hookup wires. While the definitive cause of this was not determined, no cracking was seen in the second, flight spare slip rings where the wire used was procured from Raychem as Raychem wire had been used on the rest of Windsat with no cracking. When digging into other experience with this problem it was found that the Tefzel cracking *seemed* to occur most often in the presence of elevated temperature epoxy/potting cure operations. However, no definitive cause/effect relationship was determined.

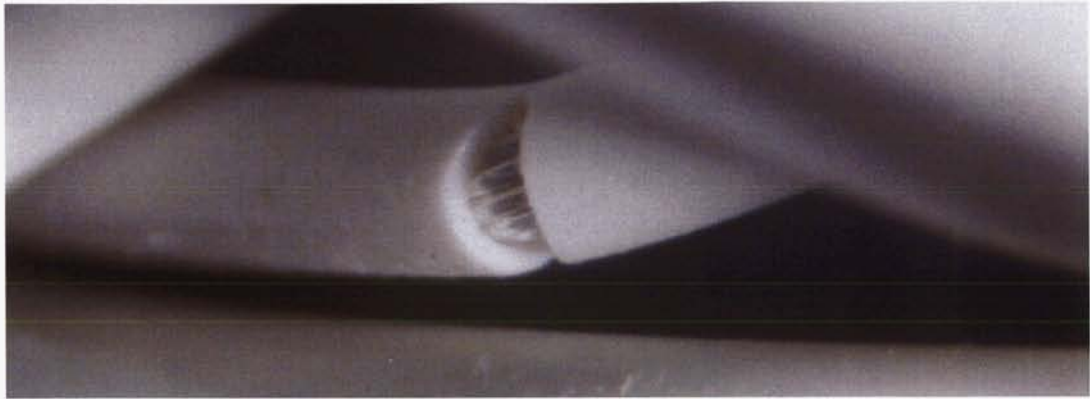


**Figure 9. Cracked Tefzel Wire**

- 3) As mentioned previously, the slip rings were cleaned and lubricated by Ball Aerospace. During cleaning an analysis of the solvent rinse was conducted, which revealed silicone contamination. The slip ring specification prohibited any silicone materials, lotions, etc from being used on or near the slip rings as silicone contamination can cause lubricant dewetting and form compounds, which result in slip ring noise. The source of the contamination was eventually traced to Kapton tape that was mislabeled by the tape vendor and contained silicone adhesive, even though it was labeled as acrylic adhesive. A lengthy cleaning process was undertaken to remove the silicone from the slip rings. If not for the extraordinarily thorough cleaning and lubrication process procedures at Ball, the slip rings would likely have had silicone contamination problems, which would have resulted in disastrous consequences. It is recommended that solvent rinse analysis be conducted during slip ring processing of slip ring assemblies.
- 4) The Windsat slip ring had 137 rings and 274 brushes in a 305-mm (12-inch) length. Slip ring-to-brush alignment was very challenging and key to proper functionality. Alignment features and tight tolerances were necessary to properly control alignment. Additionally, a detailed thermal model/analysis was performed to analyze the effect of thermal gradients/temperature on slip ring to brush alignment. Finally, displacement during vibration was analyzed to ensure that brushes would not "jump rings" during vibration testing/launch. None of these conditions presented a trivial problem. Furthermore, as the slip rings wear, they create wear debris which tends to get pushed to the side/out of the contact path with continued rotation. During normal operations the slip rings are maintained within a narrow 25-30°C temperature band. However, occasionally the spacecraft goes into a radiation upset induced safe hold which turns everything off and the slip rings cool to approximately 0°C. Starting up from this temperature results in displacement of the brushes due to differential thermal expansion and presents an opportunity for "running in the debris on the side of the road". In fact, the slip ring/brush displacement at cold temperature may have played a part in the on-orbit anomaly that will be discussed in detail later as both on-orbit BAPTA anomalies occurred within weeks of a safe hold event.
- 5) The Windsat slip rings were lubricated with a thin film of oil supplied by Ball Aerospace. During cold temperature acceptance TVAC testing (-20 to 5°C) slip ring noise was found. This noise was due to hydrodynamic effects of the thickened oil at these temperatures. It was determined that



this noise could be “burned through” with the 2 Amps of current used on the power rings but not with the 100 mA of current used on the signal rings. Additionally, the rings that exhibited oil exhibited a bead of excess oil that clung to the brush at the ring contact (Figure 10). Rings without this oil bead did not seem to show cold temperature noise. This problem was solved by 2 methods: 1) re-oiling the slip rings with a slightly lower quantity of oil which did not result in the oil beads at the ring contacts, and 2) adding a heater to the slip rings to try to keep the rings above 5°C. After retesting with the lower oil quantity there was no noise found all the way down to -20C.

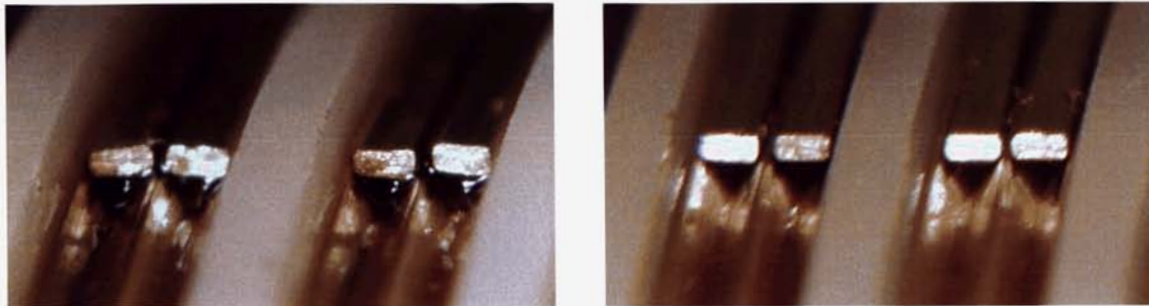


**Figure 10. Original Oil Quantity (Left)**

**Final Reduced Oil Quantity (Right)**

- 6) Since the Windsat slip rings had a high life cycle requirement and slip ring noise & wear are a function of brush force, the brush force was measured on all 274 of the slip ring brushes. This brush force inspection was a difficult, painstaking process, but it paid off in that it revealed that despite the best of efforts and tolerancing, many of the brush forces were significantly out of spec.
- 7) It is typically believed that the environment (air vs. vacuum) does not affect gold on gold slip rings but does affect silver/MoS<sub>2</sub> slip rings. On Windsat, we found that after running at 30 rpm for approximately one week in air we would get high-frequency slip ring noise. This noise would clean up / go away after several days of running at 30 rpm in nitrogen or vacuum. While there were no time/funds to investigate the mechanism for this, it is postulated that an extreme pressure additive in the oil may be oxidizing in air to form insulating compounds. In N<sub>2</sub> or vacuum this material may be worn/pushed away and cannot form in the absence of oxygen. This didn't seem to have any adverse impact on the performance of the life test units. Additionally it had no impact on Windsat as air drag limited the speed of the full up Windsat payload in air to a few rpm and there was never enough revolutions in air to run into this problem.
- 8) The Windsat slip rings are constructed from a stack of slip ring modules. Prior to the module “stacking” the individual modules were thermal cycled to screen for “bad bond” or rings going open circuit. These screening tests resulted in rejecting a module with multiple opens and finding a module with one bad circuit that was relegated to a spare, prior to wiring and any “pain”.
- 9) The slip ring brush design was an exact copy of the DSCSII design. However, since DSCS had fewer and smaller diameter rings, the brush placement differed. Unfortunately, the placement used left the tips of the brushes dangerously close to the brush/ring contact point. In fact a few of the brushes created large piles of run-in debris, which was traced to contact at the brush tip and “digging in”. Fortunately, this only affected a few brushes and enough spare rings were available to reassign these circuits.

Slip rings are very process-sensitive devices. It has taken decades to learn all of the processes that need to be controlled/paid attention to in order to produce reliable slip rings. Many of the people who “learned these lessons” have left and the program should make sure that those details have been carried forward into the current production or the “heritage” cited may not be valid. This issue was encountered when building the Windsat slip rings, which traced their heritage back to the DSCSII program, last built in the 1970's. There were actually still several people at the slip ring vendor and Ball who worked on the DSCSII slip rings. However, undoubtedly there was a lot that was forgotten, especially when it came to “why it was done that way”. The Windsat slip ring design was very similar to DSCSII but not the same. One “heritage” mistake we made on Windsat was to copy the DSCSII signal and power brush design, exactly

to print. The DSCSII unit had 12-mm (0.5-inch) diameter signal rings with correspondingly short signal brushes and 25-mm (1-inch) diameter power rings with longer power brushes. For various reasons (well thought out) Windsat ended up with both signal and power rings at 38-mm diameter (1.5 inches). The Windsat/DSCSII power brushes were much longer and had a much lower stiffness/spring rate. This made the power brushes much less sensitive to variations in brush force from misalignment and thermal excursions when compared to the shorter signal brushes. In hindsight, this was an obvious error it would have been better to not blindly copy “heritage” and optimize the brush design for brush force sensitivity – i.e., make all brushes like the power brushes.

#### Values of Thorough Testing (vs. Dumb & Happy)

This may seem obvious and not really a lesson learned, however, there is always budget and schedule pressure to reduce testing. On Windsat we did not compromise when it came to thorough testing. This had the extremely beneficial effect of catching many problems and fixing them before they were flown. However, it also had the parasitic effect of “finding lots of blemishes under a microscope” that we might have been just as happy to not know about. A highlight/recap of some of the things that were found by extremely thorough testing that would not have been uncovered with “normal testing” follows. Some of these had a big impact; others were just “interesting”.

- NRL test set designed to detect high-frequency noise finds problems not seen in typical slip ring tests
  - Found at least some cold temp noise could be “burned thru” with current
  - Found high-frequency noise in air vs. GN<sub>2</sub> & vacuum
- Found torque decreases significantly with vacuum level (<pressure=<friction)
- Found & solved cold temperature noise during acceptance testing which helped diagnose on-orbit anomaly (more on this later)
- 100% microscopic mapping of rings also helped diagnosis of anomaly & revealed cracks previously unnoticed
- Value of slip ring module level thermal cycle tests screening “bad bond”

#### **On-Orbit Anomaly Lessons Learned**

After 2 years / 33 million revolutions of nominal operation the Windsat BAPTA abruptly spun out of control (Figure 11). After a lengthy (and confusing) investigation, telemetry analysis revealed that the BAPTA resolver-based speed data was corrupt. Figure 11 shows the commanded speed, BAPTA resolver-based speed estimate, and the “true” BAPTA speed derived from spacecraft rates from the spacecraft Inertial Measurement Unit and conservation of momentum. In this figure, you can see the BAPTA speed going unstable and the true speed diverging from the resolver-based speed. Once the instability grows, the three-axis stable spacecraft begins to yaw uncontrollably, which triggers a commanded BAPTA spin-down and spacecraft “safe hold” mode. Since the data shows that the resolver system appeared to be corrupt, and the spin drive had redundant resolvers and electronics, the “B-side” was selected. The redundant B-side, however, was also found to be unstable (Figure 12). After extensive unsuccessful (and very confusing) troubleshooting, some troubleshooting commands were issued wherein the A&B sides of the BAPTA electronics were simultaneously turned on and the stationary 16-bit resolver position was queried. With the BAPTA stationary, both A and B side angles read identical (as they should) and they also read the correct angle (as roughly determined via external means). It was recognized at this point that all post-anomaly spin/troubleshooting was conducted at cold temperatures (around 5°C) as a result of the Windsat payload being off from the BAPTA induced spacecraft safe-hold. From earlier experience gained during cold temperature acceptance testing of the slip rings; it was theorized that cold temperature related slip ring noise was likely corrupting the B-side resolver which had its “transmitter” coil power passed across the slip rings. While the slip rings were able to start up at temperatures around 5°C during the first two years of operation, it was postulated that the effects of two years (33 million revolutions) of operation had resulted in a greater tendency for slip ring lubricant related noise to occur at cold temperature. Additionally, with 20/20 hindsight it would have been better to size the slip ring heater larger, but it was added late in the program when there was no more power left in the budget and no justification for a change that would “break” the power budget as the slip rings worked fine at that time all the way



down to -20C. Even with a larger slip ring heater care would need to be taken with thermal gradients and brush/ring alignment.

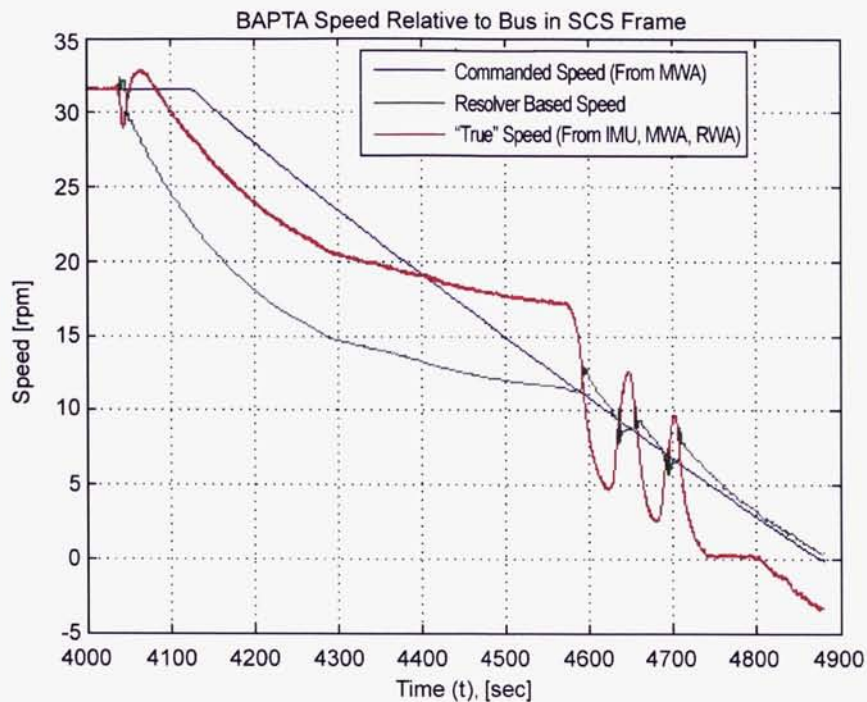


**Figure 11. Original On-Orbit “A-Side” Spin Anomaly**

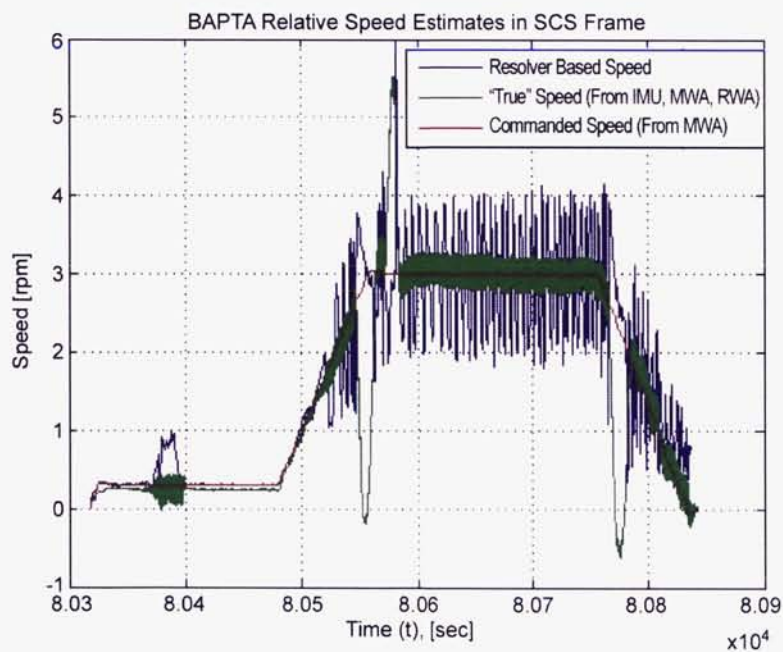


**Figure 12. Original Anomaly “B-Side” Troubleshooting Low-Speed Spin**

Additionally, it was postulated that a “blobs” of slip ring debris could have been the cause of the original A-side instability which occurred at the operational temperature of 25-30°C. However, with limited on-orbit telemetry there is no easy way to confirm this. One item of note is that while we had full electrical redundancy and multiple redundant (parallel) slip ring contacts, all of the rings have the same/common wear life (i.e., wear life is not redundant). With these anomaly theories in hand a workaround was devised to power on the payload on for several days to warm up the slip rings prior to BAPTA / momentum wheel spin up. (The payload had to be powered off during spin up to minimize the risk of blowing a fuse on the spacecraft power bus from the “peak” current draw during spin up.) On June 13, 2005 the workaround was successfully implemented and the BAPTA operated nominally on the B-side.

On October 27, 2005, however, the BAPTA went unstable again, this time on the B-side. During this second “B-side BAPTA anomaly”, the BAPTA went unstable in a manner similar to, but not quite the same as the original A-side anomaly (Figure 13).

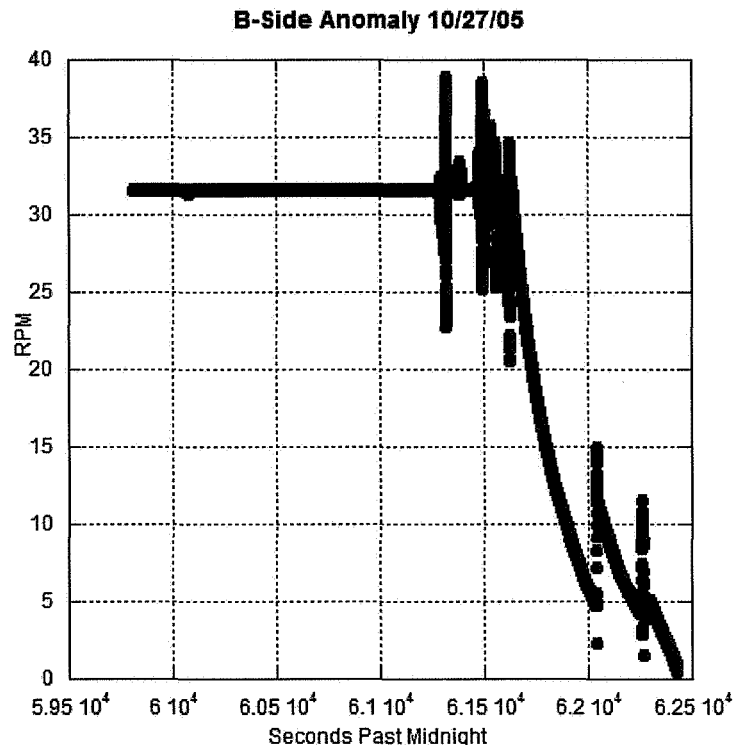


**Figure 13. Second On-Orbit “B-Side” Spin Anomaly**

Noteworthy during the B-side anomaly, the speed had several unstable “blips” followed by recoveries until it finally went fully unstable and triggered a spacecraft momentum induced safe hold and spin down (Figure 14).

The second anomaly on the B-side presented the opportunity to confirm/refute the theory that slip ring debris “ingestion” was the cause of the original A-side anomaly. If slip ring debris induced noise were indeed the cause of the A-side anomaly then there was a good chance (based on our DSCSII life test unit experience) that subsequent running had cleared the debris and “cleaned up” the noisy A-side resolver rings. Therefore, troubleshooting was conducted at low speed (0.3 rpm) on both the A and B sides of the BAPTA after the slip rings were warmed (to 15°C) to avoid the cold temperature slip ring noise phenomenon. Indeed the B-side remained noisy/unstable but the A-side was now clean/stable after the 4.5 months of additional run-time since the original A-side anomaly (Figure 15).

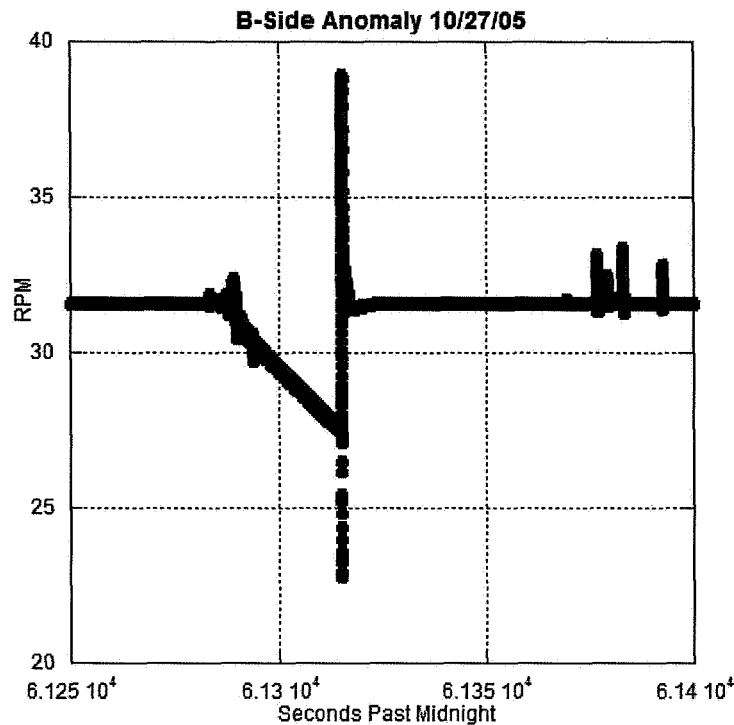


**Figure 14. Close-up of Speed "Blips" and Recoveries 2nd "B-Side" Spin Anomaly**

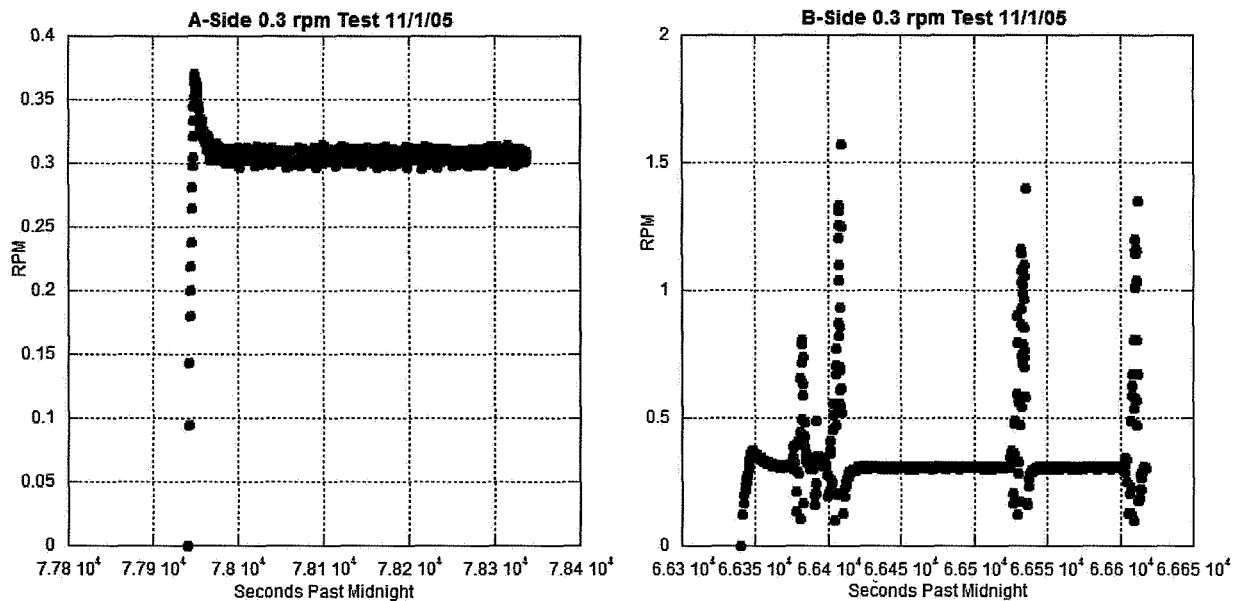


**Figure 15. Second On-Orbit Anomaly "A & B-Side" Troubleshooting**

Windsat was then successfully restored to operational status again on the *A-side* on November 6, 2005. Procedures have been developed to provide a speedy recovery should future anomalies of this nature arise. Additionally, if the condition eventually arises wherein both A&B sides are noisy at the same time it may be possible to run the motor open loop (forwards or backwards) in a troubleshooting mode to clean



up the slip rings as long as the slip rings are not noisy to the point that the motor cannot be commutated (the resolver is also used to commutate the motor). The ability to run many of these troubleshooting modes has proven invaluable in troubleshooting and recovering from problems both on the ground and on-orbit.

## **Conclusion**

The Windsat BAPTA is a long-life precision spin drive assembly with challenging requirements and a difficult development program. As of November 2005, it has operated for 2.5 years of its 3 year life goal and it continues to operate well enabling Windsat to generate good wind speed and direction data. However, after two years of operation, evidence of slip ring noise on the resolver rings has appeared which has resulted in speed anomalies requiring safe-hold recovery operations. Looking back on the experiences gained during the development and on-orbit operations some key things were done well and should be done again (good heritage) and some things could be improved next time (bad heritage). A brief recap of the key items follows:

### **What Worked Especially Well**

- **Redundancy and Robust Design Margins**  
*Without robust margins the BAPTA development schedule would have been "broken" and without redundancy (in ways unanticipated) the BAPTA would not still be operating. Windsat was a low-cost, low reliability experimental mission and a programmatic decision was made to forgo any redundancy to contain cost. However, a cost-benefit analysis was presented to management which convinced management to allow redundancy on the BAPTA (the only redundancy flown on Windsat).*
- **Partner Relationship Between Government and Slip Ring Vendor**  
*NRL and the slip ring vendor combined strengths and areas of expertise to build a better product. NRL provided assistance with bearing design and analysis as well as thermal analysis allowing the slip ring vendor to concentrate on the rest of the slip ring design.*
- **Design For Test & Troubleshooting**  
*Designing for test and troubleshooting up front allowed many problems to be solved both on the ground and on-orbit. Some key items were: the ability to spin in both directions, run open loop, and turn on both sides of the electronics simultaneously.*

### **What Could Be Done Better/Different Next Time**

- **Don't pass critical BAPTA feedback (resolver) over long-life slip rings**  
*An optical encoder was dropped early on for budgetary reasons and with hindsight one should trade alternate position feedback devices that do not require slip rings. Alternately, better methods of preventing slip ring noise from affecting resolver signals could be pursued.*
- **Noise sensitive long-life slip rings for space remain challenging**  
*Based on Windsat experience and recent development and testing on other programs a trade study should be revisited on gold vs. silver/MoS<sub>2</sub> vs. non-contacting (i.e., fiber optic, capacitive coupled) "slip rings" for long-life noise sensitive applications.*
- **Design slip ring brushes to accommodate thermal expansion**  
*Windsat copied DSCSII heritage brush design and the power brush design was good with a low "spring constant" that was insensitive to wear and thermal expansion but the critical signal brushes had a high "spring constant" and should have been designed the same as the power brushes.*

## **References**

1. Phinney, Damon, "Slip Ring Experience in Long Duration Space Applications." 20<sup>th</sup> Aerospace Mechanisms Symposium, (1986),pp 45-54.

# **JWST NIRSpec Cryogenic Light Shield Mechanism**

Kathleen Hale\* and Rajeev Sharma\*

## **Abstract**

The focal plane detectors for the Near-Infrared Spectrometer (NIRSpec) instrument on the James Webb Space Telescope (JWST) require a light tight cover for calibration along with an open field-of-view during ground performance testing within a cryogenic dewar. In order to meet the light attenuation requirements and provide open and closed fields of view without breaking vacuum, a light shield mechanism was designed. This paper describes the details of the light shield mechanism design and test results. Included is information on the labyrinth light path design, motor capability and performance, dry film lubrication, mechanism control, and mechanism cryogenic performance results.

## **Background**

A light tight cover mechanism design and development is discussed for ground testing the Near Infrared Spectrometer Instrument's focal plane detectors on the James Webb Space Telescope. The NIRSpec focal plane detectors require a light tight cover for calibration along with an open field-of-view during ground performance testing within a cryogenic dewar. These tests include exposing the detectors to infrared light for calibration in "darkness" while under vacuum at approximately 20 Kelvin (-253°C). The darkness requirement is to maintain light levels less than 0.001 electron/sec/pixel at the detectors. In order to provide this low light level during calibration and also allow the detectors to be exposed to the required light sources when needed, the light shield mechanism was developed.

## **Requirements**

The light shield mechanism is required to attenuate light in the chamber to a level less than 0.001 electron/sec/pixel before it reaches the detectors. Volume space allotted to the mechanism is 27.9 cm in diameter by 15.2 cm high (Ø11 in x 6 in). The shield must be able to open or close within about 60 seconds, operate in a vacuum ( $10^{-6}$  Torr) at 20 Kelvin, and in any gravitational orientation. The lifetime requirement for the shield is a few thousand cycles where one cycle is open and close.

When open, the shield door is to remain outside the 76-degree cone angle of the detectors' field of view. The light shield door range of rotation is about 124 degrees from open to close.

## **Shutter Light Path Design**

A labyrinth light path is created, Figure 1, by the aligning of teeth-like protrusions on the shutter door with teeth cut outs into the plate covering the detector housing, hereafter referred to as the dewar bulkhead. The door and dewar bulkhead protrusions are separated by a gap of 0.64 mm (0.025 in) to prevent any contact debris from being created during the opening and closing operation of the door. This gap allows light entrance to the path, however, the labyrinth design combined with the proper material selection and treatment forces any light entering to bounce many times off the path's walls and thus be absorbed to levels below the requirement. Aluminum 6061, which is bead blasted and black anodized, makes up both the door and dewar bulkhead.

---

\*NASA Goddard Space Flight Center, Greenbelt, MD

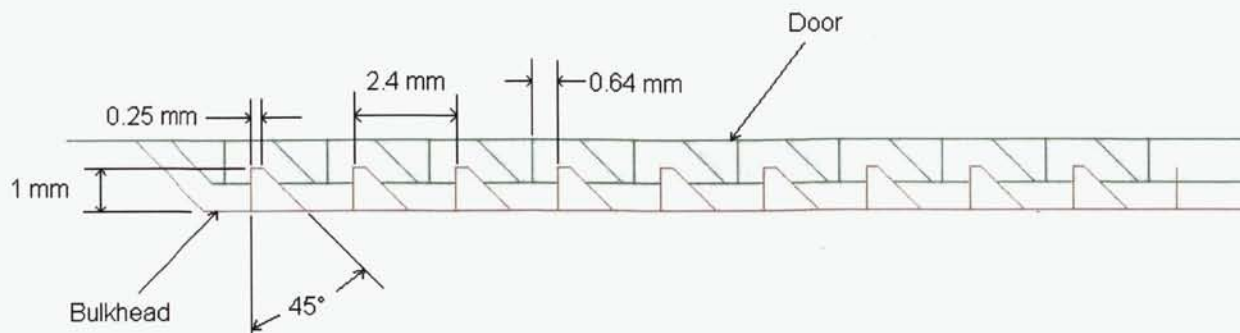


**Figure 1. Light- Path Labyrinth Cross-Section View**

Fabrication of parts was completed on the Micron 600U 5-axis high-speed milling machine as shown in Figure 2. The small sizes and angles of the light path protrusions make it necessary to use this machine. An additional advantage of the high-speed machine is the extremely low amount of stress that is added to the part by the machining as opposed to the level normally added by typical machines. Stress is a concern due to the fact that cryogenic temperatures can cause the part's stress to increase and warp the movable door. Therefore, as well as using the high-speed machine, Aluminum 6061-T651 is used to minimize stress. Aluminum 6061-T651 is heat treated to stress relieve the material.

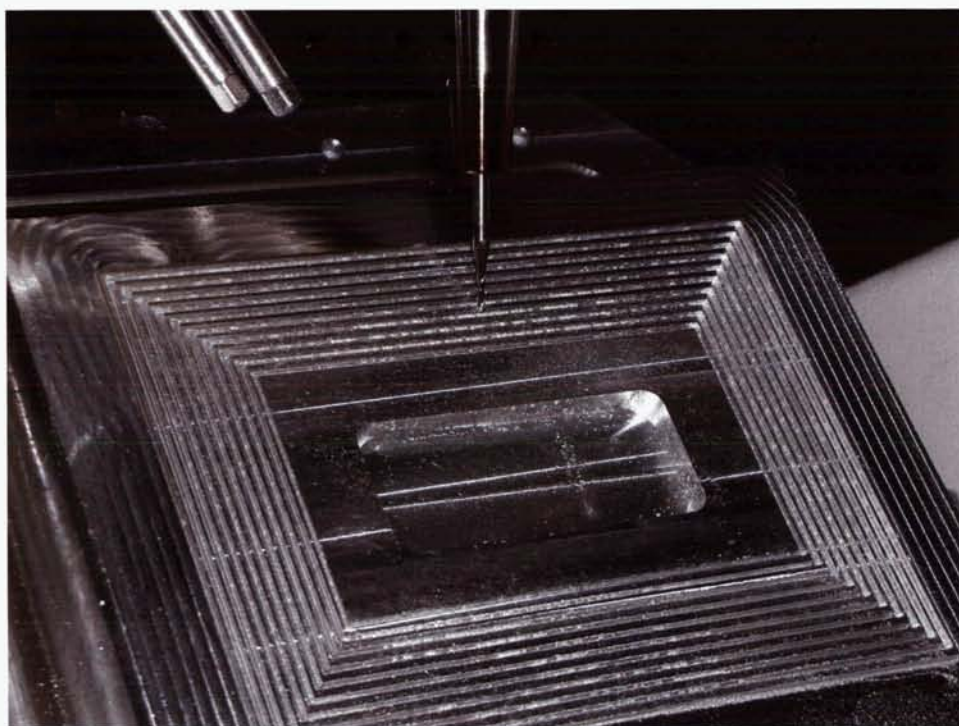


**Figure 2. Picture of door being cut on Micron machine**

After rough-cut fabrication, the door is taken and soaked in liquid nitrogen to determine if part warping at cryogenic temperatures is an issue. Key measurements taken before and after this process are compared and it is found that the door's critical dimensions do not permanently move any significant amount. Therefore, it is determined that the cryogenic environment will not warp the door and affect its operations.



Next, the dewar bulkhead plate is fabricated. Aluminum 6061- T651 is again used to minimize stress. Figure 3 shows the exploded isometric view of the mechanism.

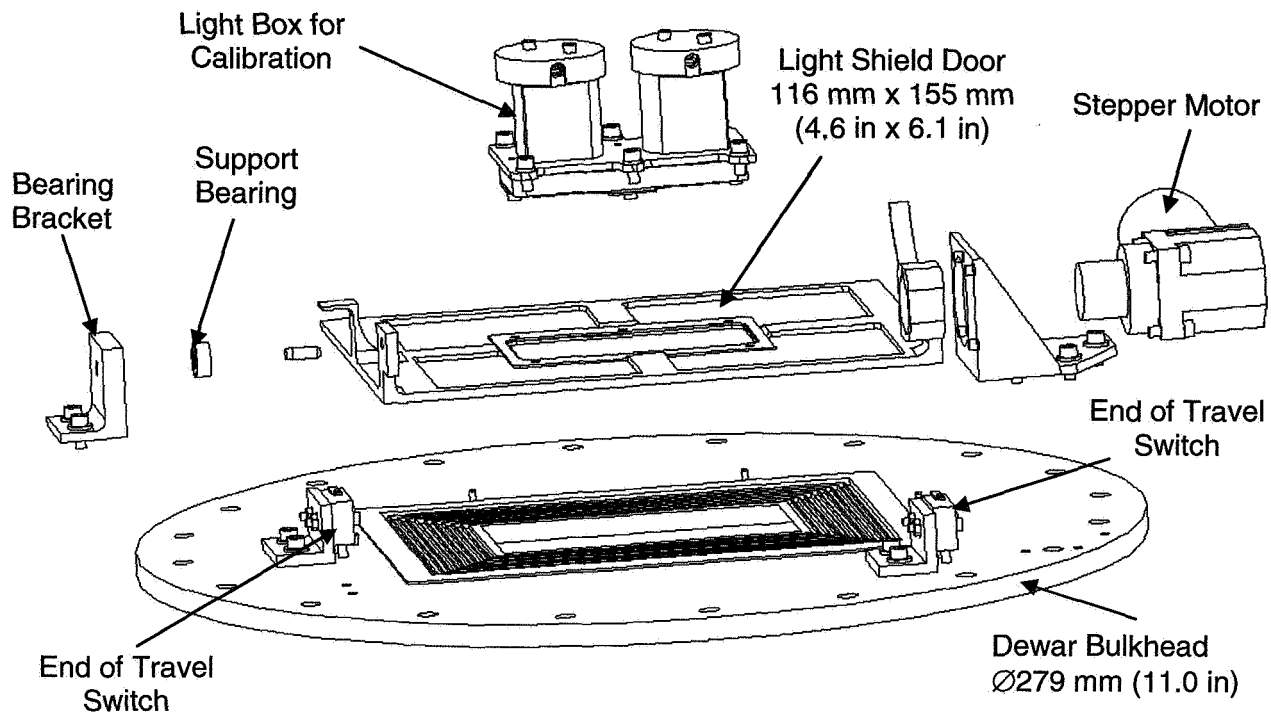


**Figure 3. Exploded Isometric View of Light Shield Mechanism**

### Motor Selection

One cryogenic compatible stepper motor is used to drive the light shield door mechanism. The motor was procured from CDA Intercorp with a right angle gear head, a planetary gear train, dry film Molybdenum Di-Sulfide ( $\text{MoS}_2$ ) coated parts, a motor shaft mounted resolver for position feedback, and a keyed motor shaft interface to the door. Motor design parameters are discussed below.

#### Torque

Analysis indicates the light shield mechanism requires, with margin, a maximum driving torque of  $0.19 \text{ N}\cdot\text{m}$  ( $1.67 \text{ in}\cdot\text{lb}$ ) in the worst-case gravity orientation. In this orientation, the door is required to be held open or closed against gravity by the motor detent alone as power must be disabled during detector tests. This motor detent torque with margin turns out to be the driving design parameter and calculates to  $0.1 \text{ N}\cdot\text{m}$  ( $0.88 \text{ in}\cdot\text{lb}$ ). A healthy factor of safety of 6 is used to bring the motor output detent torque to a  $0.6 \text{ N}\cdot\text{m}$  ( $5.3 \text{ in}\cdot\text{lb}$ ) value. The procured motor provides a measured detent torque of  $0.75 \text{ N}\cdot\text{m}$  ( $6.67 \text{ in}\cdot\text{lb}$ ).

#### Gearing

A right angle gear-head is essential for this mechanism design as the volume space available to mount the motor and mechanism to the dewar bulkhead is limited. The total motor gear ratio is 187:1 implying one motor step equals the door motion of 0.16 degree. This small step size is required so that if during door motion the motor bounces back or misses a step near the fully closed position, the gap left "open" does not allow a significant amount of light to enter the light path. Analysis confirms the gap is not large enough to degrade the light shield capability of the mechanism.

### Cryogenic Lubrication

Dry lubrication on the motor components is required for proper cryogenic temperature operation. A sputtered Molybdenum Disulfide ( $\text{MoS}_2$ ) coating was used on the motor gears, bearings, and moving parts.  $\text{MoS}_2$  was chosen for this mechanism based on the ability to provide any thickness needed and also its heritage on numerous previous flight programs such as COBE, Cassini, SIRTf, and others. Drawbacks in using many dry film lubricants, including  $\text{MoS}_2$  are that the coating should be operated in a dry oxygen and water vapor free environment. Operation should not occur at humidity levels above about 40% due to the reactivity of the coating with oxygen and water vapor.

The  $\text{MoS}_2$  dry film lubricant sputtering process was provided by Hohman Plating Inc. In a vacuum, at  $149^\circ\text{C}$  ( $300^\circ\text{F}$ ), an electron emitter breaks up the lubricant material into atomic size particles that bombard the parts. The coating particles adhere to the parts' surfaces and build up thickness over time. Coatings can be co-sputtered with different elements to improve crystalline structures and lower the friction coefficient. The majority of coatings are co-sputtered with Nickel giving a 0.02 friction coefficient. More advanced co-sputter options are Antimony  $\text{O}_3$  ( $\mu = 0.01$ ) or Antimony  $\text{O}_3$  with Gold ( $\mu < 0.01$ ). This project co-sputtered with nickel as the coefficient of friction meets the required amount and is less expensive than the other co-sputter options. Figure 4 shows the dry film thickness along the tooth of a motor gear part as seen in a cross-section view.

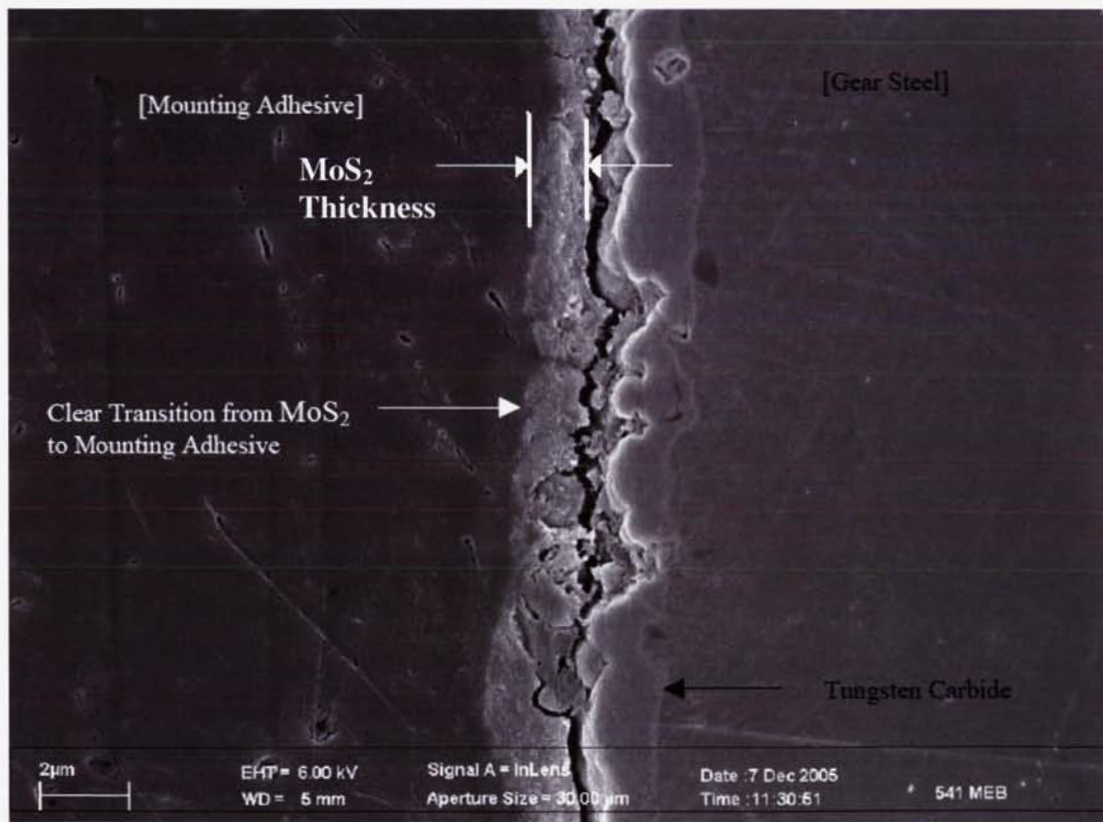


**Figure 4.  $\text{MoS}_2$  coating thickness measured along width of gear tooth near tooth tip of a representative motor gear part. Thickness measured from mounting adhesive to gap.**

Nominally, Hohman plates parts to a thickness of 3000-10000 Angstroms ( $0.3$  to  $1\text{ }\mu\text{m}$  or  $1.18 \times 10^{-5}$  to  $3.93 \times 10^{-5}$  in) over 50 minutes. Considering the low life cycle requirements of the mechanism, the associated mechanical loads it would undergo, and margin, a  $\text{MoS}_2$  coating thickness of  $2.5\text{ }\mu\text{m}$  ( $0.0001$  in) was considered. Initially, the relationship of lubricant coating buildup over time with the sputtering process was thought to be linear. However, through the coating of several sample gears, analysis shows

it to not be so. At first the thickness and time were extrapolated linearly to that for 2.5  $\mu\text{m}$  (0.0001 in) which resulted in a 3-hour long application. Destructive analysis was performed on a sample gear by the materials group at NASA Goddard, and the average thickness of the coating was measured to be 17.8  $\mu\text{m}$  (0.0007 in). Another gear sample was then coated at a lesser time of 70 minutes and the measured thickness of the coating ranged from 0.5 to 3.8  $\mu\text{m}$  ( $2 \times 10^{-5}$  to  $1.5 \times 10^{-4}$  in). Based on the gathered data shown in Figure 5, it was decided that an application duration time of 80 minutes would be sufficient for the light shield mechanism motor parts. All parts are coated for the 80-minute duration resulting in a thickness of 1.2  $\mu\text{m}$  (0.00005 in). The final dry lube coating applied to the motor parts is based on the sample gear data and the minimum motor assembly tolerances for nominal fit. After the coating process was complete, all motor parts were successfully reassembled and tested.

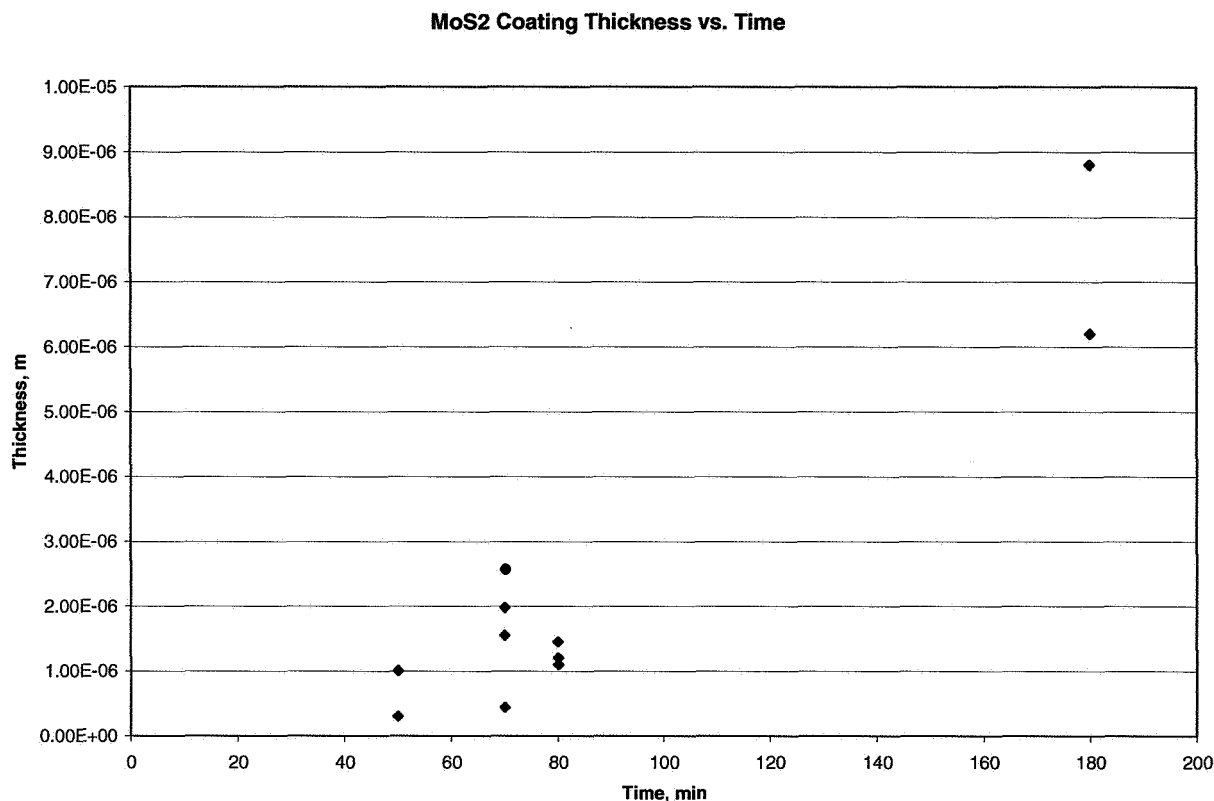


**Figure 5. Measured MoS<sub>2</sub> Coating Thickness vs. Time on a typical motor gear part**

The bearings in the motor are also dry lubricated with MoS<sub>2</sub>. Lubrication thickness is the same as that for all other motor parts, 1.27  $\mu\text{m}$  (0.00005 in). The support bearing on the opposite side from the motor on the bulkhead is a radial bearing and is not sputter coated. Instead, the support bearing is a “BarTemp” bearing from The Barden Corporation. “BarTemp” bearings have a cage made of a Teflon-coated, highly compressed material with very fine glass fibers and molybdenum disulfide impregnation. During operation, the rotation of the bearing causes the balls to rub off small amounts of the cage which coats the raceways with a thin lubrication layer.

### Mechanism Control

The light shield mechanism motor is a two phase DC stepper motor with 30 degree steps and a total right angle gear ratio of 187:1. Nominal operation occurs at 24 VDC. Since the mechanism must operate at room temperature and at 20 Kelvin, a current controlled electrical drive system is used for maintaining proper performance margins under all operating conditions. A Newport 300 Series current control amplifier drives the light shield mechanism motor. Step pulse rate and phase current levels are settable



quantities through a front panel or macro driver software which controls the mechanism to open or close the light shield door in approximately one minute. Software time out and TTL limit switch interfaces allow electronically disabling motor power redundantly with this controller. Motor resolver analog signal is read and converted to a TTL quadrature signal that the Newport controller can read. Motor power is disabled when contact is made with one of the end of travel switches in either the open or closed position of the light shield door. The motor shaft resolver is used as a method of determining the door position.

### **Over Travel Analysis**

As the light shield reaches its end of travel in either the open or close direction, it comes into contact with an end-of-travel switch. This switch then cuts off power to the motor and the door stops its motion. In the close direction there is a hard stop that does not allow the door to over travel. Travel in the open direction, however, does not have a hard stop. Therefore, stress analysis is performed on the tab that comes into contact with the switch to determine the maximum amount of force that can be handled. These calculations determine that the load felt on the tab is 20 times smaller than the yield load of the door material, including margin. Therefore, at the slow speed that the motor rotates, the tab contacting the switch will not yield if the motor attempts to continue to rotate, and the shield door will not over travel.

### **Cryogenic Testing**

Before delivery to the project, the light shield mechanism is tested in a dewar at 20K in the operational configuration. The dewar bulkhead is attached to an interface plate to mate the mechanism to the chamber. Once assembly is complete, the chamber is closed and the then rotated 180° to orient the mechanism to its operational configuration. This places the mechanism so that gravity is acting to open the door from its closed position.

*Test results are forthcoming and will be presented at the conference.*

Special thanks goes to Mike Dube and Mark Mclendon of the Materials Group at Goddard for their destructive analysis and insight in evaluating the dry film coating of motor parts.

# Development Tests of a Cryogenic Filter Wheel Assembly for the NIRC*am* Instrument

Sean McCully\*, Charles Clark\*, Michael Schermerhorn\*, Filip Trojanek\*, Mark O'Hara\*,  
Jeff Williams\* and John Thatcher\*

## Abstract

The James Webb Space Telescope is an infrared-optimized space telescope scheduled for launch in 2013. Its 6.5-m diameter primary mirror will collect light from some of the first galaxies formed after the big bang. The Near Infrared camera (NIRC*am*) will detect the first light from these galaxies, provide the necessary tools for studying the formation of stars, aid in discovering planets around other stars, and adjust the wave front error on the primary mirror (Fig. 1). The instrument and its complement of mechanisms and optics will operate at a cryogenic temperature of 35 K. This paper describes tests and test results of the NIRC*am* Filter Wheel assembly prototype.

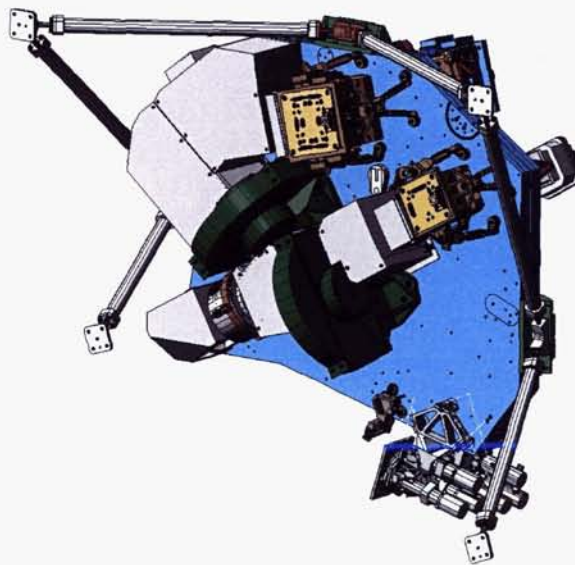


**Figure 1. The NIRC*am* instrument**

## Introduction

The Filter Wheel assembly is one of three types of mechanisms on NIRC*am*. There are a total of four Filter Wheel assemblies on NIRC*am*, and these assemblies are situated at the pupils of both the longwave and the shortwave beams for both of the NIRC*am* optical benches. The Filter Wheel assembly mission is to position optical filters and pupil lenses as well as other wavefront sensing elements into respective optic beams.

The Filter Wheel assembly prototype was built to retire certain risks and concerns. The end-of-life bearing drag torque is a critical parameter necessary in determining the drive current. The motor torque constant and phase resistance at temperature is critical to meeting operating margins for torque and power. Finally, the position control and stability using an inductive feedback position sensor and cogless DC motor needed to be characterized.

---

\* Lockheed Martin Space Systems Company, Palo Alto, CA

## Filter Wheel Assembly Design

The Filter Wheel assembly contains two independently rotating wheels with 12 optic positions each (Fig. 2). Each optic is centered on a radius that is 112.5 mm from the axis of rotation. The Pupil Wheel contains a complement of light projectors, wave-front-sensing elements, filters, coronagraphic wedges, and weak lenses. The Filter Wheel contains 5-mm filters that are tilted four degrees parallel to the plane of the optic bench. The NIRCам prescription requires the Pupil Wheel and Filter Wheels to rotate very close to one another with the final surface of the filters less than 25 mm from the first optic surface in the Pupil Wheel. The performance of the Filter Wheel assembly is driven by the requirement to locate some of the elements in the pupil wheel with a repeatability of less than 310 microns. Additionally, the target location of the prescribed element is to be adjustable on orbit through software. This performance criteria along with a very modest average thermal dissipation requirement that accompanies the 35 K operating condition make the Filter Wheel assembly design a challenge.

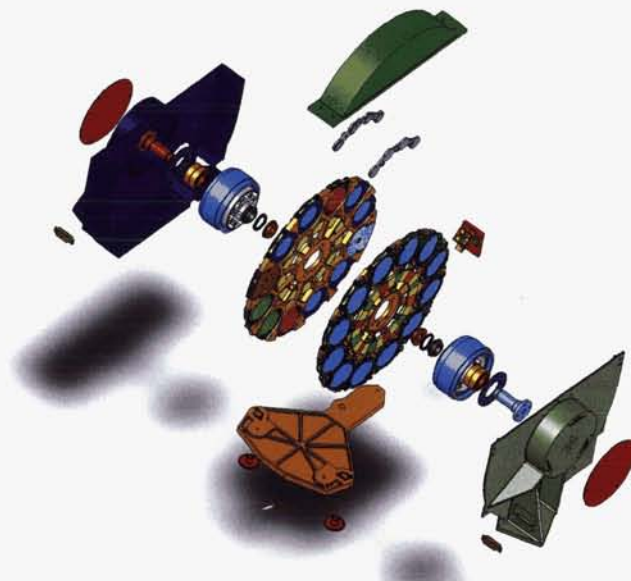


**Figure 2. The NIRCам Filter Wheel Assembly**

The team designed each wheel assembly to be mounted directly onto a custom motor rotor. This design concept is based on heritage designs that have been space qualified and flown before. It is an extremely efficient design concept for both envelope and mass concerns. Each wheel is driven by a 24-pole, three-phase, redundantly wound, cogless DC motor. This configuration minimizes the operating power and space envelope and maximizes the flexibility in commanding positions. A cogless motor has no harmonic content in the drag term, and it has no position detents. This combination of features allows for a very low drag actuator with no mechanically favored wheel positions. A 24-pole motor has the added benefit of simplifying the drive electronics operational scenario since a single 30 degree move from one optic position to another is accomplished by one complete electrical cycle.

The motor rotor is supported by a back-to-back mounted duplex bearing pair. The choice of bearing type was driven by heritage and experience. A relatively large bearing was chosen to accommodate a 50-g launch load and to extend the life expectancy of the dry film lubrication. The lubricant choice was more difficult. The final decision was based in part on an AMS paper that evaluated various lubricants [1]. Additionally, Lockheed Martin has experience with thin film lubrication on a wide variety of applications. These experiences lead to a preference for self-lubricating PTFE and MoS<sub>2</sub> retainers.

The position feedback was the last aspect to be considered. The team chose a differential inductive sensor system to measure position. Ramp targets on the face of the optical element wheels converts linear sensing devices to a rotation. This choice was driven by previous cryo experience with the



technology, envelope, power, mass, and cost concerns. It was made possible by a relatively loose position requirement.

### **Filter Wheel Assembly Prototype Design**

The prototype design represents a single actuator. The prototype design and test program goals were to confirm a bearing run-in procedure, quantify bearing, motor drag, and motor capability, characterize the inductive sensors, and finally verify the controlled repeatability performance. All tests were conducted at an operating temperature of less than 70 K.

Five 35-mm O.D. duplex bearing pairs with Teflon™ and MoS<sub>2</sub> impregnated cage material were obtained (Fig. 3). The cage material is identical to the proposed flight. The bearing size and preload is identical to the flight design. However, each prototype bearing is made from 52100 steel rather than 440C as specified for the flight program.



**Figure 3. Filter Wheel Assembly Prototype Bearing**

In addition to the bearings, two cogless DC motors were specified and procured and included a customized rotor with a feature that would accept the bearing pair and mate with the surrogate optic wheel (Fig. 4). A motor housing was designed to hold the motor stator with a unique flexure design that accounted for coefficient of thermal expansion differences between the components. A motor shaft and shaft mount was designed and fabricated. The design allowed for adjustment in the motor air-gap.

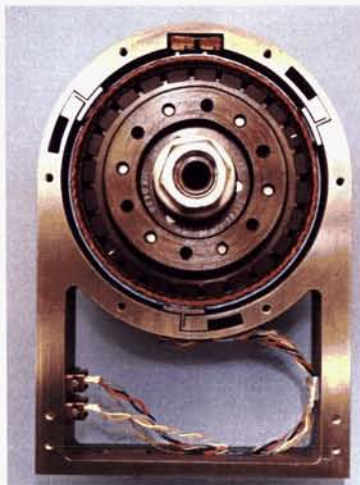


**Figure 4. Cogless Motor Installed In Prototype**

A set of inductive sensors were obtained (Fig. 5). The surrogate optic wheel was designed to provide 15-degree differential ramp targets. The sensor array and sensor track were integrated with the prototype design.

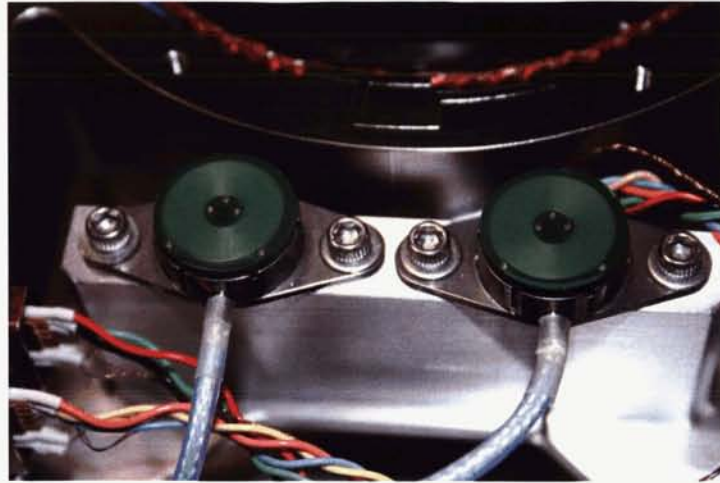


**Figure 5. Inductive Sensors**

#### **Prototype Test Configuration**

In parallel with the design and fabrication of the Filter Wheel assembly prototype, the team designed the necessary setup to test the assembly at 35 K. After selecting a cryogenic test chamber, the team specified the required test equipment. In addition, the team designed the appropriate tooling that would adequately hold the prototype during testing. In order to test the bearing and motor drag, a fixture was designed to hold the prototype within the cryo-chamber, while an external motor and encoder spun the rotor and wheel through a ferrofluidic feedthrough. A vacuum rated torque meter was coupled to the feedthrough inside the chamber to measure torque as close to the prototype as feasible.

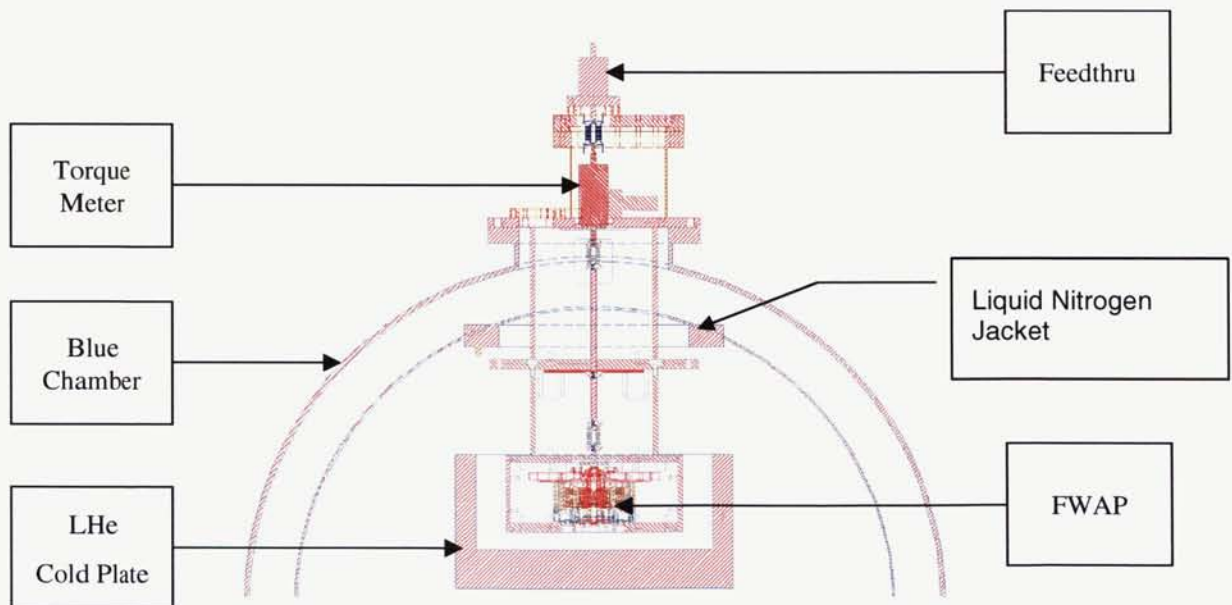


**Figure 4. Prototype Bearing Cold Test Configuration**



### **Bearing Run-in and Cryogenic Drag Test Results**

Bearing drag was the first performance characteristic tested. Each bearing was run-in at an ambient operating environment using a run-in test fixture. A ground support equipment (GSE) motor was used to rotate the motor at 40 RPMs for 200 revolutions in one direction then 200 revolutions in the opposite direction. A torque measurement at 1 RPM followed each sequence of 200 revolutions. A total of 10,000 revolutions were accomplished over a period of approximately four hours. Torque telemetry was continuously obtained by an in-line torque transducer. Post-test inspection and tests indicate that an average of 40 to 50 angstroms of Teflon lubrication was successfully transferred to the balls and races.

The bearing was then assembled onto the prototype shaft and installed into the cryo-chamber to test bearing drag at temperature. A bearing resistive torque of 5.4 mN-m (0.8 oz-in) was measured. This represents an increase of only 3.2 mN-m from the 2.2 mN-m tested at ambient.

While motor and bearing tests continued, additional bearings were run-in using the same 10,000 revolution procedure. These bearings were then inspected and characterized. Periodic inspection and photography indicates that at 20,000 revolutions, the bearing was in "as-new" condition both in terms of torque and physical condition (Fig. 5).

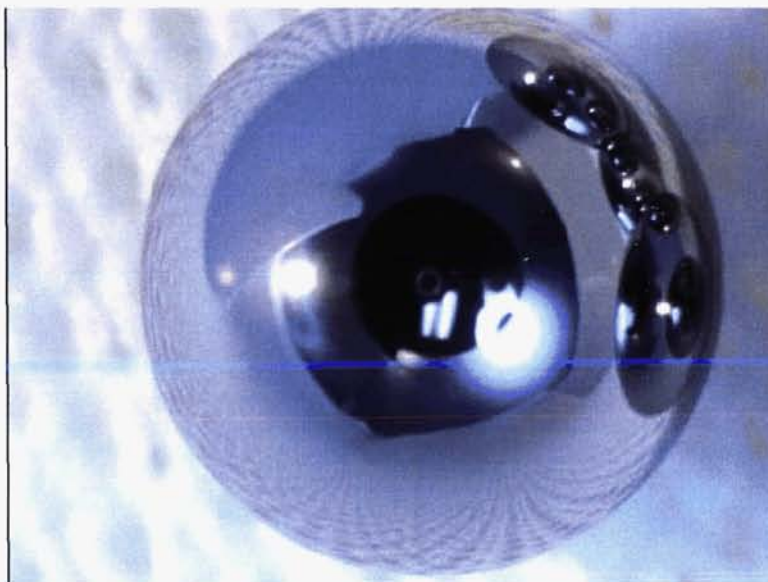


**Figure 5. Prototype Bearing Post-Test Inspection (20,110 revolutions)**

It was determined that a bearing with a measured torque in excess of 21 mN-m (3.0 oz-in) was no longer functioning properly. The torque was irregular, and it was accompanied by an audible protest or squeak. A bearing end-of-life torque limit of 14 mN-m (2 oz-in) was established using the "Knee" of the ambient torque/life curve and allowing for measurement uncertainty. This is viewed as a very conservative limit.

### **Motor and Bearing Tests**

After the bearing run-in tests were completed, the motor stator was assembled into the prototype housing for motor and bearing tests at temperature (Fig. 6). The same thermal vacuum test setup was used. A motor and bearing resistive torque of 9.6 mN-m was measured at temperature. This represents an increase of 4.2 mN-m over the bearing drag test.





**Figure 6. Prototype Bearing, Motor, and Sensor Cryo-Test Configuration**

The test configuration used to test motor and bearing drag also allowed for the measurement of the motor torque constant. By spinning the assembly at 50 RPM with the GSE motor and measuring the peak back emf voltage, the motor torque constant was determined to be 1150 mN-m/A. Through both ambient and cryo test runs, it was also shown that the torque constant was largely insensitive to the temperature and vacuum change.

Motor phase resistance dropped from 82 ohms to 2.2 ohms at temperature. This measurement was done with a simple two wire ohm meter in the prototype efforts, and the measurement includes all the GSE wire—some of it still at ambient temperatures. The flight testing will use a four-wire measurement to eliminate this measurement error. Using 2.2 ohms in the power calculation is considered conservative.

All mechanical connections to the test shaft were removed, and the assembly was tested cold under its own power. At each of the twelve positions, breakaway current was determined to be less than 10 mA. The motor was commanded to take 7 steps at a commanded current level. The motor was reset to pull it back to the motor zero position, and the commanded current level was increased. The process was repeated. Motion occurred prior to reaching a 10 mA command (Fig. 7).

A prototype control board was designed and built. Two power amplifiers (with current control) are used to generate commandable current. Since the net current into the node of a wye-wound motor is zero, the third phase is generated as a difference between the first two. The electrical cycle was divided into steps using a 12-bit controller effectively giving the ability to micro-step. The motor is driven open-loop 30-degrees (4096 micro-steps) from one position to another. Once in the approximate position, the closed loop mode is activated, and the position sensors are used to "micro-step" to a final optic position. The position signal is differentiated and used in a damping circuit while in the closed loop mode. The result is a nicely damped response. The control loop can be used to drive to any value in the position signal, but the sensor ramp has been designed (and aligned) such that each optic position is nominally represented by a zero according to the position signal.

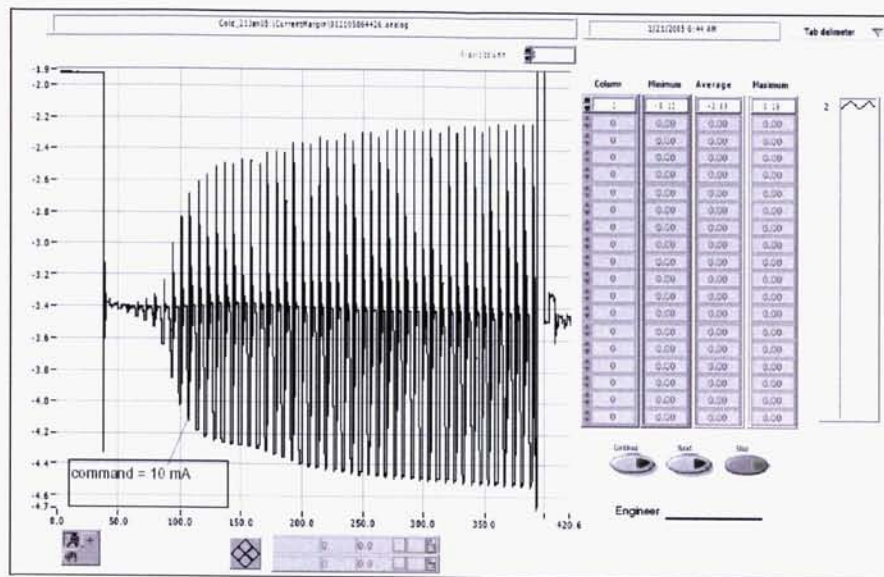


**Figure 7. Breakaway Current Tests**

### Position Control Tests

A 17-bit encoder was connected to the test shaft of the prototype in order to obtain position data (Fig. 8). The sensor track design results in 12 zero-voltage position signals and two higher voltage reference signals in a single revolution of the wheel. The sensor track was aligned to the motor zero during assembly. These data were used to obtain a voltage level of 0.09 V that corresponds to the 0.310 mm position requirement.

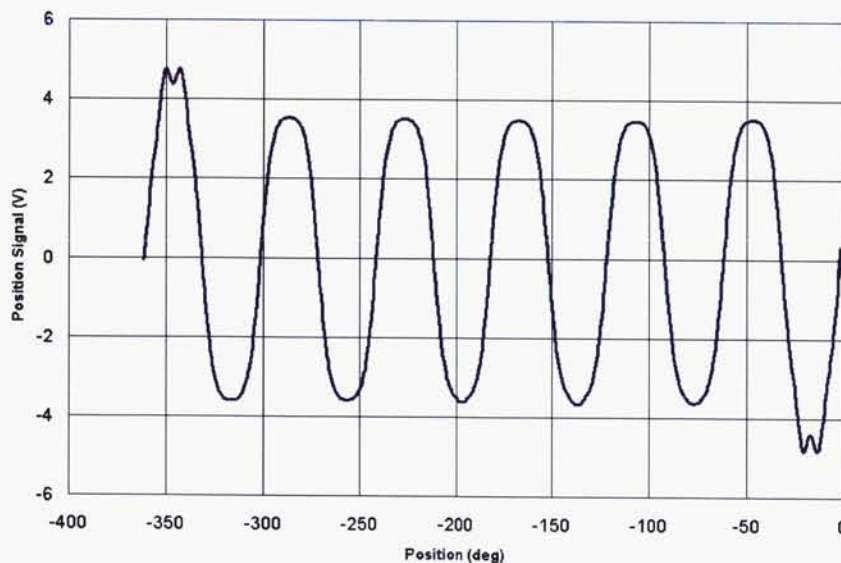


**Figure 8. Typical Voltage Response of Position Signal**

Control scripts were written to command the motor from position to position switching back and forth from open loop to closed loop modes of operation just as proposed for flight (Fig. 9). A reset was used to pull the motor to the closest motor zero position. Open loop moves were accomplished by commanding a speed, a current, and a number of steps (4096). The scripts then closed the position loop and



[illegible]

## Dither and Check Routine

It has been shown that increased friction levels reduce the powered-off position error. This is good news as this means that this particular position error will not get worse at the end of bearing life. It also provides a possible solution to the problem. After much deliberation, it was determined that introducing another source of debris into our optic system was not advisable.

236





## **Conclusions**

A calculated torque margin of 1.8 is now supported by engineering test results. A motor torque constant of 1150 mN-m/amp was measured at ambient and operating temperature and meets the specified minimum of 1100 mN-m/A. A motor drag torque of 4.7 mN-m was measured and is less than the specified maximum of 5.3 mN-m. Cold bearing testing of the FWA prototype successfully characterized the bearings at various cold temperatures and established an end-of-life bearing torque limit of 14 mN-m (2 oz-in). Further life tests are planned.

A measured motor phase resistance of 2.2 ohms results in an estimated peak power consumption of 89 mW and an average power consumption of 0.44 mW when operated at its maximum duty cycle.

Motor control and current margin have been demonstrated at a temperature of 20 K. A powered-on closed loop control error of 0.09 mm was measured at operational temperatures. A breakaway current of less than 10 mA was measured.

## **Acknowledgements**

Development of the NIRCcam instrument at the Lockheed Martin Advanced Technology Center is performed under contract to and teamed with the University of Arizona's Steward Observatory. The University of Arizona in turn is under contract to the JWST Project at the NASA Goddard Space Flight Center.

A great deal of team work was necessary to accomplish these tests. Tom Welsh, Bud Swihart, and Richard Bruner played critical roles in getting the hardware to the proper test temperature. Their efforts and dedication are greatly appreciated.

## **References**

- [1] Gould S.G., E.W. Roberts, "THE IN-VACUO TORQUE PERFORMANCE OF DRY-LUBRICATED BALL BEARINGS AT CRYOGENIC TEMPERATURES," 23rd Aerospace Mechanism Symposium, 1989.

# Cryogenic Nano-Actuator for JWST

Robert M. Warden\*

## Abstract

An extremely precise positioning mechanism has been developed for use in space for optical positioning of large mirrors. The design incorporates traditional mechanical components such as gears, bearings and flexures in a unique configuration covered by two patents. This linear actuator is capable of 10 nano-meter position resolution over a range of 20 mm and can operate under cryogenic conditions. The design, assembly, construction and testing of this mechanism are presented.

## Introduction

The James Webb Space Telescope (JWST) is configured to be a large deployable spacecraft as shown in Figure 1. A key component of JWST is the Optical Telescope Element (OTE), which consists of all the components along the optical path including the Primary and Secondary mirrors. The Primary mirror is about 6.5 meters in diameter and is made up of 18 segments. These mirrors are folded up during launch and deployed in space. Once unfolded, the mirrors must be deployed away from the launch restraints and then adjusted very precisely.

Figure 2 shows how each primary mirror segment and the secondary mirror is supported and controlled by six linear actuators to obtain six degrees of positioning control. Each mirror can be positioned in tip, tilt, piston, horizontal & vertical decentering and clocking. Two actuators are assembled into a bipod assembly as shown in Figure 3. The final hexapod configuration is made up of three bipods. In addition, each primary mirror segment features a central actuator for adjusting the radius of curvature of the segment. The positioning and focusing of the primary and secondary mirrors require a total of 144 actuators.

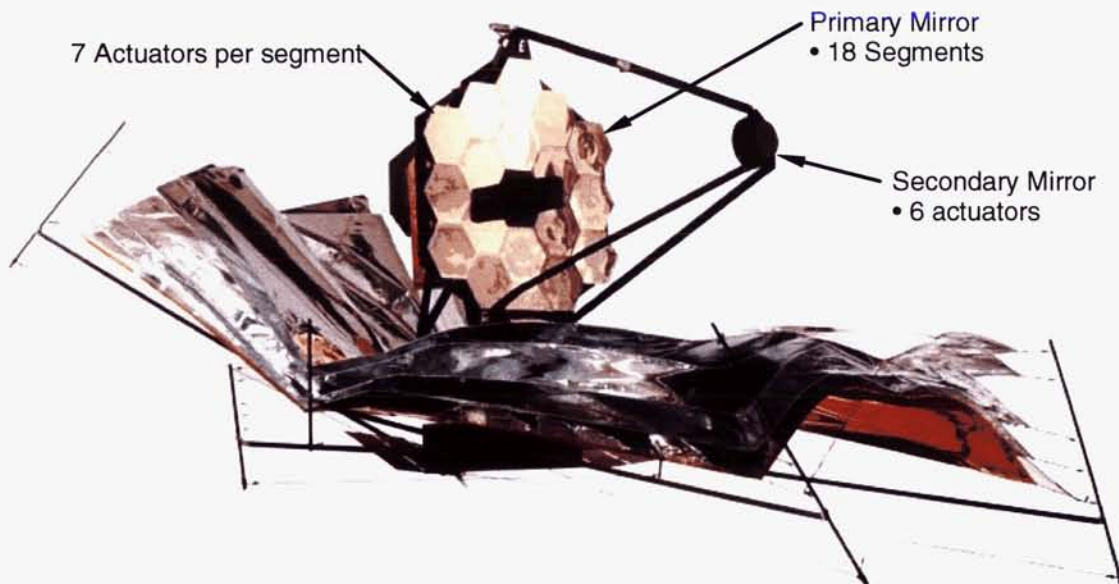


**Figure 1. James Webb Space Telescope (JWST)**

---

\* Ball Aerospace & Technologies, Boulder, Colorado



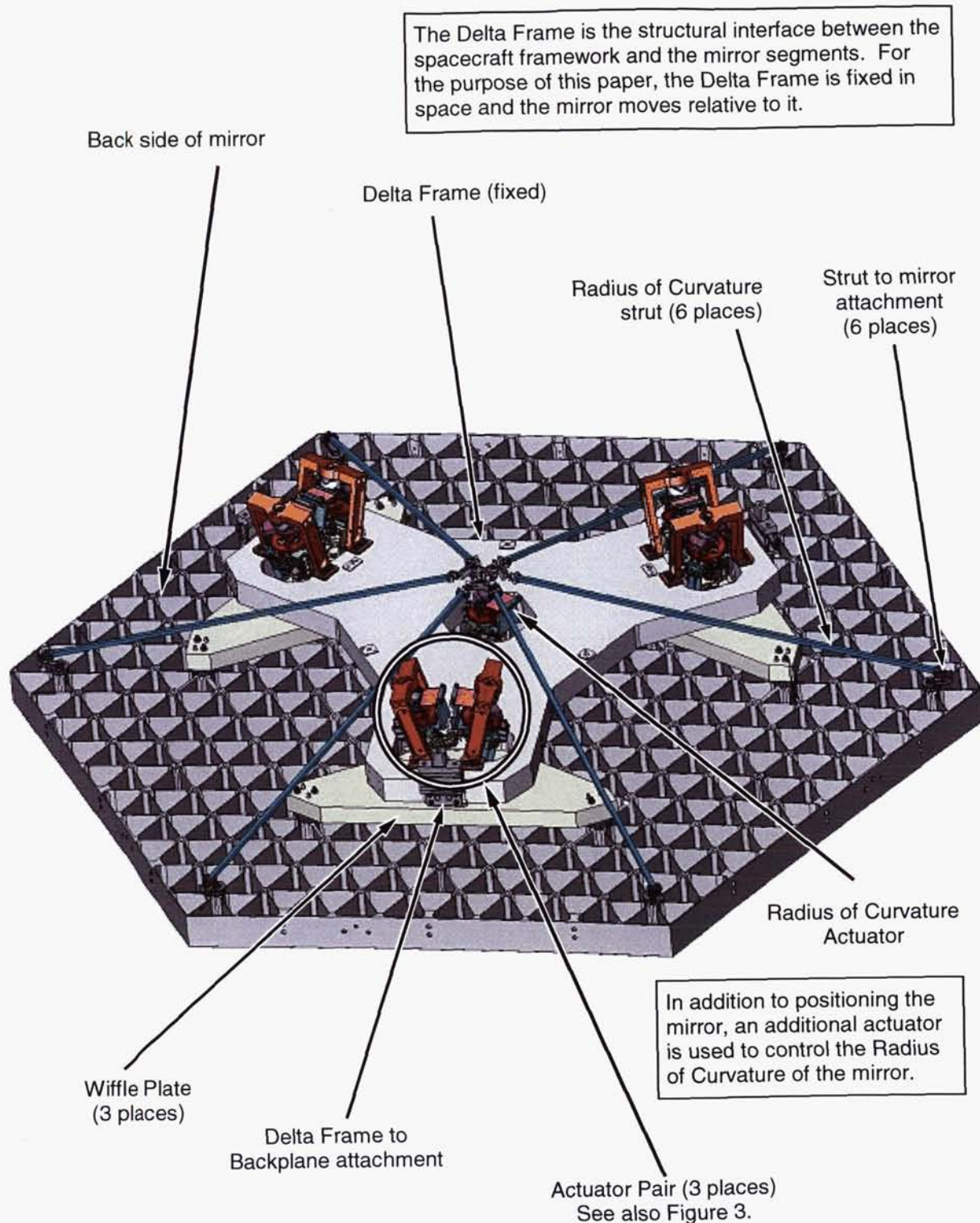
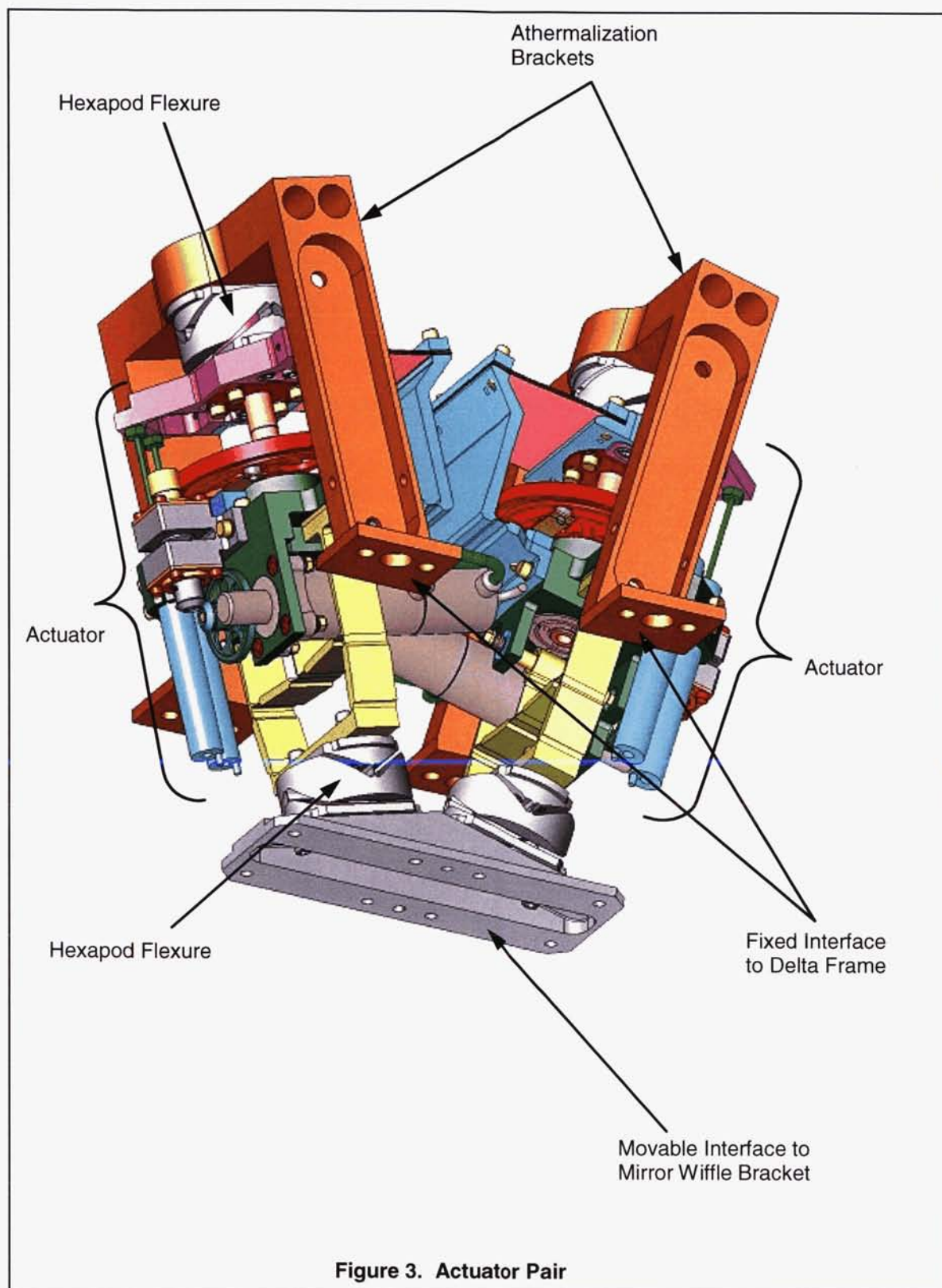


**Figure 2. Hexapod Mounting**



## Actuator Requirements

The Actuator for JWST has two top level requirements:

- I. Accurately position the mirror segments.
- II Support the mirror segments during ground test and launch

These requirements apply to the actuators supporting the 18 segments of the primary mirror as well as to the actuators that support the secondary mirror.

### Positioning requirements

The first requirement of positioning was used to generate the following derived requirements:

1. Move the mirror from the stowed position to the nominal deployed position.
2. Move the mirror from the nominal deployed position with 6 degrees of motion.
3. Position each segment to nanometer resolution.
4. Support the segments in a hexapod configuration.
5. Operate at cryogenic & ambient conditions
6. Operate over the life of the mission.

### Load Requirements

The second requirement of support was used to generate the following derived requirements:

1. Support the mirror segments during launch.
2. Support the mirror segments during ground optical testing.
3. Support the mirror segments during ground transportation.
4. Hold the mirror segments in place with power off.
5. Support the segments in a hexapod configuration.
6. Operate at cryogenic & ambient conditions

The derived requirements are summarized in Table 1.

**Table 1. Requirements Summary**

Property	Requirement	Capability	Compliance
Fine range	>7 micrometers	10 micrometers	yes
Fine step size	<10 nanometer	7.7 nanometer	yes
Fine repeatability	<3 nanometers	2 nanometers	yes
Coarse range	>20 mm	21 mm	yes
Coarse step size	<1.0 microns	0.058 microns	yes
Axial load	1890 N (425 lb)	2650 N (595 lb)	yes
Axial stiffness	24,500 N/mm (140,000 lb/in)	25,200 N/mm (144,000 lb/in)	yes
Axial holding	380 N (85 lb)	890 N (200 lb)	yes
Position feedback	20 microns	12 microns	yes
Cryogenic operation	30 K	20 K	yes
Nominal length	138.8 mm (5.5 in)	138.8 mm (5.5 in)	yes
Mass	700 gram (1.55 lb)	665 gram (1.47 lb)	yes



## Early Development

The success of the actuator is primarily due to two important inventions: the fine stage flexure and the coarse drive coupling. It is important to understand the operation of these two elements before going on to the overall actuator description. The actuator is comprised of numerous individual design elements that all work together in order to satisfy the demanding requirements of cryogenic nanometer-level positioning. However, these two inventions enable the fine adjustment capability over the long range of motion required for the actuator.

### Fine Stage Flexure

The development of the actuator began at Ball Aerospace in 1997 with the invention of the fine stage flexure. A need was established for a motion reduction device that could convert a relatively coarse input motion into a well controlled, optical-level, fine motion. It was well known that flexures work well for motion control because they enable motion without backlash or hysteresis. However, simple flexures were not able to achieve the large ratio required for this application.

The solution, partially shown in Figure 4, was the "Motion Reducing Flexure Structure", developed by Ball Aerospace and covered by United States Patent number 5,969,892 dated October 19, 1999. This compound flexure operates in two stages. As the middle of the cross bar is moved up and down, the sides are moved out and in, thereby causing a small but controlled change to the overall height. Motion reduction of up to 100:1 can be achieved using this design.

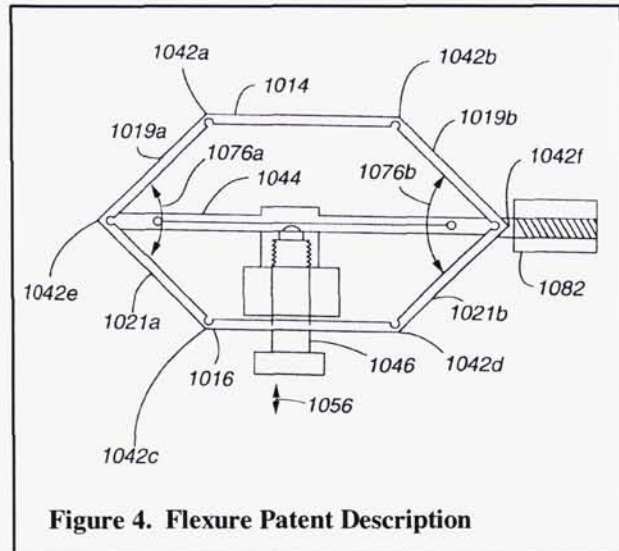


Figure 4. Flexure Patent Description

### Coarse Drive Coupling

The next development was the use of a single motor to operate both coarse and fine motion. Although the fine stage flexure provides the nanometer-range positioning accuracy needed for aligning the mirror segments, it does not accommodate the large range needed for moving the mirrors from the stowed position to the deployed position. For this reason, a coarse motion feature was needed for the actuator. It was desired to have one motor drive both the coarse motion and the fine motion.

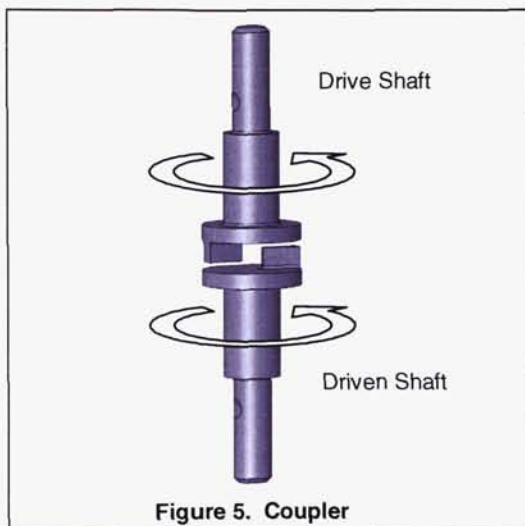


Figure 5. Coupler

To move both the fine stage and coarse stage with a single motor required the use of a coupling that could switch between coarse and fine modes or at least disengage the coarse motion. This was achieved by the invention of a tumbler type coupling, which connects the fine drive to the coarse drive as shown in Figure 5. This coupling consists of two rotating disks, each with a protruding pin. This results in a deadband or backlash of approximately 90% of the rotational input. When the motor is reversed, the drive pin backs away from the driven pin so that the coarse motion is decoupled from the drive train. In this deadband zone only the fine stage is engaged, which enables precise mirror positioning. At the end of this travel, the coarse shaft is again engaged to enable coarse motion. This mechanism was developed Ball Aerospace and is covered by United States Patent 6,478,434 dated November 12, 2002.

### Actuator Chronology

The complete development of the actuator is beyond the scope of this paper but several important milestones should be noted

- 1997 Fine stage flexure developed<sup>1</sup>: Large axial input results in small axial output due to compound flexure configuration.
- 1999 First Actuator built<sup>2</sup>: 10-mm motor, dry film lubrication on all gears and bearings, tested at cryogenic temperatures (30 K), demonstrated fine resolution of less than 10 nanometers.
- 2000 AMSD Actuator built<sup>3</sup>: ¾-inch motor, more robust, twin counter-rotating coarse drive screws, three monopods per mirror, first mirror phasing demonstrated.
- 2002 IR&D Actuator: ¾-inch motor, more modular to reduce fabrication & assembly costs, large coarse drive screw to accommodate launch loads. Never tested.
- 2003 Test Bed Telescope Actuator<sup>4</sup>: 10-mm motor, low cost, 150 units built, hexapod configuration, smaller size, flight-quality positioning, ambient conditions, new fine stage flexure design.
- 2004 Flight Actuator: ¾-inch motor, ball screw for improved axial load capability, dry lube on all bearings & gears, new fine stage flexure.

### Fine Stage Improvement

Figure 6 shows the simplified fine stage flexure. The shape is generally that of the capital letter "A". Like the original fine-stage flexure, movement of the cross-beam deflects the side beams, which, in turn change the overall height of the flexure. The cross-beam is attached to an eccentric cam shaft, which is driven by a gearmotor. As the cam shaft rotates, the cross-beam is driven up and down resulting in a sinusoidal displacement pattern. The sinusoid is distorted due to the compound nature of the geometry. The fine range of motion can be easily adjusted by changing out the pair of shims under the feet of the fine stage flexure. A change in shim thickness of about 0.1 mm (.004 in) results in a change of fine motion of about 1 micron.

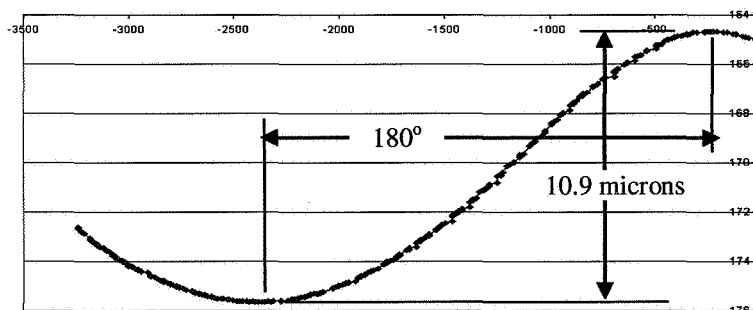
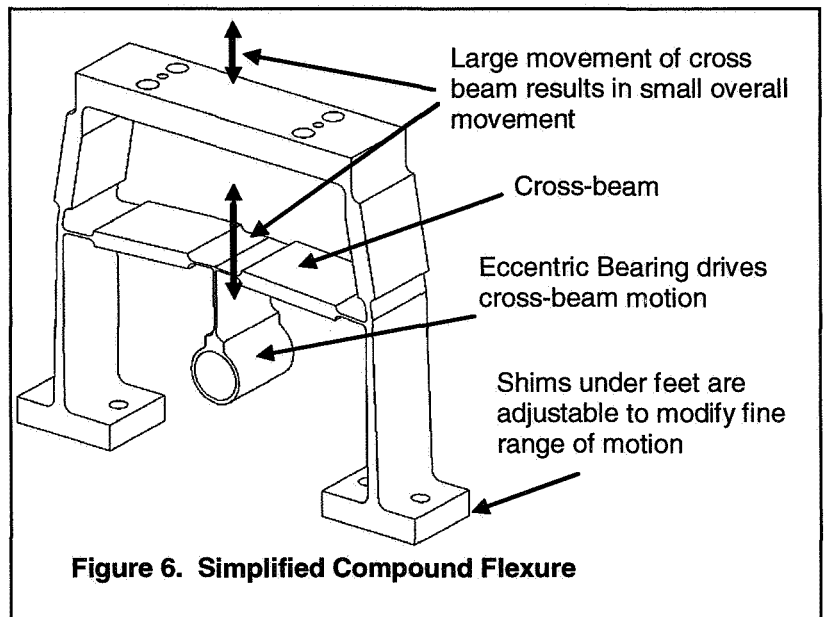


Figure 7. Fine Stage performance

Figure 7 shows an actual collection of data from the first fine range of motion test. The graph shows absolute height vs. motor steps and the distorted sine wave is clearly visible. Note that the fine range here is = 10.9 microns (0.0109 mm). Subsequent adjustment of the fine stage flexure resulted in a fine range of 10.5 microns.



## Actuator Mechanical Description

The best way to describe the functioning of this mechanism is to follow the drive train. The major components in the actuator are shown in Figure 8 and in the diagram in Figure 9. All major components attach directly to the main housing.

### Gearmotor

The drive train of the Actuator begins with a stepper motor. This type of motor is often used for positioning mechanisms because the rotation is divided into discrete steps. The motor for this application has 24 steps per revolution or 15 degrees per step. The stepper motor is attached to a 60:1 gear head and a resolver to form an integral gearmotor assembly. All bearings and gears are coated with a Ball proprietary dry film lube to enable operation at 30K.

### First Pass to Cam Shaft

The output from the gearmotor uses a simple 3:1 spur-gear pass to drive the cam shaft. The cam shaft incorporates an eccentric bearing in the middle that drives the fine stage flexure shown in Figure 8. The shaft is supported by two simple bearings that are preloaded so that the shaft is always pulled away from the gear end. The cantilevered mounting of the shaft enables the use of 1:1 right angle bevel gears to change the drive axis from horizontal to vertical.

### Second Pass to Coupling

The bevel gear pass connects to the coarse drive shaft through the coarse drive coupling as shown in Figure 5 described previously. Both sides of the coupling are supported by preloaded bearing pairs. Except for the gears, both sides of the coupling are identical to take advantage of commonality in fabrication. The drive side has a bevel gear and the driven side has a spur gear pinion attached.

### Third Pass to Coarse Drive

The spur gear pinion drives a large ring gear resulting in an 8:1 ratio. The coarse drive shaft is an 8-mm ball screw with a 2-mm pitch that is mounted as a cantilever with two preloaded bearings at one end to attach the shaft to the main housing.

### Other Components

The remaining actuator components are discussed later in the paper and include:

- Friction brake
- Torsional stabilizer
- LVDT position sensor
- Dry film lubrication

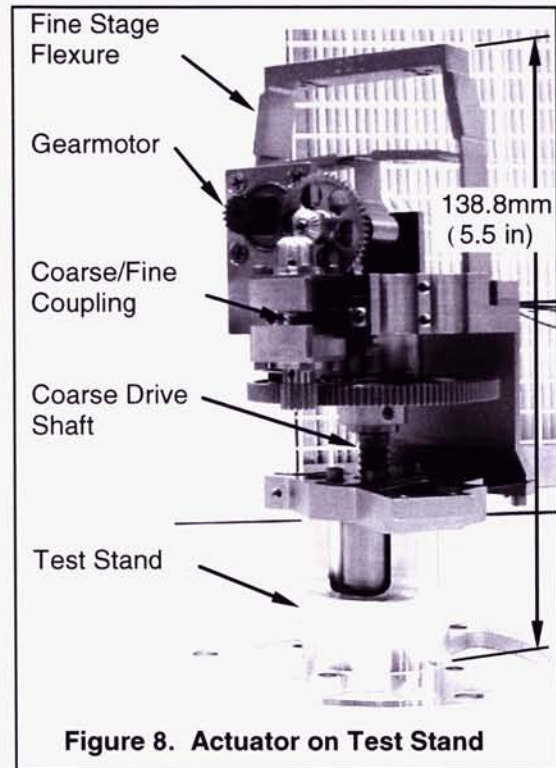


Figure 8. Actuator on Test Stand

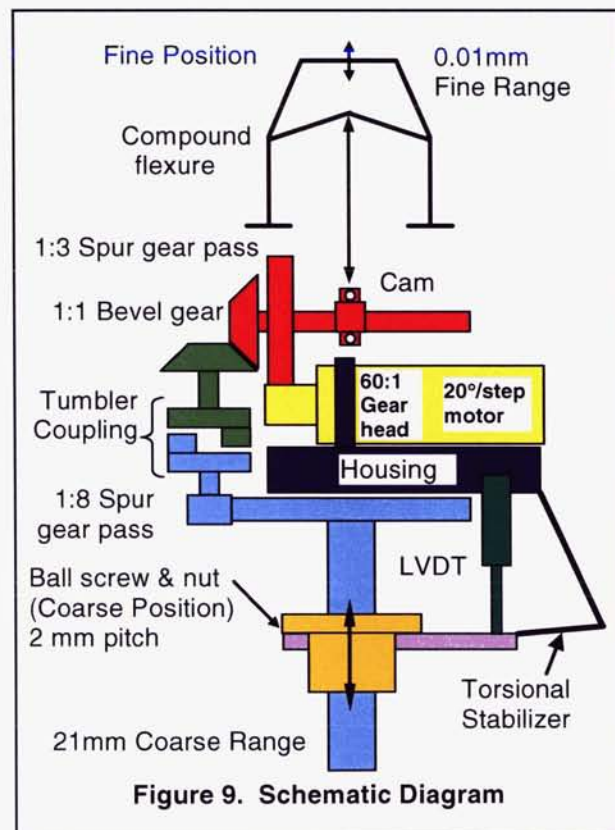


Figure 9. Schematic Diagram



## Design Discussion

Figure 10 is a cut away view of the actuator showing the preloaded bearing pairs and gear passes. Standard recommended fits and tolerances were used. These are all standard mechanical configurations derived from catalog information.

### Dry Lube

Operation at 30K prevents the use of liquid lubrication. Instead, dry film lubrication was applied to the moving surfaces of all bearings and gears. This Ball proprietary process has been used successfully on other cryogenic programs such as SIRTf and Hubble. Moving components can therefore be operated at ambient as well as cryogenic temperatures.

### Gearmotor Life

The life requirement for the gearmotor was estimated using expected operational cycles for the life of the unit. A total of 1.7 million motor revolutions were estimated. The dry film lubrication in the gearmotor has been analyzed to last at least 3 million cycles.

$$\text{Factor} = \text{spec}/\text{total} = 1.75$$

$$\text{Margin} = \text{spec}/\text{total} - 1 = 0.75$$

The gearmotor has been noted as a life limited item and motor revolutions must be recorded.

### Torque Margin

The motor is a stepper type that rotates a precise amount for each step command. Torque margin calculations were generated to compare the output torque of the motor to all of the resistance torques including friction, inertia, coulomb drag and operational loads. Appropriate safety factors were placed on the various loads including cryogenic operation. The motor shows a positive margin under all conditions.

### Friction Brake

A small friction brake was added to the actuator to prevent the coarse drive screw from back-driving operation. The axial force on the ball nut applies a torsional component to the coarse drive shaft. The coarse drive gear was chosen for the brake location because it is the largest torsional element on the coarse drive shaft thereby requiring the least force to constrain. The brake uses a double cantilevered beam to support and apply force to two Vespel buttons. The buttons slide along a raised surface on the coarse drive gear.

### Torsional Stabilizer

In order for the actuator to apply pure axial motion, the nut on the ball screw must be constrained to the main housing in such a way as to resist torsional loads but to allow axial movement. The torsional stabilizer provides this constraint by incorporating a thin flexible shear panel that resists the torque applied to the shaft while allowing the ball nut to translate. As the nut moves up and down the shaft, the flexure forms an "S" shape. A pivot flexure that is opposite the panel flexure minimizes the radial loading on the ball nut from the stabilizer.

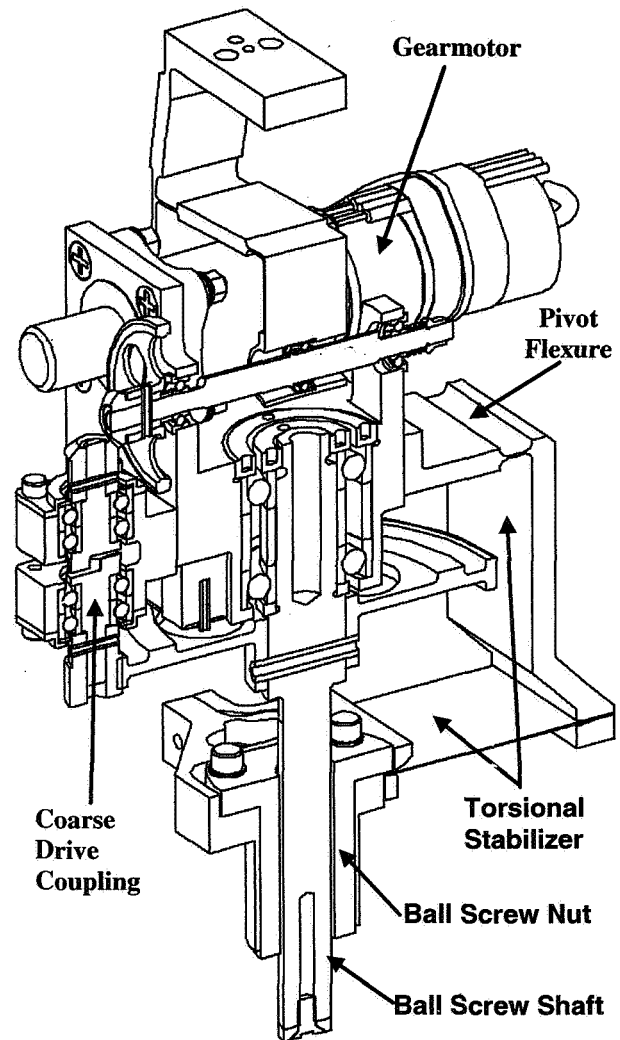


Figure 10. Section View

### Gear tooth loading

The gear teeth were analyzed using a short cantilever beam formula from Roark. The three gear passes were analyzed using the 5 g load case. The stress levels for the three passes are as follows:

First Pass = 17.0 MPa (2.47 ksi)

Second Pass = 17.4 MPa (2.52 ksi)

Third Pass = 11.4 MPa (1.66 ksi)

All gears are made of titanium, which has a yield strength of 869 MPa (126 ksi). The minimum margin of safety is therefore 49.

### Axial load requirements

Large axial loads are imparted into the actuator from two sources:

1. Launch Load:

The defined acoustic load for one mirror is 6480 N

The angle of the actuator is 15 degrees

The load is shared between all 6 actuators

$6480 \text{ N} / 6 / \cos 15 = 1118 \text{ N} (251 \text{ lb}) \times 1.4 = 1565 \text{ N} (352 \text{ lb})$ .

2. Ground Test Load:

The maximum axial force on a single actuator during ground test is 378 N (85 lb).

A factor of 5 is put on this value to protect against damage during ground test operations.

$378 \times 5 = 1890 \text{ N} (425 \text{ lb})$ .

Since the ground test load is greater than the launch load, it was used for design calculations.

### Length

The length of the actuator was calculated based on a nominal deployed actuator length of 138.8 mm. The bipod assembly is required to retract 12.5 mm to the stowed position and extend 5.0 mm to the maximum deployed position. The actuator is also required to translate the bipod at the same piston, which requires additional length.

### Launch Restraint

The original concept was to pull the mirrors down upon some mechanical hard stop until the motor stalls. There are two reasons why this concept was discarded: 1. The large force exerted by the actuator would require a huge increase in mass in order to withstand the stall forces. 2. When a stepper motor stalls, step count is lost.

Another concept was to incorporate some extra feature in order to stop the motor when a certain preload was reached. Several techniques were investigated and discarded including: load cell (adds extra wires, mass, electronics); slip or magnetic clutch (lose step count, adds mass); visual indicator (impractical for all but the outermost actuators). In all cases, the extra feature adds mass and complexity. Also, the hard stop must be designed to be loaded to some factor above launch loads multiplied by some safety factor.

The current launch restraint design is such that motion is restrained in the plane of the mirror and allowed in the direction perpendicular to the mirror. The actuators, therefore, constrain the motion of the mirror in the perpendicular direction. The actuators must withstand axial loads in both tension and compression.

### Power-train Summary

The stepper motor is integrated with a 60:1 planetary gearhead to form what is called the gearmotor. The output of the gearmotor drives a 3:1 spur gear in the first gear pass. The drive torque then branches to the fine stage and/or the coarse stage. The fine stage has a 1:1 bevel gear for the second gear pass to change the axis of rotation by 90 degrees to drive the fine stage flexure. The coarse stage has a tumbler type coupling that has 324 degrees of backlash before driving an 8:1 spur gear for the third gear pass to the coarse drive shaft. The coarse drive shaft is an 8-mm-diameter ball screw with a 2-mm pitch.

### Power Train Capabilities

Because of the numerous gear passes, it was convenient to summarize the load at each step of the power train. Starting with the gearhead output torque, Table 2 lists the load at each step. The input torque is converted to a tangential force by dividing by the radius of the pitch diameter of the gear. The Pitch Angle is also factored in as well as the resulting load on the bearings. The tangential force is then multiplied by the radius of the driven gear to obtain the torque on the driven shaft. The torque on the shaft is then used as the input torque of the next pass. The calculations shown are for the 1 g operational load.

**Table 2. JWST Power Train Calculations**

#### First Pass Calculations

Gearhead Input Torque	0.200 in-lb	0.02 N-m
Shaft Radius	0.166 in	4.22 mm
Tangential Tooth Load	1.205 lb	5.36 N
Camshaft Gear Radius	0.500 in	12.70 mm
Efficiency	0.950	0.950
Torque to Cam Shaft	0.572 in-lb	0.065 N-m

#### Second Pass Calculations

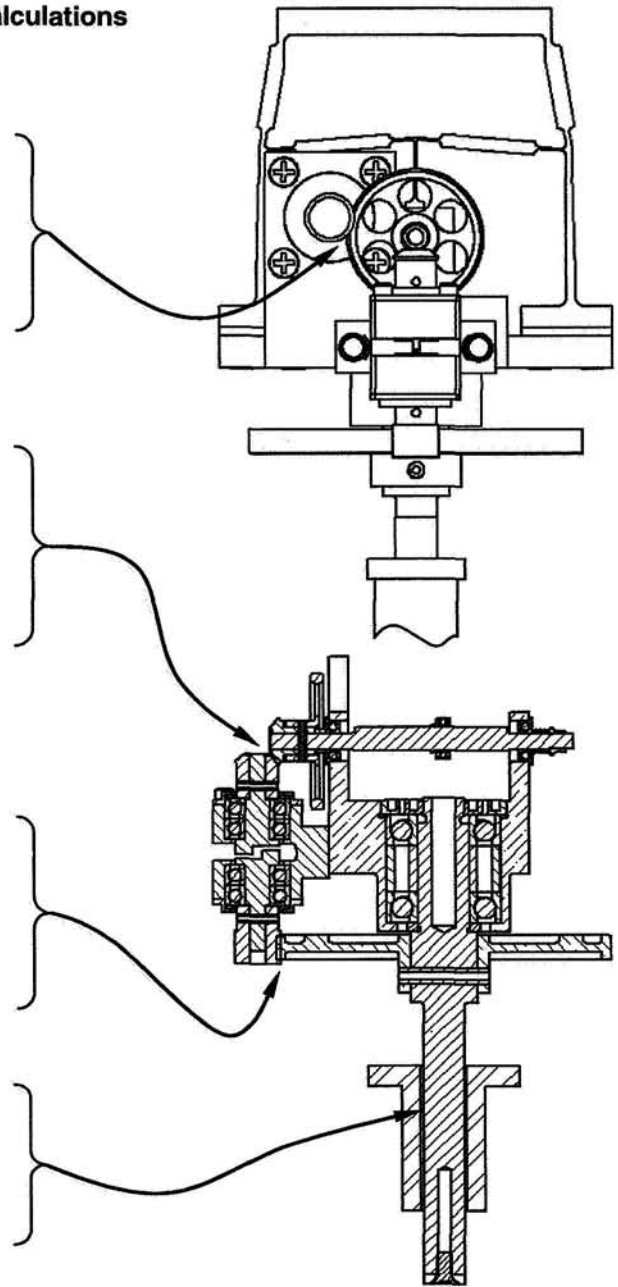
Cam Shaft Input Torque	0.572 in-lb	0.065 N-m
Bevel Gear Radius	0.166 in	4.22 mm
Tangential Tooth Load	3.448 lb	15.33 N
Bevel Gear Radius	0.166 in	4.22 mm
Efficiency	0.950	0.95
Torque to Coupling	0.544 in-lb	0.061 N-m

#### Third Pass Calculations

Coupling Input Torque	0.544 in-lb	0.061 N-m
Pinion Radius	0.156 in	3.97 mm
Tangential Tooth Load	3.481 lb	15.48 N
Coarse Gear Radius	1.250 in	31.75 mm
Efficiency	0.950	0.95
Torque to Lead Screw	4.133 in-lb	0.467 N-m

#### Lead Screw Calculations

Lead Screw Input Torque	4.133 in-lb	0.467 N-m
Brake Drag	3.000 in-lb	0.34 N-m
Lead Screw Radius	0.164 in	4.17 mm
Ball Screw Ramp	0.077 in	1.95 mm
Axial Force	90.09 lb	400.7 N





## Actuator Testing

### Testing Options

Early in the program it became apparent that the testing of certain properties of the actuator could occur at several different stages of assembly as shown in Table 3. Because some of the components are life limited and because of the relatively large quantity of units involved, it was impractical to test every property at every level. Also, it was desirable to limit cryogenic testing because it is expensive and time consuming.

**Table 3. Actuator Testing Options**

<p><b>Assembly Stage:</b> Motor only, Motor &amp; gearhead ambient, Motor &amp; gearhead cold, Actuator assembly, ambient, Actuator assembly, cold, Bipod assembly, ambient, Bipod assembly, cold, Mirror hexapod assembly, ambient, Mirror hexapod assembly, cold.</p>
<p><b>Property to be tested:</b> Motor torque, Fine range of motion, Fine step size, Fine accuracy, Coarse range of motion, Coarse step size, Coarse accuracy, Axial stiffness, Axial backdriving capability, LVDT output accuracy</p>

### Test Plan

After much discussion and trades, a testing plan was established to identify those properties that would be tested, and at what stage. It was desirable to test certain properties early in the process to determine any potential problems. The final test plan is shown in Table 4.

**Table 4. Actuator Testing Plan**

Assembly stage	Property to be tested
Motor only	Motor torque
Motor & gearhead ambient	Motor torque, gearmotor torque
Motor & gearhead cold	Motor torque
Actuator assembly, ambient	Motor torque, fine range of motion, coarse range of motion, coarse accuracy, Axial stiffness, Axial backdriving capability
Actuator assembly, cold	Motor torque, fine range of motion, fine step size, fine accuracy, coarse range of motion, coarse step size, coarse accuracy, LVDT output accuracy
Bipod assembly, ambient	Motor torque, coarse range of motion
Bipod assembly, cold	None
Mirror hexapod assembly, ambient	Motor torque,
Mirror hexapod assembly, cold	TBD

## Actuator Test Results

To date, there have been four major test activities: ambient motor tests, cryogenic motor tests, ambient actuator tests and cryogenic actuator tests.

### Ambient Testing

Figure 11 shows the combination test stand at the actuator fabricator. The fixture is used to measure axial stiffness, fine range of motion and coarse accuracy under ambient conditions. To measure the coarse accuracy, the length of the actuator was measured from stowed to deployed at every cam shaft revolution. The theoretical position was then subtracted from the measured position and the results are presented in Fig. 12. Note each point represents 0.25-mm axial movement. The accuracy requirement is 2% for this level of move, which equals 0.005 mm (5 microns). The test was performed in both the deploy (CW) and retract direction (CCW).

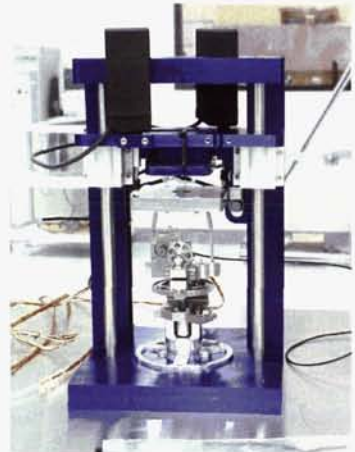


Figure 11. Test Stand

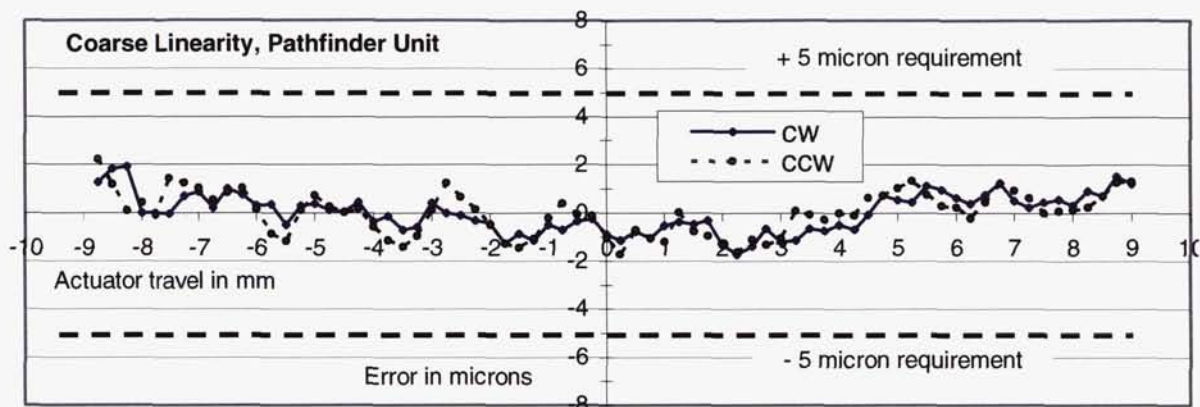


Figure 12. Coarse Linearity

### Cryogenic testing

After the actuator was delivered to Ball, more accurate tests were performed to verify cryogenic operation and fine motion characteristics. Nanometer-level measurement testing requires interferometric instrumentation, vibration compensation and special software. Up to seven actuators can be tested at once using the special setup shown in Figure 13. One of the fine motion tests is single step repeatability. The results of this test are shown in Figure 14. The motor was rotated one step clockwise then one step counter-clockwise several times. The results show an average step size of about 7 nanometers and a repeatability of 1 nanometer.



Figure 13. Cryogenic Testing at Ball

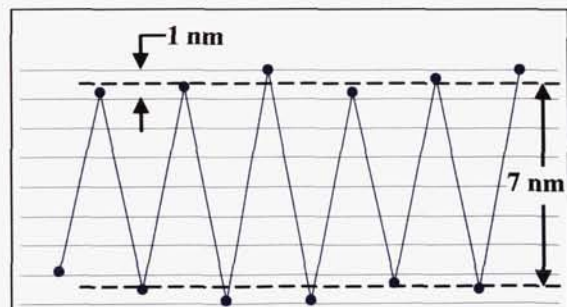


Figure 14. Single Step Repeatability



## Lessons Learned

### Mass production

One of the main lessons learned was that for mass production, it is worth some up-front time and expense to develop tooling and fixtures in order to save time later on. In order to more efficiently fabricate the 140 actuators, several mass production techniques were incorporated. For example, the application of dry film lubrication usually requires masking to prevent the dry lube from being applied to sensitive areas. This masking has traditionally been applied one unit at a time using tape or a painted on compound. For this program, however, special masking tools and holding fixtures were designed and built ahead of time to streamline this operation. Another aspect of mass production that we learned was that it is well worthwhile to spend more at the machining stage to save time during the assembly stage. For example, match drilling for alignment pins is always problematic in titanium in a clean room. For this program the alignment holes were put in ahead of time while the parts were being machined. At assembly the parts went together very easily with no match drilling required as shown in Figure 15.

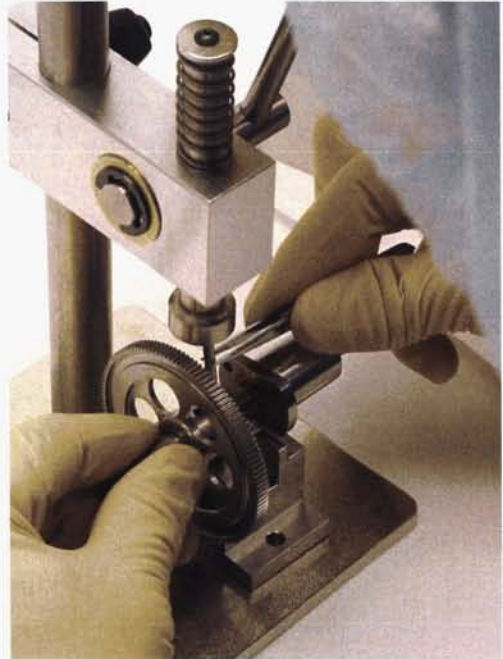


**Figure 15. Production Tooling**

### Recast from EDM

Electro Discharge Machining or EDM was used to machine many of the critical areas on the actuator because it results in very good dimensional accuracy and repeatability. However, the EDM process produces a recast layer on the surface of the part. For a flexure, this recast layer can reduce the fatigue life of the part by up to 10 times. Multiple passes in the EDM process at Ball have resulted in a thin recast layer of about 0.0033 mm (0.00013 in), which is easily removed with light chemical etching.

For one particular flexure, however, standard etching did not remove the recast layer. Additional etching to remove the recast layer made the flexure area too thin. A review of the drawing and discussions with the vendor revealed a misunderstanding of the process. A specific EDM process sequence has since been defined, which results in a thin recast layer and acceptable flexure dimensions after recast removal. Inspection techniques have also been developed to simplify the verification of recast removal.

### Thermal strapping

Titanium is a poor thermal conductor and the gearmotor generates heat during operation, which affects the length of the actuator. In order to test the actuators in a timely manner, heat straps were attached to several points on the actuator. Again with mass production as a goal, special clamps were made so that the thermal straps could be easily attached and removed.

### Pathfinder for the EDU

It is usually good practice to have an Engineering Development Unit (EDU) as a precursor to building a flight unit. JWST took advantage of this "lesson learned" that has been cited by many authors. The EDU for JWST consisted of 18 units to be used as follows: 7 actuators for the Primary Mirror Assembly, 6 actuators for the Secondary Mirror assembly, 2 actuators for a life test and 3 actuators for spares. With so many units to build, it was decided to turn one of the spare actuators into a "pathfinder" unit, which is essentially a first article development unit for the EDU. One actuator was taken from the initial build and designated as the pathfinder. This unit was the first to be assembled and the first to be tested. Any new testing or fixture was proven out on the pathfinder. To maintain schedule and to have processes verified in advance, certain shortcuts were allowed on this unit. For example, although the components were cleaned to a flight level, the pathfinder parts were not subject to an external particle count.



## **Conclusion**

The design of the Cryogenic Nano-Actuator for JWST is now complete. The EDU units have been assembled and tested. The actuators will next be assembled into bipods, which will then be integrated into the primary or secondary mirror hexapod configuration. Long lead component procurement for the flight actuators is underway. Flight actuator fabrication is scheduled to begin in the last quarter of 2006.

The design of the actuator was extremely challenging but test results show that optical level positioning can be reliably achieved using simple mechanical components. The unique combination of the patented fine stage flexure with the coarse coupling proved to be quite effective in achieving fine accuracy over a long range of travel. Mass production techniques greatly simplified the design and assembly of the actuator. Reliable operation was achieved by the use of robust components and supporting analysis.

## **Acknowledgements**

This paper presents the design of the Cryo Actuator for JWST. The design of the actuator is the result of important contributions from numerous people and organizations. I would like to acknowledge the contributions from those at Ball Aerospace including Robert Slusher, Scott Streetman, Lana Klingemann (nee Kingsbury), William Schade, Mike Matthes, Bruce Hardy and all the technicians, machinists, engineers and administrators. I would also like to acknowledge the outstanding work of outside vendors & suppliers including CDA Intercorp, All American Gear, New Hampshire Ball Bearing, Barden Bearing, ATK-Able, Next Intent, Schaevitz and Beaver Aerospace. The photographs in Figures 8, 11 & 15 are courtesy of Able. Finally, I would like to thank our customer, Northrop Grumman Space Technology (formerly TRW) and NASA Goddard.

## **References**

1. R. Slusher, "Motion Reducing Flexure Structure", U.S. Patent Number 5,969,892, Oct. 19, 1999.
2. S. Streetman, L. Kingsbury, "Cryo Micropositioner", U.S. Patent Number 6,478,434, Nov. 12, 2002.
3. Scott Streetman, Lana Kingsbury, "Cryogenic Nano-positioner Development and Test for Space Applications", in IR Space Telescopes and Instruments, Proceedings of SPIE Vol. 4850, Sep. 2002.
4. Lana Kingsbury, Paul Atcheson, "JWST Testbed Telescope", in Optical, Infrared and Millimeter Space Telescopes, Proceedings of SPIE Vol. 5487, June, 2004.

# Space Shuttle Body Flap Actuator Bearing Testing for NASA Return to Flight

Timothy R Jett<sup>\*</sup>, Roamer E. Predmore<sup>\*\*</sup>, Michael J. Dube<sup>+</sup> and William R. Jones, Jr<sup>++</sup>

## Abstract

The Space Shuttle body flap (BF) is located beneath the main engine nozzles and is required for proper aerodynamic control during orbital descent. The body flap is controlled by four actuators connected by a common shaft and driven by the hydraulic power drive unit. Inspection of the actuators during refurbishment revealed three shaft bearings with unexpected damage. One was coated with black oxide on the balls and race wear surfaces, a second contained a relatively deep wear scar, and the third with scratches and an aluminum particle in the wear track. A shaft bearing life test program was initiated to measure the wear life and explain the 5.08-micrometer wear scar. A tribological analysis was conducted to demonstrate that the black oxide coated wear surfaces did not damage the bearing, interfere with the lubrication, or cause severe bearing wear. Pre-damaged (equivalent of 30 missions), commercial equivalent bearings and previously flown shaft bearings were tested at axial loads, speeds, and temperatures seen during flight operations. These bearing were successfully life tested at 60°C for 24 hours or 90 flights. With a safety factor of 4X, the bearings were qualified for 22 flights when only a maximum of 12 flights are expected. Additional testing at 23°C was performed to determine the lubricant life and to further understand the mechanism that caused the blackened balls. Test results indicating bearing life was shortened at a lower temperature surprised the investigators. Start/Stop bearing testing that closely simulates mission profile was conducted at 23°C. Results of this testing showed lubricant life of 12 flights including a safety factor of four. Additional testing with bearings that have the equivalent of 30 missions of damage is being tested at 23°C. These tests are being performed over the Shuttle load profile to demonstrate the residual bearing life in the actuators exceeds 12 missions. Testing showed that the end of the shaft bearing life was characterized by bearing temperature rise, preload drop, and the onset of a severe wear bearing failure mechanism. The severe wear failure mechanism is characterized by rough wear scars, extensive bearing wear and steel transfer between the balls and the races.

## Introduction

The BF is part of the Space Shuttle Orbiter control system that operates primarily during the critical descent maneuvers. The Shuttle body flap is supported and controlled by four body flap actuators (BFA) sharing a common, segmented drive shaft. The common shaft is driven by the hydraulic power distribution unit. During inspection of these actuators, one of the input shaft bearings was discovered to have blackened balls and a blackened wear track in the race after the actuator had completed approximately 20 missions [1, 2]. It was deemed unacceptable for service, replaced and the used grease was discarded. Visual examinations of most of the BF actuators in the fleet revealed no evidence of blacken balls or race wear tracks in the shaft bearings. The used shaft bearings were cleaned, inspected, re-lubricated and reinstalled in the actuators or scrapped. Subsequent microscopic inspection and metrology of these shaft bearings revealed significant wear and possible plastic deformation in a second shaft bearing [3]. A third shaft bearing was found to have scratches and an aluminum particle in the wear track. To determine if actuators with used bearings were acceptable to re-fly for twelve missions, a bearing test program was initiated at the Marshall Space Flight Center.

---

<sup>\*</sup> NASA Marshall Space Flight Center, Huntsville, AL

<sup>\*\*</sup> SWALES/Goddard Space Flight Center, Greenbelt, MD

<sup>+</sup> NASA Goddard Space Flight Center, Greenbelt, MD

<sup>++</sup> SWALES/Glenn Research Center, Cleveland, OH

## Body Flap Actuator Background

The Body Flap actuator is shown in Figure 1. Several failure modes can end the life of the BF actuator bearings. Fatigue spalling, fretting fatigue, lubricant failure, high temperature oxidation, corrosion pitting, severe wear or combinations of these mechanisms can cause bearing failure. Corrosion pits or wear damage accelerate fatigue crack growth that can cause fatigue failure before the bearing reaches the B1 or B10 fatigue life. If the bearing wear life or the Braycote 601 grease life is exceeded, the bearings can fail. However, because the actuators possess very high driving torques, the worst bearing failure mode was expected to be a broken ball or bearing race that could jam the actuator as well as the common drive shaft and cause an actuator performance failure.

The design criteria for the space shuttle (OV) BFA are 100 missions and 10 years. During the 1990s, excessive BF flutter during launch and excessive BF housing corrosion led to disassembly and inspection of BF actuators. In October 2002, bearings from the S/N 402 and S/N 405 actuators were cleaned and microscopically inspected to find out if ball bearings in the BFA assemblies needed to be replaced. As part of that investigation, shaft bearing P/N 5902050, S/N V6L009, from body flap actuator S/N 402, was found to possess unusually dark wear surfaces when compared to the rest of the bearings under examination (Figure 2) [1, 2]. NASA's Engineering and Safety Center (NESC) became aware of this issue and initiate an Independent Technical Assessment to assess this bearing and all other bearings in the Shuttle's Rudder Brake and Body Flap Actuators [4].

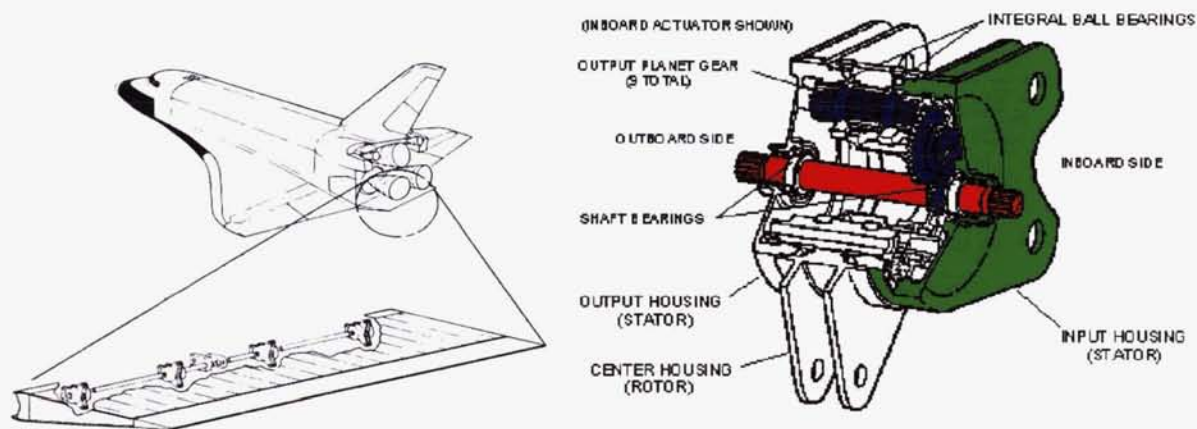


Figure 1. Space Shuttle Body Flap Actuator



Figure 2. Body Flap Shaft Bearing S/N V6L009



### Analysis of BFA Bearing with Black Balls

Visual inspection of P/N 5902050, S/N V6L009, revealed a black, tribological coating on the balls and race wear tracks (Figure 3). It should be noted that no other bearing in the Body Flap or Rudder/Speed Brake actuators was found to contain the black, tribological coating on the wear surfaces. Minor corrosion was noted on the inner and outer raceways. The grease present in the bearing was brown in appearance due to the tribological decomposition of the Braycote 601 grease and iron oxide wear debris. The recommendation based on microscopic examination analysis was to replace the bearing since the wear surfaces were black and it suffered Brinell damage during disassembly.



**Figure 3. Black bearing after sectioning and cleaning**

Note black balls and the dark bands present on the raceways.

Further work performed in 2004 by Hamilton Sundstrand, Inc. reported that the inner ring contained a black tribological coated band. The black band or wear track possessed a smooth matte finish with a grain boundary like structure. Outside the black wear track, the original surface was still evident along with the original finish marks. The outer ring contained a similar black coated wear band (Figure 4). The wear surface of the outer race was similar in appearance to the wear surfaces present on the balls.



**Figure 4. Magnified views of the black wear tracks in the inner race (left) and outer race (right) are shown. Note the false brinelling marks. The dark brown color is an optical aberration of the black color.**

#### Scanning Electron Microscopy (SEM)

Scanning electron microscopy was performed on segments of the black ball bearing by various groups [5]. The segments examined included the balls, inner raceway and outer raceway. Analysis of the balls by energy dispersive spectroscopy (EDS) revealed that the black tribological coating was composed of carbon and iron oxide. The coating was porous and appeared to be uniform over the entire ball surface. A few skid marks were noted (Figure 5). In addition, each ball possessed a moon-shaped spot that appeared to have penetrated the burnished coating. The spot was probable caused by a drop of rain

water absorbing corrosive chemical from the degraded grease and dissolving the black coating during Shuttle storage.

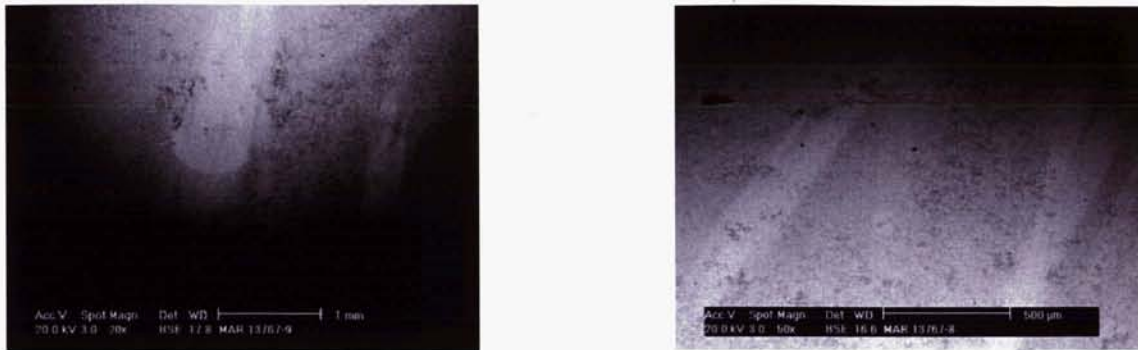


**Figure 5. Scanning electron micrograph of black ball showing spot (left) and skid marks (right)**

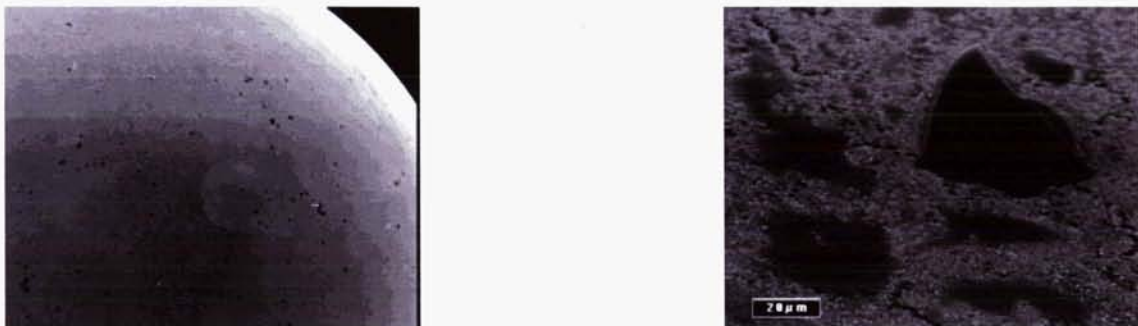


**Figure 6. Scanning electron micrographs of the black ball (left) and magnification of particle present on the ball surface (right)**

Higher magnification of the ball revealed some particles present on the ball (Figure 6). The presence of aluminum and silicon, in addition to other elements detected by EDS on these particles, were likely attributed to the bentonite clay additive present in the Braycote 601 grease and not contamination as was originally proposed. Analysis of the inner and outer raceways showed surfaces similar to the black ball. EDS performed on those surfaces detected the carbon iron oxide coating found on the black balls. Examination of the inner raceway away from the burnished band showed the original finishing marks which gradually translated into a smoother region as the burnished area was approached (Figure 7). Figure 8 shows the surface for the coating present on the black ball obtained by surface profilometry.

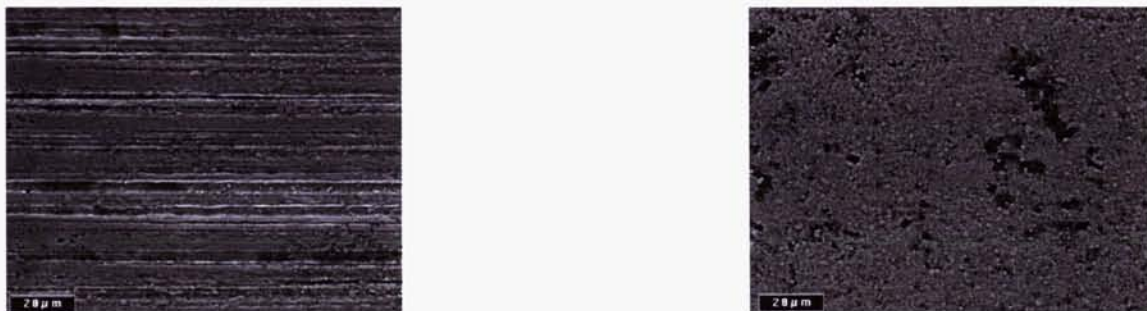


**Figure 7. Scanning electron micrograph of the outer raceway in the region above the burnished band (left), and within the burnished band (right)**



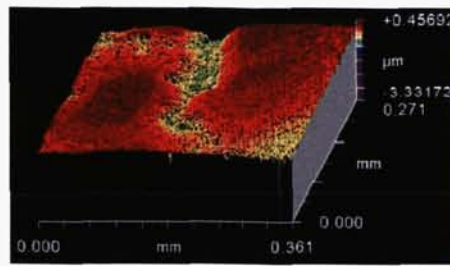


**Figure 8. Surface profilometry trace showing the coating present on the black ball including a segment of the grain boundary-like structure in the center**

#### Raman Spectroscopy

Raman spectroscopy of the black balls showed carbonaceous peaks from the carbon coating on the surface of the complex iron oxide, black, tribological coating [6]. Specifically, the diamond, D, and graphitic, G, peaks were observed confirming the presence of amorphous carbon (Figure 9).

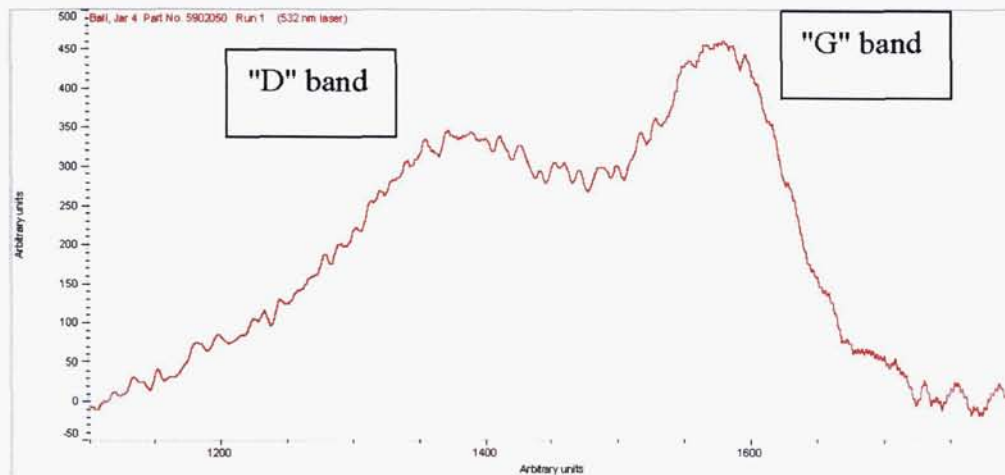


**Figure 9. Raman spectrum for black ball showing the graphitic (G) and diamond (D) peaks associated with amorphous carbon.**

#### X-ray Photoelectron Spectroscopy (XPS)

XPS was performed on the black ball at three different locations and on the inner race. Following the initial scans, depth profiling was performed by application of fifteen sputtering cycles, each lasting ten seconds, and a total sputter time of 450 seconds per location. The results show a carbon-rich coating on top of an iron oxide-rich surface. The carbon-rich top surface forms during the tribological decomposition of Braycote 601 grease and contains fluorine and sodium from the grease [7, 8]. The Raman spectrum of the carbon-rich coating is reported in the Raman spectroscopy section. Below the carbon-rich coating is the black tribological iron oxide-rich coating that also contains fluorine from the grease. At the end of the sputtering cycles, sodium was no longer present and chromium was observed in both locations in addition to carbon oxygen, fluorine, and iron (Figure 10).

#### Metallography

A black ball and a segment of the race from the blackened bearing, S/N V6L009, were metallographic cross sectioned and the tempered martensitic 52100 steel and black tribological coating examined (Figure 10 and 11) [5]. The microstructure of the black ball was consistent with properly processed 52100 temper martensite with finely dispersed carbides with a hardness of  $R_c$  64-65 from the surface into the ball. Tapered sections showed no evidence of annealing below the black tribological coating therefore the



temperature of the ball did not go above 204°C during the formation of the black tribological coating. The black coating appears to be a micron or two thick. Pits present on the cross-section were very shallow.

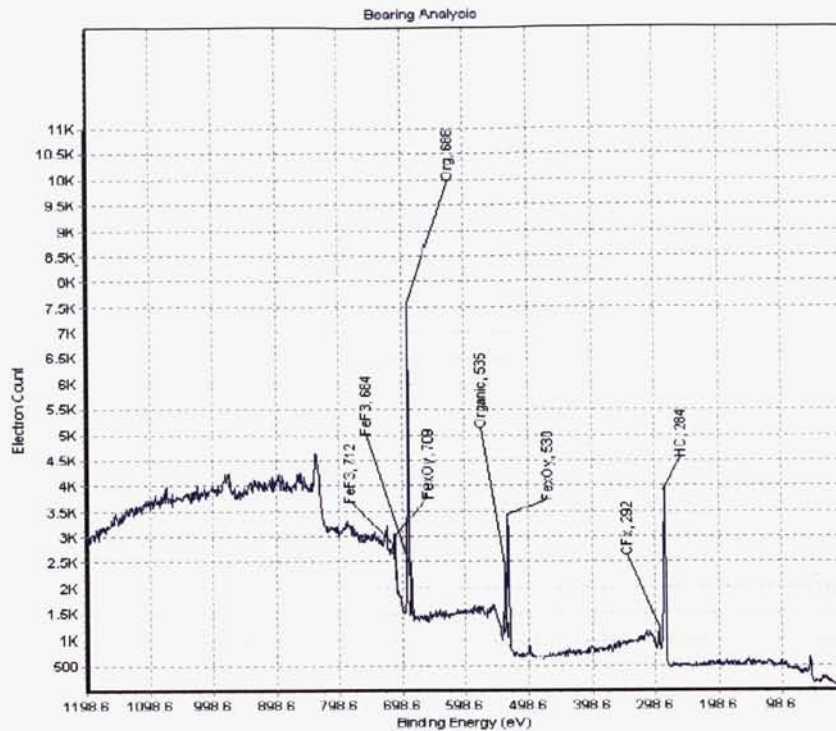


Figure 10. An XPS spectrum for black ball



Figure 11a. Metallographic section of black bearing



**Figure 11b. Metallographic section of black bearing**

### **Metrology of Previously Flown Flight Bearings**

After the discovery of the bearing with the blackened balls, seven additional BF shaft bearings were microscopically inspected and the wear depth profiles were measured. Wear was measured using a form-Talysurf measurement machine. Microscopic examination and wear depth results for these bearings are reported in Table 1. The bearings had mild surface distress but no spalling. The bearings appeared to be highly loaded with ball tracks running near the raceway shoulder. The balls showed discoloration, superficial rust stains but only S/N V6L009 was contained the black tribological coating on the ball and race wear surfaces. Metrology results show that Shuttle flights produced wear depths ranging up to 5 micrometers. The most damaged bearing was S/N V6M002. This bearing had 5 micrometers maximum wear on the inner race with evidence of plastic deformation in raceways.

**Table 1. Results of Metrology of Flight Body Flap Actuator Shaft Bearings**

Bearing Size	Bearing Serial Number	Number of Flights	Wear Depth Range (micro meter)	Microscopic Observations
106	V6M002	20	5.08	Mild discoloration
108	V6L009	20	2.23	Black complex oxide on balls and wear track
108	V89E006	19	2.23	Light gold color discoloration
108	V6L007	30	2.03	Superficial rust stains
108	V6L025	32	1.27	Slightly darken balls
106	V6M014	30	2.03	Moderate surface distress corrosion
106	V6L013	32	Wear debris build-up	Moderate surface distress, discoloration likely to lubricant degradation
106	V6L001	19	.38	Ball banding and mild discoloration and balls and races



## Bearing Testing of Body Flap Actuator Bearings

A pre-existing test rig (Figures 12 and 13) was adapted to conduct life tests on the body flap output shaft bearings (Size 106). The bearing tester supported an angular-contact bearing on each end of the drive shaft. Axial load was applied to the bearing pair and shaft by a locking mechanical screw. A drive pulley was attached to the middle of the drive shaft and was driven by a variable-speed AC motor. The bearing housing temperature was controlled by circulating ethylene glycol through coolant passages in the bearing test housings, which raised the test bearing temperature up to 70°C. During testing, the bearing axial load, shaft rotational speed, motor amps, and temperature of bearing outer races were monitored and recorded.

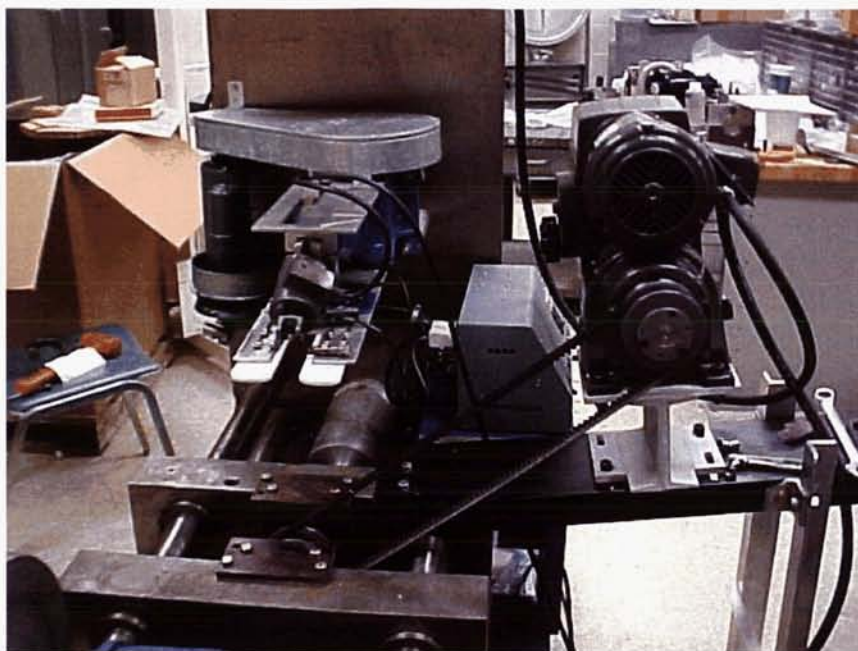


**Figure 12. MSFC Bearing Test Rig**

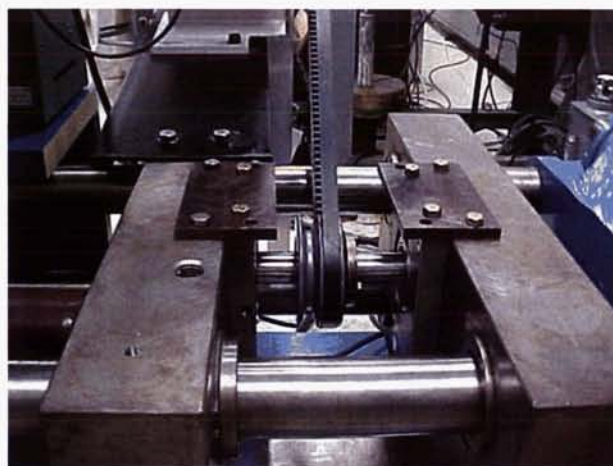


**Figure 13. Close-up view of MSFC Bearing Testing Rig**

### 48 Mission Life Test Results at 60°C

The objective of the testing was to demonstrate that previous flown and re-lubricated was acceptable for 12 additional shuttle flights with a safety factor of 4. The temperature of 60°C was selected because it



was thought that Braycote 601EF grease was shorter at higher temperature and 60°C was the highest and only temperature recorded in BF actuator system, namely in the power distribution unit.

The life test conditions for a single mission were derived from the flight load spectrum for the body flap actuator as understood early in the test program. The body flap qualification test load spectrum was made worst case to establish the single-mission life test load profile for the body flap input shaft bearings shown in Table 1.

**Table 2. Single Mission Load Profile**

Cycle	Axial load (N)	Speed (rpm)	Time (seconds)	Temperature (°C)
1	15569	80	1620	60
2	18238	70	90	60
3	19572	60	60	60
4	22241	50	30	60

With a limited supply of post-flight bearings available, initial test were performed on commercial bearings with similar dimensions to the flight bearings. Balls and cages were removed from the commercial bearings and 18 matched balls were added to make full complement test bearings, i.e., no ball separators. As shown in Table 1, S/N V6M002 had a maximum wear of 5.08 micro meters, which was higher than the other flight bearing. Two commercial bearings were loaded to 26700 N and operated for 10 minutes at 72 rpm to produce wear similar to wear measured in Shuttle flight bearing after 20 to 30 missions. After this testing, the maximum wear on a test bearing (BF-003, Table 3) was found to be 4.45 micro meter. These damaged bearings were cleaned, re-lubricated with Braycote 601EF and successfully tested for 24 hours or 48 mission life at 60°C. The bearings successfully completed this testing and about 1.27 micrometer of additional wear was observed BF-003. During testing no evidence of degradation of bearing performance was observed. Post-test inspection and metrology of the bearings showed moderate additional wear in the bearings as shown in Table 3.

**Table 3. Commercial Bearing Wear after about 25 Missions of Simulated Flight and after an Additional 48 Missions of Life testing**

Test Serial Number	Max. Wear Depth during Flight Simulation (micro meter)	MSFC Life Test Number	Max. Wear after 48 mission life test (micro meter)
BF-001	.66	LT002	2.54
BF-003	4.45	LT002	5.72

A photograph of a ball from BF-003 is shown in Figure 14. The photograph showed some banding and blue discoloration due lubricant degradation. The test lubricant was found to be in good condition. It was creamy white in color with some brown red areas caused by the early stage of lubricant degradation.



**Figure 14. Ball from BF-003 after 48 Mission life test**



Two additional 48 mission life tests were performed on previously flown flight bearings. The results of this testing are shown in Table 4. Both tests were successfully completed. No indication of lubricant failure or severe wear was observed. During the life testing, all bearings performed without anomalies and no evidence of torque increase was observed with increasing test time. In addition, no rise in bearing operating temperature was observed, which also indicated no gross degradation in bearing performance. Post-test inspection of these bearings showed moderate additional wear (Table 4). No evidence of lubricant failure, severe wear and or fatigue spalling was observed.

**Table 4. Wear for flight bearings after Shuttle Flights and after 48 missions of Additional Life testing**

Test Serial Number	Max wear before test (micro meter)	Max wear 48 mission life test (micro meter)	MSFC Life Test Number
V6M014	2.03	2.03	LT003
V6L013	Wear debris build up	.51	LT004
V6L001	.38	Wear debris build up	LT004

After testing, the lubricant appeared to be in good condition. The grease in the bearings was still creamy white with only a few areas of reddish brown discoloration (Figure 15). Balls from flight bearing showed significant banding due to normal wear and possible lubricant degradation (Figure 16).



**Figure 15. Flight bearing SN V6M013 after 48 mission life test**



**Figure 16. A ball from flight bearing V6L001 after 48 Mission of life tests**

Results of this 48 mission life test showed that 3 previously flown flight bearings and 2 pre-damaged commercial bearings successfully passed life testing for 24 hours or 48 missions at 60°C. Based on these results, it was recommended that freshly re-lubricated, pre-flown body flap shaft bearings were acceptable for 12 more flights on the Space Shuttle with safety factor of 4. When the average operation time per mission was updated to 16 minutes per mission, the bearings were found to be acceptable for 22 missions at 60°C. This recommendation was based on the assumption that 60°C was the worst-case condition for bearing lubricant life. Subsequent testing proved this assumption to be incorrect.

#### Life Testing of the Body Flap Shaft Bearings

The 48 mission life testing did not reproduce the black tribological coating on shaft test bearings, so testing with partially lubricated bearings, different temperatures, speeds, and stop-start speed profiles was continued in an attempt to produce the black tribological coating on the bearing wear surfaces, i.e. S/N V6L009. The investigators were surprised to find the life of the bearings to be 10 to 20 hours rather than the 66 hours originally required for the BF actuators. Shaft bearing life testing was redirected to measure the life of the bearing and demonstrate that 12 more Shuttle missions could be successfully accomplished.

In general, it was assumed the blackened balls were generated due to high local temperature, possibly due to lubricant degradation, and/or starvation or from an external heat source during re-entry. The objective of this testing was to generate blackened ball similar to those observed on BFA shaft bearing

S/N V6L009. A second objective of the testing was to determine the lubricant life of Braycote 601 grease used in BFA shaft bearings.

**Life Test Conditions:**

1. Size 106 commercial 52-100 steel thrust bearings were life tested.
2. A shaft with bearings mounted on the ends was thrust loaded with a locking mechanical screw.
3. The drive shaft was rotated by an electrical motor driving a pulley mounted on the shaft.
4. The bearings were tested in air at room temperature.
5. The criteria for end of bearing life were the onset of a dropping preload, bearing temperature rise, laboring of the drive motor and the onset of severe wear in the bearing.

The initial testing was performed at room temperature with continuous shaft rotation at 50 rpm. Tests were run at several thrust load levels. The tests were allowed to run until lubricant failure was detected. The results of testing are shown in Table 5.

**Table 5. Body Shaft Bearing Life Test Results Using Commercially Equivalent Bearings**

Bearing Number	Load(N)	Temp (°C)	Time(hr)	Cycles (Krev)	Failure Mode
4x Test (3 flight brgs and 2 test brgs)	Mission profile see Table 2	60	n/a	112.8	24 hrs, No failures
BF011	15569	23	11.3	33.5	Lubricant failure, Severe wear
BF012	15569	23	19	57	Lubricant failure, Severe wear
BF013	15569	23	26.3	78.9	Lubricant failure, Severe wear
BF09	20017	23	16.9	50.7	Lubricant failure, Severe wear
BF010	20017	23	16.9	50.7	Lubricant failure, Severe wear
BF008	22271	23	12.8	38.4	Lubricant failure, Severe wear

Bearing failures (lubricant failure) were observed much earlier than expected. These failures occurred much sooner than in previous 60°C, 48 mission life tests where no failures were observed. The mechanism continued to operate, but significant drops in axial load and bearing temperature increases were observed as well as copious amounts of wear debris. Post-test microscopic examination of the bearings showed two distinct wear modes.

1. Normal Wear Mode Characteristics
  - a. Race Appearance - Microscopic examination of the wear tracks in the races revealed a smooth matte finish. In some cases, the wear track was bronze colored. The bearing fabrication grinding marks were worn away.
  - b. Ball Appearance - The balls possess a shiny finish like a new ball. The shiny balls surface are often coated with a thin smeared black film covering the balls or concentrated in a wear ring pattern. The wear rings are produced when the rolls around a single axis.
2. Severe Wear Failure Mode (typical of failed bearings)
  - a. Race Appearance - Microscopic examination of the race wear tracks showed very rough surface. Wear scars form across the direction of ball motion. At higher loads and longer bearing lives, radial wear scars develop between the wear tracks and the shoulder and metal wear debris deposits on the bearing shoulder. Steel wear debris transfers from ball-to-race and/or race-to-ball. As the bearing test time in the severe wear mode increased to about 60 minutes, the transferred wear deposits turns black. The wear depth increased from 3 micrometers for normal wear to about 80 micrometers for severe wear.
  - b. Ball Appearance - undulating rather than smooth ball surfaces were observed. As the test time in the severe wear mode increased to about 60 minutes, the balls turned black.



Apparently, the black surface was formed when the worn balls heated up and oxidized during the last few minutes of the test.

In general, failed bearings exhibited severe wear. A failed bearing is shown in Figure 17 and 18. The onset of wear started when the lubricant between the ball and race was completely consumed or degraded. Shear plastic deformation occurred between the race and ball steel to cause adhesive wear or severe wear. Due to high friction and heat generation, the local ball temperatures rapidly increased and caused oxidation and discoloration of bearing balls. In some case, the balls were highly discolored and almost black. The test lubricant in the failed bearings was very dark in color with significant degradation and metallic wear debris.



**Figure 17. Failed Test Bearing BF012**

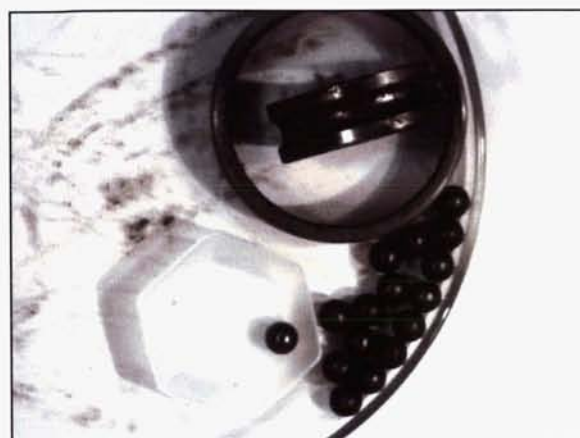


**Figure 18. Failed Test Bearing BF012 (disassembled)**

Darkened balls that were produced in testing were not identical to the black ball from V6L009. Scanning Electron Microscope examination of a failed test ball showed a texture surface. The surface of the test bearings did not have a polished finished, but appears to have been smeared with transferred steel. Some microspalling and surface cracking was observed. The flight bearing with the blackened balls (S/N V6L009) was in fairly good shape. This flight bearing did not exhibit severe wear. Balls had smooth surfaces and the raceway wear track was covered with smooth black oxide coating.

#### Life Testing at Elevated Temperature

Due to these unexpected results of lower life at room temperature, life tests at elevated temperatures were performed to confirm this trend. Tests were run at 60°C with 15569-N axial load at 50 rpm continuous shaft rotation. One test was run at 70°C under the same conditions. The same bearing test rig as previously described was used. The results are shown in Table 6 and Figure 20.

**Table 6. Results of Continuous rotation testing at elevated temperature**

Bearing Number	Load (N)	Speed (rpm)	Temp (°C)	Time (hours)	Cycles (Krev)	Failure Mode
BF015	15569	50	60	65.35	196	Lubricant failure, Severe wear
BF017	15569	50	60	39.65	119	Lubricant failure, Severe wear
BF031	15569	80	70	56.52	271	Lubricant failure, Severe wear

## NESC Bearing Testing

### Effect of Temperature on Life

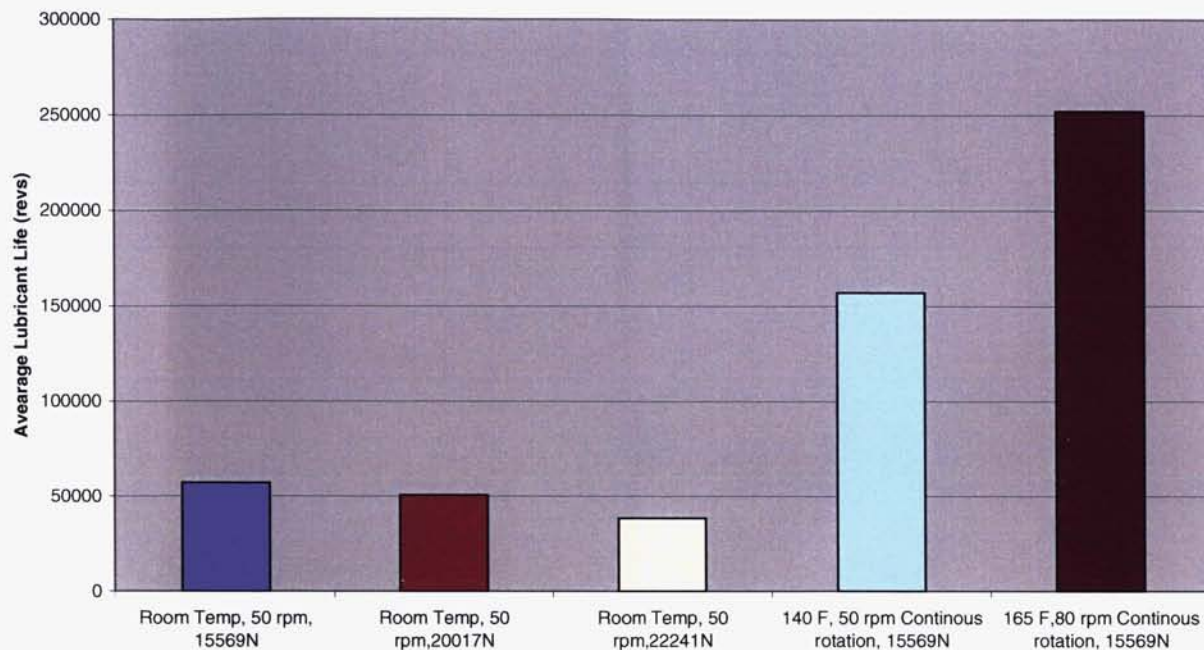


**Figure 20. The effect of temperature on lubricant life**

The results of this testing indicated that temperature had a significant effect on bearing life. Increased temperature yielded a significant increase in bearing life. The cause of this effect has not been determined. One theory is the higher temperature afforded better lubrication either by a decrease in apparent grease viscosity or by an increase in oil separation rate. This resulted in more oil available in wear contact area thus extending bearing life.

#### STOP\START Testing at Room Temperature

The testing to determine the lubricant life was performed with continuous rotation. This differs from the 48 mission life tests that had been previously performed in several ways. In the 48 mission life testing, the bearing ran at several different speeds and loads. Also, in actual BFA operation the actuator is operated for short periods of time (several minutes) then sits stationary for extended periods (months). To evaluate the effect of start\stop operation on the extension of bearing life, a series of stop\testing was performed using the same bearing test rig as previously described.

For this testing the bearing rig was run for 30 minutes at 80 rpm shaft rotation and then held idle for 30 minutes. This cycle was continuously repeated until bearing failure occurred. For a baseline comparison three additional tests were conducted with continuous rotation at 80 rpm. The results of this testing are shown in Table 7 and Figure 21.

These results showed start\stop operation has a moderate effect on lubricant life. The average bearing life for stop\start tests was 92500 revolutions which was about 30% greater than the average bearing life for the continuous rotation testing, most probably because surface tension pulls lubricant into the wear track while the bearings were stopped. These results also show that shaft speed had moderate beneficial effect on bearing life most probable because more lubricant was squeezed out of the ball race contact at lower speeds.



**Table 7. Results of Start/Stop lubricant life testing**

Bearing Number	Load (N)	Temp (°C)	Speed (rpm)	Time(hr)	Cycles (Krev)	Failure Mode
BF019	15569	23	80	20.1	96.5	Lubricant failure
BF021	15569	23	80	13.55	65	Lubricant failure
BF023	15569	23	80	14.76	51	Lubricant failure
BF026(start/stop)	15569	23	80	23.8	114	Lubricant failure
BF028(start/stop)	15569	23	80	21.31	102	Lubricant failure
BF030(start/stop)	15569	23	80	12.8	61.4	Lubricant failure

## NESC BFA Bearing Testing

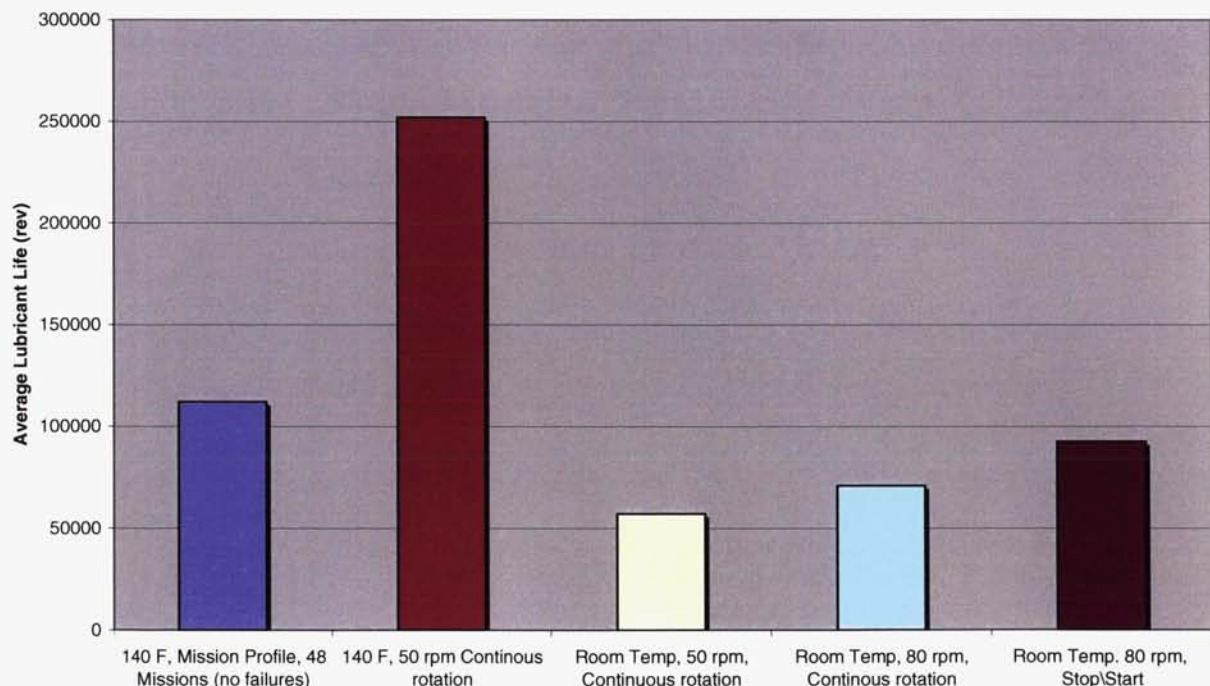


**Figure 21. Results of start/stop lubricant life testing**

The start/stop testing at 80 rpm most closely simulated the actual BFA operation. The majority (92%) cycles on the BFA are applied during ground operation under stop/start conditions. All of these cycles occurred at 80 rpm with 15569-N axial load at room temperature. The remaining cycles occurred during flight. The BFA was never operated under maximum load (22241-N load). This load occurred during ascent when the actuator is in a lock position. The actuator was operated for several seconds in space to test the actuator, but the remainder of cycles occurred during re-entry where temperature probably



reaches around 60°C. Recent reexamination of the BF actuator operation time line by the NESC showed that the actual average mission actuator operating time was 16 minutes (1280 cycles) rather than the 24 minutes. Based on these facts, the shortest lived start/stop test of 12.8 hours (61.4 cycles) was used to life the BFA shaft bearings. This calculation yielded a bearing life of 12 missions including a safety factor of 4.

### **Conclusions**

1. Initial test results of full scale bearing testing at 60°C indicated that previously flown and re-lubricated Body Flap Actuator shaft bearings were acceptable for 22 Shuttle Missions with a safety factor of 4. Subsequent bearing testing at 23°C show the lubricant life is reduced at lower operating temperatures.
2. Results of full scale bearing stop/start testing at 23°C showed that new bearings were acceptable for 12 Shuttle Flights with a factor safety of 4.
3. Efforts to duplicate the blackened balls observed on one of the Shuttle Body Actuator shaft bearings were unsuccessful. The blackened balls were produced in testing, but only after lubricant failure and severe wear are initiated. SEM analysis showed that the test blackened balls are not very similar to the flight ball. The test blackened balls were in much worse condition and had a more textured surface with small cracks observed. The flight bearing with blackened balls did not suffer a lubricant failure. The flight blackened bearing was in relatively good condition with smooth wear surface.
4. The Raman Spectroscopy, XPS and EDS analysis of the flight black ball detected the presence of carbon-rich layer on an iron oxide-rich layer and both with fluorine. The detection of amorphous carbon, fluorine and FeF<sub>3</sub> in both the carbon-rich surface layer and the iron oxide under layer were significant since local degradation of the PFPE lubricant appeared to be in part responsible for the black coating observed on the balls and raceways of P/N 5902050, S/N V6L009, bearing removed from S/N 402 BF actuator. The origin of the thicker, black iron oxide-rich layer under the carbon-rich layer is not well understood. Because it occurred only on the wear surfaces, the tribological chemical reactions in the ball/race wear interface did cause the black coating. Most investigators felt that high temperatures below 200°C contributed to the black coating formation. Local lubricant starvation within the ball path of the bearing may have generated local heating with temperatures high enough to cause the remaining lubricant film to degrade and react with the 52100 steel surface, effecting formation of a complex oxide layer that resulted in the black coating on the wear surfaces. While the system may have recovered locally after the blackened coating event, the oxide layer formed was apparently effective in separating the working surfaces of the bearing, preventing its failure, and serving as a surrogate solid film lubricant.
5. The strength, geometry, metallurgical structure and wear of the black coated bearing were found to be essentially identical to other BF shaft bearings after Shuttle flights. No evidence of severe wear was observed. Therefore, shaft bearings with black tribological coatings like S/N V6L009 are expected to perform successfully for at least 12 more Shuttle missions.
6. The severe wear mode caused failure of the shaft bearing and determined the bearing life. The onset of severe wear is thought to be caused by ball/race metal adhesion after all the Braycote 601EF grease is depleted from the interface.

### **Lessons Learned**

1. When space mechanisms are qualified by accelerated life testing, bearings should be qualified by real-time life testing. Bearings enduring the highest stresses, longest operating lives or highest temperatures in the mechanism application should be life tested as part of the qualification process.
2. Bearing life and lubricant life was found to be shorter at lower temperature even though the lubricant tribological decomposes or degrades more rapidly at higher temperature.

### **Acknowledgments**

The authors thank F. Hernandez, J. McManamen and J. Figert of Johnson Space Center; B. Heitzman and L. Salvador of Boeing; P. Munafo, P. Hall, L. Moore, H. Gibson, M. Sharp, and S. Cato of Marshall Space Flight Center; E. Devine of Swales Aerospace; E. Zaretsky and K. Street of Glenn Research Center; J. York, D. Hill and S. Tollefson of Hamilton Sundstrand; and M. Sovinski of Goddard Space Flight Center for their assistance. Without this team's support, this task could not have been accomplished.

### **References**

1. L. Hughes, Hamilton Sundstrand; Destructive Analysis of Space Shuttle Body Flap Actuator Blackened Ball Bearing, P/N 5902050, S.N V6L009, Memorandum Report 66852, February 17, 2004
2. J. York, J. Sikes, L. Hughes, Hamilton Sundstrand; Overhaul Inspection Findings for Components from Space Shuttle Body Flap Right-Hand Inboard Actuator Unit S/N 402, P/N 5003661A, Report 66442, Rev. A, January 24, 2003
3. J. York, J. Sikes, L. Hughes, Hamilton Sundstrand; Overhaul Inspection Findings for Components from Space Shuttle Body Flap Left-Hand Inboard Actuator Unit S/N 401, P/N 500141B
4. Body Flap and Rudder Speed Brake Actuator Bearing Independent Technical Assessment Final Report, NASA Engineering and Safety Center, NESC ITA 04-076-1
5. S. N. Cato, Marshall Space Flight Center; Orbiter Body Flap Actuator Bearings
6. K. Street and M. Sovinski; Analysis of Black Bearing Balls from a Space Shuttle Body Flap Actuator, Proceedings of World Tribology Congress III, Washington, D. C. September 12-16, 2005
7. P. Herrera-Fierro, M. Masuko, W. Jones, S. Pepper, Glenn Research Lab.; XPS Analysis of 440C Steel Surfaces Lubricated with Perfluoropolyethers Under Sliding Conditions in High Vacuum, NASA Tech. Memo. 106548, April 1994
8. W. Jones, Glenn Research Lab and M. Jansen, Univ. of Toledo; Lubrication for Space Applications, NASA/CR 2005-213424, January 2005

# **Bearing Development for a Rocket Engine Gimbal**

Christian Neugebauer\*, Manfred Falkner\*, Ludwig Supper\* and Gerhard Traxler\*

## **Abstract**

The bearings for a gimbal of a cryogenic upper-stage rocket engine are highly loaded, they are exposed to corrosive environment, and they have to cope with a wide temperature range down to cryogenic temperatures. A tailored single-row full-complement needle roller bearing design integrated by press fit mount technology was selected for this specific application. This paper describes the design considerations, the analysis approach, and the development test results of these bearings.

## **Introduction**

Austrian Aerospace has the privilege to develop the gimbal for the next generation upper-stage engine of the ARIANE 5 Launcher family, the VINCI engine. One of the key components of the gimbal are the bearings which

- are highly loaded by the engine operating loads and by inertial loads,
- are limited in space and mass due to stringent mass and envelope requirements,
- must tolerate considerable misalignments of the axis due to elastic deformation of the gimbal under mechanical load, and
- have to cope with harsh environmental loads and cryogenic temperatures.

The chosen bearing is a tailored needle roller bearing with specially crowned needles. To transmit the high loads, the bearing pitch circle diameter should be as large as possible. This leads to a design with a bearing integrated by press fit mount technology to allow for an undivided bearing support to find a space and mass optimized assembly design.

The design and dimensioning of the press fits was driven by the following constraints:

- Maintenance of proper fit under any thermal load-case to prevent loosening of the bearing rings in the support when experiencing thermal gradients,
- The reduction of the bearing's radial clearance during integration caused by the press fits,
- Elastic deformation of the race along the bearing axis due to the unequal stiffness distribution of the bearing housing. Such deformations may not disturb the radial clearance of the bearing.
- Roundness deviations of the race due to radial elastic deformation caused by the unequal stiffness distribution of the bearing housing.
- The unequal stiffness distribution of the bearing housing and the thin sectioned design also causes roundness deviations caused by the manufacturing process of the housing that sums up with radial elastic deformations due to the press fit.
- The design must allow the introduction of considerable axial integration forces during bearing insertion.

The development test results confirmed the chosen design.

---

\* Austrian Aerospace GmbH, Vienna, Austria



## Description of the Mechanism

The main functions of the gimbal are to fix the engine in its defined position, to transfer the thrust and all inertial forces from the engine to the stage and to allow the gimbal operation. The gimbal consists mainly of an engine-side bracket, the gimbal cross, and the stage-side bracket, connected by two pairs of bearings. The distance between the gimbal interface plates amounts to 150 mm. Four single-row needle roller bearings allow gimbal motion about two axes. The development of these bearings is described in this paper.



Figure 1. CAD model and development model of the Gimbal, with uncovered bearings

## Bearing Type, Layout and Design

Table 1 presents the main parameters of the bearings described in this paper.

Table 1. Bearing Parameters

Bearing type	Single row needle roller bearing
Material of rings and rollers	Cronidur 30
Lubricant	Sputtered Lead by ESTL, UK
Supplier of the bearing	FAG Kugelfischer AG, Germany

### Bearing Type

At an early stage of the development, the decision for rolling bearings was made due to the low friction torque and the low wear of rolling bearings. The decision for a needle roller bearing was driven by the load capability of the bearing at a given envelope restriction. This led to a one-row full-complement needle roller bearing design.

The race of the outer ring is equipped with borders to position the needle rollers in the axial direction. As no lateral force transmission by the bearing is required, the races of the inner ring are not equipped with borders.

#### Diameter / Roller Length Ratio

To achieve a certain static load rating, the bearing diameter increases if the needle length decreases. As considerable axial deflection between inner ring and outer ring was expected, a design with short needle lengths was chosen combined with a bearing diameter as large as possible to still have high load capability even if axial deflection occurs by spreading the load to a higher number of needles. Using shorter needles reduces also the impact of edge pressing.

#### Needle Roller Diameter

Investigations on the needle roller diameter were performed. It turned out that, computing the static load of needle bearings with different needle roller diameters while keeping the outer race diameter constant and also keeping the needle length constant, the load capability increased with decreasing needle roller diameter:

However, the static load capability is not the only parameter to be taken into account. The friction moment of the bearings increases with the number of rolling elements. As this effect can not be numerically evaluated for needle bearings we relied on experience from previous needle bearings. The ratio between roller diameter and roller length increases with higher roller diameters leading to less friction caused by misaligned tilted rollers.

#### Bearing Outer Ring Thickness

To distribute tensioning loads, lateral loads, and torsional loads of the gimbal on a high number of bearing needle rollers, the stiffness of the load-transferring elements, which are the bearing housing and the rings, should be as high as possible. A comparison of different thickness ratios between bearing outer ring thickness and housing thickness within the envelope constraints has been performed. The inner diameter of the bearing outer ring and the outer diameter of the bearing housing (formed by the yoke) have been assumed as fixed.

The comparison showed that the smaller the bearing ring thickness, the more stiffness is gained. The higher Young's modulus of the bearing steel Cronidur 30 (208000 N/mm<sup>2</sup>) compared to the Young's modulus of the housing of Ti-6Al-4V-ELI (110000 N/mm<sup>2</sup>) has less effect on the stiffness than a thicker rectangular section of the yoke of Ti-6Al-4V-ELI. No shear force transmission was assumed between the bearing and the housing in this comparison. Following this, the bearing outer ring thickness has to be as small as possible.

The lower limit for the bearing ring thickness is a manufacturing issue. The ring thickness must stay above 2 mm according to the bearing supplier.

#### Bearing Inner Ring Thickness

The bearing inner ring is supported stiffly by the gimbal cross, which is made of Inconel 718 (Young's modulus 205000 N/mm<sup>2</sup>). Therefore, load transfer is not a driver for the inner ring thickness. The design driver for the bearing inner ring thickness was integration issues. The gimbal cross insertion process requires a relatively small shaft diameter.

#### Bearing Sizing

The bearing pre-dimensioning was done keeping in mind above considerations and using standard formulas for full-complement roller bearings. The final bearing calculation (including Hertzian pressures in the roller needles) was then done using the results of the FEM calculation.

A coefficient of static load  $f_s$  of 0.7 was assumed as the application exhibits small angular oscillations and shock loads. The largest bearing that fits in the room given and having the necessary static load capacity was selected.

#### Bearing Ring Design

The bearing inner side is not covered by the gimbal, so borders were designed to prevent intrusion of contamination. Shoulders on the outer and on the inner rings limit the travel during the axial insertion process. Figure 2 shows the gimbal bearing design:



**Figure 2. Gimbal Bearing**

#### Outer Ring Press Fit

The operating temperature range of the gimbal is between 120 K and ambient temperature. A compression fit between the outer bearing ring and the housing, and the inner bearing and the shaft is desired at any temperature.

The material of the housing is Ti-6Al-4V-ELI. The bearing steel, Cronidur 30, has a higher coefficient of thermal expansion than Ti-6Al-4V-ELI. This leads to a decrease of compression at lower temperatures as the bearing ring shrinks more than the housing. The compensation of this effect is done by a proper dimensioned compression fit between the bearing housing and the bearing outer ring.

The dimensioning of this compression fit must also take into account the worst-case manufacturing tolerances; sufficient compression must still be granted even with the smallest outer ring diameter and the largest housing bore diameter. Combining the greatest outer ring diameter with the smallest bore diameter, the integration force of the outer bearing ring will increase. To keep this increase as small as possible, tight tolerances are given: P5 (9  $\mu\text{m}$ ) on the bearing outer ring and IT5 (13  $\mu\text{m}$ ) (in accordance with DIN 7151) on the housing bore.

The housing bore diameter was chosen to still have compression even with the smallest outer ring diameter and the largest housing bore diameter at the lowest expected temperature. The seat dimensioning provides a compression of 8...30  $\mu\text{m}$  at ambient temperature and 2...24  $\mu\text{m}$  at the operating temperature of 120K.

#### Inner Ring Press Fit

A compression fit between the bearing inner ring and the shaft is desired. The material of the shaft is Inconel 718. Inconel 718 has a higher coefficient of thermal expansion than Cronidur 30. So the same thermal expansion situation as occurs between the bearing outer rings and the yokes also occurs for the inner bearing ring seat on the shaft of the gimbal cross. Also, for the inner ring fit, a compensation using a compression seat with tight tolerances is used: P5 (8  $\mu\text{m}$ ) on the bearing inner ring and IT4 (7  $\mu\text{m}$ ) on the shaft.

The inner ring bore diameter is chosen to still have compression even with the smallest shaft diameter and the largest bearing bore diameter at the lowest expected temperature. The seat dimensioning



provides a compression of 21...36  $\mu\text{m}$  at ambient temperature and 2...17  $\mu\text{m}$  at operating temperature of 120K.

### **Selection of Bearing Material**

The selection of the bearing material had to consider the demanding mechanical and environmental loads. Among the bearing materials, firstly the traditional bearing materials AISI 52100 and corrosion resistant AISI 440C were studied. It turned out early that these materials do not have the required corrosion resistance for exposure to salt fog. A preliminary salt environment test showed severe signs of corrosion as expected for the AISI 52100, but also, although less severe, for the AISI 440C.

For this reason it was decided to use a better corrosion resistant bearing steel for the bearings of the gimbal: Cronidur 30. This material is a FAG-proprietary bearing steel that combines excellent corrosion resistance with high strength and durability [1]. A standard grade of Cronidur 30 was chosen that is also used on cryogenic applications of the U.S. space shuttle program. The corrosion resistance of this material was demonstrated in a salt spray test according to the Ariane standard salt spray test procedure that has a duration of 4 days. No signs of corruptions were visible.

### **Selection of Bearing Lubricant**

Liquid lubrication was not possible as the gimbal operates at cryogenic temperatures. After a pre-selection among available dry lubricants the following candidates were identified: sputtered  $\text{MoS}_2$ , sputtered Ag (Silver), sputtered Pb (Lead), blasted  $\text{WS}_2$  (trade name "Dicronite DL-5"), TiC coating, or an uncoated design.

An early development test showed that sputtered lead by ESTL, UK was the suitable solution. The results of the tribological tests were presented on the 37<sup>th</sup> Aerospace Mechanisms Symposium [3].

### **Design of the Bearing Support**

The design of the bearing support was driven by stringent envelope constraints and demanding stiffness specifications. To cope with the high radial loads on the bearings, it was desired to find a design that allows for a maximized pitch size diameter of the needles. A bearing support consuming little space was necessary and leads to an unconventional design solution for the bearing support:

- an un-divided yoke design, that requires axial insertion of the press-fit mounted outer rings, and
- thin walled outer bearing rings and yokes.

The bearing support consists of a circular bore in housing that has varying stiffness along its circumference: It is thin walled at the lateral faces and it is rigid at the top and at the bottom of the bearing. Compression fits are used for the bearings to allow a design consuming little space while being more rigid than a conventional, separated housing clamped by bolts.

Firstly the unequal stiffness distribution causes circularity deviations caused by changing cutting forces during machining. The weaker sections of the bearing support exhibit a larger diameter than the rigid sections caused by elastic deformation during the turning and grinding operations. These circularity deviations were measured to be 4...8  $\mu\text{m}$ .

Secondly, as described above, the bearing outer rings are situated within the bearing support using a compression fit. This compression fit causes radial load on the bearing support. This radial load deforms the bearing support made of titanium alloy. Deformation is larger in areas of the weaker sections than in the areas of the rigid sections. This circularity deviation, caused by elastic deformation was calculated by FEM analysis with 8  $\mu\text{m}$ .

The compression fit causes the outer bearing ring to follow these circularity deviations, so above two reasons lead to a circularity deviation of the race of the integrated bearing outer ring that has to be considered for the dimensioning of the bearing clearance.



**Figure 3. Bearing Support (located in the gimbal yokes)**

### **Optimization of the Needle Roller Design**

The gimbal transmits the thrust of the rocket engine to the stage. This force bends the gimbal cross. The bearing inner rings are attached to the deflecting gimbal cross whereas the bearing outer rings that are attached on the gimbal yokes do not perform a corresponding deflection. This leads to a considerable angular misalignment between the axis of the bearing inner ring and the axis of the bearing outer ring.

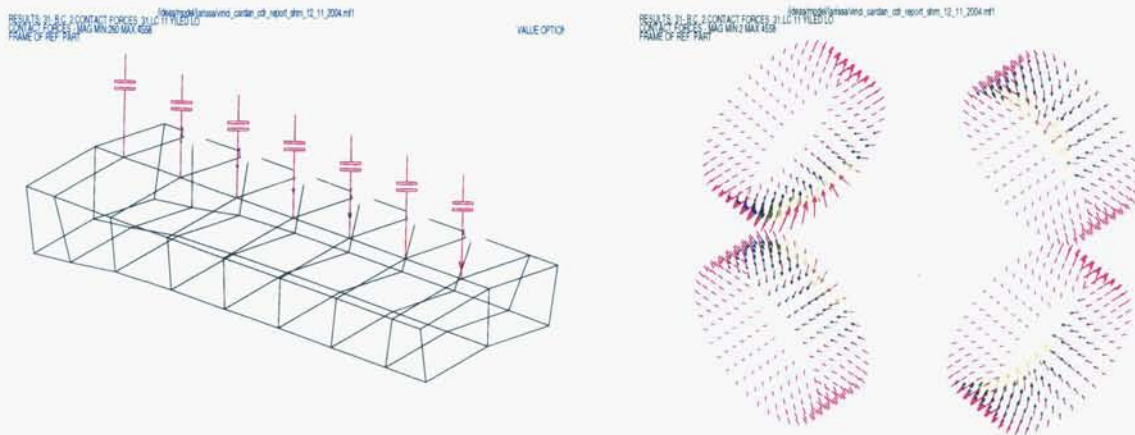
The bearing is not pre-loaded but has radial clearance. For this reason, the load distribution along the loaded bearing needle rollers is not constant but approximately triangular shaped. It was decided to study the load distribution in detail and to optimize the shape of the needle rollers to minimize the Hertzian contact stress.

The load distribution was analyzed in a detailed FEM analysis of the bearings, which included a model of each needle roller within the complete gimbal assembly so that also the impact of the stiffness of the adjacent structure was adequately modelled. In this model, each needle roller was divided into sub-segments. Each of these sub-segments has adequate stiffness and is equipped with gap-elements to simulate the bearing clearance.

Figures 4 and 5 present a typical FE model of the needle rollers attached to the bearing inner ring, and the resulting load distribution within the bearings under worst case loads. This model was used to optimize the load distribution and reduce the peak values of Hertzian stress on the needle roller by local reductions of the stiffness of the bearing support structure, and to predict the load distribution of the most loaded needle roller of the bearing.

The resulting stress distribution was used as input for the optimization of the needle roller shape. An adequate crowning of the needle was defined by the bearing supplier FAG.

Thus the bearing allows angular misalignment between the inner ring and the outer ring while transmitting the operational loads with permissible Hertzian stresses.



**Figures 4 and 5. Finite element model of the needle roller and analysis result for the needle loads**

### Dimensioning of Clearance

To reduce the bearing friction torque it was required that the bearings have positive radial clearance during the whole operation cycle. A mathematical model was established that considered:

- The reduction of the outer ring race diameter by compression of the bearing outer ring due to its compression fit in the housing. As the compression depends on the temperature, this value had to be evaluated for the whole operating temperature range of the gimbal.
- The increase of the inner ring race diameter by tension of the bearing inner ring due to its compression fit on the shaft. Also this value had to be evaluated as temperature dependent.
- The thermal elongation of the bearing steel, the Titanium alloy of the housing, and the Inconel 718 of the shaft.
- The manufacturing tolerances of the fit diameters of the outer ring and the housing as well as the inner ring and the shaft.
- The roundness tolerances of these diameters.
- The elastic deformation of the outer bearing ring in the housing due to the unequal stiffness distribution of the housing as described above.

The clearance was evaluated for the whole mission profile, using the thermal model results to apply the appropriate thermal gradients. Figure 6 shows the bearing clearance results for the whole mission profile.

### Integration of the Bearing

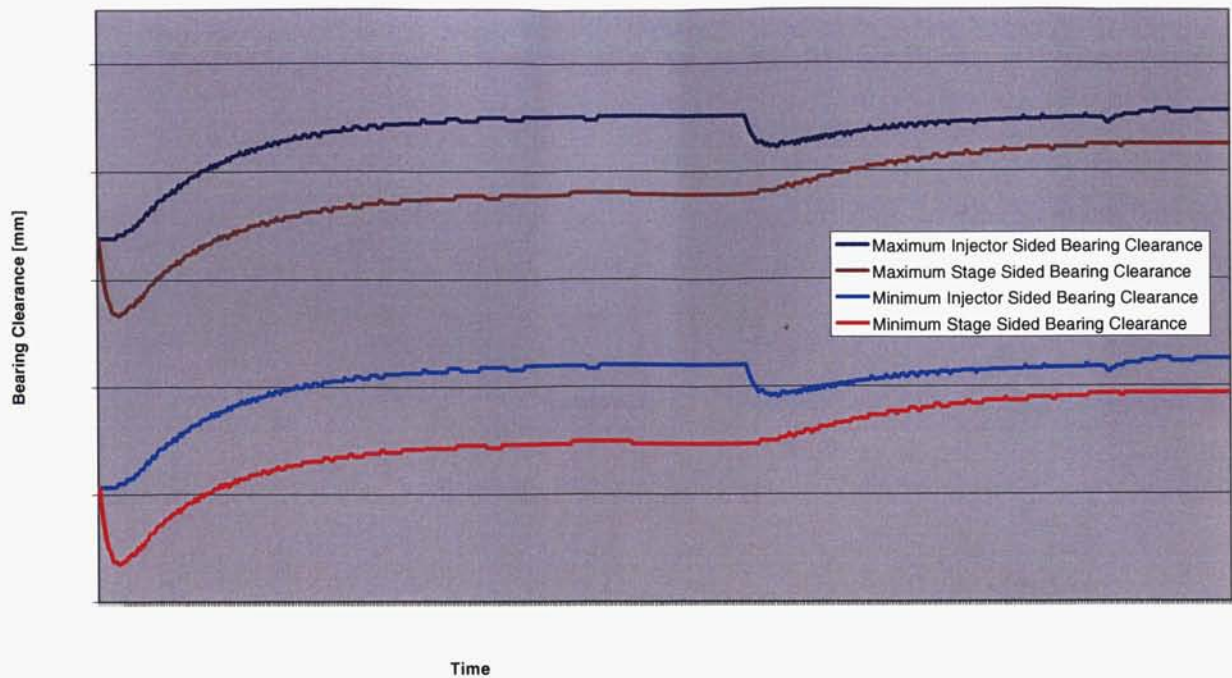
As highly pre-loaded compression fits are used for the bearings, integration by a press tool is mandatory.

The gimbal yokes and the gimbal cross are fixed in a special tool. The complete bearing assembly, comprising of the inner ring, the outer ring, and 37 needle rollers is pressed axially into the gimbal assembly by a spindle press. To ease the press process and to prevent cold welding of the parts, all contact areas are greased with Fomblin Y Z25 by Solvay Solexis, Italy. The residue is removed by cleaning after the press process.

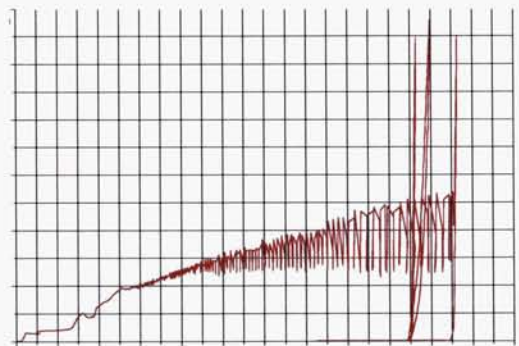
During integration, the integration force is measured by a load cell, and recorded. The press process stops when the measured integration force increases rapidly, which is an indication that the shoulders on the bearing rings are in contact with the according counter-faces of the housing and of the gimbal cross.

Figure 7 shows a typical load trace as experienced during bearing integration:





**Figure 6. Bearing clearance results for the whole mission profile**



**Figure 7. Bearing integration force versus insertion depth trace**

The trace shows a continuous increase in insertion force as the bearing slides into its seat. It is overlaid by vibrations of the setup. At a sudden point, the integration force increases rapidly signalling the completeness of the integration process.

### Development Test Setup

Testing of the bearing on bearing level was not considered necessary. The development testing of the bearing was part of the development test campaign of the gimbal assembly. For the development testing of the gimbal assembly, a dedicated test rig was developed and manufactured that allows applying the following loads simultaneously:

- Mechanical load, consisting of forces in longitudinal (X), lateral (Y, Z) direction and moment load,
- Thermal load, applied as temperature gradient between the upper and the lower gimbal interface plane,
- Dry Nitrogen atmosphere
- Gimbal movement of  $\pm 6^\circ$

During application of these loads the following measurements are continuously recorded:

- Friction torque of the bearings
- Deformation and clearance of the gimbal assembly
- Gimbal angle and gimbal count
- Forces and moment load
- Temperature of the interface planes and of 8 measurement points on the gimbal
- Strain of the gimbal structure

To allow measurement of the bearing friction torque under load and under low temperature, a special design of this test rig was developed. The gimbal assembly forms one joint of a pendulum support. The second joint is a large spherical, case-hardened contact that has a very low friction torque compared to the bearing friction torque. The pendulum is equipped with a quartz measurement plate that measures the bending moment within the pendulum. Rotation of the gimbal assembly around a gimbal axis causes friction torque that induces bending moment in the pendulum. By measuring the bending moment, the friction torque can be determined. As the location of the quartz measurement plate is distanced from the gimbal assembly and it is thermally isolated, it is possible to operate the gimbal at low temperature while the quartz measurement platform is at ambient temperature, which is necessary for high accuracy friction torque measurement. Accuracy is 10 Nm, measurement range is 300 Nm.

The mechanical loads, which are forces and a moment load, are applied by a computer-controlled hydraulic cylinder system consisting of three cylinders arranged on the test rig structure, which allows applying all the required load combinations. The loads are continuously measured by separate load cells. The gimbal motion is applied by a crank driven by an electrical motor that is supplied by a frequency converter to allow adjustment of the gimbal frequency.

The individual temperature of the interface plates is controlled by two separate temperature controllers that control the flow of liquid nitrogen through pipes embedded in the interface plates. These interface plates are thermally isolated from the test rig structure. The gimbal assembly is placed in a housing that is purged with dry nitrogen during low temperature testing. Figure 8 shows a schematic view of the test rig.

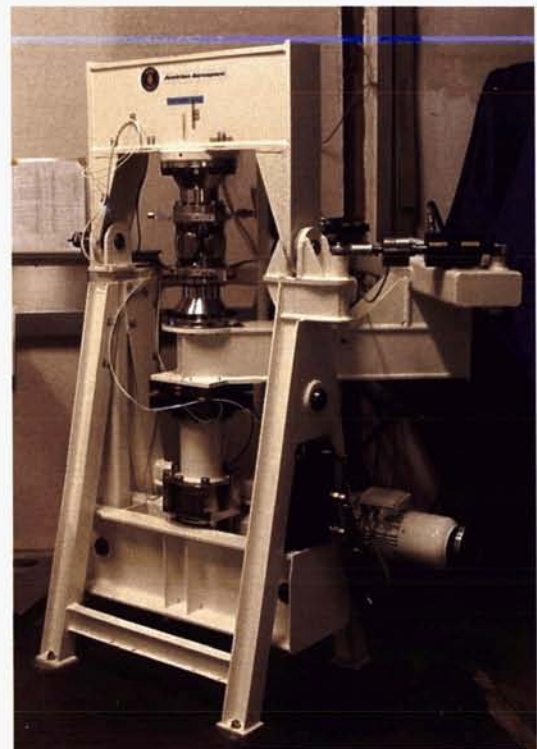
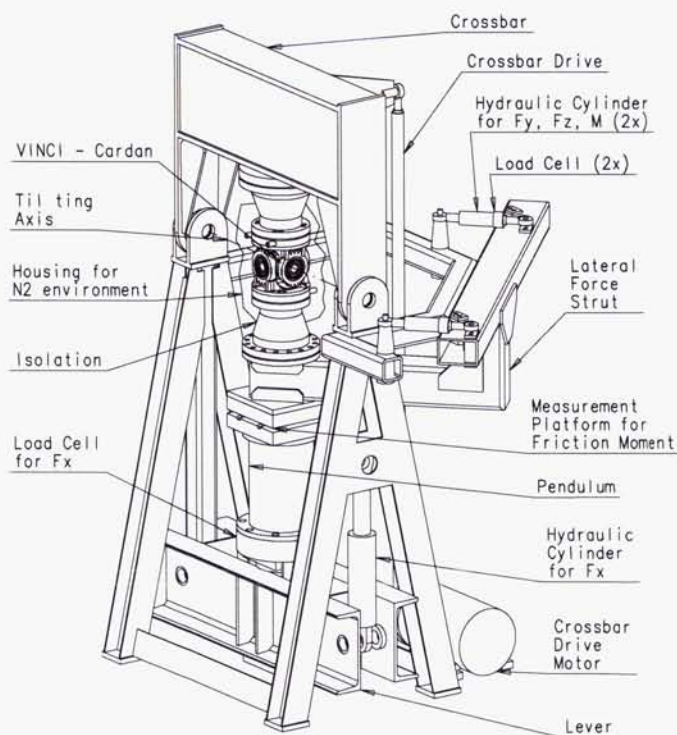


Figure 8. Gimbal Test Rig: Schematically View and Photograph



By testing the bearings at the gimbal assembly level, the bearings could be tested with representative integration such as the compression and the tension from the press fits, and with representative deflections of the rings and between the inner ring and the outer ring caused by the deflections of the gimbal structure under load.

### **Development Test Results**

The development tests comprised the environmental tests and the life test of the bearing. After these tests, the performance was verified as end-of life characteristic. An overload test concluded the bearing development test campaign.

#### **Environmental Tests**

Before the mechanical tests, environmental tests were performed to simulate on-ground and flight environmental loads such as dry heat, damp heat, thermal cycles in damp air, thermal shock and salt fog. The tests were performed in a climatic chamber.

No visual degradation of the bearings was observed. The selected bearing steel Cronidur 30 did not show any signs of corrosion. The lubricant (sputtered lead) formed lead salt as expected. Particles of this lead salt escaped from the bearing as can be seen in Figure 9.

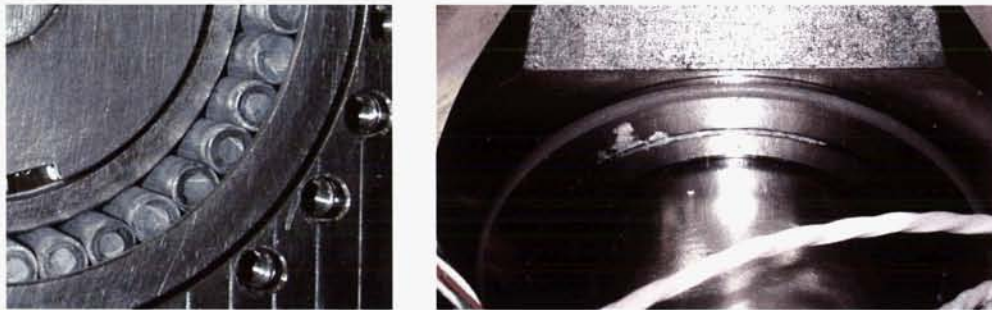


**Figure 9. Formation of lead salt on the lubricated needle rollers, escaping lead salt**

The formation of the lead salt as a consequence of the environmental testing was observed before during component level testing of the lubricants. These results were presented at the 37<sup>th</sup> Aerospace Mechanisms Symposium [3]. It is considered acceptable as the lead salt acts as protective layer which encapsulates the underlying lead. The lead salt has lubricating properties and acts as a lubricant itself. Functional performance was verified during the subsequent performance tests.

#### **Load Test**

The bearings were exposed to the mechanical design loads at ambient and at low temperature. No structural damage occurred.

#### **Friction Torque Test**

The friction torque of the gimbal assembly around one axis was measured. The result is the friction torque sum of the engaged pair of bearings. A lateral support transmits the lateral loads as the bearings support radial loads only. The friction torque of this radial support is also included in the results; however it is supposed to be negligible.

The friction torque was measured at room temperature, and at low temperature, and result was well below the allowable friction torque. This means that the lubricant performed as expected even after the harsh environmental tests.

#### **Life Cycle Test**

The life cycle test was intended as a tribological test to verify the lifetime at worst-case loads and temperature. A thermal gradient simulating the worst-case operating interface temperatures was applied.



Figure 10 presents the friction traces during the test (friction torque peaks and cycle count vs. load cycles). Gimbal operations with the worst case non operating load applied and additional gimbal operations under the worst-case operating loads were performed. The bearing friction torque was recorded during this test. The friction torque keeps approximately constant during the load cycles. No significant increase in bearing torque could be observed.

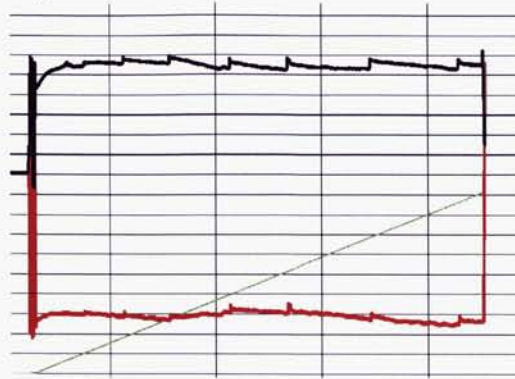


**Figure 10. Bearing friction trace during the life cycle test under operational load**

#### Clearance Test

The clearance was measured after the life cycle test as an end of life value. The measured clearance was within the clearance requirements and was according to the test prediction.

#### Stiffness Test

The stiffness of the gimbal assembly was measured. It is mainly determined by the bearings' stiffnesses. The stiffness was measured in all load directions: compression of the gimbal, tension of the gimbal, lateral force, and moment load on the gimbal. As the bearing stiffness is determined by the deformation of the contact between the races and the needle rollers, which is a Hertzian line contact, the spring rate is not constant. For this reason, the stiffness was predicted and evaluated for 50% and 100% of the maximum loads. Figure 11 shows a typical deformation versus load graph of the gimbal assembly.

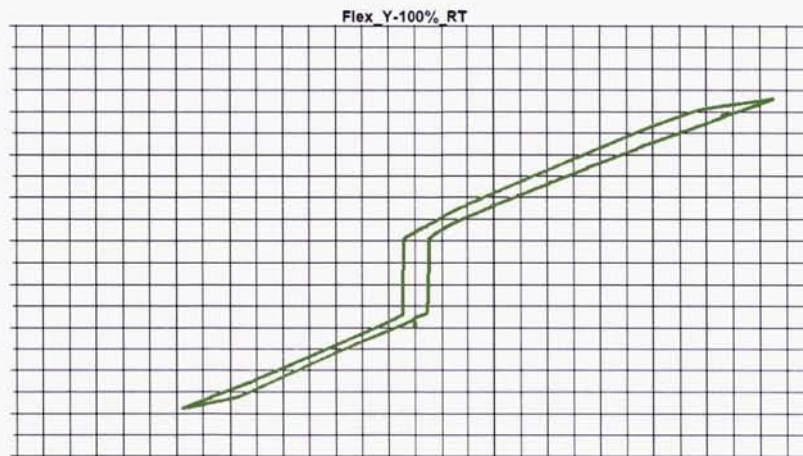


**Figure 11. Deformation versus load graph**

The graph shows the deformation versus the load in both load directions, thus the hysteresis is also shown in the graph. While recording this graph, the load direction was swapped so that during at the zero crossing of the load the bearing clearance can be evaluated from the graph.

As a result of the test, it turned out that the stiffness in longitudinal direction and in lateral direction met the predictions of the FEM analysis. However, the measured torsional stiffness was noticeably smaller than predicted.

The reason for this difference was investigated in detail. It turned out that the torsional stiffness strongly depends on the crowning of the needle rollers. The local rotation of the bearing housing is determined by the contact point of the needle rollers which is the point of torque introduction into the bearing housing.

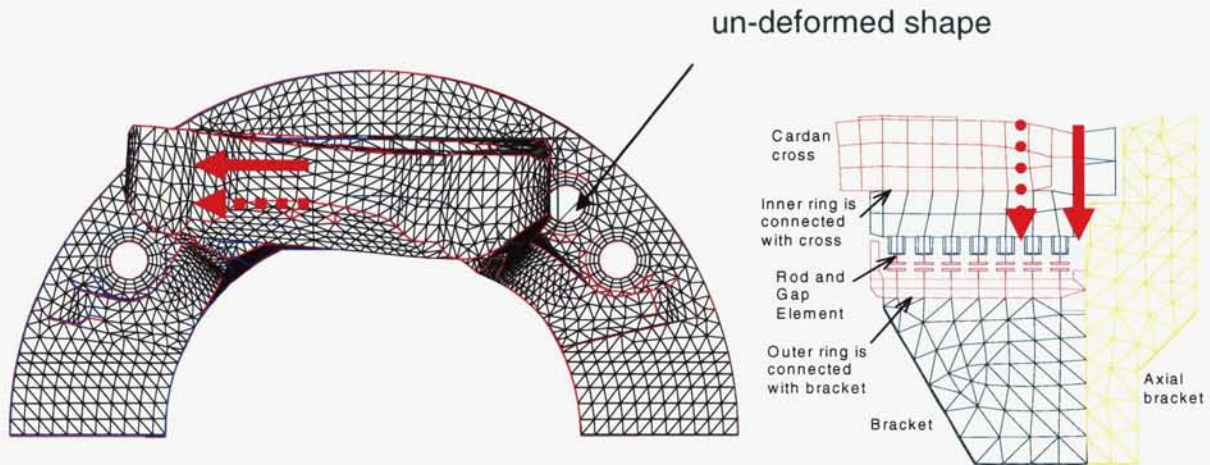


**Figure 12. Simulated deformation of the bearing housing and structural analysis model**

Figure 12 shows on the left hand side the locally rotated bearing housing, and its un-deformed shape. On the right hand side, a model detail of the structural analysis model is shown. Each needle roller is simulated by a row of 7 rod elements and 7 gap elements connected to each other. The rod element simulates the stiffness of the race/roller/race contact and the roller whereas the gap element simulates the radial clearance of the bearing.

The load introduction point is as initially resulting of the structural analysis model of the gimbal assembly is marked with a full arrow. This analysis model assumed cylindrical rollers. The dashed arrow presents an expected point of load introduction into the bearing housing as can be assumed from the stiffness test result because of the crowning of the rollers.

A refined analysis model was established to evaluate the impact of the roller crowning by variation of clearance along the needle similar to the real bearing needle shape instead using a cylindrical model for the needle rollers. It turned out that the calculated stiffness decreases due to this refined simulation of the needles. This could explain the test result.

The needle shape is optimized for stress distribution and not for optimized stiffness.

#### Life Cycle Margin Test

To verify the friction and coating behavior under higher load, the life cycle test was continued. The load was increased up to 150% of the qualification load in steps of 10%. 500 gimbal operations were performed with each load step.

Figure 13 shows the friction envelope traces in red and blue color, the counter in green line, and the compression forces (negative) in black color. The graph shows the envelope curves of the measurement platform torque which are not identical with the friction torque of the gimbal bearings themselves, however they are proportional. It showed that the friction torque increases nearly proportional with the increasingly applied test load. The friction torque kept far below the specified value even at 150% of the qualification load. The hardware under test showed no visible damage.



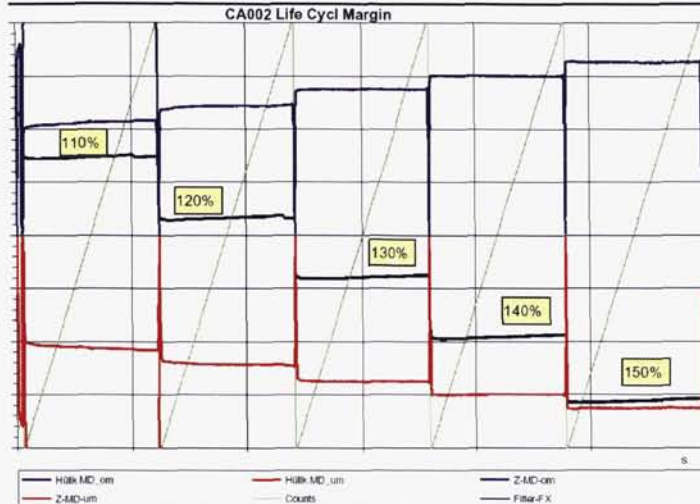


**Figure 13. Torque traces of the gimbal assembly during the life cycle margin test**

### Summary and Conclusion

It was demonstrated that the gimbal bearings were adequately designed and dimensioned and that the tribological system is capable to sustain the environmental and mechanical loads and meets the related performance requirements.

- The sputtered lead coating on the Cronidur 30 substrate provides excellent tribological behavior in terms of friction and life even after being exposed to harsh environmental loads. The expected but unintentionally produced lead salt acts also as a lubricant.
- The un-conventional bearing mount design using press fit mounts proved successful however, a careful design was necessary as dimensional changes of the bearing rings occur due to elastic deformation and due to summation of manufacturing tolerances.
- The stiffness of needle roller bearing strongly depends on their axial alignment between inner and outer ring. The crowning of the rollers must be included in the structural analysis model to allow accurate prediction of the stiffness behavior.

### References

1. Trojahn, W. et al. "Progress in Bearing Performance of Advanced Nitrogen Alloyed Stainless Steel, Cronidur 30." *Presented at the 5<sup>th</sup> International ASTM Symposium on Bearing Steels, New Orleans, Louisiana, USA - Nov. 19-21, 1996.*
2. N.N. "Space Tribology Handbook, 3<sup>rd</sup> Edition." *AEA Technology plc - ESTL Cheshire, UK, 2002.*
3. Neugebauer, C. and Falkner M. "Lessons Learnt on Cryogenic Rocket Engine's Gimbal Bearing Lubrication Selection." *Proceedings of the 37<sup>th</sup> Aerospace Mechanisms Symposium, (May 2004), pp. 137-141.*

### Remark & Acknowledgement

Ariane 5 is an ESA program, managed by CNES, prime contractor of VINCI is SNECMA. The gimbal is part of the VINCI Thrust Chamber with prime contractor EADS-ST. The VINCI gimbal has been developed under contract to EADS-ST of Ottobrunn, Germany.

Austrian Aerospace gratefully acknowledges the continuing support of all parties.





# Effect of Test Environment on Lifetime of Two Vacuum Lubricants Determined by Spiral Orbit Tribometry

Stephen V. Pepper\*

## Abstract

The destruction rates of a perfluoropolyether (PFPE) lubricant, Krytox 143AC™, subjected to rolling contact with 440C steel in a spiral orbit tribometer at room temperature have been evaluated as a function of test environment. The rates in ultrahigh vacuum, 0.213 kPa (1.6 Torr) oxygen and one atmosphere of dry nitrogen were about the same. Water vapor in the test environment – a few ppm in one atmosphere of nitrogen – reduced the destruction rate by up to an order of magnitude. A similar effect of water vapor was found for the destruction rate of Pennzane® 2001A, an unformulated multiply alkylated cyclopentane (MAC) hydrocarbon oil.

## Introduction

The destruction of liquid lubricant molecules by tribochemical attack (tribochemistry) is well-recognized, especially for perfluoropolyethers (PFPEs). The destruction or degradation can be manifested by the finite lifetime of a mechanism with a limited supply of lubricant. It is also indicated by the observation of chemical reaction films on the bearing surface, friction polymer and molecular fragments emitted into the environment. Destruction of PFPEs, in particular, has been observed in ball bearings for vacuum service in spacecraft and in eccentric bearing tests that operate in the starved or boundary lubrication regime, depleting the lubricant supply and causing bearing failure [1, 2]. Destruction of PFPEs is also a matter of concern in hard disk magnetic storage media [3]

The destruction rate of the lubricant molecules is a function of both the lubricant's chemical structure [4, 5] and bearing substrate chemistry [6, 7]. It can also depend on the test environment [8-10]. Understanding environmental effects on lubricant's destruction rate is vital to ensure that earth-based life tests of vacuum hardware provide meaningful results. Some tests are performed in 'inert' gas, such as dry nitrogen, because of significant cost and convenience advantages versus vacuum testing. However, the test chamber may still contain trace impurities that compromise the inertness of the test environment, even though the chamber may have been backfilled or purged with an inert gas such as nitrogen. Impurities such as oxygen or water vapor may be tribochemically active and change the lubricant's lifetime compared to what would be exhibited in vacuum.

In this paper, the destruction rates of Krytox 143AC™, a popular PFPE vacuum lubricant, in rolling contact with 440C stainless steel in a spiral orbit tribometer are studied for test environments of ultrahigh vacuum (UHV), dry oxygen, dry nitrogen, nitrogen containing water vapor and pure water vapor. The destruction rate is expressed as the lifetime of a finite charge of lubricant in a test and the results give a ranking of the lifetimes as a function of test environments. Some results are also presented for the effect of water vapor on the destruction rate of Pennzane® 2001A, an unformulated multiply alkylated cyclopentane (MAC) hydrocarbon oil.

## Experimental

The test instrument is a spiral orbit tribometer (SOT) depicted in Fig. 1. This rolling contact tribometer is a retainerless thrust bearing with one ball and flat races whose elements and kinematics have been described [11]. The SOT was used to observe the tribochemical destruction of lubricants in vacuum and to give a ranking of the lifetimes, or degradation rate, of two different PFPEs (Krytox 143AC™ and Fomblin Z-25™) and the unformulated Pennzane® 2001A on 52100 steel [4].

---

\* NASA Glenn Research Center, Cleveland, OH

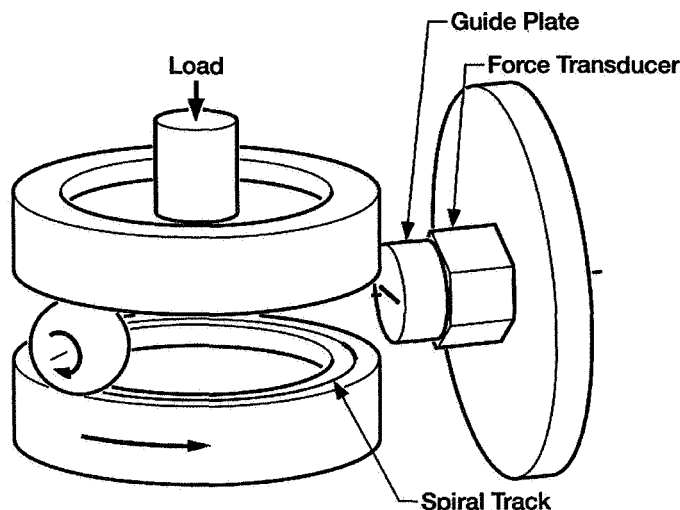


**Figure 1. Schematic of the Spiral Orbit Tribometer**

The 12.7-mm (.5-in) diameter ball and the plate specimens were 440C steel. All tests were run at room temperature at a mean Hertz pressure of 1.5 GPa and a ball orbit rate of 30 rpm (rolling velocity 0.071 m/s). The stainless steel, metal-gasketed test chamber was evacuated to  $<0.133 \times 10^{-8}$  kPa ( $1 \times 10^{-8}$  Torr) with a turbomolecular vacuum pump. A gate valve between the test chamber and the turbomolecular pump could be closed to permit the evacuated chamber to be backfilled with a particular gas. The nitrogen and oxygen supply bottles were specified to have a water vapor content of  $< 2$  ppm. The gasses were admitted into the test chamber through an evacuated and baked stainless steel transfer line and a variable leak valve. Pure water vapor was admitted into the test chamber through a variable leak valve from a water supply that had been thoroughly degassed by the freeze-pump-thaw method. Water vapor concentration in the nitrogen atmosphere test environment was determined with a thin film hygrometer (Kahn Cermet II) inserted directly into the test chamber. The hygrometer's readout in dewpoint temperature,  $T_d$ , could be converted to either partial pressure of water vapor or concentration of water vapor in ppm through the Magnus formula and then to relative humidity. Test chamber total pressure  $P$  was determined by a cold cathode ionization gauge for  $P < 1.064 \times 10^{-3}$  kPa ( $8 \times 10^{-3}$  Torr), a Pirani gauge for  $1.06 \times 10^{-3}$  kPa ( $8 \times 10^{-3}$  Torr)  $< P < 0.266$  kPa (2 Torr) and a diaphragm gauge for  $P > 0.266$  kPa (2 Torr).

The lowest reading of the hygrometer is  $T_d = -99.9^\circ\text{C}$  which corresponds to a water concentration of .014 ppm. This reading is achieved in vacuum and initially upon backfilling the chamber to an atmosphere of nitrogen. Eventually, however, water vapor accumulates in the valved-off chamber as shown in Figure 2. The accumulation is detectable after about  $2 \times 10^4$  orbits (~11 hours) and continues to increase thereafter. This water vapor is due to desorption from the chamber's unbaked interior surfaces. The lowest rate of accumulation is observed after the chamber had been evacuated for many days and then exposed to room air for a minimal time – approximately 10 minutes – during insertion of test specimens.



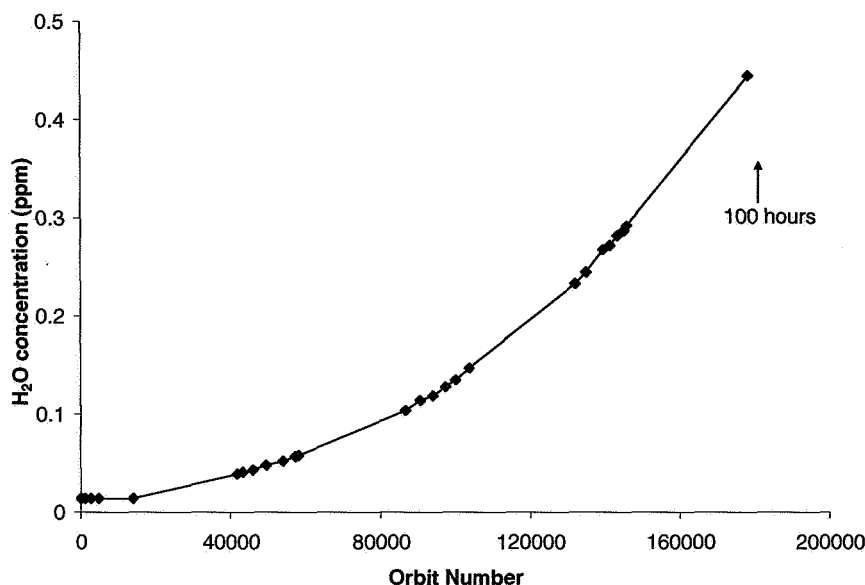


**Figure 2. Accumulation of water vapor in an atmosphere of nitrogen**

A lubricant charge of  $\sim 25 \mu\text{g}$  for the PFPE and  $\sim 20 \mu\text{g}$  for the MAC was deposited only on the ball from a gas-tight syringe containing a dilute lubricant solution in a volatile solvent. This lubricant amount was consumed in a reasonable time – from a few hours to a few days. The speed and temperature of the test are similar to values that would be seen in spacecraft bearings, with test acceleration achieved through limited lubricant. Friction is recorded as a function of ball orbit and results in a 'friction trace', shown in Figure 3. The trace exhibits constant coefficient of friction (0.134) until an abrupt increase at  $\sim 1230$  orbits. A friction coefficient exceeding 0.2 is defined as test failure, the point when the lubricant is totally consumed. Normalized lifetime is obtained by dividing the orbits to failure by the initial lubricant charge. In this test, failure occurred at 1287 orbits and the initial lubricant charge was  $25 \mu\text{g}$ , resulting in a normalized lifetime of 52 orbits/ $\mu\text{g}$ . Normalized lifetime is inversely proportional to the lubricant destruction rate.

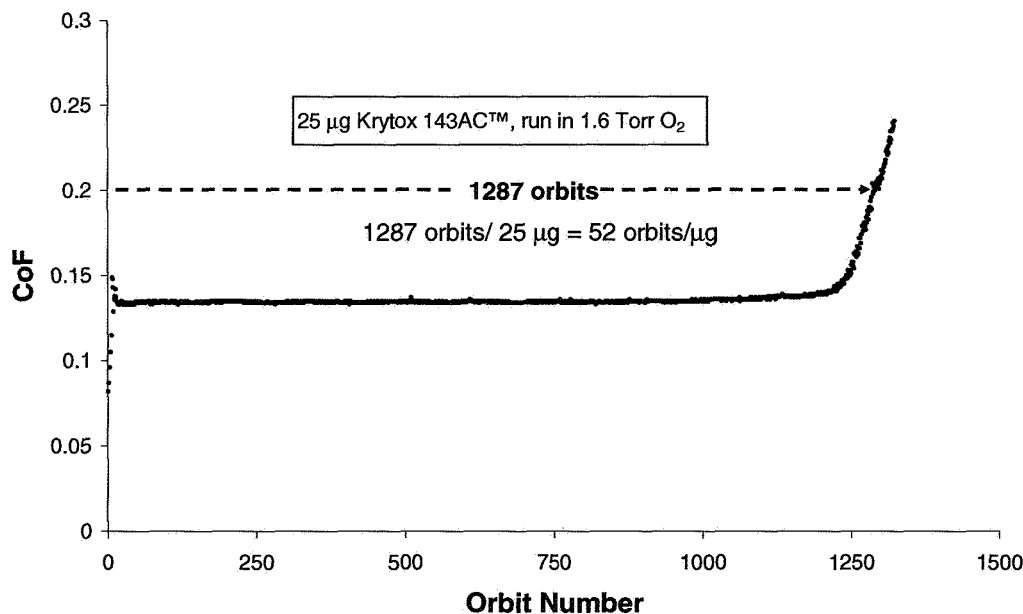


**Figure 3. Typical friction trace in SOT tests**

## Results

### Krytox 143AC™

The results of four tests of Krytox 143AC™ run in each of the five specified environments are presented in Figure 4. The shortest lifetimes are exhibited by tests run in ultrahigh vacuum (UHV). The longest lifetimes are observed by running in the presence of water vapor, with increasing lifetime corresponding to increasing water vapor concentration in the test environment. Only 16 ppm water vapor in an atmosphere of nitrogen, corresponding to a relative humidity of <0.07%, is sufficient to extend the lifetime by an order of magnitude relative to testing in vacuum. Pure water vapor itself, without its being present in nitrogen gas, also leads to lifetimes much longer than testing in vacuum. Testing in one atmosphere of “dry” nitrogen, in which the hygrometer indicated no additional water vapor above its lowest reading of  $T_d = -99.9^\circ\text{C}$  (0.014 ppm), gives lifetimes greater than the tests in vacuum, but only marginally so. Testing in 0.213 kPa (1.6 Torr) dry oxygen, corresponding to ~0.2% trace contamination of oxygen in a nitrogen atmosphere, also has little effect on lifetime relative to that in vacuum. The results presented here thus indicate that water vapor in the test environment exercises a “protective” effect on the PFPE lubricant, permitting a longer life before failure. Finally, the coefficient of friction of 0.134 was independent of the test environment and thus of the lifetime.

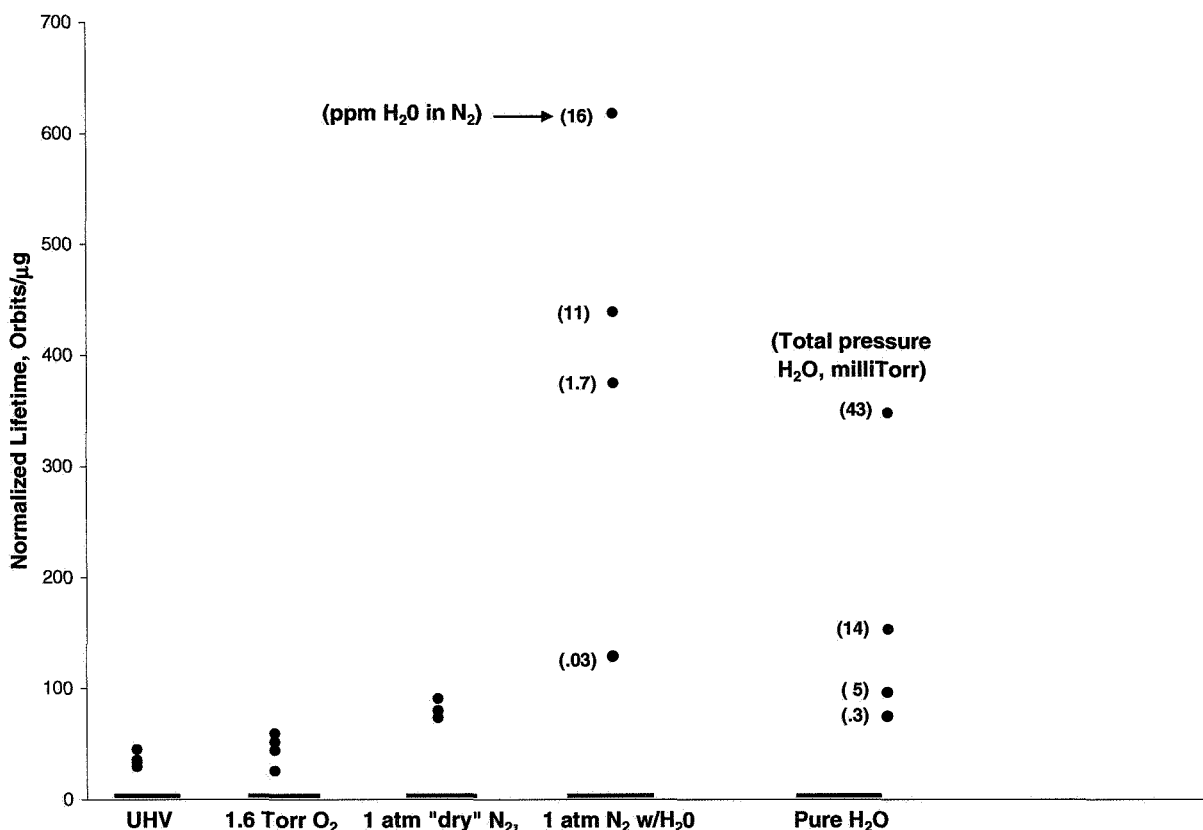


Figure 4. Normalized lifetimes of Krytox 143AC™ when testing in different environments

### Pennzane® 2001A

Friction traces for Pennzane® 2001A are plotted in Figure 5 for testing in three environments – ultrahigh vacuum, an atmosphere of nitrogen with a minimum amount of water vapor and an atmosphere of nitrogen with a greater concentration of water vapor. The normalized lifetimes for the tests are indicated above the individual traces. The minimum concentration of water vapor in an atmosphere of nitrogen was achieved simply by closing the gate valve between the chamber and the turbomolecular pump and allowing the water vapor to accumulate in a nitrogen atmosphere as shown in Figure 2. The test at 75

ppm water vapor was achieved by deliberately admitting water vapor to the isolated test chamber from the degassed water vapor source and then backfilling with dry nitrogen. The test in ultrahigh vacuum lasted much longer than that of the test of the PFPE in ultrahigh vacuum as demonstrated in [4]. The tribo-degradation rate of the MAC is much lower than that of the PFPE. The lifetime for the test in the minimum concentration of water vapor in the nitrogen atmosphere – whose evolution of concentration is shown in Figure 2 – is greater than the lifetime for the test in ultrahigh vacuum. The lifetime for the test in 75 ppm water vapor is greater still. Thus water vapor in the test environment extends the lifetime of the MAC as it does for the PFPE. As with the PFPE, the initial coefficient of friction of 0.08 is the same for all test environments, regardless of lifetime.

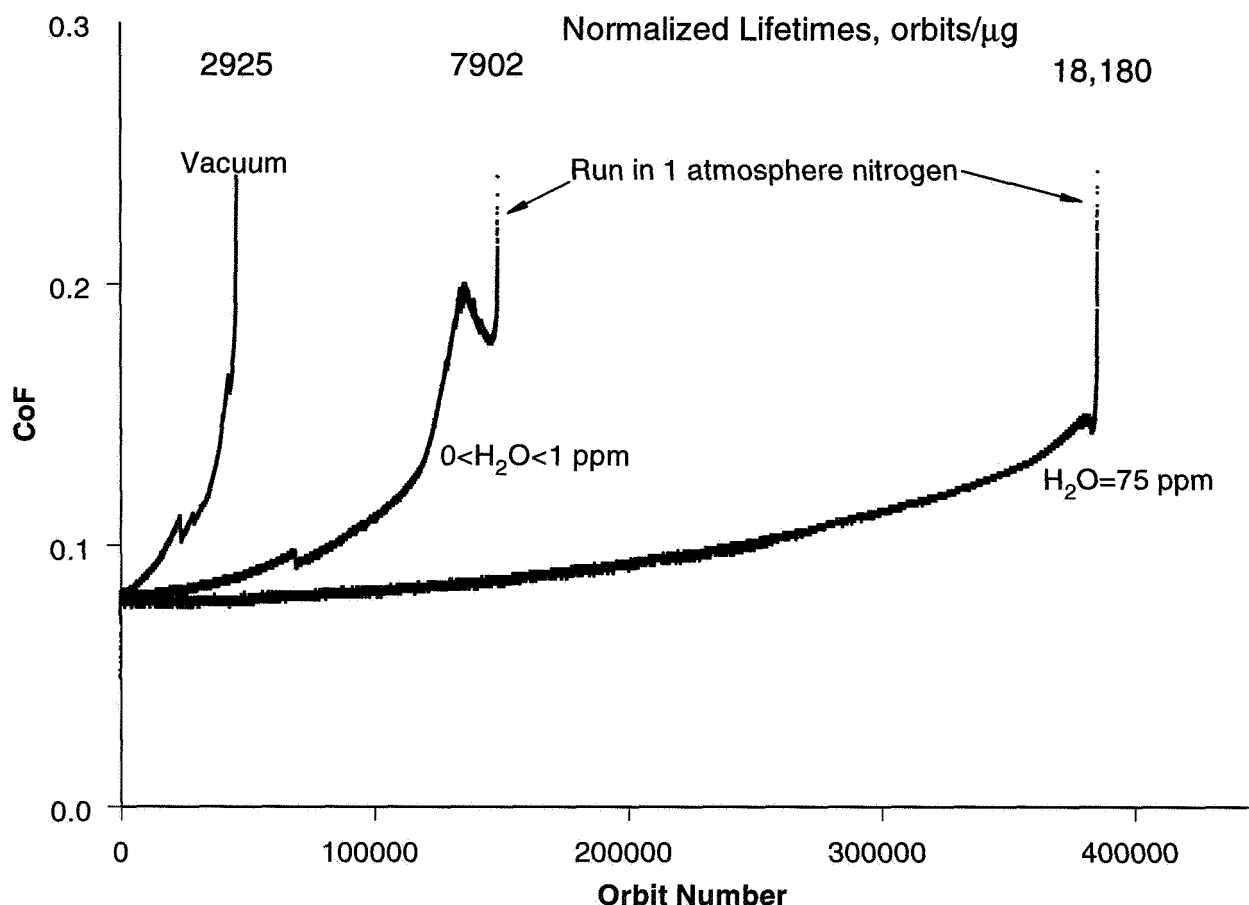


Figure 5. Friction traces of Pennzane® P2001A in different environments

### Discussion

#### Contact Conditions

The low constant friction coefficient exhibited in the tests prior to failure is an indication that the contact is lubricated. However, the state of the lubricant in the contact is not known. Cann and coworkers [12] have studied similar systems under a state of reduced availability of liquid lubricant using optical EHL. Although the lubricant charge used in the SOT is three orders of magnitude smaller than used in their investigations, the SOT system still appears to be in a state of lubrication. Cann, et al, presented an expression for the film thickness in the contact in the fully starved regime. An evaluation of their expression for the present conditions yields a film thickness that is unphysically small ( $\ll 1$  nm), confirming that the contact regime here is fully starved or parched [13]. The specific concentration of lubricant molecules in the contact is not known, except for the fact that there are enough of them to



lubricate the contact with a friction coefficient close to that exhibited by a fully flooded contact [14]. However, there are probably few enough so that an appreciable fraction of them are in direct contact with the substrate, where they are eventually consumed by tribochemical attack, indicating a failure by elevated friction (Figure 3).

In this study, the friction coefficient is independent of the degradation rate. Evidently, the process responsible for the establishment of the friction force (possibly of rheological origin) and the process responsible for the degradation (tribochemical origin) proceed independently of each other. The tribochemical events may be considered second order effects – events that occur relatively seldom compared with the rheological friction that is continuous in the contact. If the tribochemical rate of attack was higher, then the coefficient of friction might well be different for different test environments that determine different lifetimes.

#### Krytox 143AC™

The lifetime increase is evident for even very low concentrations of water vapor in the test environment. A concentration of 0.03 ppm in an atmosphere of nitrogen corresponds to a partial pressure of water vapor of 0.02 milliTor and lower concentrations may be difficult to achieve. Indeed, the somewhat longer lives for the tests in atmospheres of “dry” nitrogen (atmospheres in which the hygrometer maintained its base reading of  $T_d = -99.9^\circ\text{C}$ ) could be due to water vapor concentrations too low to be registered. The extrapolation of the data in Figure 2 to small orbit numbers indicates that there is some lifetime-extending water vapor present even for the relatively short lifetime exhibited by this PFPE. This would indicate that the lifetime tests conducted in this manner are more sensitive to water vapor than the hygrometer itself.

The tests conducted with Krytox 143AC™ in pure water vapor support the assertion that water vapor really is the cause for extended lifetimes in nitrogen atmospheres and not some other tribochemically active molecule that was introduced into the chamber along with the nitrogen. These results also indicate that life testing in “soft” vacuums of about  $10^{-5}$  Torr or less (for which water vapor constitutes a majority of the residual gas) can be as valid as testing in a better vacuum.

The null result of testing in 0.213 kPa (1.6 Torr) oxygen establishes that such trace amounts of oxygen in nitrogen cannot protect the PFPE lubricant against tribochemical attack. This result relates to a current idea that tribological stress exposes clean metal by removing the native oxide, allowing the clean metal to initiate tribochemical attack on the lubricant. However, such clean metal would be oxidized by exposure to 0.213 kPa (1.6 Torr) oxygen thus quenching any tribochemical attack by clean metal. If the oxidation is fast enough to oxidize clean metal in the contact, then these results imply that the “exposure” mechanism is not operative here and that the ball is probably rolling on the native oxide of the steel during the test.

#### Pennzane 2001A®

The friction traces in Figure 5 indicate that water vapor in the test environment also extends the lifetime of the MAC. It would be desirable to determine if there was any effect on the lifetime by testing in an atmosphere of a truly inert gas or oxygen. However, the MAC's long intrinsic lifetime allows the accumulation of water vapor in the test environment – as presently constructed – that would mask the possible effects of these species. A study of the effects of oxygen or an inert gas must be conducted in the absence of water vapor and remains to be done.

#### Mechanisms

A consideration of the mechanism by which water vapor retards the tribochemical degradation of the lubricant molecules begins with the observation that the effect is present for both the PFPE and the MAC. The mechanism is not specific to the particular lubricant chemistry and attention is thus directed to the substrate. Substrate sites (probably on the steel's native oxide) are evidently passivated by the water vapor. Water molecules might adsorb on the sites physically, that is without chemical reaction, and simply sterically block the interaction of the site with the lubricant molecule. Although this physical adsorption is well known, appreciable coverage at room temperature occurs at much higher partial pressures of water vapor [15], rendering this physisorption approach unlikely. An approach that considers the passivating chemical reaction of water with the active surface sites may be more fruitful. Lewis acid sites have received much attention in the context of PFPE degradation [16]. This approach may also work out for the sites that can attack both the PFPE and the MAC. The purely tribological results presented here offer limited chemical insight.

Other studies [8, 9] of lubricant life extension under a nitrogen cover gas have emphasized the role of an oxygen impurity component in the cover gas interacting with both an additive in the lubricant and with clean iron exposed by tribological action. The results presented here on oils without additives indicate that neither oxygen nor clean iron is a necessary aspect of life extension under an impure cover gas. Neither is the presence of an additive an essential aspect of the life extension process. Rather, the passivation of active sites on the surface of the bearing steel by water vapor is the governing mechanism that reduces the attack on the lubricant molecule itself.

#### Application to Testing

The first implication of these results for testing of space mechanisms is that life-testing devices such as bearings in a nitrogen environment to simulate vacuum is permissible with sufficient absence of water vapor. However, the severe restrictions required on the water vapor levels may eliminate any cost savings versus vacuum testing. The second implication is that the device housing may contribute water molecules to the device's environment, since water always desorbs from an unbaked surface. This water flux captured in a housing with limited access to vacuum can provide a degree of protection to the lubricant that is not available in a more open geometry such as in the present test arrangement. In this sense the present test arrangement provides a very severe test.

#### **Conclusions**

Both the PFPE and the MAC lubricants are tribochemically degraded in vacuum as evidenced by the finite lifetimes they both exhibit in these tests. Tests in controlled environments indicate the lifetime of both lubricants is extended if water vapor is present in the environment. The effect of water vapor is evident at quite low levels (<1 ppm) in the present tests. These results imply that sites must exist on the bearing steel's surface that can attack the lubricant molecules. These sites are chemically passivated by water vapor, thus reducing the attack rate and allowing a longer lubricant life. An independent understanding and chemical characterization of these sites is not available at present. These results imply that testing of those mechanisms whose life is limited by lubricant consumption in an environment with water vapor, even at very low concentrations in a nitrogen atmosphere, can lead to mechanism lifetimes that are much longer than will be realized in vacuum service. Thus in terms of a "lessons learned", it is advisable to provide water and oxygen sensors for the mechanism test environment.

#### **Acknowledgments**

I thank Dr. Kenneth W. Street for requesting tests whose results motivated this study.

#### **References**

1. Carré, D.J. "Perfluoropolyalkylether Oil Degradation: Inference of  $\text{FeF}_3$  Formation on Steel Surfaces under Boundary Conditions", *ASLE Transactions*, 29 (1986), 121-125.
2. Carré, D.J., "The Performance of Perfluoropolyether Oils under Boundary Lubrication Conditions", *Tribology Transactions* 31 (1988), 437-441.
3. Novotny, V.J., Karis, T.E. and Johnson, N.W., "Lubricant Removal, Degradation, and Recovery on Particulate Magnetic Recording Media", *Journal of Tribology*, 114 (1992), 61-67.
4. Pepper, S.V. and Kingsbury, E.P., "Spiral Orbit Tribometry – Part II: Evaluation of Three Liquid Lubricants in Vacuum", *Tribology Transactions*, 46 (2003), 65-69.
5. Bazinet, D.G., Espinosa, M.A., Loewenthal, S.H., Gschwender, L., Jones, W.R., Jr., Predmore, R.E., "Life of Scanner Bearings with Four Space Liquid Lubricants", *Proceedings of the 37<sup>th</sup> Aerospace Mechanisms Symposium*, Johnson Space Center, May 19-21, 2004.
6. Carré, D.J., "The Use of Solid Ceramic and Ceramic Hard-Coated Components to Prolong the Performance of Perfluoropolyalkylether Lubricants", *Surface and Coatings Technology*, 43/44 (1990), 609-617.
7. Jones, W.R., Jr., Jansen, M.J., Chen, G-S., Lam, J., Balzer, M., Lo, J., Anderson, M. and Schepis, J.P., "The Effect of 17-4PH Stainless Steel on the Lifetime of a Pennzane<sup>®</sup> Lubricated Microwave Limb Sounder Antenna Actuator Assembly Ball Screw for the Aura Spacecraft". 11<sup>th</sup>

*European Space Mechanisms and Tribology Symposium (ESMATS 2005)*, Lucerne, Switzerland, September 21-23, 2005.

8. Carré, D.J., "Lead Naphthenate Tribochemistry Under Vacuum and Gaseous Nitrogen Test Conditions", *Tribology Letters*, 16 (2004), 207-214.
9. Carré, D.J., "Effect of Test Atmosphere on Moving Mechanical Assembly Test Performance", *Proceedings of the 37<sup>th</sup> Aerospace Mechanisms Symposium*, Johnson Space Center, May 19-21, 2004.
10. John, P.J., Cutler, J.N. and Sanders, J.H., "Tribological Behavior of a Multialkylated Cyclopentane Oil Under Ultrahigh Vacuum Conditions", *Tribology Letters*, 9 (2000), 167-173.
11. Pepper, S.V. and Kingsbury, E.P., "Spiral Orbit Tribometry – Part I: Description of the Tribometer", *Tribology Transactions*, 46 (2003), 57-64.
12. Cann, P.M.E., Damien, B. and Lubrecht, A.A., "The Transition between Fully Flooded and Starved Regimes in EHL", *Tribology International*, 37 (2004), 859-864.
13. Kingsbury, E. P., "Parched Elastohydrodynamic Lubrication", *Transactions ASME, J. Tribology*, 107 (1985), 229-233.
14. Spikes, H.A., "Comparison of Krytox 143AB™ and 143AC™ in Prolonged Mixed Sliding/Rolling", *Report TS031/99 of Tribology Section, Department of Mechanical Engineering, Imperial College, London*.
15. Israelachvili, J.N., *Intermolecular and Surface Forces*, 2<sup>nd</sup> Ed., Academic Press, New York, 1992 and Gregg, S.J. and Sing, K.S.W., *Adsorption, Surface Area and Porosity*, 2<sup>nd</sup> Ed., Academic Press, New York, 1982, Chapter 5.5.
16. Kasai, P.H., "Perfluoropolyethers: Intramolecular Disproportionation", *Macromolecules*, 25 (1992), 6791-6799.



# **Influence of Oil Lubrication on Spacecraft Bearing Thermal Conductance**

Yoshimi R. Takeuchi\*, Matthew A. Eby\*, Benjamin A. Blake\*, Steven M. Demsky\* and James T. Dickey\*

## **Abstract**

Increasing demands on bearing performance and a lack of thermal conductance data for bearings in space applications motivated The Aerospace Corporation to study heat transfer across angular-contact ball bearings for space systems. Tests were conducted under controlled conditions including rotational speed, temperature, axial load, and vacuum environment. Bearings with Nye Pennzane SHF2001 synthetic oil were compared with dry (non-lubricated) bearings. These comparisons show that dry and oil lubricated bearings vary in thermal conductance by up to an order of magnitude. Experimental measurements also indicated that sensitivity to other variables, such as axial load and temperature, depends on whether the bearing is dry or oil lubricated, and whether it is in a static or dynamic (rotating) state. Mechanisms of heat transfer are discussed for each of these states.

## **Introduction**

In contrast to typical terrestrial applications, the absence of convection shifts the focus for thermal analysis of rotational space hardware. In vacuum environments, conductance through the bearings often provides the primary heat transfer path between the shaft and the housing. As such, temperature predictions for rotating components, such as satellite instruments, or the bearing itself require knowledge of the bearing thermal conductance. However, published literature provides little help on the subject, and thus bearing thermal conductance is usually the significant unknown in the development of a thermal model of a rotational system in space. When available, engineers often use heritage information for comparable systems with similar bearings. Significant uncertainty arises with the advent of design changes, different bearing geometry, different lubricant type or quantity, or dissimilar operational conditions. An absence of thermal conductance data leads to challenges in using thermal models for guidance in the design process.

Existing literature yields limited thermal conductance information for static and low-speed bearings [1-9] and none for high-speeds. Yovanovich [1,2] developed a mathematical model for the thermal conductance of a non-lubricated, static (non-rotating) bearing. Experimental work followed, including studies on spacecraft bearings performed by Stevens and Todd [3], from the European Space Tribology Laboratories (ESTL). They measured thermal conductance across a bearing, up to a maximum speed of 2,500 RPM, using an experimental setup designed by Delil et al [4-5]. ESTL continued to study this subject over the years, focusing on static or low-speed and large thin cross-section bearings [6-8].

Demand on bearing performance has grown and thermal concerns have increased as systems have reached higher speeds. Current momentum wheels and control moment gyroscopes typically operate at 6,000-9,000 RPM [10]. Future wheels, including energy storage flywheels, are envisioned to run at even higher speeds, above 15,000 RPM. In addition to the need for high-speed data, low-speed applications could benefit from a greater range of experimental data, and additional sources of counter verification from other researchers.

To address these concerns, an experiment was designed to assess thermal conductance of bearings in vacuum, at speeds ranging from 0 to 6,000 RPM. Controlled studies were conducted by varying variables such as axial load, thermal boundary conditions, and rotational speed, individually for parametric studies. The tests identified variables of importance for different bearing conditions, including dry, lubricated, static, and dynamic states. Finally, qualitative theories for the mechanisms of heat transfer for each of these conditions emerged.

---

\* The Aerospace Corporation, Los Angeles, CA

## Nomenclature

$G$  – conductance across the bearing  
 $N$  – number of balls in the bearing  
 $R_i$  – thermal resistance at the contact between the inner race and one ball  
 $R_o$  – thermal resistance at the contact between the outer race and one ball  
 $R_b$  – thermal resistance across inner to outer race of one ball  
 $k_i$  – thermal conductivity of the inner race material  
 $k_b$  – thermal conductivity of the ball material  
 $k_o$  – thermal conductivity of the outer race material  
 $a$  – major axis of a Hertzian contact area  
 $a_i$  – major axis of the Hertzian contact area between the inner race and one ball  
 $a_o$  – major axis of the Hertzian contact area between the outer race and one ball  
 $b$  – minor axis of a Hertzian contact area  
 $b_i$  – minor axis of the Hertzian contact area between the inner race and one ball  
 $b_o$  – minor axis of the Hertzian contact area between the outer race and one ball

## Experiment

Reference [11] provides a detailed description of the experimental setup and measurement techniques. All tests were conducted in vacuum environments of at least  $1 \times 10^{-5}$  Torr (approximately  $1.3 \times 10^{-3}$  Pa). As a summary, the experimental design matrix is outlined as follows:

1. Vary rotational speeds between 0 and 6,000 RPM. The maximum speed of 6,000 RPM is typical of a spacecraft control moment gyroscope (CMG) or momentum wheel.
2. Apply a constant pure axial load ranging from 40 to 129 N.
3. Accommodate bearings of different sizes, namely the 101 and 204-size ball bearings.
4. Test dry or oil lubricated bearings.
5. Vary the average bearing temperature.

Oil lubricated bearings were tested in either the virgin or fully run-in states. A fully run-in bearing was established by continually running the bearing at a constant speed until heat generation, torque, and thermal conductance remain unchanged (about a week of continual operation).

## Test Bearings

A 52100 steel bearing and a hybrid bearing, consisting of silicon nitride balls and 52100 steel races, were tested. Table 1 provides the specifications of the two different angular contact ball bearing sizes used. Table 2 summarizes the relevant material properties.

**Table 1. Ball Bearing Specifications**

Bearing Input	204-size	101-size	Units
Outer Diameter	47	28	mm
Inner Diameter	20	12	mm
Ball Diameter	7.94	4.76	mm
Number of Balls	10	10	
Angle of Contact	15	15	degree
Cage Material	Phenolic	Phenolic	
Cage Type	H-type, non-separable	H-type, non-separable	
Cage Land	Outer	Outer	

**Table 2. Ball Bearing Material Properties**

Property	Silicon Nitride	52100 Steel	Units
Elastic Modulus	310	210	GPa
Poisson's Ratio	0.27	0.3	
Thermal Conductivity	30	26.6	W/m-K

### Results

Following the experimental matrix, tests were performed to establish the influence of rotational speed, axial load, and temperature on bearing thermal conductance. While results for oil-lubricated bearings prove most relevant to a spacecraft application, the influence of axial load on the thermal conductance of a static dry bearing is already well known analytically [1-2]. Thus, the experimental results for a static dry bearing provide an excellent means of verifying the experimental technique. Further testing extends the results to static and dynamic (constant rotational speed) lubricated bearings, and reveals drastic shifts in the magnitude and trend of bearing thermal conductance relative to axial load and temperature.

#### Dry (Non-Lubricated) Static Bearings

The analytical relationship between thermal conductance and axial load in a non-lubricated, non-rotating bearing is well known. Yovanovich [1-2] developed the best-known analytical method, deriving the equation for bearing thermal resistance. A comparison with this model was used to verify the experimental approach, before proceeding to the more complex cases of lubrication and motion.

Figure 1 provides a comparison of experimental and theoretical bearing thermal conductance as a function of axial load at 20 °C. Both experiment and analysis agree closely in both magnitude and trend. The Figure shows that thermal conductance of the dry static bearing responds to axial load to the 1/3 power.

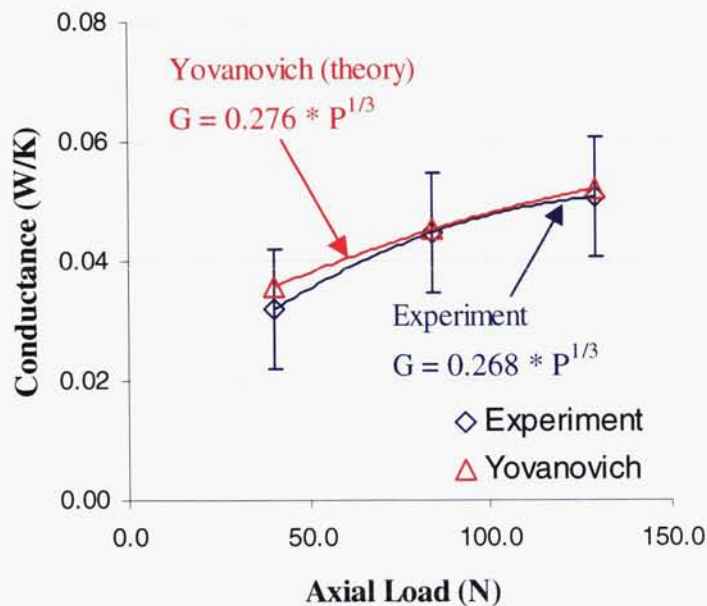


**Figure 1. Comparison of Analytical Calculation of Thermal Conductance with Experiment for a Static Dry 204-Size Hybrid Bearing at 20 °C**



Yovanovich's analysis provides an explanation for the observed trend. His model assumes the mechanism of heat transfer through a non-lubricated static bearing is pure conductance, from the hotter race, through the ball, and to the cooler race (Figure 2) and the driving source of resistance across the bearing arose from the thermal constriction region between the ball and the race contacts. This recognition presumes perfect contact (no asperities), and negligible resistance within the ball and both races.

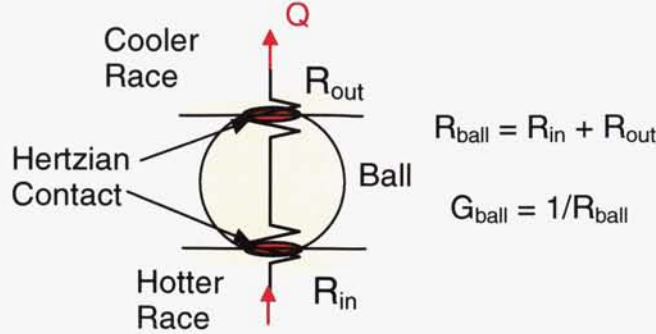


**Figure 2. Thermal Resistance Across One Bearing Ball**

As such, Yovanovich calculated the thermal resistance across a dry static bearing by modeling the ball and races as semi-infinite half-planes with the Hertzian contact area modeled as the thermal constriction region. The basic equations to calculate thermal resistance across each of the ball to race contacts are:

$$R_i = \Psi_i / 4k_i a_i + \Psi_i / 4k_b a_i \quad \text{inner race to ball thermal resistance} \quad (1)$$

$$R_o = \Psi_o / 4k_b a_o + \Psi_o / 4k_o a_o \quad \text{ball to outer race thermal resistance} \quad (2)$$

$$R_b = (R_o + R_i) \quad \text{total thermal resistance across the ball} \quad (3)$$

Where  $\Psi$  is a non-dimensional geometric factor defined as:

$$\Psi_n = \frac{2}{\pi} \int_0^{\pi/2} \frac{d\theta}{\left(1 - \frac{a_n^2 - b_n^2}{a_n^2} \sin^2 \theta\right)^{1/2}} \quad \text{where } n = i \text{ or } o \quad (4)$$

The Hertzian contact ellipse, and associated major and minor axes ( $a$  and  $b$ ), can be calculated by a number of existing programs based on classical Hertzian theory, such as BRGS10C [12]. Here, the major and minor axes are related to the applied axial load to the  $1/3$  power. Thus, the total Hertzian contact area is related to the applied axial load to the  $2/3$  power.

$$A_{\text{Hertzian}} = \pi \cdot \frac{a \cdot b}{4} \quad (5)$$

Once the resistance across each ball is known, the conductance is determined by taking its inverse. Scaling this result by the number of balls in the bearing yields the total bearing conductance (Equation 6).

$$G = N \cdot \frac{1}{R_b} \quad (6)$$

Equation 6 assumes that each ball provides an equivalent thermal pathway as a result of pure axial load, a condition consistent with our experimental setup. As the influence of axial load cancels out in the non-

dimensional parameter  $\Psi$ , only the influence on the Hertzian contact ellipse major axis remains in the thermal conductance equations of 1-3. Thus, analytically, conductance is sensitive to axial load to the  $1/3$  power. Both the magnitude and trend predicted by the analysis compared well with the experimental measurements.

Figure 3 shows the effect of the average bearing temperature (average between the inner and outer races) on thermal conductance of a dry (non-lubricated) 204-size hybrid bearing for three different axial loads. The graph shows that the conductance of the dry bearing is not strongly responsive to temperatures, especially when compared to the effect of axial load. This is attributed to the weak dependencies of the relevant material properties (thermal conductivity and Young's modulus) of the steel races and ceramic balls to temperature.

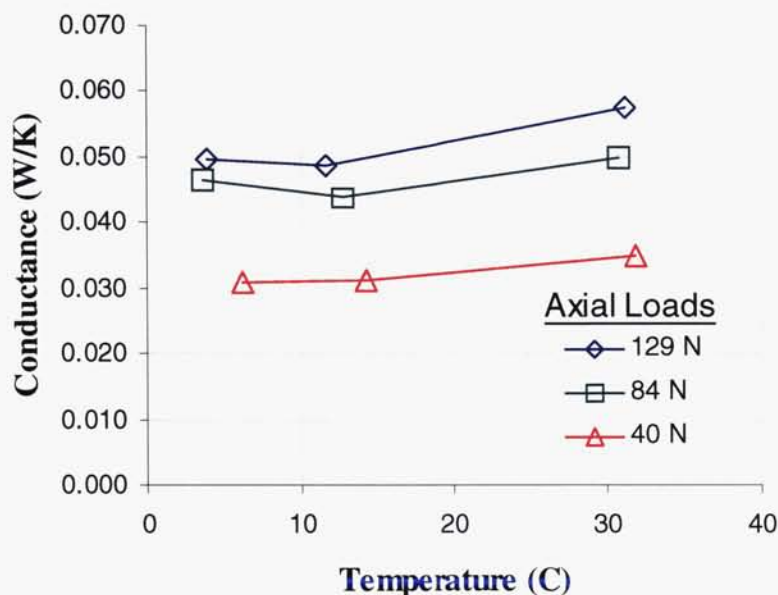


**Figure 3. Effect of Average Temperature on Thermal Conductance of a Static Dry 204-Size Hybrid Bearing**

#### Oil Lubricated Static Bearings

Yovanovich's model is a good approximation for some applications, such as dry lubricated bearings with little motion, but once lubrication is introduced into the system, bearing thermal conductance can change significantly. Figure 4 plots the static thermal conductance of a 204-size hybrid bearing in three lubrication states; dry, virgin oil lubricated, and oil lubricated after run-in. The exercised bearing was fully run-in at 6000 RPM, then brought back to 0 RPM for testing. Thermal conductance was measured for three axial loads, over a range of temperatures for each lubrication state.

The significantly higher thermal conductance of the oil-lubricated bearings, in comparison with the dry, warrants attention. To explain the difference between dry and oil lubricated bearings, Figure 5 depicts one of the ball-to-race contact regions. The mechanism of heat transfer is still pure conductance, but the large increase suggests that the lubricant meniscus surrounding the ball contributes a significant heat transfer path by increasing the constriction area at the ball to race interface. Lubricant could also potentially reduce the thermal resistance due to asperity contact at the metal-to-metal contact region; however, the close agreement between the Yovanovich model and the experiment for dry bearings suggest that this represents a secondary effect.

The large increase in thermal conductance implies that the heat path provided by the lubricant meniscus ultimately dominates, masking the influence of the Hertzian contact area. While the thermal conductance across dry bearings are driven by the size of the Hertzian contact ellipse, and thus proves sensitive to



axial load, the masking of the Hertzian contact area by the meniscus explains the minimal influence of axial loading upon the conductance of the oil-lubricated bearing. The dominance of the meniscus also explains the observation that oil lubricated bearings were found to be more sensitive to temperature, a result attributable to the higher temperature dependencies of the lubricant material properties.

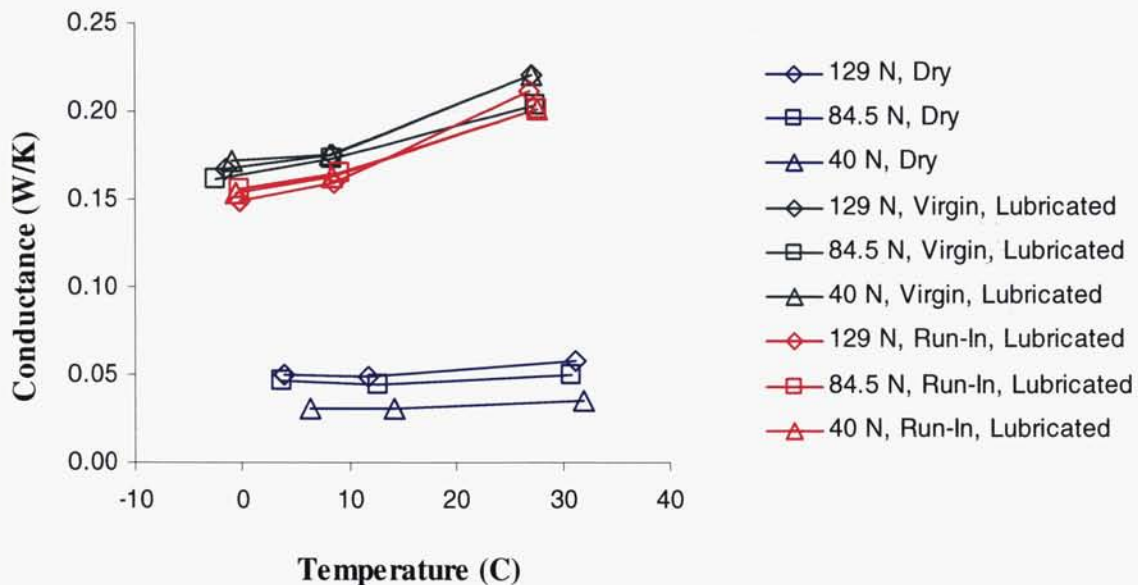


**Figure 4. Effect of Average Temperature and Axial Load on Conductance of a Static 204-Size Hybrid Bearing, for Dry and Oil Lubricated Bearings**

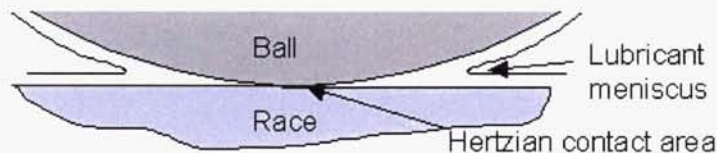


**Figure 5. Lubricant Meniscus Adds to Thermal Pathway Between Ball and Race**

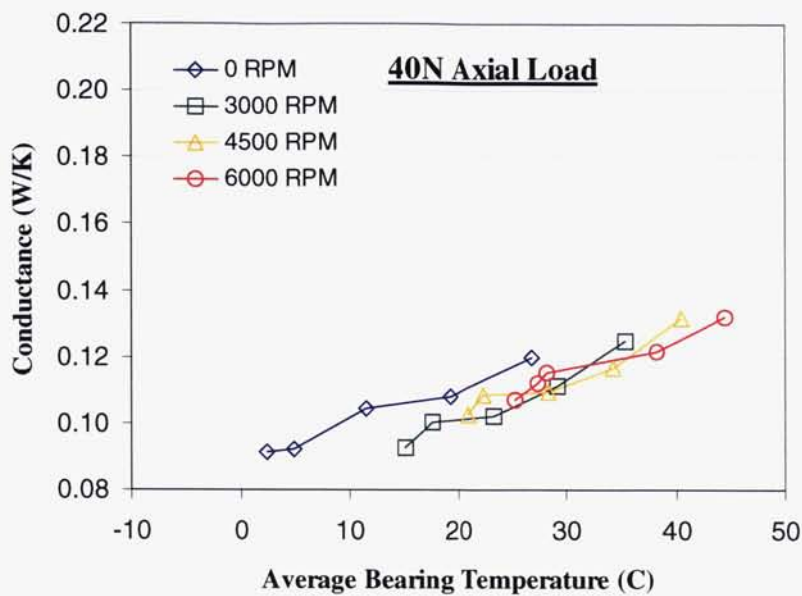
The conductance values of the virgin bearing are slightly higher than those of the fully run-in bearing, as apparent in Figure 4. This observation was attributed to lubricant loss during the run-in process, as the ball pushed excess oil out of its pathway and centrifugal forces displaced lubricant from the ball. This means that the degree of difference will be dependent upon the initial amount of lubrication and the maximum run-in speed of the bearing.

For space applications, bearings are typically lubricated once, and this lubricant may deplete over the mission duration due to various reasons, such as lubricant migration or run-in. Knowing this, one may construct bounds on static or slow moving conductance values expected throughout the spacecraft mission life. Yovanovich establishes the lower extreme bound, and test measurement of a virgin bearing establishes the upper bound. Lubricant loss can occur throughout the life of the bearing for various reasons including run-in and lubricant migration, meaning the end-of-life conductance would be somewhere between these bounds. This observation, however, does not hold for dynamic bearings.

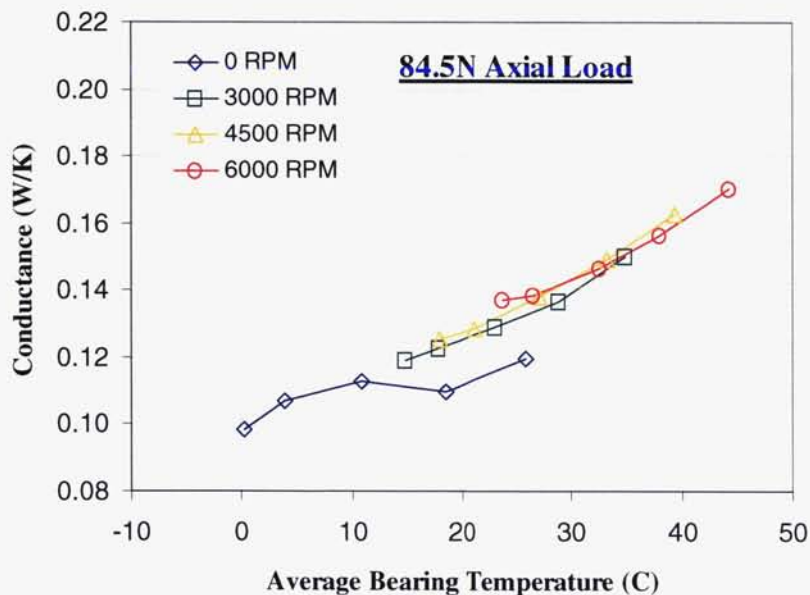


### Oil Lubricated Dynamic Bearings

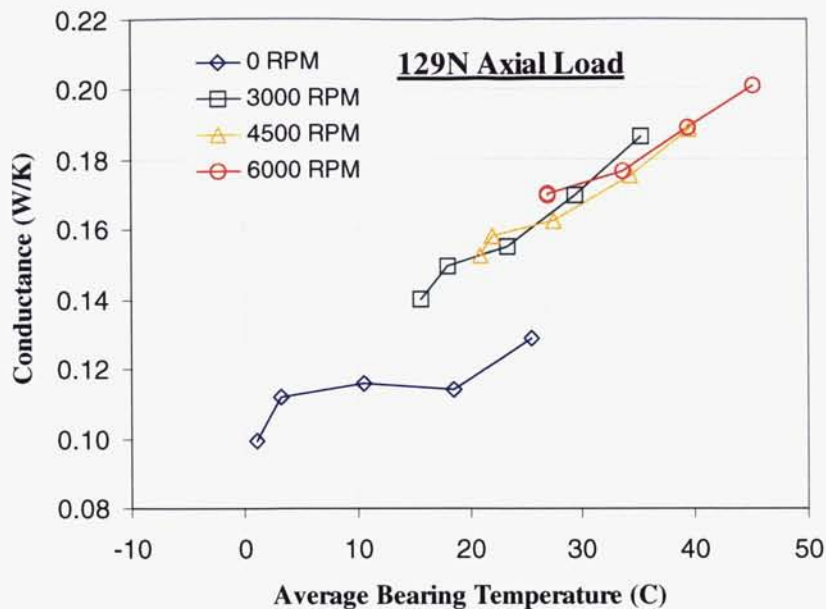
Figures 6-8 show the influence of average bearing temperature on conductance at different rotational speeds. Each figure represents a different axial load applied to an oil-lubricated bearing that had been run-in at 6,000 RPM.



**Figure 6. Thermal Conductance of a 101-Size Steel Bearing for a 40-N Axial Load**

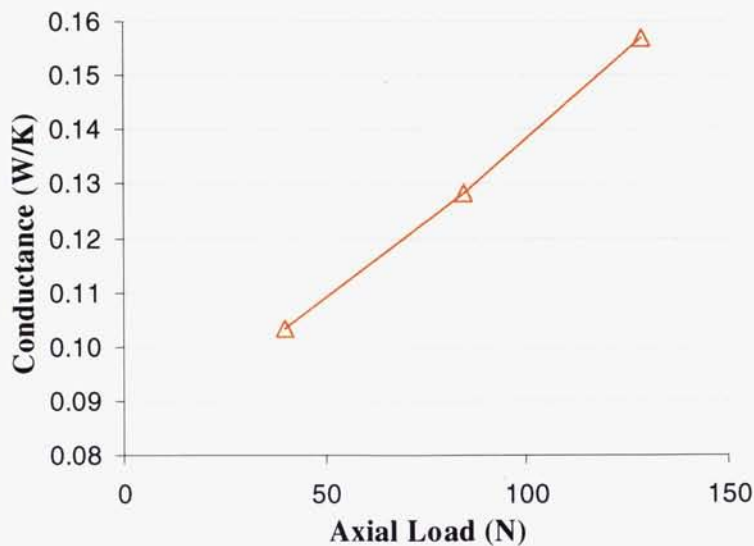


**Figure 7. Thermal Conductance of 101-Size Steel Bearing for 84.5-N Axial Load**



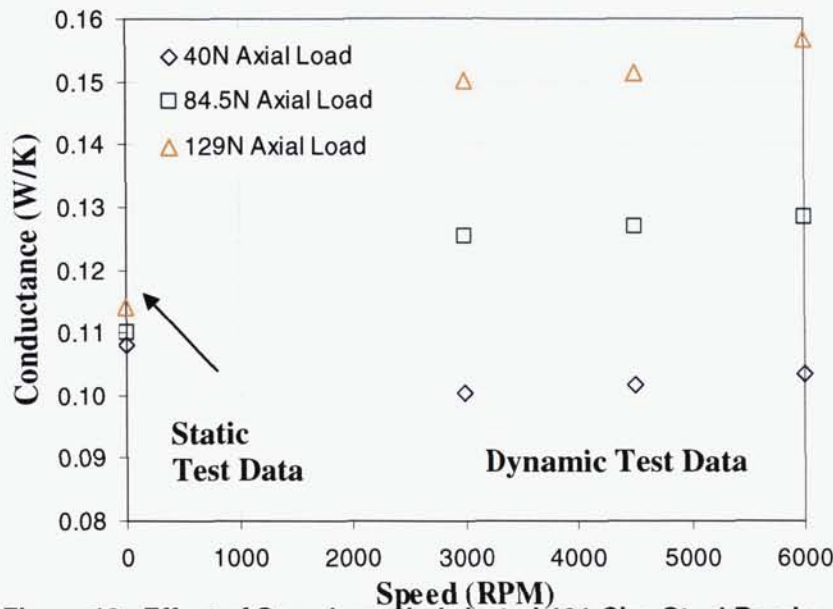
**Figure 8. Thermal Conductance of 101-Size Steel Bearing for 129-N Axial Load**

Several observations arise from these results. First, a distinct difference exists between static and dynamic bearings. Once in motion, the thermal conductance increased with temperature in a linear manner over the data range explored. Moreover, the slope and magnitude increased with axial load. To separate the response to each individual variable, Figure 9, shows the influence of axial load on the bearing at 6000 RPM and at a temperature of 20 °C. Unlike static lubricated bearings that are insensitive to axial loads, the dynamic lubricated bearing responds in a linear manner over the test range.



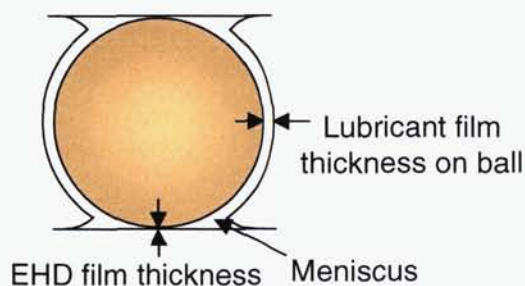
**Figure 9. Effect of Axial Load on a Lubricated 101-Size Steel Bearing at 20 °C**

Figure 10 re-plots the data to investigate the influence of rotational speed at a constant temperature (20°C). There is a distinct difference between 0 RPM and motion, which becomes more pronounced with increasing axial loads. Furthermore, contrary to intuition, at a given temperature and axial load the thermal conductance proved insensitive to rotational speeds below the run-in speed. The difference between static and dynamic bearings reflects a difference in the predominant heat transfer mechanism.



**Figure 10. Effect of Speed on a Lubricated 101-Size Steel Bearing at 20 °C**

For moving bearings, conductance through the bearing is not the primary mechanism of heat transfer. Figure 11 illustrates a ball with a lubricant film and a meniscus at the ball to race contact. The dominant mechanism of heat transfer is most likely mass transport, where the lubricant at the meniscus of the hotter race picks up heat, transports it with the ball as it rotates, then deposits heat at the cooler race. The film thickness on the ball becomes a dominant player as it determines the amount of heat transport that occurs. The ball film thickness should not be confused with the elastohydrodynamic (EHD) film thickness, which in the context of our argument has no influence on heat transport.



**Figure 11. Lubricant Distribution on Bearing Ball**

As the minimum rotational speed tested was 3000 RPM, it stands to reason that there may be a transition region between 0 RPM and 3000 RPM, where speed does influence bearing conductance. Looking through existing literature, Stevens and Todd from ESTL [3] explored the influence of speed on bearing thermal conductance at low speeds. An example of their findings, depicted in Figure 12, indicate an initial decline in thermal conductance, followed by an increase at higher speeds.



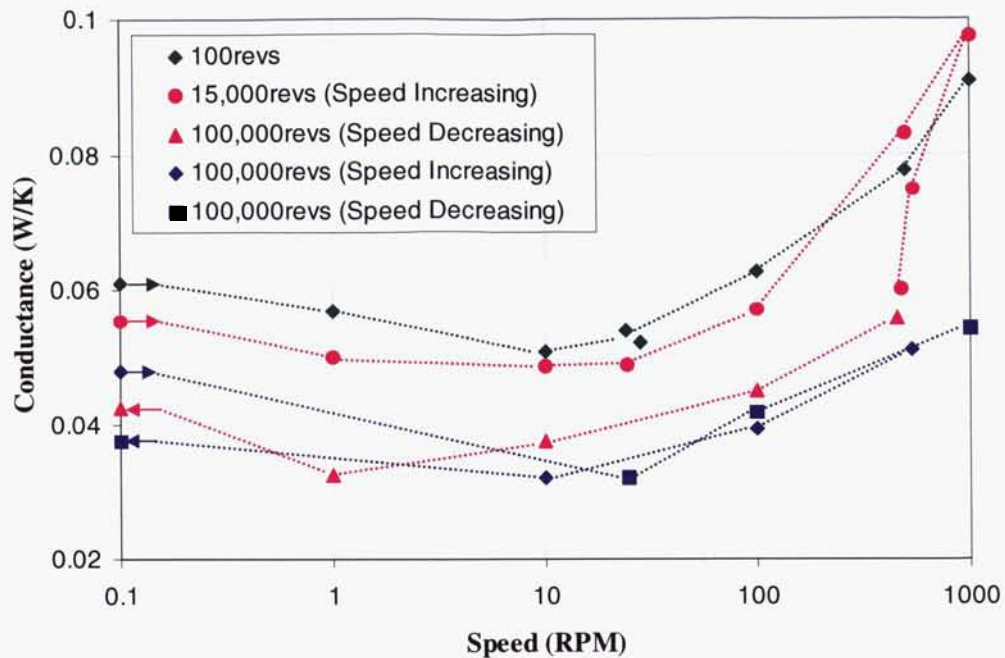


**Figure 12. Effect of Low Speeds on a 42-mm OD Bearing Lubricated with 11.4 mg of BP135 Oil with 40-N Load; Study by Stevens and Todd [3]**

Of additional relevance, Stevens and Todd [3] conducted tests multiple times with consecutively increasing or decreasing speeds. The result was a reduction in conductance occurring with additional revolutions. This is an effect that we also observed when comparing virgin and fully run-in bearings, again most likely due to the effect of excess lubricant being displaced over time. Our observations, and the literature results, indicate that this effect eventually diminishes and tests become repeatable when the bearing reaches a fully run-in state.

### Discussion

The objective of this research was to acquire a fundamental understanding of bearing thermal conductance, to establish which variables influence that property, and to determine the dominant mechanisms of heat transfer. Research results indicate that bearing thermal conductance was influenced by a number of interdependent variables, underpinned by the lubrication and the dynamic state of the bearing. Figure 13 provides a global example by plotting the influence of axial load on a 101-size steel bearing at 20 °C. The large differences in trend and magnitude between the dry and lubricated, static and dynamic bearings illustrate that the thermal analyst needs to recognize the assumptions underlying experimental data or analytical models of bearing thermal conductance.

Metal-to-metal contact, through the Hertzian contact ellipses, provided the heat transfer mechanism for dry static bearings. Experimentally, dry static bearings were found to be sensitive to axial load to the 1/3 power, as predicted by the Yovanovich analytical model, and relatively insensitive to temperature. Yovanovich's method establishes a lower bound for any bearing.

The presence of lubrication can drastically change the bearing thermal conductance. The menisci contributed an additional thermal pathway that overshadowed the conductance through the metal-to-metal Hertzian contact area. In contrast to dry bearings, the influence of axial load was negligible for static lubricated bearings, but the effect of temperature proved significant.

Mass transport of oil was considered the dominant mode of heat transfer in the lubricated dynamic bearing. Both axial load and temperature all affected this mechanism of heat transfer, and ultimately the bearing thermal conductance.

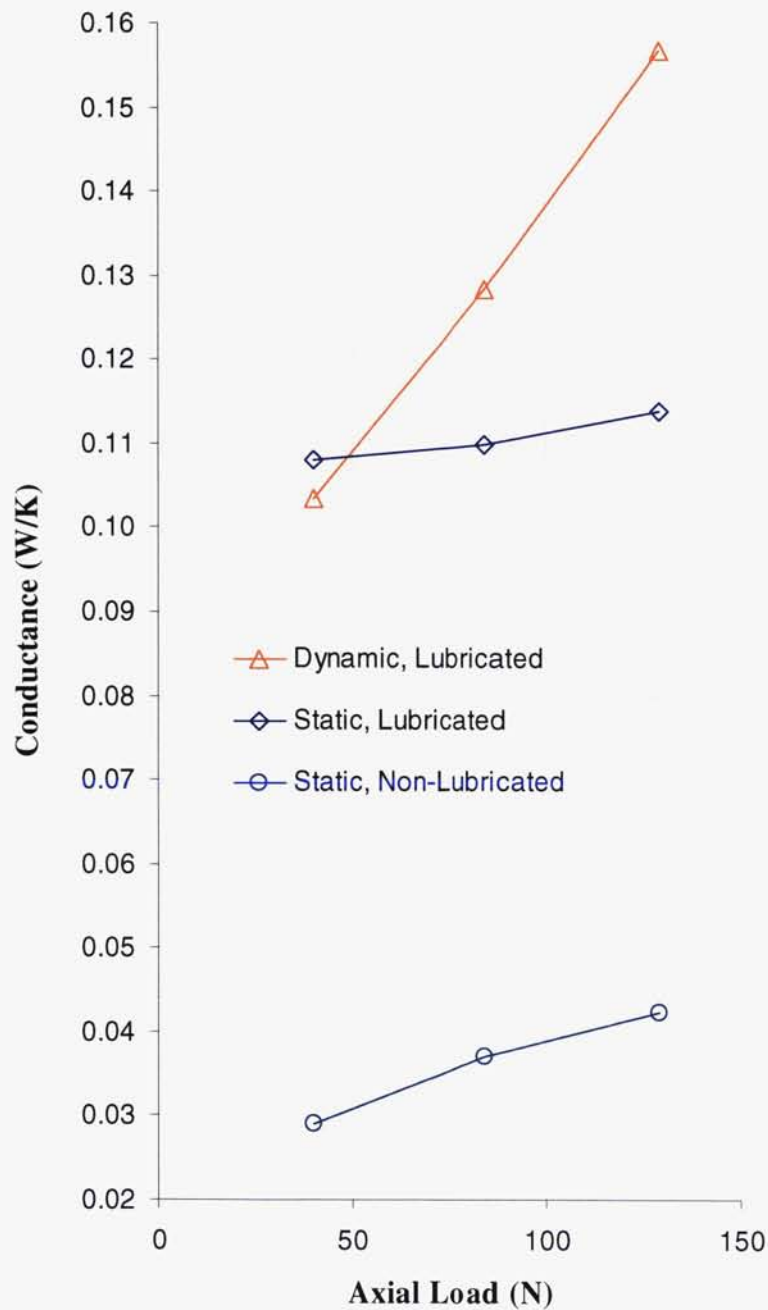


Figure 13. Effect of Axial Load on Thermal Conductance of a 101-Size Steel Bearing at 20 °C

## Conclusion

This paper has shown that lubrication or motion affects bearing thermal conductance in both magnitude and sensitivity to operational conditions, such as temperature and axial load. In practice, engineers typically use heritage information from applications using similar bearings within a comparable system to obtain an estimate of bearing thermal conductance. But in some cases heritage information is altogether lacking due to a new or a one-of-a-kind system. Engineers have often used analyses for a first-order approximation of bearing thermal conductance, but the basic analytical equations apply to a non-lubricated, static bearing. Information available on other bearing types is sometimes used as well. However, drastic difference in both thermal conductance magnitude and sensitivity to variables such as axial load and temperature is dependent on bearing lubrication and state of motion. As a consequence, engineers need to evaluate where bearing conductance data came from, what conditions it represents, and whether those conditions reflect the application at hand before using the data to predict temperatures of a rotational device in space.

## Acknowledgements

This work was funded by The Aerospace Corporation Independent Research and Development (IRAD) program. The authors will also like to extend our deepest gratitude to our management, in particular, Dr. Michael R. Hilton. It was his outstanding support that made this research possible.

## References

1. Yovanovich, M. M., "Analytical and Experimental Investigation on the Thermal Resistance of Angular Contact Instrument Bearings," Instrumentation Laboratory, E-2215 (1967), Massachusetts Institute of Technology, Cambridge, Massachusetts, 85p.
2. Yovanovich, M. M., "Thermal Constriction Resistance Between Contacting Metallic Paraboloids: Application to Instrument Bearings," *Proceedings of Heat Transfer and Spacecraft Thermal Control*, (1971), M.I.T., Cambridge, MA, pp. 337-358.
3. K. T. Stevens, M. J. Todd, "Thermal Conductance Across Ball Bearings in Vacuum," Report Number: ESA-ESTL-25, (1977), National Centre of Tribology, Risley (England), 51p.
4. A. A. M. Delil, J. F. Heemskerk, and J. P. B. Vreeburg, "Design Report on the ESRO Test Rig to Measure the Thermal Conductance and Friction Torque of Rotating Bearings in Vacuum," Report Number: NLR-TR-74069-U, (1974), 90p.
5. J. F. Heemskerk, A. A. M. Delil, J. P. B. Vreeburg, "A Test Rig to Measure the Thermal Conductance and Friction Torque of Bearings in Vacuum," *European Space Tribology Symposium*, (1975), Frascati, Italy, 18p.
6. Rowntree, R. A., Todd, M. J., "Thermal Conductance and Torque of Thin Section Four-Point Contact Ball Bearings in Vacuum," Report Number: ESA-ESTL-54, National Centre of Tribology, Risley, England, (1983), 57p.
7. Rowntree, R. A., "Stiffness, Torque, and Thermal Conductance of Thin-Section Four-Point Contact Ball Bearings for Use in Spacecraft Mechanisms," *Proceedings of the 1st European Space Mechanisms & Tribology Symposium*, (1983), Noordwijk, Netherland, pp. 91-100.
8. Anderson, M. J., Roberts, E. W., and Rowntree, R. A., "The Thermal Conductance of Solid-Lubricated Bearings at Cryogenic Temperatures in Vacuum," *Proceedings of the 30th Aerospace Mechanisms Symposium*, (1996), European Space Tribology Lab., Cheshire, England, pp. 31-45.
9. Nakajima, K., "Thermal Contact Resistance Between Balls and Rings of a Bearing Under Axial, Radial, and Combined Loads," *Journal of Thermophysics and Heat Transfer*, 9, (1995), pp. 88-95.
10. P. D. Fleischauer and M. R. Hilton, "Assessment of the Tribological Requirements of Advanced Spacecraft Mechanisms," *Materials Research Society Symposium Proceedings*, (1989), pp. 9-20.
11. Y. R. Takeuchi, J. T. Dickey, S. M. Demsky, K. K. Lue, J. J. Kirsch, P. P. Frantz, "A Methodology in Measuring Thermal Properties of Bearings in Motion," *Proceedings of the 15th Annual Thermal and Fluids Analysis Workshop*, (2004), JPL, Pasadena, CA, 25p.
12. A. Leveille, BRGS10C, (a bearing analysis code), The Aerospace Corporation, El Segundo, CA.



# **Mars Exploration Rover Potentiometer Problems, Failures and Lessons Learned**

Mark Balzer\*

## **Abstract**

During qualification testing of three types of non-wire-wound precision potentiometers for the Mars Exploration Rover, a variety of problems and failures were encountered. This paper will describe some of the more interesting problems, detail their investigations and present their final solutions. The failures were found to be caused by design errors, manufacturing errors, improper handling, test errors, and carelessness. A trend of decreasing total resistance was noted, and a resistance histogram was used to identify an outlier. A gang fixture is described for simultaneously testing multiple pots, and real time X-ray imaging was used extensively to assist in the failure analyses. Lessons learned are provided.

## **Introduction**

On the Mars Exploration Rover (MER), many angular positions required remote monitoring. An incomplete list includes the angular positions of four Steering Actuators (WSA), the azimuth, elevation, elbow, wrist and turret joints on the Instrument Deployment Device (IDD), and the azimuth and elevation axes of the High Gain Antenna Gimbal (HGAG). On the MER Lander, knowledge of the angular position of the three Lander Petals was also required. The MER avionics monitored these angular positions by reading the digital, incremental, rotary, magnetic encoder on each of the fourteen electric motor shaft inputs to these geared mechanisms. In case of encoder failure, or if avionics power and thus stored angular position data was lost, all fourteen angular positions could be determined and tracked via backup precision analog potentiometers (pots) configured to measure the output angles of the WSA, the IDD joints, the HGAG axes and the Lander Petals.

Pots were also used in the MER suspension. The left and right rocker-bogie pivots each had one pot to measure the relative angle between each bogie and its rocker arm, while a third pot in the MER differential measured the relative angle between the left and right rocker arms. In conjunction with a three-axis accelerometer providing the Rover's orientation with respect to a gravity vector, relative angle measurements from these pots allowed the Rover's complete kinematic state to be determined. Though the suspension pots were the sole source for this data, it was deemed non-critical for a nominal mission.

Pots are miniature electromechanical mechanisms and as such must pass a rigorous series of tests to be considered flightworthy. This paper will describe some of the more interesting issues that arose during qualification testing of the MER pots, detail their investigations and present their final solutions. Lessons learned along the way will be pointed out.

## **Description of Pots**

The Lander Petal, Bogie Pivot and Differential pots shared a common design based on MIL-PRF-39023; single-turn rotary pots in a metal cup with a bearing-mounted input shaft. The HGAG and WSA pots were each custom, single-turn rotary units designed to be mounted within their respective actuators, and thus had no bearings of their own.

All pots used on MER were of the precision rotary nonwire-wound (conductive plastic) type. Since the pots described in this paper (Figure 1) were provided by a single vendor, they shared basic design features such as:

- 1) An aluminum alloy "cup" which served as the frame of the pot.

---

\* Jet Propulsion Laboratory, California Institute of Technology, Pasadena, CA



**Figure 1. MIL-PRF-39023-style pot, HGAG pot, and WSA pot, from left to right**

2) A conductive plastic disk bonded to the cup. This disk contains two annular tracks: a  $<360^\circ$  resistive track (the resistance element that the wipers rub) and a  $360^\circ$  conductive track (or slip ring) co-molded into the Diallyl Phthalate disk substrate.

3) External electrical connection via three brass terminals potted into the cup on the MIL-PRF-39023-style pots, or three 28 AWG pigtailed provided on the WSA and HGAG pots.

4) Internal electrical connections made by welding, soldering or bonding with conductive epoxy, and employing solid, flat ribbon wire conductors connecting:

a) the end termination junctions of the resistance element to the "CW" and "CCW" input terminals or input pigtailed, and

b) the junction on the conductive track (slip ring) to the "W" wiper terminal or wiper pigtail.

5) Series connected wipers mounted to, but insulated from, the rotating shaft. Sweeping over both tracks, they pick up the voltage from the resistive track and send it through the conductive track (slip ring) to the wiper terminal. Wipers were comprised of multiple, thin, cantilevered contact fingers made of precious metal alloys with contact forces controlled to approximately 20g.

During calibration, each resistance element was manually trimmed to a specified linearity tolerance by scratching the surface of the conductive plastic disk with a scribe, and/or by placing dots of conductive silver paint on its surface. All resistance elements were  $6250 \pm 20\%$  Ohm and rated for 1 watt; all wiper circuits were rated to carry 10 mA. The MER avionics energized the resistance elements with 5 VDC for a power dissipation of  $<5$  mW and drew only 50 nanoAmps through the pot wiper circuits.

### Qualification Testing

To expedite matters, the MER project designated one mechanical engineer to be cognizant of all pot technical issues and qualification testing. For validation purposes non-flight Engineering Model (EM) pots were ordered and received well before the flight pots. To reduce cost and lead time, the EM pots were subjected to a reduced set of acceptance tests by the manufacturer. When the EM pots arrived at JPL they were distributed to the end users without careful inspection or electrical testing.

Most of the qualification testing on the flight pots was done by the manufacturer per a JPL-approved Acceptance Test Procedure (ATP). However, since the manufacturer did not have thermal-vacuum test chambers capable of the required  $-120^\circ$  to  $+110^\circ$  C range, the thermal-vacuum qualification tests were performed at JPL. When the flight pots were received at JPL, each was given a room temperature functional test. First the total resistance of each pot was measured. Then 5 VDC was applied across the input terminals of each MIL-PRF-39023-style pot to energize the resistance element. While its bearing-supported shaft was manually rotated, the output voltage of each pot was plotted on a strip chart recorder.



Since the HGAG and WSA pots had no bearings, each one was placed into a functional test fixture and 5 VDC was applied across its input pigtails to energize the resistance element. While its rotor was manually rotated, the wiper or output voltage of each pot was plotted on a strip chart recorder. All pots were then placed in a vacuum chamber. Once evacuated the pots were subjected to three thermal cycles of -120° C to +110° C. Finally, each flight pot was given a second room temperature functional test.

During the two functional tests, problems were noted with the following flight pots: MIL-PRF-39023-Style S/N's 1035 and 1041, HGAG Pot S/N 1017 and WSA Pot S/N 1039 (Note: all S/N's were randomly assigned by JPL). JPL Problem / Failure Reports (PFR) were initiated to describe the test failures. Shortly after the PFR's were initiated the cognizant engineer for the MER pots left JPL and I assumed her role. Though I was experienced in the construction, cleaning and use of non-flight pots, I had no knowledge of the MER pot effort prior to my taking it over. The remaining three sections of this paper discuss each of the failure investigations and present lessons learned.

### **MIL-PRF-39023-Style Pots**

#### The Initial Problem

Functional testing of the MIL-PRF-39023-style pots before and after the three thermal cycles revealed:

- a) S/N 1035's total resistance varied from approximately 5130 to 5720 Ohms as the shaft was turned, when nominally the value should have remained constant. In addition, there was an open circuit through the wiper terminal for all shaft positions, and
- b) S/N 1041 showed an open circuit through the wiper terminal for shaft positions that should have corresponded to voltage ratios between 0.0 and 0.1.

After duplicating the original functional test setup and now taking the proper precautions (see Lessons 1 - 6), the problems were verified, the out-of-spec electrical performance was characterized and a "scratchy, detent" feel was noted as the shafts were rotated.

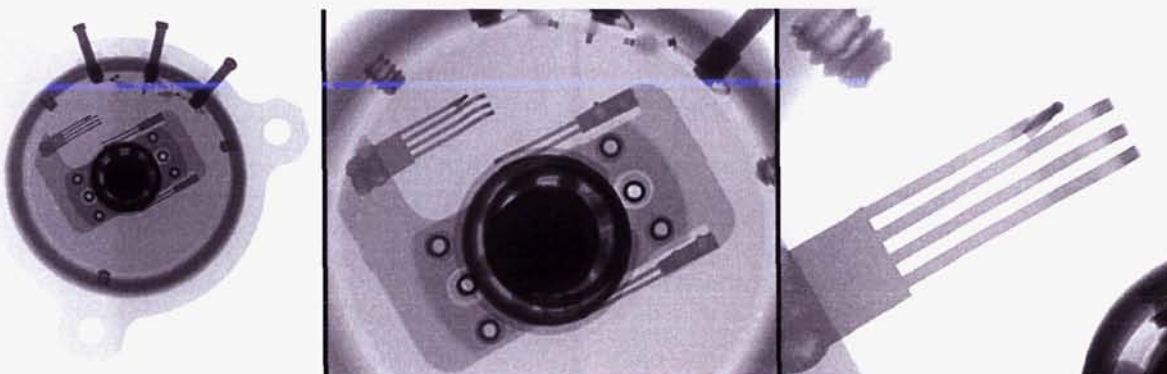


**Figure 2. X-ray images of the S/N 1041 pot at increasing magnification show wiper damage**

FeinFocus real-time X-ray images of the pots revealed wiper damage (Figure 2). Subsequent disassembly of S/N's 1035 and 1041 revealed that the resistance element wiper, slip-ring wiper and the conductive plastic disk were all damaged due to high current and/or arcing (Figure 3).

The wipers showed arc scarring: pitting coupled with discoloration and warping due to overheating (Figure 3). The end of one S/N 1035 wiper finger was burned off and embedded in its conductive plastic disk. The disks were damaged in two places: a) heavy arcing damage to the triangular shaped junction between the "CCW" end of the resistance element and the mound of conductive epoxy connecting the "CCW" terminal's flat ribbon wire, and b) light arcing damage to the slip-ring portion of the disk where one of the two slip-ring wipers was located. The carbonized shell of a "bubble" was observed across the wiper tracks on S/N 1035's conductive plastic disk where vaporized disk substrate "puffed up" the overheated top layers. There was a trough across the wiper tracks in S/N 1041's conductive plastic disk where the substrate was vaporized away.



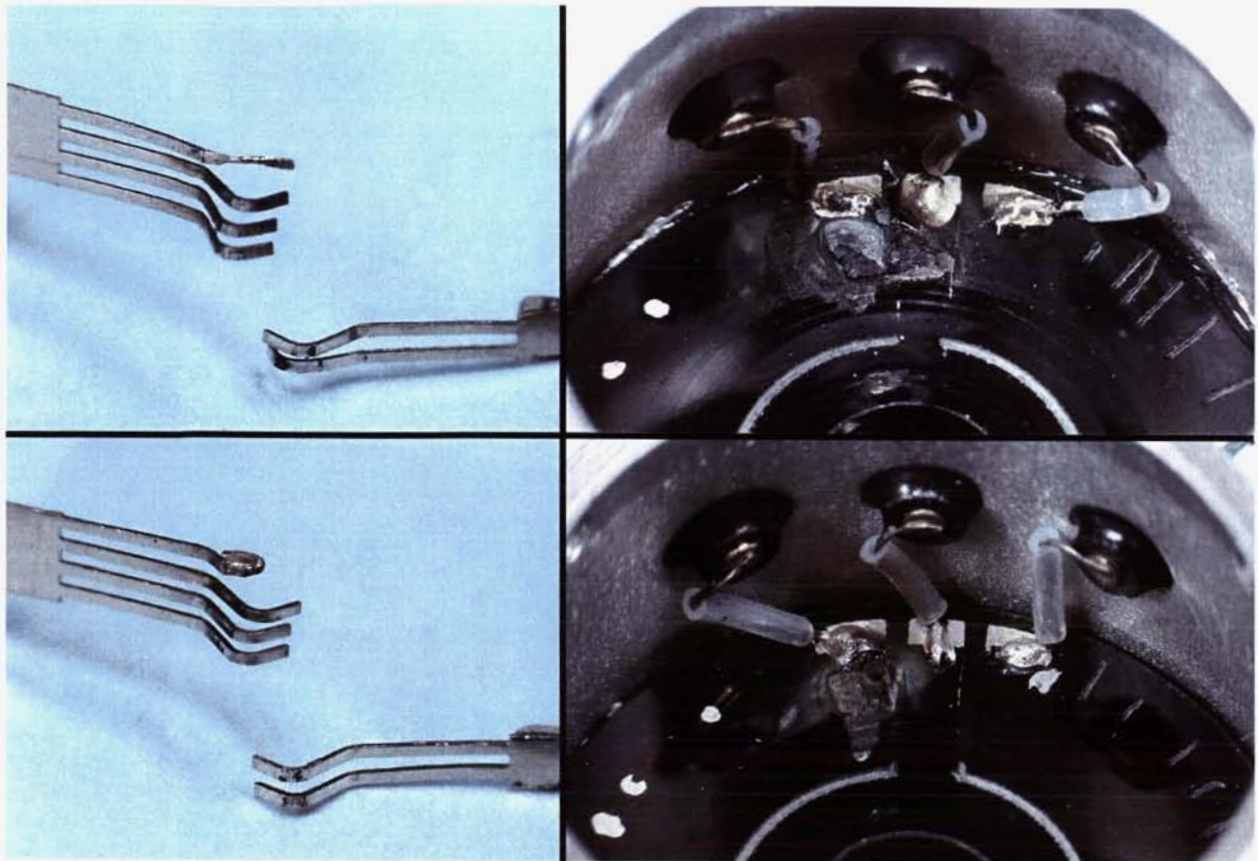


**Figure 3. Arc damage to fingers on wipers, and to conductive plastic disks on S/N 1035 and 1041**

Immediately after documenting the extensive damage in these pots, I began investigating probable causes. As I was not present during the original testing, I had to perform some detective work. I discovered that the manufacturer's rating for the current through the wiper circuit, though never specified in any of the MER pot specs, was only 10 mA. Whenever a wiper was positioned near the "CCW" end of the resistance element, a low resistance ( $\ll 500$  Ohms) circuit existed between the "CCW" and "W" terminals (Figure 4). If 5 VDC was applied between the "CCW" and "W" terminals when the wiper was positioned near the "CCW" end of the resistance element, a current well in excess of the manufacturer's rating would have flowed through the wiper circuit, damaging the pot.

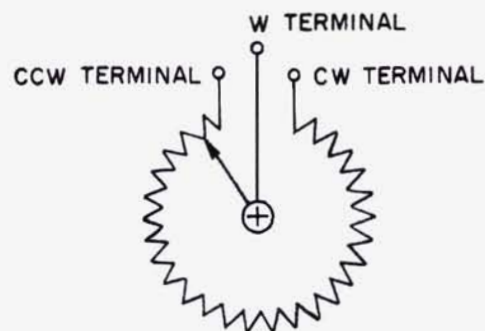


**Figure 4. The wiper position shown forms a low resistance circuit between CCW and W terminals**



The procedure that covered the functional testing of these pots read:

Set multimeter to 10 kOhm - 20 kOhm range...

Perform the following steps for each potentiometer:

1. Remove each potentiometer from its shipping container.
2. Record the resistance from the CW to the CCW terminals in the table at the end of this procedure. Resistance should be between 5 kOhm to 7.5 kOhm.
3. Remove lead from CW terminal and reattach lead onto W terminal.
4. Using a chart recorder, power supply set to 5V, and multi-meter, rotate the rotor of each potentiometer through its entire electrical range by hand. Attempt to rotate the rotor at a constant rate. Look for discontinuities or noise in the signal. Record the potentiometer part and serial number on each strip chart, and append the strip charts to this procedure.
5. Replace each potentiometer into its shipping container.

No electrical schematic was given and no polarities were mentioned. Note that step 3 left the pot's "CCW" and "W" terminals connected to test leads and implied rather than mandated the switching of the multimeter from the "Ohms" to "DCV" range. Step 4 connected a power supply but did not specify how, and though the power supply could deliver 3 amps, there was no instruction to set a current limit. Then rotating the pot ensured that the wiper would pass over the "CCW" end of the resistance element.

The same set-up was used to test all pots. Had the power supply been wired across every pot's "CCW" and "W" terminals, all pots would have been damaged identically. However, the first seven pots tested using this set-up passed. S/N 1035 was the eighth pot tested but the first one damaged. S/N 1041 was the twenty-sixth pot tested, but only the second one damaged. Therefore, it can be concluded that nominally the power supply and instrumentation were wired correctly and that the power supply was not intentionally connected across every pot's "CCW" and "W" terminals.

Close examination of the internal damage indicated that the wipers were stationary when the problem occurred. Note that Pomona Electronics brand "Minigrabber" test clips were used to connect to the pot terminals (Figure 5). When depressed, a beryllium-copper hook projects from the end of these test clips. As the procedure does not mention turning off the power supply outputs, the pots were likely hooked up to live (powered) test clips. The terminals on the MIL-PRF-39023 style pots are only 6mm apart. When attaching the powered clip meant for the "CW" terminal, it would have been very easy to bump the "W" terminal with the metal hook, or even clip it to the "W" terminal outright. If the wiper happened to be positioned near the "CCW" end of the resistance element, a high current could have flowed through the wiper circuit and caused the damage observed.

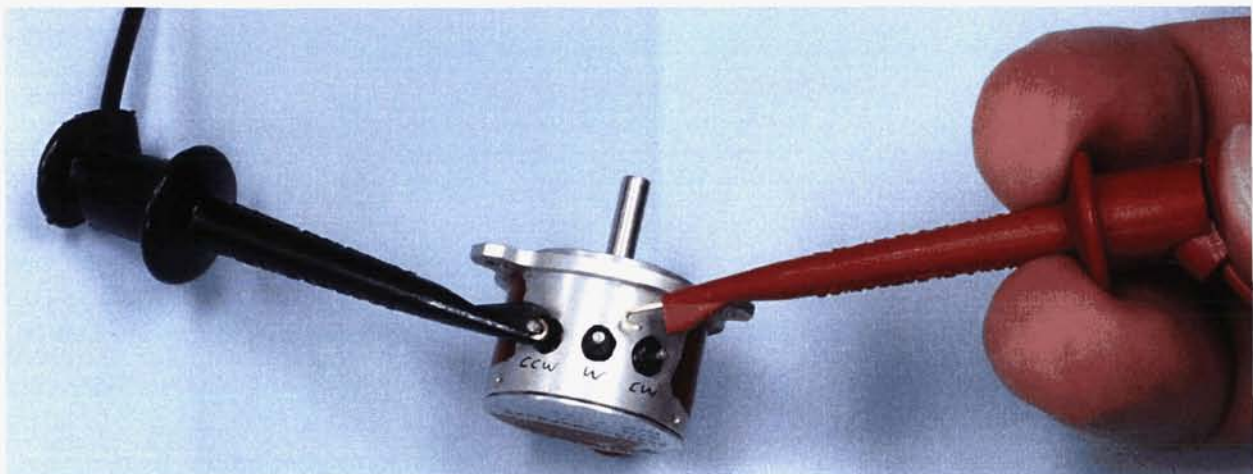


Figure 5. The live, exposed hook on the test clip is a danger to pots with closely spaced terminals

How near is "near"? Ohm's Law says that at 5 VDC, 10 mA will flow through a resistance of 500 Ohms. If the resistance between the "CCW" and "W" terminals varies from 0 Ohms to the full 6250 Ohms over the 320 degree electrical range, then a current in excess of the wiper circuit's 10 mA rating would flow if the wiper was within  $320 * (500 / 6250) = 25$  degrees of the "CCW" end of the resistance element. If the shafts were in purely random orientations when connected, one would expect  $25 / 360 = 7\%$  of the pots to be damaged. Of the 31 MIL-PRF-39023-style pots connected, two (or 6.5%) were damaged.

Based on the preceding failure analysis, this problem was attributed to test error due to a procedure fault. Pot S/N's 1035 and 1041 were scrapped. The pot specification and drawings were revised to include the 10 mA rating for the wiper circuit. The following lessons were learned:

LESSON 1. Be aware of low resistance circuits which exist between the "CCW" and "W" terminals when the wiper is positioned near the "CCW" end of the resistance element, as well as between the "CW" and "W" terminals when the wiper is positioned near the "CW" end of the resistance element. Warn of these conditions in the test procedure.

LESSON 2. In the pot specification and on the pot drawing, clearly state the current rating for the wiper circuit.

LESSON 3. Based on a fraction of this rating, set current limits on all power supplies used in pot testing.

LESSON 4. Provide an electrical schematic for connecting wires, and write detailed procedure steps.

LESSON 5. Use insulated test clips to connect to terminals that are in close proximity to each other. Alternately, solder hook-up wires to the terminals and connect leads to the wires.

LESSON 6. Turn off the power supply outputs when connecting test leads - do not hook live (powered) test leads to flight hardware.

LESSON 7. Before they are allowed to play with electricity on the job, make sure all mechanical engineers and technicians can pass the "flashlight test" (hand them a D-cell, a single piece of wire and a flashlight bulb and ask them to enlighten you).

#### The Ripple Effect

It would have been great to end the investigation there. However, every flight pot that underwent functional testing per the quoted procedure was potentially damaged and had to be proven flightworthy all over again. It was not possible to tell from the X-ray images if the conductive plastic disk was damaged, therefore the only sure way to prove that a pot was undamaged was to remove its lid and conduct a visual inspection using magnification. Each lid was retained by three equally spaced radial set screws threaded into the wall of the cup which were tightened against the bottom of a circumferential groove machined in the lid. Loosening these setscrews should have allowed the lid to be removed. But disassembly of S/N's 1035 and 1041 showed that it wasn't quite so easy:

a) one of the shaft bearings was mounted in the lid. Removing the lid thus represented major disassembly, unloading the preloaded wipers and possibly invalidating all the qualification testing performed to date, and

b) the set screws used to retain the lid had no secondary locking feature, so the original cognizant engineer required that the manufacturer apply Solithane to the set screws to bond them in. The Solithane used by the manufacturer had wicked into the circumferential groove and effectively bonded the lids to the cups. Removing the lids would contaminate the wipers, tracks and bearings with Solithane debris, requiring complete disassembly for cleaning and re-lubricating.

Time constraints necessitated an alternative though admittedly less rigorous approach. It was decided that the remaining flight pots would all be screened for any of the characteristics observed in the failed S/N's 1035 and 1041, namely:

a) out-of-spec electrical performance by electrical functional testing at room temperature, at the operating temperature extremes of  $-75^{\circ}\text{C}$  and  $+70^{\circ}\text{C}$ , and again at room temperature, and

b) any "scratchy, detent" feel as each shaft was rotated.



A complete functional test required rotating each pot while monitoring its wiper terminal voltage. This test was quickly and easily done at room temperature, but having to test 28 pots at  $-75^{\circ}\text{C}$  and  $+70^{\circ}\text{C}$  in a minimum amount of time required a different approach. A gang fixture was designed and constructed with a stationary plate that supported up to 36 MIL-PRF-39023-style pots (Figure 6). A driveshaft turned a central crank arm which rotated a second plate eccentrically. The eccentric rotation of the second plate was converted into rotation of the individual pots by a crank arm on each pot shaft.

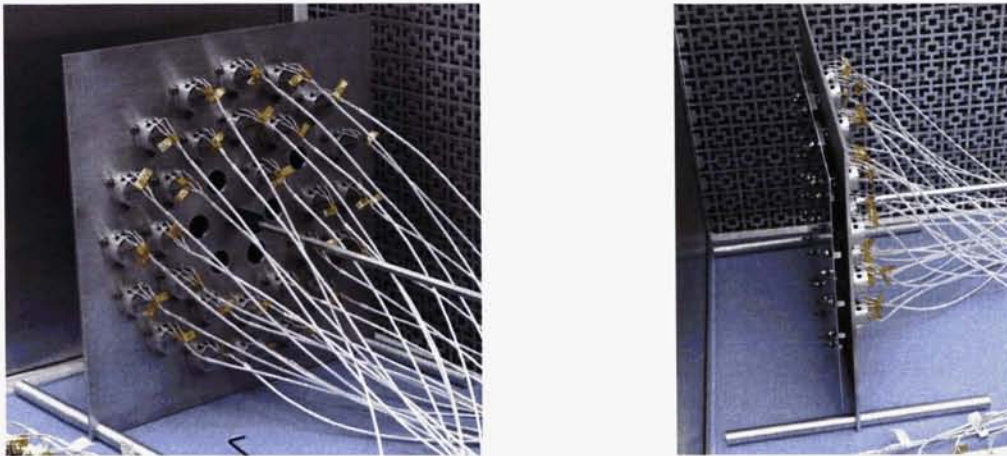


**Figure 6. Two views of gang fixture with 28 pots installed, before being placed in chamber**

This gang fixture was set up in a dry nitrogen purged thermal test chamber employing electrical heating and liquid nitrogen cooling. The driveshaft passed through an opening in the chamber wall to a gearmotor. With this set-up, electrical performance was rapidly verified at the temperature extremes in both the CW and CCW directions. The following lesson was learned:

**LESSON 8.** Don't put all your eggs in one basket. Trying out a new test procedure on all the irreplaceable flight pots in one batch is risky. It is a great deal of work to recertify potentially compromised pots for flight. Instead prove out the test procedure with a few disposable EM pots. Complete the testing and data analysis, then revise the procedure with lessons learned before applying it to any flight pots.

#### The Ripple Effect, Part II

The next step was to check for any "scratchy, detent" feel as each pot shaft was rotated. This was a very delicate task as the torque required to rotate each ball-bearing supported shaft was at most a couple of millinewton-meters. With no sensitive torquemeters available, I turned off the laminar flow benches in the clean room to eliminate their noise and vibration, turned off most of the lights to get rid of the powerline buzz, and ripped the thumb and index finger off my right glove. One by one I took each pot in my hands and rotated the shaft back and forth with my bare fingers, eyes closed and concentrating. Soon I was writing another PFR to document the very weak detent that was felt as the shaft of:

- a) S/N 1027 was rotated by hand through the  $\sim 190$  degree CW shaft orientation, and
- b) S/N's 1021 and 1036 were rotated by hand through the  $\sim 240$  degree CW shaft orientation

In each case the shaft orientation where the detent was felt did not change, even after many shaft rotations; clearly it was not caused by a bad ball in the bearing or a bad inner race. The detent on S/N 1027 occurred at the  $\sim 190$  degree CW shaft orientation which placed the wiper in the electrical dead zone of the pot so damage from high current should not have been a problem. The detents on S/N 1021 and 1036 occur at the  $\sim 240$  degree CW shaft orientation which placed the wiper far enough away from the "CCW" end of the resistance element that damage from high current should not have been possible. Functional testing at room temperature,  $-75^{\circ}\text{C}$  and  $+70^{\circ}\text{C}$  had already verified the required electrical performance for these three pots. X-ray images revealed no macroscopic wiper damage, though it was not possible to tell from the X-ray images if the conductive plastic disk was damaged. How could I be



feeling what was supposed to be a symptom of arc damage, when arc damage was absent and/or impossible? And why did these detents feel much weaker than those on S/N's 1035 and 1041? This new problem had me stumped until the shafts were rotated to the detent positions and the pots were placed back in the FeinFocus X-ray machine.

Close examination of the X-ray images showed that at the ~190 degree shaft position on S/N 1027, the wiper bracket on the shaft passed very close to the flat ribbon wire connecting the "CW" terminal to the resistance element. On most pots, the flat ribbon wires were bent towards the case immediately upon exiting the hole in the conductive plastic disk. However, on S/N 1027, the "CW" flat ribbon wire was not bent towards the case, leaving it closer to the rotating parts than usual. Careful examination of X-ray images of S/N 1027 show that the wiper bracket rubbed the insulating Teflon sleeve on this flat ribbon wire. This rubbing interference was consistent with all observations listed above, represented a new discovery, and was declared to be the cause of the detent.

The flat ribbon wires were welded to the ends of the terminals inside the pot case. However, from one pot to another there was no uniformity to the angle or direction that each flat ribbon wire pointed as it left its terminal (Figure 3). On S/N 1027, the "CW" flat ribbon wire left the "CW" terminal in a direction pointing away from its termination in the conductive plastic disk. Therefore, the flat ribbon wire had to be bent back upon itself in order to be inserted in its hole. Doubling the flat ribbon wire back on itself used up some of its finite length, and was likely why the "CW" flat ribbon wire wasn't bent towards the case when it exited its hole; there simply wasn't enough length available.

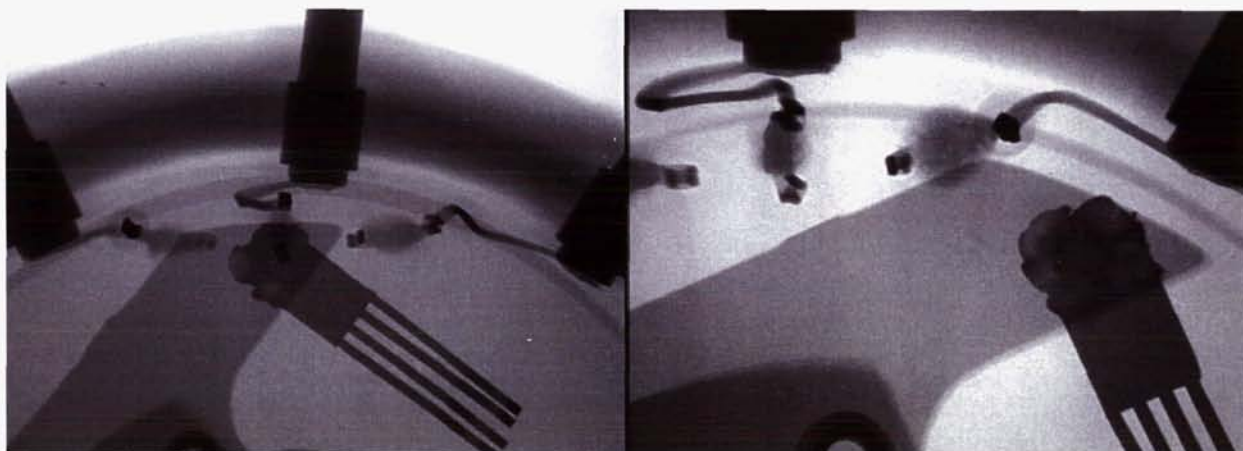


**Figure 7. X-ray images of pots show cause of detent: interfering Teflon sleeve on flat ribbon wire**

X-ray images of S/N's 1021 and 1036 (Figure 7) also showed that their wiper brackets rubbed the insulating Teflon sleeves on their flat ribbon wires. This rubbing interference was consistent with all observations listed above, and was declared to be the source of their detents as well.

Note that these three pots were never disassembled for direct visual verification because:

- a) the cover (lid) was glued on and prying open this lid would create debris which could contaminate the bearings and resistance element, and
- b) removing the lid with its integral bearing allows the shaft to tilt in the single bearing in the cup, preventing accurate checks of the clearances between the wiper bracket and Teflon sleeving, and
- c) since the detent-causing interference could be clearly seen from the X-ray images, it was not necessary to de-lid the pots.

The three pots had been subjected to 5400 revs during testing by the manufacturer and then received another 300 revs at JPL during testing on the gang fixture. The Teflon sleeve had been rubbed by the metal wiper bracket 5700 times, deflecting the flat ribbon wire each time. The number of rubs that cause failure of the flat ribbon wire was unknown, so no prediction could be made as to how much life remained.

Based on the preceding failure analysis, this problem was attributed to manufacturing error due to a faulty production process. S/N's 1021, 1027 and 1036 were labeled "Limited Use (Non-Flight Part)" and were not used for flight.

Except for S/N 1021, 1027 and 1036, all the other pots passed this screening process. Absence of any detent feel means only that the conductive plastic disk/wiper/bearings were not damaged and that there was some clearance between the rotating and stationary parts at room temperature. It was not a measure of how much clearance existed, nor was it a guarantee that clearance existed over the entire operating temperature range. However, it would have been impractical to check for detents at other than room temperature since detecting them requires a very sensitive touch in a quiet room with no vibration. This risk was accepted and the remaining pots were approved for flight use. Lessons learned include:

LESSON 9. Sometimes you have to take off the gloves. In a quiet, vibration-free room, extremely subtle mechanical effects can be felt reliably only through bare skin contact.

LESSON 10. An X-ray inspection machine with real-time imaging capabilities is an extremely valuable tool for performing non-destructive evaluation on assemblies that are sealed or for which disassembly would affect internal clearances or invalidate qualification testing already conducted.

LESSON 11. Interferences within the MIL-PRF-39023-style pots are possible. The pot manufacturer should:

- a) individually specify and inspect the angle or direction that the flat ribbon wire points as it leaves each of the three terminals. The angle should be chosen to provide a direct route to each flat ribbon wire's respective hole in the conductive plastic disk.
- b) specify and inspect that each flat ribbon wire must be bent towards the case immediately upon exiting the hole in the conductive plastic disk. This would ensure that the flat ribbon wires will be against the inner wall of the case and maximize the clearance between the rotating and stationary parts. A cutaway cover or functional gage could be designed that would permit inspection and verification of a minimum acceptable clearance.
- c) investigate a shorter wiper bracket or an alternative "lower profile" method of insulating the flat ribbon wire, to provide more clearance between the rotating and stationary parts.

#### Set Screwed

While concentrating all my tactile attention on the flight pot shafts rotating between my fingers, I noticed that many were not smooth. Close examination revealed deep impressions with raised edges that made each precision 3.170 +0.000/-0.005-mm-diameter shaft reminiscent of a bastard-cut round file. Some EM pots showed this damage as well. During testing per the ATP, the manufacturer must have used a breaker bar to repeatedly tighten R<sub>c</sub> 52 hardened steel cup-point set screws into the R<sub>b</sub> 82 annealed 303 stainless steel pot shafts. To correct this damage, the affected pots needed to have their shafts deburred with an India oilstone before I could deliver them to their end users. Deburring generates metal chips and abrasive fines, so to prevent contamination each pot was bagged and taped to expose just its shaft for deburring. After deburring was complete, the shafts were cleaned and the bags removed. The following lesson was learned:

LESSON 12. If for testing purposes EM pots are ordered and received long before the flight pots, then immediately upon receipt the EM pots should be carefully inspected and the manufacturer should be contacted about quality issues like precision shafts marred by set screws. Before fabricating the flight pots the manufacturer should be instructed to tighten setscrews against the shaft's machined flat and not its precision outer diameter, to properly control setscrew torques, to use brass or nylon tipped setscrews, and/or to switch to non-setscrew style couplings on their test equipment.

#### Observed Trends

Continuing the investigation, the total resistance measurements captured my attention next. A plot of the total resistance of the MIL-PRF-39023-style pots showed it to be decreasing with either time and/or thermal cycles. The plot in Figure 8 shows the history of these total resistance measurements with each line representing a different serial number pot. The spec for these pots was 6250 Ohms  $\pm$  20%, or 5000 to 7500 Ohms. There was minimal drift measured by the pot manufacturer before and after their thermal



testing (measurements #1 and 2), but significant drift was measured after each JPL thermal test (measurements #3 - 6). Discussion with the original cognizant engineer responsible for measurements #3 and 4 revealed that the ohmmeter was never zeroed, which would have put a constant offset error on all values measured. If that offset had been approximately -170 Ohms, there would be a uniform downward trend across nearly all measurements. I became concerned that if this trend continued, the daily thermal cycles experienced by the Rovers might cause the total resistance of the pots to drift out of spec.

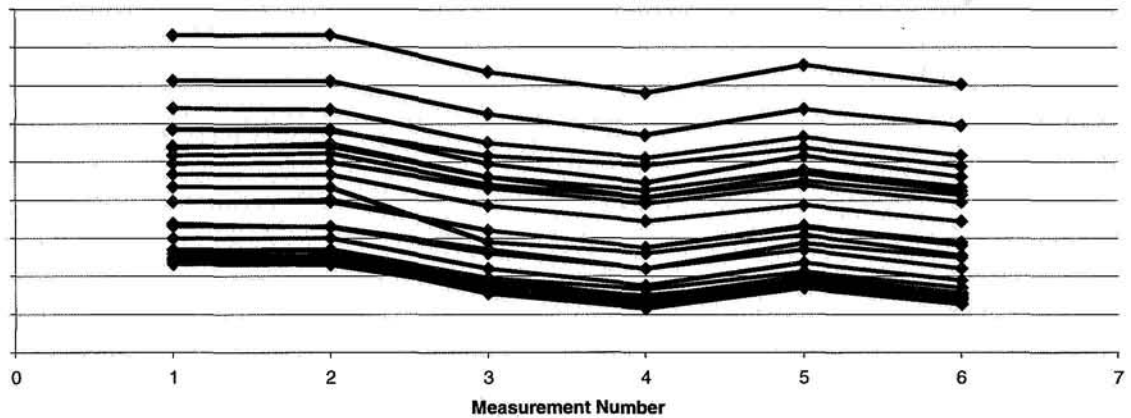


**Figure 8. Total Resistance measurement history**

When notified of this observation the pot manufacturer said that it was typical for the total resistance of a conductive plastic pot to change after thermal cycling. The mechanism was explained as follows: conductive plastic is made of carbon particles in an insulating matrix, co-cured at 160° C (and rated for operation up to 125° C). Thermal cycles change the insulating matrix on a microscopic level, allowing better conductivity between the carbon particles. Macroscopically these changes appear as a drop in the total resistance. The manufacturer said that as the number of thermal cycles builds, the rate at which the resistance drops will decrease and the resistance will eventually stabilize. The scratches and drops of silver paint used to linearize the pot have an effect on the rate at which the resistance stabilizes. The manufacturer assured me that the resistance changes would be uniform throughout the length of the resistance element and that the pot's linearity would not be affected by changes in the total resistance.

Interestingly enough, the pot manufacturer also said that just leaving the pot on a shelf for a time after thermal cycling will cause the pot to recover some, but not all, of the resistance loss which occurs during thermal cycling. They called this a "memory" effect.

**LESSON 13.** To gain insight, plot every measured quantity and look for trends. If a measurement is worth recording, it is worth plotting.

**LESSON 14.** Calibrate test equipment before using it on flight hardware. The data is only as good as the calibrations; i.e., always "zero" an ohmmeter before measuring any resistance.

**LESSON 15.** Manufacturing considerations and physical mechanisms are the reason a precision pot has the relatively loose tolerance of  $\pm 20\%$  on its total resistance.

#### Add Vent Holes, Then Glue Them Shut

MIL-PRF-39023-style pot cups trap air so the MER Environmental Requirements Engineer requested a venting analysis. I did some digging and found that during a design review early in the procurement process, the original cognizant engineer had requested that a vent hole be added, so the manufacturer drilled one in the cup between the set screws that hold the lid on. Unfortunately, the original cognizant engineer had also requested that a Solithane mixture be applied to the set screws to lock them in place. When this Solithane mixture wicked into the circumferential groove and effectively bonded the lids to the cups, it also blocked the vent path leading to the drilled vent hole. The only vent path left was the one through the shaft bearing which is undesirable because vented air often carries contamination that can become lodged in a bearing.

LESSON 16. When a design uses one feature for multiple purposes (like the circumferential groove in the lid which was used both to retain the lid and to provide a labyrinthine path for venting), make sure all the effects of even the smallest design change are well understood before approving it.

#### Turning Gold Into Base Metals

Prior to delivering the pots to the end users I noticed that the original cognizant engineer ordered the MIL-PRF-39023 pots manufactured to a drawing which specifies that its solder terminals are made from brass which has first been silver plated, and then very thinly gold plated.

JPL's internal requirements state that gold shall not be used as a surface finish for soldering, so I instructed the end users of the MIL-PRF-39023-style pots to "degold" the terminals before soldering.

LESSON 17. Soldering to gold can form brittle intermetallic compounds that can crack under thermal cycling. Gold plated conductors must have their gold plating removed by immersion in a designated solder pot, then tinned using the same processes in a different solder pot. Alternatively, gold plated leads must be tinned twice with solder wire, wicking off the solder in the first tinning to remove the gold, then tinning again.

#### Trust Nobody With Your Flight Hardware

About this time MER's Deputy Mission Assurance Manager requested a private meeting to better understand the pot details described in the PFR's. Afterward this manager asked to borrow several of the pots that had been written up, and I foolishly obliged. When I asked for my pots back, S/N 1036 could not be found: Mission Assurance had lost my flight hardware!

LESSON 18. When cognizant of flight hardware, especially small hardware, never let it out of your sight, and never, ever lend it to management.

### **HGAG Pots**

Functional testing of the HGAG pots before and after the three thermal cycles revealed that on S/N 1017 the total resistance varied from approximately 5440 to 6190 Ohm as the rotor was rotated. The total resistances of the other HGAG pots tested did not vary with rotation angle. Nominally the total resistance should remain constant.

After duplicating the original functional test setup and now taking the proper precautions (see Lessons 1 - 6), the problem was verified.

Next the build documentation was examined to determine if it held any clues to this anomaly. The pot manufacturer's ATP describes the resistance check, but does not mention rotating the rotor, nor does it specify that the total resistance must not vary with rotor angle. The spec only called for a total resistance of 6250 Ohms  $\pm$  20%. The in-process data sheet filled out by the pot manufacturer listed the total resistance as 6046 Ohms. After environmental testing, the in-process data sheet listed the total resistance as 6121 Ohms. 6121 Ohms represented a 75-Ohm increase which was not in keeping with the rest of the pots in that lot which showed total resistance changes of no more than 5 Ohms. Random rotor angles during total resistance measurement explained the 75 Ohm change, and indicated that this problem may have been inherent at assembly.

S/N 1017 was still a flight pot, so I was in no rush to tear it apart. Besides, FeinFocus X-ray images of S/N 1017 revealed no internal damage.

Instead I elected to do more testing. The pot was powered with 1.0 VDC across the input wires and the wiper voltage was measured and recorded as the rotor was rotated through 360 degrees in 5 degree increments. The wiper voltage was indeed the required linear function of rotor angle. Next the total resistance was measured and recorded as the rotor was rotated through 360 degrees in 5 degree increments. The total resistance was a smoothly decreasing function of rotor angle (Figure 9).

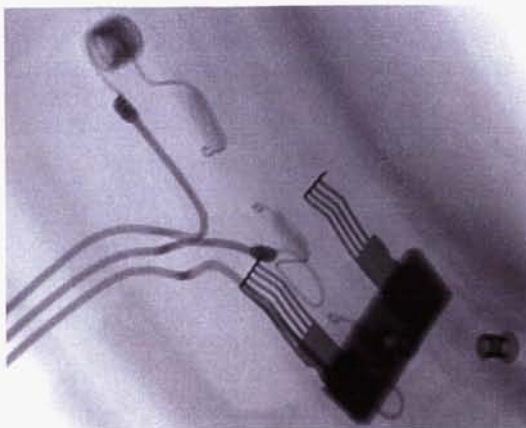


**Figure 9. X-ray image of undamaged wiper and slip ring brushes in HGAG pot**

After plotting and examining the data, I hypothesized that a high resistance leakage path between the “CCW” end termination of the resistance element and the slip ring could explain the anomaly. A schematic of a pot with an internal leakage resistance was drawn (Figure 10) and an equivalent resistance equation was written as a function of shaft angle. This mathematical model was iterated with different values of leakage resistance until the model predictions matched the measured total resistance data. Note that the 51.9 kOhm leakage resistance found in this way was 8.3 times the pot's nominal total resistance.

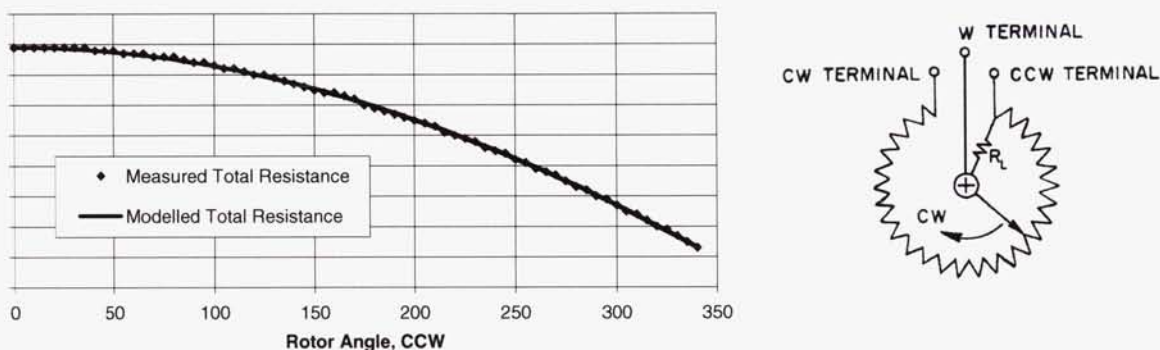


**Figure 10. Measurements match model of HGAG pot with internal leakage resistance  $R_L = 51$  kOhm**

The prediction of the model fits the data extremely well, supporting the hypothesis. The extremely linear output of this pot supports the conclusion that this leakage resistance was present all along but never discovered (because per a strict reading of the ATP instructions, no one was looking for it). Any non-linearity caused by the leakage resistance was likely removed by adding scratches and/or drops of silver paint when the pot's linearity was adjusted by the manufacturer.

True confirmation of the hypothesis requires direct measurement and so the pot was disassembled by removing the rotor from the stator. In this condition the leakage resistance could be accurately measured because the slip ring and the resistance element were no longer bridged by the brushes. With the pot disassembled, the leakage resistance measured 51.4 kOhms to the “CCW” lead, and 57.6 kOhms to the “CW” lead. Note that  $57.6 - 51.4 = 6.2$  kOhm, the nominal total resistance.

The resistance element showed a very large number of linearizing marks, with all the silver paint dots grouped in the middle of the element and all the scratches at the ends near the junctions; exactly what one would expect if the pot had been adjusted to get rid of a manufactured-in leakage resistance.

It is reasonable to ask what caused the leakage resistance. There was a concern that it could have formed from conductive debris worn off the surface of the resistance element or slip ring by a rough wiper,



and scattered between them. However that proposed mechanism was eliminated when upon disassembly the resistance element and slip ring showed no signs of wear, scraping or dusting.

The conductive plastic disk was made of carbon particles in an insulating matrix, co-cured at 160° C. It is believed that if some conductive carbon particles in the junction area were displaced from the resistance element and co-cured in place, a high resistance leakage path between the element and the slip ring would have resulted.

While the discovery of the varying total resistance was significant, S/N 1017 has always been within tolerance. Testing verified its linearity, and though it varied, the total resistance was within the  $6250 \pm 20\%$  (5000 - 7500) Ohm allowable range. Of course, this leakage resistance does waste a bit of power.

Based on the preceding failure analysis, this problem was attributed to manufacturing error due to a faulty production process. Pot S/N 1017 was labeled "Limited Use (Non-Flight Part)" and was not used for flight.

LESSON 19. Being within tolerance does not mean a pot is problem free.

LESSON 20. Unique behavior is always worth investigating until it is understood, to make sure that the problem does not affect other pots in the lot.

### WSA Pots

During functional testing of the WSA pots before the three thermal cycles, the total resistance of WSA Potentiometer S/N 1039 measured 7400 Ohms. After the three thermal cycles, the total resistance dropped to 6900 Ohms. Compared to the other WSA pots in the lot, this change was a full order of magnitude larger than expected.

After duplicating the original functional test setup and now taking the proper precautions (see Lessons 1 - 6), the problem was verified.

Next the build documentation was examined to see if it held any clues to this anomaly. The spec called for a total resistance of  $6250 \text{ Ohms} \pm 20\%$ . The in-process data sheet filled out by the pot manufacturer listed the total resistance as 7391 Ohms. After environmental testing, the in-process data sheet listed the total resistance as 7404 Ohm. While S/N 1039 was in spec, all the other WSA potentiometers supplied to JPL had much lower total resistances. A histogram of WSA total resistance values (Figure 11) clearly shows S/N 1039 to be an outlier.

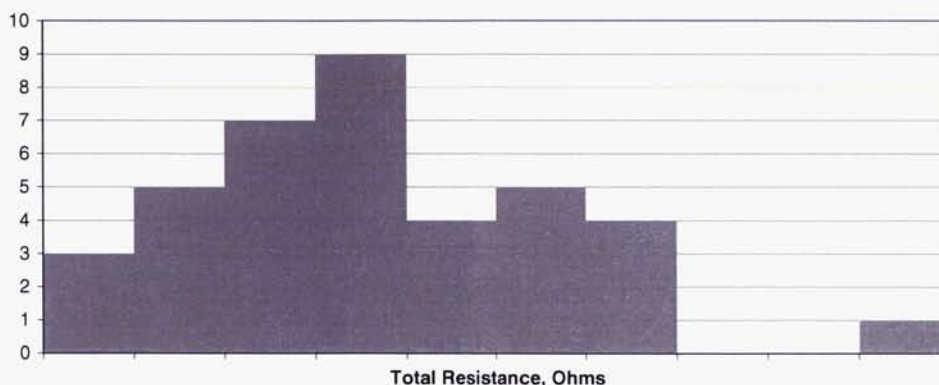


**Figure 11. Histogram of Total Resistance values showing the lone outlier, S/N 1039**

S/N 1039 was still a flight pot, so I was in no rush to tear it apart. Besides, FeinFocus X-ray images of S/N 1039 revealed no internal damage.

Instead I elected to do more testing. The pot was powered with 1.0 VDC across the input wires and the wiper voltage was measured and recorded as the rotor was rotated through 360 degrees in 5 degree

increments. The wiper voltage was indeed the required linear function of rotor angle. Next the total resistance was measured and found to be 6890 Ohm. Note that this was within the  $6250 \pm 20\%$  (5000 - 7500) Ohm tolerance allowed for this potentiometer.

When notified of this anomaly the manufacturer said that it was typical for the total resistance of a conductive plastic pot to change after thermal cycling. The mechanism was explained as follows: conductive plastic is made of carbon particles in an insulating matrix, co-cured at 160° C (and rated for operation up to 125° C). Thermal cycles change the insulating matrix on a microscopic level, allowing better conductivity between the carbon particles. Macroscopically these changes appear as a drop in the total resistance. The manufacturer said that as the number of thermal cycles builds, the rate at which the resistance drops will decrease and the resistance will eventually stabilize. The scratches and drops of silver paint used to linearize the pot have an effect on the rate at which the resistance stabilizes. The manufacturer assured me that the resistance changes would be uniform throughout the length of the resistance element and that the pot's linearity would not be affected by changes in the total resistance.

The eight flight WSA pots went through additional thermal cycling as part of the steering actuator qualification test program. After those thermal cycles, the total resistances were found to have changed by +73 to -283 Ohms. Another data point comes from the MIL-PRF-39023-style pots: between manufacture and use, the total resistance of each one dropped from 200 to 400 Ohms.

From the beginning, WSA Potentiometer S/N 1039 was an outlier, with a total resistance 750 Ohms higher than its nearest neighbor. When S/N 1039 was 5 weeks old, it took advantage of a thermal cycle to drop its total resistance by 500 Ohms to a value more in line with, but still higher than, the rest of the batch. While this drift was significant, 1039 has always been within tolerance, and testing proves its linearity. Based on the preceding failure analysis, it was determined that there was no problem with the pot. However, just to be safe, pot S/N 1017 was labeled "Limited Use (Non-Flight Part)" and was not used for flight.

LESSON 21. Drifting values and excessive variation within a lot may indicate trouble, even if the individual pots are within spec. Compare the pots to each other as well as to the requirements.

### Conclusions

As of this writing, the "Spirit" and "Opportunity" Mars Exploration Rovers have been operating on the Martian surface for over two years. In spite of the difficulties encountered during flight qualification of the MIL-PRF-39023-style pots, the HGAG pots and the WSA pots, all pots on the Rover continue to perform reliably under very harsh conditions. It is hoped that the lessons provided in this paper will help other potentiometer users enjoy similar successes.

### References

1. Iskenderian, T. "Lessons Learned from Selecting and Testing Spaceflight Potentiometers." *Aerospace Mechanisms Symposium #28*, (1994), pp. 339-358.
2. Defense Logistics Agency, "MIL-PRF-39023B Resistors, Variable, Nonwire-wound, Precision, General Specification For." Feb 1999.
3. "VRCI-P-100A, Industry Standard for Wirewound and Nonwirewound Precision Potentiometers, Terms and Definitions, Inspection and Test Procedures." Variable Electronic Components Institute, Vista, CA, <http://www.veci-vrci.com/>, 1988

# Mechanism Development, Testing, and Lessons Learned for the Advanced Resistive Exercise Device

Christopher D. Lamoreaux\* and Mark E. Landeck\*

## Abstract

The Advanced Resistive Exercise Device (ARED) (Figure 1) has been developed at NASA Johnson Space Center, for the International Space Station (ISS) program. ARED is a multi-exercise, high-load resistive exercise device, designed for long duration, human space missions. ARED will enable astronauts to effectively maintain their muscle strength and bone mass in the micro-gravity environment more effectively than any other existing devices. ARED's resistance is provided via two, 20.3 cm (8 in) diameter vacuum cylinders, which provide a nearly constant resistance source. ARED also has a means to simulate the inertia that is felt during a 1-G exercise routine via the flywheel subassembly, which is directly tied to the motion of the ARED cylinders. ARED is scheduled to fly on flight ULF 2 to the ISS and will be located in Node 1. Presently, ARED is in the middle of its qualification and acceptance test program. An extensive testing program and engineering evaluation has increased the reliability of ARED by bringing potential design issues to light before flight production. Some of those design issues, resolutions, and design details will be discussed in this paper.



Figure 1. Test subject performing a squat on ARED

---

\* NASA Johnson Space Center, Houston, TX



## Introduction and ARED Background

This paper will discuss the design, development, and testing of the Advanced Resistive Exercise Device for the International Space Station program. ARED is scheduled to fly on shuttle flight ULF2 and will be located in Node 1 of ISS. ARED is a multi-format resistive exercise machine specifically designed for a zero-gravity environment. Capable of 30 different exercises, ARED will be used daily by the astronauts aboard the ISS to counter the loss of muscle and bone mass associated with long duration human space missions. ARED is being developed at NASA's Johnson Space Center in the Biomedical System Division. The team consists of both civil servant and contractor engineers from many different organizations at JSC. ARED has been developed specifically to improve the on-orbit resistive exercise capability, reliability, and availability. The resistive force is generated by two, 200-mm (8-in) diameter dynamic vacuum cylinders. A vacuum exists on one side of the piston and atmospheric pressure exists on the other. The piston has a stroke of 30.5 cm (12 in) inside the cylinder. The cylinders are capable of delivering a nearly constant load. In combination with various mechanisms, ARED provides a range of 0 – 272 kgf (0 – 600 lbf) to the exerciser, which is important effective zero-g exercise. In addition, the flywheel mechanism simulates the inertial force component of lifting free weights in a 1-G environment. ARED thus provides a more complete weightlifting experience than any previous on-orbit resistance exercise device. It will allow astronauts to perform a wider variety of exercises at higher loads, higher speed, and longer stroke which, in turn, will enable them to maintain their health more effectively in a zero-gravity environment.

The need for ARED, arose out of reliability and performance concerns with previous resistance devices for ISS. ARED is being designed, tested, and certified for a 15-year service life, which is much longer than any previously designed device. This long service life is needed to support long duration space missions, which will require a robust and reliable weightlifting machine. ARED's predecessor, IRED, has a 0 – 136 kgf (0 – 300 lbf) load range whereas ARED will enable the crew to exercise up to 272 kgf (600 lbf). ARED will allow for a wide range of both bar exercises (squat, dead lift, heel raise, etc) and cable exercises (hip abductors, one-arm curls, etc). The load and stroke capability for bar exercises is 0 – 272 kgf (0 – 600 lbf) and a 76.2-cm (30-in) stroke. The load and stroke capability for cable exercises is 0 – 68 kgf (0 – 150 lbf) and a 183-cm (72-in) stroke. ARED's vacuum cylinders have a nearly constant loading profile, which is more medically advantageous than the varying loading profile that is provided by springs and rubber based exercise devices. In addition to providing more constant load than IRED, ARED attempts to simulate the inertia that is felt during free-weight, 1-G exercise by employing a flywheel that is directly tied to the motion of the cylinders. The differences are shown in Table 1.

**Table 1. Comparison chart of ARED vs. IRED**

	<b>ARED</b>	<b>IRED</b>
<b>Maximum Bar Exercise Load</b>	272 kgf (600 lbf)	136 kgf (300 lbf)
<b>Maximum Bar Exercise Stroke</b>	76.2 cm (30 in)	127 cm (50 in) at low loads 56 cm (22 in) at high load
<b>Maximum Cable Exercise Load</b>	68 kgf (150 lbf)	68 kgf (150 lbf)
<b>Maximum Cable Exercise Stroke</b>	183 cm (72 in)	127 cm (50 in) at low loads 56 cm (22 in) at high load
<b>1-g Free-Weight Inertial Component</b>	Yes	No
<b>Force Profile</b>	Nearly constant throughout stroke	Linearly increasing during stroke

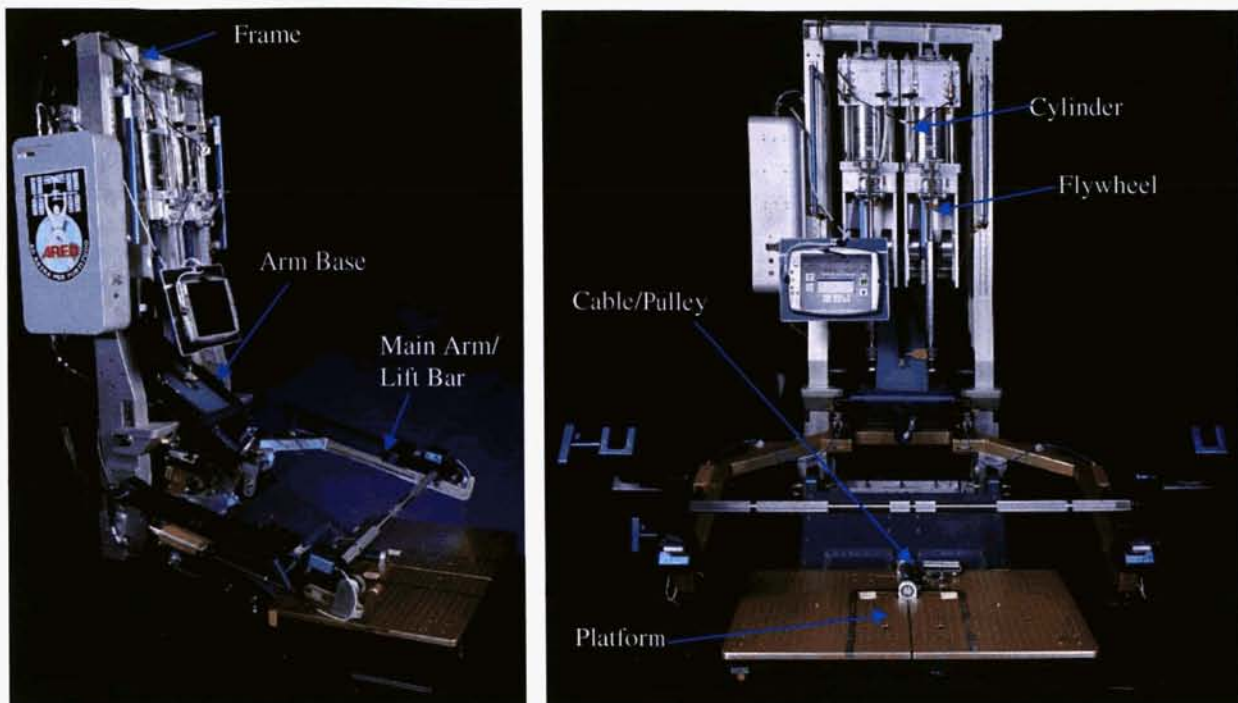


**Figure 2. ARED - Man in the Loop Testing Unit - Profile and Front View**

#### **General ARED Mechanism Overview**

ARED has seven main subsystems (Figure 2); vacuum cylinders, flywheels, frame, platform, arm base, cable-pulley, and the main arm/lift bar. A motion schematic for a squat on ARED is shown in Figure 3. The vacuum cylinders are the main generators of resistive force for ARED. The details of the cylinders will be discussed fully in the next section. The piston rods are attached to the arm base assembly.

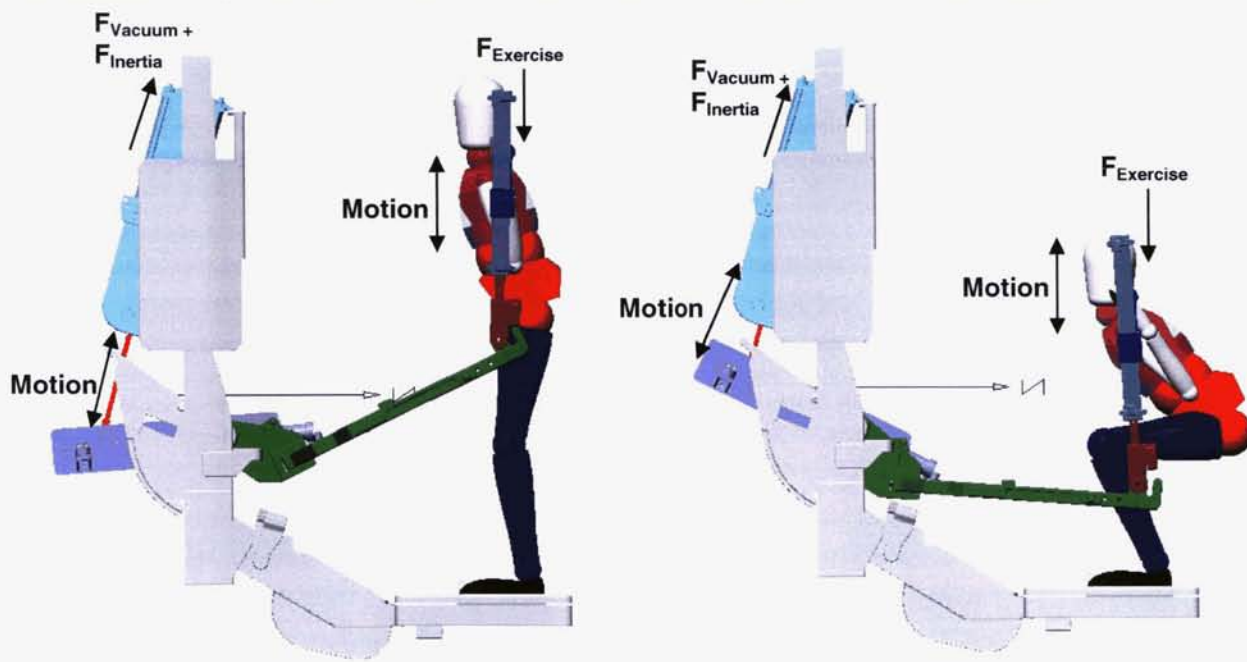


**Figure 3. Schematic of ARED showing motion and simple free body diagram**



The main purpose of the arm base assembly (Figure 4) is to provide a mechanism to adjust the load setting. A ball screw in the arm base provides this function. By turning the ball screw, the attachment point of the piston rods moves along the ball screw. This changes the moment arm between the pivot point and the cylinder load application point and allow for load adjustment at 1-lb increment. The arm base assembly transfers the load from the cylinders to both the bar and cable exercise hardware. The dual nature of the arm base minimizes the reconfiguration required to switch between the two types of exercises, resulting in a more efficient exercise routine. Details of the arm base will be discussed later.



**Figure 4. ARED Arm Base Assembly (Top Cover Removed)**

The flywheel assembly is mounted to an end cap of the cylinder and directly meshes with the motion of the piston by means of a gear and gear rack. The details of the flywheel assembly will be discussed in the next section.

The main arm and lift bar assembly (Figure 2) transfers the load from the arm base to the exerciser. The main arm assembly lifts the front end of the arm base using a contact surface. The lift bar portion of the assembly allows for bar adjustment from 25.4 cm (10 in) above the platform to 183 cm (72 in) above the platform. This wide range of adjustment allows for any bar exercise from a dead-lift to a squat and accommodates a range of human subject from 5<sup>th</sup>-percentile Asian female to 95<sup>th</sup>-percentile American male. As with free weights, the position of the bar can also be “racked” using the upper stop mechanism. The upper stop mechanism allows the crew to start the squat and heel-raise exercises from a standing position.

The cable-pulley assembly also transfers the load from the arm base to the subject. The cable arms push down on the rear portion of the arm base assembly (Figure 5). The cable-pulley assembly enables a variety of cable exercises such as one-arm cable row, hip abductions, and one-arm curls. It employs a series of pulleys, timing belts, and cables to achieve this function. One of the pulleys in the assembly is cammed to compensate for geometry changes during the stroke in order to create a constant load at the end of the exercise rope. The pulley ratios provide a maximum of 136 kgf (300 lbf) and 183 cm (72 in) of stroke.



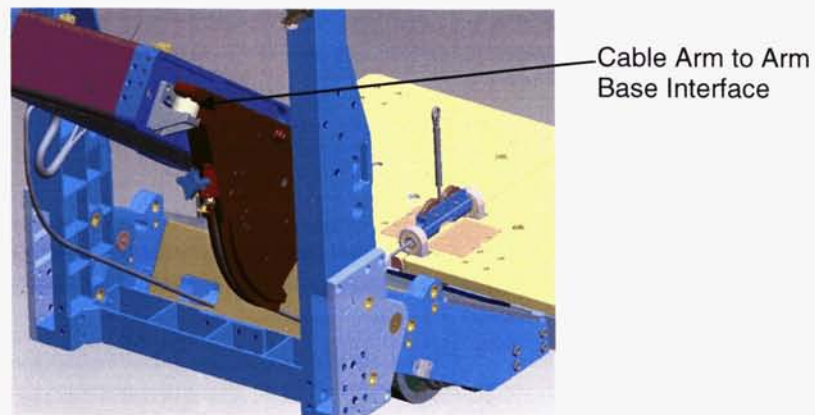


**Figure 5. Detail showing the cable arms pushing on the back of the arm base assembly**

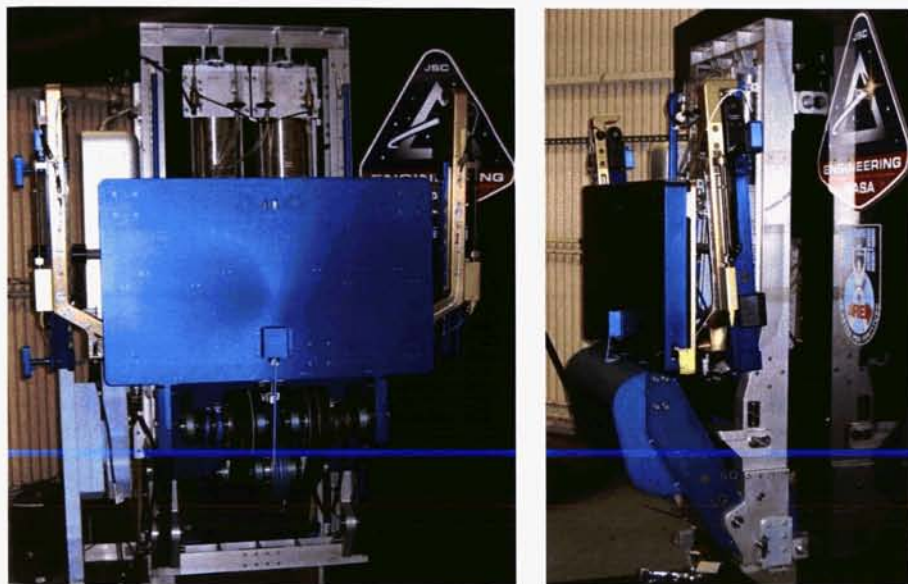


**Figure 6. ARED in the folded configuration**  
Front view shows the details of the cable pulley mechanism.

The platform (Figure 7) assembly's main purpose is to provide an adequate exercise surface and to provide containment for some of the pulleys for the cable-pulley mechanism. Its secondary purpose is to house load cells and wiring for the instrumentation system. The platform and main arm also can be folded up (Figure 6) to aid in storage and crew translation on ISS.

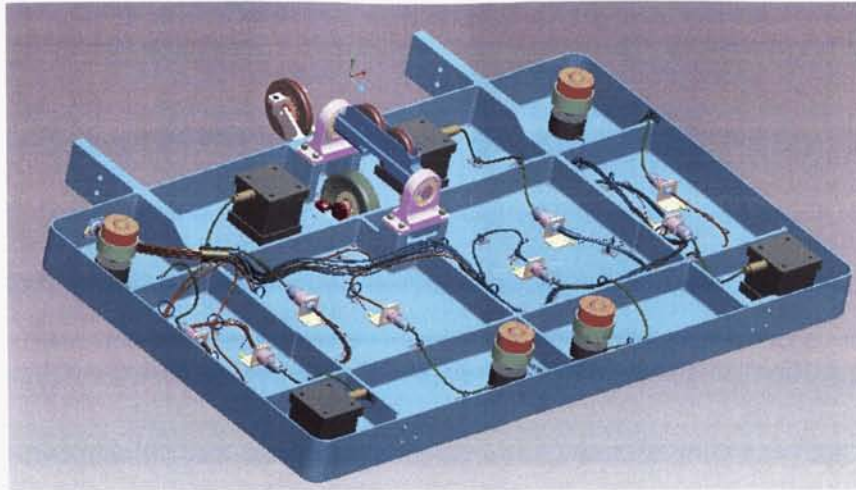


**Figure 7. Picture of the platform CAD model with the footplates removed.**  
This shows the electronics inside the platform assembly.

### **Vacuum Cylinder Design Details**

There are two vacuum cylinders (Figure 8) used on ARED. Each cylinder provides a constant 340-kgf (750-lbf) load. The design uses a standard cylinder/piston concept with endplates and four tie rods holding the assembly together.

The original cylinder shell was made of 6061-T6 Al, anodized on the outer surface, and left bare on a 16 RMS ID surface. Braycote 601 lubricant was applied to the entire ID of the cylinder shell. Early vacuum cylinder tests indicated that the surface finish of the interior surface, measured in RMS, is the critical parameter in maintaining a vacuum, while the piston is moving. The current flight design calls for a 20.3-cm (8-in) ID with an 8 RMS or better surface finish, 4.8-mm (0.19-in) wall thickness, and is 38.1 cm (15 in) in length. To achieve the best possible surface finish, three different manufacturing methods were tried; ground and honed, electro polish, and hand polish. Results showed that the ground and honed process provided a more consistent and controlled surface finish while maintaining the required roundness. To date, the best surface finish achieved is less than 1 RMS on an aluminum 6061-T6 cylinders, manufactured at the Micro-machining Department at NASA's Glenn Research Center.

The current flight piston design is made from 6061-T651 Al using a Nylon Molygard wear strip and a self lubricating Carboxylated Nitrile U-ring seal from Parker Hannifin Corporation. The open end of the U-ring seal is oriented toward the pressure side of the piston. Braycote 601 lubricant is applied to the wearstrip and u-ring seal. Three different wearstrip/u-ring seal combinations were evaluated to achieve the most efficient vacuum under dynamic conditions.

1. A single wearstrip with a single u-ring seal.
2. A single wearstrip with 2 u-ring seals.
3. A single wearstrip with a spring-energized u-ring seal.

Through a series of tests, it was determined that option 1 worked well as long as the manufacturing and assembly tolerances (Figure 8) were controlled. With such a large diameter piston/cylinder and long stroke, it was important to maintain perpendicularity and parallelism between the piston, piston shaft, and cylinder wall. A jig was designed to assist in assembling the cylinder and piston to the required alignment.



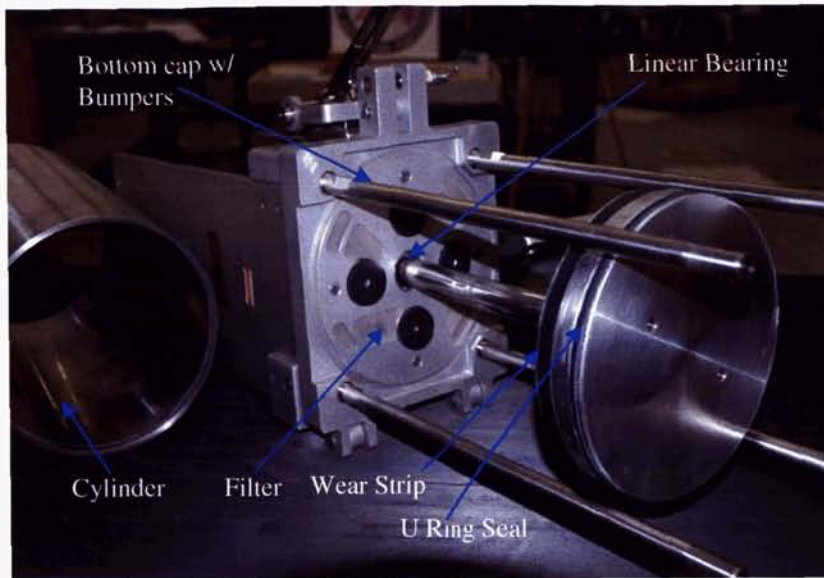


**Figure 8. Piston/Cylinder Design**

The bottom end cap design, also 6061, includes a Linear Bearing packed with Rheolube 2000 grease. This bearing interfaces with the piston shaft made of 15-5 PH stainless steel and heat treated to a H1025 condition. The shaft has a circular cross section the length of the piston stroke that interfaces with the linear bearing. The remaining portion of the shaft is rectangular for attaching a gear rack used to drive the flywheel. The bottom cap design includes a Fluorocarbon rubber bumper and a 3.2-mm (0.125-in) thick polyester grade polyurethane foam filter. The foam filter was added to the bottom end cap design to restrict airborne debris from being sucked into the cylinder. The rubber bumper prevents piston damage in the event of bottoming out during assembly (Figure 8).

The head cap, on the vacuum side of the piston, is 6061 Al and is sealed with the cylinder shell using a standard Butyle rubber o-ring seal. The head cap also includes a relief valve and a fluorocarbon rubber bumper. To evacuate the cylinder, the relief valve is opened and the piston is pushed to the top of the stroke and bottomed out against the rubber bumper. The valve is then closed (Figure 9), and a vacuum is established.



**Figure 9. Assembled Cylinders showing top caps and valves for venting/evacuation**



## Design Details – Flywheel Assembly

The flywheel assembly is the component of ARED that simulates the inertial effect of weightlifting in 1-g environment. When lifting free weights in 1-g, the total foot reaction force is dependent on the acceleration of weights on the exerciser's shoulders. While performing a squat, this inertial effect creates a spike in load at the bottom of the stroke and load relief at the top of the stroke. The exercise physiology community speculates that this inertia spike plays a major role in increasing bone density in 1-g and, by the same effect, slows the rate that bone density is lost in a zero-g environment.

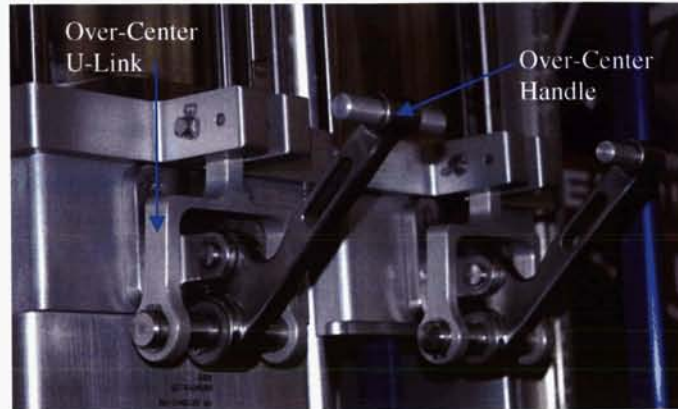


**Figure 10. Picture showing the over-center mechanisms, in the locked position, between the flywheel and cylinder assembly**

The flywheel assembly mounts to one end of the cylinder assembly. It attaches using a hinge and an over-center mechanism (Figure 10). The purpose of this attachment method is to allow for the flywheel mechanism to be engaged and disengaged depending on the exercise and the preference of the user. A U-link (Figure 11) deforms during actuation and allows for the mechanism to go over-center. The design of the U-link was challenging, because it had to elongate by 0.43 mm (0.017 in) and still be under the allowed stress limits. After using the first prototype, it was obvious that the tolerance stack-up between the hinge and the over-center mechanism made a significant difference in the over-center force. In order to better control the over-center force, an eccentric spline bushing (Figure 11) was used in the over-center handle. The hole in the bushing is 0.64 mm (0.025 in) off-set from the center of the bushing. The offset allows for small adjustment of the over-center force.

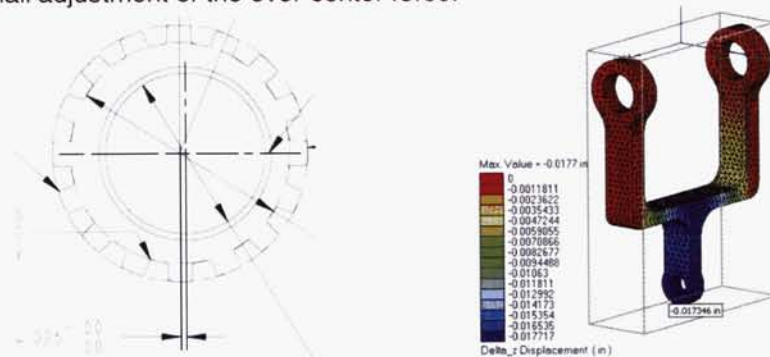


**Figure 11. Detail of spline bushing and displacement analysis of the over-center u-link.**

The heart of the flywheel assembly is a set of three gears and two inertial flywheels (Figure 12). The spur gear meshes with a spur gear rack on the piston rod which makes the motion of the flywheels directly tied to the motion of the cylinders of ARED. The flywheels provide the most load and rotate the fastest at the higher load settings of ARED due to the longer cylinder stroke. This flywheel design uses a fixed gear

ratio and a fixed mass for the flywheels. While this design is simple, it only allows for the inertia to be tuned to one combination of exercise subject mass, exercise subject deceleration, and free weight mass. The ARED flywheels do not account for the changes in the exerciser subject's mass. They do, however, adjust to the exercise subject's deceleration and free weight load. The flywheels add more load into the system at higher load settings, because the piston moves further per stroke, in the same amount of time. Also, a faster deceleration of the exercise subject causes the flywheel to decelerate faster as well. This increases the inertial load felt at the lift bar. In the beginning of the project, the flywheels were tuned to a 227-kgf (500-lbf) squat setting on ARED with a 2 second period and 76.2-cm (30-in) stroke. After ARED is on-orbit for a significant amount of time, the flywheels could be tuned to a more optimal load setting and stroke. This would need to be determined from statistical analysis of the exercise frequency, load, and stroke data from on-orbit use. A chart showing the calculated variation from the true 1-G inertia is below (Figure 13).

The assembly contains one spur gear and two helical gears. The spur gear has a 38-mm (1.5-in) pitch diameter, the large helical gear has a 127-mm (5.0-in) pitch diameter, and the small helical gear has a 38-mm (1.5-in) pitch diameter. The spur gear is made out of 17-4 PH SS and the teeth are also ion nitrided to provide a longer life of the gear teeth and to prevent pitting. The helical gears experience lower loads and are not ion nitrided. The initial prototype of the flywheel assembly used two lubrication methods to determine which would perform better. One gear set employed standard lubrication (Rheolube 2000) while the other had a ceramic dry-film lubrication called Vitro-lube. Our initial life-cycle test showed that standard lubrication was more reliable. Early in our life-cycle test, the Vitro-lube began to flake off significantly. As a result, the team opted to go with standard lubrication.

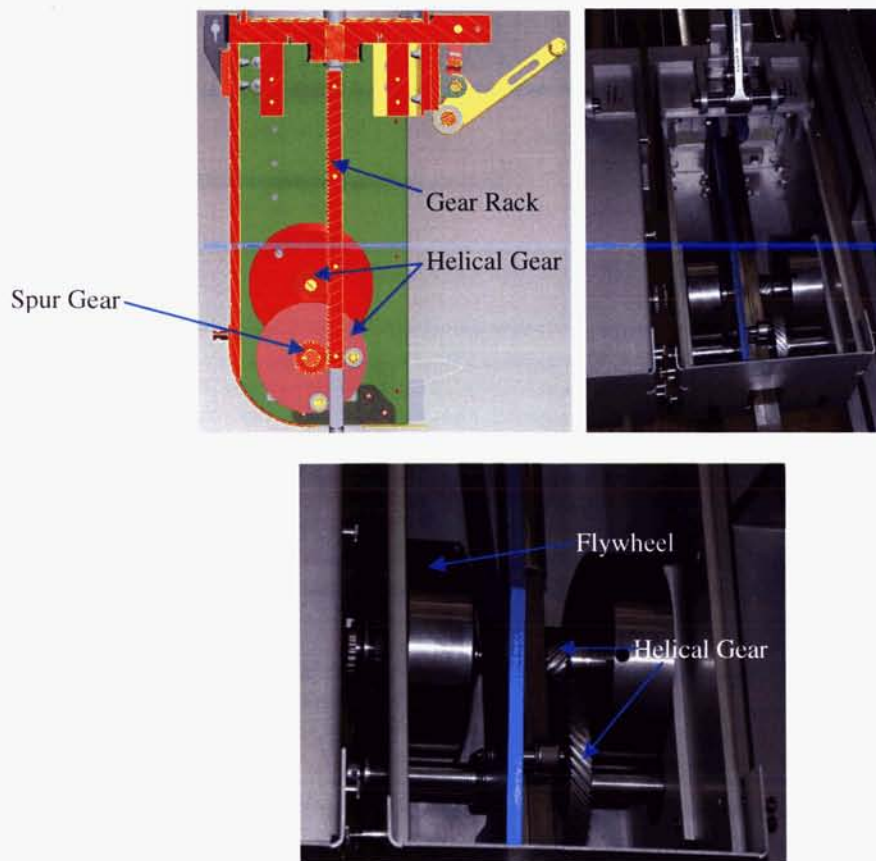


**Figure 12. Flywheel assembly with front cover removed and close up of gears and flywheels.** The spur gear is not visible. A cross-section view through the spur gear teeth is also shown for clarity.



The flywheels are 14 cm (5.5 in) in diameter and 4 cm (1.6 in) thick, stainless steel. As mentioned previously, their inertial properties and the gear ratios were specifically chosen for the 227-kgf (500-lbf) load setting on ARED. The flywheels can see a maximum speed of 800 rpm. Therefore, when the exerciser reaches the bottom of the stroke, and stops the flywheels from spinning, the flywheels could deliver a maximum of 91 kgf (200 lbf) extra at the lift bar. This would occur at the 272-kgf (600-lbf) load setting, 76.2-cm (30-in) stroke, and a 2 second period. It is highly unlikely that anyone will exercise at this load, speed, and stroke. However, these parameters were the maximum range of the project's requirements.

In order to protect the exerciser and the ARED hardware from overloading, the flywheels are directly in line with a friction disk slip-clutch. This slip-clutch is set to slip at 3.39 N•m (30 in•lbf) of torque which is less than 10% more torque than the maximum load described in the previous paragraph. The slip-clutch eliminates concerns of excessive loading being imparted on the device.

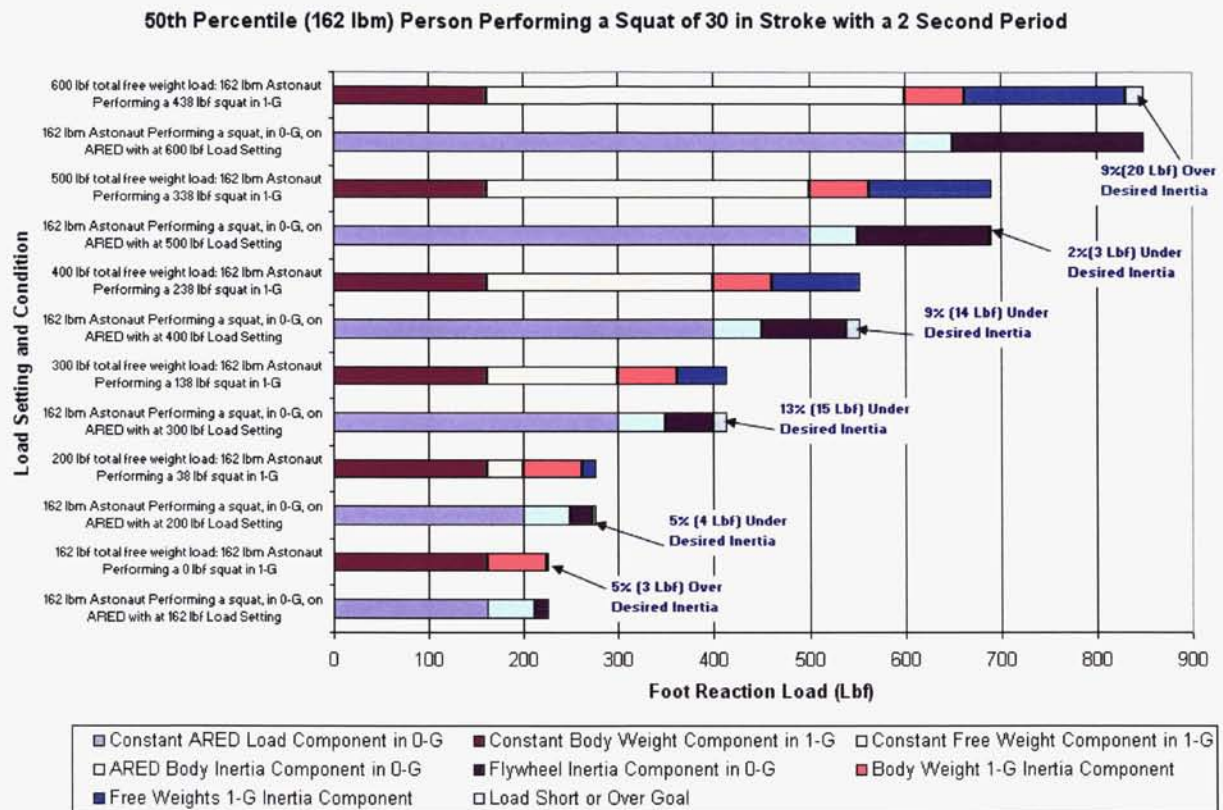


**Figure 13. Chart comparing the load contributions during 1-G free weight squat exercise and squat exercise on ARED in a 0-G environment.** This chart is for a 50<sup>th</sup> percentile astronaut performing a 76.2-cm (30-in) squat with a 2 second period at 45.4-kgf (100-lbf) increments. It shows that the inertial variation between ARED exercise and 1-G exercise is relatively small.

### Design Details – Arm Base Slider

Each cylinder shaft is attached to the arm base slider through a rod-end with a spherical bearing. The slider is attached to a ball screw, in the arm base, with a slider housing (Figure 14Figure 16Figure 17). The ball screw is used to adjust the exercise load of ARED. This is done by changing the moment arm between the pivot point of the arm base and where the cylinders attach. A scale and position indicator is provided on the arm base cover to aid in this load adjustment. The attachment to the ball screw uses a housing/slider design that follows curved tracks (Figure 17) on the sides of the arm base with cam rollers.



The track is curved to minimize force non-linearity as a function of load adjustment. The slider moves up and down inside the housing, which is attached to the ball screw, as the slider follows the tracks (Figure 17).

The life cycle design requirement for ARED is 15 years. A preliminary test was run on an engineering unit of the arm base and cylinders at various load settings. During this test, at a 181-kgf (400-lbf) load setting, the slider housing broke into 2 pieces (Figure 15) at 318,000 total cycles. After close evaluation, it was determined that the stress analysis overlooked a critical load case. There was more moment on the housing than first calculated and a fatigue analysis had not been done. As a result of the improved analysis, the slider housing was thickened and strengthened with closeout plates. The original housing was made of 7075 Al with a TufraM surface coating to increase surface hardness, extend wear, and reduce friction. During the test, the slider did not slide very well along the TufraM surface. As a result, rollers were also added to the slider design to reduce friction and to implement a zero clearance fit between the slider and housing. With the new rollers added to the slider, steel wear plates had to be added to the inside of the slider housing (Figure 16), to increase the life of the assembly.

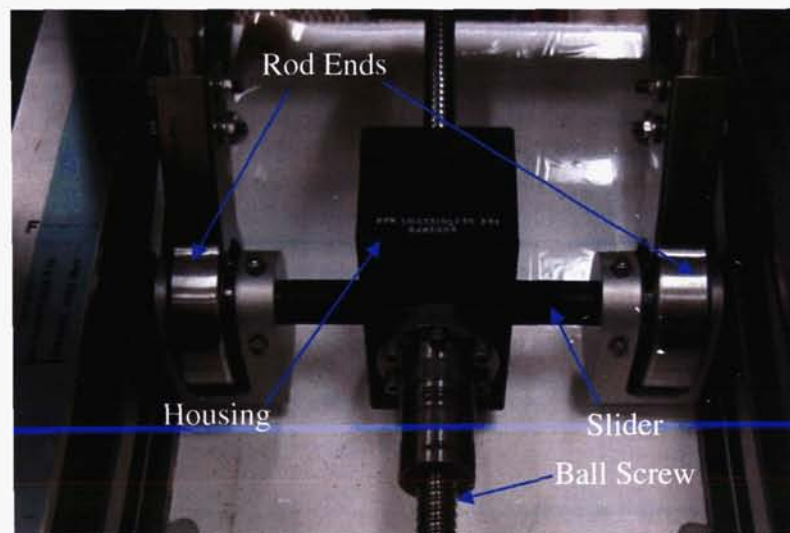


**Figure 14. Old Slider/Housing Design for Arm Base**

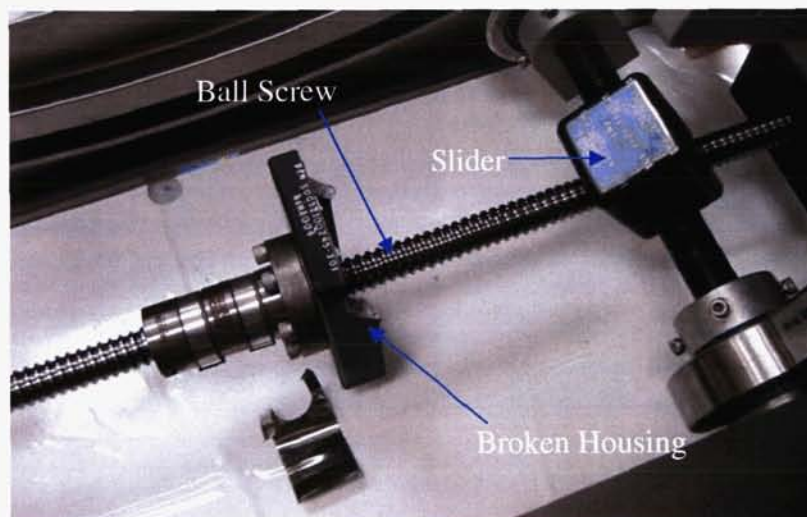


**Figure 15. Old Slider/Housing design during life cycle test showing broken Housing**



**Figure 16. New Slider/Housing Design showing slider w/ rollers and Housing wear plates**

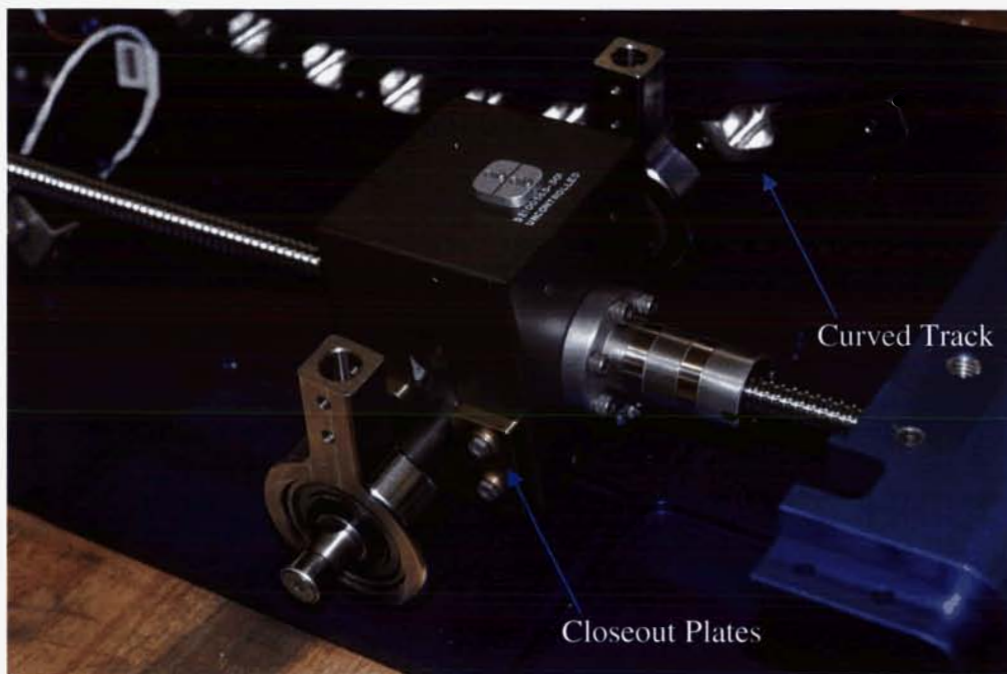


**Figure 17. New Slider/Housing design attached to ball screw showing closeout plates**

The team also performed an engineering life cycle test on the arm base/load adjustment components. This test rotated the ball screw and drove the rod ends back and forth along the length of the arm base. The purpose of this test was to prove the critical components in the arm base assembly. This test was a success and cycled the ball screw for 33,000 m (1.3 million in) of travel, before failure. Assuming a six person ISS crew and various uncertainty factors, this would be enough ballscrew life to last for ~14 years

on-orbit. According to Nook, the manufacturer of the ball screw, the failure was a classical fatigue failure of a ball screw and ball nut assembly.

### **Testing – Development**

As has been discussed, ARED is well into the testing phase of the project. Below is a summary of ARED's testing program.

#### Preliminary Life Cycle Units

Two life cycle test rigs were built. Rig 1 was intended to exercise the cylinder/flywheel, the main arm, the arm base, and the pivot arm. Rig 2 was intended to exercise the ball screw and the arm base slider housing. Rig 1 was used to evaluate different design parameters, especially in the piston/cylinder interface. At the end of development phase, rig 1 has accumulated 320,000 cycles. Rig 2, as mentioned in the previous section, produced 1.3 M inches on travel on the ball screw. Both Rig 1 and Rig 2 will be modified and upgraded to serve as the qualification lifecycle test beds.

#### Hi-Fidelity Engineering Unit

Lessons learned from testing on Rig 1 and Rig 2 were incorporated into the design. To further increase confidence in the design, a Hi-Fidelity Engineering Unit was constructed, using near-flight-quality drawings. This Hi-Fidelity Engineering Unit was used for Man-In-The-Loop testing, with the intent of evaluating human-machine interface issues and ergonomic issues. Over a period of five months, forty-three human subjects performed 700 workout sessions on this unit, accumulating over 150,000 cycles. The unit was also used extensively by the team to evaluate various design modifications as well as to develop operational and maintenance procedures. In addition, astronauts with long-duration spaceflight experience on both Shuttle and ISS were invited to exercise on ARED to identify issues unique to zero-gravity such as the location of handrails and foot restraints.

### **Certification of Flight and Qualification Units**

Having established high confidence through development testing on Rig 1 and Rig 2 and the Hi-Fidelity Engineering Unit, production of three flight-quality ARED units are underway and should be nearing completion at the time of this symposium. One unit (Dash 301) will be designated for delivery to the International Space Station, the second unit (Dash 302) will serve as the Lifecycle Qualification Unit, and the last unit (Dash 303) will be the General Qualification Unit.

The ARED Qualification and Acceptance Test Plan stipulates that each of ARED's components must be subjected to an Acceptance Vibration Test (AVT). This test is intended to be a workmanship screen. The Flight Unit, Dash 301 will then undergo a series of functional tests and packaged for launch. Dash 302, after a series of functional tests, will be installed on Rig 1 and Rig 2 and undergo continuous lifecycle testing. Current requirements state that ARED must successfully complete 1.5 M cycles on the ground in order to qualify the Flight unit for one year of on-orbit usage (6 crew members, exercising 1.5 hours per day, and 6 days per week). Results from lifecycle testing on Dash 302 will be used to determine maintenance and re-supply plan for the on-orbit Flight Unit. Dash 303, will be subjected to a launch vibration test (QVT) and an acoustic emission test. In between these tests, Dash 303 will undergo a series of functional tests.

At the conclusion of the Qualification and Acceptance Test Program, Dash 303, along with the Hi-Fidelity Engineering Unit, will become crew training units and/or research test beds for ground-based physiological studies.



## **Conclusion**

The most important lesson that the team has learned in the course of the ARED project is that prototyping and development testing is paramount and indispensable for developing a robust, reliable, complex mechanical system. Good initial designs are important as well, but nothing can replace developmental testing as a means to flush out design, manufacturing, assembly, and human-machine issues. Although not popular, a prototype-centric development phase, in advance of flight production, will result in fewer design problems, fewer modifications, fewer design iterations and, in the long run, decreases cost and schedule. As a result of ARED's extensive prototyping and testing, both in the developmental phase and the certification phase, the team is extremely confident that ARED will perform well on the International Space Station and provide years of effective resistive exercise for the crew. Furthermore, as NASA prepares to implement the President's Exploration Initiatives, ARED's technology will be mature and proven in time to support long-duration expedition to the Moon and Mars.

# Radarsat Range Adjustment Mechanism Design

Xilin Zhang\* and Sylvain Riendeau\*

## Abstract

RADARSAT (Figure 1) is a series of sophisticated earth observation satellites developed by Canada to monitor environmental changes and the planet's natural resources. RADARSAT also provides useful information to both commercial and scientific users in the fields of agriculture, cartography, hydrology, forestry, oceanography, ice studies, and coastal monitoring.

At the heart of each RADARSAT satellite, there is an advanced Synthetic Aperture Radar (SAR) payload. The SAR antenna is a 15-meter-long microwave instrument that sends pulsed signals to Earth and processes the received reflected pulses. Its on-ground test fixture has high-resolution alignment requirements. It is a challenge to any mechanical designer. The Radarsat-1 test fixture included an 18-meter-long near field range scanner, an offloaded 6 degrees-of-freedom fine adjustment system to handle and maneuver the 15-meter-long SAR antenna, an automatic closed-loop motor-driven adjustment system, and a 15-meter-long coarse adjustment table. A large R & D effort was required throughout the design, fabrication and final calibration of the equipment to ensure final success. Lessons learned from the RADARSAT-1 range alignment fixture paved the road for the RADARSAT-2 system. This type of 6 degrees-of-freedom adjustment mechanism could be very useful to all kinds of large space structures for on-ground alignment and test like solar arrays, antenna panels, etc. This paper covers the 6 degrees-of-freedom mechanism design, development, fabrication and offloading calibration method. The lessons learned during design, fabrication as well as integration and calibration are extremely useful to avoid future problems for all mechanism designers.

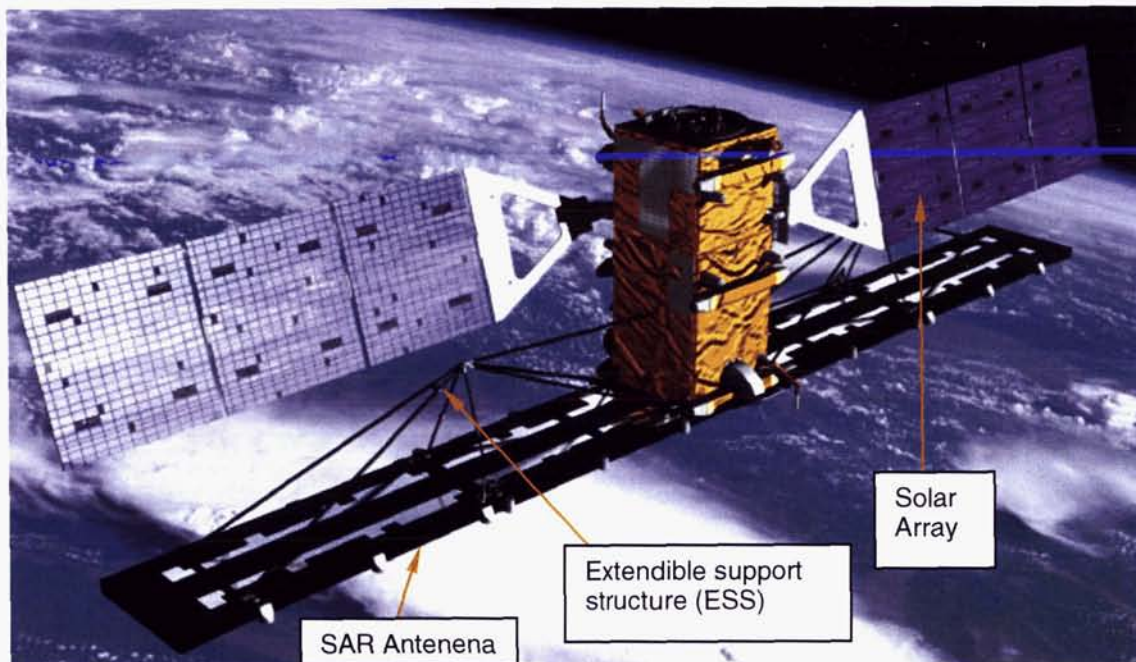


**Figure 1. RADARSAT-2  
Radarsat Mission Introduction**

\* MDA Space, Inc., Ste-Anne-De-Bellevue, Canada

Being the second largest country in the world, with a variety of landscapes and climatic conditions, Canada recognized the practical and economic benefits of using space for Earth observation early on. With global environmental monitoring and protection being a worldwide concern, Earth observation is a key priority of the Canadian Space Program, and RADARSAT was developed as Canada's flagship to pursue this priority. It is a Canadian-led project involving the Canadian federal government, the Canadian provinces, and the private sector. It provides useful information to both commercial and scientific users in such fields as disaster management, interferometry, agriculture, cartography, hydrology, forestry, oceanography, ice studies and coastal monitoring. Radarsat-2 capabilities are shown in Figure 2.

RADARSAT-1 is a sophisticated Earth observation (EO) satellite. Launched in November 1995, it provides Canada and the world with an operational radar satellite system capable of timely delivery of large amounts of data. Equipped with a powerful Synthetic Aperture Radar (SAR) instrument, it acquires images of the Earth day or night, in all weather and through cloud cover, smoke and haze.

RADARSAT-1 has proven to be an invaluable source of Earth observation data. The satellite's images are used internationally to manage and monitor the Earth's resources and to monitor global climate change, as well as in many other commercial and scientific applications. RADARSAT-1 is ideally suited to support these tasks, thanks to its right and left looking modes, wide range of beams, SAR technology, frequent revisit periods, high-quality products and fast, efficient delivery. In November 2005, Radarsat 1 celebrated its 10th anniversary and is still functioning very well in orbit.

Representing a significant evolution from RADARSAT-1, RADARSAT-2 will be the first commercial SAR satellite to offer multi-polarization - an important tool increasingly used to identify a wide variety of surface features and targets. As prime contractor for RADARSAT-2, MDA will develop, build, integrate and launch RADARSAT-2. Once operational, RADARSAT-2 will be wholly owned and operated by MDA.

To be launched in 2006, RADARSAT-2 will be lighter, cheaper, more capable, and will ensure data continuity well into the new millennium. Its enhanced capabilities include additional beam modes, higher resolutions, multi-polarization, more frequent revisits, and an increased downlink margin enabling reception of data from lower-cost receiving antenna systems.

RADARSAT-2 will carry a C-band remote sensing radar with a ground resolution ranging from a mere 3 to 100 meters. Other key features of RADARSAT-2 include the ability to select all beam modes in both left and right looking modes, high downlink power, secure data and telemetry, solid-state recorders, an on-board GPS receiver and the use of a high-precision attitude control system. Fully flexible polarization options and the ability to acquire images to the left and right of the satellite will double the accessibility swath. The three-meter resolution data generated by RADARSAT-2 will be the highest-resolution commercially available SAR data, offering enhanced detection of closely spaced objects, as well as enhanced definition of other objects.

At the heart of each RADARSAT satellite, there is an advanced Synthetic Aperture Radar (SAR) payload. The SAR antenna is a 15-meter-long microwave instrument that sends pulsed signals to Earth and amplifies the received reflected pulses. Its on-ground test fixture has high-resolution alignment requirements. The design of the required Mechanical Ground Support Equipment (MGSE) is a challenge for any mechanism engineer.

### **SAR Range Test Setup and Adjustment Mechanism Background**

The sophisticated SAR RF system requires a high-resolution adjustment mechanism for the range test setup. The four panels must be properly aligned to meet the stringent electrical performance requirements and to allow for the proper installation of the expendable support structure. The basic Mechanical Ground Support Equipment requirements for the range test are listed below:



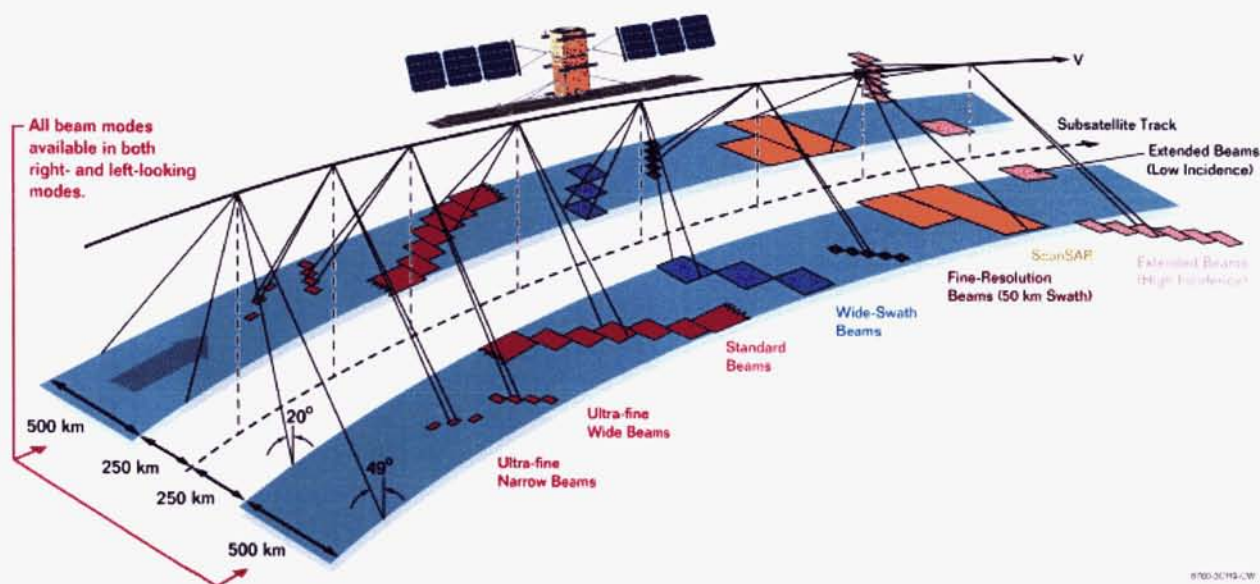


**Figure 2. Radarsat 2 Capabilities**

1. The front radiating surface flatness of SAR 15-meter-long 1.5-meter-wide panel shall be within 0.7 mm (0.028 in) to meet the fine resolution RF requirement.
2. The front surface flatness of SAR shall be adjustable in 6 degrees-of-freedom.  $\pm 12.7$  mm (0.5 in) translation in all X, Y, Z directions.  $0.35^\circ$  of rotation around X, Y, Z axes to optimize the RF performance.
3. After RF optimization, the SAR panel's positions are defined. The positions shall be able to be locked in position to allow ESS installation.
4. A heavy-duty working platform is required to locate SAR at the center of the scanner plan to allow a 1.5-meter over-scan all around the SAR.
5. SAR shall be able to move 700 mm in and out from the range scanner probe to enable the RF engineer to optimize the test distance.
6. Range Adjustment Mechanism shall allow full access for ESS, Spacecraft Y panel assembly and dummy sidewall installation after RF performance to be optimized.
7. Range platform shall be able to allow a minimum of 10 operators to be on the platform and to work at the same time.

The range test setup design (Figure 3) includes the following major MGSE assemblies to meet the above requirements:

1. 18 m x 6 m near field scanner to perform all required RF tests.
2. A range platform with 700-mm travel in and out from the scanner probe. It enables RF test engineers to optimize the SAR panels to probe distance.
3. Four support trusses and a steel structure foundation are made to support the SAR panels' test setup at the center of the scanner.
4. Dummy spacecraft sidewalls for ESS integration as well as a Y panel support to bring all necessary payload electronics up for the range test.

5. A 6 degrees-of-freedom adjustment mechanism to allow SAR panels to be located according to their designed positions on range and to optimize the RF performance.

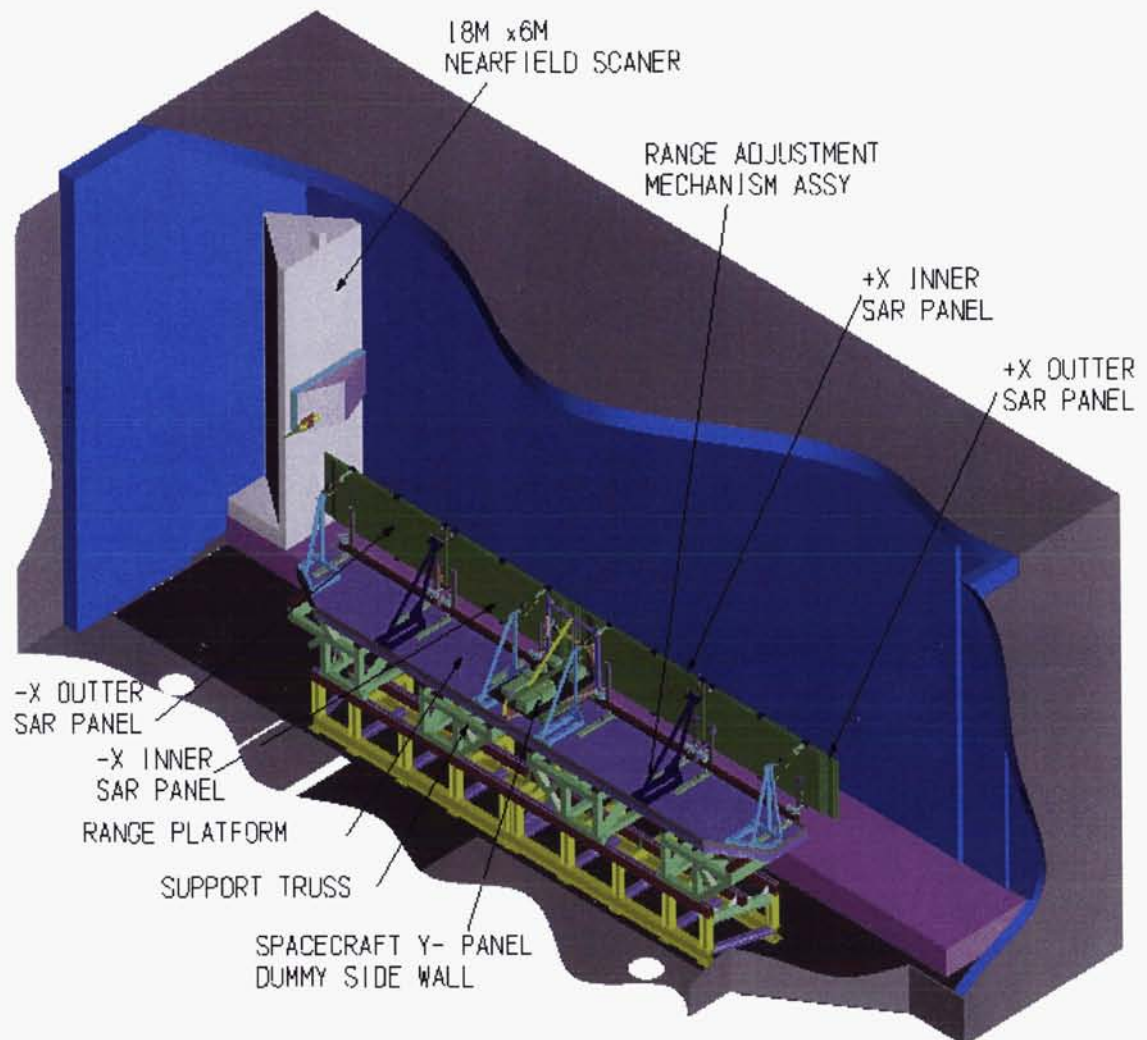


**Figure 3. Complete SAR Panel's Range Test Setup**

This paper will concentrate on the 6 degrees-of-freedom mechanism design, development, fabrication and offloading calibration method.

During the design, the fabrication, the final integration and the calibration phase, many problems occurred. The lessons learned are extremely useful to any mechanism and MGSE designer to avoid future problems.

### **SAR Range Adjustment Mechanism Design**

The SAR antenna is made of four SAR panels (+X inner and outer panels and -X inner and outer panels). Four separate panels are required to stow the antenna in the launch configuration. The extendible support structure will deploy the SAR Panels and hold them in position in orbit. During the range test, the antenna was held in position in the deployed configuration by four sets of identical/mirror-imaged mechanisms. Those mechanisms are used to adjust each panel in the required position and then hold them in place. The mechanism working principles were sketched out during the preliminary design phase. Eight different design proposals were studied, each one coming from a different design approach. A trade off analysis was performed and the Preliminary Design Review approved the principle shown in Figure 4 and detailed



below. Each set of the adjustment mechanisms has an X-direction mechanism, a Y-direction mechanism and a Z-direction mechanism. The Z mechanisms are installed directly on the range platform. The X mechanisms are seated on two Thomson linear slides. A Thomson linear shaft connects each X mechanism to a Z mechanism through two ball joints. The Y mechanism consists of two Thomson linear bearings. The linear motors/micrometers are installed on the mechanisms in every direction.

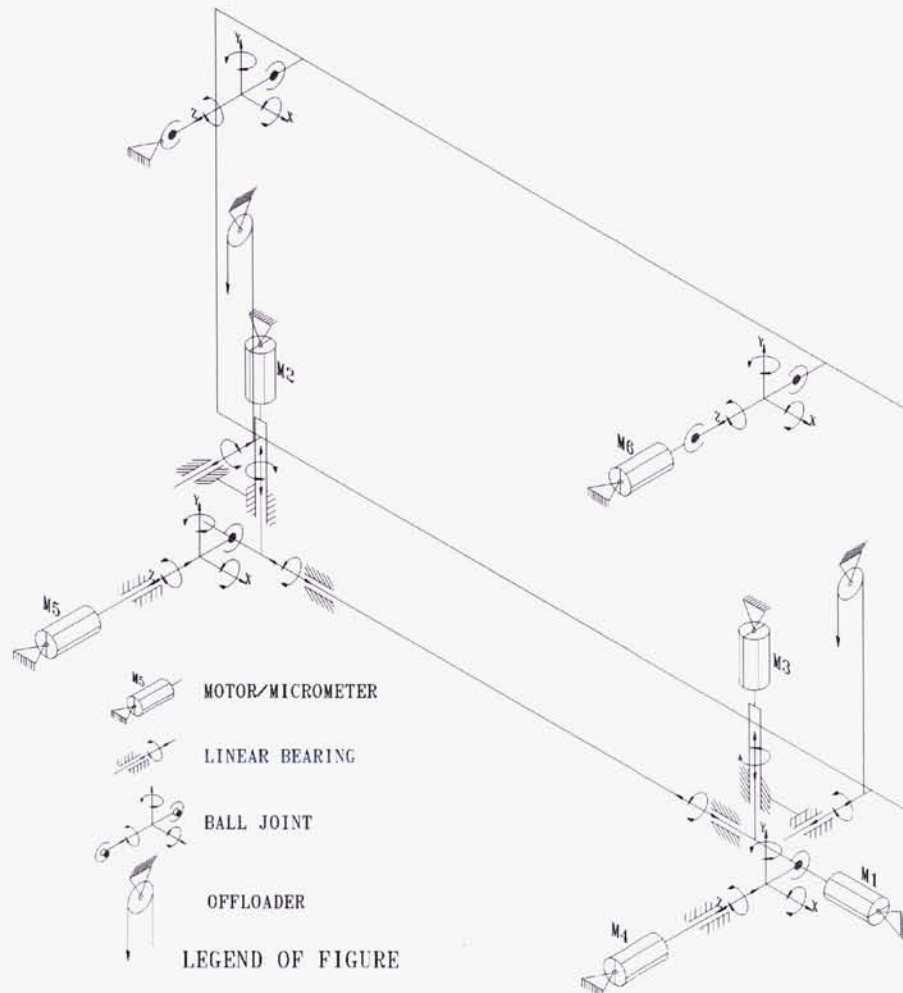


**Figure 4 SAR Range Adjustment Mechanism Design Principle**

The panel linear translations in X, Y, Z directions are very simple. The two linear motors/micrometers in the same axis need to be driven in a synchronized fashion. The rotations are achieved by driving the two motors/micrometers on the same axis for a different distance or direction. For a simple example, when the linear motors/micrometers M2 and M3 are driven in a different direction, the panel will rotate around the Z axis. If both a translation in the Y direction and a rotation around the Z axis are required, the linear actuators M2 and M3 can be driven in the same direction but for a different distance. The panel will move up or down and rotate around the Z axis.

During all the adjustment operations, the SAR panel is connected to the adjustment mechanism by three corners; the fourth corner (upper left in Figure 4) will be a safety-locking device. During the adjustment process, it has to be completely loose to give the panel the 6 degrees-of- freedom. Once the panel is in the required position, the fourth corner is locked in place with the safety-locking device.

Once the design principles are clear, many fine details have to be carefully looked at. For example, the safety issues for the operators working around the Range Fixture, the flight hardware protection, etc. The



MGSE requirements 3 through 7 mentioned earlier are addressed by other generic mechanisms. Their interaction with the 6 degrees-of-freedom adjustment mechanism needs to be carefully looked at during the detailed design phase. The final design of the 6 degrees-of-freedom adjustment mechanism is shown in Figure 5.

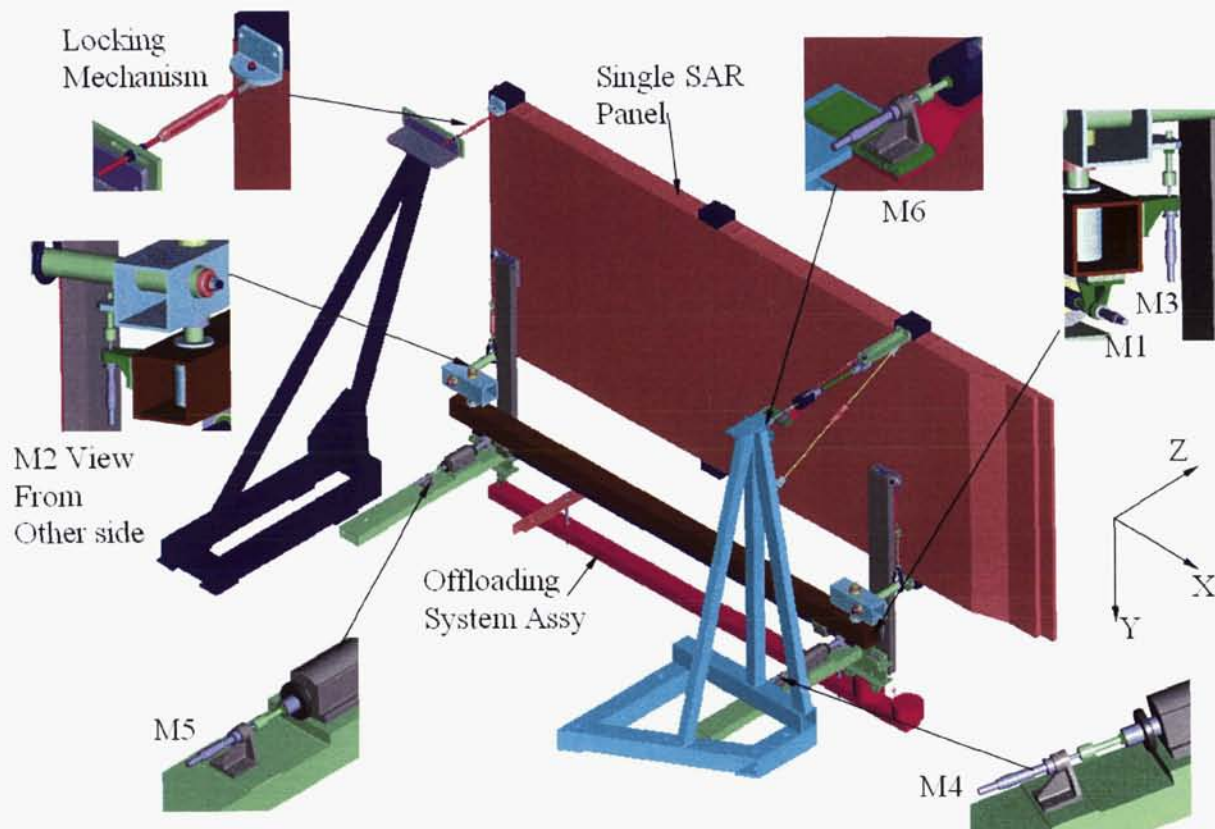


**Figure 5. Single SAR Panel Range Adjustment Mechanism**

Figure 5, extracted from the CAD model, only shows the +X outer panel range adjustment mechanism. The -X inner panel mechanism is a duplicate of this design and the other two sets of mechanisms (-X outer panel and +X inner panel) are mirror images.

#### **SAR Range Adjustment Mechanism Motor-Driven Software**

For Radarsat-1, the linear motors, with 8.2-kg (18-lb) maximum capacity and their control system are selected early in the program. Each SAR antenna panel adjustment mechanism is driven by 6 linear motors M1 – M6. The motor execution program controls the mechanism motors and give the 6-degrees-of-freedom adjustment to the antenna panels.

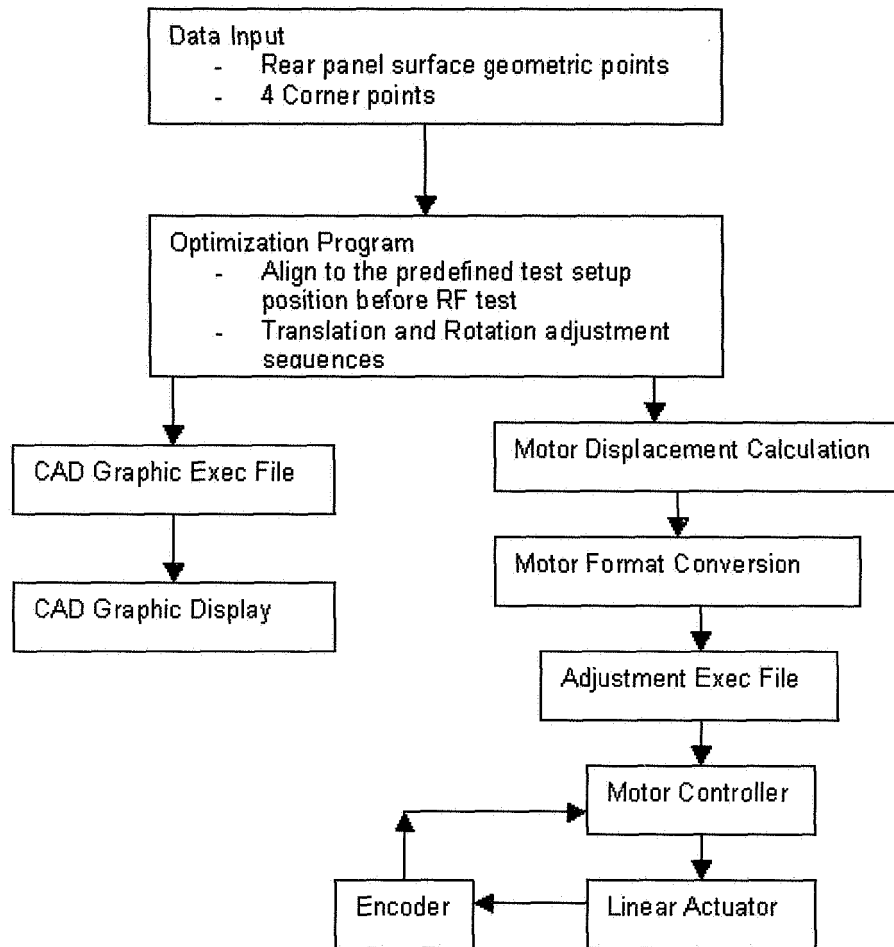


**Figure 6. Panel Adjustment Software Block Diagram**

This system is used to align the panel in the plan parallel to the scanner plan or to adjust the panels to any pre-defined test position. Also, the discrete manual input to the motion control program can drive the panel during RF testing to the optimum RF locations for each panel. This special software was developed for this specific application. The panel adjustment software block diagram is shown in Figure 6 [1] and is followed by a detailed description of the main modules.

**Data input:** Panel surface points, panel four corners points and pre-defined set up position.

**Optimization:** Determine the best-fit antenna plane.

**Adjustment sequence and actuator displacement calculation:** Calculate each of the required motor displacements from the adjustment sequence.

**CAD output:** Display the adjustment sequence on CAD screen.

**Linear motors format conversion:** Convert the required distance travel to the appropriate linear actuators format in number of encoder counts. Assign the appropriate speed to the synchronized motion.

Motor/micrometer movement to achieve translation in X, Y, Z axes direction and rotation around X, Y, Z axes are listed in Table 1. For Radarsat-1, once the SAR panel is installed on the range, the first set of panel position data was taken and the data inputted in-to the program. The software calculates the movement distance of each motor required to drive the panel in the designed position.

**Table 1. Six Degrees-Of-Freedom Linear Motor/Micrometer Adjustment**

<i>Micrometer</i>	<i>M1</i>	<i>M2</i>	<i>M3</i>	<i>M4</i>	<i>M5</i>	<i>M6</i>
<b>Translation X</b>	+ or -					*1
<b>Translation Y</b>		+ or -	+ or -			*1
<b>Translation Z</b>				+ or -	+ or -	+ or -
<b>Rotation <math>\theta_x</math></b>				+ or -	+ or -	-or +
<b>Rotation <math>\theta_y</math></b>				+ or -	- or +	+ or -
<b>Rotation <math>\theta_z</math></b>		+ or -	- or +			*1

\*1. Small adjustment might be required, but it is not the same distance as the others.

### **System Calibration and Verification**

Most large MGSE designers typically specify a pre-calibration activity to verify the system design and manufacturing before using it with flight hardware. Nobody wants to see expensive flight hardware hanging in the air waiting to be installed on a MGSE that doesn't work. To avoid surprises during the flight hardware final installation phase, a mass dummy with flight mass, CG and flight representative interfaces is designed and fabricated specifically for the calibration and verification.

The Radarsat-1 range fixture calibration went through many troubleshooting exercises; some of the problems will be discussed in the lessons-learned section. All encountered problems were resolved during the Radarsat-1 calibration and made the final integration a clean and problem free operation. These experiences paved the road for the Radarsat-2 range fixture design and calibration.

For Radarsat-2, a new mass dummy was designed. It can be calibrated to represent all four Radarsat 2 panels. Weight location and calibration hoisting points are designed to be adjustable to meet all 4 different panels' CG and mass. All linear motor/micrometer loadings are finally balanced to less than 5.5 kg (12 lb). The Radarsat-2 mass dummy calibration is shown in Figure 7.

During the calibration, each panel location was positioned relative to the others using the NFR 3-axes scanner in order to meet the design requirements. To calibrate the position of each panel, an X, Y, Z mechanical block was installed at the center of the platform as the original point. The travel of the scanner is used with a dial gage, which is installed on the near field scanner probe to precisely measure the position of each measurement point. The final calibration got the dummy panels within 0.38 mm (0.015 in) of their as-designed position. This simplifies the final SAR panel range set up installation and alignment processes.





**Figure 7. Using Mass Dummy to Pre-Calibrate the Design Setup**

#### **SAR Panel Final Range Alignment Result [2]**

The four flight SAR panels were installed on the near field range adjustment mechanism. They were positioned relative to each other and relative to the scanning plane using the NFR 3-axes. In order to facilitate the positioning of the 4 SAR panels in a later stage of integration, 16 alignment-aid interface points per SAR panel were machined on their back face. Laser tracker measurement equipment was used to determine the position of these points relative to a reference coordinate system.

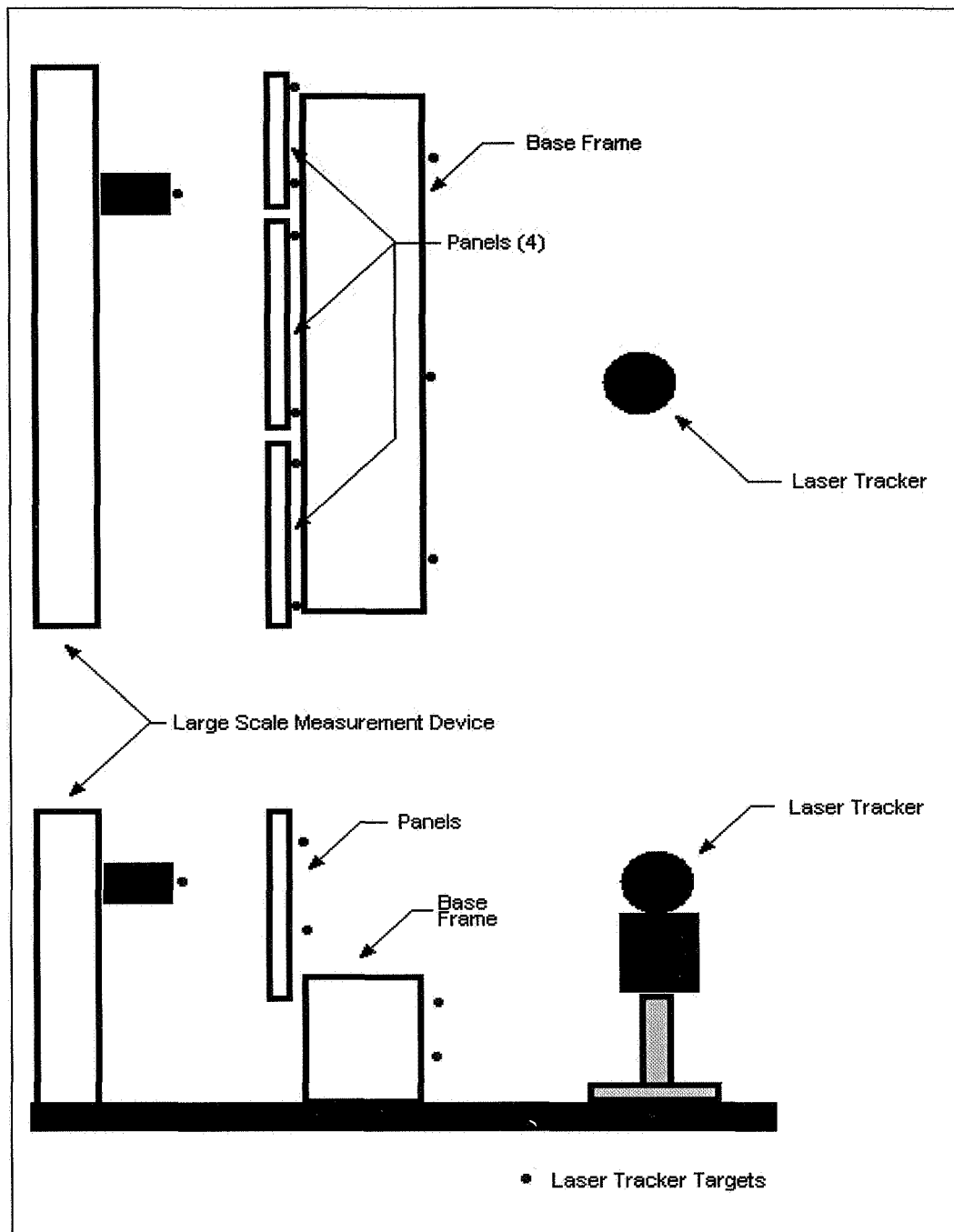


**Figure 8. SAR Panel Location Measurement Setup**

The line of sight to these points in the test range is limited due to mechanisms and guardrails in the back of the panels. Different set-ups were required. Figure 8 shows a typical set-up schematic.

The measured point positions were finally given in the mechanical build (mb) coordinate system that was predefined. Repeatability of the measurement was verified and the error from nominal position was calculated. The final Laser tracker measurement results of the three-dimensional positional errors are listed in Table 2. The error is defined as the difference between nominal and measured positions. The maximum error calculated is 0.61 mm (0.024 inch) in the X direction. The compound error is attributed to the tolerance of machining and assembly, the relative position of each panel to the reference frame and the measurement set-up accuracy.

**Table 2. Panel Measurement Point Location Error (in thousandths)**

error on location	-Xouter			-Xinner			+Xinner			+Xouter		
	dx	dy	dz	dx	dy	dz	dx	dy	dz	dx	dy	dz
P1	20	-4	-9	18	5	-2	-2	0	4	-24	5	-9
P2	12	-2	-10	10	-4	-6	-2	-3	4			
P3	13	-4	-9	15	-3	2	-4	-4	-1			
P4	18	-6	-8	18	-9	3	-5	12	-3	-17	-15	3
P5	11	-1	-6	22	2	17	-9	2	3	-24	-7	-4
P6	8	0	-11							-17	-10	-3
P7	9	-5	-8							-12	-8	4
P8	3	0	-1	18	-5	13	-8	8	-1	-20	-19	18
P9	5	-2	-11	22	9	16	-15	2	0	-21	-5	-1
P10	-2	3	-3	12	3	5	-11	3	-6	-17	-11	-6
P11	2	-7	-11	10	-1	-1	-13	-2	-7	-14	-10	0
P12	0	4	0	17	-5	0	-15	20	-4	-10	-6	6
P13	0	-9	-16	28	2	3	-1	-16	8			
P14	-4	-4	-8	27	-3	-8	-20	10	-7	-19	-12	-19
P15	-1	-9	-4	29	-14	-13	-22	-4	-9	-19	-17	-14
P16	-5	-2	3	22	4	-17	-21	10	-8	-18	-17	-7

### Lessons Learned

#### Lessons Learned 1

Linear motors with a computer software auto-adjustment system offer a nice system to have if there are several hundred panels to be adjusted, aligned and tested. They can significantly reduce the labor costs (on mass production). For single SAR requirements, it is not cost effective. For Radarsat-1, the problems with the motors, driving system and software, as well as all related troubleshooting. It became the major cost for the overall Range Fixture.

For RADARSAT-2, MDA decided to replace the system with a set of 6 (total 24) high-resolution manual micrometers, a dial gage 0,0,0 reading system and somebody on the floor with a good calculator. Good results were achieved at a fraction of the price.

#### Lessons Learned 2

Offloading point selection is critical to get ideal 0 g and *linear sliding bearing moment free* conditions. The RADARSAT-1 range fixture offloading point was first designed to be at the center of the X-direction slides with a constant-force spring offloading system. It completely failed. The 8.2-kg (18-lb) loading capacity motor can not drive the panel to move up and down at all because of the internal friction of the constant force spring and the large moment generated by the panel weight. The offloading point was finally moved as close as possible to the panel CG and a balanced-weight system was used. The moment on the sliding bearing was then removed. Before the motor installation, the moving force required to drive the panels up and down were calibrated to between 5.5 kg and 7.5 kg. The analysis shown in Figure 9 gives suggestions for offloading point selection.



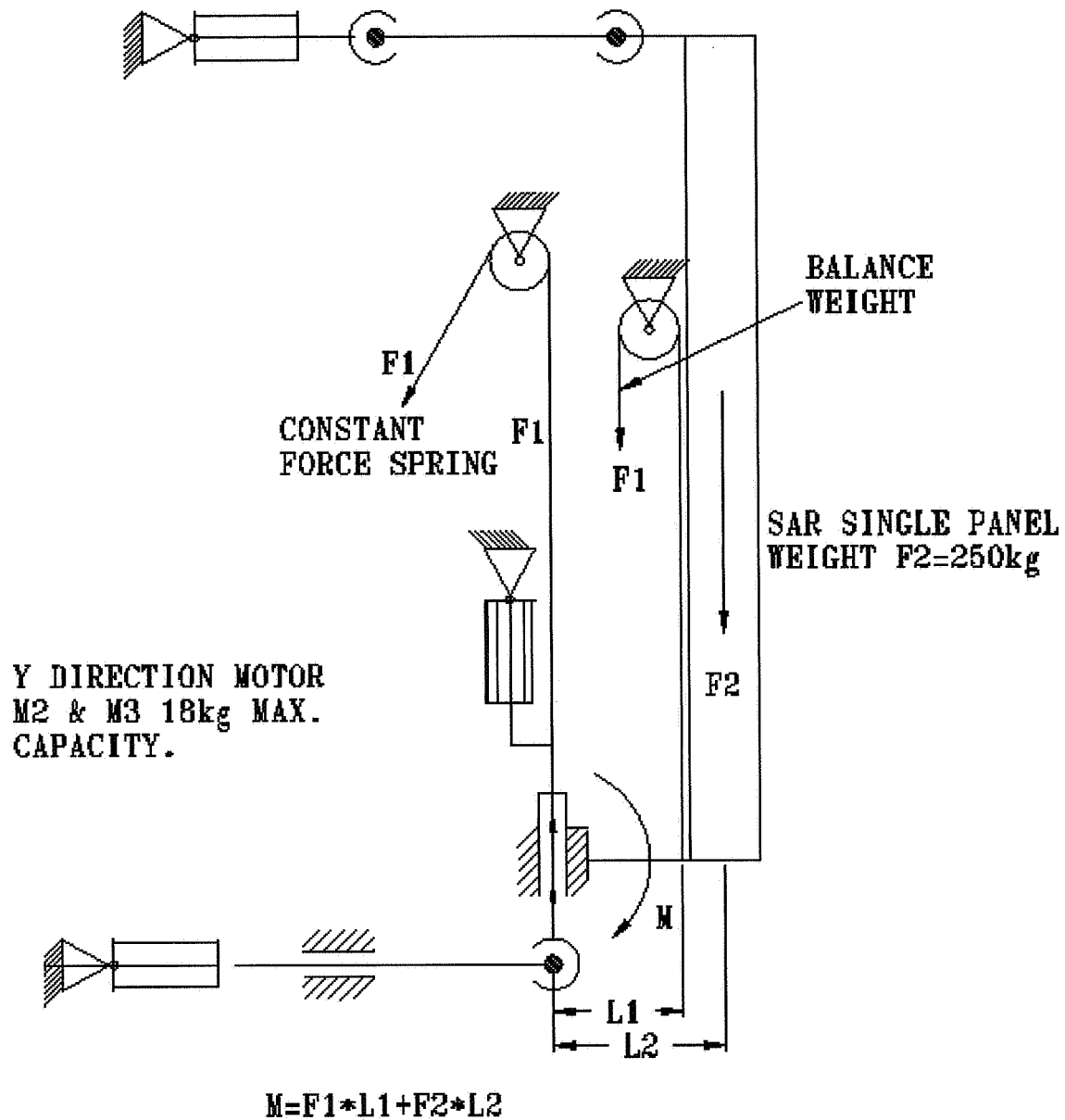


**Figure 9. Offloading Point Selection and Incorrect Offloading Point.**

From above Figure 9, one can see that with balanced panel conditions:

$$\Sigma M = 0$$

The moment M on the Y bearing shall be:

$$M = F1 * L1 + F2 * L2$$

The Radarsat-1 constant force offloading line went through Y bearing

$$L1 = 0$$

$$M = F2 * L2$$

Moment  $M$  applied to the sliding bearing significantly increased the friction. It is required to balance the moment to 0 in order to make the selected 8.2-kg loading capacity motors work for this mechanism. Following the modifications, the balanced-weight loading point was moved as close as possible to the panel CG to remove the moment from the bearing. Then, the panel can be easily driven up and down within the motor's loading capacity.

### Lessons Learned 3

The constant-force spring offloading system is not ideal for small-driving capability actuator systems because the internal friction inside the constant-force spring is significant. For the 250-kg offloading system used for Radarsat-1, the best results obtained during the calibration was a force between 28 kg and 30 kg required to move the panel up and down. It significantly exceeded the specified motor maximum capacity.

### **Conclusions**

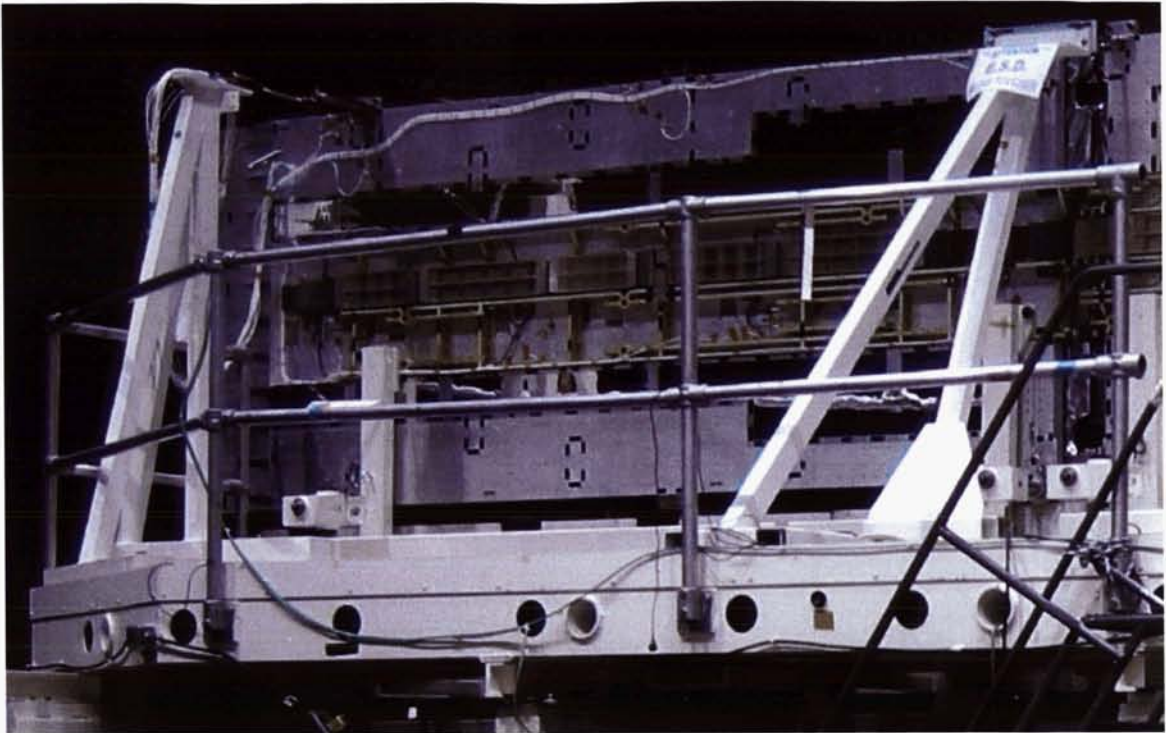
The 6-degrees-of-freedom Range Adjustment Mechanism principle was successfully used for Radarsat-1 and -2. The basic principle was debugged and improved from Radarsat-1 and successfully re-used for Radarsat-2. The mechanism is very cost effective and provides good adjustment and alignment results. The Radarsat-1 launched in 1995 for a 5 years design mission life has just celebrated its 10th anniversary and is still working very well in orbit. Radarsat-2 SAR panels were delivered to David Florida Laboratory in Ottawa for final integration and will be launched in 2006. This basic principle of the 6-degrees-of-freedom adjustment mechanism can be widely used for any on-ground large flight structure alignment and test. Offloading methods for this mechanism were presented along with the calibration of the system using a mass dummy to represent the flight hardware. Picture 1 shows the -X outer panel during the range test and Picture 2 shows the SAR system final range test.

### **Acknowledgements**

The authors would like to thank their retired colleague Alex Csaki for his technical advice through out the project. Thanks also go to Nathalie Hadida and Catherine Yi Zhang for their sincere effort in editing this paper.

### **References**

1. Derek Louie "Panel Alignment software – SAR antenna" MDA SPACE/ SPAR 823870 (Feb.1992) 6-8.
2. Erick Charbonneau "Project 6018N Radarsat-2 4-SAPA alignment report, Technical Report RML 009-2005-155.



Picture 1. SAR -X Outer Panel Range Test Setup



Picture 2. SAR Range Test Setup



# Come-Along Tool Development for Telerobotic In-Space Servicing of the Hubble Space Telescope

Jonathan Penn\*

## Abstract

The Come-Along Tool was created for the Hubble Space Telescope (HST) Robotic Servicing and De-Orbit Mission (HRSDM). During the mission, an unmanned spacecraft rendezvous with the HST and deploys a robotic arm, which manipulates the Come-Along and other robotic tools to perform servicing operations originally intended for astronauts. Developed at Goddard Space Flight Center (GSFC), the Come-Along Tool overcomes a difficult set of obstacles to open and close the HST Aft Shroud Doors by accomplishing tasks in separate robotically feasible steps. The final design incorporates lessons in functionality, operator visibility, mechanism reliability, and design for ease of robotic operation pertinent to telerobotic tool development for future missions.

## Introduction

Beginning in 1993, NASA has conducted a series of four highly successful astronaut missions to service and repair the HST, however, after the loss of the Columbia Shuttle in 2003, the next shuttle mission to deliver critical repairs to the HST was deemed unsafe for astronauts and canceled. It was at this point that the HST Program Office at GSFC, commenced developing the HRSDM, creating a unique opportunity to develop telerobotic technology. In order to replace the HST's ailing gyroscopes and batteries and add more powerful science instruments, robots would be used to eliminate the risk to human life. The HRSDM makes use of a Dexterous Robot to manipulate various robotic tools to make repairs and improvements to the HST. Operation is termed 'tele'-robotic because ground operators command the robot using telemetry.

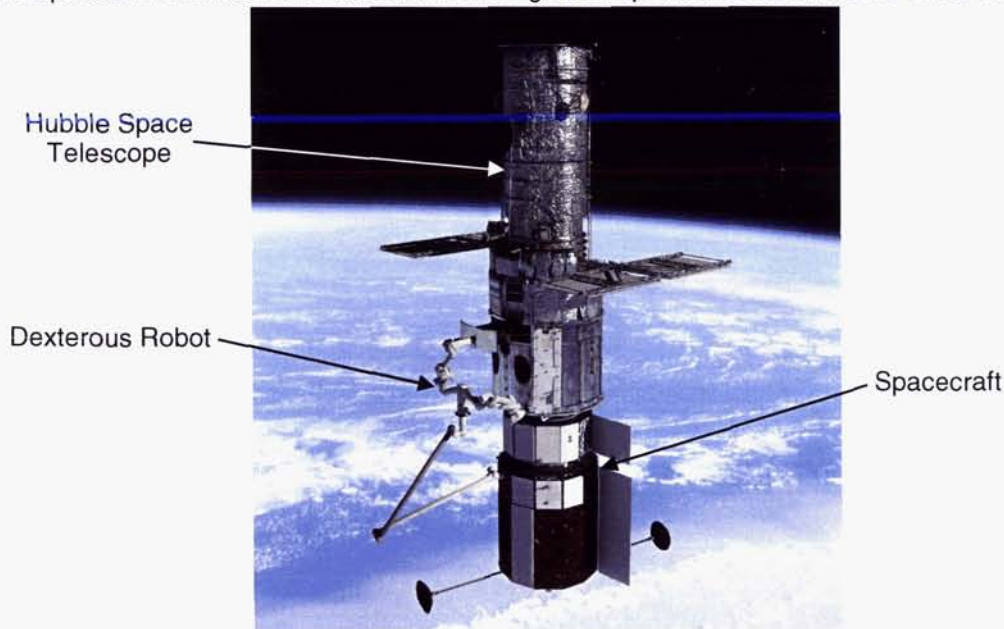


Figure 1. Robot Servicing Hubble Space Telescope

---

\* Swales Aerospace, Beltsville, MD

One of many robotic tools created for the HRSDM, the Come-Along Tool is used during the Cosmic Origins Spectrograph (COS) Task. The Come-Along Tool opens the HST Aft Shroud Doors so that the Corrective Optics Space Telescope Axial Replacement (COSTAR) can be removed and replaced by COS, improving Hubble's sensitivity to ultraviolet wavelengths by a factor of ten. Operation of the Aft Shroud Doors is a challenging undertaking that pushes the limits of what can be accomplished by a telerobotic system. Intended for use during crewmember extra-vehicular activity (EVA), these doors have proven troublesome on previous missions. During the first mission to service the HST, astronauts spent over two hours attempting to close the doors and it was concluded that the door operation is a two-person task. Even with two robotic arms, it would not be easy to mimic the dexterity of two astronauts performing EVA, and for this task, only one robotic arm is available.

The Aft Shroud Doors are difficult to operate because they have shear plates at their top and bottom that tend to jam during closing even when properly aligned. Other tasks involved with operating the doors, while easy for an astronaut, are difficult for a robotic system. Acquiring an unrestrained door was at first difficult to perform during ground testing of the robotic system because efforts to hook the handle of the door pushed the door further away. Pushing both Aft Shroud Doors closed at the same time is a two-handed astronaut operation and challenges arose designing a mechanism that could perform this using a single robotic arm.

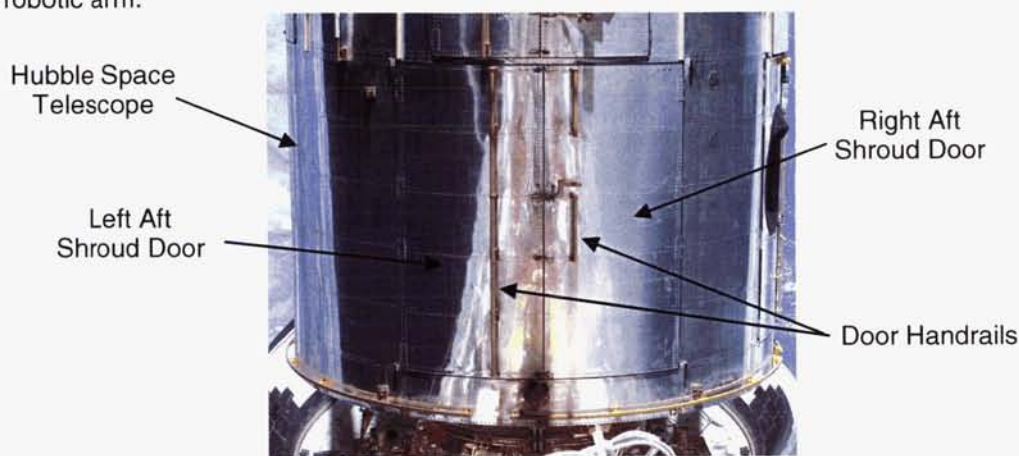


**Figure 2. Aft Shroud Doors**

Through creative problem solving and ground testing, the Come-Along Tool design evolved to overcome the difficulties associated with operating the Aft Shroud Doors in a manner that optimizes reliability, visual indication, and ease of robotic operation. The Come Along Tool is able to perform its role because it has features and an operation sequence that require the robot to move in only one degree-of-freedom at a time. Reliability is attained through use of simple, robust mechanisms and redundancy that allows the tool to perform its task even if a single failure occurs. The addition of features within the field of view of the cameras mounted on the robot allow the ground operator to watch gears rotating, discern whether the door handles are under control, and measure the tension force applied to close the doors. The ability of the tool to perform its function is further improved by combining the functionality of mechanisms to reduce the number of robotic actions and operation time. The details are further described in this paper.

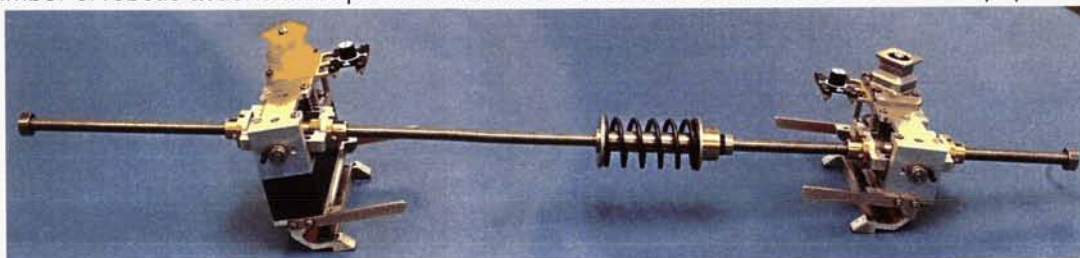


**Figure 3. Come-Along Tool**



## Background

### Robotic System

The robotic system for the HRSDM is composed of a spacecraft, a robot, and various robotic tools. The spacecraft is unmanned and intercepts the HST using a grapple arm. Once the HST is captured, the Dexterous Robot, attached to the spacecraft via a boom, is deployed to begin servicing and upgrading the telescope. The Dexterous Robot, built by MacDonald Dettwiler Robotics for use on the International Space Station, has two identical arms, one of which serves as backup in case the first fails. At the end of each arm is an Orbital Tool Change-out Mechanism (OTCM) with jaws to clamp a "Micro Fixture" interface and a socket that advances onto and rotates a 7/16-inch hex head. The Dexterous Robot was designed to move large payloads on the International Space Station, not to perform the precision operations necessary to service the HST. Bridging the gap between the Dexterous Robot and the HST, Swales Aerospace developed over twenty robotic tools for the HRSDM, each customized to specific tasks necessary to service and upgrade the HST such as manipulating connectors, attaching to science instruments, and opening bay doors.

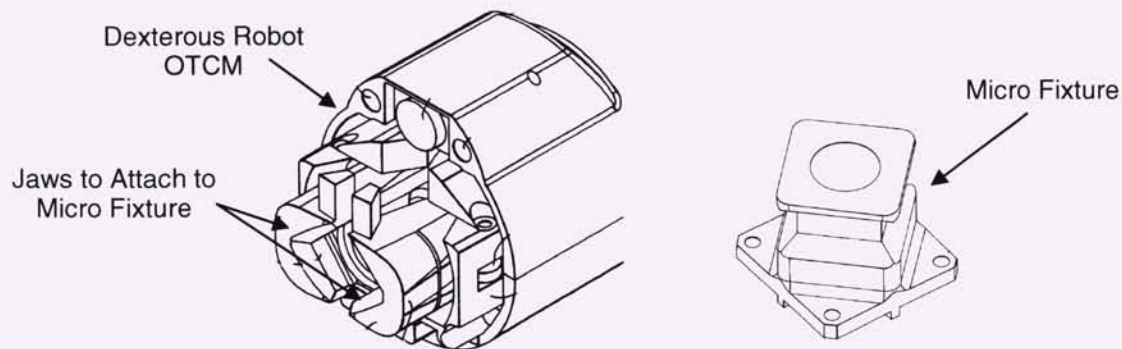


**Figure 4. Dexterous Robot Orbital Tool Change-out Mechanism and Micro Fixture**

### Worksite

The Aft Shroud Doors on the '-V2' face of the HST must be opened to access COSTAR. Restrained by four latches, the Aft Shroud Door set has gaskets along its perimeter and shear plates where the doors interface each other and the HST structure. The gaskets protect the optical equipment inside the telescope from light and contamination and become stiffer at cold temperatures. Providing attachment points for the Come-Along Tool are EVA handrails on each door.

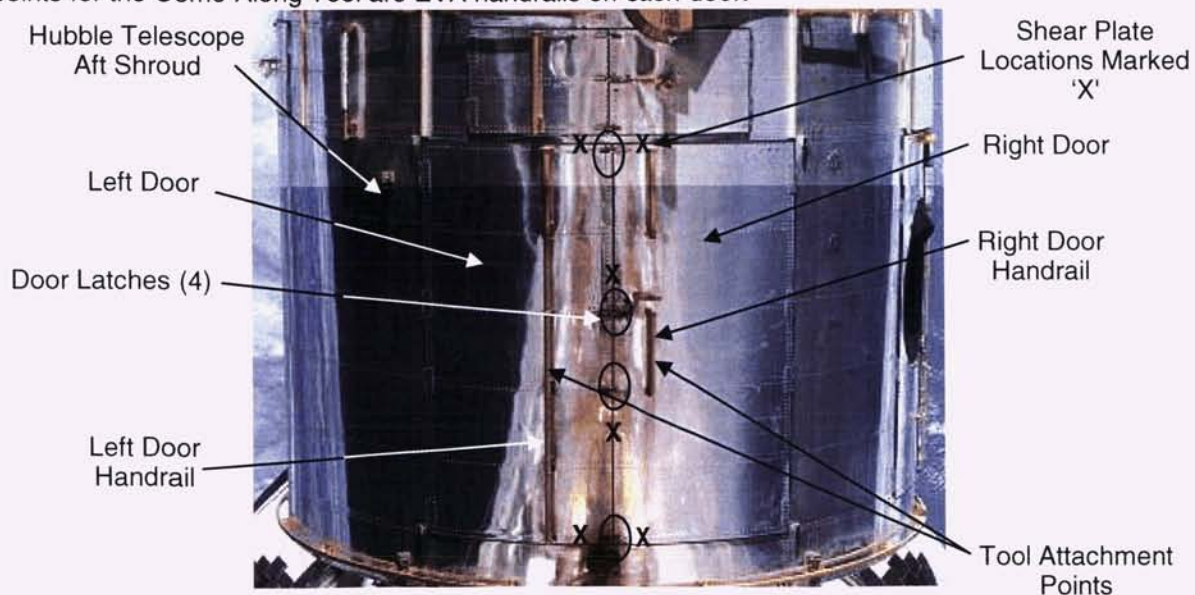


**Figure 5. Worksite**



Door operation is complicated by sets of mating shear plates at the top and bottom of each door and at the interface between the doors. These shear plates transfer structural loads from the Aft Shroud Frame and require the right door to close before the left to mesh properly. Operation of the '-V2' door set during the first mission to service the HST revealed that the shear plate on the bottom left door tends to jam even when the door is properly aligned. Temperature gradients distort the shape of the telescope's outer frame potentially exacerbating this problem.

#### System of Tools to Operate the Aft Shroud Doors

In order to perform the COS Task, the Aft Shroud Doors are operated by three robotic tools: the 90 Degree Door Latch Tool, the Door Restraint Tool, and the Come-Along Tool. The Door Latch Tool is used to release the four door latches during opening, and is used to reengage the latches once the doors are closed. Helping to control the doors once released, the Door Restraint Tool is used to hold the doors open during operations inside of the Aft Shroud, and is reconfigured to hold the doors nearly closed. The Come-Along Tool, described in this paper, controls the opening of the Aft Shroud Doors and closes and restrains the doors in the shut position.

Door Latch Tool



Door Restraint Tool

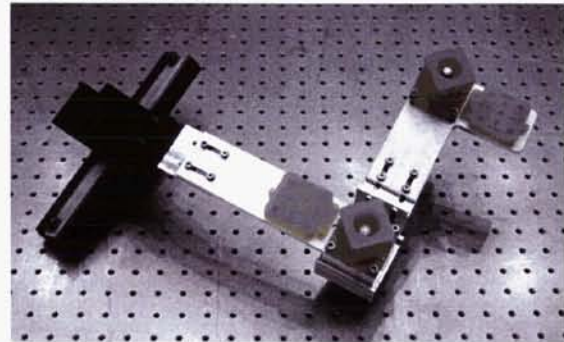


**Figure 6. The Door Latch Tool and the Door Restraint Tool**

#### Come-Along Tool Requirements

The Come-Along Tool must satisfy mission level and task specific requirements. During door opening, the Come-Along must attach to the left and right door handrails, hold the doors shut while the Door Latch Tool is used to release the latches, and slowly release the doors such that the pressure from the gaskets does not throw the doors open. The Come-Along Tool must then release from the right door handrail so that the doors can be fully opened. When it is time to close the doors, the Come-Along Tool must reacquire the handrail of the right door which is now free to move. The Come-Along Tool, hooked on to the left and right door handrails, closes the doors by applying a tension force between the two door handrails causing the doors to rotate along their respective pivot points. The tool must then hold the doors in position until the door latches can be reengaged.

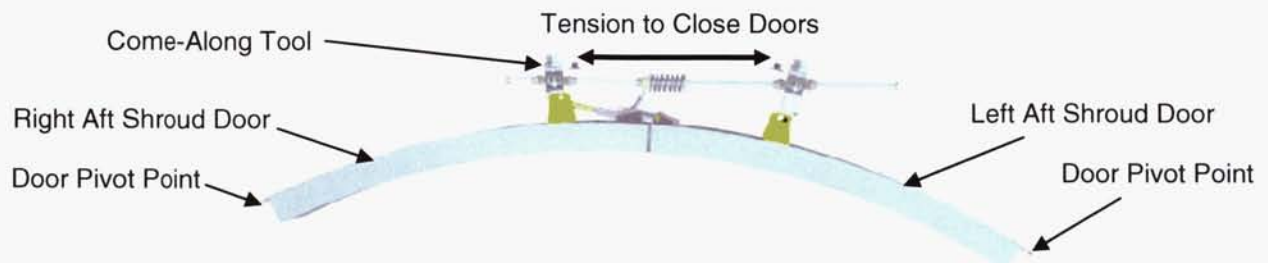


**Figure 7. Bottom View of Operation to Close Doors**

The Come-Along Tool must also satisfy requirements for design for minimum risk and single-fault tolerance, meet weight restrictions, and provide the ability to overcome jams at the door shear plates. The tool must be able to perform all of its functions using only one half of the robot's force and moment

capability in an environment that cools to below negative 80°C. Satisfying these requirements with a robotic tool that is easy to use and that provides good visual cues provided a great engineering challenge.

### Concept Development

The Come-Along Tool was developed from May of 2004 through July of 2005, culminating in an Engineering Test Unit. Tests were performed at GSFC using a door trainer constructed to flight drawings and a ground trainer Dexterous Robot. With each successive generation, features were added to incorporate lessons learned from previous testing.

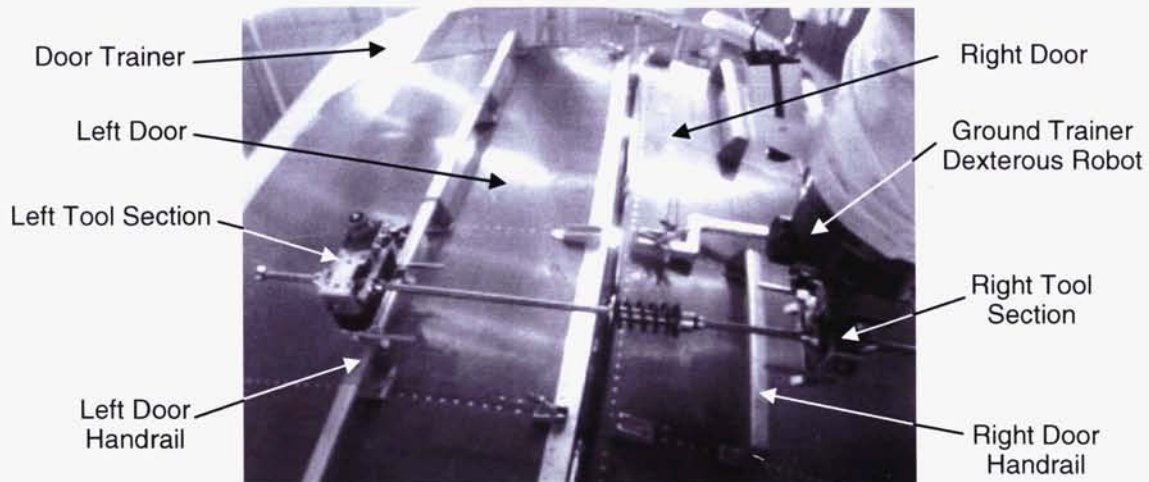


**Figure 8. Ground Testing**

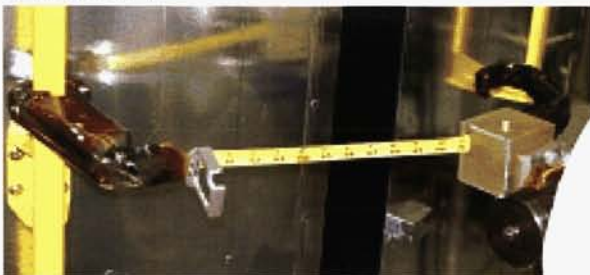
#### Generation 1

In order to begin to understand door operation using the ground trainer Dexterous Robot, a mockup of the Come-Along Tool uses hooks and a modified tape measure reel. This mockup demonstrates the ability to attach to the Left and Right Door Handrails.

#### Generation 2

This generation is more robust, containing c-clamp type jaws that actively clamp the Left and Right Handrails. The ground trainer Robot closes the doors by winding a cable reel that is coupled to a one-way ratchet, holding the doors shut.

Generation 1



Generation 2

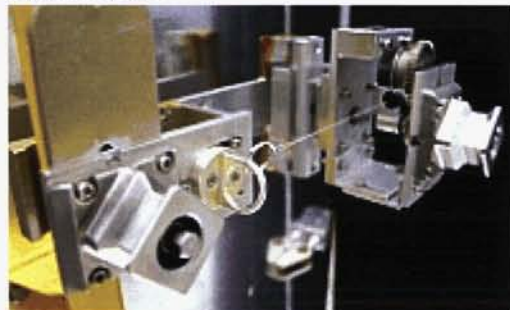


**Figure 9. Generations 1 & 2 Come-Along Tool Prototypes**



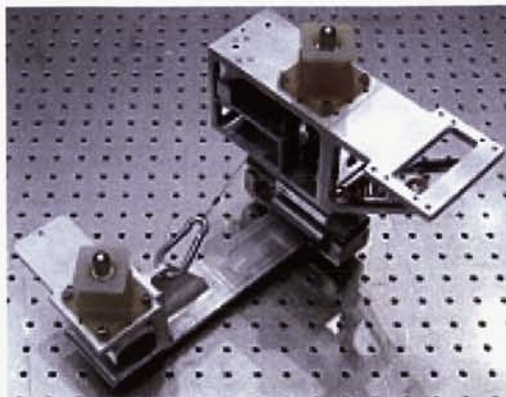
### Generation 3

With the addition of a DC motor, the third generation prototype can disengage the ratchet system and control door opening. The tool can capture the handrails when the doors are latched closed, but not in the more difficult situation in which the doors are unrestrained.

### Generation 4

In this generation, the DC motor is removed to simplify the tool. The handrail clamps are lengthened to spread the load of pitch moments induced by the ground trainer Robot to overcome door jams. Finger features are added to the clamps allowing the tool to capture the handrails of unrestrained doors.

Generation 3



Generation 4

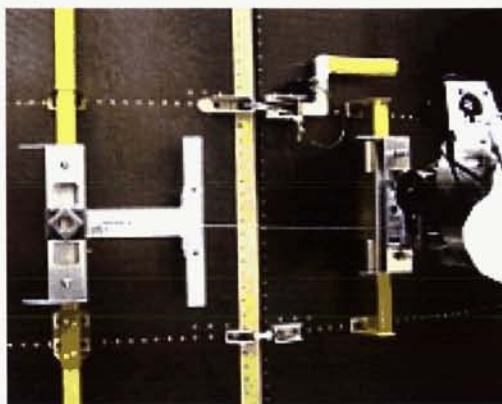


**Figure 10. Generations 3 & 4 Come-Along Tool Prototypes**

### Generation 5

The Engineering Test Unit incorporates many new design features and successfully performs all required door operations. The cable system is removed, alleviating complications associated with tethers<sup>1</sup>, and replaced with a threaded Lead Screw. This makes the tool more reliable by reducing the number of parts and providing a rigid link between tool sections. Operations of clamping the handrails, opening and closing the doors, and holding the doors in the closed position are combined into one to improve ease of robot operation. The robot grips the tool via Micro Fixture robotic interfaces. The most significant addition is the spring-loaded Lead Screw Strut, which provides visual indication of the tension force between the two doors.

The added benefit of the spring-loaded Lead Screw Strut is that it continues applying a closing tension to the slightly ajar doors. This allows the robot to release the tool and perform contingency operations in case either the left or right Aft Shroud Door is jammed.

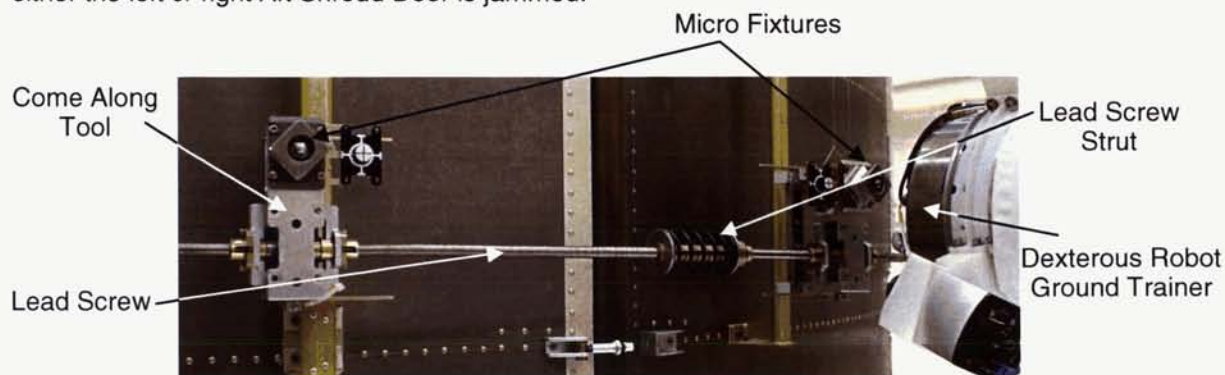


**Figure 11. Generation 5 Come-Along Tool Engineering Test Unit**



## Design for Functionality

The ability to perform certain tasks associated with operating the Aft Shroud Doors was achieved by separating operations into discrete steps that the ground trainer robot could accomplish by moving in only one degree of freedom at a time. During early phases of development of the Come-Along Tool it was difficult or impossible to acquire the handrail of an unrestrained door or overcome a door jam because complex robot movements were required that involved various combinations of translations and rotations. This approach to telerobotic operation is not effective because it assumes that a robot is able to coordinate movements with a level of dexterity approaching that of an astronaut. By breaking down movements into small simple steps, functions were made feasible.

### Acquire Unrestrained Door Handle

The task of acquiring the handrail of an unrestrained door was at first difficult and later made easy by separating operational steps. During door closure, when the doors start open and are free to move, attempting to hook a tool section onto the handrail of a door is difficult because any inadvertent bumping of the handrail sends the door off into another position. The robot then has to reposition the tool for another attempt at handrail capture. This operation is made possible by adding a 'finger' feature to the tool and first pushing the door against the door seal to lock out its movement before sliding the clamp over the handrail. This new operation requires two steps that are pure translations and can be performed easily by the robot operator. Implementing this same strategy also was successful for more difficult tasks.

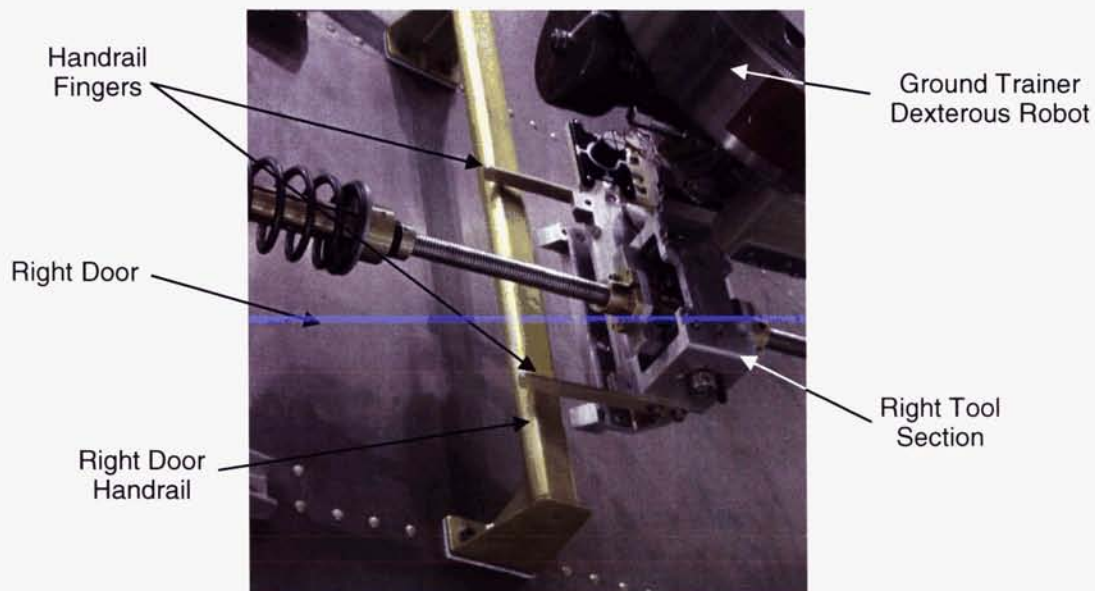


**Figure 12. Come-Along Acquiring Door Handrail**

### Overcome Door Jams

The ability to overcome door jams was achieved by separating actions into simple steps. As mentioned before, it took two astronauts working in tandem more than two hours to close the same door set during the first mission to service the Hubble Space Telescope. Door jams were induced in the ground trainer door set testing and early attempts to lift, pull, and twist the door into place were unsuccessful. Ultimately, it was discovered that applying a pitch moment to a door overcomes jams. To allow greater moment input without damaging the door handrails, the tool's handrail clamps are extended to spread the loading. Operation to overcome a door jam is made possible by completing the following steps: (1) pushing the door closed until it jams, (2) applying a pitch moment in the up or down direction to relieve the jam, and (3) completing door closure.

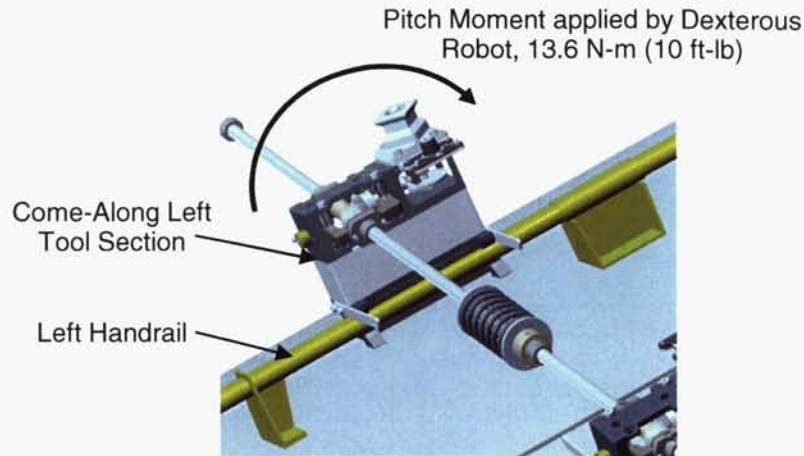


**Figure 13. Pitch Moment Application**

### **Design for Visual Indication**

Ability to view the worksite is essential to completing sequential operational steps. Mounted to the robot, cameras are intended to alert the operator if a dangerous situation arises and provide views so that the robot operator has confidence that the tool is performing as intended. However, these cameras are only effective if the tool design makes good use of them. The addition of features within the field of view (FOV) of the cameras mounted on the robot allows the operator to watch gears rotating, discern whether the door handles are under control, and measure the tension force applied to close the doors.

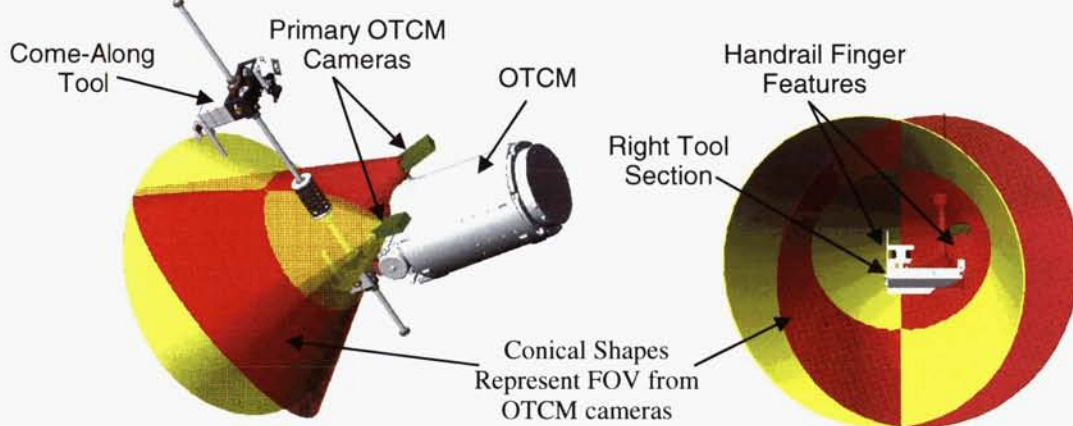


**Figure 14. Field of View**

### Handrail Capture

To hook the Come-Along Tool onto a door handrail, the robot operator needs to know the tool's distance from the handrail while making an approach. The gap between the tool and the handrail is difficult to judge when the finger feature, shown below, is in-line with the camera. To gain an offset view, the finger features are placed on the edges of each tool section at the periphery of the OTCM camera's field of view. This lets the operator discern the changing gap between the fingers and the handrail during handrail capture.



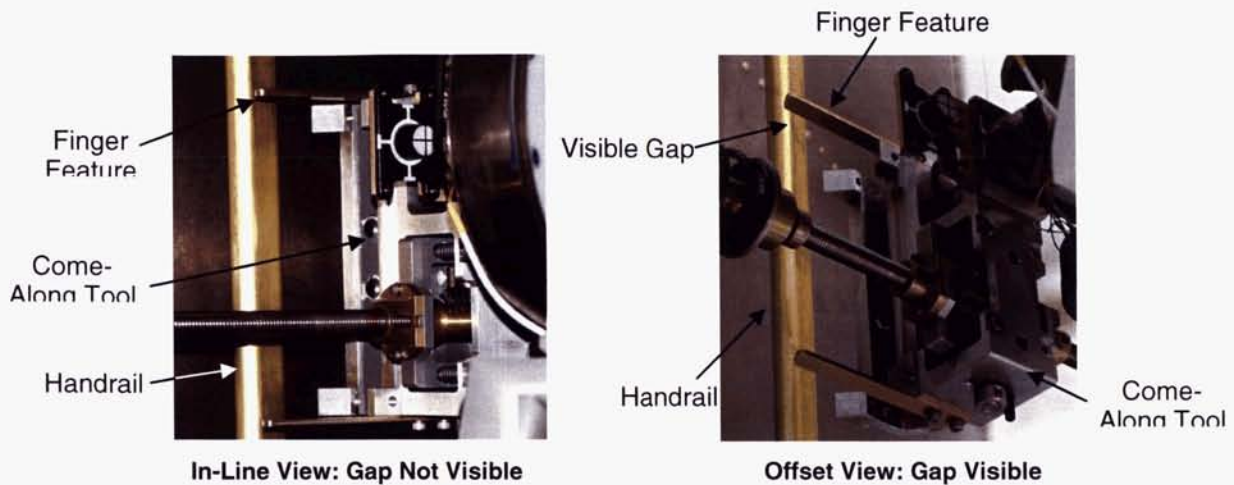


**Figure 15. Indication of Distance from Handrail**

#### Tightening and Loosening Doors

Visual indication of whether mechanisms in the tool are operating is necessary during door opening and closing. During operation, the robot operator sends a command to input torque to the tool's gear train, causing the tool to move along the lead screw which tightens or loosens the doors. Since the movement of the doors is slow, it is difficult to ascertain whether the command had the intended effect or when the operation is complete. Cutaways were added to the tool's housing so that views of rotating gears can be seen. By watching gear rotation, the operator can tell when the doors are moving and when they have stopped.

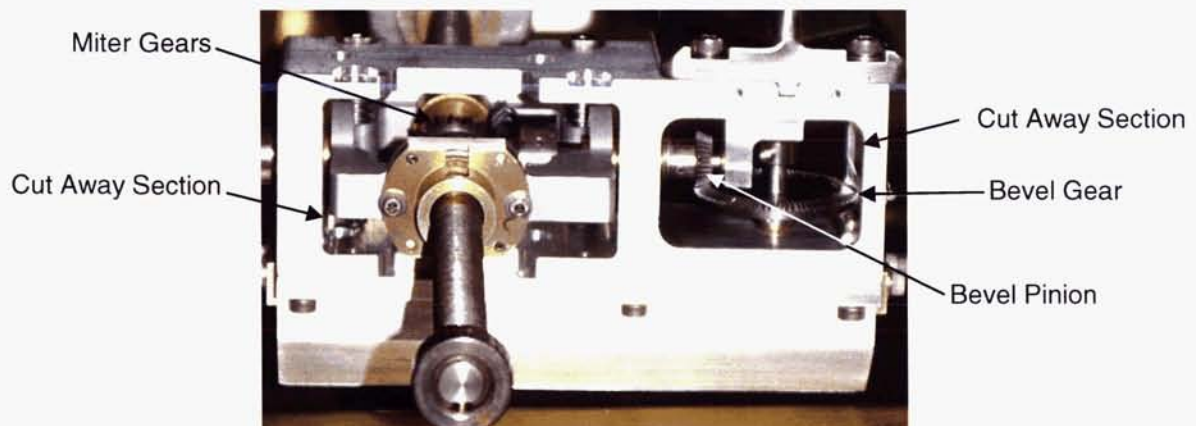


**Figure 16. View of Rotating Gears**

#### Measurement of Tension Force Between Doors

Applying tension between the doors is a sensitive operation; if the operator applies too small a force the doors will not close and if he applies too much he could damage the tool or the handrails. In order to provide the operator with force information, a spring-loaded gauge is added in line with the lead screw. The gap between the gauge housing and indication mark varies with the tension between the two Come-Along Tool Sections.



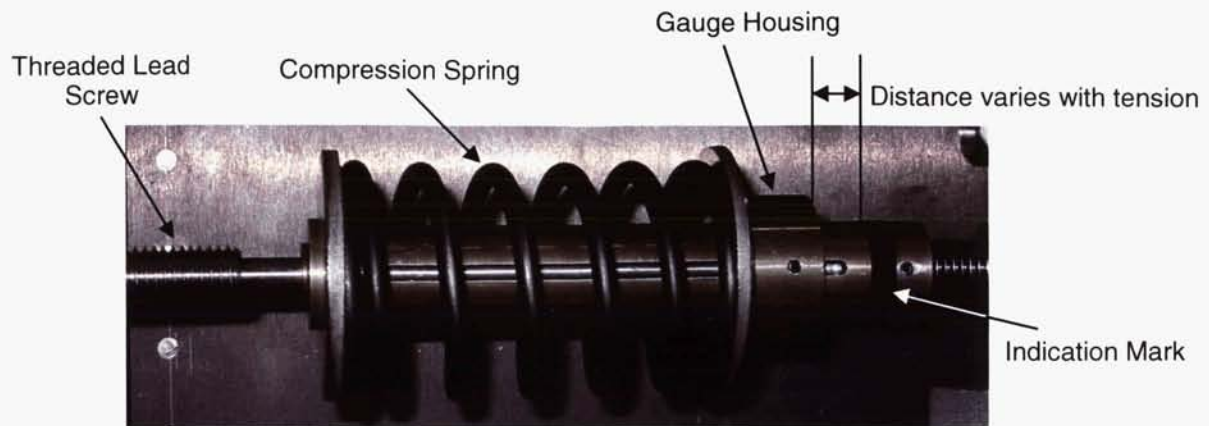


**Figure 17. Tension Indicator**

### **Design for Ease of Operation**

The Come-Along Tool is made easy to operate by minimizing the number of times the Robot must disengage and reattach since each reattachment has an associated risk of error that could cause damage to the tool, robot, or telescope. This is accomplished by allowing the robot to control all aspects of door operation using a single mechanism and by including a backup of this same mechanism.

#### Combine Operations

The Come-Along Tool is optimized for ease of operation by allowing the robot operator to control the following three functions from a single attachment point:

1. Apply tension to close the doors
2. Release tension to open the doors
3. Hold the doors in place

This is made possible by the design of the gear train. When attached to a tool section the robot powers the tool's gear train using its 'advance' mechanism. A 7/16-inch hex socket extends from the robot engaging a mating male hex in the tool. Rotational motion from the robot travels through the tool's gear train through two right angle bevel gear connections. Clockwise input rotates a nut about the lead screw causing the tool section to translate along the lead screw and apply a closing tension on the doors; a counter clockwise input causes the tool section to travel in the opposite direction along the lead screw allowing the doors to open. The non-back driving nature of the nut on lead screw connection is sufficient to lock the doors in place. This arrangement is easy to operate since the robot operator does not need to let go of or reattach to the tool during nominal operation.

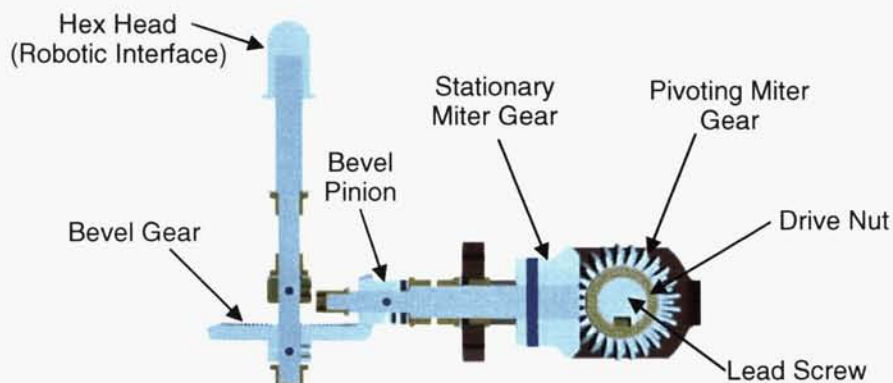


**Figure 18. Gear Train**

#### Perform Operations from Either Tool Section

Adding the same gear train mechanism on both tool sections further optimizes the Come-Along Tool for ease of operation. It was found during ground testing that the Robot must attach to a door to overcome that door's jam. In the case in which the tool lets go of one tool section and moves to the other to relieve a

jam, it does not need to move back; it can continue adding tension to the lead screw and hold the doors in the closed position using the interface on its new attachment point.

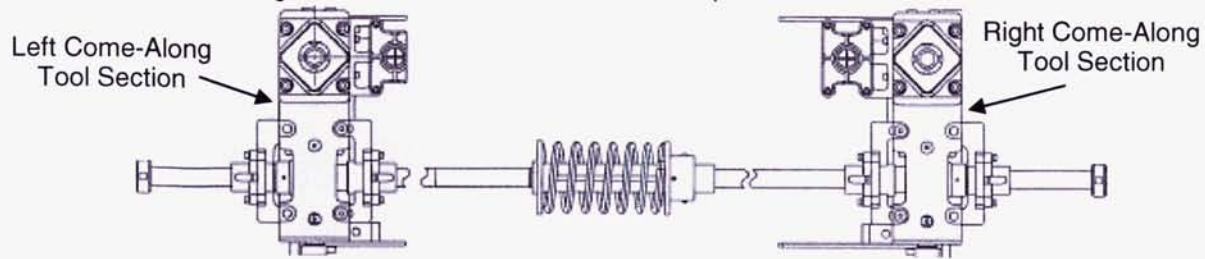


**Figure 19. Redundant Tool Sections**

### **Design for Reliability**

Reliable functioning of the Come-Along Tool is necessary to ensure that door operation is completed; if the doors are not properly closed, the HST cannot continue its science mission. Since no human will be available to perform unanticipated workarounds it is especially important the robotic tool be dependable. The robustness of the Come-Along Tool's design is due to its simple mechanisms, hard stops to prevent position overrun, and ability to continue its task if a mechanisms failure occurs.

#### Mechanical Hard Stops

The Come-Along Tool has mechanical hard stops to ensure that the tool sections do not rotate too far or run off the end of the Lead Screw. To prevent the Lead Screw from pitching out of position, the tool housing provides a stop. Collars on the edges of the Lead Screw prevent either tool section from running off.

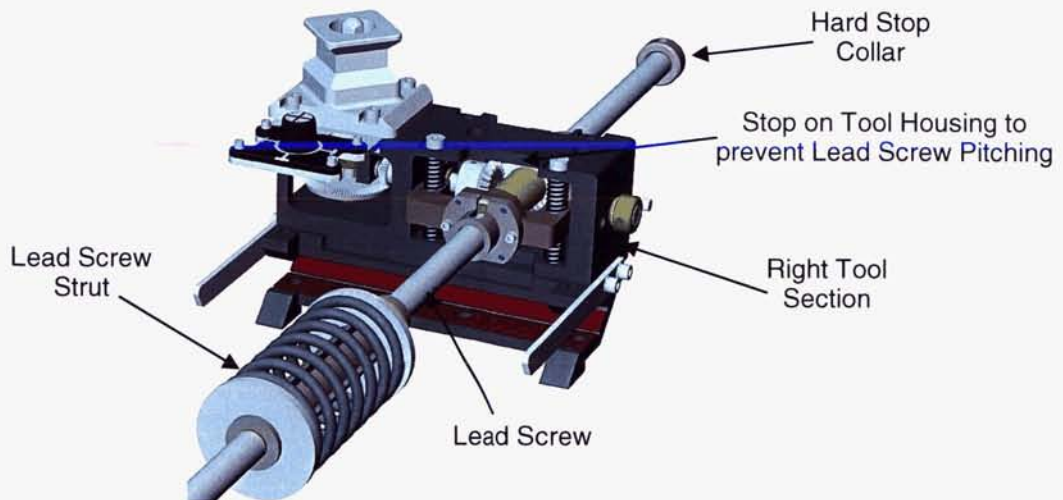


**Figure 20. Hard Stops**

#### Simple Mechanisms

In order to reduce complexity and thereby increase reliability, the Come-Along Tool incorporates simple mechanisms to hold the doors in place, provide visual indication of tension between the doors, and allow each tool section to rotate about the Lead Screw. During earlier generations of the Come-Along, a ratchet mechanism, used to lock the doors in the closed position, required a ratchet gear, pawl, pawl spring, and motor actuated pawl release. To simplify the tool, the ratchet mechanism is replaced with a nut to lead screw connection that does not allow the gear train to back drive. Avoiding use of electronics eases temperature requirements on the tool and eliminates the need for batteries.

One of the challenges of operating the Aft Shroud Doors is that the angles of the door handrails vary with the doors rotation. To remain attached to the handrails as the doors open and close, each of the tool



sections must rotate with respect to the Lead Screw. To accomplish this in a simple manner, a property of miter gear connections is used: as long as the apex of the two mating miter gears pitch cones remain aligned, one miter gear can rotate about the other. The miter gear connection allows power transfer through a rotating joint.

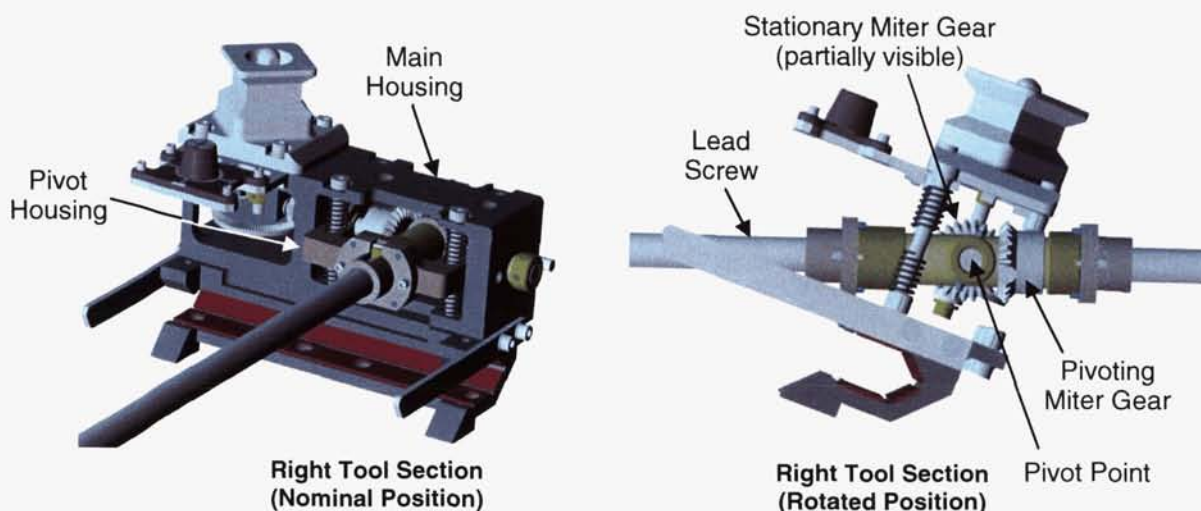


**Figure 21. Rotation Relative to the Lead Screw**

#### Single Fault Tolerance

One of the mission level requirements of the Come-Along Tool is that it be single fault tolerant, meaning that it shall continue to operate even if any single mechanical failure occurs. The tool accomplishes this by including a redundant tool section. Should a part on one tool section fail, the other tool section can be used to continue operating the Aft Shroud Doors.

#### **Conclusion**

Reliable operation of the Aft Shroud Doors with the Come-Along Tool is critical to performing the COS Task and achieving the scientific objectives of the HRSDM. The tool's current design overcomes a difficult set of obstacles to make door operation possible. Through testing and development of the tool, we gained insight regarding Aft Shroud Door operation, reliability issues involved with Robotic Tool design, and the use of telerobotics.

Robotic missions require a high level of reliability since there are no humans to perform unanticipated 'work arounds'. After first struggling to operate more complicated prototypes, the Come-Along Tool design was optimized through use of simple and redundant mechanisms. Functions for closing the doors, clamping the handrails, and holding the doors in place were combined into one. If any part of one tool section fails, redundant features on the other tool section can be used to complete operation.

Important lessons were also learned about telerobotic operation. Using the force-feedback capability of the robot, it was discovered that certain human operations could be performed robotically. The simple task of acquiring the handrail of an unrestrained door was at first difficult to perform with the robot, and later made easier by adding additional features, such as Handrail Fingers to the tool and adjusting the door capture operation to first press the door shut. The execution of operations to overcome door jams successfully combines the capabilities of a robotic tool and robot to perform a difficult task that requires two astronauts working in tandem.

The results of developing the Come-Along Tool are applicable not only to the HRSDM, but also to future robotic missions as we begin to realize NASA's vision for space exploration. Development of the Come-Along Tool furthers NASA's goal to "...implement a safe, sustained, and affordable robotic and human program to explore and extend human presence across the solar system...."<sup>2</sup> The Come-Along Tool's



ability to operate interfaces made for humans and coordinate with other robotic systems is pertinent to the next generation of space exploration in which robotics will play a key role.

### **References**

1. Tomlin, Faile, Hayashida, Frost, Wagner, Mitchell, Vaughn, and Galuska. "Space Tethers: Design Criteria." *NASA Technical Memorandum 108537* (July 1997).
2. Martin, Gary L. "Level 0 Exploration Requirements for the National Aeronautics and Space Administration." *NASA Document No.: SA-0001* (4 May 2004), p. 5.

### **Acknowledgements**

Development of the Come-Along Tool would not have been possible without the thoughtful work of Dick McBirney, Jenny Xu, Carl Anders, Randal Frey, Kevin McMennamin, Justin Cassidy, Paul Nikulla, John Bishop, and Giles Robinson. Thank you for your help and insight.



# Planetary Airplane Extraction System Development and Subscale Testing

John E. Teter Jr.\*

## Abstract

The Aerial Regional-scale Environmental Survey (ARES) project will employ an airplane as the science platform from which to collect science data in the previously inaccessible, thin atmosphere of Mars. In order for the airplane to arrive safely in the Martian atmosphere, a number of sequences must occur. A critical element in the entry sequence at Mars is an extraction maneuver to separate the airplane quickly (in less than a second) from its protective backshell to reduce the possibility of re-contact, potentially leading to mission failure. This paper describes the development, testing, and lessons learned from building a 1/3 scale model of this airplane extraction system. This design, based on the successful Mars Exploration Rover (MER) extraction mechanism, employs a series of trucks rolling along tracks located on the surface of the central parachute can. Numerous tests using high speed video were conducted at the Langley Research Center to validate this concept. One area of concern was that although the airplane released cleanly, a pitching moment could be introduced. While targeted for a Mars mission, this concept will enable environmental surveys by aircraft in other planetary bodies with a sensible atmosphere such as Venus or Saturn's moon, Titan.

## Introduction

The ARES project will employ an airplane as the science platform to closely survey the surface, identify the constituents of the atmosphere, and assess the residual magnetism of Mars. In order for the airplane to arrive safely in the Martian atmosphere, a number of sequences must occur, starting with Earth launch and ending with deployment. The airplane will be launched from Earth inside a protective aeroshell attached to a spacecraft. It will cruise for almost a year from Earth to Mars. Then, arriving at Mars it will begin the Entry, Descent, and Deployment (EDD) sequence. Figure 1 shows the stages of EDD. Many sequences must occur quickly to allow the plane to fly in the Martian atmosphere. Upon arrival at Mars, the protective forward aeroshell will separate from the spacecraft and coast into the atmosphere of Mars. After atmospheric drag has slowed the assembly to approximately Mach 2, a supersonic parachute will deploy to slow the craft further allowing the forward heatshield to separate. At this point, the airplane will be safely tucked in the swinging and turning backshell, which is suspended from the parachute. Now the final deployment sequence of the airplane begins. The backshell must ascend 0.7 meter relative to the airplane extraction system to expose the airplane. The extraction system will then release the airplane. In less than two minutes, the airplane will fall under the restraint of a drogue chute, unfold, pull up, and fly above the surface of Mars.

This paper concentrates on the mechanical extraction system developed to separate the airplane from its protective backshell. Since the folded tail of the airplane is not sufficient to support the airplane launch loads, a secondary structure is required to extend past the folded wings and tail to attach to the main body of the airplane. This multi-legged, tripod structure which connects the airplane to the backshell has been dubbed the Airplane Extraction System (AES).

---

\* NASA Langley Research Center, Hampton, VA



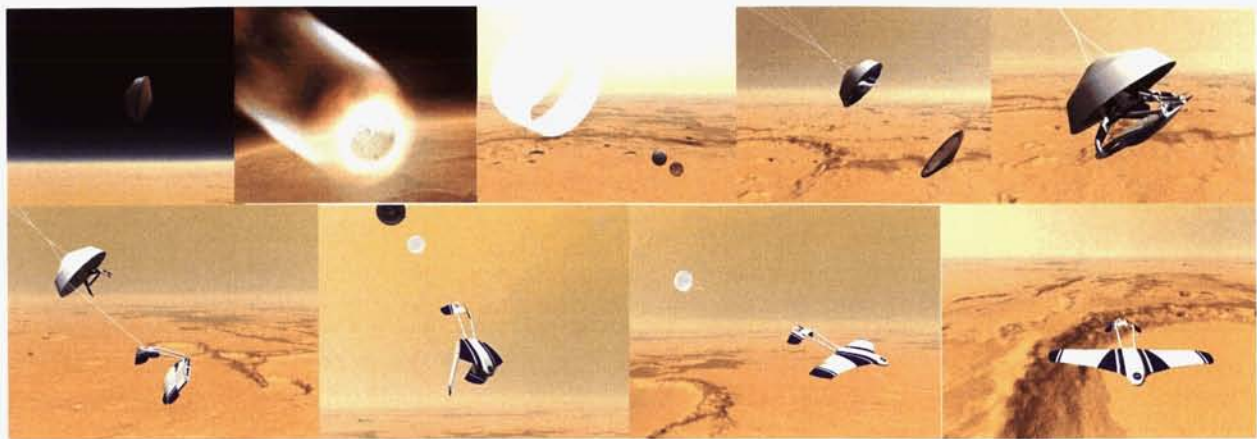


**Figure 1. ARES Entry, Descent, and Deployment sequence**

### **Concept Description**

The primary functions of the AES are to support the airplane through launch, interplanetary cruise, and entry; and then to guide the airplane safely out of the backshell during extraction. During launch, cruise, and entry, the airplane is held by three kinematic mechanisms to prevent stresses from building up in the airplane structure by allowing the aeroshell and airplane to deform independently. During the extraction phase, six pyrotechnic separation nuts will fire releasing the AES and airplane assembly. The backshell will be free to roll up the AES guided by rollers on the AES's central ring and tracks on the backshell's parachute can. The forces of differential aerodynamic drag between the backshell's high drag supersonic parachute and the low drag free falling AES/airplane assembly will cause the separation. As the parachute can reaches the end of the AES, a second set of pyrotechnic separation nuts will release the airplane from the AES. The folded airplane is then in free fall in the atmosphere until the drogue chute is deployed (Figure 2). The following tests verify the extraction function of the airplane extraction system.



**Figure 2. Extraction concept. Left illustration shows stowed airplane stowed inside the backshell just after heatshield release. Right illustration shows the extracted airplane prior to release from the AES.**

### AES Requirements

#### **Key AES Requirements:**

- Hold 175-kg airplane securely through Earth launch, interplanetary cruise, and Mars entry
- Guide the airplane out of the backshell and release it in the Martian atmosphere
- Reduce stresses on the airplane due to thermal expansion and contraction
- Low mass
- Fit within the volume of a bi-conic, 2.65-meter-diameter aeroshell
- Airplane/AES minimum natural frequencies, 15-Hz lateral, 35-Hz axial
- Withstand 15-g launch loads

### AES Description

The AES shown in Figure 3 is approximately 2.4-meters wide, 0.9-meter tall, with a mass of 56 kg. It is composed primarily of titanium tubes. Hard stops on the top of the central ring prevent the AES from coming off the parachute can.

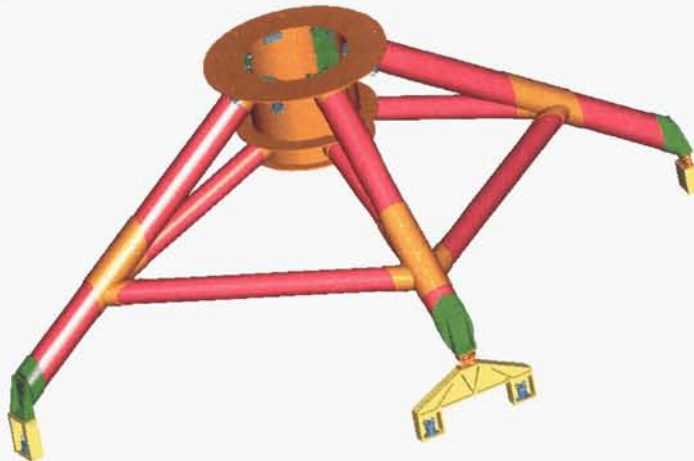


**Figure 3. Airplane Extraction System**

### AES Roller Configuration

Central to the success of the AES is the roller configuration. The configuration is based on the successful MER extraction hardware modified to work with an airplane. Like MER, three tracks are equally spaced on the central parachute can. However, the vertical spacing of the rollers along the track is much greater. The nominal clearance between each pair of rollers and the track is  $\pm 0.25$  mm. The clearance in the system ensures there is no binding as the backshell is pulled away. Yet, the tolerances are close enough to guide the backshell without damaging the plane. The clearances are needed to compensate for machining tolerance stack-ups and thermal growth. Theoretically, this system will still work even if the rollers do not turn, although sliding friction would result. Figure 4 through Figure 8 show the various movements allowed. In each figure, the illustration on the left shows a schematic top view. The red ring and rollers represent the AES. The blue cylinder with three protuberances represent the parachute can and tracks. The right illustration shows a schematic side view for each figure. The four red circles represent one vertical set of AES rollers. The blue rectangle represents one parachute can track. Table 1 summarizes the movements.

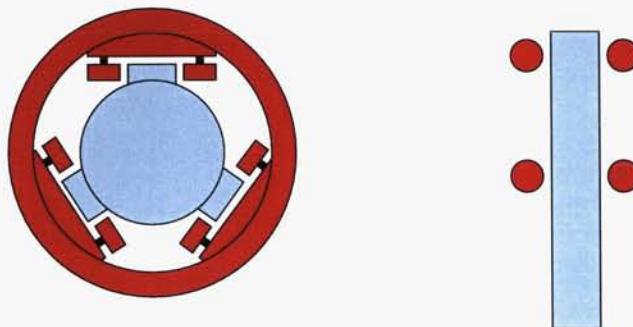


**Figure 4. AES roller configuration, nominal clearance**

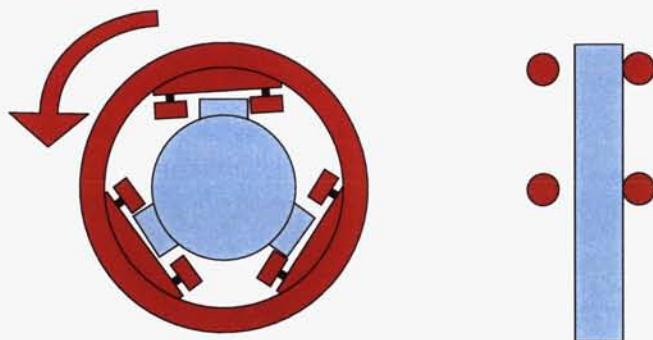


Figure 5. AES roller configuration, axial rotation

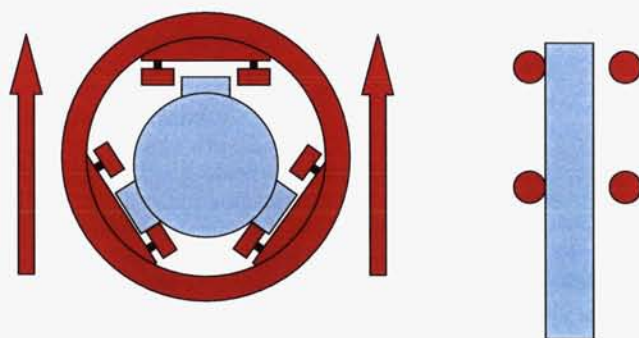


Figure 6. AES roller configuration, radial thrust

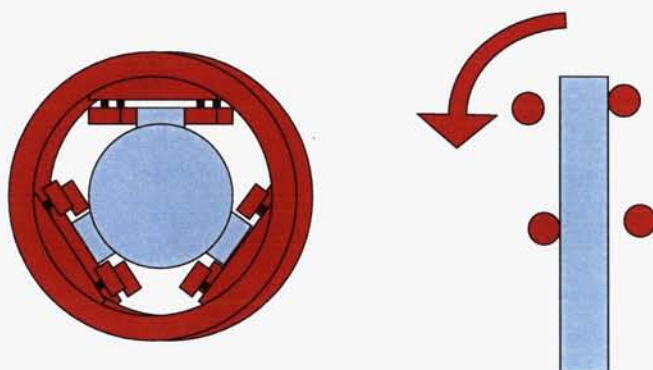
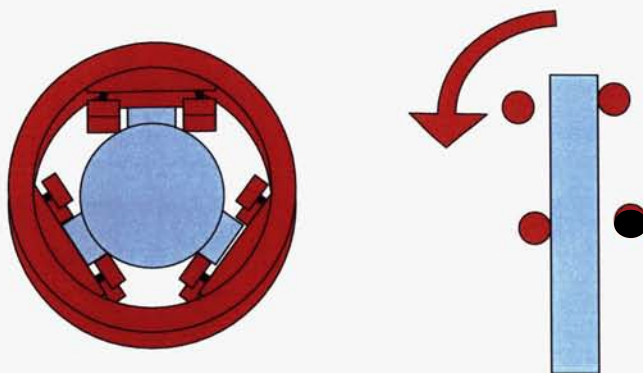


Figure 7. AES roller configuration, X tilt





**Figure 8. AES roller configuration, Y tilt**

**Table 1. AES Clearances and Maximum Movements**

Nominal	$\pm 0.25$ mm clearance between rollers and track
Radial Thrust	$\pm 0.28$ mm side to side thrust
Rotate	$\pm 0.1$ deg axial rotation
X Tilt	$\pm 0.1$ deg tilt from vertical axis
Y Tilt	$\pm 0.09$ deg tilt from vertical axis

### Test Description

In order to demonstrate the extraction design approach and operation of the AES, a functional 1/3 scale model of the backshell, AES, and airplane was created. To simulate the potential orientations in which separation would occur, the model was statically held at various angles and rotations on an A-frame in the high bay of building 1250 at NASA Langley Research Center. Figure 9 shows the test apparatus. Earth gravity was used to simulate the differential drag between the backshell and AES/airplane assembly. Although in actuality the backshell, AES, and airplane are in freefall together, practical considerations for testing dictated that the backshell be held statically for this set of tests. The relative motion is still the same and most of the dynamics are captured. A scale of 1/3 was chosen for ease of manufacturing and handling while testing. High-speed video was used to determine proper extraction. Figure 10 shows a multi-exposure sequence of a typical test.

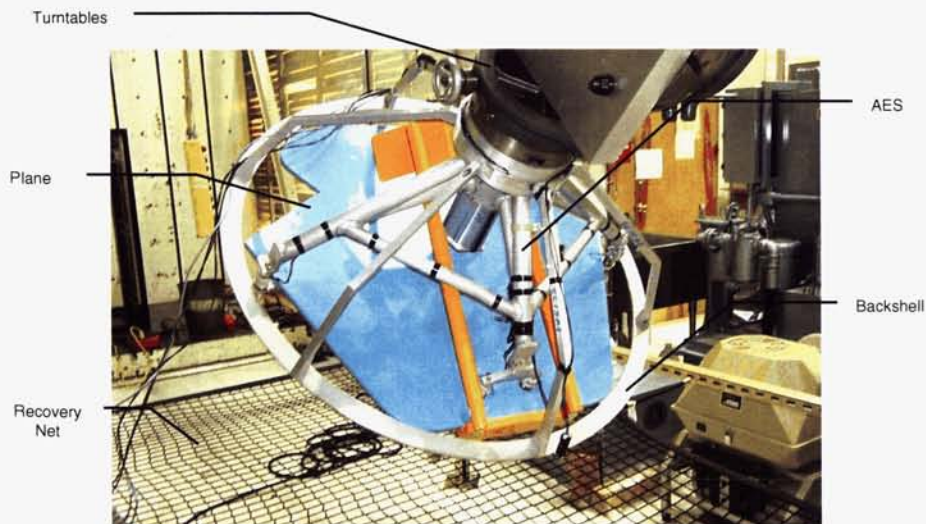


**Figure 9. AES test apparatus**

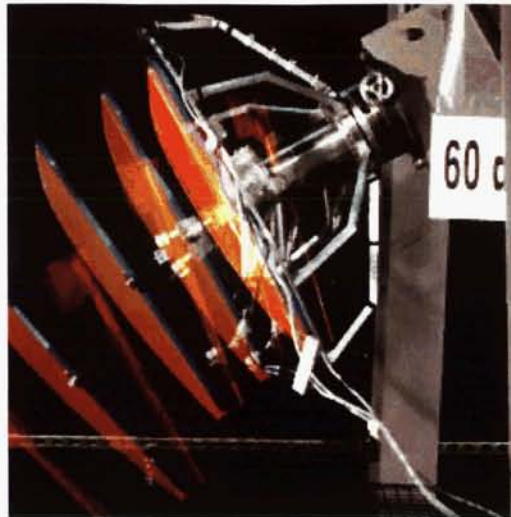


**Figure 10. Multiple exposure picture of a typical extraction test**

#### Key Test Objectives

Key test objectives were:

- Demonstrate proof-of-concept for an airplane extraction system from a backshell under various axial and lateral loading conditions.
- Demonstrate no binding as the airplane extraction system/airplane assembly rolls down the parachute can.
- Demonstrate dynamic clearance between the backshell, the airplane extraction system and the airplane.
- Determine the timing sequence for airplane release.
- Determine effects of the kinematic mounts on release of the airplane.
- Determine electrical cable clearances.
- Determine airplane attitude after release.

#### **Test Hardware**

The 1/3 scale model of the backshell, AES, and airplane were not miniature replicas of the full scale concept. Because of cost, schedule, and practical considerations, some compromises were made. Figure 11 shows a CAD model of the test backshell, AES, and airplane. The following sections give a brief description of the major components.



**Figure 11. 1/3 scale model of the backshell, AES, and airplane**



### Backshell

The scale-model backshell is an aluminum skeleton structure that represents the interior volume of the full-scale backshell. Its mass properties are not represented because it is a form only, static structure. The backshell skin has been eliminated in order to have a clear view of the extraction sequence.

### AES

The scale-model AES is made of welded aluminum for ease of construction. It has approximately equivalent mass, cg, inertia and leg stiffness as the full scale titanium structure. The central cylinder is missing some stiffening rings for ease of manufacture, but they were needed only for high launch loads (15g) and not lightly loaded (2g) extraction loads.

### Airplane

The scale-model plane is a foam, fiberglass, and wood structure. The airplane represents the correct mass properties and roughly the correct volume. However, the stiffness of the airplane has not been matched. The mass, cg, and inertias are scaled from the full-scale airplane. The plan form of the airplane is correct as well as the positioning of the tail booms.

### Kinematic Mounts

The kinematic mounts duplicate the correct function but are greater mass because miniature spherical bearings were not readily available. The fixed point, hinge point, and swivel points of attachment between the AES and airplane functionally match the full-scale model.

### Release Mechanism

The full-scale AES and airplane are released with pyrotechnic separation nuts (Figure 12). To reduce cost and safety concerns, electromagnets were used on the scale model. While electromagnets do not release as cleanly (residual magnetism, longer response time) as pyrotechnics, these devices allow for multiple tests without replacing hardware. The electromagnets also increase the mass of the AES.

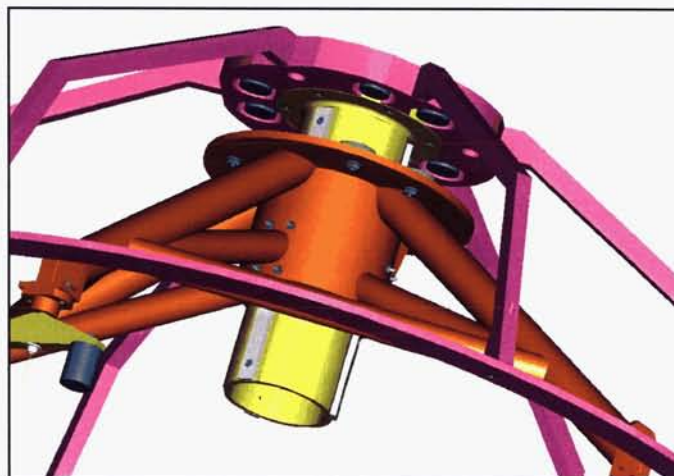


**Figure 12. 1/3 scale model release mechanism**

### Parachute Can

The parachute can is made of thick aluminum for ease of manufacturing as opposed to the thin titanium on the full-scale hardware. Also, a steel track instead of an aluminum track was used because of its durability.

### Rollers

The rollers for the scale model are mounted on three independent rings for ease of construction and the ability to move their locations easily (Figure 13). The full-scale AES has three axial trucks instead of three rings. The important parameter is the location of the rollers in relation to the tracks and not the structure that holds them.



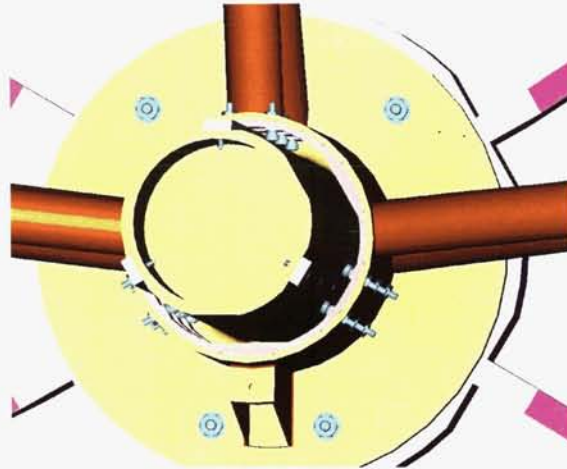


**Figure 13. 1/3 scale model rollers**

#### Scaling

The apparatus is dynamically scaled to 1/3 with the proper mass, center of gravity, and inertia properties. The scaling factors are summarized in Table 2.

**Table 2. Scaling Factors**

Property	Units	1/3 Scaling Factor Fraction	1/3 Scaling Factor Decimal
Length	m	1/3	.333
Mass	kg	$(1/3)^3 = 1/27$	.037
Time	sec	$(1/3)^{0.5}$	.577
Density	kg/m <sup>3</sup>	$(1/3)^3 / (1/3)^3$	1
Velocity	m/sec	$(1/3) / (1/3^{0.5})$	.192
Acceleration	m/sec <sup>2</sup>	$(1/3) / (1/3^{0.5})^2 = 1$	1
Force	kg*m/sec <sup>2</sup>	$(1/3)^3 * 1 = 1/27$	.037
Pressure	N/m <sup>2</sup>	$(1/27) / (1/3)^2 = 1/3$	.333
Rotation	deg/sec	$1 / (1/3^{.5})$	1.732
Inertia	kg* m <sup>2</sup>	$(1/3)^3 * (1/3)^2 = 1/27 * 1/9 = 1/243$	.0041

#### Mass Properties

The mass properties of the apparatus are summarized in Table 3. The full scale information was extracted from a ProEngineer CAD model of the ARES concept. The actual scale model information was extracted from an as built ProEngineer CAD model with selected information verified by measurement. The actual hardware corresponds well to the calculated properties. The mass of the airplane increased from configuration 1 to 2 to better reflect the calculated mass. The mass of the AES was greater because the electromagnets holding the airplane are heavier than an equivalent pyrotechnic device would be. The full-scale airplane has a slight x cg offset, however, the x cg of airplane2 is essentially zero for ease of

manufacturing but the error is negligible. The airplane inertias about the center of gravity are higher than prescribed but still within reason.

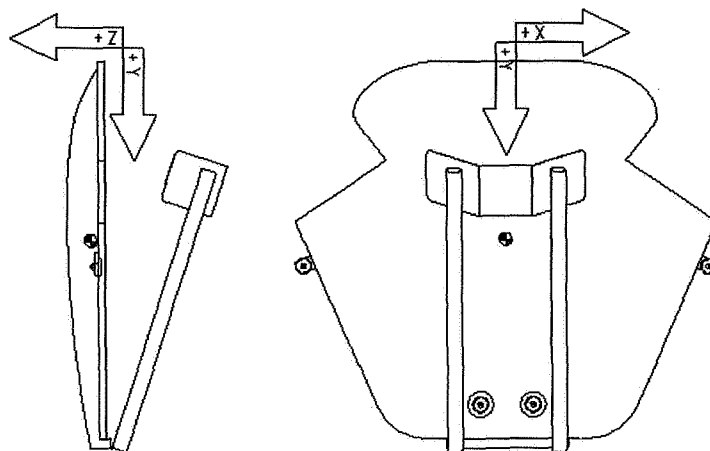


Figure 14. Airplane coordinate system

Table 3. Mass Properties

Item	Unit	Full Scale	1/3 Scale Factor	1/3 Scale Model Calculated	1/3 Scale Model Actual	Percent of Calculated
Mass	$(1/3)^3 = 1/27$					
Airplane configuration 1	kg	170	0.037	6.296	5.176	82.2%
Airplane configuration 2	kg	170	0.037	6.296	6.17	98.0%
AES	kg	56	0.037	2.074	2.81	135.5%
Backshell	kg	149.2	0.037	5.526	5.5	99.5%
cg	1/3					
from airplane coordinate system						
Airplane1 x cg	mm	13.47	0.333	4.49	0.003	0.1%
Airplane1 y cg	mm	1222.00	0.333	406.93	410	100.8%
Airplane1 z cg	mm	193.80	0.333	64.54	69.9	108.3%
from airplane coordinate system						
Airplane2 x cg	mm	13.47	0.333	4.49	0.002	0.0%
Airplane2 y cg	mm	1222.00	0.333	406.93	414	101.7%
Airplane2 z cg	mm	193.80	0.333	64.54	71.9	111.4%
from separation airplane						
Backshell y cg (axial)	mm	529.00	0.333	176.16	138	78.3%
Inertia	$(1/3)^3 * (1/3)^2 = 1/27 * 1/9 = 1/243$					
from airplane coordinate system						

Item	Unit	Full Scale	1/3 Scale Factor	1/3 Scale Model Calculated	1/3 Scale Model Actual	Percent of Calculated
Airplane1 lxx	g-mm <sup>2</sup>	2.99E+11	0.0041	1.23E+09	1.06E+09	86.1%
Airplane1 lyy	g-mm <sup>2</sup>	2.12E+10	0.0041	8.72E+07	9.76E+07	111.9%
Airplane1 lzz	g-mm <sup>2</sup>	3.01E+11	0.0041	1.24E+09	1.09E+09	88.0%
from airplane cg						
Airplane1 lxx	g-mm <sup>2</sup>	3.83E+10	0.0041	1.58E+08	1.79E+08	113.6%
Airplane1 lyy	g-mm <sup>2</sup>	1.49E+10	0.0041	6.13E+07	7.27E+07	118.6%
Airplane1 lzz	g-mm <sup>2</sup>	4.61E+10	0.0041	1.9E+08	2.32E+08	122.3%
from airplane coordinate system						
Airplane2 lxx	g-mm <sup>2</sup>	2.99E+11	0.0041	1.23E+09	1.29E+09	104.8%
Airplane2 lyy	g-mm <sup>2</sup>	2.12E+10	0.0041	8.72E+07	1.10E+08	126.1%
Airplane2 lzz	g-mm <sup>2</sup>	3.01E+11	0.0041	1.24E+09	1.31E+09	105.8%
from airplane cg						
Airplane2 lxx	g-mm <sup>2</sup>	3.83E+10	0.0041	1.58E+08	2.18E+08	138.3%
Airplane2 lyy	g-mm <sup>2</sup>	1.49E+10	0.0041	6.13E+07	7.86E+07	128.2%
Airplane2 lzz	g-mm <sup>2</sup>	4.61E+10	0.0041	1.9E+08	2.76E+08	145.5%
from backshell cg:						
Backshell lxx	g-mm <sup>2</sup>	7.45E+10	0.0041	3.07E+08	3.59E+08	117.1%
Backshell lyy	g-mm <sup>2</sup>	1.21E+11	0.0041	4.98E+08	4.90E+08	98.3%
Backshell lzz	g-mm <sup>2</sup>	7.20E+10	0.0041	2.96E+08	3.59E+08	121.2%

### Results

There were no major surprises in testing. The airplane released cleanly in all cases. The kinematic mounts did not interfere with the release of the airplane. Yet several improvements can be made. Figure 15 shows pictures of the first four tests.

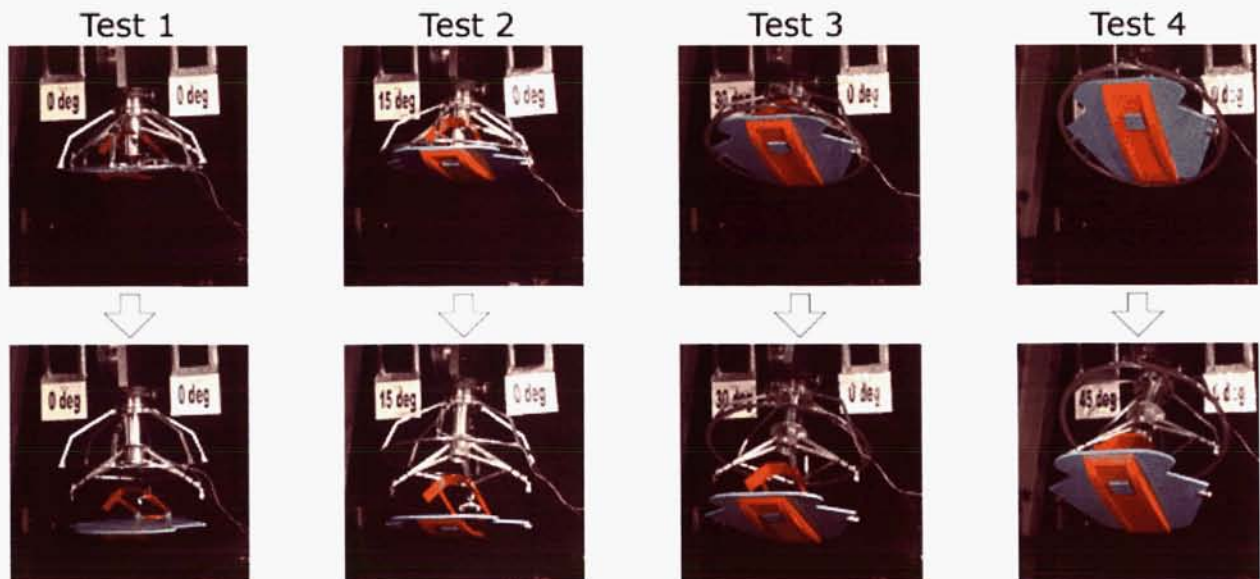


Figure 15. Setup and release of test 1 - 4



Table 4 shows the test matrix. The azimuth refers to the position of the airplane about the release axis. Zenith refers to the position of the apparatus in reference to the vertical. Zero degree is vertical. The roller configuration column refers to the placement of the rings of rollers vertically along the central canister. The first group of tests positioned rollers in all three possible location, top, middle, and bottom. The second group of tests positioned roller sets only on the top and bottom ring. The release trigger point refers to the point at which the airplane is released relative to the top of the parachute can. The airplane was tested in two configurations. The first one had a smaller mass than the second. The video number refers to the video file name. The frame rate was reduced from 500 to 250 frames/sec for some of the high zenith angle tests in order for the video data for each test to fit on one compact disc.

Tests 1 – 39 were conducted with the video camera isometric to the test apparatus to capture movement in all three axes. For tests 40 – 47 several improvements were made. The video camera was moved perpendicular to the motion of the airplane and targets were added. These improvements allowed specific points on the airplane to be tracked without compensating for the angle of the video camera. LED indicator lights showing power to the AES and airplane electromagnets were placed in the camera's field of view. This gave precise information as to when the AES and airplane were released.

**Table 4. Airplane Extraction System Test Matrix**

Test #	Azimuth (deg)	Zenith (deg)	Roller Configuration	Release Trigger Point	Airplane Configuration	Video #	Frame Rate (frame/ sec)
1	0	0	top, mid, bottom	bottom	1	test1a	500
2	0	15	top, mid, bottom	bottom	1	test2	500
3	0	30	top, mid, bottom	bottom	1	test3	500
4	0	45	top, mid, bottom	bottom	1	test4a	500
7	45	30	top, mid, bottom	bottom	1	test7	500
10	90	15	top, mid, bottom	bottom	1	test10	500
11	90	30	top, mid, bottom	bottom	1	test11	500
12	90	45	top, mid, bottom	bottom	1	test12	500
15	135	30	top, mid, bottom	bottom	1	test15	500
18	180	15	top, mid, bottom	bottom	1	test18	500
19	180	30	top, mid, bottom	bottom	1	test19	500
20	180	45	top, mid, bottom	bottom	1	test20	500
21	0	60	top, mid, bottom	bottom	1	test21	250
23	90	60	top, mid, bottom	bottom	1	test23	250
25	180	60	top, mid, bottom	bottom	1	test25	250
26	0	75	top, mid, bottom	bottom	1	test26a	250
28	90	75	top, mid, bottom	bottom	1	test28	250
30	180	75	top, mid, bottom	bottom	1	test30	250
32	0	60	top, mid, bottom	bottom	2	test32	250
33	0	75	top, mid, bottom	bottom	2	test33a	250
36	0	60	top, mid, bottom	50%	2	test36	250
37	0	75	top, mid, bottom	50%	2	test37	250
38	180	75	top, mid, bottom	bottom	2	test38	250
39	90	75	top, mid, bottom	bottom	2	test39	250
40	0	30	top, bottom	bottom	2	test40	500
41	180	30	top, bottom	bottom	2	test41	500
42	90	30	top, bottom	bottom	2	test42	500

Test #	Azimuth	Zenith	Roller Configuration	Release Trigger Point	Airplane Configuration	Video #	Frame Rate
43	0	45	top, bottom	bottom	2	test43	500
44	180	45	top, bottom	bottom	2	test44	500
45	180	60	top, bottom	bottom	2	test45	500
46	0	60	top, bottom	bottom	2	test46	500
47	35	0	top, bottom	bottom	2	test47	500

### Objectives Met

**Table 5. Objectives Met**

Objective	Met	Comments
Demonstrate proof-of-concept for an airplane extraction system from an aeroshell under various axial and lateral loading conditions	Yes	Concept works
Demonstrate no binding as the AES/plane assembly rolls down the parachute can	Yes	AES/airplane assembly does not bind, even with damaged rollers
Demonstrate dynamic clearance between the aeroshell, the AES and the airplane	Yes	No clearance problems
Determine timing sequence for airplane release	Yes	Airplane release at bottom of the stroke is fine
Determine effects of kinematic mounts on release of the airplane	Yes	Kinematic mounts do not effect release negatively
Determine electrical cable clearances	Yes	No cable hang-ups
Determine airplane attitude after release	Yes	Determined from video

### Problems Discovered

One point of interest was that the bottom rollers were damaged after many tests because the airplane extraction system would rebound after airplane release. This is not a problem for the actual flight since the AES must only work once and is then discarded, but it may be a problem if ground testing is required on flight hardware. A wedge or positive stop at the end of travel is being considered to eliminate this motion.

High-speed video revealed a pitching motion in the airplane after it was released for some extreme orientations. This is a problem in two ways. First, the pitch may cause the airplane to hit the backshell or AES under certain circumstances, although it was not observed in this set of tests. Second, the airplane now is starting to tumble. This motion must be counteracted by the drogue chute to avoid problems while unfolding the tail and wings. The ideal case would be to have the airplane to separate without a pitching moment.

There are several possible causes for this pitching. Since the AES and airplane are not symmetric about the vertical parachute can axis, there is a cg offset. This offset can cause the airplane to pitch after separation. Second, after the next to the last set of rollers leaves the track, the AES is free to pitch slightly under the influence of gravity and aeroloads. Third, the electromagnets used to release the airplane and the airplane extraction system contains residual magnetism after they are turned off. Sometimes this causes the aft end of the airplane to release after the wing points have separated. This influence appears small, and will be eliminated with pyrotechnics for the flight hardware. Design modifications are being considered to address the other issues.

### **Future Work**

The next series of subscale tests should have the entire backshell, AES, and airplane assembly free fall in order to capture the effects of dynamics as the backshell rotates and swings during entry. This complex interaction should reveal new insights.

A full-scale high-altitude balloon drop test is scheduled for 2006. This test will include a form, fit and function backshell, AES, and airplane called the High Altitude Drop Demonstrator 2. The goal of the test is to verify all aspects of the EDD at simulated Mars conditions from 30,000 meters in Earth's atmosphere.

### **Conclusions**

Extraction is a critical event in the entry, descent, and deployment sequence for the Mars airplane. This development and subscale testing proves the viability of the concept. Subscale testing demonstrated a clean release of the airplane in every instance. Yet testing also showed that pitching of the airplane needs to be addressed.

### **References**

Wright, Henry S. et al., *ARES Mission Overview – Capabilities and Requirements of the Robotic Aerial Platform*, AIAA 2003-6577

Levine, Joel S. et al., *Science from a Mars Airplane: The Aerial Regional-Scale Environmental Survey (ARES) of Mars*, AIAA 2003-6576

MER Aeroshell Critical Design Review presentations, May 30-31, 2001

### **Acknowledgements**

I would like to acknowledge the contributions of the many people who made this development a success:

- Henry Wright for funding and guidance
- Charles Bailey and Joseph Hickman for assembling and modifying hardware
- Tom Lash and Norman McRae for development of the electromagnetic release system
- Paul Bagby for capturing high-speed video
- Gary Qualls for photogrammetry





# **“Digital” SMA-Based Trailing Edge Tab Actuators for Aerospace Applications**

Robert M. McKillip, Jr.\*

## **Abstract**

A novel approach for providing aerodynamic control using collections of discrete active tab devices was completed recently under an Army-sponsored Phase II SBIR program, and is being developed further as part of a NASA-sponsored effort on UAV control. Each tab incorporates a patented bistable design that uses SMA wires for transitioning between one of two deflection positions, thereby providing a localized perturbation to the sectional aerodynamics at the location of the lifting surface trailing edge. By arranging several such tabs spanwise along a wing or rotor blade, incremental adjustments may be made using these tabs to perform aerodynamic reconfiguration, tracking adjustments on rotor blades, or primary flight control. The device has been prototyped as part of these SBIR research programs, and has been designed so that it may be retrofit on existing rotor blade systems and UAV platforms to support further application development in a variety of aeronautical applications. The underlying concept of using SMA-based actuation for configuration control is directly extendable to additional aerospace systems, including spacecraft applications.

## **Rotor Blade Tracking Application**

Development of the underlying concept for SMA-based actuation of a bistable device originally grew from the desire to provide in-flight adjustment of rotor blades to minimize one-per-revolution vibration. Blade one-per-revolution vibration is often a result of blade aerodynamic and mass mismatch between blades of a given rotorcraft’s “blade set”. This mismatch may be a consequence of assembly tolerance or from unequal wear on in-service blades, and often can be alleviated through placement of balance weights and aerodynamic perturbations via adjustments of both swashplate links and trailing edge tab deflection angles. Aerodynamic adjustments that minimize vibration also typically minimize blade “tracking” deviations, and thus the blade’s track is used to optimize the adjustment process. Traditional blade tracking adjustments are performed by maintenance personnel using specialized hardware, coupled with a series of flight test measurements, to attempt to optimize blade aerodynamics across the helicopter flight envelope. This process is often expensive, as it tends to be iterative in nature. In fact, some current operational military helicopters must devote nearly 10% of their flight hours to track and balance activities.

Clearly, in-flight tracking capability would significantly reduce this cost burden, as all tab tracking changes could be made in one flight without the requirement for periodic landings to stop the rotor and perform manual adjustments. In addition, since tracking adjustments would be easier, they could be performed more often, on an as-needed basis, *thereby providing “trickle-down” benefits of reduced vibration exposure and hence longer service lives for dynamic components*. This motivation spawned the development of the SMA-based actuation system described here, in that the tab deflection adjustments would be performed using SMA wires as the prime mover for an electrically-actuated tracking tab device.

## **“Digital” Tab Implementation**

The system initially developed under U.S. Army Phase I SBIR funding initially replaced the maintenance specialist’s adjustment tools with a pair of agonist-antagonist SMA wires, so that the imposed moments generated from the SMA wire’s phase change would provide plastic deformation of a metal trailing edge tracking tab mounted on the rotor blade (Figure 1). While successful at the conceptual demonstration stage, this design required a means of sensing the blade tab angle in order to properly control the SMA wire material properties to position the tab deflection to a desired angular orientation. In addition, the hysteresis inherent in the SMA wire’s thermal properties made closed-loop control challenging for this application implementation. Under Phase II, this concept was replaced with a “digital” tab device, whereby each discrete tab uses SMA wires to move between one of two positions, thereby significantly reducing

---

\* Continuum Dynamics, Inc., Ewing, NJ

the complexity of both the associated control system (proportional/servo control becomes simply “on/off”) and the tab position sensing (“up/down”) (Figures 2 through 4). Aerodynamic “resolution” of adjustment is provided through the incorporation of several tabs in a spanwise fashion, thus providing true “digital” adjustment for blade tracking.

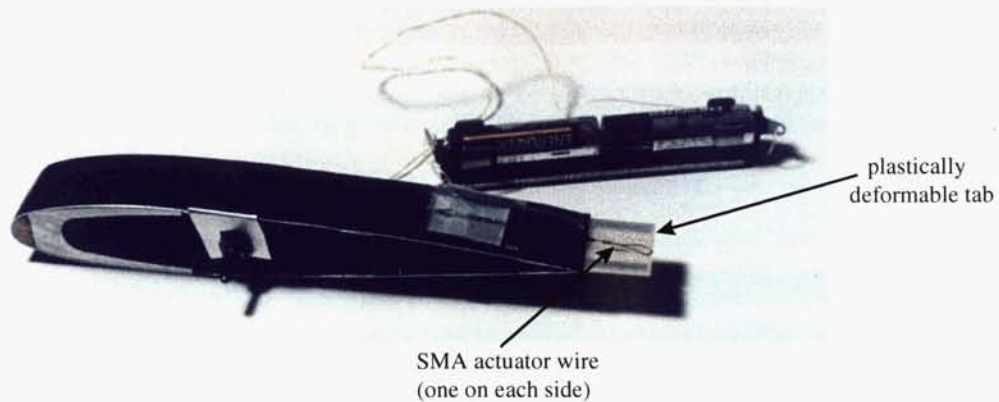


**Figure 1. Phase I concept demonstration for agonist/antagonist SMA-based tracking tab concept.**



**Figure 2. “Digital” tracking tab demonstration concept on trailing edge of a CH-47 blade.**

This design approach change incorporates all the features of the agonist/antagonist plastically-deforming tab, namely:

- Use of SMA wires as prime movers driving pre-stressed structural components in a hybrid fashion provides large strain and force capability for the actuator system, without the attendant bulk required with other “smart” or active materials for enhancing actuator mechanical advantage
- Electric power is only used during transitions for changing tab position
- The devices are retrofit-capable onto existing rotor blades
- The tabs are adjustable in-flight
- The physical size and weight is minimal due to the use of SMA wires as the prime mover

In addition, the digital concept includes the following unique advantages:

- Position sensing is trivial, in that only one of two possible states may exist
- The precise shape of the device is dictated from geometric features of the base material
- Control of the device is simplified to a “change position” command
- Use of multiple spanwise units provides robustness as an individual unit failure implies only a partial degradation in total system performance



- Design of the SMA wire is simplified to specifications on maximum stress/strain required for transition
- Maximum power required is that required to heat only one SMA wire, since the tabs are transitioned sequentially

The basic actuation concept is described referring to Figure 3. Figure 3a shows a notched flat plate element that deflects out-of-plane to the plate when points A-B are forced together. The surface buckles elastically into one of two stable positions, determined by the manner in which the points are drawn together. Figure 3b illustrates the plate prior to installation of the actuation wires but installed on the trailing edge of an airfoil. The deflection results from the pre-stress introduced in the plate, and studies to date have shown that trailing edge deflection angles of  $\pm 25^\circ$  are achievable for acceptable levels of plate stress. Figure 3c schematically shows the pre-strained SMA wires attached to the upper and lower surfaces which, when heated, result in shortening of the wire and a “snap-through” and locking of the plate into the “mirror” position. The heating is directly accomplished by running a current through the wire, since SMA wires have relatively high resistivity. The innovations in this actuator are two-fold:

- The structural or load-bearing component of the actuator is a very simple machine (a notched flat plate). This component is readily fabricated and encapsulated to form a useful aerodynamic surface, and has no bearing surfaces.
- Power is only required to transition the actuator from one position to the mirror position. Once the transition is made, the power to the actuating wire is cut-off and the actuator is “locked” into position as a consequence of its geometric compound curvature.



**Figure 3. Schematic of “SNAP” trailing edge tab:**

**(a) undeformed base plate**

**(b) stressed plate on airfoil t.e.**

**(c) tab with SMA wires**

### Rotor Blade Tracking Testing Activities

Testing of this device to support the rotor blade tracking application included benchtop functional tests, high dynamic pressure tests, high centrifugal field tests, and actual on-rotor testing. These data were used both to support analytical model development for design, and to validate configuration choices for construction and wire attachment.

#### Tab Actuator Benchtop Testing

While an analytical model for tab design was under development, a series of tests were performed on an oversize representation of the tab configuration of Figure 3. These tests were undertaken with the goal of generating a database for analytical model correlation, as well as validating a scaling analysis for performing “nomogram”-like design calculations for similar tab geometries. Aluminum sheets of approximately 4 cm by 8 cm were constructed with a center stress-relief hole, and an offset stud was mounted near the center of the tab, from which a wire cable was mounted in series with a strain gauge load cell. Tests were performed to measure the tab deflection angle with applied cable load, much like an SMA wire would generate on the actuator tab, and notes were made of the displacement and force levels just prior to tab snap-through. These data, taken over a range of tab length to width ratios, thicknesses, offset stud locations, and initial wire pre-strains were ultimately used to validate both in-house CDI finite element (FE) code predictions and commercial FE simulations.

Whereas the super-scale tab testing only included one nominal wire orientation for applying pop-through forces on the base tab material, several different arrangements were fabricated and evaluated at design scale on the benchtop. Two of these configurations, termed pre-prototype configurations, are shown in Figures 2 above and 4 below. Figure 2 oriented the SMA wires in a nominal spanwise orientation, while Figure 4 shows the SMA actuator wires aligned with the blade chord direction. Both configurations could be made to operate successfully, but it was found through assembly of several units that wire pre-tensioning was easiest to perform for the chordwise orientation. Thus, the ultimate configuration, that of a

pair of wires (upper and lower) aligned in a "v"-pattern orientation about the stress relief hole borrowed more heavily from the design experience of the device of Figure 4.

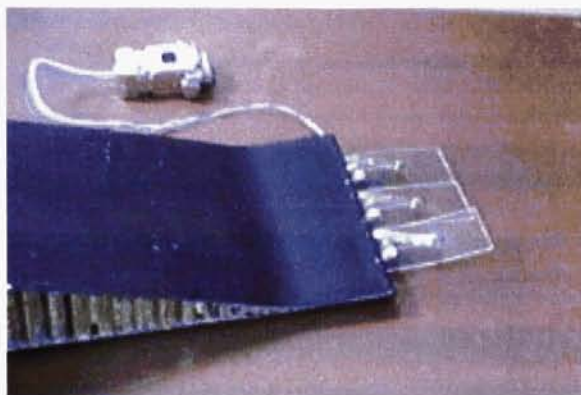


**Figure 4. Pre-prototype benchtop demonstrator tab arrangements, SMA wires mounted on offset studs in chordwise orientation.**

Several base tab materials were evaluated for use, including spring steel, aluminum sheet, and various plastics. Based upon earlier discussions with Boeing engineers about the desire to remove metals from rotating components on aircraft to reduce aircraft signatures, it was felt that the tab design could best support U.S. Army interests if it were made of non-metallic material. Lexan plastic (polycarbonate) was found to have sufficient robustness to effects of temperature and UV radiation that it became the default base material for subsequent actuator design concepts. In addition, aluminum was ruled out when it was determined that the anticipated stresses built up in the outer layers of the base tab material could experience fatigue failure after many pop-through cycles of the tab actuator.

Since further development called for testing of the tab assembly on a full-size rotor system, most likely provided from an aircraft manufacturer or helicopter operator, bonding of the tabs to helicopter blades was required to be a reversible process. Several adhesives and solvents, along with manual installation and removal techniques, were evaluated for their capability to provide sufficient strength in both shear (to counter centrifugal loads) and peel (to maintain bond strength during pop-through and under aerodynamic loading). Tab coupons were manufactured and bonded to aluminum plate and the trailing edge of a composite CH-47 blade section, in order to evaluate shear and peel strength of the combined tab/bonding agent/blade system. Shear tests were instrumented using an in-line load cell, and peel strength was checked manually. Many bonding agents exhibited good shear strength but poor peel performance. Some bonding materials showed good strength in both directions, but poor resistance to applied heat. Ultimately, an epoxy was identified that showed excellent bond strength, and acceptable solvent-based removal performance, for both metal and composite skin blades; this material was used in all subsequent tests performed on combined blades and active tab assemblies.

#### Two-Dimensional (2D) Section Testing

Two separate 2D tests were performed using the active tab assembly. The first was using CDI's 30-cm x 30-cm low turbulence wind tunnel to assess anticipated aerodynamic drag effects of the tab on rotorblade performance. The second was a high dynamic pressure test, to check the two-position tab's potential to pop-through under loading when the section is generating significant lift. This latter experiment used a novel mounting arrangement in order to perform hydrodynamic testing from the side of a small power boat in the Delaware River. Each is described below.

CDI's low turbulence wind tunnel was used to conduct tests on two-dimensional airfoil sections to determine the effectiveness of proposed actuation concepts. The 30-cm x 30-cm tunnel can generate up to 36 m/s flows, which, although not representative of the anticipated aerodynamic environment for the actuators, was suitable for providing a "first look" at aerodynamic drag effects generated by the addition of trailing edge treatments on the airfoil sections.

A two-dimensional section representative of a Bensen B8-M autogiro rotorblade was constructed and installed in the tunnel, mounted on top of a 6-component strain gauge balance. Data from comparison of the baseline section with a full-span tab system shows an increase in a few "counts" of drag on the section (Figure 5). Later testing that included mock-ups of the supporting SMA wires and associated electronics showed these added effects to be minimal, and thus the original data as shown here was used in generating pre-test predictions for full-size rotor tests to follow.

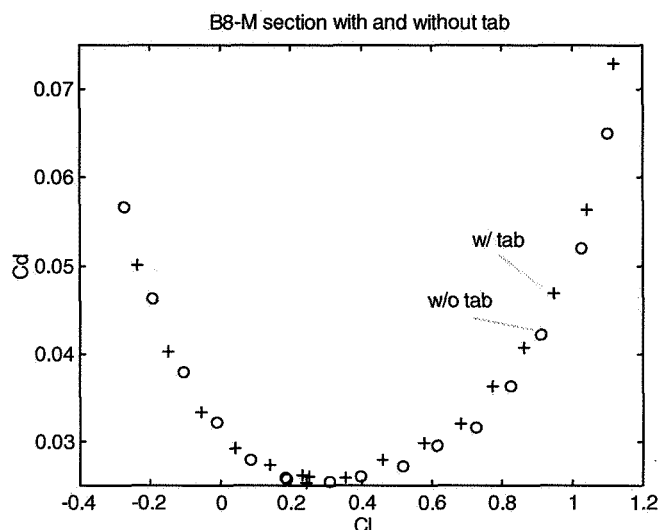


**Figure 5. Two-dimensional section polar from CDI's low turbulence wind tunnel.**

One of the concerns associated with the trailing edge tab design was that the stiffness of the tab geometry would be sufficient to support the sectional pressure difference expected in flight. Design of the tab actuator represents a tradeoff between sufficient base tab material stiffness, in order to provide aerodynamic control, and enough compliance to permit motion with the application of SMA-wire induced strains.

Typical tracking tab locations are near the 75% radius location, so for a typical helicopter tip speed between 200 m/s and 213 m/s, the dynamic pressure at the tab location is approximately 40 N/m<sup>2</sup>. Duplicating this dynamic pressure in a wind tunnel or other aerodynamic facility is difficult and expensive, so an alternative testing method was employed. Since the density of water is approximately three orders of magnitude greater than air, equivalent dynamic pressure may be achieved at speeds of approximately 7.7 m/s. Thus, dynamic pressure tests on a tab-equipped UH-60 helicopter blade airfoil section were performed using a special "oar" with a representative airfoil and two-position tab attached to the end, with the oar placed into the water aside a small power boat. The airfoil was mounted on a long pole to permit its being placed sufficiently far away from the side of the boat hull to eliminate any surface effects from the boat displacement when traveling under power. Instrumentation consisted of a digital inclinometer for measuring approximate angle of attack of the foil, and a handheld GPS unit for measuring boat hull speed. Runs were taken in both upstream and downstream directions on the Delaware River, and despite extremes of both dynamic pressure and high angles of incidence (up to 0.3 radian), the two-position tab did not "pop" through to its alternate position from differential pressure on the tab.

Another operational concern for proper tab actuation was the anticipated high centrifugal environment anticipated for tabs mounted at the 75% radial location. For UH-60 size rotors, this loading can approach 550 g's, and thus the tab may "pop through" from inertial loads, or the SMA wire may deform on the tab under its own centrifugal load, effectively "using up" the available strain energy and rendering the tab inoperative. The latter was surmised to be the case for early versions of SMA-based flap actuators, developed by CDI for application to the V-22 tiltrotor blades on a model rotor set; ultimately, the wire-based actuation mechanism had to provide mechanical guides for the chordwise-oriented actuator wires to eliminate the centrifugal distortion. Although the prototype tab actuator developed here has wires



oriented chordwise, supporting calculations showed that they would not be subject to large strains due to their minimal size and weight.

Testing was nonetheless performed on the tabs using a four-foot diameter model rotor, with the operating rpm boosted to 550 in order to expose the tabs to representative centrifugal loads. In these tests, the tabs were mounted at the blade tip to provide maximal centrifugal stresses for the wires. Testing revealed no problems with the tabs reversing their positions at these g-levels, thus providing confidence for ultimately testing the units on a full-size rotor system.

#### Full Size Rotor Testing

The full-size rotor system used for evaluating the prototype actuation system was a Bensen B-8M autogiro ("gyrocopter"), available for use at CDI (Figure 6). The advantage of using the autogiro test platform is the ease of access to a man-rated rotor system, with all of the system integration issues associated with a full-size flight vehicle. Since that aircraft is an autogiro, and not a helicopter, an alternate means of spinning the rotor was required so to avoid having to fly the aircraft with the tab devices installed. This drive system consisted of a pre-rotator assembly that used a flexible shaft that could be driven by a pulley mounted inboard of the propeller hub on the autogiro's engine.



**Figure 6. Autogiro with 65 HP engine and drive system used in full-size rotor tests.**

Test objectives were twofold for the full-size rotor experiments: first, it was desired to demonstrate tab effectiveness in controlling tracking angle of the rotor blades from positioning of individual tabs on the rotor; and second, it was desired to assess the rpm range over which reliable electrical actuation of tab displacement could be achieved.

Tabs were installed onto the Bensen blade set from the 0.71 to the 0.80 radius location, with each tab assembly fabricated using an aluminum base plate holding four 2.5-cm by 5-cm tabs. Three tab plates were mounted on each blade, with a Lexan separator plate bonded between the blade surface and the mounting plate in order to facilitate removal of the tab system from the blade at the conclusion of the test program (the removal agent for the tab system is known to attack certain plastics). To simplify the test program, only one set of four tabs was fabricated using SMA wires, since the purpose of the test was to demonstrate performance and not provide a complete system installation. As a result, the control electronics were mounted at the rotor hub, and separate flat ribbon wires were attached to the bottom of the blade to provide electrical power to each SMA tab. While a true prototype installation would include local surface-mounted MOSFETs for control of individual SMA wire excitation at each tab plate, this simplification helped expedite the completion of the full-size rotor test program. Details of the tab mounting arrangement may be seen in Figure 7, and the hub electronics in Figure 8.

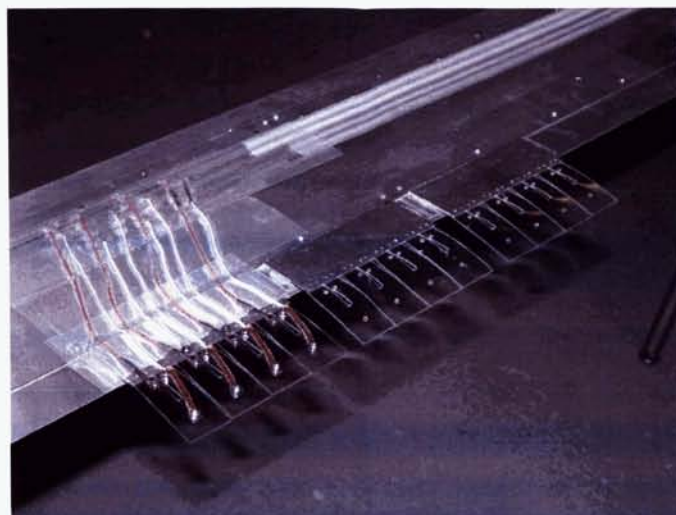


**Figure 7. SMA-driven bi-modal tabs on underside trailing edge of Bensen B8-M blade section.**

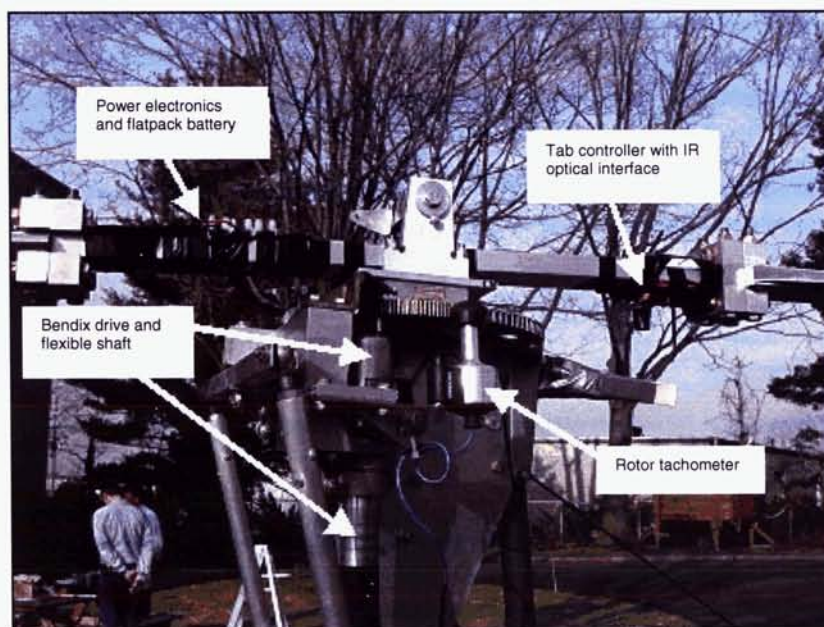


**Figure 8. Details of hub on Bensen autogiro test platform.**

In order to check blade track angle, a separate video camera installation was mounted in the rotor plane, with a calibration card constructed and the blade ends colored (white/black) to differentiate them on the videotape. The videotape was then viewed on a frame-by-frame basis to measure the blade tip position as a function of tab deflection angle. For the extreme case of all tabs on the "black" blade deflected down, and all tabs on the "white" blade deflected up, a tip deflection difference of 3.9 cm was measured from scaling displacements from the video monitor. This compares favorably with a predicted value of 4.5 cm, since the predicted displacement does not account for any lift rolloff at the most inboard and outboard locations of the deflected tab assemblies. Screen capture of the rotor plane video may be seen in Figure 9.





**Figure 9: Still video of white and black blade position from rotor plane camera.**

Post-test analysis and further development testing revealed that the Lexan plastic material used to form the base bender element eventually took a “set” due to the continued exposure to bending stresses, and thus developed a preferential orientation that would make the tabs less robust. As a result, further development produced a tab with equivalent stiffness but no tendency to plastically creep, due to the use of spring steel for its bender element. Shown in Figure 10 is a demonstration article that incorporates a steel base with Kapton tape overcoat and flush attachments of the SMA wire assemblies, along with the flatpack 6 volt battery used for its actuation.



**Figure 10. Metal-based tab demonstration device with flatpack battery.**

### **Distributed UAV Flight Control Application**

High-altitude, long-endurance (HALE) remotely-operated aircraft (ROA), or unmanned aerial vehicles (UAVs), are designed to operate at extreme altitudes for many days, in order to serve as platforms for science missions, earth observation, or communications and data relay stations. In order to meet the long duration requirements for these missions, these aircraft are designed to minimize drag and weight, and thus are characterized by having large wing spans and significant aeroelastic response under both steady and dynamic loading conditions. This inherent flexibility in these aircraft may sometimes lead to flight dynamics issues and instabilities, as witnessed with the breakup of the HELIOS aircraft over Hawaii during flight investigations while operating with alternate energy sources.

These aeroelastic issues may be mitigated to a considerable extent for these vehicles if the loading on the large aspect ratio wings may be redistributed in flight, using distributed multiple actuators. Such an approach provides enhanced robustness to the aircraft platform, in that multiple actuators would easily accommodate the failure of a few to respond to commands, but if these actuators were conventional, servo-type systems, this feature would be overshadowed by an unacceptable weight and power penalty.



Conventional electric servo actuators incorporate electric motors that drive a gear train that ultimately is connected to a control arm, on which is also mounted a potentiometer for sensing actuator displacement. Thus, the positioning control and the actuator impedance are provided only while the electric motor draws power from its energy source. Use of the SMA-based actuator described for the rotor blade tracking application would be an ideal alternative, in that it would permit spanwise distributed load modification with minimal electrical power expended during the reconfiguration process. NASA is presently sponsoring CDI in an SBIR effort directed at investigating the use of these snap-through SMA-based actuators in support of HALE-type UAV aircraft control. Results to date in this investigation are described below.

#### UAV Application Design Challenges

Since the detailed design specifications for a future NASA HALE ROA/UAV are yet to be completed, it was felt prudent to consider HALE vehicle operating features in the actuator design, but size the actual device to be more immediately applicable to potential test platforms, such as CDI's 2m span electric radio control (R/C) model aircraft, and the two NASA Dryden's APV-3 test aircraft. Fortunately, these two platforms are roughly the same size, and thus it was decided to base the actuation sizing on a compromise that would accommodate each aircraft type. Fundamental to each actuation concept is its application in a distributed fashion, so that several (possibly many) of them would be arrayed along the trailing edge of the UAVs lifting surfaces. Sizing of each individual actuator was selected to provide:

- Desired flight control forces/moments, dictating a minimum ratio of actuator to surface chord length;
- Appropriate speed of actuation, thus impacting maximum wire diameter used;
- Sufficient stiffness to support operational aerodynamic loads, fixing a minimum thickness for the base material.

Key factors in the design considerations applied included operational environment, endurance, robustness, actuator weight and power consumption. HALE ROA/UAV systems operate at altitudes in which the ambient air temperature is approximately  $-48^{\circ}\text{C}$ , and thus the actuator may require insulation on its wires to mitigate the power lost through ambient cooling to the atmosphere. Endurance requirements for these actuators would flow from possible HALE missions lasting from several days to several weeks. While use of multiple, distributed actuators provides some robustness relief in that single actuator failures represent graceful degradation of control capability (vs. catastrophic), the actuators nonetheless should be capable of accommodating multiple flights/missions without replacement. Standard practice for SMA wire-based actuators has shown that as long as the wire strains are kept below 3% in actuation cycles, millions of repetitions are possible. For the actuation systems here, actual wire stress changes in the discrete actuation system varied from 0.5% to 1.0% depending upon end termination of the wire that stretches across the base tab material.

Robustness design goals imply that all material stresses are kept well below limiting values, and the opportunity for failure be mitigated as much as possible. The actual stresses on the base plate assemblies are well within linear bounds below yield, and failure modes were reduced in the actuation elements by reducing the number of parts required in assembly. Toward this end, use was made of custom-fabricated SMA wires having metal balls welded onto their ends. By using a welded ball with a diameter twice that of the wire, the wire could be "dropped into place" on the base tab assembly through insertion into a slot created in the base manufacturing process. This approach provided a convenient mechanical means for coupling the SMA wire to the base material (i.e., the actuator armature), but continued experimentation with this approach revealed that the stress imposed at the junction of the weld could be past yield if the wire were tensioned at an angle nearly parallel to the surface of the base tab. Put another way, the ball end fitting was not adequate if the wire had significant non-axial stresses at the weld point. This observation resulted in a design having an offset mount for the actuating SMA wires.

Weight considerations on the actuation schemes, both continuous and discrete, were actually a secondary issue, as it was a fall-out effect from material choice based upon actuator performance requirements. Basic stiffness requirements dictate a minimum actuator thickness, and the fact that the buckling-enhanced actuation concept routinely induces stresses on the base material showed in previous actuator implementations that plastic base structures are inadequate due to their creep properties. Thus, the design of these actuation systems has routinely used tempered steel (spring sheet stock) for the base plate material. Despite the use of steel components, the net weight of these actuators, when compared against conventional servo-system components, is almost insignificant.

Power consumption issues, however, show a clear bias in favor of the use of discrete actuator concept, when possible, over any continuously deflectable device. When comparing power required to hold a given actuator position, the discrete actuation concept requires none, while a conventional servo-based (motor driven) actuator will require steady currents of roughly comparable levels. This is in large part due to the fact that static servo holding stiffness operates the underlying electric motor at near stall torque levels, a very inefficient regime for these electromechanical components. Protracted operation holding a given deflection would impose a significant power drain on the HALE aircraft, limiting its endurance.

Two design variants were investigated, where the wire was electrically actuated at each end with a potential applied across the entire wire length, and a second where the wire was grounded on both ends and an additional electrical connection was made at the center of the SMA wire. Initial work with the center actuated design revealed that adjustment of wire tension through the height change of the center actuation point was difficult to achieve repeatedly. Subsequent work with the end-point actuated tab system showed that it suffered in being able to repeatedly actuate the system without shearing off the ball end fittings. Thus, the final configuration realized in this design process was a hybrid design that incorporated features from both the center point actuation design and the end point actuation system. Shown in Figure 11 is the dual tab assembly, where two SMA wire-actuated discrete tabs are mounted to a "sandwich" of printed circuit board, with the two tensioning straps having a triangular shape added to promote the snap-through effect of the base tab when the wires are tensioned. This tab design also incorporated customized screw-adjustable crimps at the inner edge of the tab assembly, permitting rapid wire tensioning for optimum tab performance.

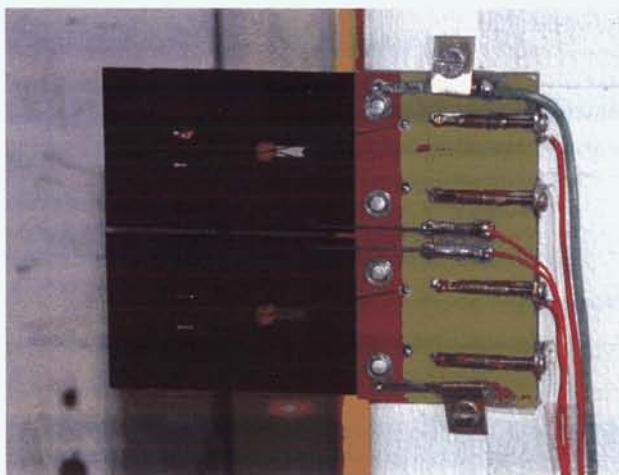


**Figure 11. Final Phase I configuration for dual discrete tab system.**

#### Electronic Integration Design/Testing

Electronics and software design for controlling the groups of individual tab actuators has been investigated as part of the integration work, since the collection of multiple tabs would be interfacing to a single standard servo connector for both the flap and the aileron assemblies for applications to both CDI's R/C airplane and the APV-3 wing. While having multiple tab actuators provides a means of mechanical redundancy for providing trailing edge control, both signals and power must be supplied to all to make them function as a group. Brute force approaches for directly wiring each and every tab actuator to a central controller would be unacceptably heavy and complex, due to the massive amount of wire required for providing current to each individual SMA wire. Instead, electronics incorporating extremely small microcontrollers is being used for a serial-bus network that determines which actuator to energize and for how long. The target microcontroller is the Microchip PIC12F675 family, an 8-pin SO-8 surface-mounted device that has an internal clock and is reprogrammable in-circuit via FLASH memory.

Two schemes were investigated for localized control and communication on this serial bus network for interconnected tab actuators. The first involves the direct device addressing from a "master" microcontroller for actuation, whereby a master/slave(s) network is constructed with the master requesting



an individual tab to change its state through serial commands that include the identifier of the tab device. The second scheme attempts to eliminate the assignment (and/or cataloging) of individual tab actuator identification codes by incorporating a "daisy-chain" interconnection of the tabs, where the most inboard tab microcontroller strips off the first command signal (pulse) and sends the rest down the serial databus to all the other actuators. This scheme allows for identical software to run on all tab actuator microcontrollers, but interrupts the signal coming from the master unit at each tab station, potentially impacting robustness. However, this same re-broadcasting technique can also be viewed as boosting the signal of the transmitted pulse train as the signals propagate spanwise from inboard to outboard actuator unit.

Printed circuit boards compatible with the dual tab design seen in Figure 11 are shown in Figure 12, along side the tab assembly and a pen for scale comparison. The board has solder pads that directly accept a programming header so that software changes may be made in-circuit, if necessary.

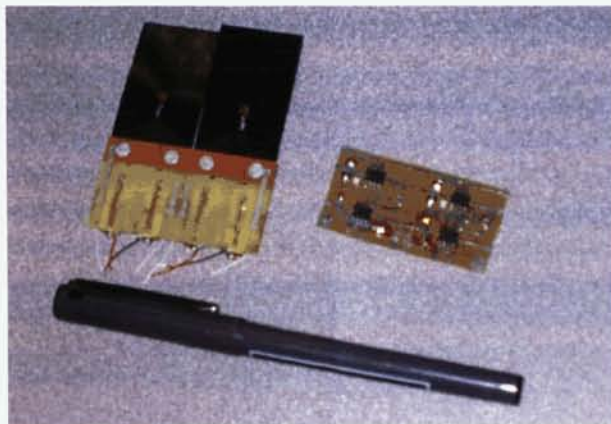


**Figure 12. Dual tabs and associated PB with surface mount PIC microcontroller and dual power MOSFETS.**

Installation of the actuators on CDI's model aircraft was expedited through the use of an extra control channel for the model. Since this model lacks a rudder, an additional control channel was available from the hand controller that had an output on the aircraft receiver, but not servo actuator that would connect to it. Thus, an auxiliary roll command channel was constructed using the output of the rudder command to drive a "master" microcontroller that, in turn, sent out serial daisy-chain tab command signals to both the left and right wing actuators. This model arrangement was flown, and found to exhibit moderate roll effectiveness, despite the fact that a full span complement of active tabs was in fact not driven from these serial command sequences. Testing on this configuration continues, along with integration efforts to support tests on NASA's APV-3 aircraft.

### **Other Possible Aerospace Applications**

Other aerospace applications suggest themselves for use of this actuation concept. While initially developed as a trailing edge control component, the fundamental nature of an SMA-actuated over-center spring like system has a variety of other possible uses. The essential features of this actuation concept are captured in a simple example. If a structural member, such as a beam or plate, is buckled and placed between two end constraints (either pinned or cantilevered), the beam (or, actuator "armature") will assume one of two possible equilibrium shapes, representing the minimum stress condition that satisfies the end conditions (Figure 13). By attaching pre-strained, opposing SMA wires on each side of the buckled member, and heating the most elongated SMA wire, one may induce a moment within the buckled structure (at the SMA connection points) that forces the base material back toward its other equilibrium position. As this induced moment is increased, the buckled structure will eventually move to a shape where the incremental moment required to produce additional motion vanishes, and then rapidly switch, or "snap" or "pop", to its other equilibrium position. This behavior is often called "snap-through" or "oil-canning" in the structural community, and is characterized by linearly elastic material properties but large (nonlinear) deformations.



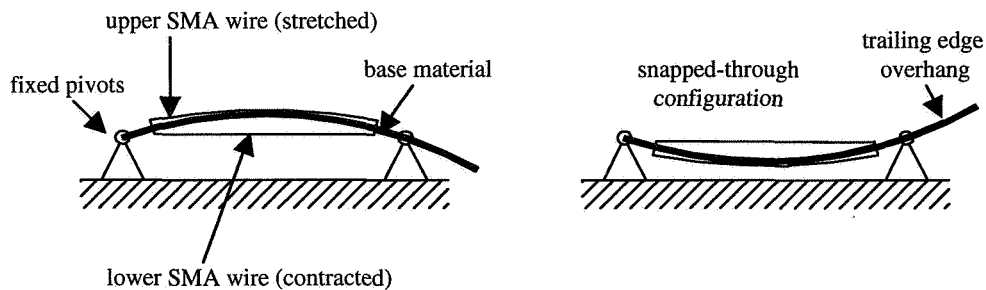


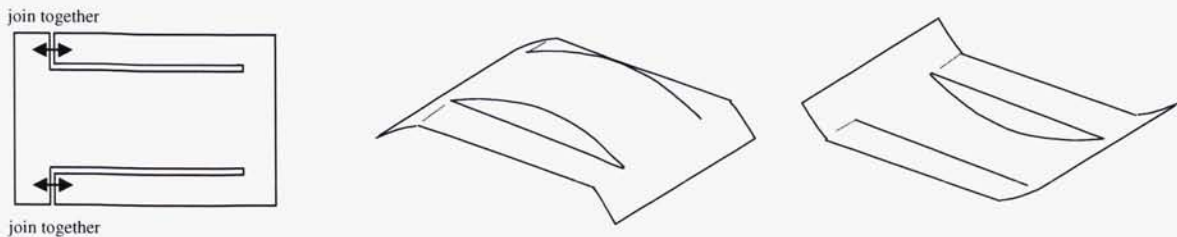
**Figure 13. One-dimensional example of a “snap-through” SMA-driven actuator, showing pinned constraints and optional overhang.**

The actual work performed by this type of actuator as prime mover can come from several sources:

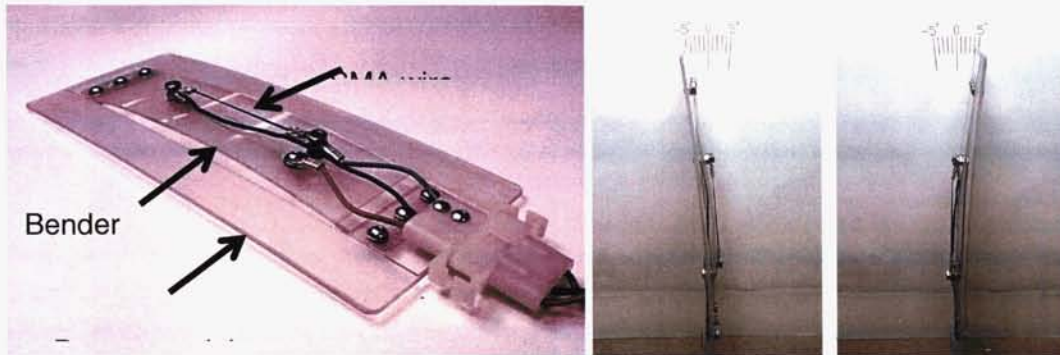
- the linear motion of the center of the buckled beam may be used to drive a linkage between two different locations;
- the change in slope of the end points of the beam may be incorporated as a form of angular orientation or camber control;
- the snap-through in one direction may influence the convex or concave shape of a doubly-curved planar surface (such as on the trailing edge tab device above); or
- the buckled structure may induce relative forces and moments between two disparate locations on a flexible base structure (particularly if the base material has cantilever end constraints).

A simple comparison with a notional miniature linear actuator for aerospace use [1] reveals this concept's considerable advantages over motor-driven mechanisms. If one matches the end-point stroke and displacement of the device of [1] using the linear motion of the snapping arch shown above, one realizes a *weight reduction of 91%*, since the pre-stressed snap-through element performs the same useful work as a stepping motor/ball screw combination. This weight savings is effectively due to the replacement of a motor-driven system with a “reversible actuated spring” unit. Of course, similar devices may be combined in series or in parallel to provide complex, large deformations in multiple directions as a complete mechanism system. Several examples will be sketched below to better visualize these configurations.

Figure 14 shows a method for forming a bi-stable actuator from a flat plate that produces a change in slope between its two ends. The center portion of the stamping comprises the buckled member, while the two side strips, when joined as shown, provide the geometric constraint that keeps the center piece pre-stressed. SMA wires mounted on the upper and lower surface of the buckled member are used to “pop” the device between the two possible stable positions. Figure 15 shows a three-position actuator, similar to that in Figure 14, but uses two nesting pre-stressed members that are cantilever-mounted on either side of a cut-out rectangular base support. By snapping one or the other pre-stressed arches through the cut-out area, one can generate three different slopes between the ends of the base support, or equivalently, an up-neutral-down type of output for the end displacement (Figure 16). Simple extensions to that mechanism, ones that include other nested buckled members above and below these two, provide even higher “resolution” of the relative angles between the two end points of the buckled members. Combinations of these three-or-more-position actuators distributed across a planar surface could provide complex warping of the base plate or planar surface to provide localized camber and shape control. Several actuators ganged in *series* would produce additive changes in base material slopes, or, very large end displacements (Figure 16). This large motion response is possible even while limiting the strain of the SMA wires to less than 3%, a level that is suitable for millions of cycles of operation.



(a) stamping (b) assembled,  $\frac{3}{4}$  view (c) popped-through,  $\frac{3}{4}$  view  
Figure 14a-c. Bi-stable actuator formed from a flat plate, incorporating three parallel strips.



d) demonstration device implementation and actuation response  
Figure 14d. Bi-stable actuator formed from a flat plate, incorporating three parallel strips.

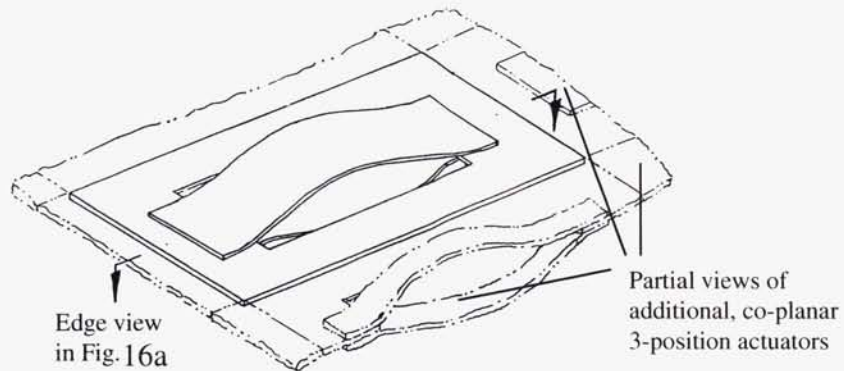


Figure 15. Co-planar three-position actuators for compound geometry control.

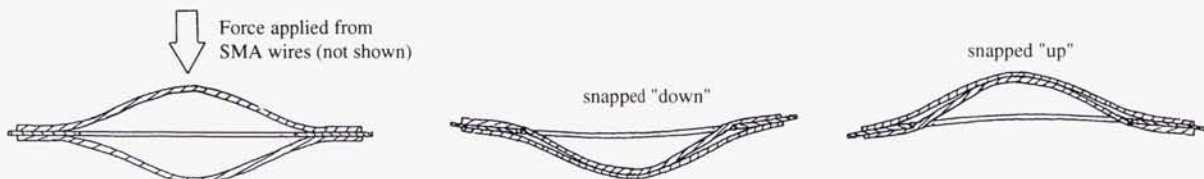
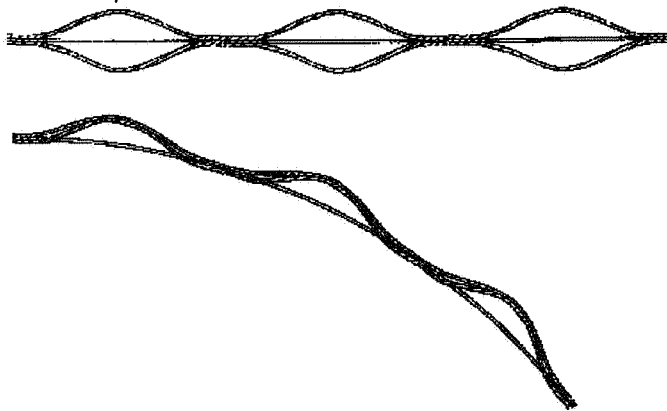


Figure 16a. Three-position actuator showing base support bending from snap-through action.



**Figure 16b. Three-position actuator in series arrangement for large displacement application.**

### **Conclusions**

An actuation system incorporating SMA wires to reorient a buckled member has been described, with a focus on its use as a trailing edge control device for aerodynamic modifications. Applications to helicopter rotor blade in-flight tracking, and UAV spanwise aerodynamic load control have shown that the small form factor, minimal power requirements, and simplicity of design make it an attractive alternative to conventional aerodynamic control effectors. Future use in other aerospace applications will benefit from the attractive weight and size offered in such a device.

### **References**

- Asadurian, A., "Miniature Linear Actuator," Proc. 34<sup>th</sup> Aerospace Mechanisms Symposium, NASA CP-2000-209895, May 2000.
- Bilanin, A. J., and McKillip, R.M., Jr., "Actuation Device with At Least Three Stable Positions," U.S. Patent No. 6,345,792, February 12, 2002.
- McKillip, R.M., Jr., "Remotely Controllable Actuating Device," U.S. Patent No. 5,752,672, May 19, 1998.
- McKillip, R.M., Jr., "'Digital' Tracking Tabs for One-per-Rev Vibration Reduction," Proc. 59<sup>th</sup> AHS Annual Forum, Phoenix, AZ, May 2003.
- McKillip, R.M., Jr., "Actuating Device with Multiple Stable Positions," U.S. Patent No. 6,220,550, April 24, 2001.



# Development of a Forced Oscillation System for Measuring Dynamic Derivatives of Fluidic Vehicles

B. C. Trieu\*, T. R. Tyler\*, B. K. Stewart\*, J. K. Charnock\*, D. W. Fisher\*,  
E. H. Heim\*, J. Brandon\*, and S. B. Grafton\*\*

## Abstract

A new Forced Oscillation System (FOS) has been designed and built at NASA Langley Research Center that provides new capabilities for aerodynamic researchers to investigate the dynamic derivatives of vehicle configurations. Test vehicles may include high performance and general aviation aircraft, re-entry spacecraft, submarines and other fluidic vehicles. The measured data from forced oscillation testing is used in damping characteristic studies and in simulation databases for control algorithm development and performance analyses.

The newly developed FOS hardware provides new flexibility for conducting dynamic derivative studies. The design is based on a tracking principle where a desired motion profile is achieved via a fast closed-loop positional controller. The motion profile for the tracking system is numerically generated and thus not limited to sinusoidal motion. This approach permits non-traditional profiles such as constant velocity and Schroeder sweeps. Also, the new system permits changes in profile parameters including nominal offset angle, waveform, and associated parameters such as amplitude and frequency. Most importantly, the changes may be made remotely without halting the FOS and the tunnel.

System requirements, system analysis, and the resulting design are addressed for a new FOS in the 12-Foot Low-Speed Wind Tunnel (LSWT). The overall system including mechanical, electrical, and control subsystems is described. The design is complete, and the FOS has been built and installed in the 12-Foot LSWT. System integration and testing have verified design intent and safe operation. Currently it is being validated for wind-tunnel operations and aerodynamic testing. The system is a potential major enhancement to forced oscillation studies. The productivity gain from the motion profile automation will shorten the testing cycles needed for control surface and aircraft control algorithm development. The new motion capabilities also will serve as a test bed for researchers to study and to improve and/or alter future forced oscillation testing techniques.

## Introduction & Background

Forced oscillation testing is traditionally used to investigate the dynamic derivatives of vehicle configurations. A model is oscillated one frequency at a time at various amplitudes. Balance data, angular position and rate data are measured and recorded. The data set corresponding with a model mass and inertias is reduced to determine the dynamic derivative coefficients. The coefficients are used in damping characteristic studies, and used in simulation database for control algorithm development and performance analyses. Test vehicles may include high performance and general aviation aircraft, re-entry spacecraft, submarines and other fluidic vehicles.

Historically, the forced oscillation testing hardware has been an induction motor driving a crank and linkage mechanism to provide oscillatory motion. Figure 1 shows an existing system, formerly designed and built for the 30- by 60-foot Langley full-scale tunnel that can be configured to oscillate a model in roll, yaw and pitch. The system is limited to sinusoidal motion having the frequency controlled by motor speed and the amplitude determined by the mechanical linkage. Oscillatory frequency may be changed remotely by changing the motor speed. However, to change amplitude, the oscillation hardware and the tunnel must be halted and the linkage mechanism manually reconfigured.

---

\* NASA Langley Research Center, Hampton, VA

\*\* Vigyan, Inc., Hampton, VA

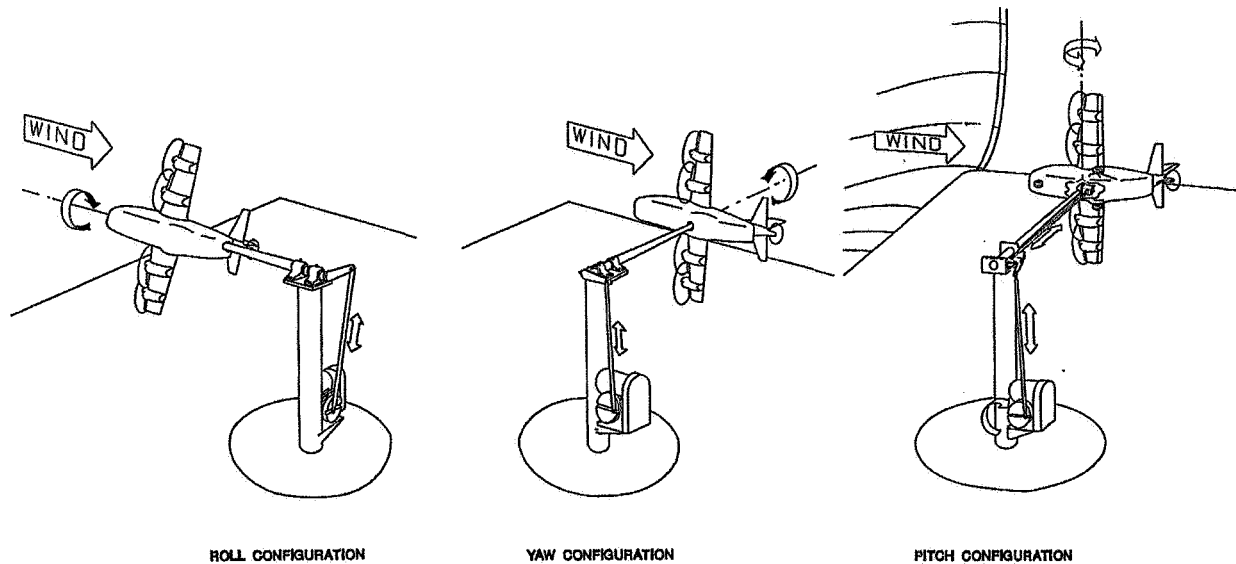


**Figure 1. Existing Forced Oscillation System (FOS)**

The existing system is operationally inefficient thus keeping wind tunnel productivity low. Beside the need to halting the wind-tunnel and the FOS system for amplitude change, the inherent one frequency at a time data gathering is slow and time consuming. Many data points are needed to construct a frequency response curve for any given aerodynamic derivative coefficient, and there are many coefficients for any given vehicle configuration.

In addition to operational inefficiency, the motion generated by the existing system is limited to sinusoidal profiles only. Other motion profiles including ramp and arbitrary waveforms are useful in aerodynamic testing. Low-speed constant ramp may be useful for quasi-static testing; and arbitrary waveforms as used in Schroeder sweeps can improve dynamic testing efficiency by measuring the full frequency response spectrum of the aerodynamics behavior instead of the traditional method of one frequency at time testing<sup>1</sup>.

The vision for a new FOS is to create a system that greatly enhances forced oscillation testing capabilities. The new system should be able to oscillate not only in sinusoidal motion but also other profiles that may be beneficial for aerodynamic testing. The system should enhance productivity such as reducing model setup time and reducing run time needed to collect a data set.

### **System Requirements**

The overall design goals of the new FOS included the ability and flexibility to oscillate a model in sinusoidal as well as non-sinusoidal motion profiles. The system should be able to operate safely and efficiently – it should be able to operate with different amplitudes and frequencies as well as different motion profiles without the need to stop the test and mechanically change the system.

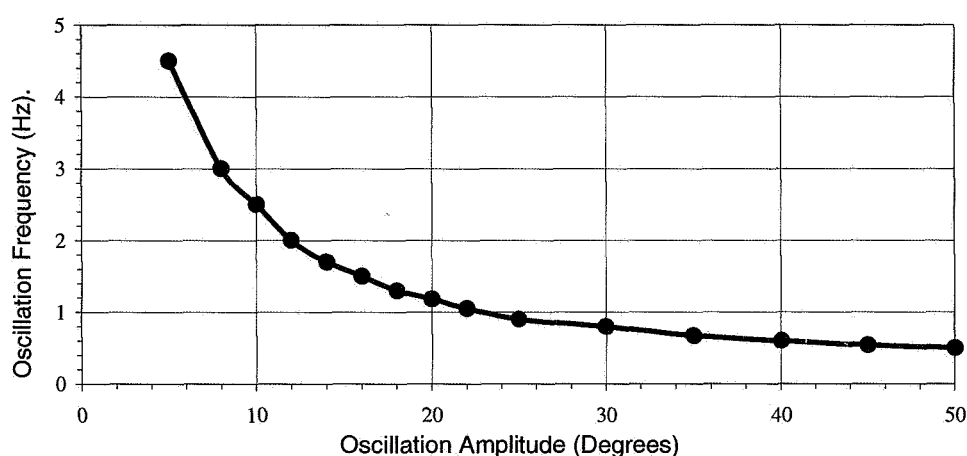
Technical requirements for use in the design of the system were derived from free-flight models. Often, it is desirable to use the same model for lower development cost; i.e., the same model design may be used in wind tunnel, free flight, and drop model tests. Using the same model type of same scale has the added benefit of avoiding potential inconsistencies which can occur from dynamic scaling.

The two model classes used to establish requirements were based on typical fighter configurations with characteristics listed in Table 1.

**Table 1. Model Characteristics**

Model Class	"90-lb"	"200 lb"
Length, L	1.83 m	3.05 m
Wing Span, b	1.22 m	2.83 m
Mass, M	40.8 kg	90.7 kg
Roll Inertia, $I_x$	1.36 kg m <sup>2</sup>	5.69 kg m <sup>2</sup>
Pitch Inertia, $I_y$	10.71 kg m <sup>2</sup>	40.00 kg m <sup>2</sup>
Yaw Inertia, $I_z$	11.39 kg m <sup>2</sup>	42.44 kg m <sup>2</sup>

Traditionally, models are sinusoidally oscillated to determine the dynamics derivatives of a vehicle configuration and then scaled for use in the full-size vehicle control and stability system studies. For the model sizes in Table 1, Figure 2 shows the theoretical desired frequency versus amplitude of oscillation for a non-dimensional frequency constant  $k$  of 0.18. For the selected constant  $k$  and model classes, the dynamic free stream velocity is usually limited to low speed dynamic pressures<sup>2</sup>.

**Figure 2. Theoretical frequency vs. amplitude of oscillation**

The 12-Ft Low-Speed Tunnel was selected as the primary facility for the new FOS. The tunnel has a dynamic pressure of up to a  $Q$  of 48 kPa (7 psf) ( $V = 23.5$  m/s (77 ft/sec) at standard sea level conditions) which meets the frequency scaling factor and satisfies the low speed requirement. In addition, this tunnel has an arc-sector model support system that provides pitch and yaw static positioning of a model and can be modified for use with the new forced oscillation system. However, the existing 12-Ft arc-sector support model system was designed for static testing only with loading limitations as listed in Table 2. The model support system needs to be analyzed for the additional dynamical forces to prevent overloading and to prevent undesirable structural vibrations. From the static load limitations, the existing model support system can sustain the 200-lb model class but with reduced normal force capacity (712 N or 160 lbf).

Along with model support system limits, the balance used to measure dynamics and aerodynamic forces during testing also imposes additional design constraints to the system. For both the 90-lb and 200-lb model classes, the FF-10 balance was used. Table 2 also lists balance loading limits.

Additional derived requirements for performance and operational efficiency included:

- Range of displacements  $\pm 170$  deg
- System accuracy  $\pm 0.05$  deg

Finally, the new FOS must be integrated with the existing model support system, data acquisition system and tunnel safety operations.



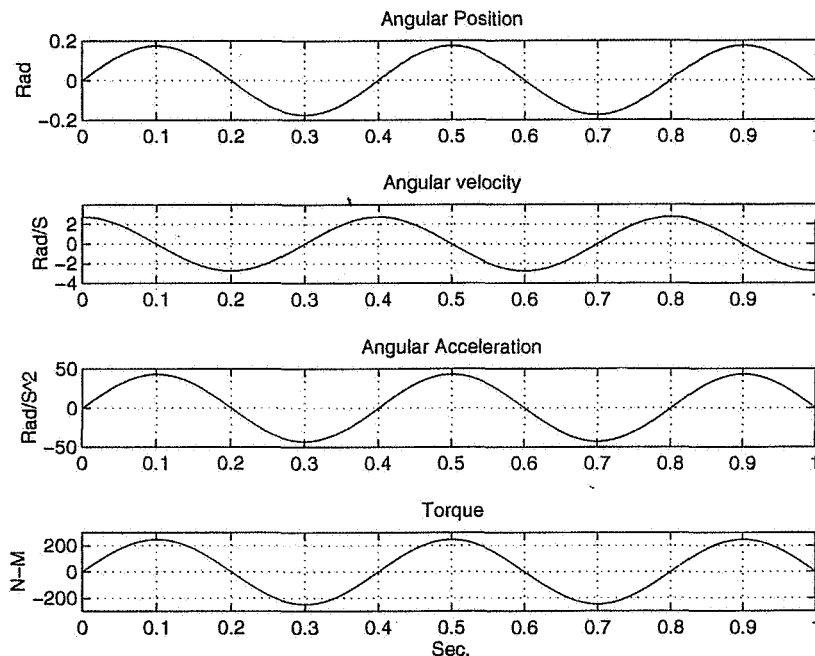
**Table 2. Loading Limitations**

	12-Ft Model Support System	FF-10 Balance
Model Mass	81.65 Kg (180 lbf)	--
Normal Force	800.68 N (180 lbf)	1780 N (400 lbf)
Axial Force	800.68 N (180 lbf)	890 N (200 lbf)
Side Force	800.68 N (180 lbf)	890 N (200 lbf)
Roll Moment	101.7 N-m (900 in-lbf)	141 N-m (1248 in-lbf)
Pitch Moment	203.4 N-m (1800 in-lbf)	226 N-m (2000 in-lbf)
Yaw Moment	203.4 N-m (1800 in-lbf)	226 N-m (2000 in-lbf)

**Design Analysis**

Concept studies were performed to arrive at a system design that would satisfy the design goals for conducting dynamic derivative studies. Instead of using mechanical linkages to achieve motion profiles, the new design is based on a tracking principle where a desired motion profile is achieved via a fast closed-loop positional controller. The motion profile for the tracking system is numerically generated and thus not limited to sinusoidal motion. It permits non-traditional profiles such as constant velocity and Schroeder sweeps. This new design approach simplifies the mechanism design but requires more emphasis on drive system and motion control design as well as system integration.

From the model classes and motion profile requirements, inverse analyses were performed to determine the required actuating torque and speed to achieve the desired frequency and amplitude. Figure 3 is a typical inverse dynamic analysis. Using the roll inertia for the 200-lb model, the peak torque of 246 N-m is required to generate an oscillation of  $\pm 10$  degrees at 2.5 Hz as shown. Analyses were performed for frequency and amplitude combinations as shown in Figure 2. Table 3 summarizes the inverse dynamic analysis results for sinusoidal motion profiles meeting the theoretical frequency versus amplitude of oscillation curve.

**Figure 3. Inverse analysis result for a motion profile of 10 degrees at 2.5 Hz**

**Table 3. Inverse dynamic analysis results for determining peak torque**

Freq (Hz)	Amp (deg)	Torque (Nm)	Speed (RPM)
0.5	50	50	26.2
0.6	40	57	25.1
0.8	30	76	25.1
0.9	25	80	23.6
1.2	20	114	25.1
1.5	15	133	23.6
2.5	10	247	26.2
3.0	8	284	25.1
4.0	6	378	25.1
4.6	5	417	24.1

From the inverse dynamic analyses, the torque and speed required to generate the sinusoidal motion are used to design and size the actuator system. Table 3 indicates that a torque multiplier is needed to meet the high torque and low speed requirements. High performance servo drive systems (for low and medium inertia rotors) of interest are capable of about 3000 RPM at a rated constant torque. The required high output torque and cyclic loadings lead toward a cycloid drive for long life and high momentary overload margin. The reduction ratio of the cycloid torque multiplier is selected to match motor speed and rotor inertia with expected total inertia load<sup>3</sup>. Typical high performance servo drives are tuned to operate most stable when having a reflected inertia ratio of about 5:1. Optimization of design parameters including motor torque, speed, reduction ratio, reflected inertias and spatial constraints for packaging led to the system as designed.

Another consideration is the dynamic loading on the existing arc-sector model support system generated by the new FOS. The system was designed for static loading only. The dynamic load induces unwanted vibration and may excite natural modes in the system. Modal analyses were performed to determine the natural frequencies and modes of the modified model support system. Figure 4 shows the first 5 modes and their frequencies. As shown, the lowest natural frequency for mode 1 is near 4.55 Hz. This is near the high frequency end of the theoretical oscillation curve shown on Figure 2. Care must be taken to operate the FOS near this high frequency range. Other than that, the modified model support system can accommodate the dynamic frequencies induced by forced oscillation testing.

### **System Description**

Figure 5 shows the new FOS as installed in the 12-Foot LSWT. Figure 6 shows the schematic of the overall system as implemented in the tunnel. As shown, the system may be controlled from the test section or from the control room via a laptop computer. The LabVIEW based PXI real-time controller (RTC) from National Instruments has custom developed software modules that manage the FOS including system safety, communication, operations, and motion control according to user input and system feedback.

The system safety module monitors and controls the 230VAC power to the servo drive system, safety interlocks including control-keyed switches, Emergency Stops, end-of-travel limits (software and hardware), and communications among user interface computers, and RTC controller. The system also monitors safe operations from the existing arc-sector model support system. The communication module connects the RTC with the user interfaces to process user inputs and provides system status. The motion control module executes the positional closed-loop algorithm to track motion profiles as requested by a user. The block diagram in Figure 7 shows how the motion tracking is achieved. As shown, the velocity loop of the motor is internally managed and controlled by the BDS4 servo amplifier. The control algorithm commands the velocity signal based on the error signal generated by the commanded motion profile and the encoder feedback signal. For system verification and validation, a PID algorithm is used. For more complex motion profiles, different control algorithms may be explored in the future.

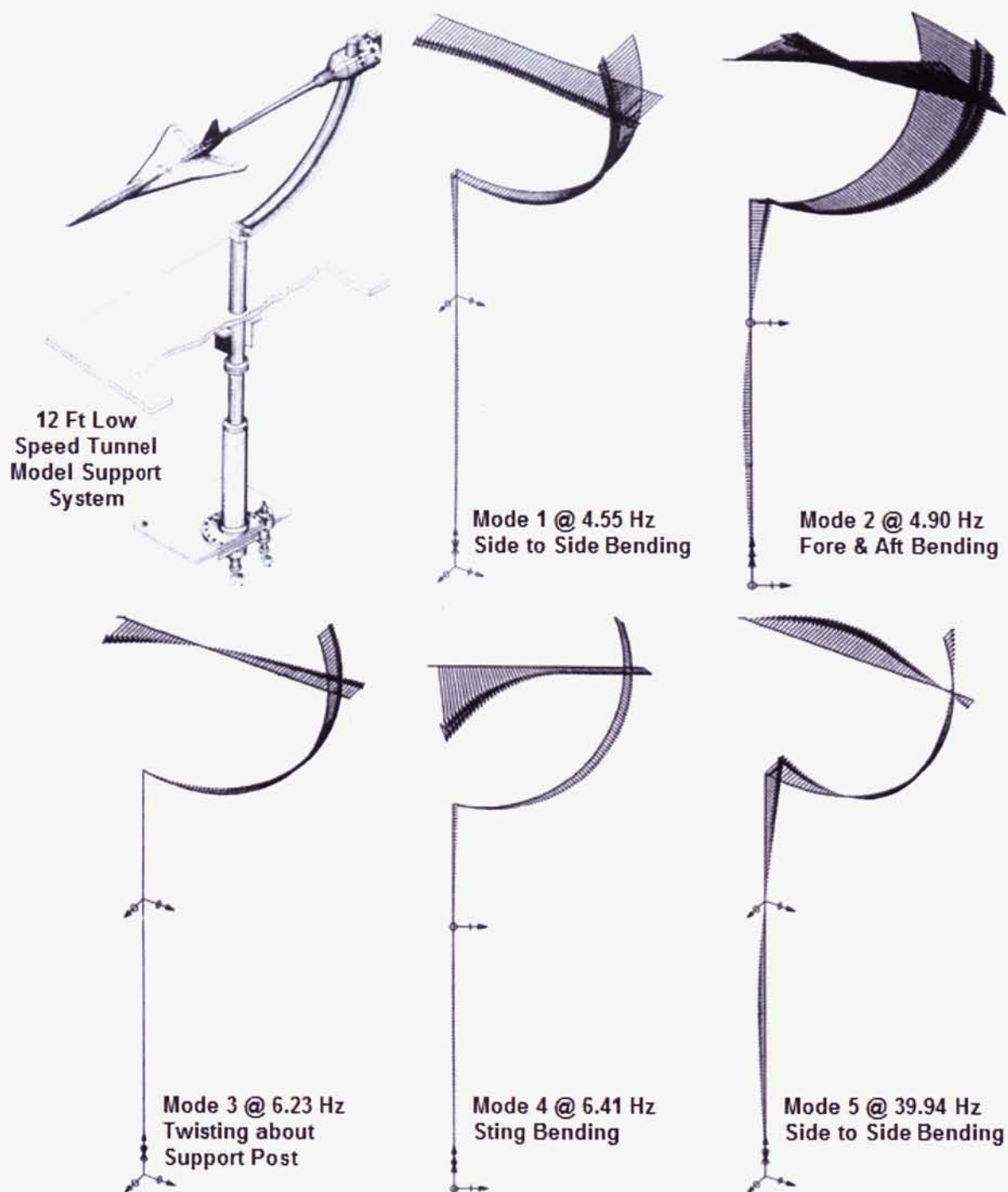


Figure 4. Modal analysis results for the arc-sector model support system



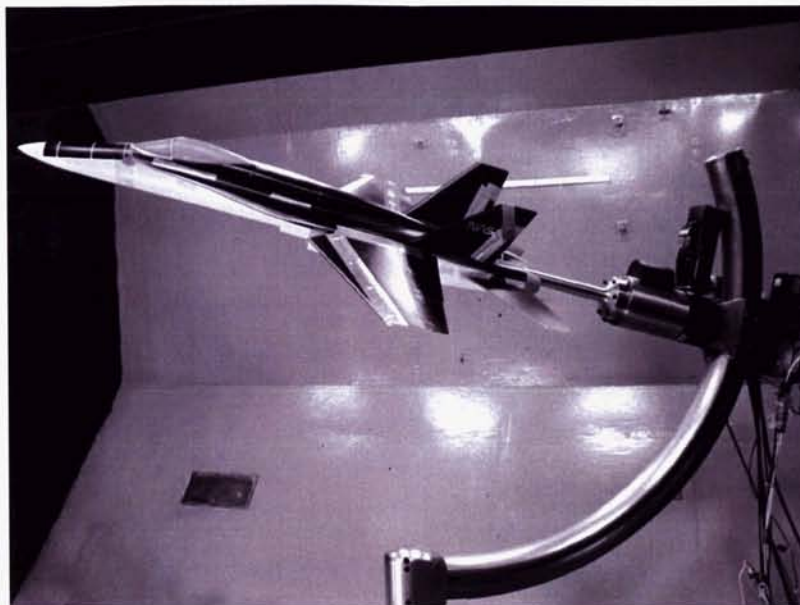


Figure 5. FOS installed in the 12-Foot Low-Speed Wind Tunnel (LSWT)

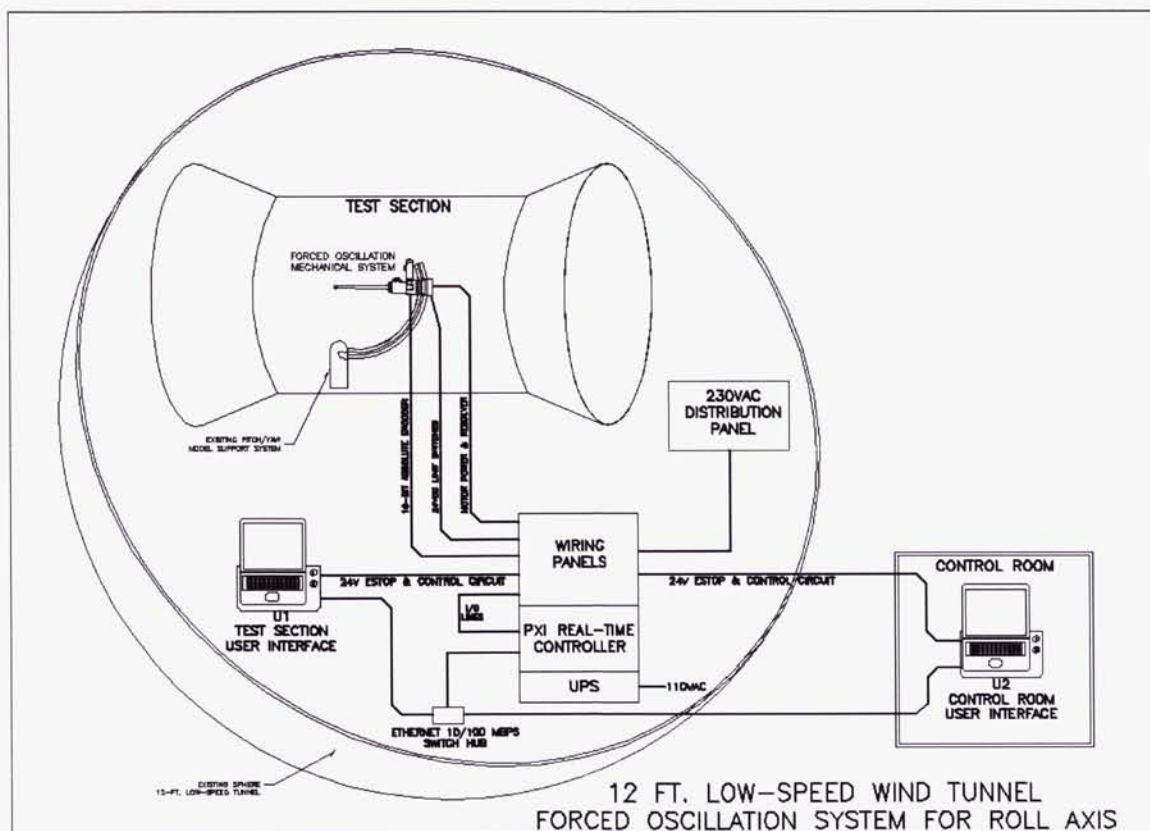
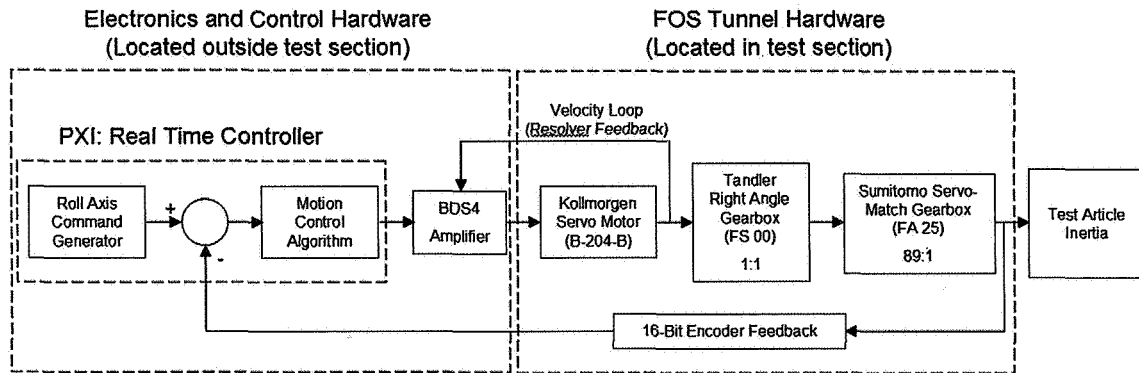
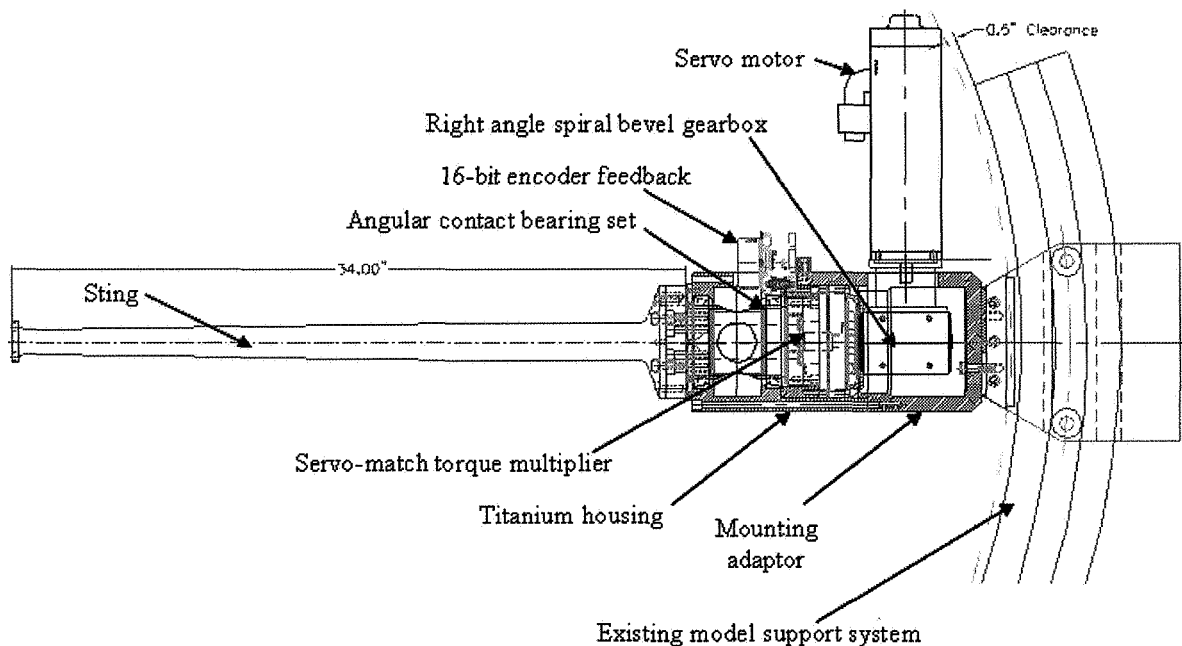


Figure 6. Schematic of the overall FOS in 12-Foot LSWT



**Figure 7. FOS block diagram**

The mechanical subsystem of the new FOS is defined by the hardware located in the test section of the wind tunnel. This subsystem consists of all the drive system components and mounting hardware. Figure 7 shows a FOS block diagram which provides the flow description for all the major components, and Figure 8 shows a cross-section of the mechanical subsystem. The existing arc-sector model support system provides static orientation in pitch and yaw; and the new FOS provides roll attitude and dynamic roll motion control. The FOS is driven by a high performance Kollmorgen servo motor. This servo motor incorporates high energy rare earth neodymium-iron-boron magnets to provide a high torque-to-rotor inertia ratio as well as exceptional continuous torque and peak torque performance. This motor has a peak speed of 3600 RPM with a peak torque of 13.8 N-m and a continuous stall torque of 4.7 N-m.



**Figure 8. Cross-section of the FOS assembly**

Minimizing intrusion to the tail end of the model and potential aerodynamic interference, the overall length of the FOS was shortened by utilizing a right angle drive at the motor interface. Even though this increased the frontal aerodynamic area of the FOS, the motor is still located within the frontal area of the existing model support arc-sector and therefore overall tunnel flow is minimally affected. The right angle drive is a Tandler spiral bevel, low backlash gearbox. The main function of this gearbox is to optimize

packaging. It provides a 1:1 gear ratio. This gearbox was procured with a flanged input interface and a hollow shaft output interface. The flanged input interface provides a bolt-on interface for the motor with misalignments handled by an integrated flex coupling.

The output of the Tandler gearbox drives a Sumitomo Servo-Match Gearbox which is a low-backlash precision cycloid torque multiplier designed for heavy duty industrial robotic applications. The Sumitomo gearbox has a reduction drive ratio of 89:1. The Sumitomo input interface is a hollow shaft of the same diameter of the Tandler gearbox. A precision manufactured shaft with machined keyway provides the drive interface and a precision machined adapter plate provides the housing interface and alignment between the two gearboxes.

A machined drive shaft is coupled to the output half of the Sumitomo drive. The drive shaft is supported by a pair of matched angular-contact ball bearings. The bearing set is sized to react to the cyclic bending, side and axial loads resulting from aerodynamic and oscillatory dynamic forces. The drive shaft with the bearing set effectively decouples the Sumitomo drive from all but rotational loads and provides an interface for sting attachment. A 16-bit encoder measures the rotation of the drive shaft which provides the sting's angular position. It is used in the closed-loop motion control.

All of the mechanical components, except the servo motor are mounted inside a cylindrical, titanium housing. Titanium was chosen for its strength and lightweight properties. The additional weight of the FOS, compared to the weight of the existing model support sting and mounting hardware, decreases the existing model support system model weight capability.

Attaching the FOS to the existing model support system required a rigid interface that could tolerate high side and torsional loading. A tapered dovetail with bolts was chosen for this interface. The existing sting adapter was also modified as shown in Figure 9 to match this same dovetail interface so both the FOS and existing sting can be quickly interchanged for various testing needs. A removal bolt is also designed into the interface to force the tapered dovetail joint apart for FOS and sting removal.

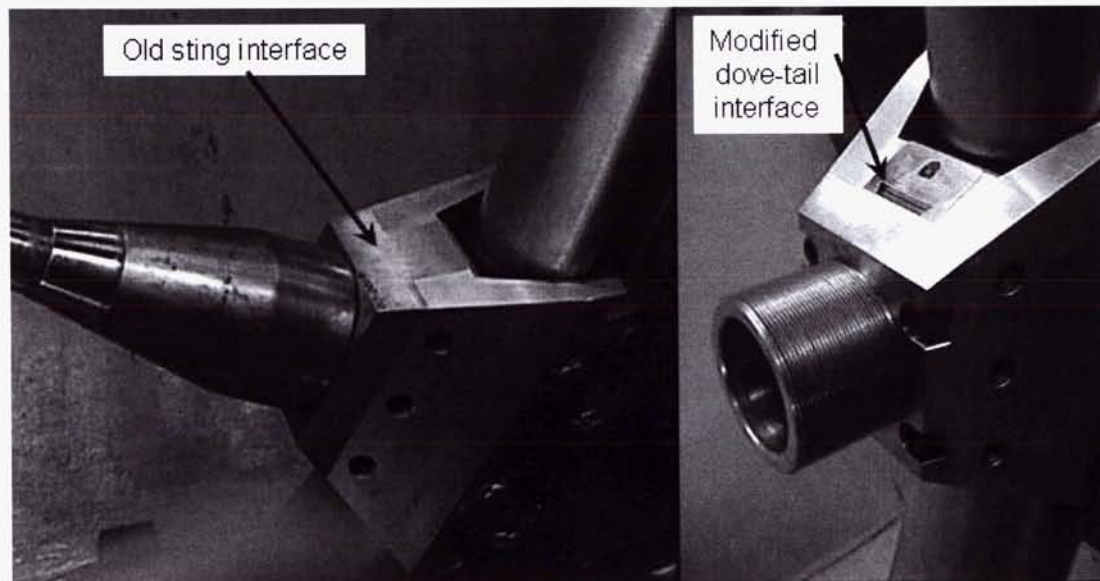


**Figure 9. Comparison of existing to modified sting interface**

The expected system performance for this design for a 200-lb model is shown in Figure 10. By generating and plotting the various performance curves along with the desired theoretical curve from Figure 2, it was determined that the first limiting loading factor for roll oscillation testing is the model support system; and the next factor is due to the load limits of the balance used for measuring aerodynamic loads. The FOS



can conceivably exceed the load capability of the test infrastructure. It should also be observed that the drive system is not limited by its speed but by the maximum motor torque.

Similarly, the expected system performance for a 90-lb model is shown in Figure 11. However, for the much smaller model class, the entire theoretical frequency versus amplitude curve (Figure 2) is achievable. The limiting factor for the system is due to motor speed except at frequency greater than 3.4 Hz, where the limiting factor is the motor torque.

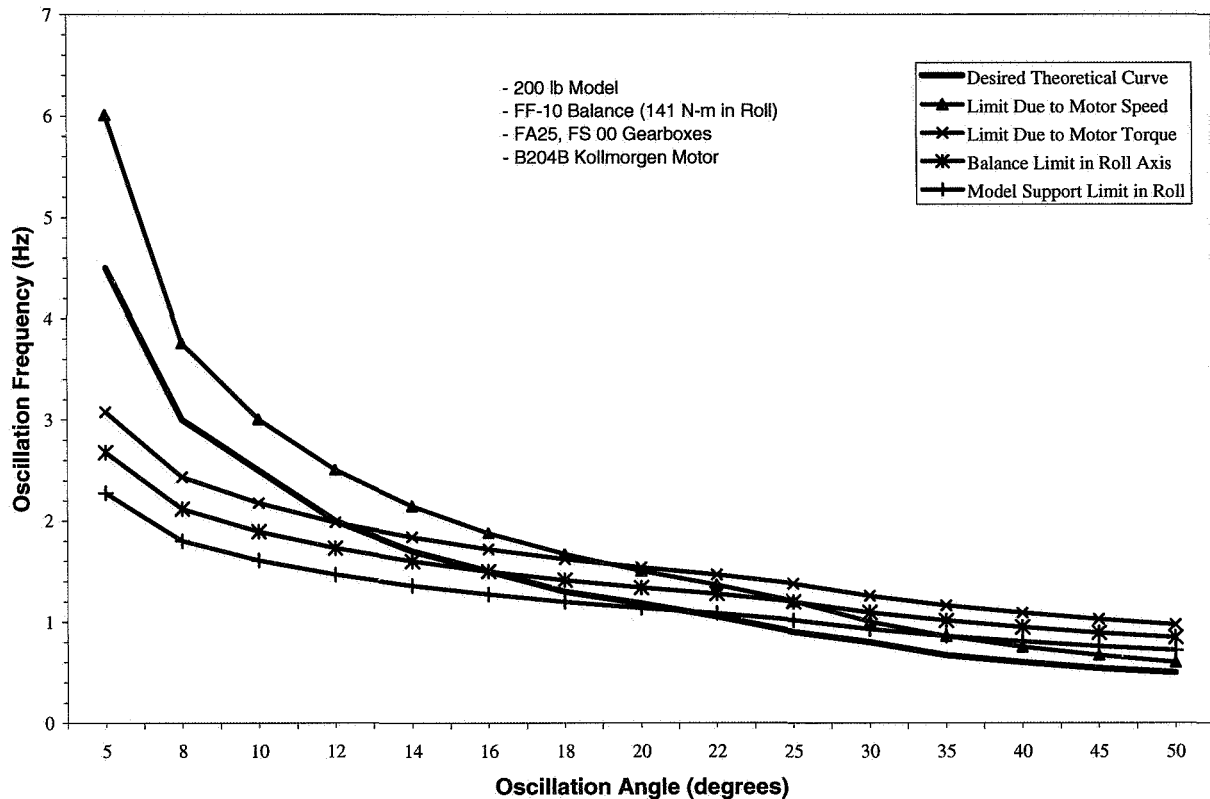


**Figure 10. Predicted performance curve for a 200-lb model**

### System Integration and Testing

System integration testing was done outside the tunnel in a controlled environment by installing inertia bars on the FOS to verify performance under simulated loading conditions. Various runs were made with varying amplitude and frequencies gradually approaching the limitations of the hardware.

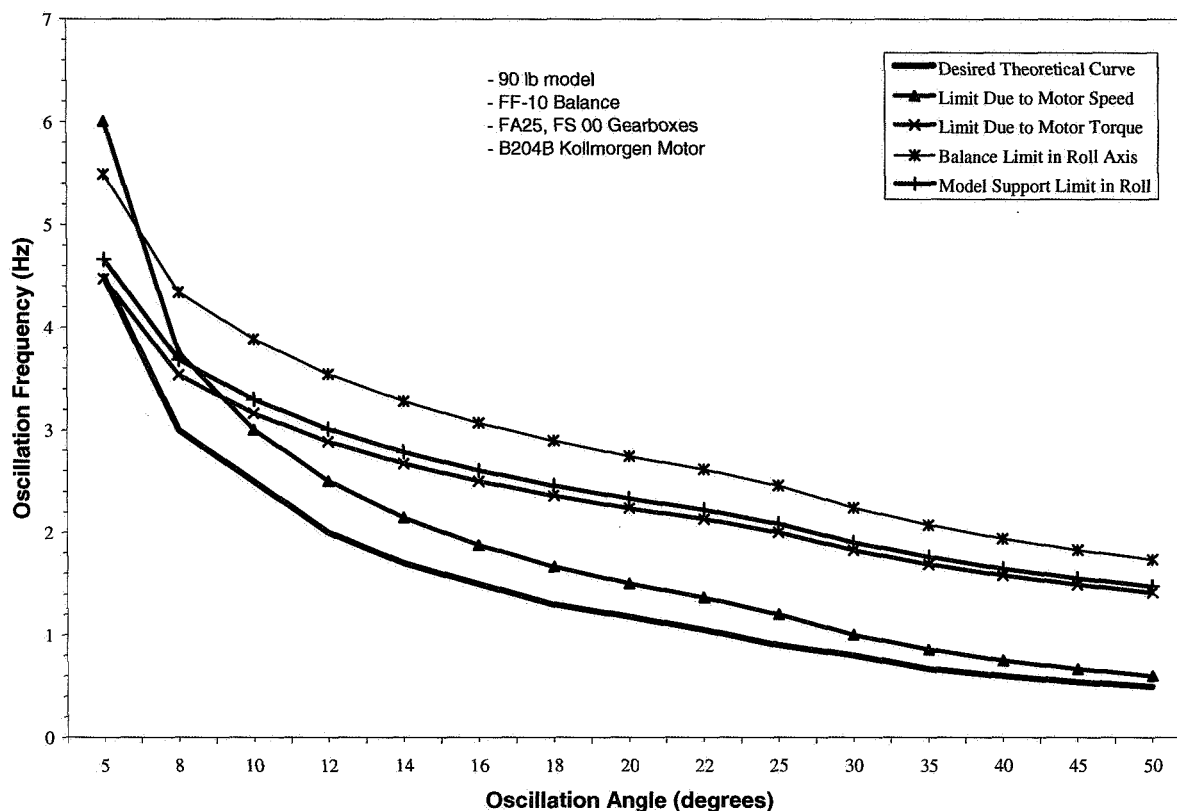


**Figure 11. Predicted performance curve for a 90-lb model**

The hardware ran well at low frequencies and low amplitudes. However, degradation in performance occurred at higher amplitude profiles. As one of the trouble-shooting methods, a torque wrench was used to record the required moment at the motor input interface. The test showed that the torque varied significantly per revolution of motor. A probable cause for the variation is due to an internal alignment problem at one of the drive component interfaces.

To isolate and locate the problem, the mechanical subassembly was disassembled and all the individual components were inspected. No anomalies were discovered and all parts were machined within tolerances as specified. The mechanical drive system was carefully reassembled with emphasis on even and opposite torqueing of all bolt patterns and with careful inspection to assure that no contamination or irregularities were present on the critical interfaces. The reassembled unit was then tested again to determine torque consistency per motor revolution. The subsequent test showed a slightly increased overall torque as compared to the previously lowest measured torque but with almost no variation per revolution.

Once reassembled, verification tests of the FOS demonstrated the expected performance and system safety. Figure 12 shows a response to a sinusoidal command input of 0.5 Hz at 5-degree amplitude. As shown, the system tracked the roll command to within 3 percent of amplitude. Figure 13 shows the encoder output from an excerpt of a Schroeder sweep command input. This demonstrates the new capabilities as envisioned for the new FOS.

Integration and testing have verified system operation and safety. The system still needs to be evaluated to characterize the performance over the full operational envelope. Validation testing with known inertias

is also required, and is underway to confirm system implementation and test techniques. Certification and approval for wind-tunnel operation is being processed currently.

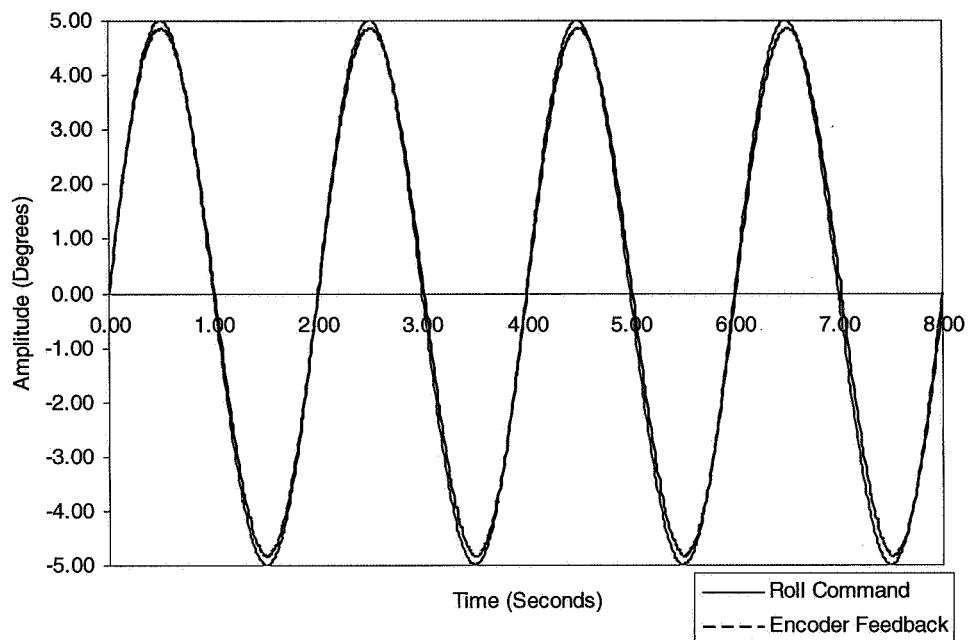


**Figure 12. Typical encoder output signal**

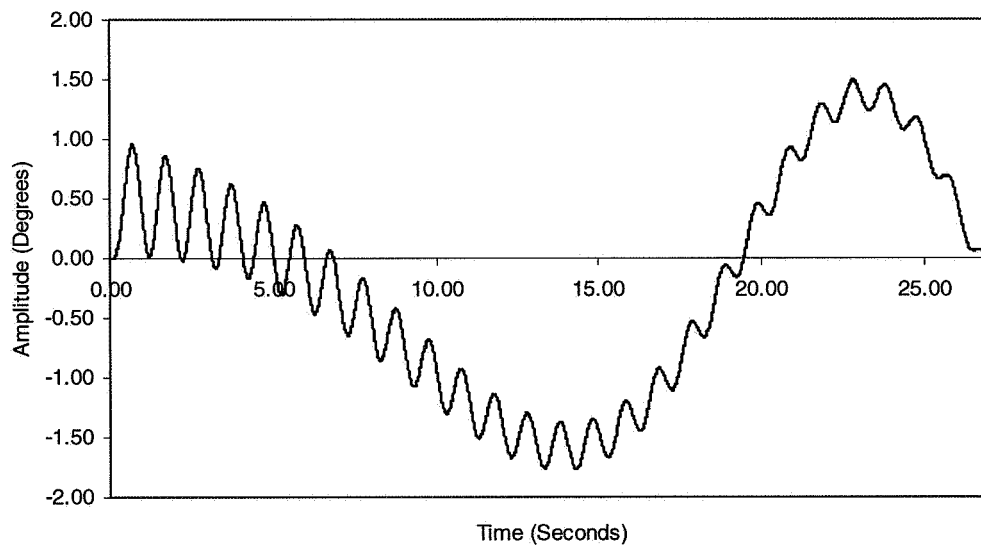


**Figure 13. An excerpt from a Schroeder sweep**



## **Conclusion**

A new Forced Oscillation System (FOS) has been designed and built that will provide new capabilities and flexibility for conducting dynamic derivative studies. The new design is based on a tracking principle where a desired motion profile is achieved via a fast closed-loop positional controller. The motion profile for the tracking system is numerically generated and thus not limited to sinusoidal motion. This approach permits non-traditional profiles such as constant velocity and Schroeder sweeps. Also, the new system permits changes in motion parameters including nominal offset angle, waveform and its associated parameters such as amplitude and frequency. Most importantly, the changes may be made remotely without halting the FOS and the tunnel.

System integration and testing has verified design intent and safe operation. Currently the FOS is being validated for wind-tunnel operations and aerodynamic tests. Once complete, the system is a major enhancement to forced oscillation studies. The productivity gain from the motion profile automation will shorten the testing cycles needed for control surface and aircraft control algorithm development. The new motion capabilities also will serve as a test bed for researchers to study and to potentially improve and/or alter future forced oscillation testing techniques.

## **References**

1. Murphy, Patrick C. "Estimation of Aircraft Unsteady Aerodynamic Parameters from dynamic wind Tunnel Testing", *AIAA 2001-4016*.
2. Etkin, Bernard and Reid, Lloyd D. "Dynamics of flight – Stability and Control", 3<sup>rd</sup> Edition, John Wiley & Son, Inc. 1996.
3. Armstrong, Richard W. "Load to Motor Inertia Mismatch: Unveiling the Truth", Drives and Controls Conference, Telford England, 1998.



REPORT DOCUMENTATION PAGE				Form Approved OMB No. 0704-0188	
<p>The public reporting burden for this collection of information is estimated to average 1 hour per response, including the time for reviewing instructions, searching existing data sources, gathering and maintaining the data needed, and completing and reviewing the collection of information. Send comments regarding this burden estimate or any other aspect of this collection of information, including suggestions for reducing this burden, to Department of Defense, Washington Headquarters Services, Directorate for Information Operations and Reports (0704-0188), 1215 Jefferson Davis Highway, Suite 1204, Arlington, VA 22202-4302. Respondents should be aware that notwithstanding any other provision of law, no person shall be subject to any penalty for failing to comply with a collection of information if it does not display a currently valid OMB control number.</p> <p><b>PLEASE DO NOT RETURN YOUR FORM TO THE ABOVE ADDRESS.</b></p>					
1. REPORT DATE (DD-MM-YYYY) 01- 05 - 2006		2. REPORT TYPE Conference Publication		3. DATES COVERED (From - To)	
4. TITLE AND SUBTITLE 38th Aerospace Mechanisms Symposium			5a. CONTRACT NUMBER		
			5b. GRANT NUMBER		
			5c. PROGRAM ELEMENT NUMBER		
6. AUTHOR(S) Boesiger, Edward A. (Compiler)			5d. PROJECT NUMBER		
			5e. TASK NUMBER		
			5f. WORK UNIT NUMBER 8100310712		
7. PERFORMING ORGANIZATION NAME(S) AND ADDRESS(ES) NASA Langley Research Center Hampton, VA 23681-2199			8. PERFORMING ORGANIZATION REPORT NUMBER  L-19245		
9. SPONSORING/MONITORING AGENCY NAME(S) AND ADDRESS(ES) National Aeronautics and Space Administration Washington, DC 20546-0001			10. SPONSOR/MONITOR'S ACRONYM(S)  NASA		
			11. SPONSOR/MONITOR'S REPORT NUMBER(S) NASA/CP-2006-214290		
12. DISTRIBUTION/AVAILABILITY STATEMENT Unclassified - Unlimited Subject Category 37 Availability: NASA CASI (301) 621-0390					
13. SUPPLEMENTARY NOTES Edward A. Boesiger: Lockheed Martin Space Systems Company, Sunnyvale, California NASA Langley point of contact: James E. Wells An electronic version can be found at <a href="http://ntrs.nasa.gov">http://ntrs.nasa.gov</a>					
14. ABSTRACT  The Aerospace Mechanisms Symposium (AMS) provides a unique forum for those active in the design, production and use of aerospace mechanisms. A major focus is the reporting of problems and solutions associated with the development and flight certification of new mechanisms. Organized by the Mechanisms Education Association, the National Aeronautics and Space Administration and Lockheed Martin Space Systems Company (LMSSC) share the responsibility for hosting the AMS. Now in its 38th symposium, the AMS continues to be well attended, attracting participants from both the U.S. and abroad. The 38th AMS, hosted by the NASA Langley Research Center in Williamsburg, Virginia, was held May 17-19, 2006. During these three days, 34 papers were presented. Topics included gimbals, tribology, actuators, aircraft mechanisms, deployment mechanisms, release mechanisms, and test equipment. Hardware displays during the supplier exhibit gave attendees an opportunity to meet with developers of current and future mechanism components.					
15. SUBJECT TERMS Actuators; Bearings; Deployment; Design; Gimbals; Mechanisms; Release; Test; Tribology					
16. SECURITY CLASSIFICATION OF:			17. LIMITATION OF ABSTRACT	18. NUMBER OF PAGES	19a. NAME OF RESPONSIBLE PERSON
a. REPORT	b. ABSTRACT	c. THIS PAGE			STI Help Desk (email: <a href="mailto:help@sti.nasa.gov">help@sti.nasa.gov</a> )
U	U	U	UU	418	19b. TELEPHONE NUMBER (Include area code) (301) 621-0390